THE LOCALISATION OF EROSIONAL DENUDATION DURING THE GROWTH AND DECAY OF THE PYRENEAN OROGEN

by

Matthew Gibson

Thesis submitted for the degree of Doctor of Philosophy
University of Edinburgh
2004

THE LOCALISATION OF EROSIONAL DENUDATION DURING THE GROWTH AND DECAY OF THE PYRENEAN OROGEN

by

Matthew Gibson

Thesis submitted for the degree of Doctor of Philosophy
University of Edinburgh
2004

Declaration

I declare that this thesis is my own work and of my own composition, and that all other contributions have been dutifully acknowledged and cited.

Abstract

Erosional denudation represents the principal mechanism through which compressional mountains systems are exhumed and is a fundamental parameter in their mechanical and geomorphological development. Exhumation gradients within the central Pyrenean interior have been identified by synchronous periods of exhumation and sedimentation. There is no structural or metamorphic evidence to indicate that tectonic denudation in this region has occurred, hence, the distribution of exhumation was principally controlled through spatially heterogeneous surface erosion. The controlling parameters on the spatial variability of erosion in the Pyrenees and the implications for the developing mountain belt are, to date, poorly understood.

In this study, spatial and temporal gradients in erosion-driven exhumation within the central Pyrenees are quantified and the mechanisms through which they were generated are investigated. To this aim, a multidisciplinary approach is adopted. Low temperature thermochronology (apatite (U-Th)/He, apatite fission track and zircon fission track) is applied to constrain time-temperature histories and to characterise the regional distribution of exhumation during active orogenesis and during the post-orogenic period. Geological field data from the orogenic interior and from adjacent sedimentary basins are used to provide constraints on the tectonic evolution of the area.

Results indicate the history of erosional denudation during and after orogenesis is considerably more complex than previous models envisaged and is governed by a number of discrete physical mechanisms. During active orogenesis, exhumation was controlled by the strongly spatially variable distribution of tectonically-forced rock uplift and the associated control on erosion. During the post-orogenic period, spatial variability in exhumation was maintained, but was principally governed by externally-forced shifts in the evolution and denudation of the south Pyrenean landscape.

Errata

A revised edition of Table 4.2 is located in Appendix II at the back of this thesis. Relevant changes occur in the data columns entitled; '^{238}U (ng)', 'F^t correction (%)', and 'Corrected age (Ma)'. The correction to the data manifests as a systematic increase in the He age.

Revision was necessary owing to the recent identification of an instrument calibration error, which initially occurred prior to the onset of this study. The ^{235}U spike, used as a known value against which the ^{238}U liberated from apatite samples was measured (see Appendix I), was found to have become fractionally diluted from its assumed concentration. This error was not identified for some time because the laboratory standard used, Durango apatite, has a naturally high Th/U ratio and, thus, the small discrepancy in the ^{235}U spike concentration did not measurably alter the He age standards.

The revised data (see Appendix II) and the modified interpretations have been included in a paper submitted for publication in the journal Basin Research, entitled 'Gibson, M., Lynn, G. P. and Sinclair, H. D. (in press) Localisation of erosional denudation: Growth and decay of the Pyrenean orogen'.

Acknowledgements

I would principally like to thank and acknowledge Hugh Sinclair for advice, discussion and direction in every aspect of this work over the duration of the Ph.D. I would also like to extend my sincere gratitude and thanks to Fin Stuart for continued guidance, support and technical instruction.

Thanks also to a variety of people who have at some point assisted, advised or helped in some way; Bet Beamud, Mark Beaumont, Charlotte Cederbom, John Craven, Patience Cowie, Sorcha Diskin, Ray Donelick, Margaret Donelick, Daniel Garcia-Castellanos, Linda Kirstein, Gwilym Lynn, Josep Anton Muñoz, Ann Menim, Mark Naylor, Paul O'Sullivan, Cristina Persano, John Underhill, Stewart Jamieson, Jaume Vergés, Nicola White.

This research was funded through a NERC PhD studentship (NER/S/A2000/03351).

Contents

Page

Chapter One: Introduction 1

Chapter 1

Introduction

Objectives: The primary objectives of this chapter are to discuss the research motivation driving the study, to outline the specific scientific objectives and to summarise how the work is presented.

Chapter 1 – Introduction

1.1 Research motivation

Erosional denudation is a fundamental parameter in the mechanical and geomorphological development of evolving compressional mountain belts (Ring et al., 1999; Schlunegger and Willettt, 1999; Willettt, 1999; Beaumont et al., 2001). It represents the outward flux of mass from the orogenic system, via mechanical and chemical surficial processes, and is the principal mechanism through which mountain systems are exhumed (Ring et al., 1999; Willettt, 1999). The importance of the role of surface processes in orogenesis is exemplified by recent studies which indicate that the spatial variability of erosion may govern the distribution and style of orogen-scale tectonic deformation, due to the modification of gravitationally-induced stresses, and exert the principal control over the gross geomorphic nature of mountain belts (Beaumont et al., 1991; Avouac and Burov, 1996; Willettt, 1999; Willettt et al., 2001; Reiners et al., 2004).

The recent increase in the application of low temperature thermochronometers, however, has demonstrated that the long-term erosional history of mountain systems is significantly more complex than early models predicted (e.g. Morris et al., 1998). Preserved exhumation gradients within orogenic interiors, commonly identified by abrupt discontinuities in isotopic cooling ages, have been interpreted to represent strongly heterogeneous spatial distributions of surface erosion (e.g. Kamp et al., 1992; Seward and Mancktelow, 1994; Wobus et al., 2003; Foeken et al., 2003). Constraining such exhumation gradients, and understanding the associated mechanisms through which surface erosion was localised or accelerated within specific spatial or temporal domains, is a fundamental requirement for understanding mass flux within orogenic systems and for constructing viable geodynamical models of the evolution of a given mountain belt.

The Pyrenees is an asymmetric, doubly-convergent orogen formed through Mesozoic and Cenozoic collision between the Afro-Iberian and Eurasian plates. The history of shortening and deformation have been well constrained within the fold and thrust belts to the north and south of the mountain belt and have been used to infer stages of growth in the adjacent orogen (e.g. Puigdefábregas et al., 1992; Vergés et al., 1992; Vergés et al., 1995; Meigs and Burbank, 1997). The modern-day macro-structure of the interior of the range has been well-documented and a number of geodynamical models have been proposed to explain the tectonic evolution which culminated in the present structural geometry (e.g. Muñoz, 1992; Puigdefábregas et al., 1992; Beaumont et al., 2000). However, owing to the inherently difficult nature of investigating the history of eroded terrains, there remains a significant lack of constraints on the manner in which the internal parts of the orogen evolved. Previous fission track studies have estimated that within the south central region of the orogenic interior up to 15 km of crust was removed during a period of rapid exhumation during Late Palaeogene times (Fitzgerald et al., 1999). Balanced geological cross-sections and restorations likewise infer significant mass removal (15-20 km) from the central Axial Zone during this period of growth (Muñoz, 1992; Vergés et al., 1995). This time interval, however, also correlates with the accumulation of a thick sequence of largely undeformed synorogenic conglomerates that onlap the orogenic interior less than 12 km to the south (Mellere, 1992; Beamud et al., 2003). The synchroneity of unroofing and sedimentation within such a limited spatial domain defines a large magnitude exhumation gradient within the evolving orogen. As there is no structural or metamorphic evidence to indicate tectonic denudation of the central Pyrenees occurred, exhumation must have been principally driven through processes of erosional denudation. Neither the mechanisms through which such gradients in erosional denudation were generated, nor the tectonic implications for the developing mountain belt, have been investigated within the Pyrenees.

1.2 Thesis objectives – A multidisciplinary approach

The principal scientific objectives of this work can be outlined, as follows;

(1) to document the spatial and temporal distribution of exhumation gradients across the central and southern Pyrenees during active orogenesis and during the post-orogenic period;

(2) to investigate the mechanisms through which the distribution of exhumation was spatially and temporally controlled during these intervals, and;

(3) to consider the inherent implications for existing geodynamical models of Pyrenean growth, evolution and decay.

In order to achieve these objectives, a multidisciplinary approach has been adopted. A range of low temperature thermochronometers (apatite (U-Th)/He, apatite fission track and zircon fission track) are applied to constrain the time-temperature histories of a number of granitic massifs and volcanic provinces within the central and southern Pyrenees. This data is used to identify and characterise temporal and spatial gradients in exhumation preserved within the bedrock geology. Field data from the major tectonic contacts surrounding the sampling sites and from the adjacent sedimentary basins is used to provide constraints on the tectonic evolution of the region. The exhumational record and the geological data are then synthesised to develop an understanding of the specific mechanisms that may have controlled the spatial and temporal distribution of erosional denudation during the growth and decay of the Pyrenean orogen.

This integrated study represents a unique approach to investigating the development of the Pyrenean orogenic interior. The application of a number of thermochronometers, comprising a range of temperature sensitivities, allows the documentation of long-term cooling histories and potentially enables the transition between deep-level exhumation processes and those operating in the near-surface realm to be fully bridged. The use of vertical-profile sampling strategies, additionally provides a means to detect subtle changes in the derived erosional histories over relatively short temporal intervals. Combined with the constraint of geological field data, this study allows different components of the Pyrenean system to be evaluated within a single, holistic and coherent study.

1.3 Thesis structure

Following this introduction, Chapter 2 provides a review of the relevant published data and interpretations pertaining to the evolution of the central Pyrenean orogen. This chapter places the present study into a scientific context and provides an archive of reference material for the reader. The chapter is subdivided into four main sections; (2.1) 'An historical perspective', places the present study in the context of previous Pyrenean research, (2.2) 'Geological setting', provides a summation of the tectonic, structural and stratigraphic research on central Pyrenean evolution, (2.3) 'Models of orogenic evolution', reviews the geodynamical and numerical modelling of the Pyrenees, and (2.4) 'Thermochronological studies in the Pyrenees', summarises the high and low temperature thermochronlogical data and interpretations from the region.

Chapter 3 provides a review of the principles and applications of low temperature thermochronology and outlines the specific methodology used in this study. The inclusion of this extended summary is intended to supply the reader with a thorough background in the way in which thermochronological data is processed and to provide a rationale for the techniques later applied. This chapter is subdivided into five sections. The first two sections, (3.1) 'Principles of (U-Th)/He thermochronology' and (3.2) 'Principles of fission track thermochronology', summarise the theory upon which the techniques are based and addresses the relative merits and limitations of both systems. The subsequent two sections, (3.3) 'Thermal modelling' and (3.4) 'Denudation histories', review the procedures for deriving information on exhumation from isotopic ages and time-temperature evolutions. The final section, (3.5) 'Application of thermochronology to Pyrenean orogenesis', documents the procedures and assumptions applied in this thesis.

In Chapter 4 the thermochronological datasets and thermal modelling results are presented and the interpreted exhumation histories discussed. In the first two sub-sections, (4.1) 'Sampling strategy' and (4.2) 'Apatite chemistry and mineralogy', the sample profiles and localities are outlined and the geochemical data from the rocks are reviewed. The two subsequent sections, (4.3) 'Fission track results' and (4.4) 'AFTSolve thermal modelling', contain the apatite/zircon fission track data and modelling solutions, and are followed by (4.5) 'AHe results' and (4.6) 'AFT-AHe integrated-thermal modelling', in which the apatite He data and modelling solutions are presented. The thermal histories derived from the data are outlined in (4.7) 'Time-temperature evolutions', and the interpreted histories are then modelled in (4.8) 'PeCube modelling'. In the two final sections, (4.9) 'Pyrenean exhumation' and (4.10) 'Localised erosional denudation', the link between the derived thermal histories and the distribution of erosional denudation is discussed.

In Chapter 5, new geological field data from the central Pyrenees is presented and compiled with existing data from the region and from sedimentary basins adjacent to the Pyrenees. The primary goal of this chapter is to provide constraints on the tectonic evolution of the regions from which the thermochronological samples were taken. The five geographical regions, (5.1) 'North Maladeta Zone', (5.2) 'South Maladeta Zone', (5.3) 'Nogueres Zone', (5.4) 'Morreres Zone' and (5.5) 'Ebro Basin and offshore Zone', are discussed in detail from north to south. For each region a review of the published work is outlined, followed by the presentation of field data from this study and a brief interpretative summary.

In Chapter 6, the exhumation histories and the geological field data are synthesised and used to constrain large-scale models of the evolution of the central Pyrenees. The history of orogenic growth and decay is partitioned into three discrete sections and discussed at length. Potential ambiguities and weaknesses in the interpretations are considered and the route for future research is suggested.

In Chapter 7, the wider implications of this work are considered and the major conclusions from this thesis are reviewed and summarised.

Chapter 2

Geological review

Objectives: The objectives of this chapter are to present a broad review of the published research that is relevant toward understanding the orogenic evolution and exhumational history of the central Pyrenees. This will be used as an archive of reference material and to provide a geological context and scientific basis for this thesis.

Chapter 2 – Geological review

The Pyrenean orogen extends over 1500 km, from Provence in southern France to the Cantabrian platform in northern Spain, and separates the Iberian peninsula from the rest of the European continent (**Fig. 2.1**). The range forms a linear, east-west trending drainage divide and defines a strong orographic transition from the relatively precipitous northern flank to the semi-arid southern flank. This zone of extreme topographic relief was recognized by 19th century geologists as representing an Alpine-age collisional belt, despite showing no obvious structural continuity with the Alpine Mediterranean orogen further to the east.

A large volume of literature has been published covering the structural, stratigraphic and tectonic development of the central Pyrenean range. The compact and relatively uncomplicated nature of the mountain belt, and the excellent exposure afforded at the present erosional level, has resulted in the area being intensively studied and promoted as a simple comparative model for more complex collisional systems. This chapter begins with a brief review of this published literature over the last century, from which the current work can be placed in the appropriate historical context (Section 2.1). This is followed by summaries of the Iberian tectonic setting and of the major litho-stratigraphic and structural elements of the orogen. Emphasis is placed only on the previous work which provides the necessary geological background, or holds direct relevance, for this study (Section 2.2). Crustal-scale geological and numerical models of the orogen are reviewed, discussed and their implications considered (Section 2.3). Likewise, previous exhumation studies are evaluated and the interpretations from these studies, regarding issues such as orogenic mass flux and erosional denudation, are briefly discussed (Section 2.4).

2.1 An historical perspective

In 1903 a six-volume treatise of geological interpretations of the Pyrenees was published (Carez, 1903) and initiated a long history of geological investigation. Early work by Dalloni (e.g. Dalloni 1910; Dalloni, 1913) represented pioneering work in understanding and documenting the development of orogenic compressional regimes. Until the early 1950's, however, much of the published literature concentrated primarily on the sedimentary geology of the Mesozoic lithologies. Subsequent work from the late 1950's to the early 1970's, pioneered by Dutch and French-Spanish collaborations (e.g. De Sitter & Zwart, 1962;

Zwart, 1979; Séguret, 1970), promoted the re-mapping and intensive documentation of much of the Palaeozoic interior of the Axial Zone (Fig. 2.1) and enabled advanced interpretations of the tectonic evolution of the mountain belt to be proposed.

Numerous crustal models were published for the central Pyrenees during the mid 1980's offering a variety of crustal geometries and pre-orogenic structural configurations (e.g. Williams, 1985; McCaig, 1986). However, the proposed models remained invariably speculative owing to the lack of geophysical data from the orogen. In 1989, a 250 km long, deep seismic survey across the central core of the orogen, from the Aquitaine basin to the Ebro basin, was published as part of the ECORS study (Etude Continentale et Oceanique par Reflexion et Refreaction Seismique; Roure et al. 1989). This seismic profile provided the necessary constraints to enable Pyrenean workers to resolve deep-crustal geometries and proffer a number of contrasting balanced solutions (e.g. Roure et al. 1989; Choukroune, 1989; Muñoz, 1992,). These crustal sections, generated for the central Pyrenees, have provided a rigid structural framework from which absolute crustal shortening values and mass balance calculations have been proposed (e.g. Muñoz, 1992), and upon which crustal sections for the eastern and western Pyrenees have been based (e.g. Vergés et al., 1995).

The last decade of central Pyrenean research has seen a large commitment toward reconstructing the progressive structural and sedimentological evolution of the excellently-exposed South Pyrenean- and North Pyrenean Thrust Belts (SPTB and NPTB, respectively) (Fig. 2.1). The application of seismic reflection and borehole data to delineate geological structures and strata has become an increasingly important technique in this field of study (e.g. Vergés, 1993; Sans et al., 1996). In addition, the readily-dateable, syn-orogenic molasse which drapes many of the major structures have been used to provide rigid time constraints on the Tertiary tectonic activity (e.g. Holl and Anastasio, 1993; Hardy and Poblet, 1994; Meigs, 1997). This alliance of well-constrained surface exposure combined with an impressive network of seismic profiles and borehole data, has promoted the fold and thrust belts as a test-bed for structural geology and thrust wedge theory and associated models of orogenic development (e.g. Meigs and Burbank, 1997; Puigdefàbregas et al., 1992).

Recent years have witnessed a universal surge of interest from the tectonic geo-science community toward achieving a more holistic understanding of orogenic growth and mass flux. The interplay of the controls on the growth of orogens, and particularly the role of exhumation, erosion, climate and the implications for landscape evolution, have been intensively explored through theoretical modelling and case studies (e.g. Tippet and Kamp, 1993; Willett et al., 1993; Avouac and Burov, 1996; Ellis et al., 1999; Schlunegger and

Willett, 1999). In addition, significant advances have been made toward demonstrating the applicability of Critical Couloumb wedge models to the predictibility of orogenic evolution (e.g. Davis et al., 1983; Dahlen, 1984; Lawton et al., 1994; Bombalakis, 1994; DeCelles and Mitra, 1995). Following this mode of investigation a number of workers have begun to attempt to characterise the long-term evolution of the Pyrenean orogen and to reconsider the interplay and feedbacks between tectonics, surface processes and mass flux on the mountain belt scale. This has required a progressively more integrated approach and has been attempted through the documentation of orogenic mass flux, principally through the application of low-temperature thermochronology, combined with structural geology and sedimentology (e.g. Morris et al., 1998; Fitzgerald et al., 1999) and through geodynamical numerical modelling (e.g. Chery et al., 1991; Beaumont et al, 2000).

2.2 Geologic setting

Inherent in achieving an understanding of the mechanical development of the mountain belt and the implications for exhumation processes is the need to place the modern-day setting into a rigid tectonic and geological framework. In this section the regional plate kinematic and tectonic history is reviewed and a generalised pre-Alpine lithostratigraphy for the central Pyrenees is considered. A focus is placed, however, on the major Alpine morphotectonic units and macro-structural geometries across the ECORS line as it is this which holds greatest relevance for this study.

2.2.1 Tectonic history

The present-day configuration of the major morphtectonic units of the Iberian peninsular (Pyrenees, Betic Cordillera, Iberian Range, Catalan Coastal Range, etc.) reflect a 300 Myr history of relative movements and interactions between the Iberian, European and African plates. As plate rotation, divergence and convergence replaced each other as the dominant tectonic forcing, the major orogenic and basinal settings continued to evolve. The interpretation of magnetic anomalies and tectonic lineations has enabled the production of detailed plate kinematic models and the reconstruction of the complex tectono-sedimentary basin development.

The Mesozoic history of the Pyrenees reflects the initiation of sea-floor spreading in the central North Atlantic, Bay of Biscay, and the anticlockwise rotation of the Iberian plate and it's related wrenching in the North Pyrenean fault zone (Puigdefàbregas and Souquet, 1986). During the Tertiary, the tectonic history is largely dominated by a strong N-S compressional regime in which major deformation occurred at the Iberian plate margins (**Fig. 2.2**). This protracted history can be divided into three evolutionary stages in geological time: (i) Stephanian to Valanginian, (ii) Valanginian to Santonian and (iii) Santonian to mid Miocene.

2.2.1.1 Stage One – Stephanian to Valanginian

An initial stage of sinistral strike-slip movement (Lucas, 1985) along inherited, E-W, NE-SW and NW-SE oriented fractures, evolved into a dominantly transtensional and extensional setting during late Stephanian and Permian (304-255 Ma). This period is documented by a sequence of correlative volcanics, ranging from andesite-rhyolite to basalts, and corresponding sedimentation of alluvial fan deposits, red mudstones, local slope breccias and abundant volcaniclastics in small, asymmetric, fault-bounded basins (Puigdefàbregas and Souquet, 1986; Besly and Collinson, 1991).

Generalised extension was maintained during the Triassic leading to basin widening and the development of widespread braided fluvial systems grading into lagoonal deposits and accompanied by the widespread extrusion of basaltic 'ophites' (Boillet, 1984; Curnelle, 1989; Puigdefàbregas and Souquet, 1986).

NE-SW faults controlled carbonate shallow marine sedimentation during the Liassic, and persisted throughout the lower and middle Jurassic (205-170 Ma) as widespread platform conditions prevailed (Puigdefàbregas and Souquet, 1986). Continued extension resulted in the fragmentation of the existing Hercynian basement and initiated the intracontinental Aquitaine basin (Pinet et al., 1987), though is regarded to precede the major rifting associated with the opening of the central Atlantic.

2.2.1.2 Stage Two - Valanginian to Santonian

Recent palaeomagnetic data from the Algarve indicates that during the Barremian (127-121 Ma) the Iberia microplate accomplished a significant rotation with respect to the European plate (Moreau et al., 1997). Moreau et al. (1997) suggest this rotation event was contemporaneous with other tectonic events occurring in the western Tethyan realm and occurred whilst Iberia was acting as an independent plate between Africa and Eurasia. After this period of rapid rotation, Iberia likely followed Africa in its eastward trajectory and continued moderate, small amplitude rotations with respect to both the Eurasian and African plates (Moreau et al., 1997).

Iberian rotation may have been promoted through the rifting of the northern continental margin of the Bay of Biscay and between the Grand Banks and Portugal. However, this period of continental breakup and associated crustal thinning commenced in earnest during the Aptian (121 Ma) (Masson and Miles, 1984; Pinet et al., 1987). This northward extension of the Atlantic spreading centre caused a major reorganisation of regional plate kinematics and likely resulted in the reactivation of normal faults as strike-slip faults and the development of flower structures. The opening of the Bay of Biscay ensured that net plate motions were transtensional, despite being dominated by sinistal kinematics associated with the opening of the spreading central Atlantic (Vincent, 1993).

This transitional period toward a more transtensional tectonic regime is characterised by discontinuous sedimentation and localised erosion. Rapid subsidence occurred in a number of sub-basins (e.g. The Parentis, Adour and East-Central Pyrenean basins; Puigdefàbregas and Souquet, 1986) though overall sedimentation rates remained low. N-S extension with associated NNW-SSE transtension resulted in NW-SE trending rhombic sub-basins separated by intermediate thresholds. These sub-basins are filled with marginal Urgonian carbonates onlapping a discontinuous bauxite fringe (Peybernes and Souquet, 1984: Puigdefàbregas and Souquet, 1986). By middle Albian times (~110 Ma), sinistral wrenching along the North Pyrenean Fault Zone (NPFZ), between the Iberian and European plates, produced large strike-slip troughs and transtensional flysch basins. Global sea-level rise, during the Cenomanian transgression (98-93 Ma), promoted basin widening and the associated deposition of shelfal and turbiditic carbonates (Peybernes and Souquet, 1984; Puigdefàbregas and Souquet, 1986). Strike-slip deformation within the thinned crust of the NPFZ resulted in the emplacement of lower crustal granulites and upper mantle ultrabasic rocks (Vielzeuf and Kornprobst, 1984).

2.2.1.3 Stage Three – Santonian to mid Miocene

With the continued, albeit reduced, anticlockwise rotation of Iberia relative to Eurasia, the dominantly sinistral transtentional relationship was progressively augmented with compressional deformation in the Pyrenean zone, increasing in intensity from west to east (Roest and Srivastava, 1991). Srivastava et al. (1990) suggest this period of NE-SW compression during Upper Cretaceous times was consistent with the early phase of deformation in the Pyrenees and with the North Pyrenean Fault representing the boundary between Iberia and Eurasia (Srivastava et al., 1990; Roest and Srivastava, 1991).

Displacement of the African plate relative to the European plate during Palaeocene and early Eocene times is regarded to have been largely N-S oriented with subduction of oceanic crust accommodating the principle shortening (Sanz de Galdeano, 1996; Smith, 1996). Compressional deformation across the Pyrenees until the Bartonian (41 Ma) was relatively small and contemporaneous with some translational movement along the North Pyrenean Fault (Roest and Srivastava, 1991). Roest and Srivastava propose that the plate boundary shifted to the south during the upper Eocene (~37 Ma) and, when combined with contemporaneous extension in the King's Trough to the west, heralded the onset of up to 100 km of N-S compression across the Pyrenees. The transmission of deformation across the entire Iberian plate, resulting in limited subduction of oceanic crust in the Bay of Biscay and strong compression in the Pyrenean chain, is attributed to the continued northward trajectory of the African plate (Boillet, 1984; Sanz de Galdeano, 1996). This proposed second wave of compressional tectonics, initiating in Late Eocene times and maintained to Early Miocene times, is supported by the second phase of Pyrenean folding (Mattauer and Henry, 1974; Roest and Srivastava, 1991). This transition to purely plate convergence conditions heralds the onset of macro-thrust sheet transport and the emergence of the inner part of the Pyrenean chain (Puigdefàbregas and Souquet, 1986). The progressive migration of the Ebro-foreland basin toward the south (Sanz de Galdeano, 1996) is also testament to the continued deformation and growth of the orogenic mass.

Srivastava et al. (1990) propose that by early Miocene times (~20 Ma) Iberia had begun to move as part of the Eurasian plate, with its southern boundary along the Azores-Gibraltar fracture zone. This is considerably later than the youngest age-constrained compressive deformation in the Pyrenean fold and thrust belt (~26 Ma) (Meigs et al., 1996; Meigs, 1997) and in the Iberian and Catalan Coastal Range (Guimera, 1984).

2.2.2 Major structural elements

The central Pyrenees can be broadly categorised into four major structural units, as defined by their deformational state and the lithostratigraphic units of which they are comprised (**Fig. 2.1**). In a N-S transect from the northern deformation front in the Aquitaine Foreland Basin to the southern Ebro Foreland Basin, broadly congruent with the ECORS profile, the four elements are (i) The North Pyrenean Thrust Belt (NPTB), (ii) The North Pyrenean Fault Zone (NPFZ), (iii) The Axial Zone, and (iv) The South Pyrenean Thrust Belt (SPTB).

The major structural geometries have been constrained through numerous field studies across the orogen and further refined using subsurface data from the ECORS deep seismic profile (e.g. Séguret, 1964; Zwart, 1979; Fischer, 1984; Perbernes and Souquet, 1984; Vielzeuf and Kornprobst, 1984; Williams, 1985; McClelland and McCaig, 1989; Choukroune, 1989).

2.2.2.1 The North Pyreanean Thrust Belt

The NPTB is structurally located between the Aquitaine foreland basin and the subvertical North Pyrenean Fault Zone, to the north and the south respectively (**Fig. 2.3 & 2.4**). It consists of folded and northward imbricated thrusts involving Mesozoic sediments with local windows into the Hercynian-age basement culminations (Barousse, Milhas, Trois Seigneurs, Arize and St. Barthelemy Massifs) (Fischer, 1994). The Upper Cretaceous flysch series (Coniacian to Maastrictian) unconformably overlies the basement and exhibits a non-metamorphic and weakly deformed character (Muñoz, 1992).

The Trois Seigneurs Massif and its' unconformable strata share a sub-vertical south-vergent thrust contact with the heavily deformed Mesozoic metamorphic terrane to the south at the NPFZ (Vielzeuf and Kornprobst, 1984). The Arize culmination, immediately to the north, is observed in cross-section to overthrust Upper Cretaceous turbidites at both its northern and southern extremes, defining a basement pop-up structure. The allochthoneity of this unit, as proposed in early work by Fischer (1984), has since been further constrained through the seismic imaging of Lower Cretacous turbiditic series directly beneath the overthrust massif (Choukroune et al., 1989). Similarly, the St. Barthelemy massif to the east is structurally situated in the hangingwall of the same north-vergent thrust (Fischer, 1984; Deramond et al., 1993). Choukroune et al. (1989) suggest the basement massifs were bound by Albian-age normal faults which have been significantly reactivated during later compressional events (Choukroune et al., 1989; Desegaulx et al., 1990).

Northward, the Camarade basin, bound by the overthrusting Arize massif and by the North Pyrenean Frontal Thrust , contains folded Lower Cretaceous (Albian to Cenomanian) flysch series. The frontal thrust delineates the northern extreme of emergent thrust surfaces in the region, though foreland-vergent anticlines in the Mesozoic to middle Eocene strata to the north are likely associated with frontal duplex systems on blind frontal thrusts (Peybernes and Souquet, 1984; Desegaulx et al., 1990).

Through the application of sequence stratigraphical analysis, Deramond et al. (1993) suggested shortening within the NPTB occurred primarily during Cretaceous times. However, the deformation of the Eocene Poudingue de Palassou formation, with overlying and undeformed Oligocene molasse drapes, indicates activity at the deformation front, north of the emergent frontal thrust, to have continued until approximately the Eocene-Oligocene boundary (33.7 Ma). In addition, AFT cooling ages of 38.2, 33.7, and 39.8 Ma from the Arize and Trois Seigneur Massifs, suggest exhumation of the basement massifs occurred into the upper Eocene (Morris et al., 1998). Both the frontal deformation and the late-stage exhumation of the internal massifs are likely associated with continued activity along the blind Sub-Pyrenean frontal thrust, the sole thrust into which NPTB structures detach at depth.

2.2.2.2 The North Pyrenean Fault Zone

The NPFZ is a striking E-W linear feature that delineates the northern boundary of the Pyrenean Axial Zone (Fig. 2.1). It is characterised by a narrow belt of anastomosing faults which juxtapose Jurassic and lower Cretaceous metamorphics against lower crustal granulites and upper mantle lherzolites (Vielzeuf and Kornprobst, 1984; Muñoz, 1992).

The North Pyrenean Fault developed during the sinistral displacement of Iberia on the already thinned Middle Cretaceous continental crust. Emplacement of lower crustal and upper mantle lithologies is associated with syn-rift thermal upwelling and alternating tensional and compressional stresses in the subsequent transcurrent fault zone (Vielzeuf and Kornprobst, 1984). High temperature-low pressure metamorphism, associated with high heat flow values during crustal thinning, developed synchronously or immediately after the formation of Albian-Cenomanian flysch pull-apart basins. Dating of both metamorphic and magmatic minerals from the NPFZ yields ages of mid-Albian to mid-Coniacian age (Montigny et al., 1986; Goldberg et al., 1986).

Seismic refraction and teleseismic data indicate the Moho discontinuity is offset vertically approximately 15 km beneath the NPFZ (Choukroune et al, 1989). Differential thickening of the Iberian crust, compared to the pre-collisional thinning of the European crust, is a likely explanation for this observed Moho step (Choukroune et al., 1989; Roure et al., 1989; Muñoz, 1992; Casas et al., 1997). Based on this, the NPFZ was considered to represent the axis or suture zone of the mountain belt and thereby define a boundary which separates material accreted from opposing underthrust plates (Choukroune, 1976; Morris, 1998). Plunge variations in subhorizontal stretching lineations within the NPFZ are noted by Fischer (1984) to closely relate to the position of lateral/oblique walls and thrust flats in the

North Pyrenean Thrust belt. This rotation of originally horizontal lineations over basal thrust culminations, and the presence of well-defined south dipping reflectors in seismic profiles, is regarded as strong evidence of the allochthonous nature of the Iberian-European contact, now located over the European plate (Fischer, 1984; Choukroune etal, 1989). This relationship is further constrained through imaging along the ECORS profile which depicts a northward transport of the NPFZ and also, by implication, the North Pyrenean Thrust Belt, from the point of lower crustal convergence or 'singularity' (Roure et al., 1989; Choukroune et al., 1989; Willett et al., 1993). This relationship, therefore, requires that the North Pyrenean Thrust Belt was formed prior to its overthrusting of the European plate, though with later reactivation of its structures during Eocene times.

2.2.2.3 The Axial Zone

The central Pyrenean Axial Zone is bound by the NPFZ and the South Pyrenean thrust belt, to the north and south, respectively (**Fig. 2.5**). Hercynian basement lithologies and their Mesozoic cover rocks display mountain belt-scale thrusting acquired during Pyrenean crustal shortening (Choukroune et al., 1989). Neither basement nor cover rocks display evidence of Alpine-age magmatism or significant metamorphism.

The majority of the lithologies represent a protracted history of Palaeozoic deposition and Hercynian-age deformation (Zwart, 1979). Large spatial variations in the Palaeozoic stratigraphy occur across the Axial Zone (Fig. 2.5), however the central Pyrenean succession can be characterised as follows: Orthogneiss massifs (e.g. Canigou, Aston-Hospitalet) in the east have been interpreted as both Precambrian basement and as intrusive Cambro-Ordovician granites to the overlying Cambro-Ordovician quartz- and graphite-phyllites and the intercalated limestones (Cavet, 1957; Hartevelt, 1970; Zwart, 1979). The Silurian epoch is represented by a very uniform development of black, carbonaceous shales which are overlain by highly variable and fossiliferous Devonian limestones, dolomites, shales and quartzites (Mey, 1968; Mey et al., 1968; Zwart, 1979). These pass upwards, in some areas unconformably, into a host of pre-Variscan Carboniferous sub-facies, including nodular limesones, cherts, greywackes and occasional conglomerates. Several large and elongate, E-W oriented granodioritic bodies occur in intrusive relationships within the Palaeozoic stratigraphy, often with the contact metamorphic aureoles still in situ (e.g. Maladeta, Marimaña, Riberot) (Mey, 1968; Zwart, 1979). The post-Variscan succession (**Fig. 2.6**) is largely represented in the southern extreme of the central Axial Zone, with only limited outcrops in the higher relief core of the range. Upper Carboniferous (Westphalian) deposits record predominantly fluvial and lacustrine environments with sub-aerial tuffs and pyroclastics (Aguiro, Erill Castell and Malpas Formations) (Mey, 1968; Besly and Collinson, 1991). Overlying Permian and Triassic strata are dominated by red sands and muds which pass upwards into the dominantly marine facies of the Mesozoic (Zwart, 1979).

The central Axial Zone is comprised of stacked Hercynian basement thrust sheets with localised outcrops of deformed Triassic and Permian cover rocks. The main thrust sheets are Rialp, Orri and Nogueres.

The structurally lowest of these is the Rialp thrust sheet and is only briefly exposed within three complex tectonic windows along the Pallaresa valley of the south central Pyrenees (**Fig. 2.7**). Triassic strata display N-S folds with an west-dipping axial planar cleavage and are observed to be truncated by overthrust Cambro-Ordovician and Silurian-Devonian rocks (Puigdefàbregas et al., 1989; Muñoz, 1992). The truncating structure, representing the south-vergent floor thrust to the overlying Orri thrust sheet, dips slightly at surface and describes an open anticline (Muñoz, 1992). Importantly, this relationship demonstrates the allochthoneity and southward transport of the overthrusting mass. The Orri thrust sheet exposure forms much of the southern central Axial Zone and, in particular, the broad anticlinal Orri Dome (Zwart, 1979). Palaeomagnetic and structural studies within the area to the west of this feature, across the ECORS line, indicate a similar deformation and doming to be of Alpine age (McClelland and McCaig, 1989; Bates, 1989).

The uppermost of the basement-involved thrust sheets is the Nogueres Zone, which outcrops in a longitudinal belt at the southern extreme of the central Axial Zone (Dalloni, 1930). Over-steepened thrusts bounding Hercynian basement and Permo-Triassic cover rocks display downward-facing hangingwall anticlines and localised north-dipping Alpine cleavage (Séguret, 1964; Séguret, 1972). These structural geometries have been used to infer that the palaeozoic blocks represent 'noses' of allochthonous thrust nappes (Séguret, 1964; Séguret, 1974; Williams, 1984). Lower Nogueres units are differentiated from the Upper Nogueres units by the presence of thick Stephano-Permian sequences below the Triassic strata and the nature of the Hercynian facies (Mey, 1968; Puigdefàbregas et al., 1989) (**Fig. 2.8**). These stratigraphical characteristics have been used to propose potential source areas for the southerly transported blocks of the Upper Nogueres Zone. Muñoz (1992) rejects the Llavorsi thrust as a possible root zone and, instead, suggests the thrust bounding the Llavorsi syncline to the north is a more appropriate source region. This implies a southward displacement of the Upper Nogueres zone on the tens-of-kilometre scale and displacement of the Lower Nogueres units on the kilometric scale (Puigdefàbregas, 1989; Muñoz, 1992). The northern area of the central Axial Zone is deformed by faults which have steep to vertical dips and are upthrown to the north (Zwart, 1979).

2.2.2.4 South Pyrenean Thrust Belt (SPTB)

The South Pyrenean thrust belt comprises thrusted and faulted Mesozoic and Palaeogene rocks (Muñoz, 1992). It is located south of the Axial Zone and north of the undeformed Ebro pro-foreland basin. Within the central Pyrenees, three major units (Sierres Marginales, Montsec and Boixals) have been southwardly transported and imbricated across autochthonous Palaeogene and Mesozoic cover rocks of the Ebro basement (**Fig. 2.9**). The SPTB represents classical evaporitic decollement tectonics; exhibiting large-scale translation of thrust blocks along basal detachments without inducing penetrative hangingwall deformation, and the formation of narrow, salt-cored anticlines and broad synclines (Choukroune etal, 1989; Muñoz, 1986, Vergés et al., 1992).

The Boixals thrust sheet, the most northerly of the SPTB series, is bound to the north by the south-dipping Morreres Backthrust. Folded Cretaceous limestones and breccias are juxtaposed next to Triassic ophites and marls across a steep north-vergent fault contact (Puigdefàbregas et al., 1989). This has been interpreted as a passive-roof thrust to the south Pyrenean thrust sheets during Axial Zone development (Banks and Warburton, 1986; Muñoz, 1992). The mainly lower Cretaceous shallow water marine succession of the Boixals thrust sheet are bound to the south by the Boixals thrust, buried along much of its length by the onlapping Maastrictian Aren sandstone. Where emergent, the Boixals thrust has a well developed kilometric-scale fault propagation anticline with opposing forelandward syncline displaying onlapping and syntectonic, footwall growth strata (Deramond et al., 1993; Bond and McClay, 1995).

Immediately to the south, the Montsec thrust sheet defines a broad synclinal structure within which the Tremp-Graus basin is located. Upper Cretacous limestones and lower and middle Eocene clastic rocks have been transported up to 10 km over the Montsec thrust (Muñoz, 1992; Burbank, 1992). Enhanced stratigraphic thicknesses of the Cretaceous carbonate succession on the hangingwall of the Montsec thrust have been used to infer this structure represents an original upper Cretaceous extensional fault (Reynolds, 1987).

The Sierres Marginales thrust sheets are located between the Montsec thrust and the southern deformation front (South Pyrenean Main Thrust) (Muñoz, 1992). A characteristically thin Mesozoic succession is overlain by Palaeocene and lower Eocene Alveolina limestones which, in turn, are unconformably overlain by syn- and post-tectonic upper Eocene and lower Oligocene conglomerates, sandstones and gypsum (Pocovi, 1978; Muñoz, 1992). South of the Sierra Marginales thrust sheets, at the frontal tip line or structural front of the SPTB, foreland sediments are deformed into anticlines by blind frontal thrusts and frontal thrust-wedge geometries (Williams and Fischer, 1984; Vergés and Muñoz, 1990; Sans et al., 1996).

Principle piggy-back thrusting commenced within the SPTB during upper Thanetian times (<55Ma) and continued, episodically, to the upper Oligocene (~26 Ma) **(Fig. 2.10)** (Meigs, 1997). Inversion of the Organya extensional basin during upper Campanian to Maastrictian (~72 Ma) times heralds the onset of Pyrenean contraction in the southern foreland (Bond and McClay, 1995). The progressive rotation and tectonic enhancement of intraformational unconformities within the onlapping Aren sequence demonstrates the continuation of shortening across the Boixals thrust into the lower Palaeocene (Deramond et al., 1993; Bond and McClay, 1995). To the south, shortening is marked by both the southward translation of the Montsec thrust sheet and the initial displacement of the Sierra Marginales across the foreland basin succession during the Ypresian (Williams and Fischer, 1984; Burbank et al., 1992; Vergés, 1993). Restored sections indicate displacement values on the Montsec and Sierra Marginales thrusts reached up to 6 km and 14 km, respectively, prior to the upper Priabonian (36 Ma) (Vergés, 1993; Vergés et al., 1992). Shortening continued along the Sierra Marginales and also, by implication, the southward piggy-back transport of the overlying SPTB, through to the latest Rupelian (29.5 Ma) (Meigs et al., 1996; Meigs and Burbank, 1997). Up to 29 km of additional translation across the foreland basin sequence was achieved during this period, though with very limited hindward deformation in the overriding thrust belt (Meigs et al., 1996). A final deformational pulse generated minor thrust displacement and tightening of existing fold structures within the Sierra Marginales frontal structures before the end of the tectonic activity in lower Chattian times (Meigs et al., 1996; Meigs, 1997).

The isolation of discrete deformational episodes within the polydeformed SPTB has been largely achieved through the stratigraphic and geometrical analysis of Eocene to Oligocene age continental deposits which drape the major structures (e.g. Deramond et al., 1993; Burbank et al., 1992; Meigs et al., 1996; Meigs, 1997; Beamud et al., 2003). Coarse alluvial conglomerates and fluvial sandstones are distributed across the southern region displaying pre-, syn- and post-tectonic associations with the underlying duplexed lower thrust system. Areally large, subhorizontal masses also cover much of the interior of the foreland thrust belt lying with angular unconformity over older rocks and onlapping onto the southern margins of the Axial zone (Mellere, 1993; Coney et al., 1996). Undeformed exposures of the sediments range from ridge crests of up to 1500 m elevation in the southern thrust belt to the base of steeply-incised canyons at the modern base-level at elevations of < 500 m (Coney et al., 1996). The distal equivalents of the northern proximal conglomerates and sandstones are the extensive sheets of upper Eocene to lower Miocene alluvial-fluvial channel and floodplain sandstones and shales and playa-lake deposits which fill the Ebro basin to the south (Dañobeitia et al., 1990; Coney et al., 1996; Pérez-Rivarés et al., 2002). These units are up to 3km thick in the central foreland basin and overlie southward-thinning lower to middle Eocene marine strata, possibly deposited when a marine gateway to the Atlantic was open at the western edge of the foreland. Isolation of the basin and the development of internally-drained continental sedimentation likely occurred in the late Eocene in response to uplift of the surrounding Iberian range and Catalan Coastal Range (Riba et al., 1983; Puigdefàbregas et al., 1986).

2.2.3 Pyrenean macro-structure

When the main structural elements of the Pyrenees are considered holistically, the mountain belt can be observed to display many large-scale characteristic geometries of doubly-vergent, continental collisional mountain belts (Willettt et al., 1993). However, there are a number of salient features of the Pyrenees which warrant particular attention and which must be integrated into any potential geodynamical model:

Relationships of the basement-involved thrust sheets within the central Axial zone require that structurally higher units are allochthonous and southerly-vergent over structurally lower units. Furthermore, the Alpine-age faults which bound the thrust blocks display a distinct and characteristic geometry; fault surfaces are steep and southerly-dipping in the Nogueres Zone in the south of the Axial Zone, display a flat-lying attitude over the Rialp tectonic window and progressively increase in dip toward the north (Zwart, 1979; Choukroune, 1989; Muñoz, 1992). In the north of the Axial Zone south-vergent thrust surfaces have been back-steepened or even overturned. Importantly, throughout the Axial Zone the pervasive main-phase Hercynian cleavage remains parallel or sub-parallel to the Alpine-age thrust surfaces (**Fig. 2.11**) (Zwart, 1979; Muñoz, 1992). This suggests late-stage folding of both Hercynian- and Alpine-age structures and fabrics during orogenesis.

Seismic imaging of the NPFZ indicates that it is truncated at depth by a gently south-dipping detachment, likely to represent the sole thrust to the North Pyrenean Thrust Belt. This requires that the NPFZ has been transported to the north and retained its subvertical orientation during convergence (Choukroune, 1976). Furthermore, late-stage shortening at the north Pyrenean deformation front suggests the northerly-vergent NPTB has also been transported away from the orogenic axis.

Other important features of the Pyrenees worthy of note include, the lack of strong internal deformation of all Mesozoic and Tertiary rocks outside of the NPFZ and the lack of any granitic plutonism or migmatisation during orogenesis (Choukroune et al., 1989).

2.3 Models of orogenic evolution

Collation of the numerous field-based studies and the deep seismic imaging projects from recent years offer significant constraints on the major structural geometries within the Pyrenean orogen. The configuration of these large-scale fault structures, regional fabrics and deep crustal geometries, in turn, provide a rigid skeleton around which potential models of orogenic evolution must ultimately strictly adhere to.

Such models, be they interpretative geological, sandbox analogue or numerical, potentially provide key insights into the evolutionary stages of the mountain belt and thus enable predictions to be made which can be tested in the modern setting. Similarly, temporally-constrained geological events from the mountain belt can be used to offer vital information for the construction of the orogenic models.

In this section the Pyrenean crustal models based on structural, stratigraphic and seismic data from the last 20 years are evaluated and discussed. Likewise, the available numerical models which have been used to investigate Pyrenean evolution, or concepts relevant to Pyrenean evolution, are considered.

2.3.1 Geological models

Early models of Pyrenean structural evolution have shifted from autochthonous to allochthonous conceptions. The Leiden University defended a purely autochthonous interpretation, suggesting Hercynian basement blocks within the southern Axial Zone had been locally upthrust along north-vergent structures (Mey, 1968; Fontboté et al., 1986). In the seventies, French workers documented thrust relationships from the Nogueres Zone, which they regarded as evidence of allochthonous origins (Séguret, 1970; Choukroune and Séguret, 1973). General acceptance of this interpretation (Zwart, 1979) promoted an essential shift in the understanding of Pyrenean structure and marked the onset of a number of allochthonous-based evolutionary models.

Choukroune and Séguret (1973), and others French workers, proposed the influence of superficial gravimetric sliding of thrust nappes accounted for significant amounts of mass transfer (**Fig. 2.12**). They envisaged the initial early uplift of the central core of the mountain belt was followed by both northward and southward gravity-driven sliding of thick Mesozoic sequences overlying the Triassic evaporitic decollement.. The component of horizontal compression and associated gravity sliding, accounting for up to 50 km of thrust movement, was interpreted as the fundamental forcing of mass transport.

In the early eighties, additional data was collected from seismic and gravity surveys and interpreted to show crustal thickening below the Axial Zone, a Moho step beneath the NPFZ and thinner crust on the northern side of the Pyrenees (Daigniéres et al., 1982). A group of British geologists contested these early interpretations and, employing recently developed ideas on thrust geometries, formulated radically new models of Pyrenean development based on the concept of thin-skinned tectonics (Fischer, 1984; Williams, 1985; Williams and Fischer, 1984). Early models incorporating gravitational gliding were rejected on the basis of two primary reasons; (i) field relationships indicated the central Axial zone was not uplifted until later in the Alpine evolution, when the fold and thrust belts were already in situ, and (ii) there was no strong structural evidence to support gravitational collapse, such as extensional features in the hinterland portion of the thrust sheets (Williams and Fischer, 1988).

The thin-skinned model describes the development of the orogen over a relatively shallow decollement above undeformed lower crust in the Axial Zone (**Fig. 2.13**) (Williams and Fischer, 1984; McCaig, 1986). All thrusts are assumed to have originated at shallow angles (<30°) with subsequent steepening attributed to the stacking of lower imbricates into antiformal thrusts or to backthrusting (McCaig, 1986). Therefore, the Pyrenees were considered as an asymmetrical chain with a prevailing south displacement of thrust sheets, north-Pyrenean structures thus representing secondary thrusts, interpreted as backthrusts from the southerly-vergent system (Fontbote etal., 1986; Williams and Fischer, 1984). Importantly, this model required that the trace of the NPFZ is allochthonous and must be displaced at least 60 km from any original crustal root (Williams, 1985; McCaig, 1986). The central Axial Zone was interpreted to constitute a large antiformal stack formed through the stacking of south-vergent basement thrust sheets, evidenced in the modern setting through the revelation of thrust repetition in the eroded Rialp tectonic window.

Owing to the unavoidably speculative nature of the deep crustal geometries below the Pyrenees at this time, strong critical reactions were lodged against the thin-skinned model of orogenic evolution. Séguret and Daigniéres (1985, 1986) proposed a 'vertical-tectonic model', in which N-S shortening within the Axial Zone is accommodated by superficial thrust displacements at the surface which pass downwards into a zone of penetrative ductile deformation (**Fig. 2.14**). Alpine thrusts were envisaged to rapidly steepen downwards and the absolute displacements to reduce to negligible values with depth (Séguret and Daigniéres, 1986). Shortening was considered to be principally achieved south of the NPFZ in the eastern and central Pyrenees, and north of the NPFZ in the western part (Séguret and Daigniéres, 1986). Importantly, this 'inhomogenous strain model' implied considerably reduced overall orogenic shortening (55 km in the west; 80 km in the east) in comparison to the low-angled thrust trajectory thin-skinned model (106 km in the central Pyrenees) (Séguret and Daigniéres, 1986; Williams and Fischer, 1984).

Both opposing structural models remained consistent with the development and dominance of south-directed thrusting and the formation of an Axial Zone antiformal stack. The principal contrasts between the models being the geometry, and therefore associated shortening, of these structures at depth. Fontbote et al. (1986) suggest the proposed rapidly-shallowing upwards faults could not have long horizontal displacements, the Axial zone lacking any evidence of widespread Alpine deformation in the exposed Hercynian basement. Likewise, McCaig (1986) argues that although there is good evidence that both shallow thrust faults and steep shear zones formed within the same orogen, it is the shallowly-dipping structures that accommodated the large majority of horizontal crustal shortening. However, the same shallowly-dipping structures, inherent in the thin-skinned model, appeared to show major discrepancies with the geophysical data which depicted a Moho step linked to the surface trace of the NPFZ.

With the completion of the ECORS seismic profile across the uplifted core of the Pyrenees came the much needed additional constraints on the deep crustal geometries. Interpretations from a number of workers (e.g. Choukroune et al., 1989; Roure et al., 1989; Desegaulx et al., 1990) suggested the NPFZ could not be extended directly downward and, therefore, was not connected to the gravity-imaged Moho step (Desegaulx et al., 1990). Instead, it appeared the North Pyrenean massifs had, along with the NPFZ, been thrusted northward over the European plate (Choukroune et al., 1989), as originally envisaged by William and Fischer (1984). However, seismic data from within the central Axial Zone depicted the downward steepening of deep crustal reflectors, defining a clear v-shaped geometry of the crustal fabric, far below the structural levels for the postulated thin-skinned basal detachment (Choukroune etal., 1989). Additional complexities were also revealed through length and surface measurements along the gently northward dipping Iberian plate (Desegaulx, 1990). Large discrepancies were observed between the estimated length for the top of the Iberian Palaeozoic basement, and the actual length of the layered lower crust imaged on the ECORS line (Roure etal, 1989; Muñoz, 1992).

Evidently, the two end-member solutions proposed for the evolution of the Pyrenees could no longer accommodate the available geological and geophysical data. A model incorporating the deep crustal structural lineaments of the orogen, whilst also emphasizing the allochthonous nature of the major thrust sheets was required.

Roure et al. (1989) proposed a tectonic scenario whereby poorly imaged Iberian lower layered crust is currently stacked beneath the Axial Zone, imbrication accounting for the shortfall in imaged section (**Fig. 2.15**). High reflective events below the NPFZ are interpreted to be layers of European lower crust, across which the NPFZ and the thrust belt have been transported. The Moho step is regarded to coincidentally lie below the offset surface trace of the NPFZ (Roure et al., 1989). The importance of tectonic inheritance in this mode of evolution is highlighted by Desegaulx et al. (1990). Reactivation and inversion of pre-existing Hercynian fault lineaments, operative when the fault plane is consistent with stress field orientation, is regarded as the principal forcing behind the modern orogenic geometries.

Similarly, Muñoz (1992) maintains the pre-existing structural geometries have defined the lithospheric evolution of the orogen (**Fig. 2.16**). However, in this case, a model of tectonic delamination is favored, whereby the flattening of existing Cretaceous extensional structures over the lower layered crust cause detachment between the Iberian upper and lower crust during Pyrenean inversion and thrusting (Muñoz, 1992). According to the model, the upper crust, constituting the duplex antiformal stack in the southern Axial Zone and imbricate stack in the northern Axial Zone, detached from the lower crust along a detachment level located at a depth of 15 km (Muñoz, 1992). The lower seismic layered crust, together with the lithospheric mantle, is regarded to have been subducted into the mantle. An overall shortening of 147 km, and of 110 km of subducted lower crust, is required to satisfy this favored geometric solution, significantly more than proposed in earlier models (eg. 100 km; Roure et al., 1989). Subsequent balanced restorations from the eastern Pyrenees have yielded similar estimates of orogenic contraction (125 km; Vergés et al., 1995).

2.3.2 Numerical Models

The application of numerical modelling to investigate the evolution of the Pyrenees has been largely focused on the flexural behavior of the continental lithosphere during collision and on the importance of inherited crustal lineaments on the orogenic evolution and the modern-day structural configuration.

Desegaulx et al. (1990) model the development of the mechanical and flexural behavior of the lithosphere during and after Pyrenean compression. They conclude that late Jurassic to Early Cretaceous stretching produced a variation of the elastic thickness, and therefore rigidity, of the plate. This variation, it is postulated, can be linked to subsequent characteristics of Pyrenean orogenesis and structural development. Namely, the northerly subduction of the Iberian plate relative to the European plate; contrasts between the elastic thickness of the Iberian and European plates, and distinctive patterns of uplift associated with post-orogenic 'unflexing'. The influence upon central Pyrenean uplift is interpreted to show initial rapid uplift in the northern sector and a delayed uplift to the south, a pattern which is broadly corroborated by early fission track work (Desegaulx et al., 1990; Yelland, 1990).

Similarly, to demonstrate the interactions between plate boundary forces and pre-existing crustal asymmetries, Chery et al. (1991) modelled the thermomechanical evolution of an initially thinned and thermally perturbed continental lithosphere, using the Pyrenees as a structural framework. Model predictions, from a finite element formulation, were compared and contrasted against ECORS seismic interpretations. Model runs with initial configurations displaying lithospheric thinning north of the pre-orogenic NPFZ, and the associated thermal perturbations, typical of asymmetric transform plate boundaries, were observed to reproduce very closely the broad deformation pattern imaged within the Pyrenees.

More recently geodynamical numerical modelling has been coupled with crustal structural restorations in order to investigate the role of crustal heterogeneities and surface processes on controlling asymmetric shortening across the Pyrenean orogen (128 km across the southern wedge and 37 km across the northern one) (Beaumont et al., 2000). Model reproductions of Pyrenean balanced cross sections are attained by providing the pre-collisional crust with asymmetric mid-crustal weaknesses with a stepped increase in strength toward the converging plate. This promotes the subduction of the modelled Iberian lower crust and associated lithospheric mantle and, together with additional stratigraphic detachments, reproduces the broad character of the Axial Zone antiformal stack with some accuracy (**Fig. 2.17**) (Beaumont et al., 2000). The inferred zones of weakness are attributed to the flattening of Late Cretaceous extensional faults at mid-crustal depths, as previously postulated by Muñoz (1992). The strain partitioning and clear asymmetry of the Pyrenean double-wedge can be further enhanced in the model by inferring lower denudation rates on the retro-side of the orogen. This, combined with the effect of weakening of the pro-crust, acts to reduce retrothrusting and increase southern Axial Zone exhumation (Beaumont et al., 2000).

2.4 Thermochronological studies in the Pyrenees

A number of radiometric dating techniques have been applied to constrain different aspects of Pyrenean evolution. In this section, relevant thermochronological studies are reviewed and the implications for timing and exhumation are discussed.

2.4.1 'High-temperature' radiometric systems

Within the Hercynian basement of the Axial Zone, Rb-Sr whole rock dating has yielded Cambro-Ordovician ages for gneissose bodies and Permo-Carboniferous ages for granitic massifs (Jaeger and Zwart, 1968). This has been interpreted to show that any measured thermochronological ages younger than approximately 260 Ma represent post-emplacement thermal events (Garwin, 1985). Syntectonic metamorphism of Mesozoic sediments within the NPFZ is dated at around 90 Ma through the application of K/Ar techniques (Albarede and Michard-Vitrac, 1978; Montigny et al., 1986; Choukroune et al, 1989). This is regarded to be associated with the mid Cretaceous emplacement of hot ultramafic rocks (Lherzolites) during transpressional deformation (Albarede and Michard-Vitrac, 1978). Axial Zone muscovite ages immediately south of the NPFZ yield ages from 264 to 285 Ma, and have been interpreted, within error, to represent undisturbed Hercynian cooling ages (Michard-Vitrac and Allegre, 1975; Jager and Zwart, 1968). In contrast, mixed biotite ages (118 to 230 Ma) from the Axial Zone have been regarded as being non-uniformly reset during the mid-Cretaceous thermal event (Jager and Zwart, 1968). Alpine-age movements along major structural lineaments, such as the Merens fault, and hydrothermal activity in active mylonite zones have been confirmed within the central and eastern Axial Zone (McCaig and Miller, 1986; Wayne and McCaig, 1998). Ar^{40}-Ar^{39} muscovite ages indicate shear zones were active <100 Ma and likely about 50 Ma ago (McCaig and Miller, 1986). Similarly, Rb-Sr and U-Pb ages from a mixed suite of altered wall rocks and shear veins suggest retrogressive shear zones were active between 47-50 Ma (Wayne and McCaig, 1998).

2.4.2 'Low-temperature' radiometric systems

In order to investigate the latter stages of the thermal histories of rocks currently at the surface, and thus to shed more light on Alpine-age and late-stage activity, isotopic systems with significantly lower closure temperatures have also been employed. Single-elevation apatite fission track (AFT) and zircon fission track (ZFT) samples from independent massifs from the central-eastern Pyrenees were interpreted by Garwin (1985) to indicate broad structural partitioning across the range. Early Oligocene to Early Miocene AFT ages (27-17 Ma) and Middle Eocene ZFT ages (~40 Ma) from the southern-eastern Axial Zone contrast sharply with Early Eocene AFT ages (32-48 Ma) and a range of Cretaceous ZFT ages from the NPFZ (Garwin, 1985). These data were considered to reflect that the NPFZ samples had been partially reset by the Cretaceous thermal event and had been structurally distinct from the southern Axial zone during the Eocene culmination of the Pyrenean orogeny. Data from both thermochronometers were taken to represent a southward progression in the axis of maximum uplift during orogenesis. Calculated average uplift rates of 0.4 km Myr^{-1} for the Axial Zone are derived from samples with both AFT and ZFT ages. Deviations from the expected age-altitude correlation, that is decreasing age with decreasing elevation, are regarded as an artefact of uplift of non-coherent tectonic units, with younger samples being structurally placed above relatively older samples (Garwin, 1985).

Yelland (1990) applied fission track analysis on a suite of apatite crystals from independent basement and granitic massifs across the central and eastern Pyrenees. Long mean track lengths (13.3-14.6 μm) and low standard deviation (0.9-1.7 μm) in the northern Axial Zone were regarded to contrast with short mean track lengths (11.9-13.9 μm) and high standard deviations (1.3-3.2 μm) in the south (Yelland, 1990). This contrast was interpreted to show an initial period of rapid Palaeocene-Eocene uplift in the northern Pyrenees followed by a protracted period of less rapid uplift in the southern Pyrenees. Again, the southward migration of exhumation maxima during orogenesis is interpreted from the younging of ages from the NPFZ to the southern Axial Zone.

Morris et al. (1998) applied a selection of these AFT analyses from the central and eastern Pyrenees to evaluate the spatial and temporal variability in the magnitude of erosional denudation from Middle Eocene to the Late Miocene times (~40-10 Ma) (**Fig. 2.18**). Modelled thermal histories were derived from single-elevation samples. An assumed geothermal gradient was used to convert the modelled time-temperature plots into time-depth plots and, by inferring all exhumation to be accountable to erosional denudation, to contoured denudation maps of the central and eastern Pyrenees. Morris et al. (1990) conclude that variations in denudation through time are localised and are not influenced by the major bounding structures. Maximum amounts of denudation are achieved during the interval of 35-30 Ma at maximum rates of 240 mm kyr^{-1}. However, spatially averaged denudation rates between 40 Ma and 10 Ma show little temporal variation across the study area.

Apatite fission track analysis of three vertical profiles by Fitzgerald et al. (1999), however, suggest a strong temporal and spatial variation in rates of exhumation through Palaeogene times. Vertical profiles were sampled from a north-south transect across the central Pyrenees, incorporating the Lacourt, Riberot and Maladeta Hercynian granite massifs **(Fig. 2.19)**. The Lacourt profile (578 m) was interpreted to depict the base of an exhumed partial annealing zone (see section 3.2.3) and the onset of a period of rapid exhumation. This was based primarily on track length distributions and the age elevation profile, with ages between 55±3 to 37±1 Ma. The base of the palaeo-partial annealing zone is regarded to be at a modern-day elevation of 1 km and with a ~50 Ma age. The Riberot profile (1143 m) yielded ages ranging from 44±4 to 36±2 Ma, with a broadly positive age-elevation correlation. Derivation of exhumation rates from this plotted slope, which is not regarded by Fitgerald et al. (1999) to have been influenced by isothermal perturbation, yields averages of 173 ± 80 m Myr^{-1}, ± 1σ. The Maladeta profile (1725 m), the largest and most southerly profile, yielded ages ranging from 34±4 to 21±3 Ma. The age-elevation plot is regarded by Fitzgerald et al. to document two distinct periods of the cooling history within the southern Pyrenees. The upper part of the profile is considered to reflect a period of very rapid exhumation, resulting in the uppermost 8 samples (~900 m) showing similar ages of 35 to ~32 Ma ± 1σ with high mean track lengths ($\geq$ 13.8 μm). During this period Fitzgerald et al. (1999) calculate up to 15 km of crust was exhumed at rates of up to 2-4 km Myr^{-1}. The lower section of the profile is interpreted to represent the upper part of a palaeo-partial annealing zone formed during a period of relative thermal and tectonic stability. This is characterised by relatively low mean track lengths ($\leq$ 13.6 μm) and an age transition from 31±3 to 21±3 Ma. The Maladeta profile is considered to record the abrupt transition, at ~30 Ma, from a period of rapid exhumation to one of thermal and tectonic stability during the 'post-orogenic period (Fitzgerald et al., 1999).

Extrapolation of the lower part of the Maladeta profile to the modern day indicates 2-3 km of post-orogenic exhumation must have occurred in order for the sampled fission track ages to be at the surface. Numerical modelling of the fission track data by Fitzgerald et al.

(1999) suggests this rejuvenation cannot have occurred before ~5-10 Ma so as to allow the full development of a palaeo partial annealing zone during at least 20 Myr of thermal stability.

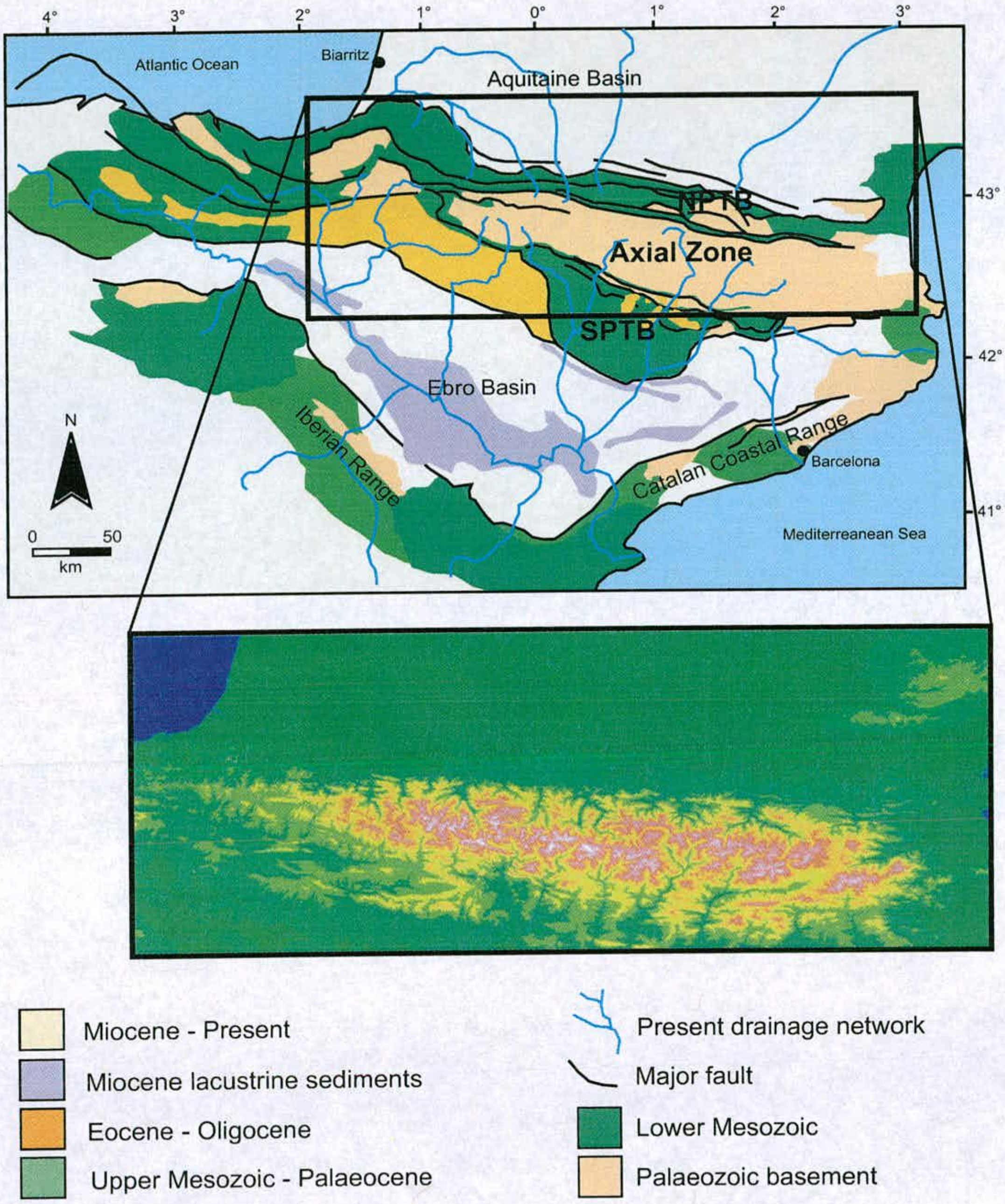

Figure 2.1 (a) Geological map of the Pyrenees, Catalan Coastal Ranges, and Iberian Range bounding the Ebro Foreland Basin. Major structural lineaments are outlined in bold black lines. Present day drainage networks are highlighted in blue (Garcia-Castellanos et al., 2003). (b) 90-metre DTED digital elevation model of the Pyrenean range highlighting the strong topographic relief and east-west trending drainage divide separating France and Spain.

Fig. 2.1

Geological map and 90m Digital Elevation Model of the Pyrenees

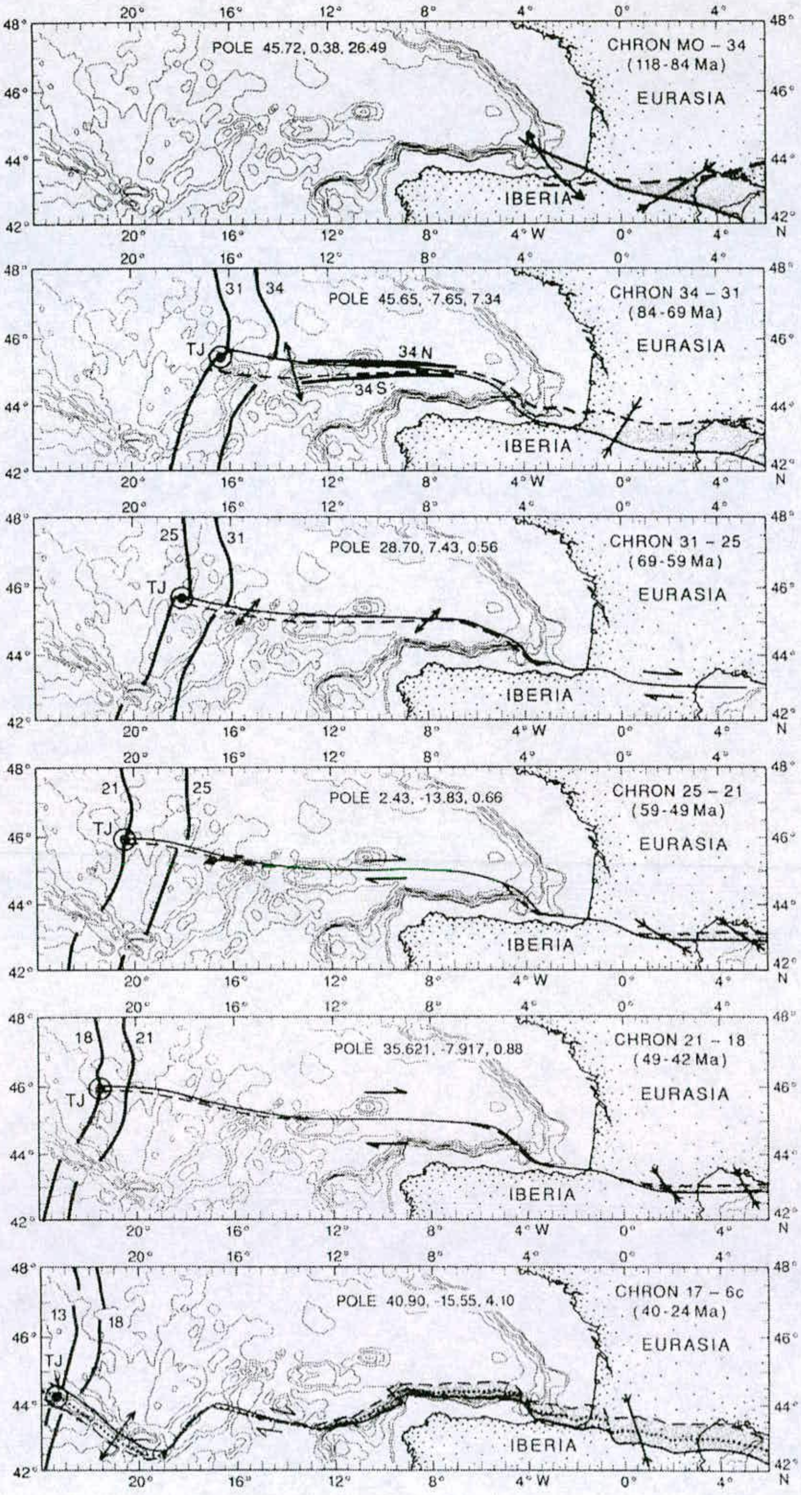

Figure 2.2 Motion between Eurasia and Iberia represented by the difference between solid and dashed lines, superimposed on the present day bathymetry. Magnetic isochrons indicate the start and end of each interval and shaded areas indicate compression (Roast and Srivistava, 1991). The tectonic history is largely dominated by a strong N-S compressional regime in which major deformation occurred at the Iberian plate margins during the anticlockwise rotation and northward translation of the Iberian plate.

Fig. 2.2

Tectonic evolution of the Iberian Peninsular

(Roest and Srivistava, 1991)

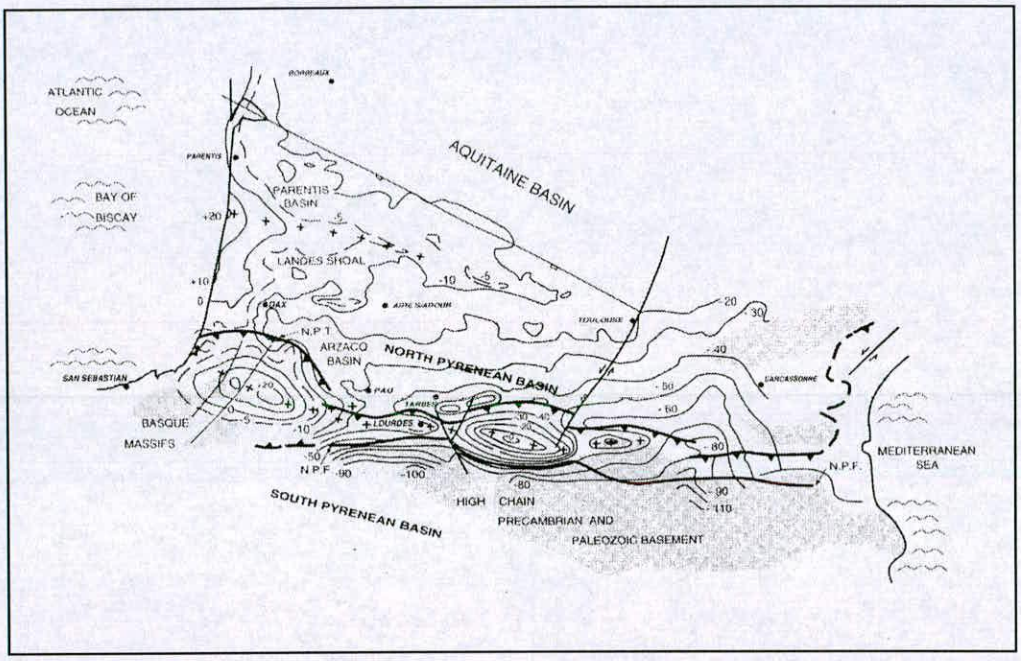

Figure 2.3 Gravity (Bouguer anomaly) and structural map of the Aquitaine Basin and North Pyrenean Thrust Belt. The 'heavy' anomaly in the central zone likely corresponds to the stacking of heavy Palaeozoic structural slabs in the central North Pyrenean Thrust Belt. The northern thrust front of the range is highlighted in bold black line (modified from Bourrouilh et al., 1995).

Fig. 2.3
Gravity map of the Aquitaine Basin
(Bourrouilh et al., 1995)

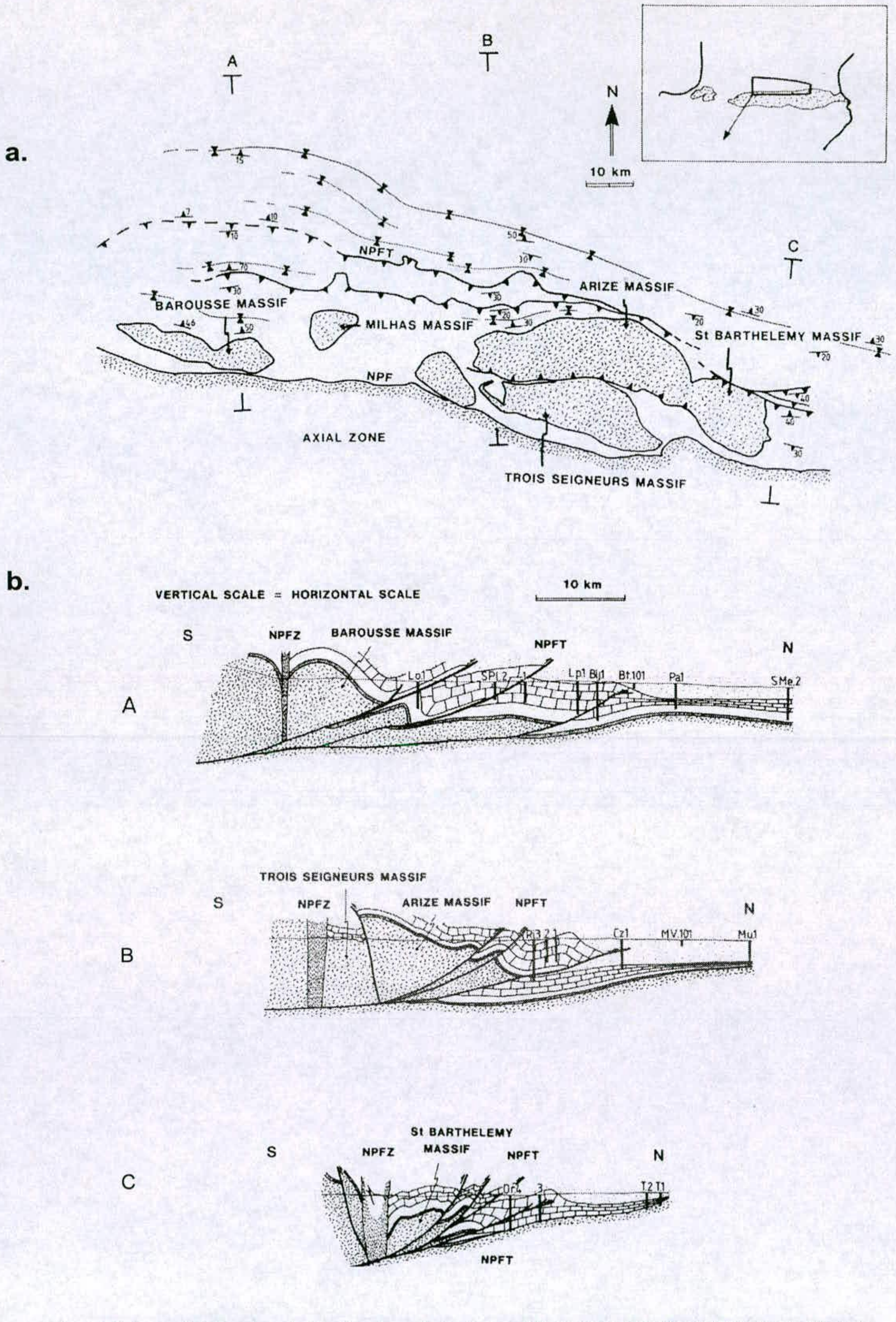

Figure 2.4 (a) Regional structural geology map of the central Northern Pyrenean Thrust Belt showing the major subdivisions and lines of section (A, B, C). Hercynian basement is stippled; NPF=North Pyrenean Fault; NPFT=North Pyrenean Frontal Thrust. (b) Balanced sections along lines A, B, and C. The reference lines used by the authors, which are assumed to be horizontal, are base of the Palaeocene (A and C) and base of the Eocene (B).

Fig. 2.4

Structural geology of the North Pyrenees

(Fischer, 1984)

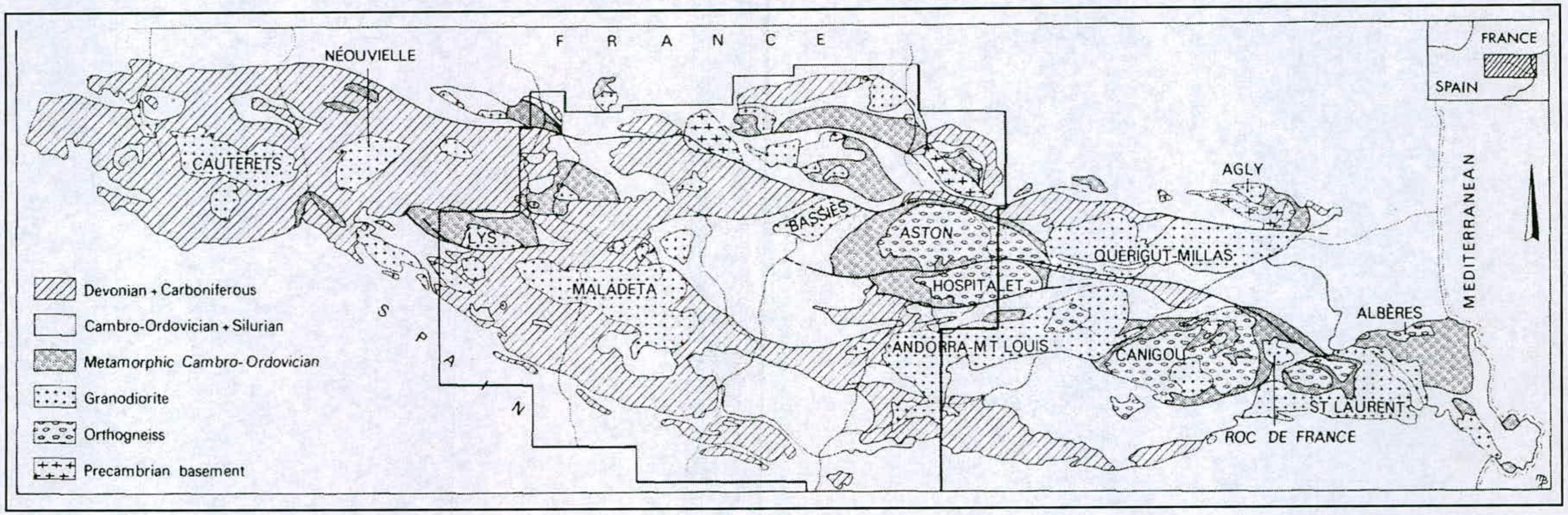

Figure 2.5 Regional geology map of the Palaeozoic basement of the Pyrenean Axial Zone (taken from Zwart, 1979). The isolated Hercynian-age granidioritic massifs and pre-Cambrian basement massifs dominate the high topography in the range.

Fig. 2.5
Geological map of the Axial Zone
(Zwart, 1979)

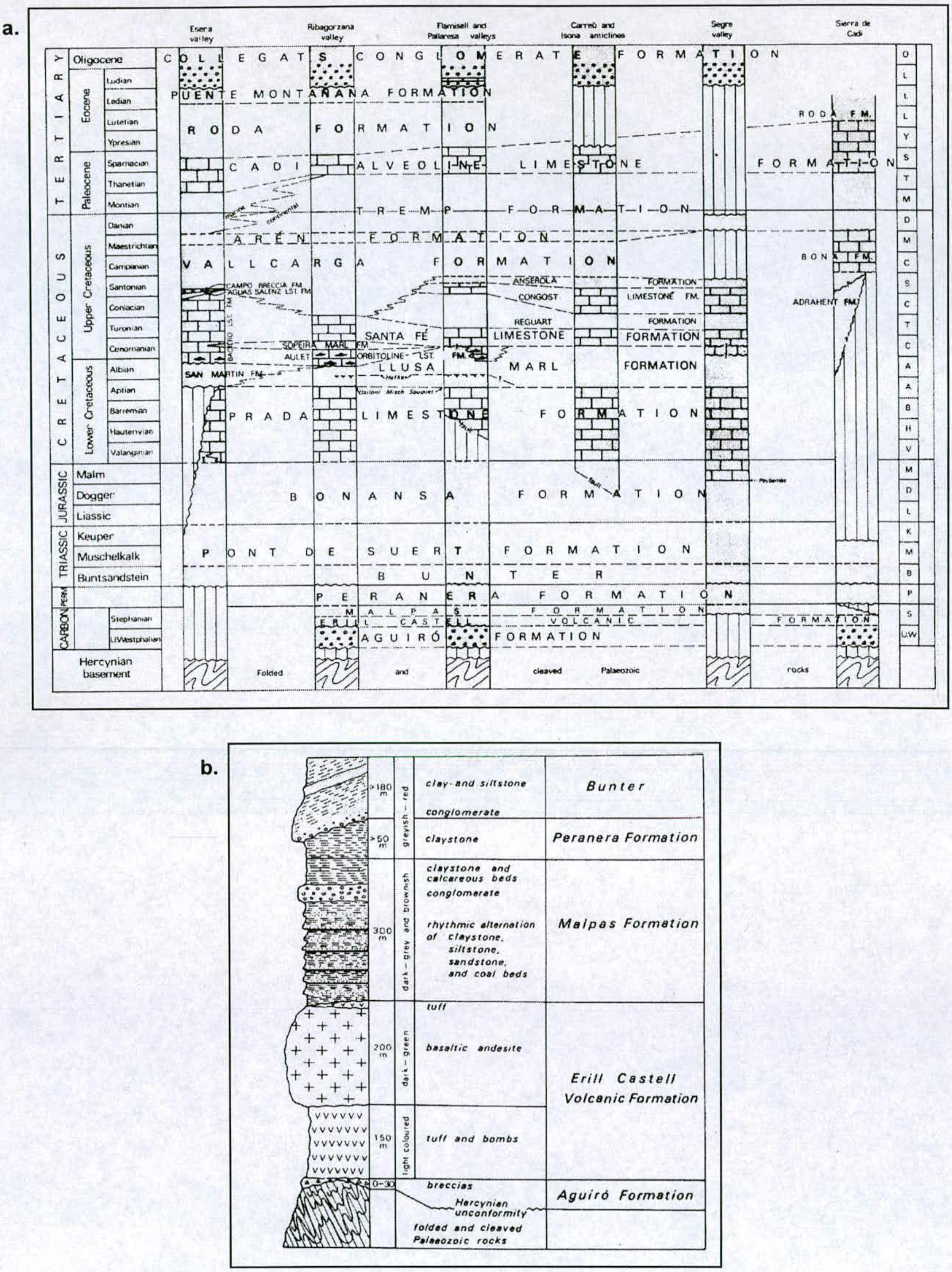

Figure 2.6 (a) Post-Hercynian stratigraphy of the central Pyrenees showing the transition from previously folded and cleaved Palaeozoic lithologies, through dominantly fluvial, lacustrine and volcanic Carboniferous sediments, Permo-Triassic fluvial redbeds, to the dominantly marine facies of the Mesozoic and early Tertiary. Late Eocene to Miocene conglomerates unconformably overlie the sucession (Zwart, 1979). (b) Detailed stratigraphic section of the post-Hercynian Carboniferous, Permian and Triassic sediments and volcanics of the south, central Pyrenees (Mey, 1968)

Fig. 2.6

Post Hercynian stratigraphy of the central Pyrenees (Mey, 1968; Zwart, 1979)

Fig. 2.7

Structural section through the Nogueres Zone along the ECORS profile
(Muñoz, 1986)

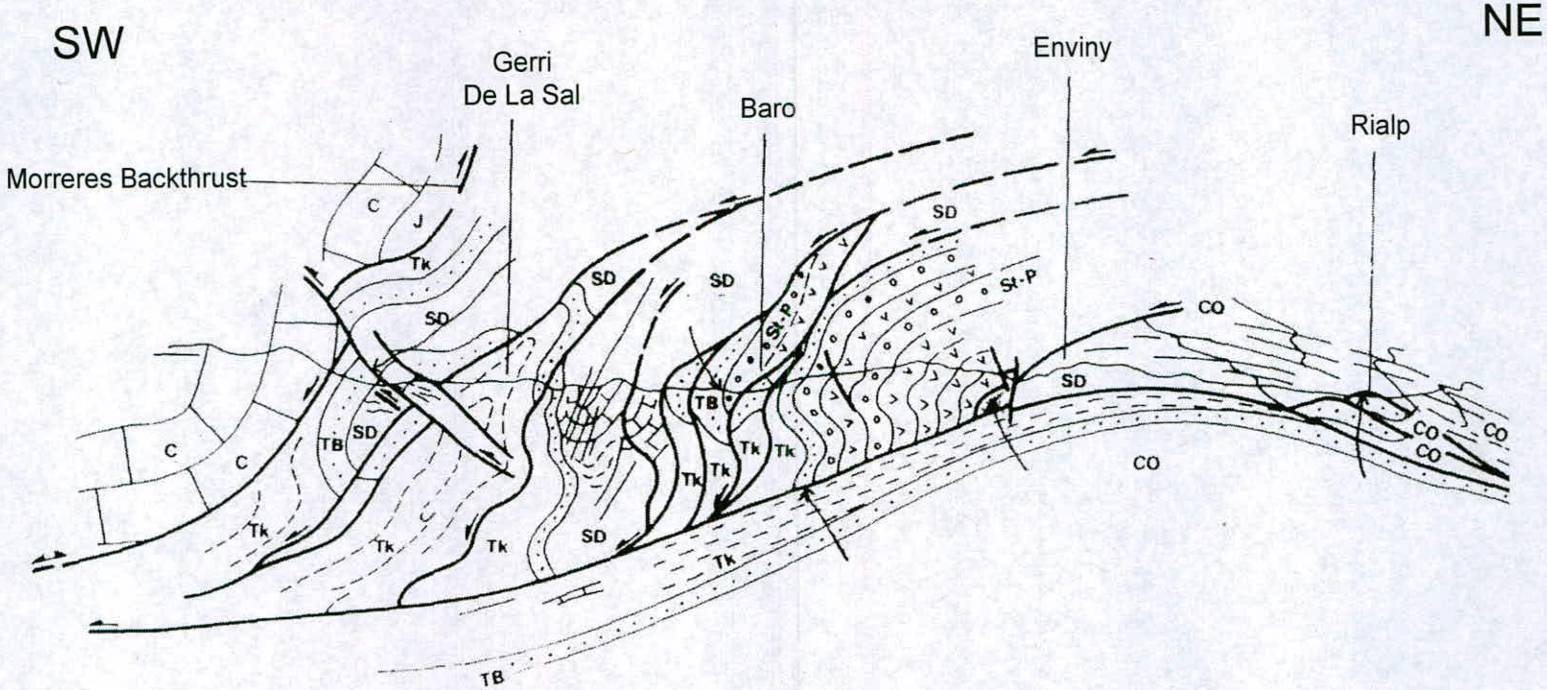

Figure 2.7 Section through the Nogures Zone in the region of the ECORS profile and the Rialp tectonic window. The Triassic strata of the Rialp block (base) display N-S folds and are truncated by overthrust and south-vergent Palaeozoic rocks of the overlying Orri block (Muñoz, 1986)

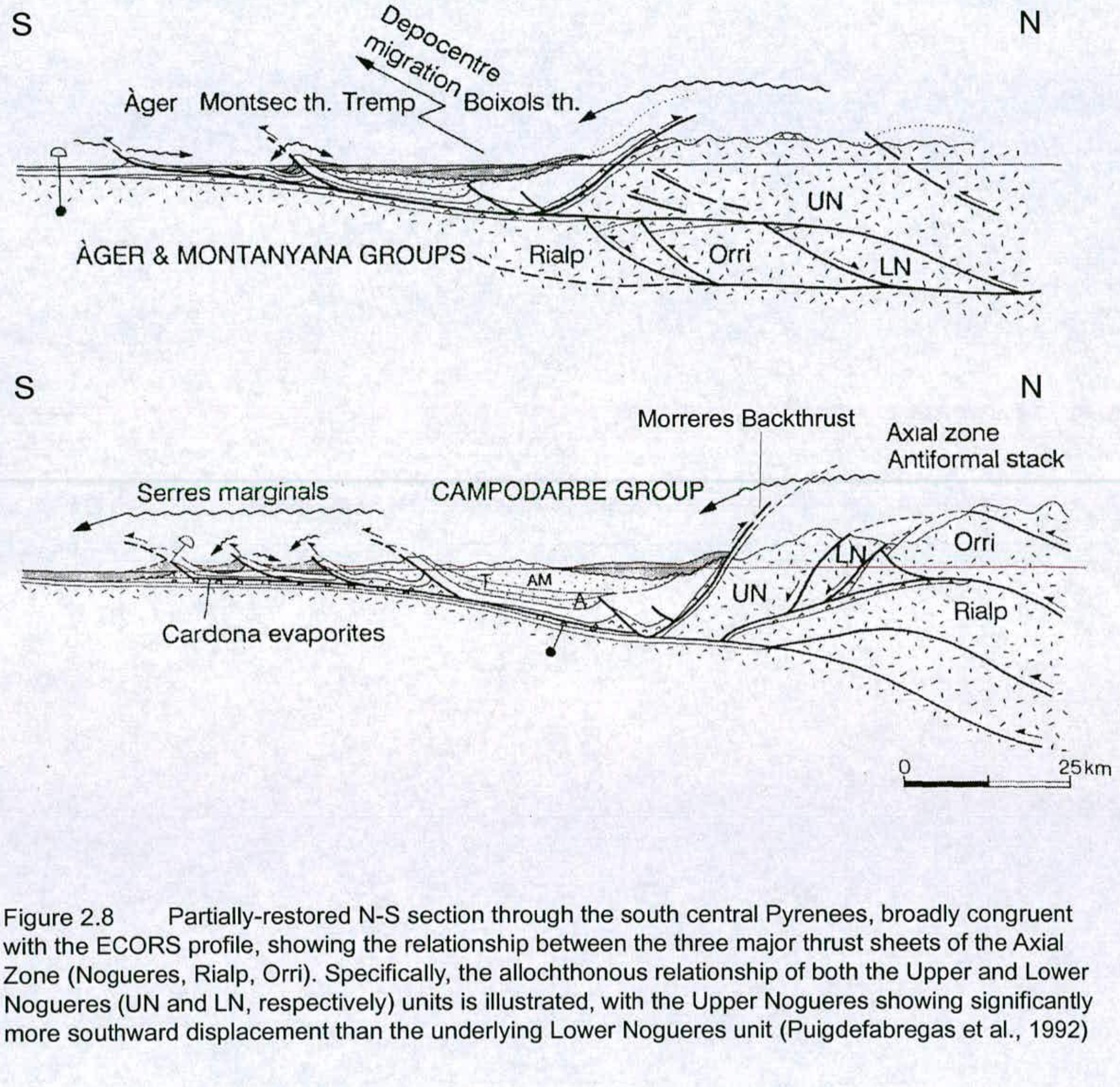

Figure 2.8 Partially-restored N-S section through the south central Pyrenees, broadly congruent with the ECORS profile, showing the relationship between the three major thrust sheets of the Axial Zone (Nogueres, Rialp, Orri). Specifically, the allochthonous relationship of both the Upper and Lower Nogueres (UN and LN, respectively) units is illustrated, with the Upper Nogueres showing significantly more southward displacement than the underlying Lower Nogueres unit (Puigdefabregas et al., 1992)

Fig. 2.8

Partially restored N-S cross section through the south central Pyrenees (Puigdefabregas et al., 1992)

Fig. 2.9

Balanced cross section on the south Pyrenean fold and thrust belt
(Verges and Muñoz, 1990)

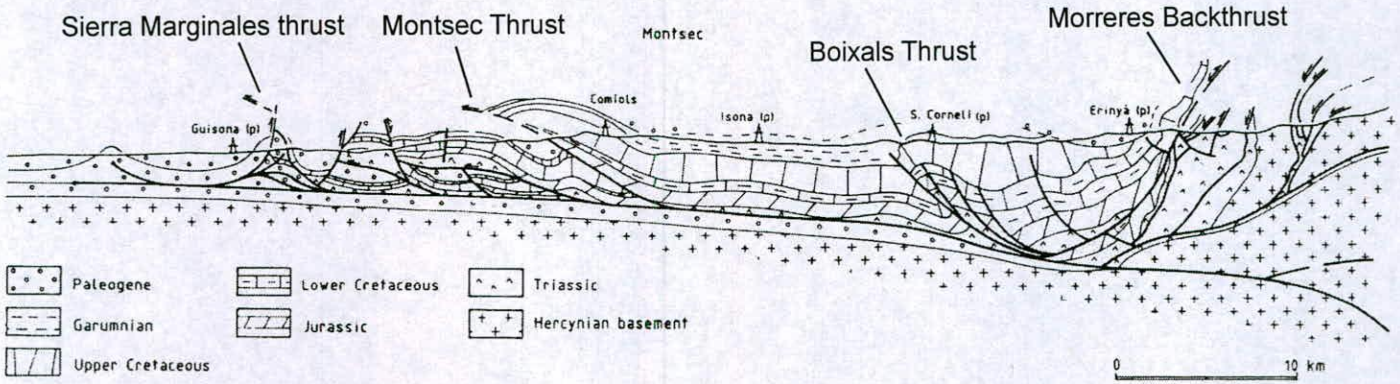

Figure 2.9 Balanced section of the cover thrust sheets across the south central Pyrenees, congruent with the ECORS profile. The SPTB comprises three major thrust sheets, from north to south, the Boixals, the Montsec and the Sierra Marginales. The Morreres Backthrust represents the northern boundary of the SPTB and separates it from the Nogueres Zone located to the north. The Sierra Marginales represents the southern boundary of the SPTB and separates it from the undeformed Ebro Basin to the south. (Verges and Muñoz, 1990)

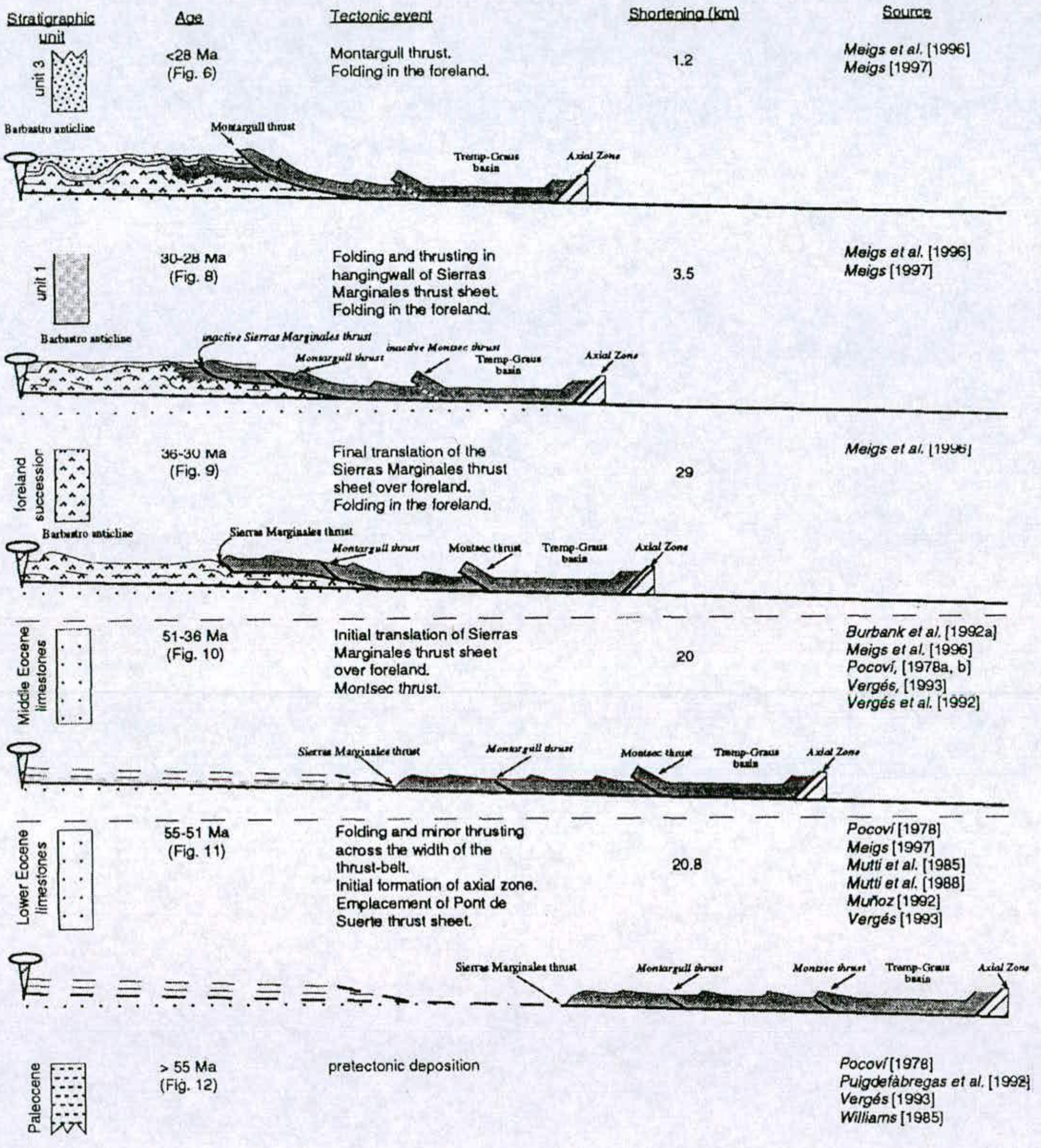

Stratigraphic unit	Age	Tectonic event	Shortening (km)	Source
unit 3	<28 Ma (Fig. 6)	Montargull thrust. Folding in the foreland.	1.2	*Meigs et al.* [1996] *Meigs* [1997]
unit 1	30-28 Ma (Fig. 8)	Folding and thrusting in hangingwall of Sierras Marginales thrust sheet. Folding in the foreland.	3.5	*Meigs et al.* [1996] *Meigs* [1997]
foreland succession	36-30 Ma (Fig. 9)	Final translation of the Sierras Marginales thrust sheet over foreland. Folding in the foreland.	29	*Meigs et al.* [1996]
Middle Eocene limestones	51-36 Ma (Fig. 10)	Initial translation of Sierras Marginales thrust sheet over foreland. Montsec thrust.	20	*Burbank et al.* [1992a] *Meigs et al.* [1996] *Pocoví*, [1978a, b] *Vergés*, [1993] *Vergés et al.* [1992]
Lower Eocene limestones	55-51 Ma (Fig. 11)	Folding and minor thrusting across the width of the thrust-belt. Initial formation of axial zone. Emplacement of Pont de Suerte thrust sheet.	20.8	*Pocoví* [1978] *Meigs* [1997] *Mutti et al.* [1985] *Mutti et al.* [1988] *Muñoz* [1992] *Vergés* [1993]
Paleocene	> 55 Ma (Fig. 12)	pretectonic deposition		*Pocoví* [1978] *Puigdefàbregas et al.* [1992] *Vergés* [1993] *Williams* [1985]

Figure 2.10 Summary diagram of the tectonic development and shortening across the SPTB constrained through the dating and structural analysis of syntectonic sediments draping the major structures (Meigs and Burbank, 1997). Total shortening measured for a given interval is quoted in kilometres and is approximately scaled on a horizontal axis.

Fig. 2.10

Tectonic development of the south Pyrenean thrust belt (Meigs and Burbank, 1997)

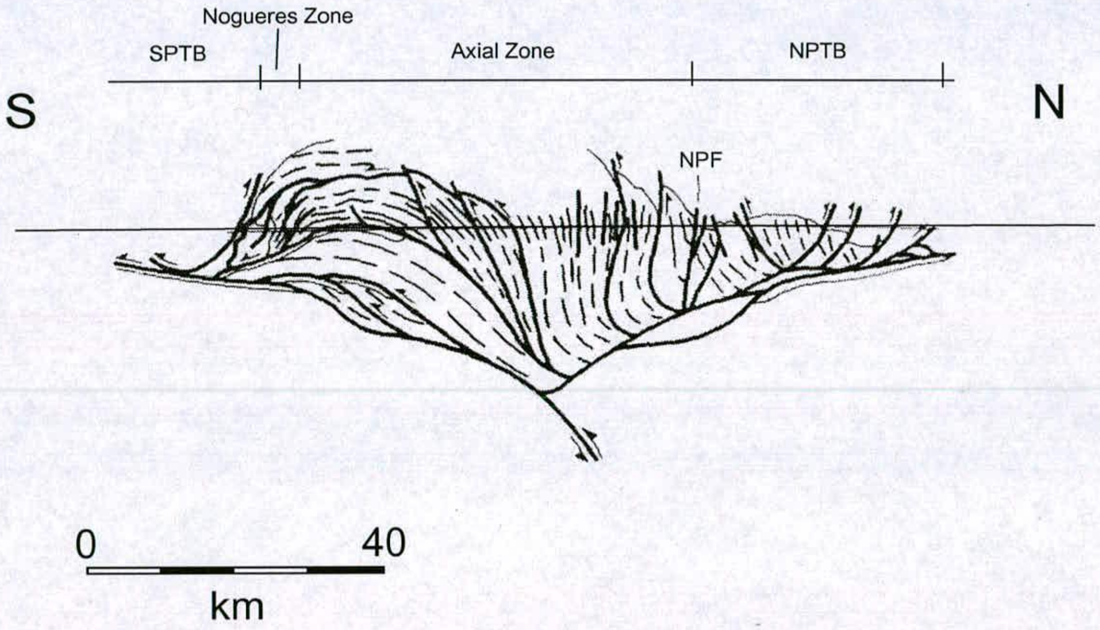

Figure 2.11 Geometrical relationship between Alpine thrusting of Palaeozoic blocks and the Hercynian fabric within the Axial Zone (Muñoz, 1992). Bold black lines represent major Alpine-age thrusts and dotted lines represent the Hercynian fabric. Fabric and thrusts are sub-parallel, or form a small angle, and define the geometry of the Axial Zone antiformal stack.

Fig. 2.11
Relationship between Alpine thrusting and Hercynian cleavage
(Muñoz, 1992)

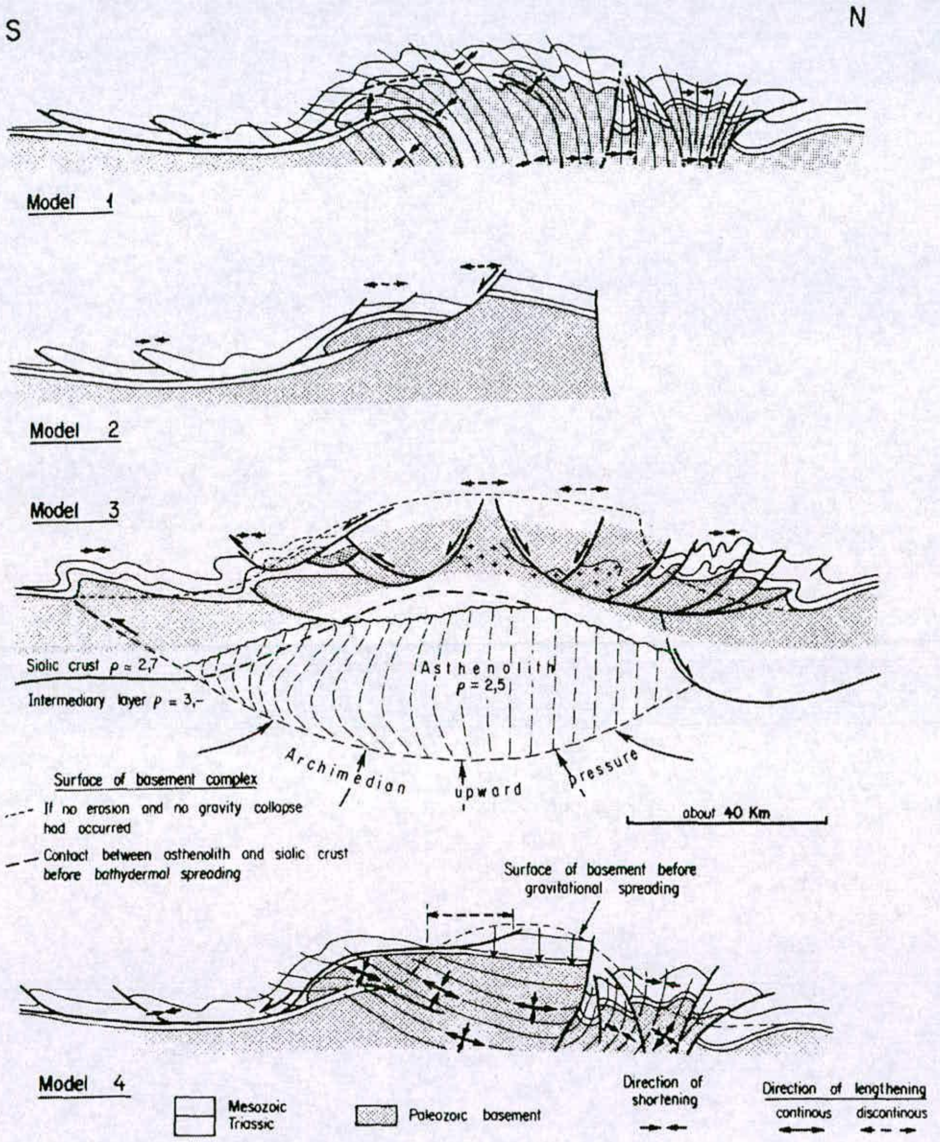

Figure 2.12 Four geodynamical models of the formation of the Pyrenees proposed by Choukroune and Seguret (1973). All fours models rely on the controlling influence of superficial gravimetric sliding along Triassic evaporite decollements to produce significant mass transfer to the north and south after early uplift of the central core of the range.

Fig. 2.12

Geodynamical models of Pyrenean evolution
(Choukroune and Seguret, 1973)

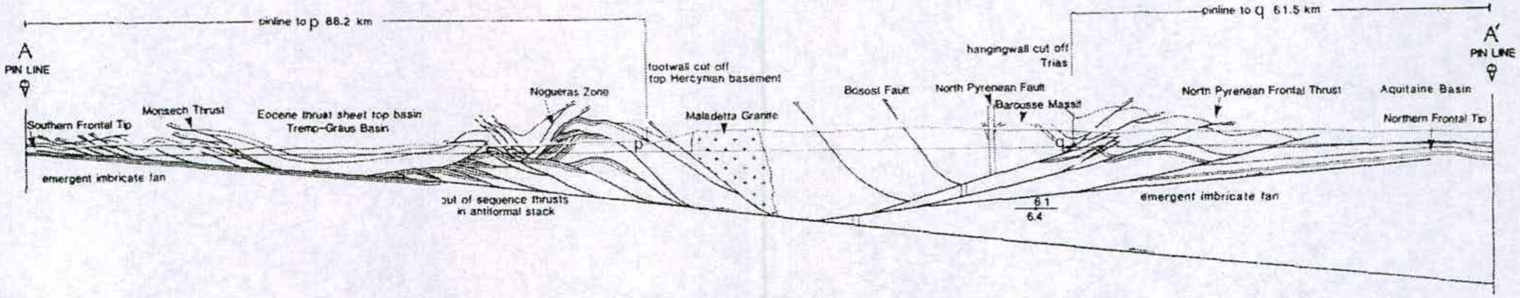

Figure 2.13 Balanced section through the central Pyrenees (Williams and Fischer, 1984). This interpretation required the orogen to form over low-angle decollements and to lie above undeformed lower crust in the Axial Zone. The Pyrenees were considered as an asymetrical chain with a prevailing south displacement of thrust sheets, north Pyrenean structures thus represented secondary thrusts, interpreted as backthrusts from the south-vergent system.

Fig. 2.13

Balanced thin-skinned cross section across the central Pyrenees
(Williams and Fischer, 1984)

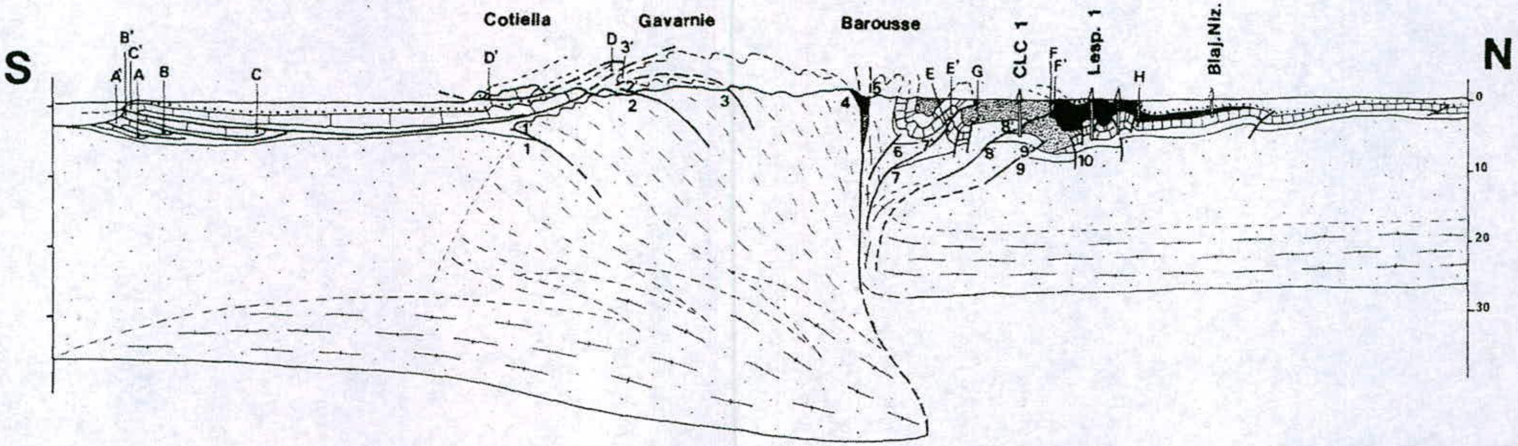

Figure 2.14 N-S section through the central Pyrenees (Seguret and Daignieres, 1986). In this 'vertical-tectonic model' the authors proposed significant amounts of shortening within the Axial Zone was accomodated by penetrative ductile deformation at depth, with discrete thrust displacements being only superficial structures. Overall shortening was considered to be significantly less than in previous models and to have been principally accomodated south of the NPFZ in the central region.

Fig. 2.14

N-S cross section of Pyrenean 'vertical' tectonic model (Seguret and Daignieres, 1986)

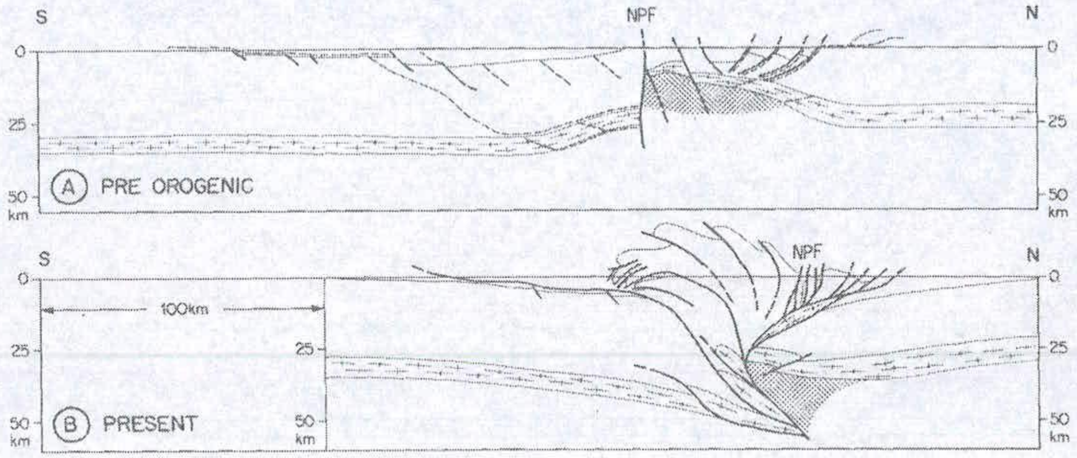

Figure 2.15 Balanced N-S section through the central Pyrenees along the ECORS profile (Roure et al., 1989). This interpretation was based upon the seismic data from the ECORS profile and proposes Iberian lower layered crust is stacked and imbricated beneath the Axial Zone. The reactivation and inversion of pre-existing fault lineaments, operative when the fault plane is consistent with the stress field orientation, is the governing factor behind the formation of the Axial Zone antiformal stack.

Fig. 2.15

Balenced N-S cross setion along ECORS profile (Roure et al., 1989)

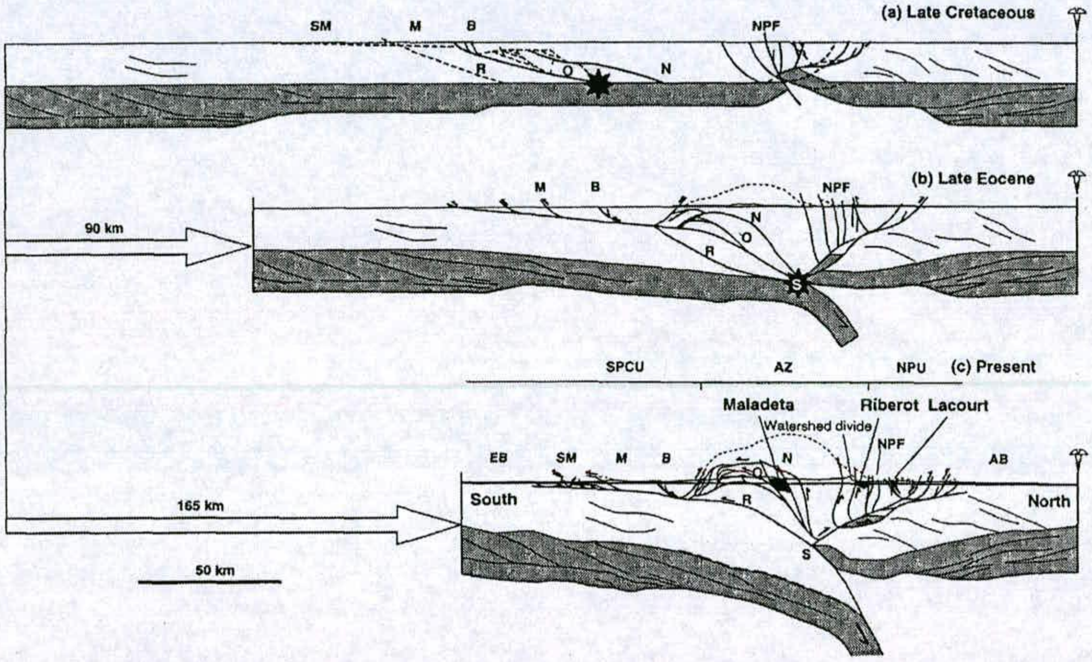

Figure 2.16 Late Cretaceous to Present tectonic evolution of the Pyrenees along the ECORS profile (Muñoz 1992; Fitzgerald et al., 1999). SPCU=South Pyrenean Central Unit; NPU=North Pyrenean Unit; SM=Sierra Marginales; M=Montsec; B=Boixals; R=Rialp; O=Orri; N=Nogueres; EB=Ebro Basin; AB=Aquitaine Basin. Tectonic delamination is proposed, whereby the flattening of existing Cretaceous extensional structures over the lower layered crust causes detachment between the upper and lower layered crust during Pyrenean inversion. Overall shortening values of 147 km for the upper crust, with ~15 km of vertical exhumation in the Nogueres and Orri thrust sheets, have been proposed.

Fig. 2.16

Tectonic evolution of the central Pyrenees
(Muñoz, 1992; Fitzgerald et al., 1999)

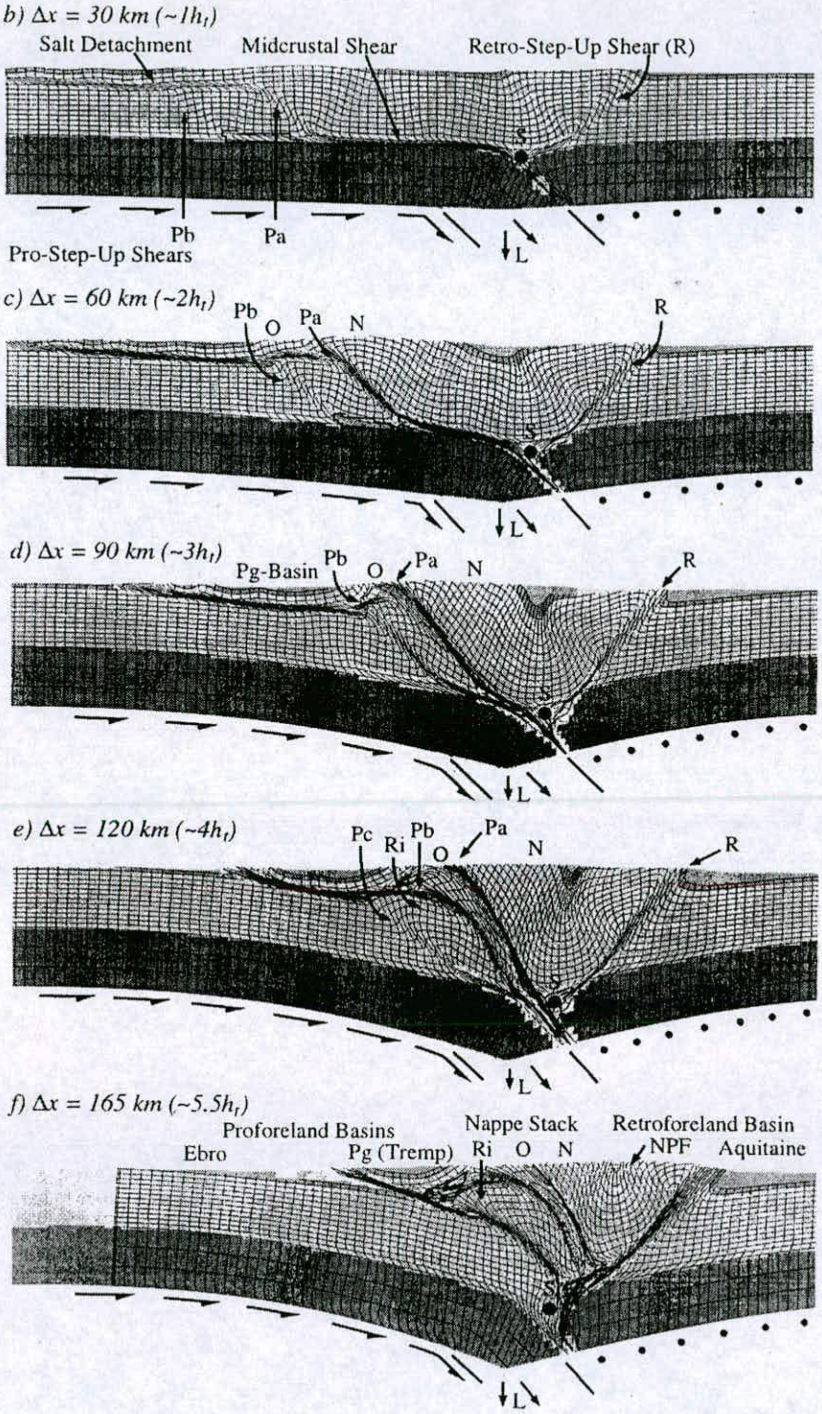

b) $\Delta x = 30\ km\ (\sim 1h_t)$

c) $\Delta x = 60\ km\ (\sim 2h_t)$

d) $\Delta x = 90\ km\ (\sim 3h_t)$

e) $\Delta x = 120\ km\ (\sim 4h_t)$

f) $\Delta x = 165\ km\ (\sim 5.5h_t)$

Figure 2.18 Comparison of observed transported and rotated Palaeozoic blocks with that predicted by Lagrangian grid numerical models (Beaumont et al. 2000). The macro-geometries of the orogen are accurately replicated by applying pre-determined structural lineaments with extremely low mechanical strengths. For the model run above, inferred cleavage orientations in the Palaeozoic basement dip moderately to the north prior to convergence and are assumed to be an inherited fabric which pervades the entire upper crust.

Fig. 2.17

Numerical modelling of central Pyrenean evolution

(Beaumont et al., 2000)

Fig. 2.18
Apatite fission track data and thermal modelling
(Yelland, 1990; Morris et al., 1998)

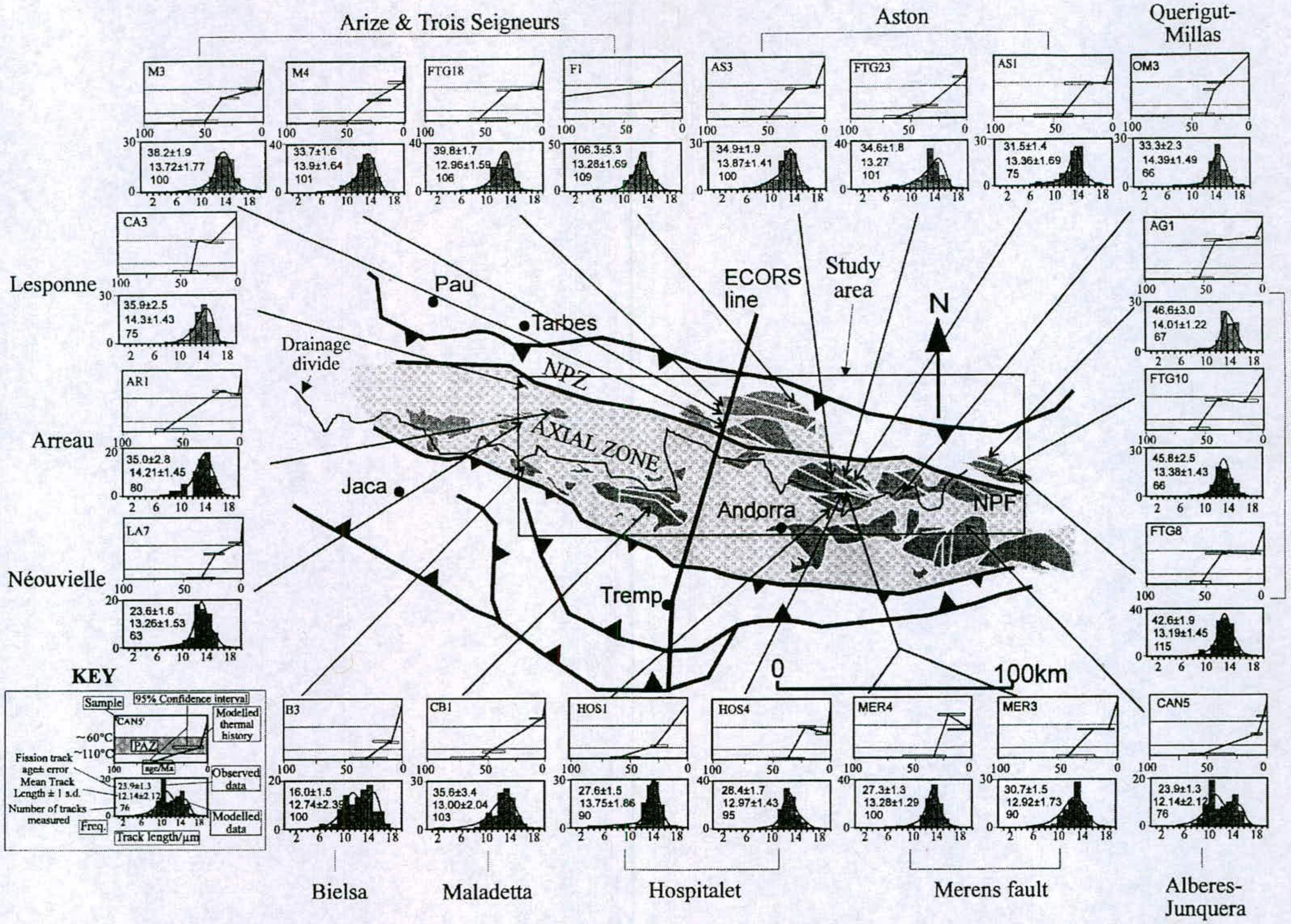

Figure 2.18 Apatite fission track data (Yelland, 1990) used by Morris et al. (1998) to model the spatial and temporal variability in the magnitude of erosional denudation from the mid-Eocene to the upper Miocene. Only one sample was retrieved from each sampling locality and the fission track data was modelled to provide cooling histories and, by inference, histories of erosional denudation over a large spatial domain.

Fig. 2.19
Vertical profile apatite fission track data
(Fitzgerald et al., 1999)

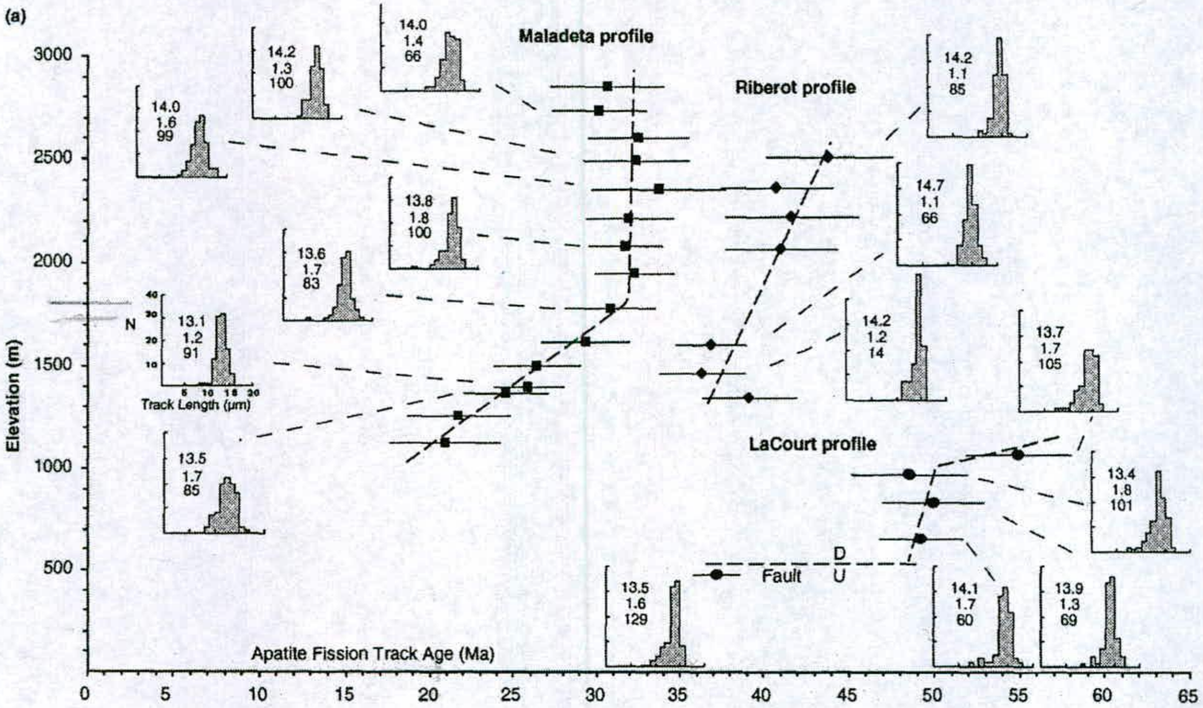

Figure 2.20 Apatite fission track age versus sample elevation plot for the Maladeta, Riberot and Lacourt massifs, with a selection of the track length distributions displayed as histograms (Fitzgerald et al., 1999). The age-elevation relationships were interpreted by Fitzgerald et al. to show initiation of relatively rapid exhumation at Lacourt at ~50 Ma, the continuous and steady exhumation at Riberot between ~35 and 45 Ma, and the rapid exhumation at the Maladeta until ~30 Ma which was followed by a period of thermal and tectonic stability and the formation of a partial annealing zone until ~5 Ma.

Chapter 3

Low Temperature Thermochronology

Objectives: The objectives of this chapter are to provide a review of the principles and applications of low temperature thermochronology and to outline the specific methodology used in this study. The strategies and assumptions used to convert cooling ages into exhumation histories are also discussed and provide a basis for interpreting the data presented in the subsequent chapter.

Chapter 3 – Low temperature thermochronology

The application of temperature-sensitive radiometric dating methods has provided earth scientists with ways of placing absolute time constraints upon processes influencing the upper crustal environment. With the use of temperature as a proxy for depth, the cooling histories of individual rock samples, or suites of samples, can be used to document the displacement of the rock column toward the surface at specific geographical localities. Bedrock is progressively exhumed by either tectonism or erosion, or both, and therefore transits up the geothermal gradient that universally characterises the earth's crust. In this way relative motions of bedrock can be calibrated against shallow level tectonics, surface processes and even landscape evolution (Kohn and Green, 2002). Furthermore, regional rates and patterns of exhumation over large temporal periods can be accurately estimated within well-defined spatial domains (Gleadow and Brown, 2000).

This chapter outlines the principles upon which (U-Th)/He (section 3.1) and fission track (section 3.2) thermochronology is based and addresses the relative merits and limitations of both systems. Numerical modelling of thermochronological data is briefly discussed (section 3.3) and the techniques used to derive information on denudational histories from thermochronological data are summarised (section 3.4) with particular reference to their application in orogenic systems. Finally, the methodology used in this study for both the thermochronological analysis and the modelling of the resultant data is outlined (section 3.5) (see also Appendix I).

3.1 Principles of (U-Th)/He thermochronology

Apatite (U-Th)/He (hereafter referred to as AHe) thermochronology is based on the principle of ingrowth of ^{4}He (α-particles) produced by U and Th series decay within certain minerals (Zeitler et al., 1987). Zeitler et al. (1987) proposed that the apatite ($Ca_5(PO_4)_3(OH, F, Cl)$ crystal lattice was retentive to such helium ingrowth over geological time-scales and subsequent studies have indicated that volume diffusion of ^{4}He is controlled by thermal activation above a 'closure temperature' (Wolf et al., 1996; Warnock et al., 1997). This suggests that the absolute abundance of the daughter product, in any given crystal is governed by the parent element concentration and the length of time since diffusion of He from the crystal stopped. The quantity of radiogenic ^{4}He, assuming no extraneous sources of He or subsequent He loss, can thus be expressed by the following equation:

$$^{4}\mathrm{He} = 8\,^{238}\mathrm{U}(e^{\lambda 238t}-1)+7/1.37.88\,^{238}\mathrm{U}(e^{\lambda 235t}-1)+6\,^{232}\mathrm{Th}(e^{\lambda 232t}-1) \qquad (1)$$

Where ^{4}He, U and Th refer to present-day concentrations, *t* is the time since He accumulation commenced or the AHe age, and λ's are the decay constants of the respective decay series (Farley, 2002; Ehlers and Farley, 2003). Therefore, as the absolute abundances of both parent (U and Th) and daughter (He) elements can be measured in any given sample, the time since diffusive loss stopped can be accurately determined. Importantly, the characteristics of He diffusion (and other factors influencing He loss) must be clearly understood before geological significance can be attributed to the derived AHe 'age'.

3.1.1 He diffusion behaviour

Most studies investigating the temperature control of He diffusion in apatite have been achieved through step heating experiments (e.g. Zeitler et al., 1987; Lippolt et al., 1994; Farley, 2000). Such studies have shown that He diffusion in Durango fluorapatite[1] obeys an Arrhenius relationship, at least at temperatures less than ~265°C (Wolf et al., 1996; Wolf et al., 1998; Farley, 2000), suggesting that thermal activation is the controlling parameter on He loss from the crystal lattice (Farley, 2000). The manner in which diffusivity scales with temperature can be expressed by the following relationship:

$$D/a^2 = D_o/a^2 e^{-Ea/RT} \qquad (2)$$

Where D is diffusivity, D_o the diffusivity at infinite temperature, E_a the activation energy, R the gas constant, T the temperature (°K), and *a* the diffusion domain radius (Fechtig and Kalbitzer, 1966). Diffusive loss appears to be unaffected by the cumulative fraction of gas released, which has been interpreted to indicate the presence of a single diffusion domain (Farley, 2000). This is further supported by the observation that He diffusivity scales with the inverse square of the grain size, suggesting that the grain itself is the diffusion domain (Farley, 2000; Farley, 2002). Importantly, this implies the relevant dimension for diffusion is

---

[1] Durango: $Ca_{9.83}Na_{0.08}Sr_{0.01}REE_{0.09}(PO_4)_{5.87}(SO_4)_{0.05}(CO_3)_{0.01}(AsO_4)_{0.01}F_{1.90}Cl_{0.12}(OH)_{0.01})$ (Young et al., 1969)

the prism radius of the apatite crystal, which represents the shortest pathway for He loss through the isotropic lattice, with prism length being of secondary importance (Farley, 2000; Farley 2002).

Data from several apatites indicate that the closure temperature (T_c) for He is ~65-70°C, for a cooling rate of 10 to 20°C Myr^{-1} and apatite prism diameter of 60 μm (Wolf et al, 1996; Ehlers and Farley, 2003; Farley 2000). As the diffusivity must scale with grain size, the closure temperature also scales similarly. Variation associated with this effect has been noted to be as much as ±5°C when grain radius varies from 50 to 150 μm (Ehlers and Farley, 2003).

3.1.2 α–particle ejection

^{4}He α particles produced by U- and Th-series decay are emitted with sufficient energy to travel significant distances through the apatite lattice (Ziegler, 1977; Farley et al., 1996) (**Fig. 3.1**). A fundamental requirement of employing the AHe system as a thermochronological tool is to be able to account for the potential loss or gain of the daughter product associated with this effect. The spatial separation between parent and daughter nuclei may result in the underestimation of the AHe age, when α particles are ejected from crystal edges, or the overestimation of the AHe age, when α particles are implanted from surrounding grains. Importantly, only the outermost ~20 μm of a crystal is affected as this is the maximum average value at which a parent nuclei is one stopping distance from the crystal boundary (Ziegler, 1977; Farley et al., 1996). However, as the vector which the emitted particle follows is random, the probability of α ejection or implantation, even from a parent nuclei located at a crystal edge, can only reach a maximum of 50%.

It is generally assumed that the effects of α implantation from outside the crystal boundaries are negligible. This assumption is valid for most apatite-bearing igneous lithologies, as the likelihood of α implantation is trivial due to the low statistical chance of being located close to other U- and Th-bearing minerals (e.g. apatite, zircon, monazite) (Farley, et al., 1996).

Therefore, the overall magnitude of the recoil effect is a singular function of the amount of α particles ejected from the crystal edges. This is determined by the surface-to-volume ratio and the distribution of parent atoms relative to the surface (Ehlers and Farley, 2003). Farley et al. (1996) note that failure to correct for the effects of α-ejection greatly impedes determination of precise AHe ages.

3.1.3 α–particle ejection correction

Mathematical frameworks for the quantitative evaluation of the effects of α-particle ejection on AHe ages have been formulated (Farley, et al., 1996; Farley, 2000). In order to apply these corrections the dimensions of the crystal must be accurately measured and the distribution of the parent nucleides within the crystal lattice must be quantified, or otherwise assumed to be homogenous (Farley, 2002). Recent work has underlined the importance of accounting for the effects of a heterogenous distribution of U and Th within the crystals analysed (Farley et al., 1996; Meesters and Dunai, 2002). However, as it is generally not possible to date grains in which zonation has been accurately quantified, either homogeneity is assumed or zonation is characterised from a selection of different crystals from the same sample.

Solutions have been calculated for the appropriate α-ejection correction (F_T: Farley, 2002) to the surface to volume ratio (β value), of a number of simple grain geometries, including spheres, cylinders and cubes (Farley et al., 1996). The geometry that most closely describes natural apatite is an isotropic, symmetrical, hexagonal prism. This has been modelled by Farley (2002) to be:

$$F_T = 1 + a_1\beta + a_2\beta^2 \qquad (3)$$

Where, the surface to volume ratio is given by $\beta = (2.31L+2R)/(RL)$ for a hexagonal prism (R is the half distance between opposing apices, L is the length), and a_1 and a_2 are coefficients obtained through iterative modelling (Farley et al., 1996; Farley, 2002).

As noted above, the magnitude of α-ejection or 'F_T parameter', the factor by which the measured age must be divided to obtain the α-ejection-corrected age, is dependent upon the surface-to-volume ratio, the distribution of parent elements and the α stopping distance (Farley, 2002). Consequently, the physical dimensions of the crystal to be dated becomes of primary importance. Crystals with relatively small values of β (large prism widths) require a small F_T correction, whereas those with large β values (small prism widths) require larger F_T corrections (Farley, 2002) **(Fig. 3.2)**. In order to apply an accurate F_T correction to measured AHe ages it is necessary to select grains with euhedral crystal morphologies, thereby allowing accurate measurement of prism widths and lengths and enabling the crystal terminations to be appropriately characterised.

3.1.4 Interaction of diffusion characteristics and α-ejection

An additional effect that should be noted is generated by the interaction of diffusion processes and α-ejection within the realm of the grain edge. As discussed above, α–ejection acts to deplete the relative abundance of He nuclei in the outermost 20 μm of the crystal. This acts to effectively reduce the He concentration gradient between the edge of the crystal and the diffusion domain (Farley, et al., 1996; Farley, 2000). As a consequence, the rates of He diffusion, which are driven by the concentration gradient, are also reduced causing modest increases in the AHe closure temperature of ~2%, or ~1.3 °C for a T_c of 65 °C (Farley, 2002). This effect is rendered negligible in crystals which cool rapidly (>10°C Myr^{-1}) through temperatures at which the AHe technique is sensitive (Farley, 2002; Meesters and Dunai, 2002).

3.1.5 AHe Partial Retention Zone (PRZ)

The extrapolation of laboratory-based diffusion studies to geological time-scales and temperatures has to a large extent been validated by numerous studies of natural samples documenting predicted patterns of diffusivity behavior (e.g. House et al., 2002; Warnock et al., 1997; Wolf et al., 1996; House et al., 1997). Samples extracted from boreholes with established geothermal gradients have yielded vertical profiles which depict a zone of rapidly decreasing ages with increasing depth, or increasing temperature, culminating with near-zero age samples at the base of the zone (e.g. Warnock et al., 1997). Wolf et al. (1998) name this the 'Partial Retention Zone' (PRZ) and define it to be the range of temperatures where AHe ages fall from 90% to 10% of the time for which a sample is isothermally held **(Fig. 3.3)**. This zone reflects the progressive increase in diffusive He loss, with increasing depth. Theoretically, at a given depth, samples held close to the closure temperature achieve a steady-state age whereby He production by U- and Th-decay is equal to the rate of diffusive He loss (Wolf et al., 1998). Both model predictions and studies in the natural setting indicate that He is completely lost from apatite above ~80°C and almost totally retained below ~40°C (Stockli et al., 2000; Wolf et al., 1998). Importantly, the range of absolute temperatures that defines any PRZ is determined by the amount of time the rock column is held at a given temperature (Wolf et al., 1998).

AHe ages reflect the passage of a sample through the PRZ. Samples which cool at slow rates between ~65 and ~40°C (e.g. ~1.2 °C Myr^{-1}: Reiners et al., 2003) will suffer a sustained period of partial diffusive loss of ^{4}He, such that the measured age does not reflect the time at which the sample passed through a specific closure temperature (Stockli, 2000). In addition, the sample will have spent substantial time at temperatures where small differences in the rate of He loss will propagate into large differences in AHe age (Ehlers and Farley, 2003). Therefore, variation of the factors that control He production and loss in samples, such as U- and Th- zonation or grain size, will generate large differences in the measured AHe age. In contrast, samples which pass rapidly through the PRZ (e.g. >10 °C Myr^{-1}: Farley, 2000) have little opportunity for partial diffusive loss and, thus, record the timing through the closure temperature and show little sensitivity to variations in grain size or the effects of zonation. As noted previously, the closure temperature (T_c) for the AHe system is determined by a number of factors, including grain size, and cooling rate, but is regarded to fall within the range of 60-75°C (Wolf et al, 1996; Ehlers and Farley, 2003; Farley 2000).

3.1.6 Extraneous He sources

The most widely adopted procedure for AHe dating involves the heating of apatite crystals to temperatures at which ^{4}He is liberated from the crystal lattice without structural damage or melting. This He concentration is measured, often as a ratio against a known ^{3}He 'spike', and then the samples are dissolved in weak nitric acid, and U and Th abundances measured by inductively-coupled plasma mass spectrometry.

Any He that has not been produced by U- or Th-decay will affect the apparent cooling age of a crystal. Mineral inclusions with high U and Th concentrations, such as zircon and monazite, are often found in apatite and may introduce a large excess of He during heating of the host crystal. These phases are not dissolved, and their contribution of U and Th is not analysed. Consequently, apatite crystals with undetected mineral inclusions may yield erroneously high AHe ages. Microscopic examination of the apatite crystals, prior to analysis, is thus required to ensure no other mineral phases are present. SEM backscatter images have been used to demonstrate the relatively common occurrence of heterogeneously-distributed sub-microscopic inclusions within apatite (e.g. Ehlers and Farley, 2003). Such effects likely contribute to the common difficulty in reproducing AHe ages within the theoretical analytical uncertainty (e.g. Spotila et al., 2004).

3.2 Principles of fission track thermochronology

Fission track dating is the study and characterisation of the effects, as opposed to the products, of a mineral-hosted radioactive decay scheme. Fission tracks are damage features produced when charged nuclear particles travel through insulating solids, rendering intense atomic-scale disruption to the crystal lattice (Ravenhurst and Donelick, 1986) (see **Fig. 3.4**). In apatite and zircon fission track dating (AFT and ZFT, respectively) the natural spontaneous decay of ^{238}U yields positively-charged fission fragments which transit the crystal at 180° from each other, stripping electrons from atoms in the surrounding lattice. The repulsion of the resulting ions then produces a linear damage trail at the ηm scale (Fleischer et al., 1975; Paul and Fitzgerald, 1992), each fission track being the product of a single spontaneous fission event (Brown et al., 1994). These 'fission tracks' can then be enhanced in size, to the μm scale, through the application of a chemical etchant and observed and quantified under high-power optical microscopes.

3.2.1 Fission track age dating and 'Closure Temperature'

As with the AHe technique, fission track age dating requires an estimate of the relative abundance of both the amount of radiogenic decay and the original parent isotope (^{238}U). The determination of both of these values can be achieved by quantifying the amounts of fission track damage within any given sample.

The natural, or spontaneous, fission tracks within a crystal represent a direct measure of the amount of radiogenic decay, or daughter product, and can be quantified under the microscope. The abundance of the parent ^{238}U can be determined by irradiating the sample with low-energy thermal neutrons, which induces fission of ^{235}U. As the natural ratio of ^{235}U/^{238}U is constant, the amount of fission track damage caused through the induced fission of ^{235}U can be used to accurately determine the absolute amount of ^{238}U. Following this technique, the fission track age of a given sample can be expressed as:

$$t = \frac{1}{\lambda_d} Ln\left(\lambda_d \frac{\rho_s}{\rho_i} \rho_d \zeta g + 1 \right) \qquad (4)$$

where t is the fission track-derived age; ρ_s and ρ_i are spontaneous and induced track densities; λ_d is the decay constant associated with α-particle decay of ^{238}U; ρ_d is the track density of a uranium-bearing glass standard used to monitor the neutron flux to which the sample has been exposed (dosimeter); g is the geometry factor and accounts for the omission of half the effective volume between the production of spontaneous tracks and the production of induced tracks, as the crystal must be halved to allow exposure of an internal surface; and ζ is the calibration factor for individual operators, determined through a number of calibrations of known age standards combined with a given dosimeter (Gallagher et al., 1998).

In the simple scenario, where a sample cools rapidly and the transition from zero-retention to complete-retention of fission tracks is achieved quickly, the observed fission damage will accurately record cooling of the crystal through the apatite fission track closure temperature (T_c). As discussed below, T_c is influenced by a number of factors but is generally regarded to fall within the range of ~110±10 °C (Gleadow and Brown, 2000; Balestrieri et al., 2003), and thus lies physically below the AHe closure temperature in the earth's thermal field.

3.2.2 Fission track length data

All newly-formed fission tracks display a characteristic track length of ~16μm, when etched using standard procedures (Gleadow et al., 1986). However, they are meta-stable features, as displaced atoms gradually diffuse to the original and more ordered state through time. Rates of track annealing are sensitive to, amongst other factors, temperature (Gleadow and Brown, 2000).

As the determination of a fission track age is reliant upon randomly-orientated fission tracks intersecting a given polished surface within the crystal, it follows that a shorter track length has a lower probability of intersecting the surface than a long track length (Laslett et al., 1982; Laslett et al., 1984) **(Fig. 3.5)**. This results in lower apparent track densities for a sample with annealed tracks and, therefore, an age that is relatively younger (Gallagher et al., 1998). Individual tracks will shorten to a length which is characteristic of the maximum temperature to which it has been exposed. Therefore, as the production of tracks is a continuous process, an individual crystal will have an array of track lengths, ranging from those newly-formed (~16μm) to those which have suffered annealing (<16μm).

It is obviously of great significance then to have a clear understanding of the distribution of fission track lengths in order to fully appreciate the significance of a fission track age. In addition, the two components can be compiled and used to quantitatively reconstruct the thermal history experienced by the sample (Gallagher et al., 1998).

3.2.3 AFT Partial Annealing Zone (PAZ)

Above temperatures of ~110±10 °C, all fission tracks, in Durango-type apatites, are considered to have been 'instantaneously' annealed on geological timescales (Laslett et al., 1987). The rate of annealing decreases rapidly with falling temperature and is extremely slow at temperatures less than ~60°C. The earth's near surface is characterised by a zone in which all fission tracks are annealed to some degree, the extent being determined by the residence time at a given temperature and apatite composition. This has been named the apatite fission track Partial Annealing Zone (PAZ) (Wagner and Van Den Haute, 1992; Fitzgerald et al., 1995). In a similar manner to that of the AHe Partial Retention Zone, ages decrease with increasing depth and culminate in near-zero age samples at the base of the PAZ (**Fig. 3.6**) (e.g. Gleadow and Duddy, 1981).

The implications for age determinations using fission track thermochronology is similar to that of the (U-Th)/He system. Samples which are exhumed rapidly through the AFT-PAZ experience little opportunity for track annealing and so the cooling age is representative of passage through the specific closure isotherm (110±10 °C). However, samples that reside within the AFT-PAZ for protracted periods have experienced annealing of all fission tracks, and so the cooling age is also progressively reduced.

3.2.4 Apatite fission track annealing

Considering the obvious importance of track lengths within any sample, it is a fundamental requirement of the correct interpretation of fission track ages that the annealing behaviour of tracks in apatite is well constrained and quantified. A number of laboratory experiments have been conducted in order to understand the annealing characteristics (e.g. Green et al., 1986; Laslett et al., 1987; Donelick et al., 1999). These studies have provided empirical calibrations which demonstrate the relative importance of a number of factors in controlling the annealing rate. Importantly, the relevant atomic-scale physical processes are still poorly understood (Gallagher, 2000), and so all annealing models are based upon empirical data which is extrapolated to geological time-scales and temperatures.

The key physical parameters that have been considered to control annealing kinetics are temperature and time. However, a number of other variables observed within natural apatites have been demonstrated to exert a strong influence. For instance, Cl-rich apatites have been shown to be significantly more resistant to annealing than F-rich apatites (e.g. Gleadow and Duddy, 1981). The relative atomic proportions of hydroxl and rare earth elements (REE) are also regarded to represent a controlling variable (Carlson, 1990; Carlson et al., 1999). In addition, the disparity between un-annealed track lengths in geological samples and those induced in the laboratory (typically 1-1.5μm shorter) suggest the characteristics of low temperature annealing are also not appropriately constrained (Donelick et al., 1999).

Owing to the large number of possible parameters that influence apatite annealing, the manner in which apatite populations are kinetically classified, and the way the fission track data is subsequently modelled, varies. A number of kinetic algorithms have been formulated to predict annealing behaviour as a function of specific parameters. Cl-content, and to a lesser extent OH-content, is often used as a proxy for annealing rates (e.g. Green, 1995). However, as demonstrated in Carlson et al. (1999), no single parameter or obvious combination of parameters can currently account for the kinetic variation observed among different apatite varieties. Barbarand et al. (1997) postulate that the rate of annealing is proportional to the crystal lattice cell dimensions, which reflects bulk chemical composition, and so can be used to quantify kinetics for a given population. Likewise, Donelick et al. (1999) use the solubility of apatite, as defined by the physical dimensions of the fission track etch pits parallel to the crystal c-axis (Dpar value), as an analogue of the crystal kinetics. Fission tracks exhibiting low Dpar values are considered to represent mineral compositions that anneal rapidly, as defined by a number of potential parameters, including Cl-content and OH-content. Tracks that exhibit high Dpar values represent compositions that anneal more slowly. Thermal histories derived through modelling of fission track age and length data, therefore, are highly sensitive to the choice of kinetic algorithm used.

3.2.5 Zircon fission track annealing and kinetics

A number of studies have shown that the kinetics of the zircon fission track (ZFT) system is broadly similar to the apatite system (Geotrack, 2004), albeit requiring significantly higher temperatures to induce annealing of tracks. However, unlike apatite fission tracks, the annealing characteristics of those in zircon are still not adequately constrained. This is due in particular to the current lack of knowledge on the influence of composition and of accumulated radiation damage to its annealing behaviour (Rahn et al., 2004). The latter effect is dominantly the result of ^{238}U decaying in a multi-step process to Pb. This produces intense microscopic-scale α-damage within the crystal, which may culminate in complete metamictisation, causing profound changes in the physical attributes of the structure and may lead to additional technical difficulties relating to anisotropic etching of the fission tracks (Rahn et al., 2004). The extent of α-damage depends upon the amount of time spent in temperatures immediately below the ZFT Partial Annealing Zone (PAZ). In turn, as samples enter the ZFT PAZ annealing of fission tracks will occur at a rate which is a function of the accumulated α-damage density and with the U-content of the sample (Rahn et al., 2004).

However, the relationship between α-damage intensity and the resultant fission track annealing rates has not been fully investigated, empirically or otherwise.

As a direct consequence there remains serious discrepancies between laboratory and field-based constraints on the effective closure temperature of the system. These discrepancies are likely to be exacerbated by strong variations in sample preparation and analysis techniques between different workers and through the lack of sufficient characterisation of older zircons with respect to age and track density (Rahn et al., 2004).

A number of experimental annealing studies have shown the complete removal of induced and etched fission tracks at 400-800°C on short time-scales in the laboratory (e.g. Yamada et al., 1995) and at 200-350°C over geological time-scales (e.g. Tagami et al., 1995). Importantly, closure temperatures have also been investigated in geochronological field studies and do not require time frames to be scaled up from the experimental. Of particular importance are those studies which have used neighbouring geochronologic systems, such as the apatite fission track and the biotite K/Ar system, to constrain and calibrate zircon ages against a thermal frame of reference (e.g. Soom and Hurford, 1990; Scott et al., 1998; Batt et al., 1999; Bernet et al., 2002). Such studies have proposed closure temperatures ranging from 196±18°C (Bernet et al., 2002) to 255°C (Brandon et al., 1998) in areas which have been demonstrated to have exhumed monotonically from temperatures where complete annealing of zircon fission tracks occurred to temperatures regarded to be below the ZFT T_c. Importantly, as with the apatite fission track system, the closure temperature scales with the cooling rate, with higher cooling rates promoting an increase in the closure temperature. Brandon et al. (1998) apply both experimental annealing data and use geochronologic field constraints to propose a closure temperature range of 210-245°C for α-damaged zircons, with a corresponding increase of cooling rates of 1 to 40°C/Myr, respectively **(Fig. 3.7)**.

3.3 Thermal modelling of thermochronological data

As outlined in sections 3.1 and 3.2, the interpretation of thermochronological cooling ages as reflecting a particular event or passage through a specific closure temperature can only be applied in samples that have experienced rapid cooling through the relevant closure temperature (Farley et al., 2002). All other cooling ages reflect the accumulation of radiogenic decay products, or decay damage, plus the partial restoration of the sample to it's previous state, with zero decay products, owing to residence in either the partial retention- or partial annealing zone.

Consequently, numerical modelling of cooling ages, along with other sample-specific parameters, such as track length distributions and Dpar values for fission track samples, or grain dimensions and zonation characteristics for (U-Th)/He samples, is required. A number of numerical models have been formulated for different radiometric systems which enable the interactions between given samples and specific thermal histories to be predicted (e.g. Gallagher, 1995; Ketcham et al., 2000; Dunai et al., 2003; Ehlers and Farley, 2003). However, the model output is clearly dependent upon the annealing or diffusion algorithms used and the laboratory techniques applied to quantify the thermochronlogical cooling ages (Barbarand et al., 2003).

'Forward' modelling techniques are used to calculate the thermochronological ages, and also the track length distributions for AFT samples, resulting from a known or estimated thermal history, as a function of the kinetic models imposed (Gleadow and Brown, 2000). Alternatively, the process can be inverted, where a given thermochronological age, and other appropriate parameters such as track length distributions or grain size dimensions, are used to define a series of plausible thermal histories (e.g. Ketcham et al., 2000). It is invariably the case that a large number of time-temperature (*t*-T) histories may share an equal statistical chance of producing a given cooling age, and so additional *t*-T constraints are often imposed, such as stratigraphic or crystallisation ages (Ketcham et al., 2000).

3.4 Denudation histories from thermochronological data

AFT and, more recently, AHe thermochronometry has been applied in a number of convergent orogenic settings to provide quantitative information on crustal exhumation. The sensitivity of these systems to low crustal temperatures enables insights to be gained on processes which potentially govern rates of cooling, such as tectonic- or erosional denudation. Therefore, if the thermal history of samples can be ascertained or, more specifically, the manner in which a given sample cools through low temperatures in the crust, then the relative timing, rates and amounts of exhumation, and by inference denudation, can be estimated. A number of different methods have been applied to determine accurate denudation histories from mineral cooling ages.

3.4.1 Thermal reference frame method

Firstly, if the mineral ages can be shown to represent cooling through a specific closure temperature, then different thermochronometers from the same rock sample can be used to track its passage through successively lower temperature isotherms (e.g. Balestrieri et al., 2003). In this way, the progressive displacement of the rock column toward the free cooling surface, associated with unroofing through denudation processes, can be documented (**Fig. 3.8**). Demonstrating that a cooling age represents closure of the specific radiometric system can be achieved through thermal modelling of the age in association with track length data, for the fission track system, or grain size and zonation effects, for the AHe system.

In order to convert estimated closure temperatures to palaeodepths, and therefore attach an absolute value to amounts and rates of exhumation, the cooling ages must be considered with regard to a thermal reference frame or geothermal gradient. Through this technique, time-averaged exhumation rates can be estimated over very large temporal domains which may far exceed those achieved through analysing samples using only one thermochronometric system.

A requirement of attaching a thermal frame of reference to a particular thermochronological age is to account for a number of parameters which may govern at what paleodepth closure of the radiometric system took place. This palaeodepth is defined by the closure temperature of the specific mineral, which, as noted in sections 3.1 and 3.2, is known to scale with a number of variable parameters such as cooling rate, chemical composition and grain size, and by the thermal regime of the crust at the time of sample closure. A number of variable factors, associated with ongoing exhumation and interaction with the free cooling surface, however, dictate the nature of the geothermal gradient within any given section of the rock column.

As erosion progressively displaces the rock column toward the surface, heat is correspondingly advected upwards until thermal relaxation occurs and the initial, or a new found steady-state, thermal regime is reached (Mancktelow and Grasemann, 1997; Brown and Summerfield, 1997). If exhumation commences abruptly this may result in the dramatic increase of the near-surface geothermal gradient compared to its pre-exhumational thermal state (**Fig. 3.9**). The magnitude of this effect is a function of the rate of exhumation, the temperature of the rock before exhumation occurred and, to a lesser extent, the duration of exhumation and the pre-exhumational geothermal gradient (Brown and Summerfield, 1997; Moore and England, 2001). Numerical modelling of these advective influences on the thermal regime have indicated the effects to only be significant when the denudation rate is relatively high (>300 mMa^{-1}: Brown and Summerfield, 1997; 1000 mMa^{-1}: Brandon et al.,

1998) and the depth of denudation occurring at these rates exceeds several kilometres prior to the sample passing below its specific closure temperature (Brown and Summerfield, 1997). Importantly, the timing at which a sample cools below a particular closure temperature is relatively insensitive to the effects of advection, and so determining the timing of onset of a period of denudation is not inhibited (Brown and Summerfield, 1997).

The local thermal regime may also be strongly influenced by the presence of large wavelength surface topography. As the wavelength of topography increases, the distortion of a given isotherm from the horizontal becomes more enhanced (Mancktelow and Grasemann, 1997). This effect decreases exponentially with distance from the finite topographic surface (Braun, 2002). Therefore, for thermochronometers characterised by low closure temperatures, such as AHe and AFT, the closure temperature isotherm can become significantly perturbed in high relief settings. The direct implication of this is that the palaeodepth of the closure isotherm may be substantially increased/decreased and deformed as a function of the overlying topography (**Fig. 3.10**).

Previous workers (e.g. Brandon et al., 1998; Balestrieri et al., 2003; Reiners et al., 2003) have applied erosion models to relate closure temperature, depth, exhumation rate, and age as a function of the following parameters; pre-exhumational geothermal gradient, thermal diffusivity, depth to constant temperature, and mean annual surface temperature. Diffusion and annealing characteristics from the applied thermochronological system are also required in order to predict the interaction between the evolving thermal regime and the generated mineral cooling age. These techniques allow the prediction of the temperature and palaeodepth of a specific closure isotherm at a specific time and, thus, enables the amount of exhumation to the mean elevation to be calculated since mineral closure occurred. To account for elevation differences between sampling sites, relative to the mean elevation of the long-wavelength topography, an elevation correction is also added to derive total exhumation depth (Reiners et al., 2003; Brandon et al., 1998). Therefore, total exhumation for each sample is given by the derived closure depth plus the difference between the sample collection elevation and the mean elevation (**Fig. 3.11**). The rate at which exhumation occurred is thus determined by dividing the calculated closure depth by the measured thermochronological age. Importantly, application of the technique assumes that constant exhumation in a given area has occurred since movement of the sample through the closure depth and, therefore, provides only time-averaged rates since closure. This may be verified by interchronometer age differences and age-elevation relationships from vertical transects (Reiners et al., 2003).

3.4.2 Spatial reference frame method

If a suite of samples are collected over a range of elevations but from within a limited spatial domain, thereby utilising the surface topographic relief, the resultant thermochronometric ages can be considered to be fixed to a known vertically-defined frame of spatial reference. In principle, this can be considered to represent a 'vertical' section of the rock column and thus will depict progressively younger cooling ages, with increasing palaeodepth, as the samples passed through the closure isotherm (Balestrieri et al., 2003). By attaching the ages to a spatial (vertical) frame of reference, the reliance upon crudely estimated geothermal gradients for calculating denudation rates is eradicated **(Fig. 3.12)** and the absolute amount of denudation for the sampled profile remains unchanged. Consequently, the gradient of the slope defined by plotting thermochronometric age against elevation, or palaeodepth, represents the vertical velocity of samples relative to the relevant closure isotherm (Reiners et al., 2003).

However, as outlined by Gallagher et al. (1998), there are a number of potential over-simplifications that must be considered when interpreting data in terms of quantifying the rates at which denudation occurred using this method.

As with the thermal reference frame technique, the deformation of isotherms by surface topography may significantly influence the manner in which thermochronologic ages are set as the sampled rock column is progressively exhumed. As noted by Stüwe et al. (1994), samples associated with a 'vertical' frame of reference generally also have a significant lateral component, commonly spanning topographic profiles with a given wavelength. A consequence of this is that samples from the same profile may have markedly different amounts of exhumation required to transport them from the closure isotherm to a mean elevation. In particular, the depth to the closure isotherm is likely to be greater under valleys than under ridge crests (Reiners et al., 2003) **(Fig. 3.13)**. The differences decrease with depth and higher temperature isotherms or, for a given temperature isotherm, with decreasing topographic wavelength (Braun, 2002; Reiners et al., 2003).

In addition, if the closure isotherm was perturbed to a similar orientation to that of the modern surface then the implicit assumption that the sampled rock column transited the closure isotherm on a perpendicular trajectory is invalidated. This will result in high elevation samples yielding relatively younger ages and low elevation samples yielding relatively older ages (Stüwe et al., 1994; Mancktelow and Grasemann, 1997) **(Fig. 3.14)**. Consequently, the denudation rates derived from the gradient of the age-elevation relationship will be over-estimated. The discrepancy between the real and the apparent denudation rate becomes of increasing importance for faster rates of cooling (Stüwe et al., 1994). Braun (2002) has also highlighted the potential inversion of age-elevation relationships caused by the reduction of relief after the samples have passed through the relevant closure temperature.

With increased parallelism of isotherms at the time of mineral closure toward the orientation and angle of the sampled profile, the amount of exhumation required to exhume a non-vertical profile through the T_c reduces. Therefore, a sub-vertical profile in an area with perturbed isotherms may only indicate the maximum amount of exhumation required. The derivation of absolute rates of exhumation also requires corrections to be applied to the 'apparent' exhumation rate depicted by the age-elevation profile. Following the procedures of Braun (2002), the correction factor applied is based upon the ratio of relief on specific closure isotherms to the relief of topography of a given wavelength, also known as the admittance ratio, α. The 'model' exhumation rate can then be derived as it is equal to the 'apparent' exhumation rate multiplied by $(1-\alpha)$ (Braun, 2002; Reiners et al., 2003). A number of numerical models have been formulated (e.g. Braun, 2003; Ehlers et al., 2003) to simulate different exhumational and topographic evolutions and their impact on a given thermal regime and the derived cooling ages (e.g. House et al., 1997; Pik et al., 2003). Models such as the finite element code 'Pecube' (Braun, 2003) were developed specifically to solve the three-dimensional heat transport equation in uplifting and eroding lithospheric blocks which have an evolving, finite-amplitude surface topography. This enables time-temperature (*t*-T) histories of model rock particles, defined by delineating specific areas on an imposed digital topographic surface, to be generated for a given history of exhumation and topographic evolution. These t-T paths can then be input into thermochronometer-specific forward modelling software to generate model ages and age-elevation profiles.

In addition to isothermal perturbations influencing the age-elevation relationship, effects associated with the thermochronometric systems themselves may also produce 'apparent' rates of exhumation which do not necessarily reflect true values. Samples that have resided in a PRZ or PAZ (section 3.1.5 and 3.2.3, respectively), and have been exhumed to the surface by a successive period of accelerated exhumation, will provide a clear positive age-elevation relationship that does not document the exhumational history (Fitzgerald and Gleadow, 1990). Instead, the cooling age profile represents a protracted period of time when the rock column was in thermal stability, the decrease in age with depth being determined by the progressive influence of diffusion at higher temperatures. Therefore, the quantification of denudation rates is only achievable by exclusively considering the age-elevation profile from below the palaeo PRZ or PAZ, or below the profile break-in-slope (**Fig. 3.15**). This demonstrates the importance of identifying what trends are represented by a particular suite of samples (Gallagher et al., 1998). As noted previously, this can be achieved through careful consideration of grain size-to-age correlations or track length information, in the (U-Th)/He and fission track system, respectively.

Finally, the role of tectonics, both before and after mineral closure, must be firmly established before a 'vertical' profile can be properly interpreted in terms of exhumational history. Firstly, the style of the denudation being documented must be clearly established. For example, if samples are collected from the footwall of a large normal fault, then cooling ages may be very similar, irrespective of elevation. However, the steep gradient of the resulting age-elevation plot does not necessarily correspond to the rate at which tectonic denudation occurred. Areas characterised by only erosional denudation will not show this type of effect. Secondly, the occurrence of late-stage deformation after the cooling ages in a vertical profile have been determined, particularly in convergent orogenic settings, must also be considered. Any form of rotation or offset, if not identified, precludes the quantification of the rates of denudation because the gradient of the age-elevation slope is artificially increased or decreased (e.g. Johnson, 1997).

3.5 Application of thermochronology to Pyrenean orogenesis

As outlined in Chapter 1, the primary objective of applying thermochronological analyses in this study is to investigate to what extent exhumation, driven by erosional denudation, was partitioned and localised in the interior of the range during Pyrenean orogenesis and during the 'post-orogenic' period.

This is achieved by deriving specific information on the erosional histories from four structural domains in a north-south transect across the central Pyrenees. Mineral cooling ages, and other thermochronometer-specific data, from both vertical profiles and single-elevation samples, are modelled to derive statistically-acceptable thermal histories for each sampling zone. The thermochronological data will then be used to identify strong spatial variability in exhumation at specific temporal intervals. The magnitude and spatial distribution of this exhumational partitioning will be used to assess potential controlling mechanisms which can then be corroborated through field geology. In order to maximise the extent of the exhumation record documented, a number of thermochronometers with markedly different temperature sensitivities are applied (apatite (U-Th)/He (AHe), apatite fission track (AFT) and zircon fission track (ZFT)).

3.5.1 (U-Th)/He analytical methodology

Rock samples were weighed, measured and outer surfaces cleaned prior to undergoing mineral separation procedures. Individual blocks were disaggregated into gravel-size particles using a hydraulic rock splitter and jaw crusher. This sediment was further reduced to coarse-sand size fractions through the use of a roller mill.

After cold-water cleaning the samples were divided according to magnetic susceptibility using a Frantz Isodynamic separator. Non-magnetic fractions were further separated using gravimetric contrasts in dense solutions (lithium polytungstate: density 2.82 gmL^{-1}, viscosity 10cP) to isolate the heavy mineral fractions, including apatite and zircon (see Appendix I for full mineral separation procedures).

Individual apatite crystals were screened under plane and cross-polarised light at 218X magnification for mineral contaminants, structural defects, appropriate morphology and size. The physical dimensions of between 5-15 inclusion-free crystals per sample were measured and packed into stainless steel capsules and wrapped in degassed Cu foil. Variation of grain diameter was minimised within individual aliquots to reduce the standard deviation of the recoil correction within each population to ±0.5% (Farley et al., 1996). Where possible, perfectly euhedral crystals with similar length-to-width ratios were used for analysis. The character of all crystal terminations was recorded to be either 'normal', 'parallel' or 'irregular' (**Fig. 3.16**) and, along with the physical dimensions, used to provide the appropriate α-ejection correction following the procedures of Farley (2002). Where enough contaminant-free apatite was recovered, individual sample analyses were reproduced in duplicate or triplicate (Ehlers and Farley, 2002).

All (U-Th)/He analyses were performed at the Scottish Universities Research and Reactor Centre, East Kilbride, Glasgow. Samples were heated in a double-walled resistance furnace at ~950°C for 35-minute intervals. The liberated gas was purified on hot and cold TiZr getters and liquid nitrogen-cooled charcoal trap for 10 minutes after heating. ^{4}He abundance was measured relative to a 99.9% pure ^{3}He spike in a Hiden HAL3F mass spectrometer. Samples were checked for quantitative degassing of He by subsequent reheating for 35-minutes.

Capsules were extracted from the furnace and the samples dissolved in 5% nitric acid and spiked with 3 ng ^{230}Th and 1.3 ng ^{235}U, and U and Th concentrations measured by VG PlasmaQuad 2 ICP-MS (see Appendix I for full (U-Th)/He analysis methodology).

The analytical uncertainty on age determinations for the AHe laboratory is ≤6% and is derived from replicate analyses of Durango apatite standards. Typically, multiple aliquots of the same sample yield a reproducibility of ±8-10% (Persano et al., 2002).

3.5.2 Fission track analytical methodology

The mineral separates used for AHe dating were also used for AFT determinations. All fission track slides were prepared and analysed at Apatite to Zircon Inc., Idaho, USA. Coarse apatite separates were mounted in epoxide resin and cured for 1 hour at 90°C. Internal crystal surfaces were exposed using 0.3μm Al_2O_3 slurries on a polishing wheel. Spontaneous fission tracks intersecting the polished surface were then etched in 5.5N HNO_3 for 20 seconds (±0.5) at 21°C and densities counted using both reflected and unpolarized transmitted light at 1562.5x magnification.

For apatite track-length analysis the grain mounts were irradiated with ^{252}Cf-derived fission fragments in a nominal vacuum chamber to maximise track-length distribution measurements following the procedure of Donelick and Miller (1991). After re-etching, as outlined above, the length and crystallographic orientation, with respect to the c-axis, of natural, horizontal confined track lengths was determined at 1562.5x magnification with attached projection tube and digitizing tablet.

Fission track ages were determined by placing low-uranium muscovite sheet against the polished and etched grain mounts prior to irradiation at the Washington State University nuclear reactor (45 minutes at thermal neutron fluence of 10^{16} neutrons/cm^2 at 1MW power level; position D9). Similar mica sheets were placed next to ^{235}U-doped CN-1glass for standardization purposes. The mica sheets were immersed in 48% HF at 20°c (±1°c) for 15 minutes (±15 seconds) in order to reveal fission tracks induced through irradiation. Fission track ages were calculated using the radioactive decay equation (4) with an analyst zeta calibration factor of 113.8±2.9. Annealing kinetics were inferred using the arithmetic mean of 1-4 measured Dpar values (μm units) per grain. (see Appendix I for full AFT analysis methodology).

3.5.3 Quantification of parent nuclide distribution

The distribution of U within the analysed samples was estimated by quantifying the extent of fission track zonation within representative AFT slides. This was achieved using a Zeiss axioplan stereoscopic microscope, a projection tube and a digitizing tablet, calibrated against a micrometer, in the Earth Sciences department of the University of Glasgow. One hundred apatite crystals were selected, under x1100 magnification, from the AFT grain mount according to crystal morphology, physical dimensions and lack of structural damage or mineral inclusions. These were considered to represent similar crystals to those used for (U-Th)/He analysis. The induced track distribution of each crystal, from the fission of ^{235}U, was then observed on the adjacent muscovite sheet (external detector) and the homogeneity of the parent nuclide discerned. For heterogeneous U distributions the crystals were categorised into either 'rim-enriched' or 'core-enriched' varieties and the enriched zone measured. Previous studies of geochemical variations in natural apatites suggest the distribution of ^{238}U and ^{232}Th is well characetrised by the distribtuion of ^{235}U (Dempster et al., 2003). This relationship is assumed in the apatites used in this study.

3.5.4 Quantification of apatite/inclusion composition

In order to determine the chemical composition of the apatite species analysed, and of sub-microscopic mineral inclusions within the crystals, representative samples from each locality were imaged and analysed using a Scanning Electron Microscope (SEM) facility (Philips XL30CP) at the University of Edinburgh SEM facility. The size and morphology of the samples were determined by mounting them upon adhesive analytical stages and gold-coating them, in order to minimise charging under the electron beam, and using Secondary Electron (SE) imaging with an accelerating voltage of 20keV and a working distance of 10mm.

Geochemical contrasts and mineral inclusions were highlighted using polished and carbon-coated samples and the Backscatter Electron (BSE) detector, also using a 20 keV accelerating voltage and a working distance of 10mm. Different minerals and phases were identified as different greyscale tones according to the mean atomic number of the relevant mineral.

Qualitative analysis of the elements present in the phases was achieved by using, together with the BSE imaging, Energy Dispersive Spectrometry (EDS) and the PGT Spirit X-ray analysis system. Apatite and inclusion compositional data are presented and discussed in chapter 4.

3.5.5 Modelling of thermochronological data methodology

All AHe and AFT ages and track length parameters were modelled using thermochronometer-specific software to derive time-temperature histories (*t*-T) histories which were consistent with the data. In order to provide additional constraints the (U-Th)/He and fission track modelling was integrated for samples where both were determined. This enables cooling ages from more than one temperature range to be attributed to specific sections of the same *t*-T path, whilst satisfying the diffusion or annealing characteristics for each system.

AFTSolve©, developed by Richard Ketcham and Donelick Analytical Inc. (2000), was used to 'reverse' model all the measured fission track ages and track length distributions, and DeComp (Meesters and Dunai, 2002) was used to model the (U-Th)/He data, following the procedures outlined below.

3.5.5.1 Numerical modelling of fission track data

For each apatite fission track sample, model ages and track length distributions were calculated for between 10,000 to 50,000 randomly-generated *t*-T histories. Predicted age and track length parameters for each thermal history were then considered against the measured fission track age and track length data. The assignment of relative 'merit of fit', between the modelled and measured values, is based upon two numerical tests which evaluate the degree of statistical precision and is outlined in Ketcham et al. (2000). The two tests are combined to provide a single 'merit function' (Ketcham et al., 2000) which allows *t*-T paths to be evaluated against each other. *t*-T paths with a merit function of 0.5 were deemed to have a 'good fit', whilst those with a value of 0.05 were deemed to have an 'acceptable fit'. All values above 0.05 indicate that the model has not failed the null hypothesis test that forms the basis of the statistical test (Ketcham and Donelick, 2000).

Model runs were generated using the minimum number of imposed thermal restrictions on the *t*-T paths. This was done to promote flexibility in path generation and thus to allow all statistically valid thermal histories to be considered. Starting conditions for each model run began above the total annealing temperature of the most resistant apatite being modelled, as defined by the Dpar values for each sample. The age at which this thermal constraint was imposed was determined by multiplying the oldest pooled fission track age by 1.5. This technique ensured that all *t*-T paths initiated in a state of total annealing and, thus, the entire fission track data set was determined by the modelled history. An end-constraint for all model runs was also defined in order to only allow thermal histories which culminated with surface temperatures (10° C) at 0 Ma.

A Monte Carlo algorithm was used to generate the random *t*-T paths as this is considered most suited to mapping out the full potential breadth of time-temperature possibilities within limited imposed thermal constraints (Ketcham et al., 2000). The Dpar value was used to define the kinetic populations (see section 3.2.4) and the annealing model used was that published by Ketcham et al. (1999). This combination was employed because the empirical data, upon which the annealing model is based, is derived from Dpar measurements of a variety of apatite compositions and kinetic groups, and provided the most versatility for modelling the data. Where more than one kinetic population had been defined for an individual sample, through Dpar analysis, the overall population was divided into subsets that exhibited relatively uniform behavior. As noted by Ketcham and Donelick (2000), this generally corresponds to two end-member populations, which were modelled, and a highly transitional intervening population which was not modelled.

The procedure outlined above generates an envelope in time-temperature space within which all the *t*-T paths produced by the numerical model, which show a pre-defined statistical precision with the measured AFT data, are accommodated (**Fig. 3.17a**).

3.5.5.2 Numerical modelling of integrated AFT and AHe data

To further constrain the thermal history of the sampled profiles the integration of the fission track-based *t*-T paths with the lower temperature AHe data is necessary. This enables a number of *t*-T paths to be discriminated from the many statistically-viable alternatives which satisfy the fission track data and which are represented within the AFTSolve thermal envelopes. A number of thermal histories can be derived that are consistent with both thermochronometric systems and thus a larger part of the temperature range and exhumational record. In addition, the remaining thermal histories predicted through modelling of the fission track data can be rejected on the basis that they are not compatible with the lower temperature data.

Individual *t*-T paths, for samples which had been analysed for both AFT and AHe, were exported from the AFTSolve software as a numerical series of time-temperature co-ordinates. These values were then downloaded into DeComp (Meesters and Dunai, 2002). Age derivation in DeComp, from a user-defined thermal history, is based upon the ^{4}He production-diffusion equations presented by Meesters and Dunai (2002). The program enables AHe ages to be generated for a given *t*-T path for apatite crystals of known diffusion parameters, alpha-emission distance, parent nuclide zonation characteristics and physical dimensions. As the algorithm used in the software takes into account the effects of alpha-ejection, the predicted AHe ages must be considered to represent ages that have not had a F_T correction applied.

For each sample modelled, the default settings for the diffusion parameters and alpha-emission distance (20μm) were retained (Ziegler, 1977; Farley et al., 1996). The distribution of parent nuclides within the crystals was regarded to be homogenous (section 4.3.4) and the mean prisms diameters for individual sample aliquots were used for the physical dimensions of the diffusion domain.

A maximum of 50 'appropriate' AHe ages were generated from the exported AFT-derived thermal histories. 'Appropriate' model ages are defined as those which lie within the analytical uncertainty of any of the uncorrected AHe data. If appropriate ages were not produced additional *t*-T paths were generated in AFTSolve, up to a maximum of 250,000. If the available thermal histories could still not produce suitable AFT and AHe ages, the statistical 'goodness of fit' boundary conditions, as defined in the AFTSolve model runs, were relaxed to 0.05 or 'acceptable' levels (see section 3.5.5.1). This has the effect of producing additional *t*-T paths with slightly reduced statistical confidence in the fit between measured and modelled fission track datasets, but which still indicate the model has not failed the null hypothesis that forms the basis of the statistical test. If the AFT-derived thermal *t*-T paths could still not be reconciled with the AHe ages then thermal constraints, up to a maximum of two, were imposed on the starting boundary conditions for the fission track modelling. This has the effect of generating *t*-T paths with the same statistical precision to the measured data but within specific *t*-T constraints, so as to induce the model to output *t*-T paths which are likely to reproduce the AHe age. Samples in which both the modelled AFT and AHe data could still not be matched within the analytical uncertainty and reproducibility of the technique were considered to not be reconcilable.

The procedure outlined above generates a maximum of 50 *t*-T paths for each individual sample. Each alternative *t*-T history pass pre-defined statistical thresholds for both the actual fission track and AHe data (**Fig. 3.17b**).

3.5.6 Interpreting denudation from thermochronological data

As outlined in section 3.4, deriving information on erosional histories, and in particular erosion rates, from mineral cooling ages commonly utilises a number of implicit and explicit assumptions about the thermal structure of the crust and about the manner in which the rock column is displaced toward the surface. By assuming various thermal and geomorphological boundary starting conditions, the evolution of the thermal structure, with respect to the evolving topography and imposed exhumation histories and cooling rates, may be synthetically modelled (e.g. Brandon et al., 1998; Reiners et al., 2003). Through this technique the precise temperature and palaeodepth of a mineral closure isotherm (T_c) in a particular location may be estimated and, thus, the thermochronological data used as a proxy for erosion rates.

However, it is important to recognise that in areas undergoing active orogenesis the thermal and topographic 'starting conditions' for such a model are purely speculative. This is particularly the case in regions which have not been exhumed at continuous rates, but instead over a number of transient exhumational 'events', and in thermochronological studies which do not document the entire exhumational history, but instead document from a point in time during active exhumation. Previous studies in the Pyrenees (e.g. Fitzgerald et al, 1999) indicate that the application of low temperature thermochronology on samples extracted from the orogenic interior will document complex histories and will not record them from their initiation. Consequently, any thermo-kinematic modelling of this region would be founded upon a number of unconstrained input parameters and would generate a variety of alternative output scenarios which could only be reliably discriminated from each other by the application of higher temperature thermochronometers.

3.5.6.1 Estimating values of exhumation

The fundamental objective of this study is to simply identify relative differences in the magnitude and timing of exhumation, driven by erosional denudation, between different crustal sections of the Pyrenees. To achieve this it is necessary to be able to estimate at what depths in the crust, both relative and absolute, specific samples were at specific times during Pyrenean mountain-building, rather than to quantify the rates at which they were displaced toward the surface. By identifying areas that have been exhumed to greater extents than others, constraints on the mass flux during orogenesis can be established and the mechanisms through which it is localised be investigated. Therefore, it is most appropriate to interpret the thermochronological data in a relatively simplified manner and to defer to the least interpretational data treatment, without recourse to applying complex, unconstrained, and largely speculative thermal modelling. Thus, we provide a range of reasonable input parameters that define the thermal regime and we assume the most simple starting topographic scenario. In this manner it is possible to derive a range of acceptable values of exhumation for specific sites whilst imposing the fewest assumptions upon the data. The input parameters used in this study are listed below:

1. As there are no independent constraints on the palaeo-geothermal regime of the Pyrenean crust, we provide minimum and maximum values for the sampling region. The present-day upper-crustal (10 km) geothermal gradient is ~28°C km^{-1} within the Pyrenees (Zeyen and Fernàndez, 1994) and previous thermochronological studies have used estimated values of 25-30°C km^{-1} during orogenesis (Morris et al., 1998; Fitzgerald et al., 1999). We use minimum and maximum values of 25-35°C km^{-1}, respectively, for the upper crust and a mean surface temperature (T_s) of 10°C. As this range is applied to the entire study area, any inaccuracies associated with applying an incorrect palaeo-geotherm would not affect relative differences in exhumation and would only scale-up or scale-down the absolute values, and is thus of relatively limited importance. It is worth noting, however, the profound influence an inaccurately estimated geothermal gradient would have on attempting to calculate exhumation rates from the data.

2. As there are no available independent constraints on the topographic evolution of the orogen, we assume that at the time of mineral closure the largest-scale morphology of the mountain belt approximated that of the modern system; that is to say, mean elevations on the orogenic-scale and the approximate positioning of the main drainage divide have been retained during orogenesis. This notion is to some extent supported by numerical models which indicate large-scale topographic steady state is achieved rapidly during the early growth of an orogen (Batt and Braun, 1999; Willett et al., 2001). It is also assumed that the broad geometry of the isothermal surfaces were largely parallel to the mean elevation of the longest wavelength topography (~150 km), upon which small wavelength perturbations were locally imposed (Brandon et al., 1998; Reiners et al., 2003).

3. We assume the T_c values for the radiometric systems applied fall within pre-defined temperature ranges, as determined by a variety of possible cooling rates. It is not appropriate to apply specific T_c values because the thermal regime immediately prior to the time of mineral closure remains unconstrained, and thus, the T_c value cannot be precisely determined. The end-member closure temperature values for rapidly cooled samples (5 to 20°C Myr^{-1}) are 65-75°C T_c for the AHe system (effective mean crystal radius of 80 μm for this study) (Farley, 2000), 105-115°C T_c for the AFT system (assuming Durango apatite composition;

after Laslett et al., 1987), and 210-245°C T_c for the α-damaged ZFT system (Brandon et al., 1998; Rahn et al., 2004).

These parameters and assumptions enable the range of palaeo-depths at which specific thermochronological ages were set to be calculated. The implications and limitations of these assumptions on palaeo-closure depths are further discussed in Chapter 6. In order to convert the palaeo-depths to the value of exhumation required to transport the samples to the surface, it is necessary to (i) correct for the variation in sampling elevation and (ii) to quantify the uncertainty of these values due to isothermal perturbations.

(i) As the amount of exhumation is defined as that which is required to transport a given sample from the T_c to the mean elevation, it is necessary to correct for the variation in elevation with respect to the mean value. This correction value, or 'effective elevation' (el_e) (Brandon et al., 1998), is then added to the inferred closure depth; thus total exhumation is equal to closure depth plus the difference between the sample collection elevation and the mean elevation of the sampling area (Brandon et al., 1998; Reiners et al., 2003). The mean elevation for the closely-spaced Axial Zone sampling localities (section 4.1) was determined from a 44 km^2 tile of ~90-metre SRTM digital topography data (U.S.G.S., 2004) and using ArcInfo software (ESRI, 2000). The same procedure was followed for sites outside of the Axial Zone, though local tiles of topography were sampled around specific sites.

(ii) As noted in section 3.4.1, the presence of high relief valleys and ridges may locally perturb isothermal surfaces by significant amounts. Consequently, the calculated palaeodepth of any T_c may be substantially increased or decreased as a function of the overlying topography. However, the extent of these perturbations cannot be reliably constrained because the nature of the topography in the interior of the mountain belt during orogenesis can only be speculated upon. In this study it is therefore assumed that any local thermal perturbations away from the large-scale geometry, which was described by the mean elevation and large wavelength of the mountain belt, are characterised by those that are imposed by the local topography in the modern setting. That is to say, the amplitude and wavelength of the modern short-wavelength topography in the central Axial Zone is a broad approximation of the local topography during the time of mineral closure, and therefore topographically-induced isothermal perturbations are also similar for a given set of uplift rates and thermal parameters. We also assume the advective influences of increased rates of exhumation on the thermal regime did not increase the local geothermal gradient beyond the temperature range given above (25-35 °Ckm^{-1}).

By applying these assumptions and employing the calculations of Stüwe and Hintermüller (2000), it can be shown that the magnitude of the topographic relief within the modern Pyrenean setting would induce perturbations of ~0.23 m on the 70°C isotherm (~T_c for the AHe system), ~0.13 km on the 110°C isotherm (~T_c for the AFT system), and ~0.02 km on the 225°C isotherm (~T_c for the ZFT system) for a maximum uplift rate of 2 km Myr^{-1} in a steady-state setting (thermal diffusivity (K): 31.536 km^{2}Myr^{-1}, depth (L) and temperature (TL) of the lower boundary: 100km and 1000°C, respectively, Uplift rate (U): 2 kmMyr^{-1}, Wavelength (I) and Amplitude (H) of topography: 8 and 1.2 km, respectively). This provides, therefore, an envelope of potential uncertainty on the ranges of exhumation amounts derived from the thermochronological data. Importantly, this estimation of isothermal perturbation must be considered a maximum value for the thermal steady state scenario as it is based upon the greatest topographic dimensions in the sampling areas and upon a two-dimensional representation of infinitely linear valley-ridge topography, whereas the true three-dimensional 'peak' topography of the region would have significantly less ability to perturb isotherms (Stüwe and Hintermüller, 2000; Reiners et al., 2003).

In summary, by combining the above ranges of T_c for each radiometric system with the assumed ranges of geothermal gradients during mineral closure, and taking into account the assumed mean annual surface temperature, a minimum and maximum value for the palaeo-depth at which the T_c resided may be calculated. Therefore, if it is assumed the exhuming rocks pursued an approximately vertical trajectory from the point of mineral closure to its position at the surface, the absolute amount of exhumation, plus the uncertainty imposed by the maximum topographic perturbation of isotherms, may be estimated by the following equation (5):

$$E \pm \mathrm{d}z_c = \frac{T_c - T_s}{\mathrm{d}T / \mathrm{d}z} \tag{5}$$

Whereby, E is the total exhumation, and by inference erosion, required to displace the rock from the closure temperature to the 'effective elevation' (el_e) at the surface, dz_c is the possible change in palaeo-depth of the specific closure temperature associated with topographic perturbations, T_c is the closure temperature of the thermochronometer, T_s is the surface temperature, and dT/dz is the geothermal gradient.

A potential oversimplification of this methodology, however, is that the calculations to define isothermal perturbations assume the system is maintained in thermal steady state and, therefore, cannot account for highly transient thermal effects, such as thermal relaxation following rapid pulses of exhumation (Lock and Furlong, 2003). Furthermore, a number of workers have also demonstrated the strong relationship between increasing and decreasing topographic relief, and the associated changing isothermal perturbations, with changes in the rock uplift rate as the landscape approaches or moves away from topographic steady-state (Burbank and Pinter, 1999; Schmidt and Montgomery, 1995).

3.5.6.2 Topographic and thermal Modelling ('Pecube')

In order to objectively assess the assumptions used above and the potential influence of a non-steady state thermal regime and a highly variable topographic evolution, the AHe data from this study was also modelled by G.J. Lynn and the author (Gibson et al., submitted) using the finite-element code 'Pecube' (Braun, 2003) (section 3.4.2). This enables *t*-T histories to be synthetically generated, and cooling ages forward-modelled using thermochronomter-specific modelling programs, for a given exhumation history and topographic evolution. The boundary conditions, topographic and exhumational parameters used, and the model results are discussed in chapter 4.

3.5.6.3 Estimating rates of exhumation

As noted previously, calculating rates of exhumation from the thermochronological data is not of primary importance for this study. However, it should be considered what information can be reliably derived without additional assumptions being invoked. As the total amount of exhumation that is required to transport specific samples to the surface can be calculated, and the precise age of the sample is documented with one or more thermochronometer, it appears to be a simple operation to convert the depth-to-age ratio to a time-averaged rate of exhumation. However, to follow this procedure would be to assume the rate at which exhumation had occurred since mineral closure to its appearance at the surface had been constant and continuous. During the transition from active orogenesis to the post-orogenic period this is likely to be a highly erroneous and unwarranted assumption (e.g. Lock and Furlong, 2003) and would provide only acceptable rates for an unacceptable scenario. Likewise, to assume age-elevation relationships from samples from the vertical profiles perfectly characterise the rate of vertical velocity which the rock column exhumed through the appropriate T_c, is to assume that the near-surface isotherms were entirely unperturbed from the assumed horizontal geometry. Again, this is likely to be erroneous in an actively exhuming region (e.g. Braun, 2002) and thus, where discussed, all age-elevation relationship-derived rates are considered only to be maximum values. The relative steepening or shallowing about a kink in an age-elevation profile, however, could only be achieved by either an effectively instantaneous and significant change in the near surface thermal perturbations, presumably by a dramatic shift in local topography (Van der Beek et al., 2004), or by an increase or decrease in the exhumation rate. The effects of changing topography are addressed through PeCube modelling in Chapter 4 and are shown to be of limited importance with the scale of topographic wavelength documented in the sampling areas. Therefore, the steepening or shallowing of AER profiles is considered to be attributable to the relative acceleration or deceleration of exhumation rates in specific areas.

3.5.6.4 Additional considerations

Implicit in the procedure for calculating the amount of erosion required to exhume from T_c to the surface is that the rock particles were transported to the surface along vertical kinematic geometries, and that erosion occurred perpendicular to that path. Similarly, it is assumed that relative sample depths were constant and remain equivalent to the modern elevation differences. Any component of lateral advection, presumably driven by horizontal shortening, would lengthen the path that a thermochronometer would have to take to be exposed at the surface (Brewer et al., 2003). As noted by Batt and Brandon (2002), the higher the temperature at which the radiometric system closes, the higher the potential for accumulating lateral, as well as vertical, displacement with respect to the thermal field. Consequently, values of total erosion may be significantly more erroneous derived from the ZFT system than for values derived from the AHe system. With continued low-angle lateral advection, such as observed with subhorizontal thrusts, the erosional denudation of the thrust sheet may be significantly larger than the exhumation. Previous thermochronological studies in the Pyrenees (e.g. Fitzgerald et al., 1999; Morris et al., 1997), however, have regarded the influences of thrust trajectory to be negligible, and the primary influence of cooling in the upper crust to be governed by erosional denudation perpendicular to exhumation trajectory. This is largely based upon the assumption that underplating is the primary process driving erosion trajectories, and that the horizontal advection of rock particles is negligible. As an initial approximation of the distribution of erosion, this will also be assumed in this study and discussed further in Chapter 6.

Finally, it must also be considered whether the processes which act to exhume, and thus cool, the rock column are achieved primarily through tectonic denudation, such as extensional unroofing (Platt, 1986), or through erosional denudation. As there is no structural or metamorphic evidence to suggest that the central Pyrenean orogen has undergone any significant extension during its' Tertiary evolution (e.g. Zwart, 1979), we assume the latter alternative.

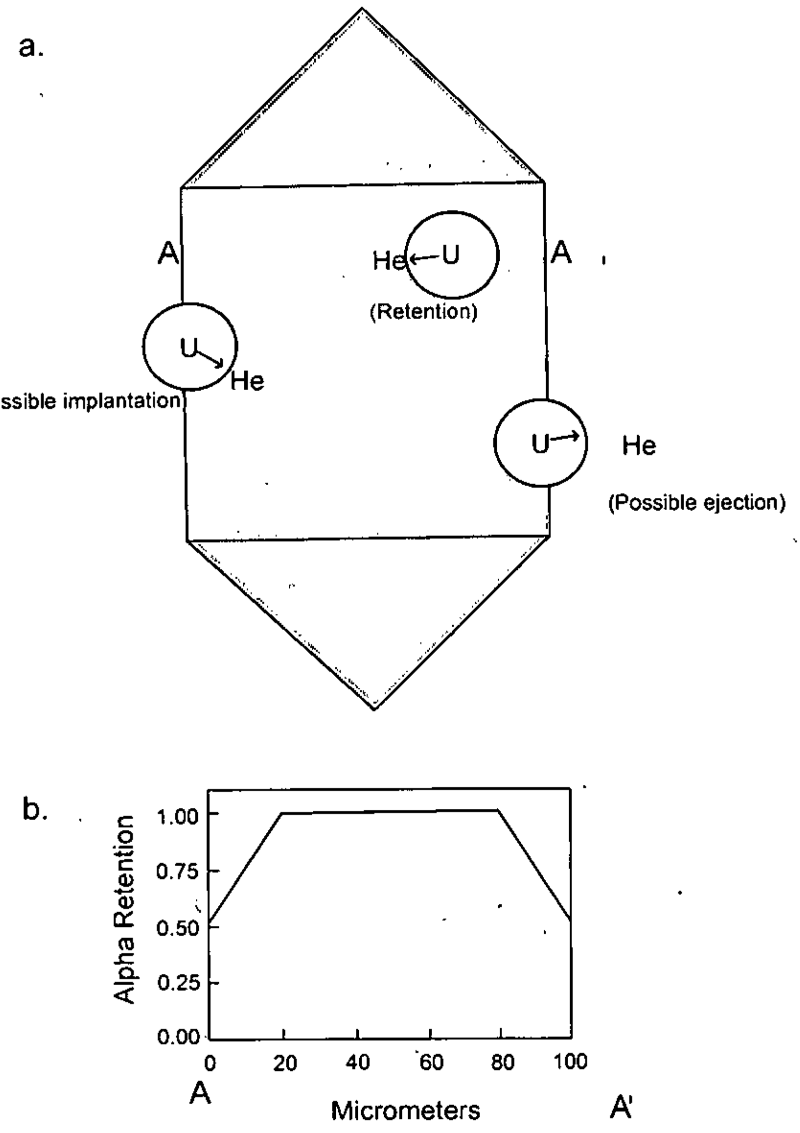

Figure 3.1 (a) The potential possibilities of He retention associated with the long stopping distances of α-particles from the site of parent nuclides in apatite; namely, α-ejection, α-implantation or α-retention. Nuclides located at the edge of the crystal boundaries have a 50% statistical chance of either retention or ejection (white circles define locus of points where He particle may come to rest). (b) Schematic representation of the change in α retention from the crystal boundary to the crystal core along the path A-A' (Farley, 2000)

Fig. 3.1

Nuclide stopping distances in apatite (Farley, 2000)

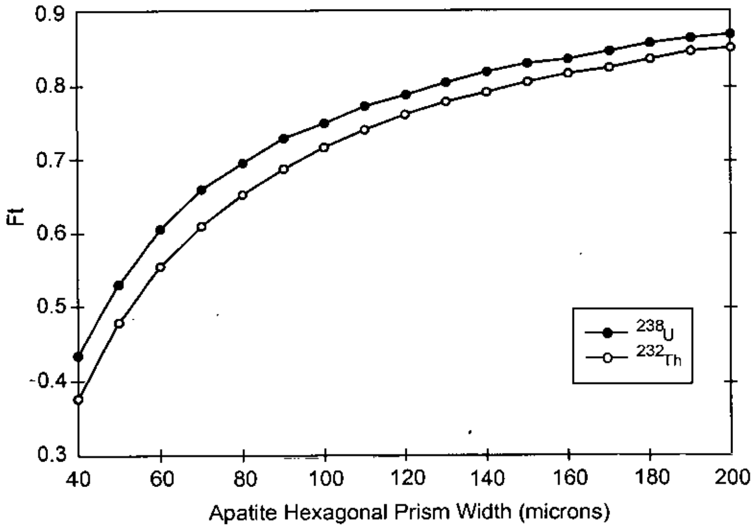

Figure 3.2 Plot depicting the Ft value (total fraction of α particles retained in the crystal) as a function of crystal diameter. This correlation is determined by the decrease in the surface-to-volume ratio with progressively larger crystal diameters. The difference between the $_{238}$U and $_{232}$U is associated with slightly different decay energies (Farley, 2000).

Fig. 3.2
Ft value as a function of crystal diameter
(Farley, 2000)

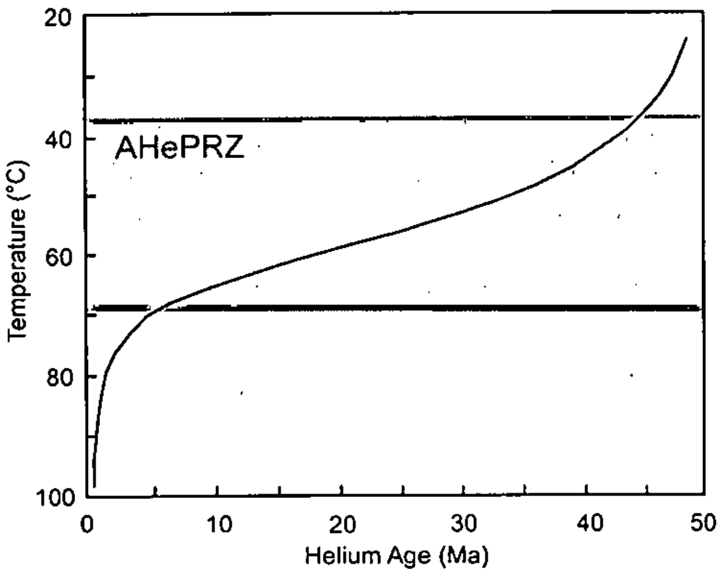

Figure 3.3 Plot depicting the He age range as a function of temperature for an isothermal holding time of 50 Myr. The He-PRZ (shaded region) is the temperature range in which He ages change most dramatically with temperature variation. He ages immediately below the He-PRZ have very high activation energies and diffusion rates and thus accommodate little $_4$He and yield a ~zero age Wolf et al., 1998).

Fig. 3.3
He age as a function of Temperature
(Wolf et al., 1998)

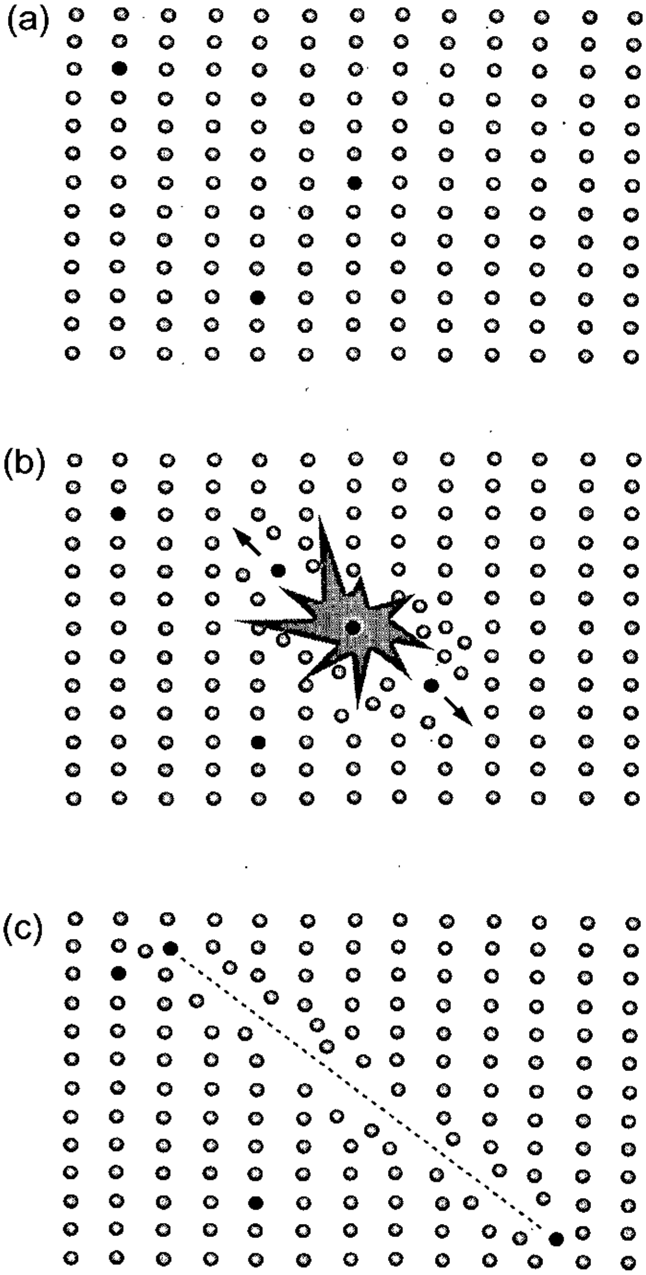

Figure 3.4 Cartoon representation of the 'ion spike explosion' model and the formation of fission tracks within an atomic crystal lattice. (a) parent nuclides (dark circles) are randomly distributed within the lattice. (b) Spontaneous fission of $_{238}$U generates two charged particles which recoil at 180° and act to electron-strip atoms in the surrounding lattice. (c) Fission particles lose energy through electron gathering and atomic collision and leave a damage trail or fisssion track at the ηm scale (Gallagher et al., 1998).

Fig. 3.4
'Ion spike explosion' model
Gallagher et al., 1998)

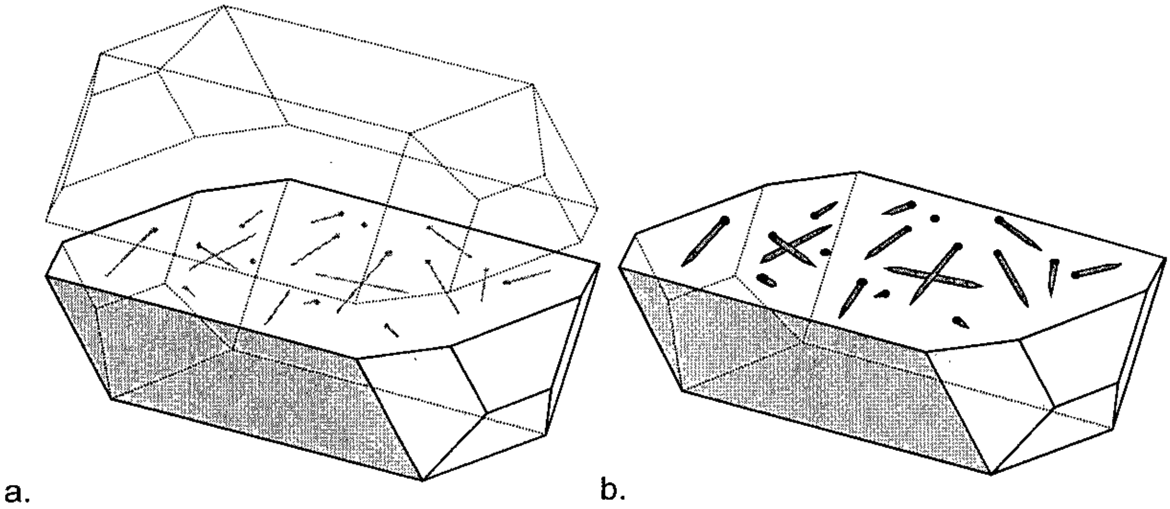

Figure 3.5 (a) Crystals are polished to reveal an internal surface which intersects with a number of fission track damage trails from the spontaneous nuclear fission of $_{238}$U. If the tracks have been annealed, and thus are shorter, the likelihood of them intersecting the polished surfaces are diminished and so the track density and, therefore, the calculated AFT age is lower. (b) When the surface is chemically etched the damage trails are enlarged to the µm scale and can be observed with an optical microscope. Tracks which do not intersect the surface but have a conduit for the etchant to reach them are also etched.

Fig. 3.5
Internal surfaces and confined fission tracks
(Gallagher et al., 1998)

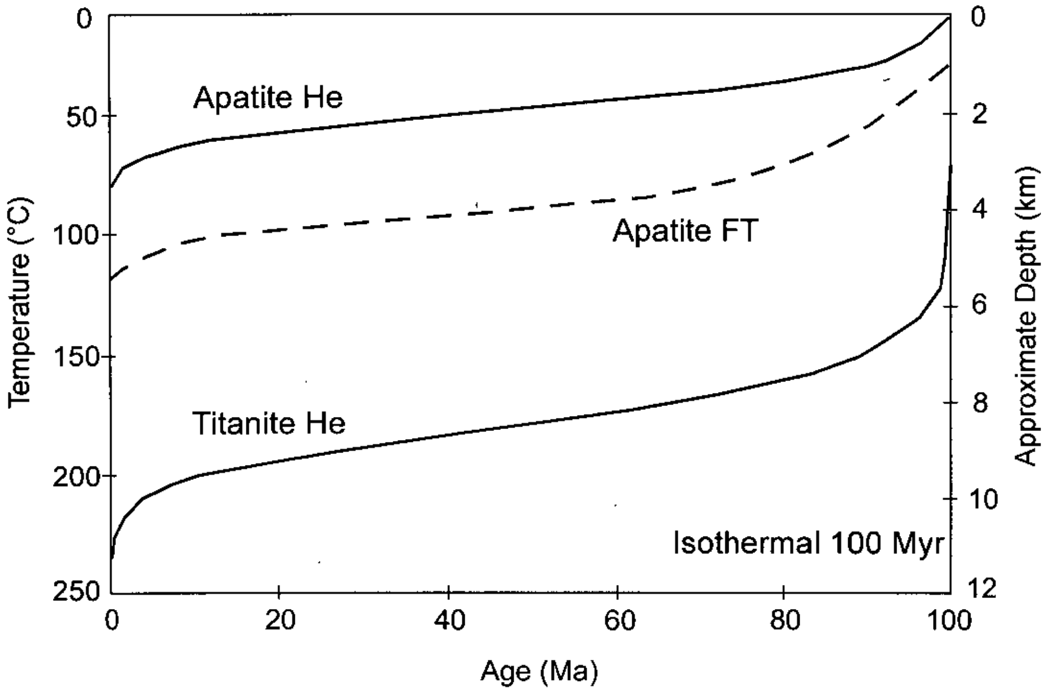

Figure 3.6 Plot depicting variation in AFT age as a function of temperature in an 100 Myr isothermal holding model. From low to high temperatures: the He Partial Retention Zone (PRZ); the AFT Partial Annealing Zone and the Titanite Partial Retention Zones, respectively (Farley, 2000).

Fig. 3.6

He age as a function of temperature

(Farley, 2000)

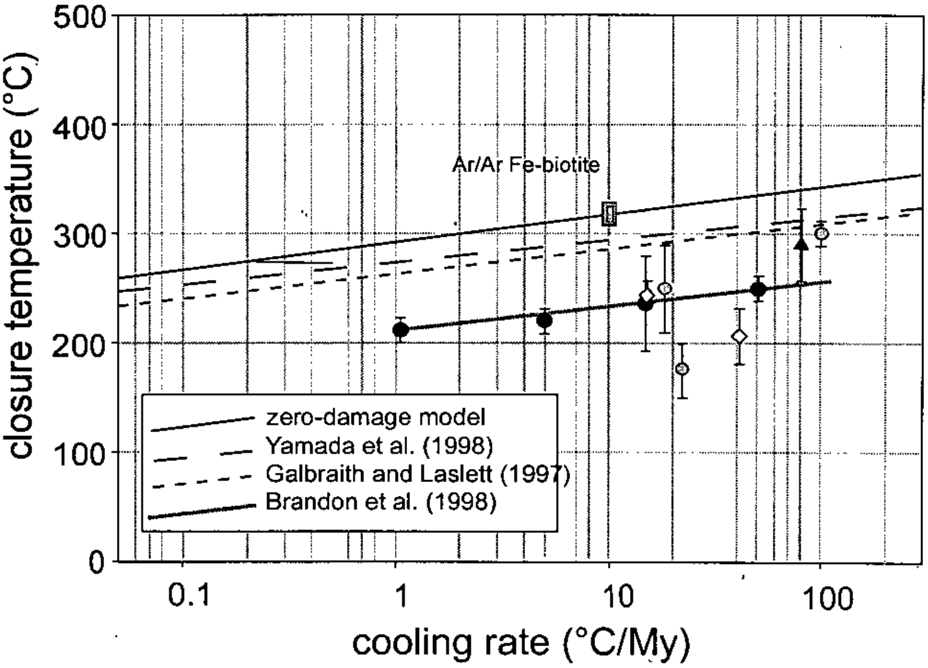

Figure 3.7 Plot depicting closure temperature variation as a function of cooling rate. Laboratory values calculated for zero-damaged zircons (upper line) (Rahn et al., 2004) and for low damage models (lower two lines) (Tagami et al., 1998; Galbraith and Laslett, 1997). Laboratory predictions compared to geologic constraints from the literature; (grey line: Brandon et al., 1998, based on direct comparison between Ar/Ar age spectra of Kfs), (black: Scott et al., 1998), (grey: Batt et al., 1999), (white: Hoish et al., 1997), (open diamond: Harrison et al., 1979).

Fig. 3.7
ZFT Tc as a function of cooling rate
(Rahn et al., 2004)

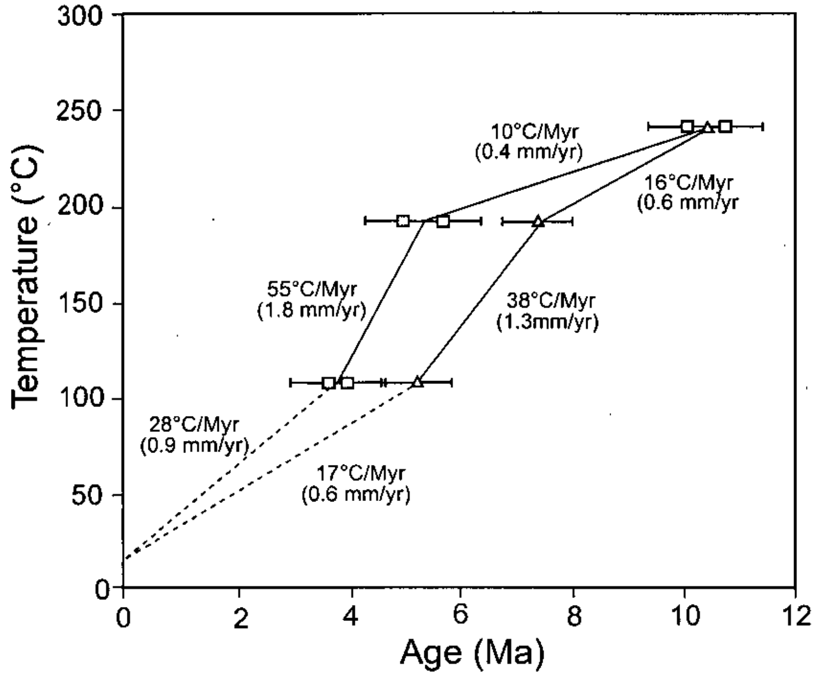

Figure 3.8 Plot depicting the mineral cooling ages for three differant thermochronometers (ZFT, AFT and ZHe) for samples from the Apuane Alps (Balestieri et al., 2003). Cooling rates, and thus exhumation rates, are time-averaged and are calculated assuming a geothermal gradient of 20°C/km.

Fig. 3.8

Exhumation rates from multi-chronomter studies
(Baliestrieri et al., 2003)

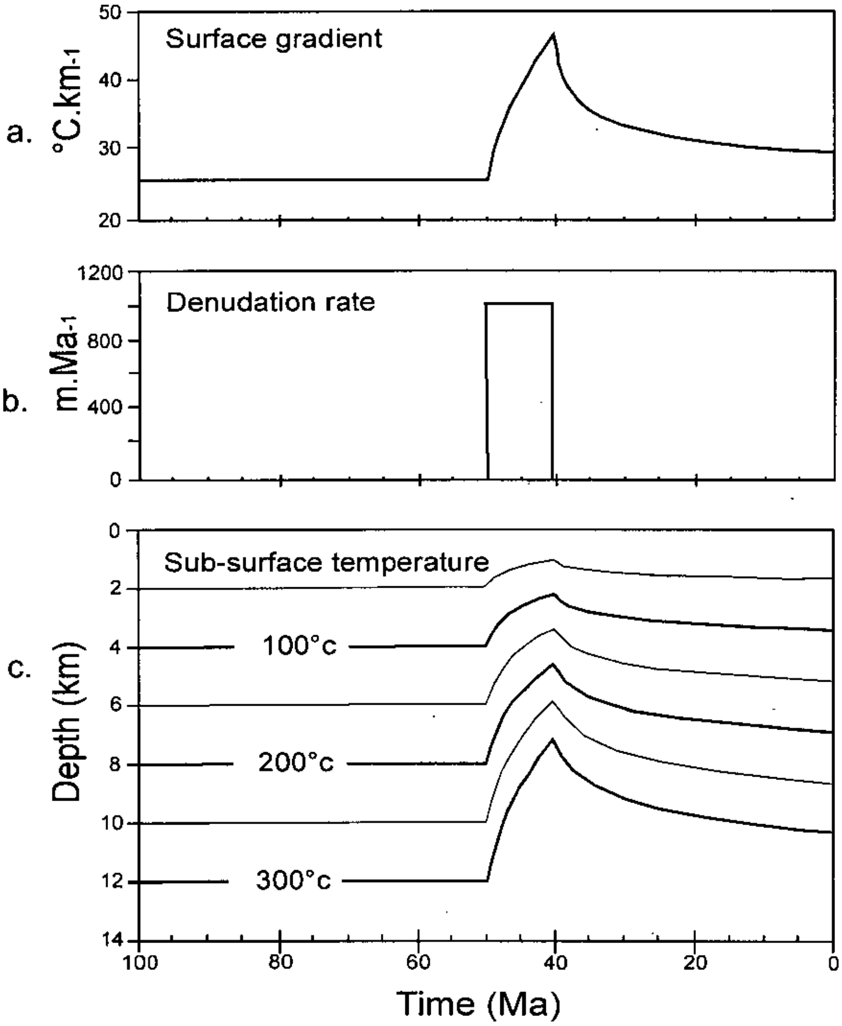

Figure 3.9 An illustration depicting the thermal effect of denudation and the resulting advection of heat towards the free cooling surface. Isotherms are 'dragged' upwards during the period of rapid denudation before relaxing to the earlier thermal steady-state (Brown and Summerfield, 1997). The example given by Brown and Summerfield (1997) applies a 'square pulse' denudational episode at a rate of 1000 m Ma -1 and lasting for 10 Ma that removes 10 km of crustal section with an initial steady-state geotherm of 25°C km -1.

Fig. 3.9
Thermal effects of denudation
(Brown and Summerfield, 1997)

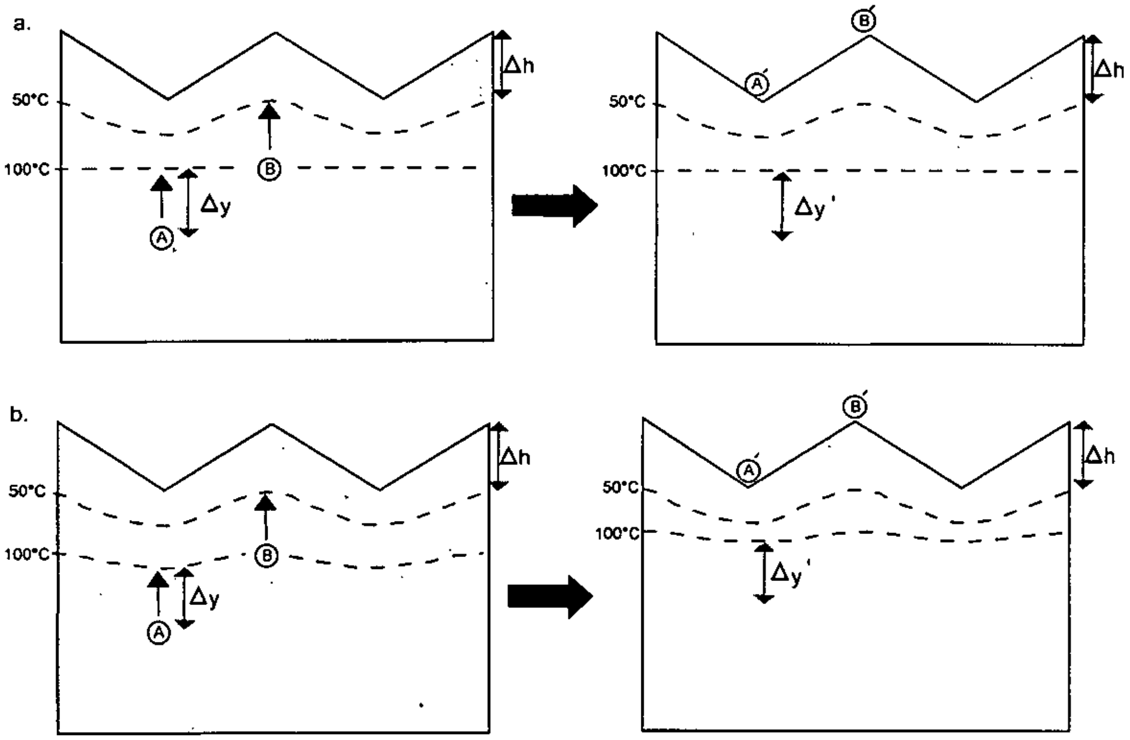

Figure 3.10 A cartoon highlighting the influence of topographic relief on a closure temperature isotherm of 100°C and on the calculation of exhumation amounts and rates based on two samples, A and B. (a) There is no advection of heat and the relief does not affect the paleodepth of the closure temperature below a mean elevation.Therefore, $\Delta y' = \Delta y = \Delta h$. (b) The closure temperature is perturbed by the topographic relief and advection of heat is assumed. Therefore, $\Delta y'$, Δy and Δh are unequal. (Mancktelow and Grasemann, 1997)

Fig. 3.10
Influence of topographic relief on Tc isotherms
(Mancktelow and Grasemann, 1997)

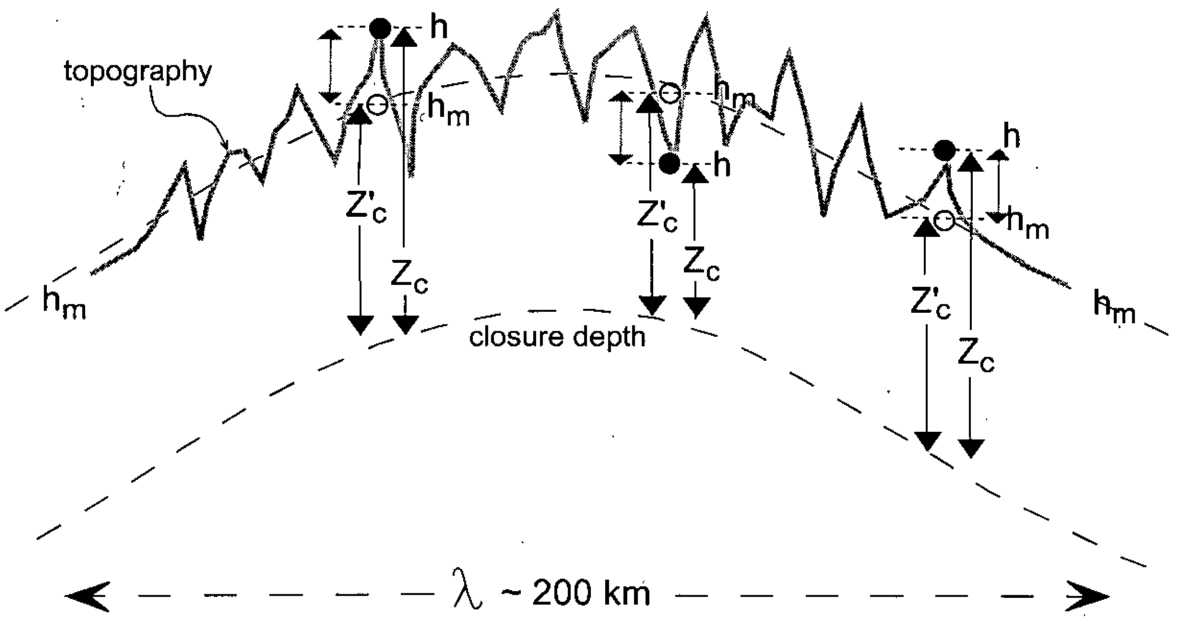

Figure 3.11 Schematic representation of mountain topography and the method for correcting for the variation in elevation in differant samples. This enables all elevations to be normalised to a mean elevation above the *Tc* isotherm, and assumes the *Tc* isotherm remains parallel to the longest wavelength topography of the mountain belt (Reiners et al., 2003). *Z'c*=nominal depth to the *Tc'; hm*=mean elevation of the mountain range; Total exhumation rate since closure *(Zc)* = *Z'c* + *(h-hm)*. Apparent exhumation rates, after elevation correction and topographic correction, are then the ratio of *Zc* and observed age (Reiners et al,. 2003).

Fig. 3.11
Elevation correction in vertical profile sampling
(Reiners et al., 2003)

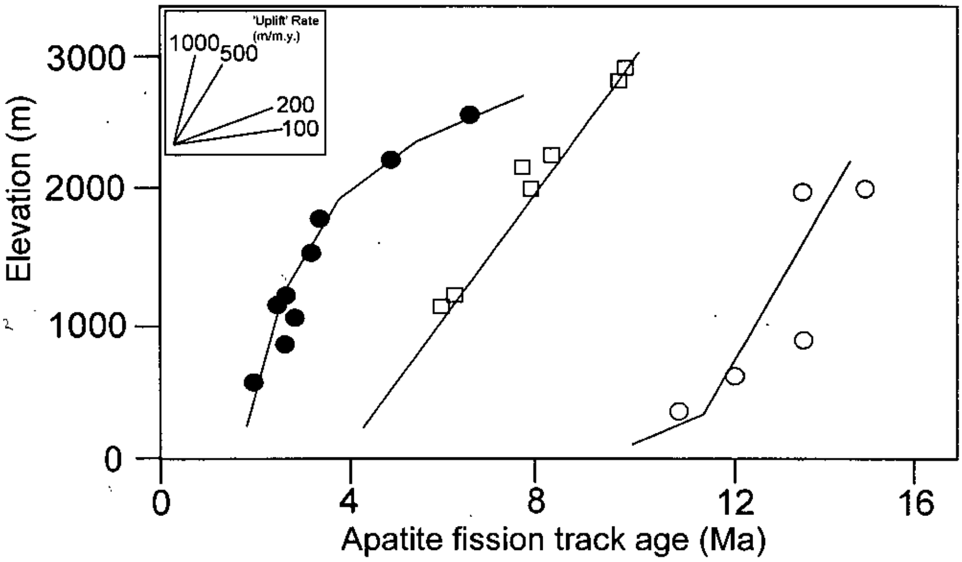

Figure 3.12 Plot depicting AFT age-elevation profiles from the European Alps (Wagner et al,. 1977). Slopes defined by the AFT ages were interpreted to reflect denudational cooling, with increasingly steep lines reflecting increasingly rapid rates of exhumation. Note, measurements did not account for fission track annealing (Gallagher et al., 1998).

Fig. 3.12
AFT age-elevation profiles from the European Alps
(Wagner et al., 1977)

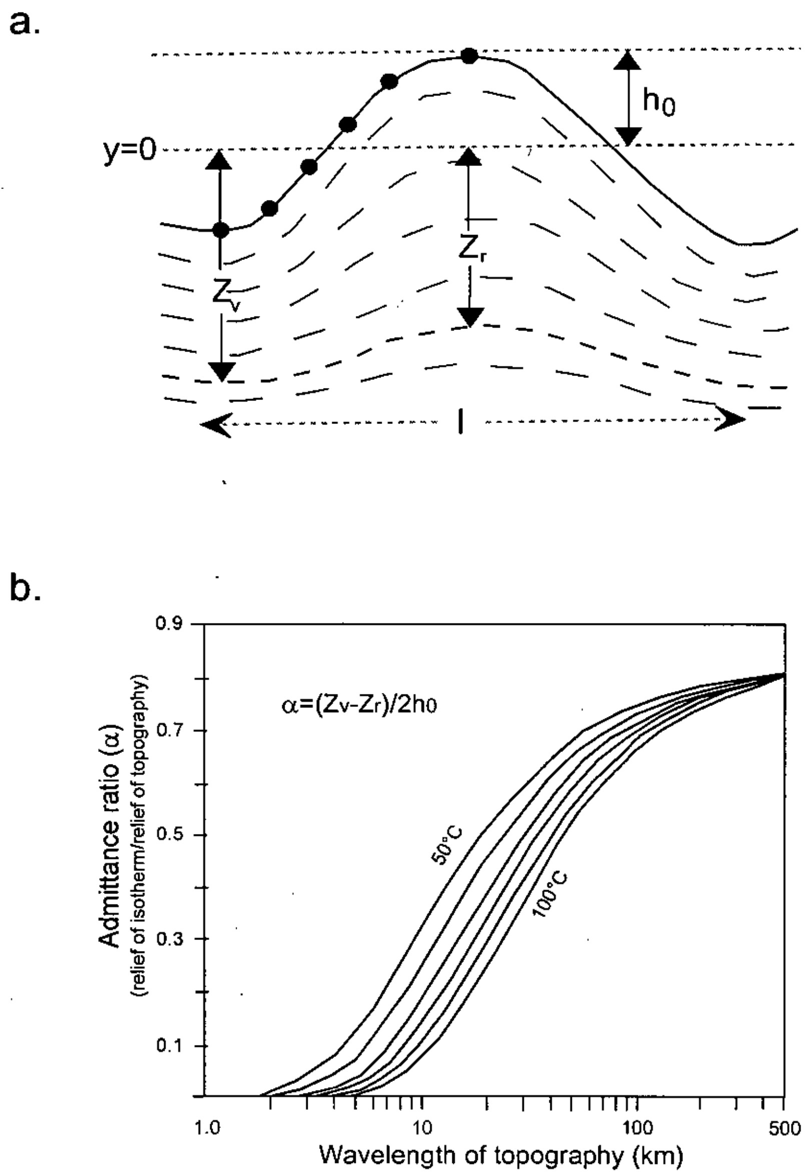

Figure 3.13 (a) Schematic illustration of the influence of local topography on *Tc* isotherms under a 'vertical' transect. The relief has amplitude of *2ho* and samples are collected over l / 2. The depth of a specific isotherm, as measured from a mean elevation *(y=0)* is greater under valleys *(Zv)* than under ridges *(Zr)* (Reiners et al., 2003). Therefore the perturbation level value *(±x)*, for a given topography, must be added to exhumation values. (b) Plot depicting the variation in admittance ratio α (after Braun, 2000) as a function of topographic wavelength. α is the ratio of relief on an isotherm to relief on the overlying topography, α = *Zv-Zr)/2ho.*

Fig. 3.13
Influence of local topography on Tc isotherms under a 'vertical' transect
(Braun, 2000; Reiners et al., 2003)

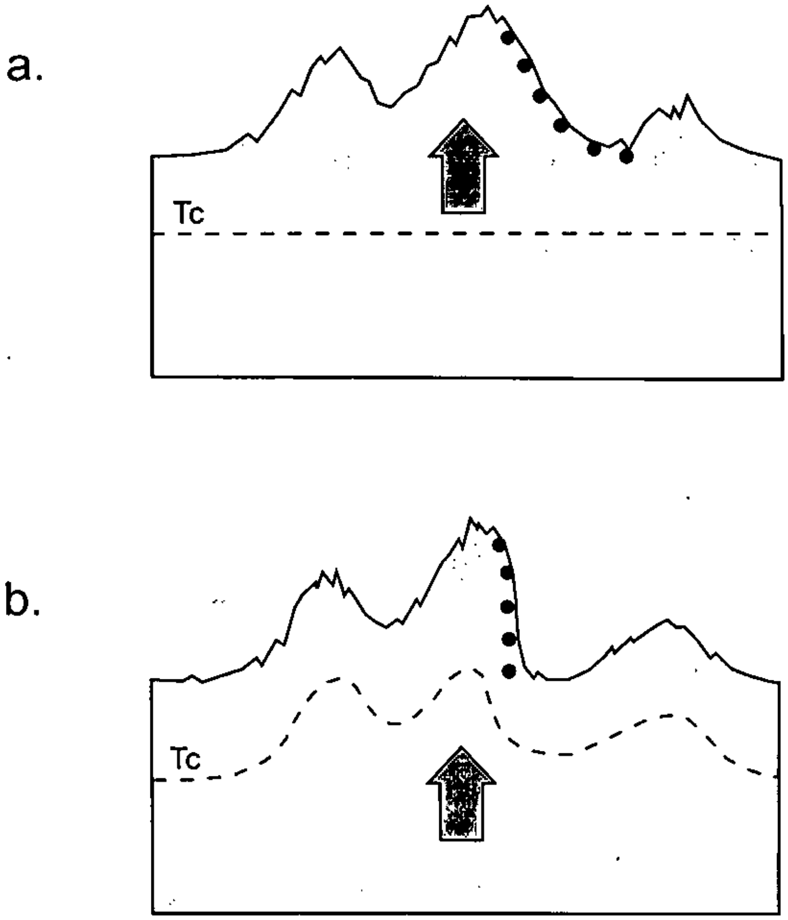

Figure 3.14 Cartoon depicting the assumptions often imposed in one-dimensional interpretations of low temperature thermochronological data. (a) The critical isotherm displays horizontal geometry and is parallel to the geoid, despite being overlain by extreme topography which acts to perturb the near surface isotherms. (b) The *Tc* isotherm follows the topography in perfect parallel and the sampled profile is entirely vertical with no lateral dimension (Stuwe et al., 1994).

Fig. 3.14
One-dimensional interpretations of AFT data
(Stuwe et al., 1994)

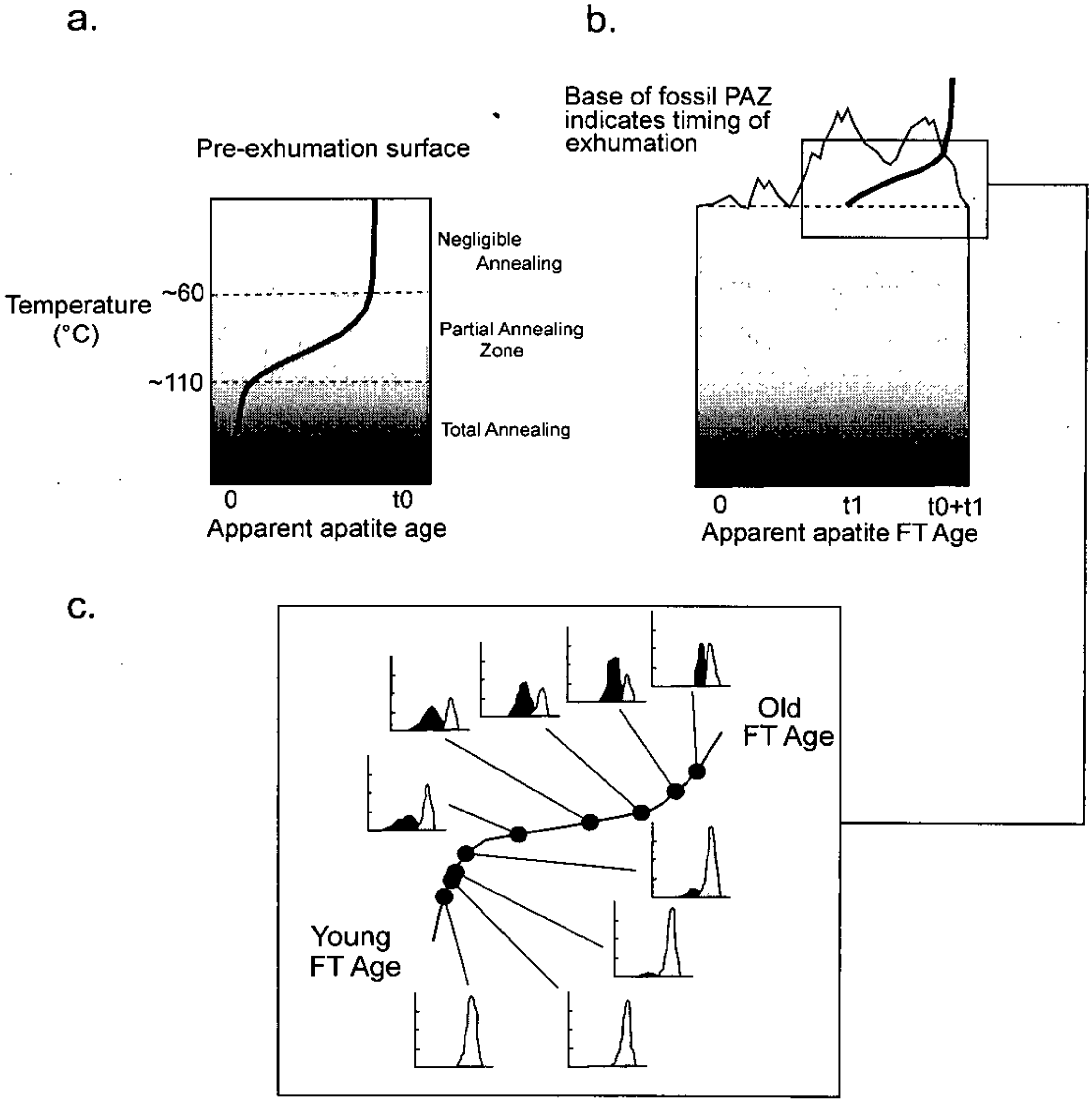

Figure 3.15 Schematic diagram outlining the exhumed partial annealing zone concept (Fitzgerald et al., 1995; Gallagher et al., 1998). (a) The pre-denudation apatite fission track age crustal profile, with the initial fission track age as t0. The illustrated crustal profile has required isothermal holding to allow PAZ formation. Denudation at time t1 exposes differant levels of the preserved PAZ while the deeper samples begin to retain tracks. (b) The expected trend in the fission track age data with respect to elevation. Note, therefore, that the gradient of the slope preserved in the paleo PAZ does not reflect the rate at which the rock column was exhumed.Only the data below the break in slope reflect a cooling event. (c) Track length distribution can be clearly divided into two types: those formed prior to cooling (dark shading) and those formed after cooling (light shading). The tracks formed after cooling are all long. (Gallagher et al., 1998).

Fig. 3.15
Exhumed Partial Annealing Zone (PAZ) concept
(Fitzgerald et al., 1995)

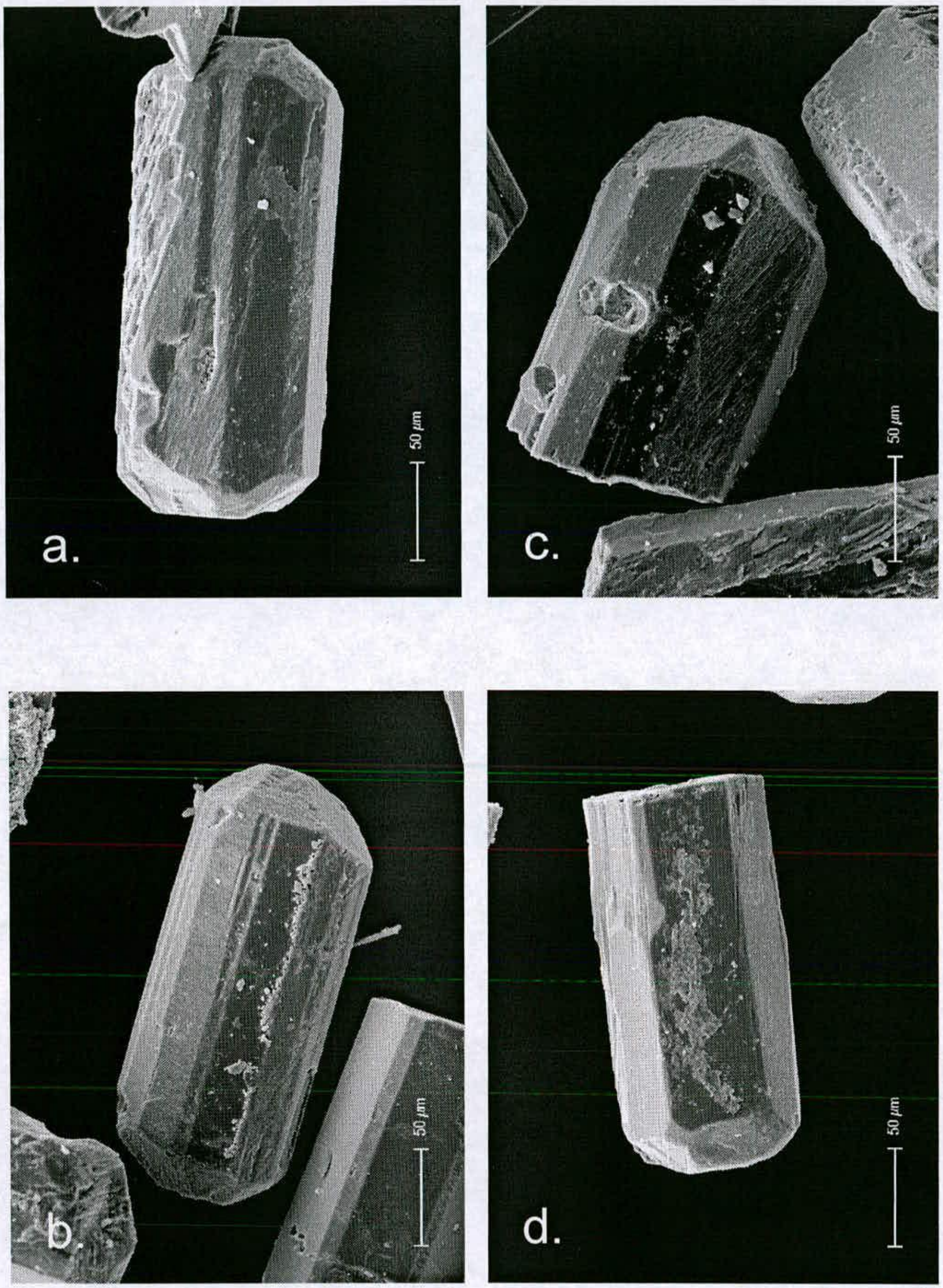

Figure 3.16a Scanning electron micrograph (SEM) images if individual apatite crystals of various morphology, size and condition. (a, b) Euhedral crystal morphologies with two undamaged crystal terminations. Crystal length measured from tip to tip. (c, d) One undamaged crystal termination and a 'parallel' crystal termination. Long axis measured from undamaged crystal tip to flat crystal termination.

Fig. 3.16a
SEM images of apatite crystals

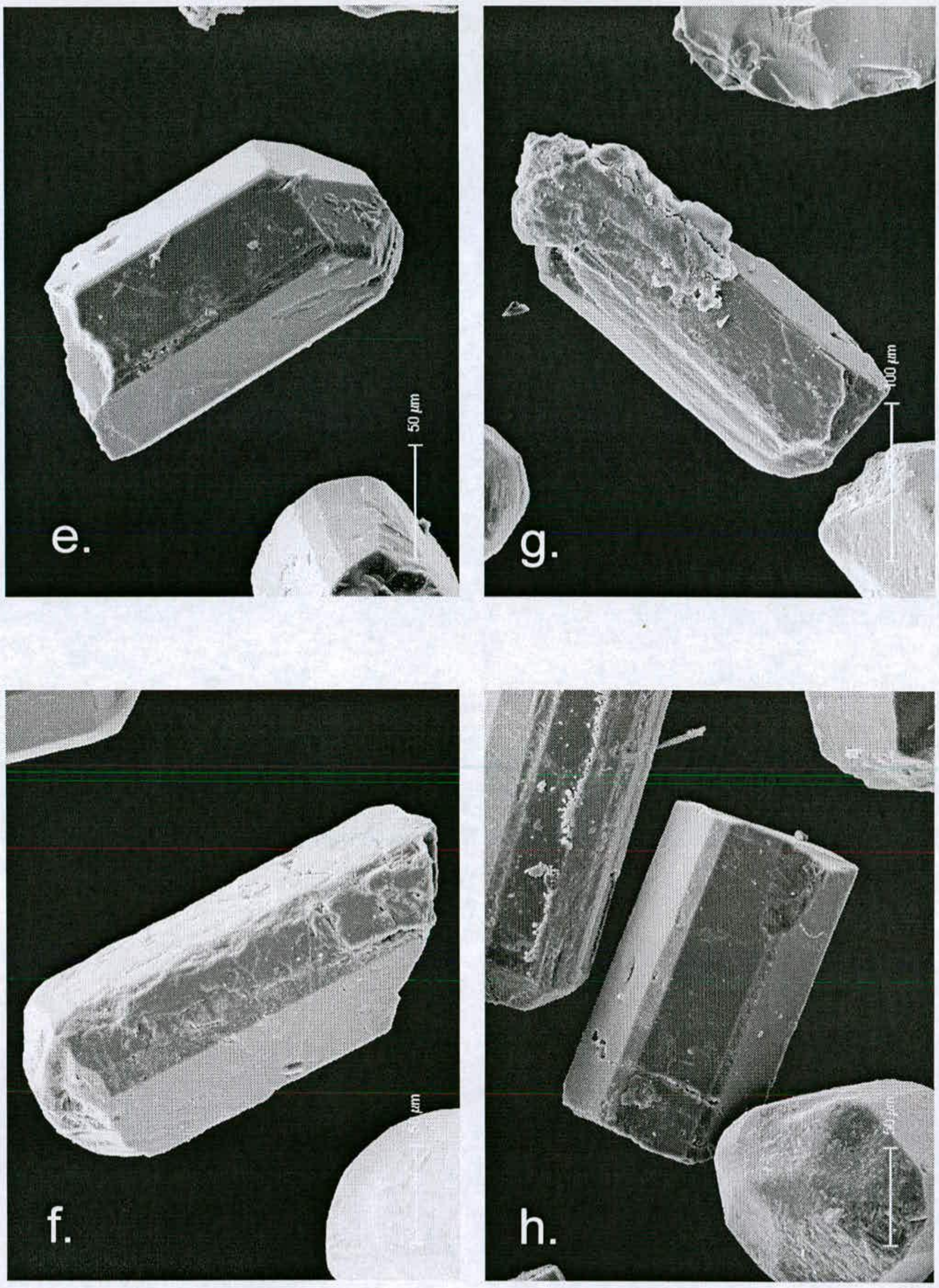

Figure 3.16b (e,f) One undamaged crystal termination and an 'irregular' crystal termination. Long axis measured from undamaged crystal tip to halfway between undamaged crystal body and irregular termination. (g) Subhedral crystal morphology; crystal types avioded for analysis as dimensions difficult to accurately determine. (h) No natural terminations. Long axis measured between two flat crystal terminations.

Fig. 3.16b
SEM images of apatite crystals

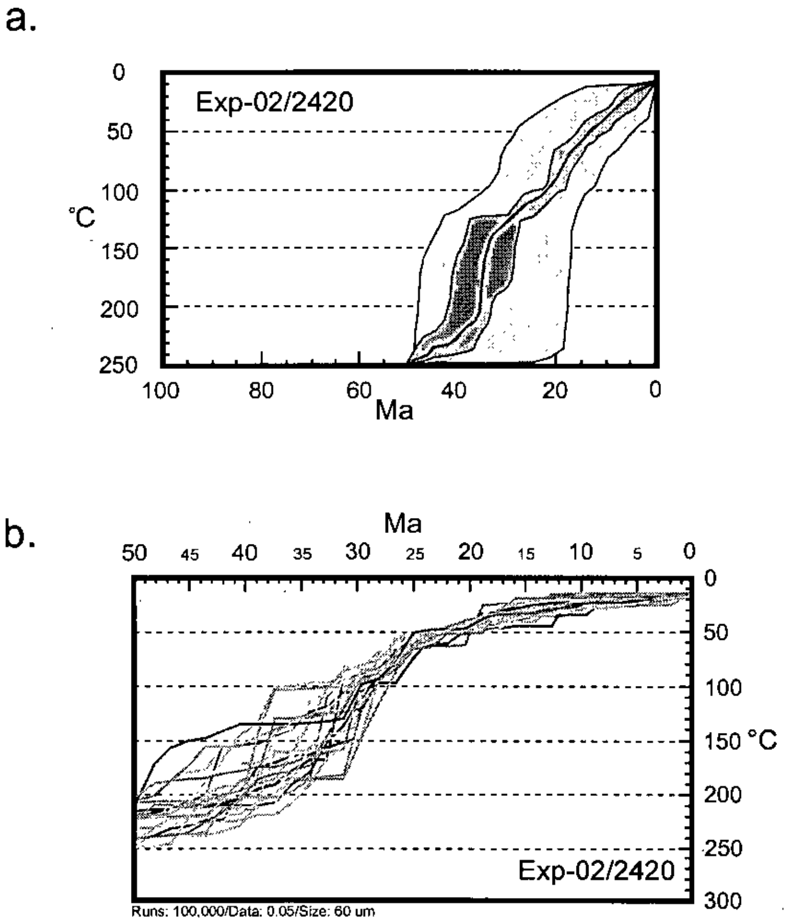

Runs: 100,000/Data: 0.05/Size: 60 um
t-T: 0 Ma (10°C), 60 Ma (150-250°C)
Modelled He age min/max: 5.4-6.4

Figure 3.17 (a) Example output from AFTSolve thermal modelling of apatite fission track data. Plot area depicts time-temperature space, within which an infinite number of t-T paths may be plotted. Two t-T envelopes are shown: the dark grey envelope depicts the t-T space in which all the thermal history solutions that have a statistical fit with the measured data over a value of 0.5 are plotted (see text). The light grey envelope depicts the t-T space in which all the thermal history solutions that have a statistical fit with the measuted data over a value of 0.05 are plotted (see text). All t-T solutions within either envelope pass the null hypothesis for the measured AFT data and are considered potential thermal history solutions. The black line depicts the statistically best fitting t-T solution. (b) Example output from the DeComp forward modelling of individual t-T solutions, derived from AFTSolve, which generate appropriate He ages. Individual t-T solutions in differant tones run through time-temperature space. The input paramaters for each model are noted below the time-temperature plot - 'Runs': the amount of t-T solutions tested in AFTSolve to generate thermal envelopes; 'Data': the statistical threshold of fit between the modelled and the measured AFT data, below which t-T solutions were rejected; 'Size': size of the input diffusion domain (mean diameter of the apatite crystal analysed); 't-T': time temperature constraints through which accepted t-T solutions must pass; 'Modelled He age min/max': the modelled age range generated by the model run.

Fig. 3.17

AFTsolve and DeComp modelling output

Chapter 4

Pyrenean exhumation from low temperature Thermochronology

Objectives: The primary objective of this chapter is to document the time-temperature history of four areas in the southern and central Pyrenees using low temperature thermochronology and thermal modelling. This information is then used to characterise the spatial and temporal distribution of erosional denudation during and after orogenesis.

Chapter 4 – Pyrenean exhumation from low temperature thermochronology

Rock cooling histories obtained through the application of isotopic thermochronometers can be used as a proxy for exhumation and to provide quantitative constraints on the temporal and spatial variability of denudation. The objectives of this chapter are to document the time-temperature (*t*-T) histories of four areas in the central Pyrenees, and to convert this data into a meaningful understanding of the local exhumational record. This is used to assess how erosional denudation, the driving force of exhumation in the central Pyrenees, varied spatially both during and after orogenesis.

These objectives are achieved through the application of apatite (U-Th)/He (AHe), apatite fission track (AFT) and zircon fission track (ZFT) thermochronology, following the procedures discussed in section 3.5. The sampling strategy and rationale is outlined (section 4.1), followed by a summary of the chemical and mineralogical characteristics of the apatite crystals from the samples (section 4.2). The AFT/ZFT datasets are presented (section 4.3) and modelled to derive thermal histories (section 4.4), followed by presentation of the AHe datasets (section 4.5) and integrated (AFT-AHe) thermal modelling (section 4.6). The *t*-T histories produced by combined AFT and AHe data are discussed (section 4.7) and modelled with varied topographic evolutions using 'PeCube' (section 4.8). From this data the exhumation histories of the four regions is compiled (section 4.9) and the record of erosional denudation summarised (section 4.10).

4.1 Sampling strategy

Four sub-vertical profiles were sampled from high-relief Hercynian granodioritic massifs and Carboniferous volcanics from the Axial Zone of the south central Pyrenees (Marimañi Massif, Maladeta Massif, Barruera Massif, and Montardit volcanics) **(Fig. 4.1a-d)** and from single-elevation samples from the Erill-castell volcanics from the central Nogueres Zone (**Fig. 4.1e-h**). All samples (10-20 kg) were extracted from fresh, unweathered bedrock exposures located more than 100 m from any evidence of late-stage thermal activity, such as vein systems or shear heating.

The locations of the sampling sites were chosen to define a broadly north to south transect that was orientated perpendicular to the strike of the mountain belt and approximately congruent with the ECORS deep seismic profile (Choukroune et al., 1989). Parts of this region have been sampled in previous low- and high-temperature thermochronometric studies (e.g. Garwin, 1985; Morris 1998; Morris et al., 1998; Fitzgerald et al., 1999) and the stratigraphic and structural history of the adjacent fold and thrust belt to the south has been extensively documented (e.g. Vergés and Muñoz, 1992; Vergés et al., 1992; Mellere, 1993; Meigs et al., 1996; Meigs and Burbank; 1997). By sampling within the same region of the Pyrenees the new data from this study can be allied with the considerable constraints afforded by the previous studies to allow more robust interpretations to be made of the mechanical and thermal evolution of the area.

4.1.1 The Marimañi profile

The most northern Hercynian massif sampled (Marimañi) is located immediately to the west of the ECORS line (**Fig. 4.1a**). A sample profile was taken from near the summit of Tuc de Baciver (2635 m) down the south-western flank of the mountain to the granite intrusive contact (2030 m) at approximately 150 m intervals. The massif is bounded to the south and north west by large sub-vertical faults and is located within the headwaters of the northerly-draining catchment of the Aquitaine Basin.

Sample	*Elevation (m)*	*Grid Reference*
MM-02/2635	2635	3564 3106
MM-02/2440	2440	3520 3064
Mar-00/2304	2304	3480 3019
Mar-00/2200	2200	3464 3007
Mar-00/2030	2030	3422 3007

4.1.2 The Maladeta profile

The profile spanning the greatest vertical distance (1110 m) was sampled in the Estany Gento region on the south-east flank of the Hercynian Maladeta granitic massif (**Fig. 4.1b**). The highest sample was taken from near the summit of Pala Pedregos (2889 m) and the lowest at Pantà de Sallente (1760 m). The Maladeta massif is located within a coherent structural block that is bounded to the north and south by major Alpine-age faults. The main Pyrenean drainage divide runs east-west through the massif, though the sampled profile is located within the headwaters of the south-draining catchments of the Ebro Basin.

Sample	*Elevation (m)*	*Grid Reference*
Mal-00/2870	2870	3769 0914
Mal-00/2765	2765	3778 0871
Mal-00/2650	2650	3772 0858
Mal-00/2440	2440	3736 0846
Mal-00/2360	2360	3675 0850
Mal-00/2250	2250	3631 0829
Mal-00/2140	2140	3574 0838
Mal-00/2030	2030	3513 0867
Mal-00/1920	1920	3518 0848
Mal-00/1760	1760	3483 0805

4.1.3 The Barruera profile

The most westerly profile was sampled on the south-eastern flank of Corona del Pinar (2053) within the small Barruera massif, north of Barruera village (**Fig. 4.1c**). The highest sample was taken at an elevation of 1750 m and the lowest at 1150 m. The massif is situated ~15 km along strike and ~4 km south of the Maladeta profile and is also located within the southern-draining catchments of the Ebro Basin. However, the two massifs are structurally separated by Alpine-age east-west striking faults.

Sample	*Elevation (m)*	*Grid Reference*
Bar-02/1750	1750	1990 0995
Bar-02/1695	1695	1995 0987
Bar-02/1150	1150	2032 0925

4.1.4 The Nogueres profile and single-elevation samples

Immediately south of Montardit village a sub-vertical profile of four samples was extracted from volcaniclastic and pyroclastic deposits of the Permo-Carboniferous Erill-Castell succession (Soriano et al., 1996) (**Fig 4.1d**). The uppermost sample was taken from an elevation of 1280 m and the lowest at 805 m.

Five single-elevation samples were also collected from lower relief outcrops exposed along the strike of the most southerly Axial Zone and Nogueres Zone (**Fig 4.1e-h**) (area e=Col; areas f and g=Sas; area h=Esc). Sampling localities range along strike from the village of Escané, in the west, to Coll d' Olli, in the east. All samples are located within the

Nogueres zone, which is structurally higher than the underlying Axial Zone. The samples from the Sas area (Sas-02/1490 and Sas-02/1540) and from the Coll d' Olli area (Col-00/1490 and Col-00/1540) are located to the north and south of major thrust structures.

Sample	*Elevation (m)*	*Grid Reference*
Mon-02/1280	1280	4290 9445
Mon-02/1085	1085	4335 9460
Mon-02/960	960	4365 9475
Mon-02/805	805	4400 9495

Sample	*Elevation (m)*	*Grid Reference*
Esc-02/1250	1250	0915 0325
Sas-02/1490	1490	2280 9795
Sas-02/1580	1580	2315 9790
Col-00/1490	1490	2894 9655
Col-00/1540	1540	2879 9610

4.2 Apatite chemistry and mineralogy

The chemical composition of representative apatite crystals from samples from each profile were determined following the procedures outlined in section 3.5.4. All samples yielded fluor-apatite compositions ($Ca_5(PO_4)_3(OH,F)$) (see Appendix II for full analytical dataset). Consequently, the fission track annealing kinetics and He diffusion characteristics of the crystals used for thermochronological analysis were assumed to be comparable to Durango apatites (~0.45 wt. % Cl; Green et al., 1986; Laslett et al., 1987; Farley, 2000).

Quantification of the distribution of parent elements within the samples was performed following the procedures outlined in Section 3.5.3. Apatites in all but two of the samples displayed homogenous U and, by inference, Th (section 3.5.3). Out of 100 crystals analysed from each of Mal-00/1760 and Mal-00/2650, six and eight crystals, respectively, displayed a moderate enrichment of parent elements in the outer 10 to 15 μm of the crystal. As noted in section 3.1.6, a non-homogenous distribution of the parent elements within an apatite crystal may significantly influence the measured AHe age. On average, 8 to 10 crystals were used for a single AHe age determination for Mal-00/1760 and Mal-00/2650, respectively (section 4.4). The likelihood of including one of the zoned crystals is, thus, very small and the potential impact on the corrected AHe age of including one zoned crystal is negligible. Therefore, no zonation correction was applied to the AHe ages from these samples.

Following the procedures outlined in section 3.5.4, apatite separates from a number of representative samples which were not used for AHe analysis, were analysed by Back-Scatter Electron (BSE) imaging. All the samples analysed yielded a number of crystals containing randomly-distributed, sub-microscopic mineral inclusions (<2 μm diameter). Quantitative elemental analysis indicated the inclusions were primarily of zircon composition ($Zr[SiO_4]$) **(Fig. 4.2a-d)**.

4.3 Fission track results

AFT analysis was peformed on a selection of samples from each profile and ZFT analysis was performed on a single sample from each profile. Age and track length data is summarised in **Table 4.1**.

Zircon fission track ages range from Middle Jurassic to Lower Eocene in age, and are in accord with previous ZFT studies (e.g. Garwin, 1985). All AFT ages are of Oligocene age, or younger, in accord with previous south Pyrenean AFT studies (e.g. Garwin, 1985; Yelland, 1990; Morris et al., 1998; Fitzgerald et al., 1999). AFT ages are plotted against elevation for the four profiles and the track length distributions for individual samples are superimposed next to the appropriate age data **(Fig. 4.3a-d)**. A composite age-elevation plot is compiled which shows the AFT ages from all the profiles **(Fig. 4.3e)** and the ZFT ages plotted against elevation **(Fig. 4.3f)**

4.3.1 Marimañi age-elevation profile

The ZFT cooling age of the uppermost sample in the Marimaña profile (2635 m) is 49.7±3.1 Ma. The AFT cooling ages range from 27.6±2.4 Ma (Mar-00/2200 m) to 36.6±3.2 Ma (MM-02/2440 m). Mean track lengths range from 14.19±0.12 μm (std. dev. 1.37 μm) (Mar-00/2304 m) to 14.32±0.07 μm (std. dev. 1.0 μm) (Mar-00/2030 m). AFT ages depict moderate scatter about a vertical to steeply-positive, linear correlation with elevation **(Fig. 4.3a)**.

The steeply-positive orientation of the linear age-elevation profile indicate that the Marimaña AFT ages likely document a period of rapid cooling through partial annealing temperatures during early Oligocene times. The long mean track lengths and small standard deviations are also consistent with this primary interpretation.

4.3.2 Maladeta age-elevation profile

The ZFT cooling age from the lowermost sample in the Maladeta profile (1760 m) has a Lower Eocene age of 49.3±2.6 Ma. AFT cooling ages are similar to those recorded in the Marimañi region, ranging from 27.7±2.5 Ma (Mal-00/2030 m) to 33.1±3.4 (Mal-00/2870 m). Mean track lengths range from 13.73±0.18 μm (std. dev. 1.33 μm) (Mal-00/1760 m) to 14.27±0.15 μm Ma (std. dev. 1.7 μm) (Mal-00/2870 m). A best-fit linear regression through the AFT ages depicts a steeply positive age-elevation profile (**Fig. 4.3b**).

The steep to vertical orientation of the linear age-elevation profile suggests the Maladeta AFT ages also document a period of rapid cooling through partial annealing temperatures during early Oligocene times. The long mean track lengths and low standard deviations are consistent with this interpretation. The slightly lower mean track length of the lowermost sample may indicate a longer residence time within the AFT PAZ.

4.3.3 Barruera age-elevation profile

The ZFT cooling age for the lowermost sample (1150 m) of the Barruera profile is 104±7 Ma. AFT cooling ages range from 19.5±3.2 Ma (Bar-02/1695 m) to 21.4±2.0 Ma (Bar-02/1150 m). Mean track lengths range from 13.18±0.15 μm Ma (std. dev. 1.69 μm) (Bar-02/1150 m) to 14.17±0.23 μm Ma (std. dev. 1.45 μm) (Bar-02/1695 m). A vertical to sub-vertical age-elevation relationship is depicted by the AFT data (**Fig. 4.3c**).

The steep to vertical orientation of the AFT age-elevation profile likely indicates that the Barruera profile cooled rapidly through partial annealing temperatures during earliest Miocene times. The long mean track lengths are largely consistent with this interpretation, though the lowermost sample, with a slightly shorter mean track length, may have cooled at a relatively slower rate through partial annealing temperatures.

4.3.4 Nogueres age-elevation profile

The ZFT cooling age for the lowest elevation sample in the region (Mon-02/805) is 159±33 Ma and is the oldest fission track age in the dataset. AFT ages from the Montardit vertical profile range from 17.2±3.4 Ma (Mon-02/960) to 26.2±3.1 Ma (Mon-02/1280), with mean track lengths ranging from 13.75±0.21 μm (std. dev. 2.23 μm) (Mon-02/1280) to 14.76±1.23 μm (std. dev. 2.76 μm) (Mon-02/960). AFT ages from the remaining single-elevation samples of the Nogueres Zone range from 25.5±3.1 Ma (Esc-02/1250) to 30.2±4.1 Ma (Col-00/1540), with mean track lengths ranging from 13.62±0.33 μm (std. dev. 1.73 μm) (Col-00/1540) to 14.16±0.14 μm (std. dev. 1.59 μm) (Sas-02/1490). A best-fit linear relationship through all the Nogueres Zone samples depicts a shallow positive age-elevation **(Fig. 4.3d)**.

The positive correlation of age and elevation depicted by the three Montardit AFT samples may indicate progressive cooling through partial annealing temperatures. The mean track length data for the upper two samples is consistent with this interpretation, though the lowermost sample, yielding only six confined tracks, cannot be confidently interpreted. The remaining single-elevation samples align broadly along the same age-elevation profile, despite being spatially separated over a large area, and show similar mean track length values. This may indicate the Nogueres region underwent a similar thermal evolution during early Oligocene times.

4.4 AFTSolve thermal modelling

AFTSolve modelled thermal histories and fitting statistics are presented in **Fig. 4.4a-t** for the AFT age and track length data, following the procedures outlined in section 3.5.5. Each plot depicts two time-temperature (*t*-T) envelopes which represent 'good' (dark grey) and 'acceptable' (light grey) statistical fits between the model and the measured data (section 3.5.5 for discussion). Where only 'acceptable' fits are shown the model did not generate any 'good' fits with the AFT data. Importantly, the envelopes only represent *t*-T space in which the model thermal solutions are accommodated and do not imply that all thermal histories within that area are feasible. A representative *t*-T path is depicted by the statistically best-fitting thermal history generated by the model runs.

It is of importance to recognise the limitations of the thermal model solutions generated by AFTSolve from the AFT data (see also section 3.5.5.1). Firstly, any solutions generated from sample datasets that do not have sufficient available track length data (>25 confined tracks; Donelick, pers Comm., 2003) must be regarded with caution and used only in conjunction with data from adjacent samples. Secondly, as the kinetic algorithms used to generate the thermal histories in AFTSolve are based entirely upon empirical apatite fission track data (Ketcham et al., 2000; Ketcham and Donelick, 2000), the constraint on t-T histories at temperatures outside the AFT PAZ are extremely limited and, consequently, should not be relied entirely on for interpreting the lower temperature (<~75°C) thermal evolution. To avoid this problem additional modelling software is used (DeComp; Meesters and Dunai, 2002) in conjunction with the corresponding AHe ages (section 4.6).

4.4.1 Marimaña profile - AFTSolve thermal modelling

The modelled *t*-T envelopes, based upon the AFT data from the Marimaña profile, indicate similar thermal evolutions for all five samples in the profile (**Fig. 4.4a-e**). At 45 Ma all the *t*-T solutions are at temperatures above partial annealing temperatures. By 30 Ma, the temperature ranges have reduced dramatically and bracket a thermal window of between ~25° to 120°C, in all but one of the samples (Mal-00/2200). This sample also exhibits a low temperature minimum (40°C) but retains a large temperature maximum above PAZ temperatures (240°C). The statistical best-fit thermal history for each model run depicts a period of rapid cooling through AFT Partial Annealing Zone (PAZ) temperatures over a brief period of 2-4 Myr at intervals between 36 to 28 Ma (e.g. Mar-00/2304: 34 to 36 Ma; MM-02/2440: 26 to 30 Ma). By 20 Ma all of the modelled thermal histories predict all samples were at temperatures below the AFT PAZ, ie. 15 to 70°C. By 10 Ma the temperature ranges have decreased, with maximum values all below 45°C.

The AFT ages, the age-elevation relationship, track length distributions, and the AFTSolve-derived thermal histories, are consistent with all the samples from the Marimañi profile documenting a broadly similar cooling history over the temperature window at which the AFT technique is sensitive. Both data and models support a period of rapid cooling, during which the profile was displaced up the local thermal gradient and through the AFT PAZ at some time interval during latest Eocene to early Oligocene times (~36 to 28 Ma).

4.4.2 Maladeta profile - AFTSolve thermal modelling

AFTSolve model results for the Maladeta AFT data also depict good consistency between samples (**Fig. 4.4f-i**). At 40 Ma the t-T solutions are poorly constrained and at temperatures above the AFT PAZ. By 30 Ma the minimum temperature for all the thermal envelopes reduce dramatically to between 30°C (Mal-00/2870) and 85°C (Mal-00/2030). The upper temperature values in this time interval are largely unchanged since the 40 Ma interval. The statistical best-fit thermal history for each model run depicts a period of rapid cooling through AFT PAZ temperatures over a period of up to 3 Myr. This occurs at slightly different times in the interval between 32 to 28 Ma (e.g. Mal-00/2870 and Mal-00/2250, respectively). By 20 Ma the thermal envelopes are within or below PAZ temperatures and lie within ranges of 15° to 100°C, defined by Mal-00/2870 and Mal-00/1760, respectively. At 10 Ma temperature ranges have decreased, with Mal-00/1760 depicting the highest temperature of 65°C. The statistical best-fit *t*-T solutions all indicate prolonged thermal stability after rapid cooling to temperatures below the AFT PAZ.

Models results and the AFT ages and parameters are consistent with the rapid cooling of the entire profile through partial annealing temperatures between ~32 to 28 Ma. The slightly shorter mean track lengths of the lowermost sample in the profile (Mal-00/1760) may indicate that it resided within the PAZ for a longer duration.

4.4.3 Barruera profile - AFTSolve thermal modelling

Modelling of the Barruera AFT data yields *t*-T solutions which are similar for all three samples (**Fig. 4.4j-l**). At 40 Ma the *t*-T paths are above PAZ temperatures. By 30 Ma the minimum temperatures have reduced to upper PAZ temperatures of ~100°C. Best-fit *t*-T solutions indicate that transition through PAZ temperatures occurred over an interval of <4 Myr for the two upper samples (Bar-02/1780 and Bar-02/1695) and over a period of up to 8 Myr for the lowermost sample (Bar-02/1150) after 22 Ma. Model *t*-T paths for the lower sample indicate that initial transit through the PAZ was relatively rapid, but may have slowed significantly prior to cooling below ~70°C. By 10 Ma, the best-fit *t*-T paths indicate all the samples were at temperatures cooler than the PAZ.

The age-elevation relationships and model results indicate the samples underwent similar thermal histories, with transition through PAZ temperatures from ~21 Ma onwards. The lower sample may have resided within these temperatures for slightly longer.

4.4.4 Nogueres profile - AFTSolve thermal modelling

AFTSolve thermal modelling of the Nogueres profile samples generates *t*-T envelopes which are all broadly similar (**Fig. 4.4m-o**). Prior to 35 Ma all the t-T solutions predict all samples are at temperatures above the AFT PAZ. The statistically best-fitting *t*-T solutions indicate passage through PAZ temperatures did not occur until between ~25 to 18 Ma. *t*-T paths for the upper samples suggest transit through this temperature window occurred over 5-6 Myr. The lower sample indicates this occurred effectively instantaneously, however, it is important to recognise that the model result for Mon-02/960 is based upon only six confined tracks, and so meaningful conclusions cannot be drawn from it. By 10 Ma, the models predict that all the samples except Mon-02/960 had cooled below the PAZ.

4.4.5 Nogueres single-elevation samples – AFTSolve thermal modelling

As the remaining samples from the Nogueres Zone were collected along a 35 km strike-parallel section, and therefore do not constitute a vertical profile or represent the thermal evolution of the rock column, the modelled thermal histories from discrete sampling areas are considered individually from west to east.

Sample Esc-02/1250 (**Fig. 4.4p**), yielding an AFT age of 25.5±3.1 Ma and mean track lengths of 13.83±0.19 µm, generates a thermal solution which indicates the sample was above PAZ temperatures until at least 35 Ma. However, the best fit *t*-T solutions indicate the sample did not pass through PAZ temperatures until between 25 and 18 Ma and over a period of up to 8 Myr. All the possible *t*-T solutions indicate the sample had passed beyond temperatures at which significant annealing of the fission tracks could have occurred by 10 Ma.

Samples Sas-02/1580 and Sas-02/1490, yielding respective AFT ages of 25.9±3.6 and 30.1±2.7 Ma and mean track lengths of 13.85±0.26 and 14.16±0.14 µm, yield similar AFTSolve thermal modelling results (**Fig. 4.4q & r**). At 45 Ma, the temperature minima for the *t*-T envelopes are above PAZ temperatures. The statistically 'good' thermal histories indicate passage through the PAZ temperature window did not occur until between 30 to 20 Ma, with the best-fit solutions indicating 30 to 27 Ma. Transit through PAZ temperatures likely occurred over 4-6 Myr. By 10 Ma, thermal models indicate the samples were above PAZ temperatures.

Samples Col-00/1540 and Col-00/1490, yielding respective ages of 30.2±4.1 and 27.6±3.7 Ma and mean track lengths of 13.62±0.33 and 13.80±0.22 µm, also yield similar modelled histories. The *t*-T windows depict a broad range of time in which the samples transited PAZ temperatures. However, the best-fit solutions indicate they cooled into PAZ temperatures at 33 and 27 Ma, respectively (**Fig. 4.4s & t**). The thermal model for both samples depicts a moderately slow transition to low temperatures of ~6 Myr for the lower sample, and ~8 Myr for the upper sample. Both thermal models indicate the samples had cooled below temperatures at which annealing occurred by 10 Ma.

In summary, the five AFT samples taken at various altitudes along strike of the Nogueres zone generally depict cooling through PAZ temperatures between 30 and 20 Ma.

The modelled thermal histories depict transit through this temperature took 5-8 Myr. Despite the samples being collected in different geographical locations, when the AFT ages are plotted against elevation with the AFT ages from the Noguères profile, a clear positive and linear age-elevation relationship is defined **(Fig. 4.3d)**. This may indicate that the region of the Nogueres Zone in which the samples were collected shared a similar low-temperature cooling history.

4.5 AHe results

(U-Th)/He ages were determined on apatites from all samples which yielded sufficient inclusion-free crystals of the appropriate morphology and size (see section 3.1). AHe cooling ages are presented in **Table 4.2** (see Appendix II for full dataset).

Eight analyses (marked with square brackets in Table 4.2), from a total of 48, yielded AHe ages which were significantly older than their corresponding AFT age and older than other replicate analyses from the same samples. These ages were considered to be erroneously old as the thermal sensitivity of the AFT system is higher than that of the AHe system and, therefore, cannot cool through the lower temperature system first.

The reproducibility of the remaining analyses in the dataset is variable. Previous studies have demonstrated that replicate analyses of single samples in the SUERC He laboratory yields an average variation of ±8 to 10% (Persano et al., 2002). There are a number of samples which reproduce well within this prescribed analytical uncertainty (e.g. Mal-00/2870, Mal-00/2650, Mal-00/1760, Bar-02/1695, Mar-02/2635 and Mar-00/2030). A proportion of the samples, however, reproduce only within 15-30% of each other (e.g. Mal-00/2440, Mal-00/2250, Mal-002030, Mal-00/1920, Mar-00/2200) and occasional samples reproduce to worse than 30% (e.g. Mal-00/2765 and Bar-00/1150). As outlined in section 3.1, several factors may adversely affect the reproducibility of the He age of apatites from a single rock sample.

Zonation of the parent element is unlikely to account for the scatter in the replicate analyses. Zonation is restricted to a small percentage of crystals in two of the samples which yielded reproducible ages (Mal-00/1760 and Mal-00/2650) (section 4.3.4). The potentially significant impact of crystal size variability between different replicates of the same sample (Reiners and Farley, 2001) can also be confidently discounted. The variation in crystal diameter within a single aliquot was maintained to <20% and the dimensions were also combined into the F_T correction, following the procedures of Farley (2002). As the samples analysed were generally of a small and uniform size range (see Table 4.2) the effects on the derived AHe age, even in slowly cooled samples, would not be in excess of the analytical uncertainty (Dunai et al., 2003). Consequently, variability in crystal dimensions cannot have played an important role in reducing the precision of reproducibility outside the uncertainty of any individual analysis.

The most likely factor which imposed control over the poor reproducibility of AHe ages was the presence of U- or Th-rich mineral inclusions or ^{4}He-rich fluid inclusions. Microscopic screening and BSE imaging of apatite grains from a number of samples (section 4.2) indicates submicroscopic zircon inclusions are common within the apatite population.

As the U and Th content of zircon is high relative to apatite, radiogenic decay produces relatively large quantities of He. This is recoiled from the mineral inclusion into the apatite crystal lattice, approximately ~20 μm. Apatites that contain inclusions, therefore, will accumulate ^{4}He in excess of that derived from U and Th decay from the apatite lattice. As the zircon inclusions are probably not dissolved during the AHe analytical procedure, the U and Th within the inclusion is not measured. Consequently the apparent parent to daughter element ratio within the apatite is decreased and the derived AHe age will be erroneously old. If the crystals used for BSE imaging are characteristic of those used for (U-Th)/He analysis, then the poor reproducibility of a number of samples can be reliably attributed to undetected zircon inclusions in the apatite crystals.

Previous workers have considered that good age reproducibility renders it appropriate to allow confidence in the mean values of the combined ages, plus their analytical uncertainty (e.g. Persano et al., 2003; Spotila et al., 2004). In poorly reproduced samples with only 2-3 replicates, however, the mean AHe age, and the uncertainty of the mean age, are essentially undefined and cannot be used to reliably represent an individual sample. All AHe ages which are younger than their corresponding AFT age are potentially unaffected by inclusion-derived He. Bearing this in mind, the most circumspect approach is to plot all the measured ages that are less than, or equal to, their respective AFT age. This ensures that no AHe ages are assumed to be inaccurate and, in effect, provides minimum and maximum ages for each elevation. The data range from upper Oligocene to Upper Miocene and are plotted against elevation in **Fig 4.5a-c** and in a composite plot in **Fig. 4.5d**. Any interpretation of the data must be a demonstrably unique solution for the age range for each sample and must be compatible with the overall age-elevation relationship.

4.5.1 Marimañi age-elevation profile

AHe ages from the Marimañi profile **(Fig 4.5a)** range from 23.2±1.4 Ma (Mar-00/2200:2) to 33.7±2.0 Ma (MM-02/2635:2). Replicate analyses yield good age reproducibility in all but one of the samples (Mar-00/2200). The profile defines a linear and positive age-elevation relationship constrained at the highest and lowest elevations by ages that have been reproduced in triplicate within the analytical uncertainty (MM-02/2635 and Mar-00/2030). Two of the three samples from intermediate elevations (MM-02/2440 and Mar-00/2304) are constrained by single AHe ages, though both depict decreasing ages at progressively lower elevations. Sample Mar-00/2200 is constrained by two AHe ages which reproduce just outside their respective analytical uncertainties. Regression analysis of the data provides a moderately steep best-fit solution with an R^2 value of 0.614 and a gradient of 0.040 km Myr^{-1}.

4.5.2 Maladeta age-elevation profile

AHe ages from the Maladeta profile **(Fig. 4.5b)** range from 7.8±0.5 Ma (Mal-00/2030:1) to 29.9±1.8 Ma (Mal-00/2440:5). Replicate analyses yield variable standards of age reproducibility. A number of samples analysed in triplicate reproduce within the analytical uncertainty (e.g. Mal-00/1760, Mal-00/2650, Mal-00/2870) and constrain the top and bottom of the age-elevation profile. Others display a larger scatter outside the analytical uncertainty (Mal-00/2440 and Mal-00/2765). A positive age-elevation gradient is clearly discernible in the upper section of the profile, above ~2100m. Below ~2100m this relationship changes to one of age-invariance with elevation and is characterised by a linear, vertical to subvertical best-fit and with a marked improvement of AHe age reproducibility.

Owing to the spread of ages, particularly in the higher elevation samples, this interpretation of the data is non-unique. An alternative interpretation is to suggest that the ages are scattered about a linear, positive gradient spanning the vertical length of the profile from 1760 to 2870 m elevation. Regression analysis of the data provides a best-fit correlation with a gradient of 0.042 km Myr^{-1} and an R^2 value of 0.49. The two interpretations of the Maladeta data would require markedly different cooling histories and will be explored through thermal modelling of the dataset (section 4.6.2). An additional observation to make of the Maladeta profile is that samples yield systematically younger AHe ages, for similar elevations, to those observed in the Marimañi profile.

4.5.3 Barruera age-elevation profile

The Barruera profile (**Fig. 4.5c**) depicts AHe ages that range from 7.6±0.5 Ma (Bar-02/1150:2) to 14.9±0.9 Ma (Bar-02/1150:1). Replicate analyses yield good reproducibility for the upper elevation sample and poor reproducibility for the lower elevation. The profile is difficult to interpret with confidence, owing to the relatively few samples and the poor reproducibility of the lowermost age. The highest elevation sample reproduces within the analytical uncertainty (Bar-02/1695) and depicts very similar ages to those at the base of the Maladeta profile. If the age of Bar-02/1150 lies within the age range of the two replicates, the trendline can be inferred to be vertical to sub-vertical.

4.6 AFT-AHe integrated thermal modelling

For the eleven samples which yielded enough apatite crystals for both AFT and AHe analysis (MM-02/2635, MM-02/2440, Mar-00/2304, Mar-00/2200, Mar-00/2030, Mal-00/2870, Mal-00/2250, Mal-00/2030, Mal-00/1760, Bar-02/1695, Bar-00/1150), the thermal histories are integrated, using both AFTSolve and DeComp (section 3.5.5.2) in order to provide additional constraints on the cooling history. The modelled *t*-T paths, input parameters and forward model AHe ages are presented in **Fig. 4.6a-k**. Each plot depicts a maximum of 50 *t*-T paths generated by AFTSolve, consistent with the measured fission track data and with DeComp modelling of the AHe age from the same sample.

4.6.1 Marimaña integrated thermal modelling

As with the AFTSolve thermal models, the integrated *t*-T paths from the five Marimaña samples depict similar thermal histories (**Fig. 4.6a-e**). In order to generate *t*-T solutions for four of the five samples, the statistical boundaries of the AFT data were set to 'acceptable' levels (section 3.5.5.2). This was required because the original AFTSolve solutions for MM-02/2440, Mar-00/2304, Mar-00/2200 and Mar-00/2030 only yielded solutions at 'acceptable' levels of statistical fit with the data (Fig. 4.3a-e). *t*-T paths were generated at 'good' levels of statistical precision for MM-02/2635, but show little variation from the other model runs. No appropriate modelled AHe ages could be generated for sample Mar-00/2304.

All of the *t*-T paths suggest samples were at >110°C prior to ~35 Ma. From approximately 30 Ma temperatures reduce over a period of 2-3 Myr to lowermost PAZ temperatures. This short cooling 'event' is common to the large majority of *t*-T solutions for all four samples. Moderate variations between samples are observed in the timing of onset of this rapid cooling event, though most are bracketed in the time interval between ~34 to 28 Ma. All *t*-T solutions depict a subsequent period of relative thermal stability after the pulse of rapid cooling. Time-temperature trajectories indicate samples may have resided in AHe PRZ temperatures, for up to 10 Myr, prior to monotonic cooling to the modelled surface temperature (10°C).

4.6.2 Maladeta integrated thermal modelling

Modelling of the Maladeta AHe ages and parameters, using *t*-T paths derived from the AFTSolve solutions, shows significant differences between the four available samples (**Fig. 4.6f-i**). In order to generate *t*-T paths the level of statistical fit was lowered to match that yielded by the AFTSolve model runs. No appropriate AHe ages could be generated for sample Mal-00/2030.

t-T solutions for Mal-00/2870 (Fig. 4.6f) depict poorly constrained histories prior to ~30 Ma, followed by a period of cooling to ~70°C, by ~25 Ma. This interval represents rapid cooling of all *t*-T paths and through AFT PAZ temperatures over 2 to 3 Myr. This is followed by a period of relative thermal stability in which *t*-T paths are maintained within AHe PRZ temperatures until up to ~12 Ma. After this time the model solutions indicate samples cooled to less than ~35°C.

Model ages generated by *t*-T solutions for Mal-00/2250 (Fig. 4.6g) show good agreement with the upper range of AHe ages defined by Mal-00/2250:1 and Mal-00/2250:2, but not with the significantly younger Mal-00/2250:3. Between 20 and 13 Ma, all *t*-T paths record slow cooling within AHe PRZ temperatures, prior to cooling to less than 40°C by ~10 Ma.

The closest fit between model and measured AHe ages for Mal-00/1760 (Fig. 4.6h) were generated by *t*-T paths depicting a two-phase cooling history separated by a prolonged period of relative thermal stability; *t*-T solutions indicate cooling through AFT PAZ temperatures had occurred by ~25 Ma and was followed by stability above AHe PRZ temperatures for up to 16 Myr. The second stage of cooling commences between ~10 to 7 Ma and is maintained for a short duration of 1 to 3 Myr. After this event all *t*-T paths are at temperatures below the AHe PRZ and cool slowly to 10°C by 0 Ma. The modelled ages for these t-T solutions are up to 1 Myr older than the uncorrected measured ages. The vast majority of AFTSolve solutions depict a steady and continuous cooling history after ~30 Ma

(Fig. 4.6i). Importantly, these *t*-T paths generate model ages which are significantly older (up to 7 Myr) than the uncorrected AHe ages of Mal-00/1760.

4.6.3 Barruera integrated thermal modelling

Model results for the Barruera data are well constrained and show limited variability between different *t*-T paths. Cooling trajectories for Bar-02/1695 (**Fig. 4.6j**) depict transition through AFT PAZ temperatures by 18 to 12 Ma, followed by an acceleration of cooling rates at ~10-12 Ma for up to ~3 Myr. By ~8 Ma, all *t*-T paths are cooler than AHe PRZ temperatures.

Model *t*-T paths for Bar-02/1150 (**Fig. 4.6k**) depict a slight increase in cooling rates for 4 to 5 Myr until ~20 Ma. This is followed by a period of relative thermal stability, during which *t*-T paths are retained within AHe temperatures for up to 8 Myr. At ~8 Ma, cooling rates in all the *t*-T solutions dramatically increase for 2 to 3 Myr. This is followed by a period of slower cooling to present day.

4.7 Time-Temperature (*t*-T) evolutions

By compiling the cooling ages, the age-elevation relationships, thermochronometric parameters and thermal modelling results from each profile, the *t*-T history since Early Eocene times can be documented for each location.

4.7.1 Marimaña *t*-T evolution

The ZFT age of the uppermost sample from the Marimaña region indicates the top of the profile was above ~210°C by earliest Middle Eocene times (~49 Ma). The uniformly long mean track lengths and low standard deviations exhibited by all AFT samples from the Marimaña, are indicative of rapid cooling of the entire profile (~600 m) through the AFT PAZ. This cooling event is constrained by the *t*-T envelopes depicted in all the AFTSolve thermal models to have occurred during Early Oligocene times (~34 to 28 Ma). Hence, the uppermost sample of the profile cooled from above ZFT annealing temperatures to at least 600 m above AFT annealing temperatures during the time interval between 49 to 28 Ma.

The AHe ages of the uppermost sample from the Marimañi profile are indistinguishable, within analytical uncertainty, from the corresponding AFT age. This is consistent with the rapid cooling through the AFT T_c and the AHe T_c. This is supported by the rapid cooling of the lower elevation AFT samples. The remaining samples from the AHe profile yield progressively younger ages with decreasing elevation. Model results are consistent with a period of rapid exhumation through AFT partial annealing temperatures, followed by slow cooling and protracted residence in AHe PRZ temperatures for up to 10 Myr. It is unclear whether the gradient of the AHe age-elevation profile documents a palaeo-AHe PRZ or the vertical velocity at which the profile was exhumed through the PRZ.

4.7.2 Maladeta *t*-T evolution

The ZFT age of the lowermost sample from the Maladeta region indicates the base of the profile was above ~210°C by earliest Middle Eocene times (~49 Ma). Long mean track lengths, low standard deviations and the relative age-invariance with decreasing elevation, are compatible with the rapid cooling of the profile (~1100 m) through AFT partial annealing temperatures. This is further supported by the AFTSolve thermal modelling results which depict steep *t*-T trajectories through the PAZ during Early Oligocene times (~34 to 28 Ma). The slight shortening of mean track lengths in the lowest elevation sample indicates additional annealing that may identify a decrease in cooling rates prior to the transition of the base of the profile to temperatures cooler than the AFT PAZ.

The AHe ages from the Maladeta profile are significantly younger than the corresponding AFT ages. Ages from samples above ~2100 m decrease progressively with elevation. DeComp modelling results are compatible with protracted exhumation through AHe PRZ temperatures for these samples. In contrast, ages from samples below ~2100 m show little variation with elevation. Model results are compatible with an abrupt increase in cooling rates and the rapid transition of the lower samples through AHe PRZ temperatures during Late Miocene times (~10 to 7 Ma), followed by slower cooling to the present day.

4.7.3 Barruera *t*-T evolution

The ZFT age (104±7 Ma) for the lowest elevation sample from the Barruera profile significantly predates the onset of Pyrenean orogenesis (Roest and Srivistava, 1991) and records an earlier cooling history. This implies that the rocks now exposed in the Barruera region were at temperatures cooler than ZFT annealing temperatures throughout Pyrenean mountain-building processes. The AFT ages of the Barruera profile show no significant variation with elevation. The relatively long mean track lengths for the upper two samples, combined with low standard deviations, indicate a relatively rapid transit through PAZ temperatures. The lowermost sample has shorter mean track lengths suggesting moderate annealing associated with a slightly slower passage through the same temperature interval.

This notion is supported by the AFTSolve model *t*-T paths, which depict transition through PAZ temperatures during Lower Miocene times (~20±2 Ma) at faster rates for the upper two samples.

The AHe ages from the Barruera profile are ~10 Myr younger than their corresponding AFT ages and show limited variation with elevation. DeComp modelling predicts a pronounced increase in rates of cooling through AHe PRZ temperatures during Late Miocene times (~10 to 8 Ma), followed by constant cooling rates to 0 Ma.

4.7.4 Nogueres *t*-T evolution

The ZFT age (159±33 Ma) from the lowest elevation sample in the Nogueres Zone is also significantly older than the onset of mountain-building. This indicates the region was at less than ZFT annealing temperatures from at least mid-Tertiary times.

The AFT ages and track length data for both the profile and single-elevation samples are consistent with the progressive exhumation of the region through Upper Oligocene and Lower Miocene times (~30 to 20 Ma). The age-elevation relationship depicts a low gradient, linear best-fit. Thermal modelling of the data in AFTSolve supports the interpretation of a relatively slow transition through PAZ temperatures.

As there were no AHe analyses performed on the Nogueres samples, owing to poor apatite yields, no further thermal constraints are available and the history less than 70°C remains undocumented.

4.8 PeCube topographic and thermal modelling

The *t*-T histories derived from the thermochronological data document the passage of the sample profiles through the thermal field of the upper crust. To relate this thermal evolution to a meaningful understanding of exhumation, and the processes that controlled it, the state of the thermal field at the time of mineral cooling must be considered.

As discussed in Chapter 3, there are a number of factors which may perturb the temperature regime in the shallow crust and so may strongly influence thermochronological data. Of primary importance are the effects of isothermal perturbation by surface topography, the upward advection of heat during rapid exhumation, and the downward migration of heat associated with thermal relaxation after advection. In order to assess the extent that the *t*-T histories are a function of the mechanisms that controlled exhumation, or simply a function of transiting a perturbed and dynamic thermal regime, it is appropriate to synthetically model the system.

The finite-element code 'PeCube' (Braun, 2003) is applied to simulate different thermal and topographic scenarios and to assess their impact on model AHe ages (Lynn, pers comm.; Gibson et al., submitted). Ages from the other thermochronometric systems are not modelled as it is assumed that the influences of thermal perturbations are greatest for the lowest temperature system. The code was developed to solve the three-dimensional heat transport equation in uplifting and eroding lithospheric blocks which have an evolving, finite-amplitude surface topography (Braun, 2003). *t*-T histories of rock particles can be generated for an exhuming crustal block with a pre-defined surface topography. These *t*-T paths can then be input into thermochronometer-specific software to forward-model cooling ages (Braun, 2002; Braun, 2003).

A 44 km^2 sample of ~90 m SRTM (Shuttle Radar Topography Mission) data (U.S.G.S., 2004) topography from the central Pyrenees (**Fig. 4.7a**), incorporating the sampling localities, was downgraded in resolution to a grid of 1 km^2 nodes using ArcInfo software (ESRI, 2000) (**Fig. 4.7b**). For each experiment, this grid was delineated as the end-point topographic configuration reached by the model before present-day (0 Ma). *t*-T paths were generated for a number of exhumational and topographic scenarios (see below) and were used to forward model AHe ages. Model *t*-T paths are a function of only two variables imposed on each experiment, namely a temporally-variant exhumation history and a specific topographic evolution. AHe ages were calculated for a range of apatite crystal sizes (66 to 130 μm diameter) using DeComp (Dunai et al., 2003). An age-elevation profile was generated by each model run at the geographical location and elevation of the samples in the Marimaña and Maladeta profiles, as these offered the largest and most interpretable datasets.

4.8.1 Model boundary conditions

The boundary conditions used to simulate the upper crustal thermal structure are defined by the following parameters which were assumed to be spatially uniform and non-variant with time: heat diffusivity (25 km^2 Myr^{-1}), heat production (23.44 °C Myr^{-1}), crustal thickness (20 km), and crustal basal temperature (500°C). Each model run was initiated at 45 Ma and terminated at present-day (0 Ma). At 45 Ma isotherms are distributed uniformly with depth, giving a geothermal gradient of 25°C km^{-1}. However, during periods of exhumation, the isotherms are advected towards the cooling surface (Brown and Summerfield, 1997), thus temporarily increasing the geothermal gradient during model runs up to values of ~40°C km^{-1}.

4.8.2 Model parameter I – Exhumational evolution

A period of rapid exhumation, with a vertical velocity of 0.5 km Myr^{-1}, was imposed on all runs from 36 to 30 Ma. This was done to simulate the period of rapid cooling observed in all the AFT data from the Marimaña and Maladeta profiles, and in previous AFT studies from this region (e.g. Fitzgerald et al., 1999). This rate represents a minimum value based on previous estimates of exhumation at this time (Fitzgerald et al., 1999) and may be significantly increased with little effect on the derived model ages. Importantly, it generates model AFT ages of ~30±3 Ma with long mean track lengths (~14μm) for the samples from both profiles. This is consistent with the AFT data both from this study and with previous datasets (Fitzgerald et al., 1999).

The post-30 Ma exhumational history was assumed to be one of two possible alternatives. The first scenario assumes that after the decline of exhumation at ~30 Ma the exhumation velocities were slow and continuous (0.053 km Myr^{-1}) to the present-day. The rate used represents the minimum value required to exhume the samples from above the AFT PAZ to the surface in 30 Myr. This continuous and slow exhumation is intended to represent a simplified modelling analogy of the *t*-T paths derived from the Marimaña data and Maladeta data (above ~2100 m). This protracted history of exhumation also represents a simplified modelling analogy for that predicted for post-orogenic settings (Pinet and Souriau, 1988; Baldwin et al., 2003; Reiners et al., 2003).

The second scenario assumes that exhumation is negligible immediately after the decline of tectonism at ~30 Ma, but resumes at accelerated rates (0.275 km Myr^{-1}) between 12 and 8 Ma, and then significantly declines (0.0625 km Myr^{-1}) from 8 Ma to present. This scenario, of thermal stability punctuated by pulses of accelerated exhumation, is intended to represent a simplified modelling analogy of the *t*-T paths derived from the lower Maladeta samples and interpreted from the Maladeta age-elevation relationship. The vertical velocities are the minimum values required to exhume samples through the AHe PRZ during the 12 to 8 Ma interval, and subsequently to their present elevations from 8 Ma. Alternative values are also experimented with for the Marimaña model profile in order to assess the impact of varying exhumation rates. All exhumation rates for each model run are presented in **Table 4.3**. For simplicity it is assumed rates were continuous during the designated intervals, however, it is the total amount of exhumation during the given time-period that is of primary importance and not the maintenance of a singular vertical velocity.

4.8.3 Model parameter II – Topographic evolution

In order to test the relative impact of different topographic evolutions on model AHe ages, three end-member scenarios were tested against both exhumational histories. As there are no independent constraints on the topographic development in the area, it is necessary to assess the impact of decreasing, increasing and unchanging relief, with respect to the modern topography. For the pulsed exhumational history it was assumed that the abrupt changes in vertical velocity coincided with the changes in relief, and for the continuous exhumational history it was assumed the relief changes occurred progressively through time. For the first topographic scenario it is assumed a topography identical to that in the modern system was created by 30 Ma and has been retained to present-day. For the second scenario it is assumed that a very low amplitude (essentially flat) topography was sustained until at least 30 Ma. The modern topography was carved from this progressively from 30 Ma (continuous exhumation) or rapidly between 12 to 8 Ma (pulsed exhumation). For the third scenario it is assumed that a high amplitude topography (50% larger than the modern system) was present until 30 Ma. This amplitude was then reduced to the modern topography progressively from 30 Ma (continous exhumation) or rapidly between 12 to 8 Ma (pulsed exhumation).

4.8.4 PeCube model results

Model ages are presented as two linear age-elevation profiles, corresponding to the ages predicted for apatites of 66 and 130 μm diameter, and are plotted with the measured AHe data to allow direct comparison (**Fig. 4.8a, b**). The corresponding *t*-T profile and topographic scenario are located above and to the side, respectively, of the age-elevation plots for each model run.

Model ages for the Maladeta profile (**Fig. 4.8a**) display a negligible degree of variability as a function of changing topography. In contrast, the two exhumational scenarios yield markedly different results; age-elevation relationships generated from the pulsed exhumational history show a relatively good fit to the measured AHe ages (Runs 1, 3 and 5), whereas profiles generated by the continuous exhumation depict a linear trend significantly outside the uncertainty of the AHe data (≤15 Myr) (Runs 2, 4 and 6).

Owing to the negligible impact of topographic variation, only the constant relief scenario is presented for the Marimaña profile (**Fig. 4.8b**). Instead, the two exhumational scenarios are run with varying vertical velocities (**Table 4.3**). For pulsed exhumation, the model ages are consistent with the measured data when exhumation rates are significantly reduced (Run 9) and show a large discrepancy when the same values are imposed as those used for the Maladeta profile (Run 7). For continuous exhumation, however, the model ages fit with the measured data with the same rates as used in the Maladeta profile (Run 8), but show much reduced compatibility when the rates are lowered (Run 10).

4.8.5 PeCube discussion and summary

The modelling results demonstrate the limited influence that topographically-induced isothermal perturbation imposes on the AHe ages and derived *t*-T histories. A larger impact may have been generated if the profiles had a significantly greater horizontal spatial component, thereby sampling the larger topographic wavelength of the orogen. However, in this case, no additional corrections are necessary and it can be assumed that the age-elevation relationships from the Marimañi and Maladeta profiles are largely a function of the exhumation history. Furthermore, as the evolution of topography in the area is unlikely to have undergone such an extreme history as depicted in the end-member scenarios, the true extent of thermal perturbation caused by this effect is likely to be considerably less than that depicted in the models.

The PeCube modelling demonstrates that the AHe (and AFT) ages for samples from the Maladeta profile cannot be resolved by a *t*-T history characterised by slow and protracted exhumation. The age-elevation relationship, however, can be accurately reproduced by a model that imposes a period of protracted thermal stability after the 36-30 Ma rapid cooling/exhumation event followed by an abrupt rejuvenation of exhumation at approximately 10 Ma. During the initial period of exhumation (36-30 Ma), 1100 m of rock column is exhumed rapidly through the apatite fission track PAZ. This is consistent with the generation of a vertical age-elevation profile of Early Oligocene apatite fission track ages combined with long mean track lengths in the Maladeta profile. Exhumation subsequently declines and the profile languishes at constant or negligibly decreasing depths, with the upper elevation samples being held within the AHe partial retention zone, and the lower samples below it, for at least 18 Myr. Exhumation processes are abruptly rejuvenated at around 12 Ma and the lower samples rapidly cool through temperatures at which the AHe system is sensitive. This is compatible with the upper samples from the profile (>2100m) depicting a palaeo-PRZ and the lower samples, yielding elevation-invariant ages, recording rapid exhumation at 8-12 Ma.

Simulations of the Marimaña profile, in contrast, indicate a markedly different *t*-T history is required in order to generate ages which are compatibile with the AHe data. The two scenarios, which cannot be reliably discriminated from each other, suggest the Marimaña either progressively exhumed at a rather constant and slow rate from 30 to 0 Ma, or underwent a pulse of exhumation between 12 to 8 Ma but at rates significantly less than recorded by the Maladeta profile.

Model results for both profiles indicate that the amount of exhumation required to transport the samples from the AHe PRZ temperatures is ~1.6 km. This suggests that immediately after rapid exhumation the geothermal gradient increased from 25°C km^{-1} to ~40°C km^{-1}. This increase is caused by the upward advection of heat during rapid exhumation and declines through time as the thermal field relaxes to it's former state (Brown and Summerfield, 1997). This is a transient effect which diminishes during the subsequent periods of relative thermal stability.

4.9 Pyrenean exhumation from low-temp thermochronology

As noted in chapter 3, all cooling documented in the profiles is assumed to be associated with 'exhumation', or the displacement of the rock column toward the surface. To assess the temporal and spatial variability in exhumation, it is necessary to quantify it during specific intervals of time and at specific localities. This can be achieved by employing the *t*-T histories derived from the thermochronological data from the four profiles, and by making a number of fundamental assumptions regarding the thermal structure of the crust at the time of mineral cooling.

In this study it is assumed the isotherms in the upper crust remained approximately parallel to the orogen's large-scale morphology during mountain-building, and that this gross morphology was not significantly different from the present day (section 3.5.6.1). All estimates of exhumation in the following section represent minimum and maximum values based on a range of geothermal gradients (25 to 35 °C km^{-1}), a range of closure temperatures (AHe: 65 to 75°C; AFT: 105 to 115°C; ZFT: 210 to 245°C) and a surface temperature of 10°C (section 3.5.6.1). The uncertainty on the palaeodepths of the closure isotherms, associated with topographically-induced isothermal perturbation in a thermal steady-state setting, is 0.236 km for the AHe system, 0.125 km for the AFT system, and 0.023 km for the ZFT system (section 3.5.6.1; Stüwe and Hintermüller, 2000). The PeCube modelling results indicate that these geothermal gradients and mineral closure temperatures are at least reasonable for the interpreted exhumation histories. However, model results indicate that during and after periods of rapid exhumation the geothermal gradients may temporarily increase to ~40°C km^{-1}. Assuming a geotherm of 25 to 35°C km^{-1} may lead to a modest over-estimation of the amount of exhumation. The modelling results also suggest the impact of topographically-induced thermal perturbation is very small and of similar magnitude to that estimated. The mean elevation used to calculate the 'effective elevations' (el_e) (section 3.5.6.1) for the Marimaña, Maladeta and Barruera Axial Zone sampling localities is 1.87±0.35 km. The mean elevation used for the Nogueres Zone samples is 1.34±0.22 km.

The regional variability of exhumation over time is presented in the next section. The time periods used are defined by the cooling 'events' derived from the thermochronological data. The derived exhumational histories and values are further discussed in Chapter 6.

4.9.1 Pre-Oligocene (~34 Ma) exhumation

The ZFT ages from the Marimaña and Maladeta profiles are very similar (~50 Ma) and are consistent with both regions being exhumed through ZFT annealing temperatures by Lower Eocene times. The difference in effective elevations between the samples (MM-02/2635: el_e = +765 m; Mal-00/1760: el_e = -110 m) dictates that they may have undergone different amounts of exhumation relative to the mean elevation since closure in the ZFT system. Values range from 6.7 to 9.9 km and 5.7 to 9.1 km, for the Marimaña and Maladeta ZFT samples, respectively, if it is assumed the ZFT ages represent closure ages. Two explanations for the potential relative difference in exhumation are plausible; (i) a significant amount of the rock column at both localities cooled through the ZFT PAZ by ~50 Ma, and yield no ZFT age variability in the profiles. In this scenario, the apparent variation in exhumation between the two sites would simply be associated with the different elevations at which the rocks were sampled. Alternatively, (ii) the two profiles cooled progressively through ZFT PAZ temperatures, and so only samples from specific elevations would yield a ~50 Ma age. For this scenario the Marimañi region must have since undergone preferential exhumation to elevate it to its higher elevation. This scenario would suggest the Marimañi region had been exhumed up to 0.87 km more than the Maladeta region. However, owing to the considerable overlap in exhumation estimates, associated with the large range of ZFT T_c applied, it is not clear if differential exhumation is documented. As there are no further constraints available on the Eocene cooling history, such as additional ZFT ages from different elevations in the two profiles, the two different scenarios cannot be reliably discriminated from each other.

The Barruera ZFT age (104 Ma) is significantly older than the onset of mountain-building and so, by inference, records a thermal history from an earlier stage of crustal evolution. This highlights a significant exhumation gradient that occurred during Pyrenean orogenesis between the Barruera and Marimaña/Maladeta regions, with less exhumation recorded by the Barruera profile. The absolute difference in exhumation cannot be accurately quantified, because it is not known from what depths below the ZFT PAZ the Marimaña and Maladeta samples have been transported prior to ~50 Ma, nor at what depths above the ZFT PAZ the Barruera sample resided prior to ~50 Ma. The maximum value of exhumation for the Barruera profile since the onset of orogenesis must lie in the range between 5.1 to 8.5 km, and the minimum value must be greater than the depth of the AFT T_c (2.7 to 4.2 km). The ZFT age from the Nogueres Zone is also older than the time of onset of the Pyrenean orogeny. This indicates that the lowest elevation sample in the region has likewise not been exhumed from depths greater than the ZFT PAZ and thus may share a similar early exhumational history to the Barruera region.

In summary, strong spatial variability in exhumation is clearly documented by the distribution of ZFT ages during orogenesis prior to ~34 Ma. Maximum depths of exhumation occur in the Marimaña and Maladeta regions, with significantly less in the adjacent Barruera region to the south and in the Nogueres region on the southern flank of the range. Previous AFT studies and numerical modelling of the central Pyrenees have predicted maximum exhumation to have occurred significantly further south, above the structural culmination of the Axial Zone antiformal stack (Muñoz, 1992; Fitzgerald et al., 1999; Beaumont et al., 2000). Overall values of exhumation in the Axial Zone since the samples cooled through ZFT T_c, calculated for the Marimaña and Maladeta regions, range between ~5.5 to ~9.5 km. These values are considerably less than those previously predicted from AFT studies and restored structural cross-sections for the central Axial Zone region (Muñoz, 1992; ~15 km; Fitzgerald et al., 1999).

4.9.2 Lower Oligocene (~34 to 28 Ma) exhumation

The AFT data from the Marimaña and Maladeta profiles are consistent with rapid exhumation of the regions through AFT partial annealing temperatures during Lower Oligocene times. The vertical difference between the upper- and lowermost samples, indicate a maximum of ~0.6 and ~1.1 km of crustal removal may be documented by the Marimaña and Maladeta profiles, respectively. As the upper sample from the Marimaña profile also has an AHe age within error of the AFT age, it implies that 1.1 to 1.6 km of crust was removed from above the Marimaña profile since closure of the AFT system. The total amount of exhumation required to transport any of the samples from the AFT T_c to the mean elevation since mineral closure is ~2.7 to 4.2 km. As both profiles record the same period of cooling at the same elevations it cannot be determined if there was differential exhumation at either site.

The base of the Maladeta profile and the top of the Barruera profile have an almost identical effective elevation (-0.110 and -0.120 km, respectively). Despite this, the Barruera data indicates the profile was at more than ~110°C during Lower Oligocene times, while the Maladeta region was rapidly exhuming. By considering both AFT and ZFT data, a significant exhumation gradient is apparent between the Barruera and the Marimaña/Maladeta regions; as the Marimaña and Maladeta profiles exhumed from temperatures above the ZFT T_c to below the AFT T_c between ~50 and 30 Ma, the Barruera region was retained at temperatures between the ZFT and AFT closure isotherms. Maximum values of exhumation for the sample at the base of the Barruera profile during this interval is ~2.5 to 4.6 km.

The Nogueres Zone samples are significantly lower in elevation that those from the Marimaña/Maladeta region, and so the AFT data are difficult to directly compare. During Lower Oligocene times the high elevation Nogueres samples transited the AFT PAZ at relatively slow rates and were at <60°C at a time similar to the Barruera samples. The amount of exhumation required to transport the lowest elevation AFT sample to it's position in the modern landscape is 2.3 to 3.8 km since Lower Oligocene times.

In summary, during the time interval between 34 to 28 Ma, the strong spatial variations in exhumation documented prior to this period are maintained. The greatest amount of exhumation is recorded by the Marimaña and Maladeta profiles during a period of rapid cooling. The Nogueres profile was also exhuming through PAZ temperatures, though probably at much slower rates. In contrast, the Barruera profile, which is located between the Nogueres and Marimaña/Maladeta regions, was at higher temperatures during this interval and records significantly less exhumation. The data support previous interpretations which depict a period of rapid exhumation within the central Axial Zone during Lower Oligocene times, associated with an acceleration of tectonically-driven rock uplift (Fitzgerland et al., 1999). However, previous workers have assumed exhumation at this time occurred over a large, diffuse area of the south central Pyrenees, centred on the culmination of the Axial Zone antiformal stack (Morris et al., 1998; Fitzgerald et al., 1999; Beaumont et al., 2000). The limited amount of exhumation documented in the nearby Barruera profile indicate this is unlikely. Instead, exhumation was localised to the north, as documented in the Marimaña and Maladeta profiles.

4.9.3 Upper Oligocene to Mid Miocene (~28 to 12 Ma) exhumation

The AHe data from the Marimaña profile and PeCube thermal modelling indicate that from ~28 Ma until at least ~21 Ma, slow exhumation or thermal stability occurred. The amount of exhumation required to transport the lowest elevation sample to it's current position in the landscape since ~20 Ma is 1.7 to 2.8 km. Regression analysis of the data depict a cooling rate of 0.05 km Myr^{-1}. Using this value in PeCube modelling of the data generates the measured age-elevation profile. If exhumation was continuous at this rate, and prolonged thermal stability did not occur, the Marimaña region would exhume only ~0.8 km during upper Oligocene to Middle Miocene times.

The AHe data from the Maladeta profile also depict a period of either slow exhumation or thermal stability between ~28 and 12 Ma. PeCube and thermal modelling of the data indicate the age-elevation profile is most compatible with a protracted period of thermal stasis. Despite the Maladeta profile depicting a very similar thermal history to the Marimaña profile during this interval, the same AHe ages are persistently at higher elevations in the modern topography. This can be demonstrated by comparing the required exhumation ranges for two samples of similar age from either profiles; the base of the Marimaña profile ($el_e = +0.160$ km) requires 1.7 to 2.8 km exhumation since ~24 Ma, whilst the top of the Maladeta profile ($el_e = +0.930$ km) requires 2.5 to 3.5 km exhumation since ~24 Ma.

The Barruera AFT data and thermal modelling indicate a period of relatively rapid exhumation occurred at ~20±2 Ma. This is only unambiguously documented in the upper two samples, which are within 100 m in elevation of each other, with the lower sample indicating significantly more annealing and slower transit through PAZ temperatures. This may suggest the ~20 Ma exhumation 'event' recorded in the Barruera profile was of a relatively small magnitude. This is consistent with it not being documented in the nearby Marimaña or Maladeta profiles at ~20 Ma by either the AFT or AHe thermochronometers.

The ~20 Ma event depicted in the Barruera profile is not observed in the Nogueres AFT data. Instead, the data are consistent with slow and protracted exhumation of the region during Upper Oligocene to Middle Miocene times. The age-elevation profile indicates slow exhumation rates of 0.045 km Myr^{-1}. If this rate was maintained for the 28 to 12 Ma interval, 0.7 km of crust would have been exhumed in this time.

The decline of Pyrenean orogenesis has been proposed to occur within Upper Oligocene times. Structural studies within the southern fold and thrust belt indicate a cessation of tectonic shortening by ~29 Ma, with minor reactivation of activity until ~28 Ma

(Meigs et al., 1996; Meigs, 1997). Fission track studies have interpreted the decline of exhumation in the western Maladeta at ~30 Ma to mark the end of major tectonics (Fitzgerald et al., 1999). Sea-floor spreading data, however, indicates Iberian convergence and Pyrenean shortening was maintained until at least ~23 Ma (Srivistava et al., 1990; Roest and Srivistava, 1991). The reduction of exhumation documented in this study from ~28 Ma onwards, is consistent with the decline but not the cessation of major tectonics and likely heralds the onset of the final stage of active, but markedly reduced, orogenic growth. The cooling documented at ~20±2 Ma documented in the Barruera profile is the latest recorded exhumational 'event' within the tectonically-active Pyrenees.

4.9.4 Post-Middle Miocene (~12 Ma) exhumation

AHe data from the Marimaña profile document the exhumation history until ~20 Ma. If the best-fit line through the age-elevation data is projected (i.e. continuous rates of exhumation since Lower Miocene times) apatites at 0.9 km elevation are predicted to have an AHe age of 0 Ma. This is ~1 km below the regional mean elevation. Assuming a geothermal gradient of 25 to 35 °Ckm^{-1} and a surface temperature of 10°C, would not be at sufficient temperatures to cause total He diffusion and to generate a 0 Ma age and suggests that exhumation rates since 20 Ma have not been continuous and must have increased at some time.

The Maladeta AHe ages and thermal modelling indicate exhumation rates abruptly accelerated at ~10±2 Ma. PeCube results are compatible with this interpretation and suggest rates of 0.26 km Myr^{-1} between 12 to 8 Ma are sufficient to generate the age-elevation profile. At least 0.27 km of the rock column at the base of the Maladeta profile exhumed rapidly through the AHe PAZ temperatures. In reality, this value may be considerably larger as the vertical extent of the exhumation event is not documented. In order to exhume the lowest elevation sample of the Maladeta profile to it's current position since ~10 Ma requires 1.5 to 2.5 km to be removed. AHe ages and thermal modelling of data from the Barruera profile are also compatible with an abrupt acceleration of exhumation at ~10±2 Ma. The required exhumation to transport the bottom sample to it's position in the modern topography is 0.9 to 1.9 km. After ~8 Ma the exhumation history is undocumented by the AHe data.

Previous studies have documented that the cessation of Iberian plate convergence and tectonic shortening occurred by 23 Ma (Srivistava et al., 1990; Roest and Srivistava, 1991). AHe ages and modelling of data from the Maladeta and Barruera profiles in this study indicate exhumation was abruptly rejuvenated at ~10 Ma, during the 'post-orogenic' period.

This event is not recorded in the Marimaña profile but PeCube modelling indicates it may have occurred but with less overall exhumation. Forward modelling of Oligocene AFT data by Fitzgerald et al. (1999) predicted that exhumation rates may have accelerated during Mio-Pliocene times. The rejuvenation of exhumation documented in this study is inconsistent with previous empirical and theoretical studies of post-orogenic topography which predict exhumation rates should exponentially decline after the cessation of tectonics (e.g. Pinet and Souriau, 1988; Pazzaglia and Brandon, 1996; Baldwin et al., 2003; Reiners et al., 2003).

4.10 Localisation of erosional denudation: A summary

Exhumation within the central Pyrenees was demonstrably variable across the south central region both during and after orogenesis. There is no structural or metamorphic evidence within the region to indicate exhumation has been influenced by tectonic denudation of the crust. Therefore, it is assumed that the singular driving mechanism behind the documented patterns of exhumation was the spatial and temporal variability in the rate at which erosional processes denuded the surface and hence, exhumed the rock column. Gradients in exhumation between adjacent regions, therefore, represent the localisation and spatial partitioning of processes of surface erosion.

A number of time intervals in the history of the sampling region are characterised by clear spatial gradients in the rates at which surface erosion operated and the amount of exhumation which resulted. These can be summarised, as follows:

a. From Early Eocene to Early Oligocene times, erosional denudation was focused in the region of the Marimaña Massif and the Maladeta Massif, both in the central Axial Zone. The Marimaña massif may have undergone slightly more exhumation (~0.9 km) at this time, though this cannot be unequivocally confirmed by the data. The syn-orogenic erosional history of both regions is dominated by a period of rapid exhumation between ~34 to 28 Ma. Erosional denudation in the Barruera region, which is also located in the central Axial Zone, was significantly less during the same interval (2.4 to 4.6 km). The exhumation histories from neither Barruera nor Nogueres record a period of accelerated erosion between ~34 to 28 Ma.

b. During Late Oligocene and Early Miocene times, erosional denudation was dramatically reduced in all regions except the Barruera area. Denudation was maintained or temporarily reactivated here during Lower Miocene times, though this event is not recorded in the surrounding regions.

c. During Middle to Upper Miocene times, or during the 'post-orogenic' period, rates of erosional denudation were dramatically rejuvenated in at least the Maladeta and Barruera regions. Erosion rates in the Marimaña region may have also increased, but at lower rates than recorded in the southern areas.

Documenting the spatial and temporal variability of erosion is of limited value for understanding the evolution of an orogen if the mechanisms that controlled it are not understood. Of primary importance for this study is to assess what forcing could have initiated periods of rapid or rejuvenated erosion, and what mechanisms could have isolated and accommodated the effects in specific spatial domains. By doing this, the erosion histories can be placed within a geological context and their impact on Pyrenean evolution be more fully understood.

Fig. 4.1 Geological and topographic location map of sampling area

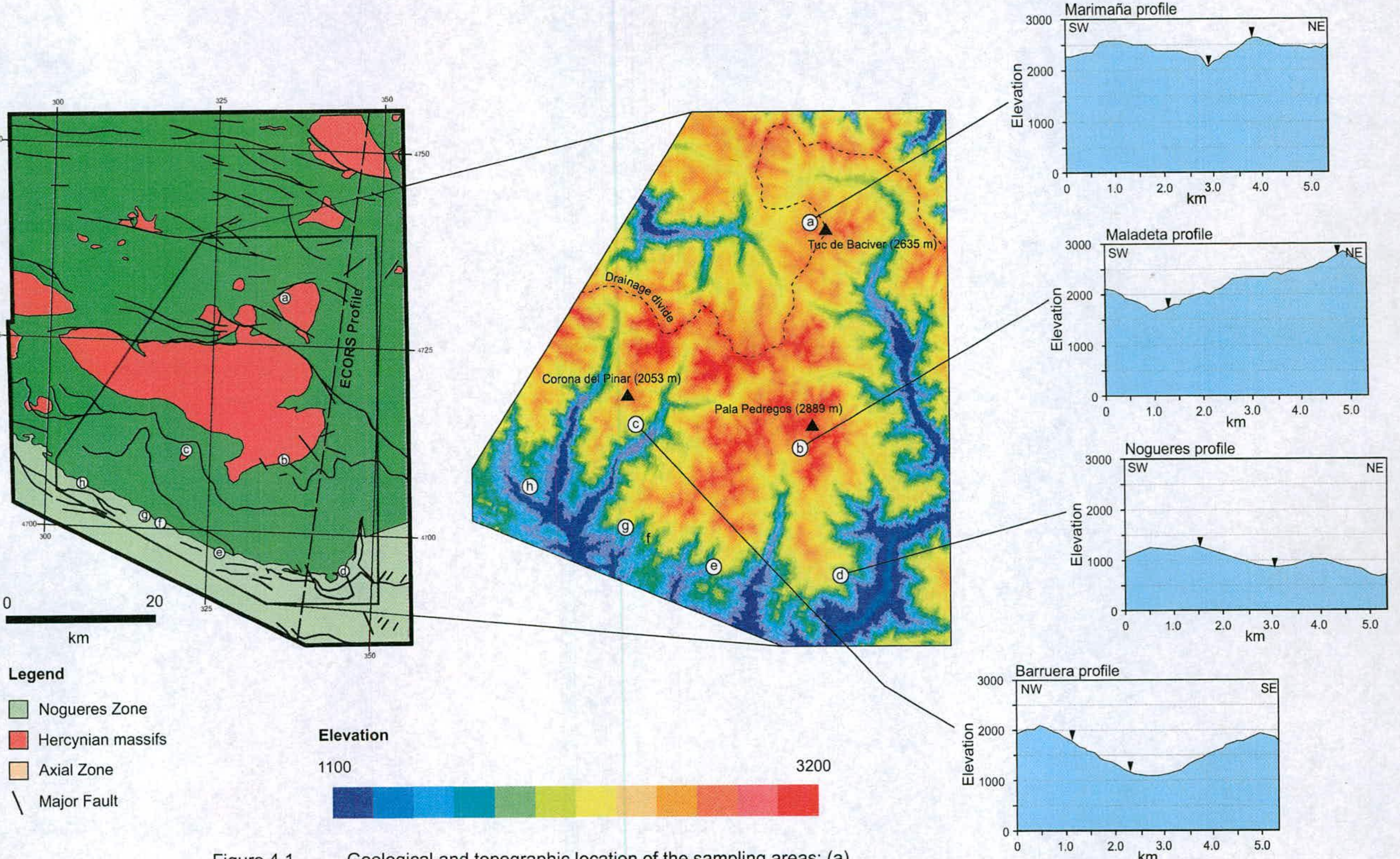

Figure 4.1 Goelogical and topographic location of the sampling areas: (a) Marimañi profile, (b) Maladeta profile, (c) Barruera profile, (d) Nogueres profile, (e-h) Nogueres single elevation samples.

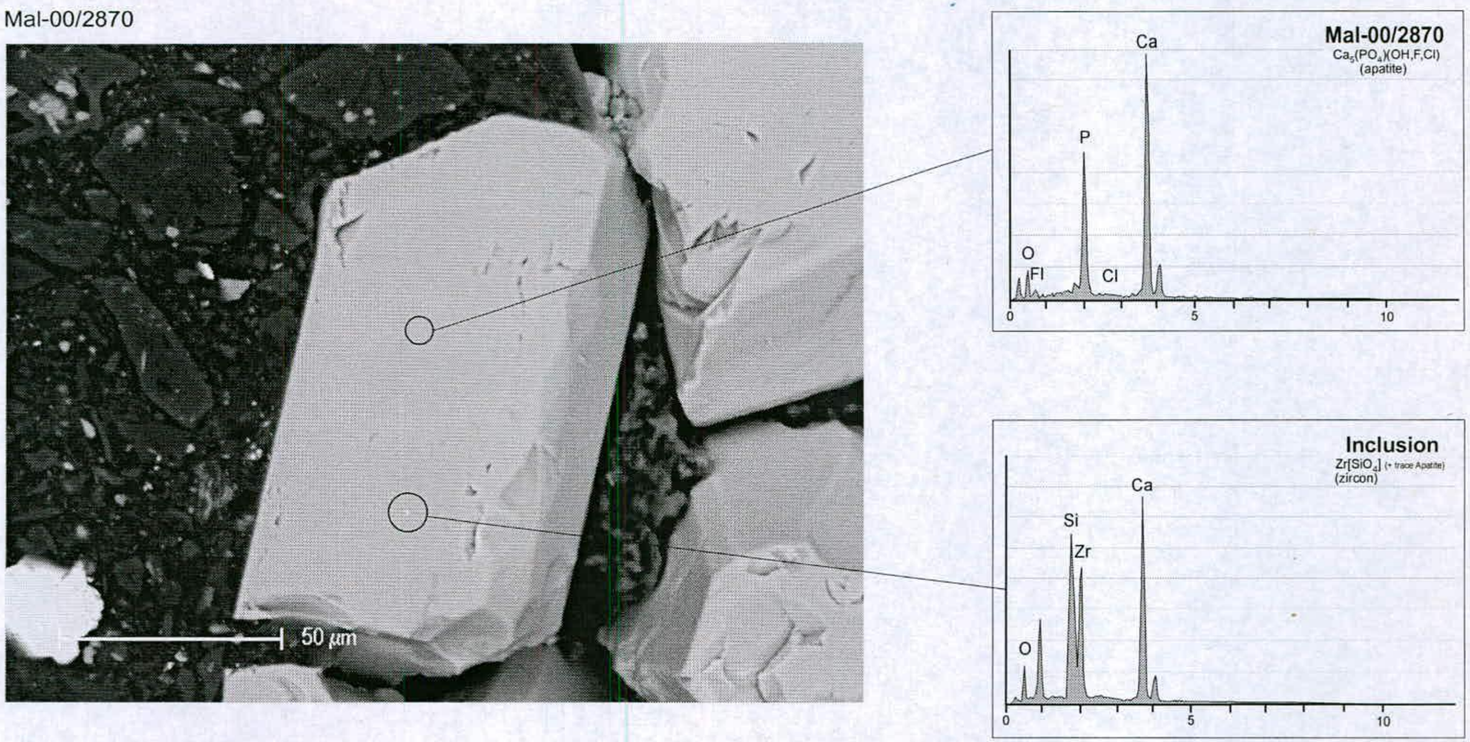

Figure 4.2a Backscatter Electron (BSE) images of apatite crystals with mineral inclusions of the <1μm scale. Each inclusion can be identified from the host apatite by a clear variation in greyscale tones according to the mean atomic number of the inclusion phase. Quantitative analysis of the elemental presence in the inclusions, achieved using Energy Dispersive Spectrometry (EDS) analysis, is shown with strong elemental peaks (annotated). (4.2a) Mal-00/2870, (overleaf) (4.2b) Mal-00/2440, (4.2c) Mal-00/2250, (4.2d) MM-02/2440.

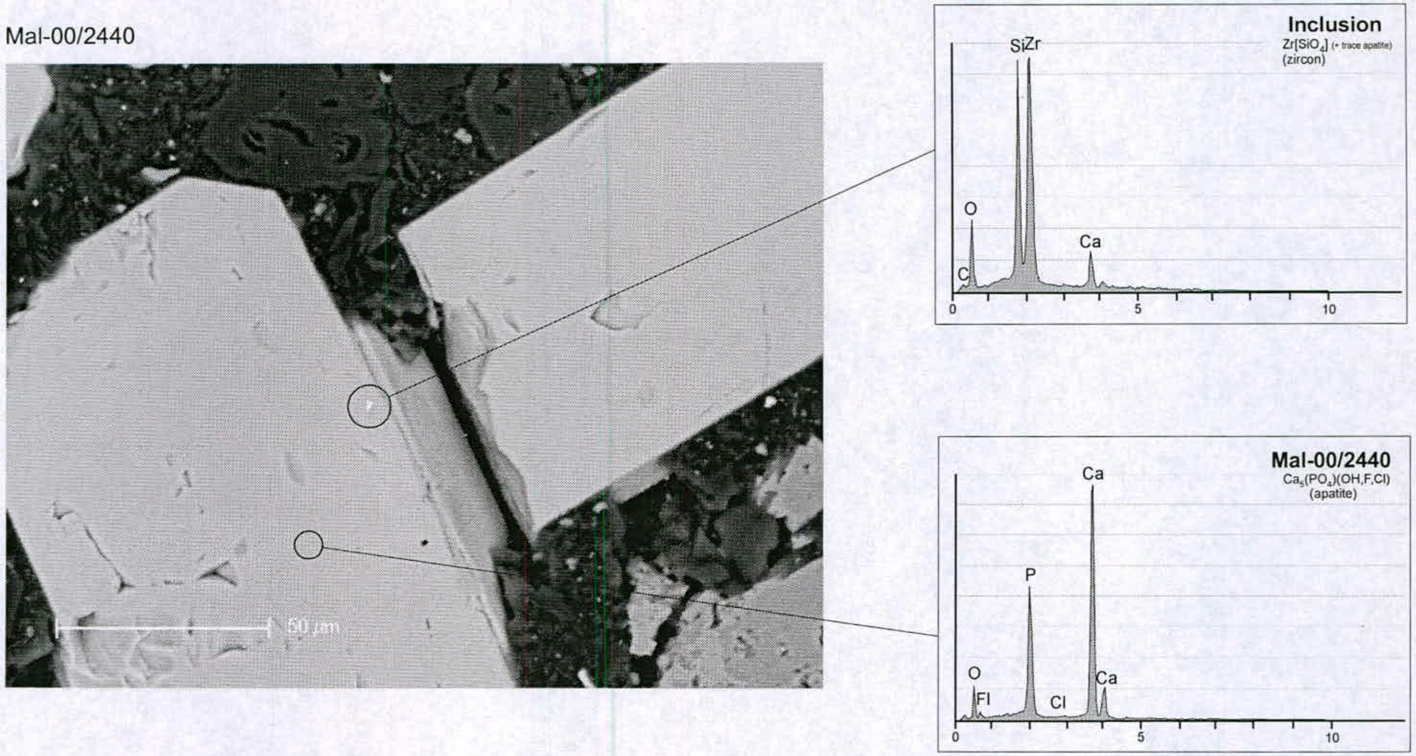

Fig. 4.2b

Elemental analysis of Apatite and inclusions (continued

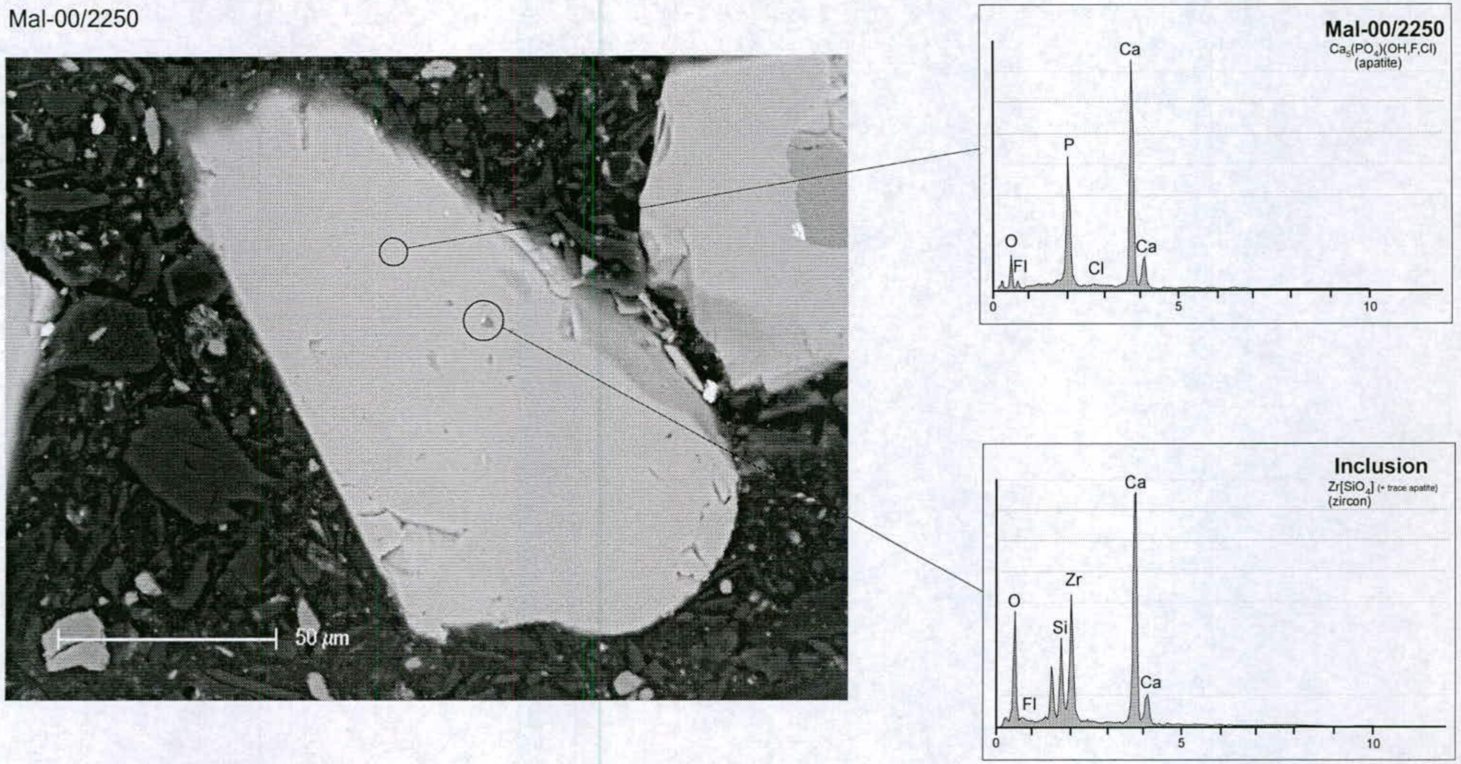

Fig. 4.2c
Elemental analysis of Apatite and inclusions (Continued)

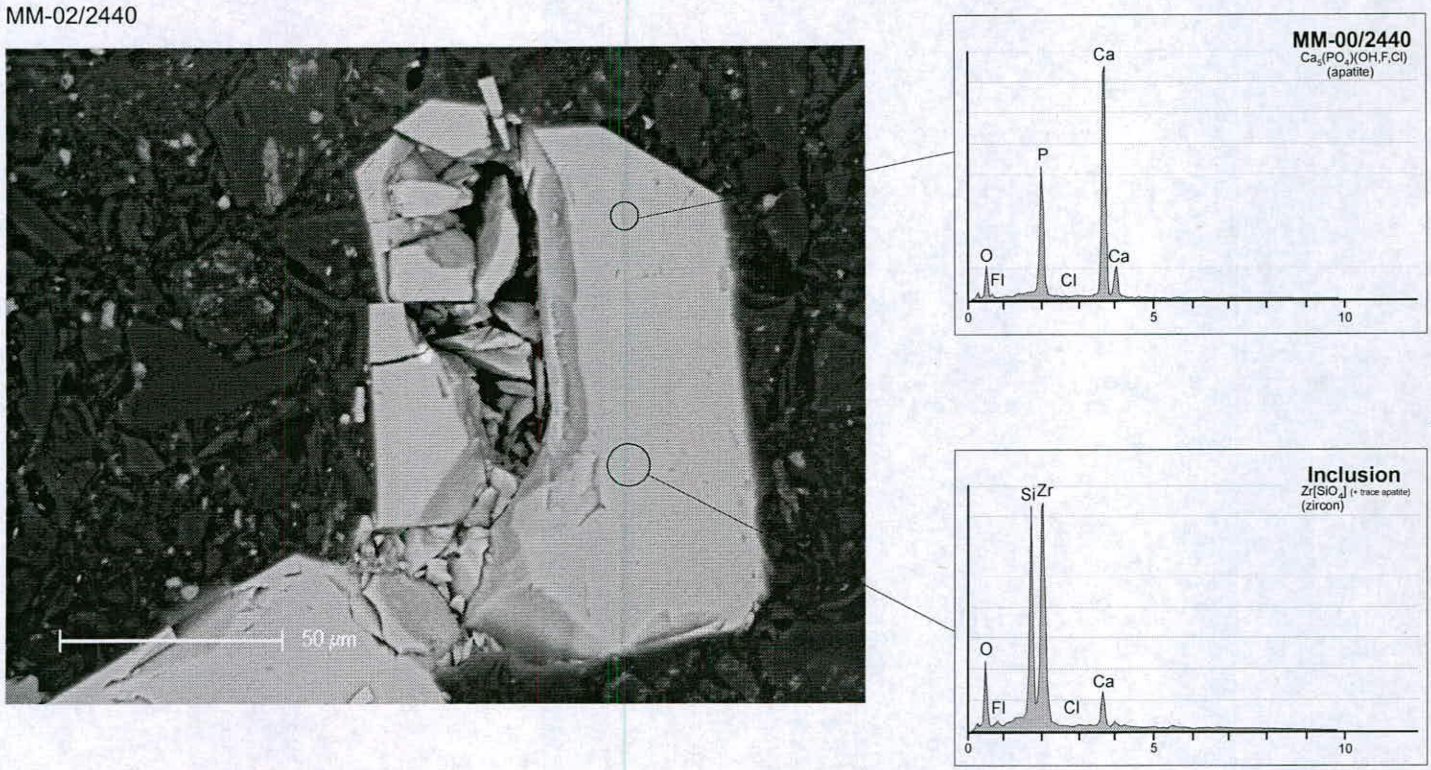

Figure 4.2d
Elemental analysis of Apatite and inclusions (continued)

Sample ID	Grid Ref.	Ps (Ns) (10^6 tracks cm^{-2})	Pi (Ni) (10^6 tracks cm^{-2})	Pd (Nd) (10^6 tracks cm^{-2})	Grains (dmnls)	Dpar (μm)	Dper (μm)	Chi^2	Zeta (±1 SD.)	Pooled Age (Ma)	Tracks (tracks)	Mean Length (μm)	Std Dev (μm)
Marimaña													
MM 02/2635	3564 3106	0.346 (181)	2.153 (1126)	3.546 (4176)	25	1.72	0.53	23.926	113.28±2.9	32.4+/-2.8	125	14.28+/-0.14	1.58
MM 02/2440	3520 3064	0.319 (181)	1.747 (992)	3.538 (4176)	25	1.68	0.51	30.269	113.28±2.9	36.6+/-3.2	130	14.19+/-0.11	1.27
Mar-00/2304	3480 3019	0.311 (147)	2.012 (951)	3.977 (4146)	24	1.86	0.41	101.28	113.28±2.9	34.9+/-3.6	136	14.19+/-0.12	1.37
Mar-00/2200	3464 3007	0.265 (177)	2.166 (1447)	3.979 (4146)	25	1.81	0.41	34.337	113.28±2.9	27.6+/-2.4	201	14.28+/-0.09	1.21
Mar-00/2030	3422 3007	0.256 (171)	1.825 (1218)	3.982 (4146)	24	1.77	0.41	16.387	113.28±2.9	31.7+/-2.8	201	14.32+/-0.07	1.00
Maladeta													
Mal-00/2870	3769 0914	0.171 (121)	1.176 (833)	4.019 (4146)	25	1.83	0.44	23.509	113.28±2.9	33.1+/-3.4	137	14.27+/-0.15	1.70
Mal-00/2250	3778 0871	0.132 (108)	1.058 (865)	4.016 (4146)	25	1.81	0.42	31.21	113.28±2.9	28.5+/-3.0	117	14.02+/-0.14	1.54
Mal-00/2030	3772 0858	0.235 (160)	1.930 (1313)	4.005 (4146)	25	1.69	0.39	30.985	113.28±2.9	27.7+/-2.5	126	13.88+/-0.10	1.08
Mal-00/1750	3736 0846	0.139 (107)	1.095 (844)	4.013 (4146)	24	1.84	0.43	21.568	113.28±2.9	28.9+/-3.1	53	13.73+/-0.18	1.33
Barruera													
Bar-02/1750	1990 0995	0.094 (37)	0.882 (347)	3.505 (4176)	17	1.82	0.52	18.489	113.28±2.9	21.2+/-3.7	41	13.95+/-0.29	1.80
Bar-02/1695	1995 0987	0.108 (41)	1.100 (419)	3.513 (4176)	17	2.08	0.78	12.08	113.28±2.9	19.5+/-3.2	41	14.17+/-0.23	1.45
Bar-02/1150	2032 0925	0.265 (146)	2.482 (1366)	3.521 (4176)	24	1.78	0.55	22.783	113.28±2.9	21.4+/-2.0	126	13.18+/-0.15	1.69
Nogueres													
Col-00/1540	2879 9610	0.131 (66)	0.977 (494)	3.985 (4146)	39	2.00	0.51	28.425	113.28±2.9	30.2+/-4.1	28	13.62+/-0.33	1.73
Col-00/1490	2894 9655	0.142 (65)	1.163 (533)	3.988 (4146)	40	2.27	0.58	41.694	113.28±2.9	27.6+/-3.7	94	13.80+/-0.22	2.15
Mon-02/1280	4290 9445	0.181 (86)	1.357 (646)	3.472 (4176)	25	2.08	0.67	25.677	113.28±2.9	26.2+/-3.1	118	13.75+/-0.21	2.23
Mon-02/1085	4335 9460	0.183 (45)	1.481 (365)	3.480 (4176)	25	1.93	0.55	16.328	113.28±2.9	24.4+/-3.9	81	13.99+/-0.21	1.91
Mon-02/960	4365 9475	0.201 (29)	2.326 (335)	3.489 (4176)	9	1.97	0.56	21.80	113.28±2.9	17.2+/-3.4	6	14.76+/-1.23	2.76
Esc-02/1250	0915 0325	0.172 (83)	1.321 (639)	3.464 (4176)	25	2.04	0.62	36.416	113.28±2.9	25.5+/-3.1	84	13.83+/-0.19	1.71
Sas-02/1580	2315 9790	0.167 (60)	1.257 (453)	3.447 (4176)	25	2.00	0.82	28.375	113.28±2.9	25.9+/-3.6	26	13.85+/-0.28	1.40
Sas-02/1490	2280 9795	0.259 (157)	1.685 (1020)	3.439 (4175)	24	2.16	0.67	23.45	113.28±2.9	30.1+/-2.7	133	14.16+/-0.14	1.59

Table 4.1(a)

Apatite fission track data

Sample ID	Grid Ref.	Ps (Ns)	Pi (Ni)	Pd (Nd)	Grains	Q	Pooled Age
		(10^6 tracks cm^{-2})	(10^6 tracks cm^{-2})	(10^6 tracks cm^{-2})	(dmnls)	(dmnls)	(Ma)
Marimaña							
MM 02/2635	3564 3106	7.168 (812)	5.606 (635)	0.578 (4072)	20	0.021	49.7+/-3.1
Maladeta							
Mal-00/1760	3483 0805	8.175 (1240)	6.448 (978)	0.578 (4072)	20	0.004	49.3+/-2.6
Barruera							
Bar 02/1150	2032 0925	18.023 (1165)	6.730 (435)	0.578 (4072)	16	0.056	104+/-7
Nogueres							
Mon 02/805	4400 9495	16.146 (124)	3.906 (30)	0.578 (4072)	3	0.139	159+/-33

Table 4.1(b)
Zircon fission track data

4.3a Marimaña AFT profile

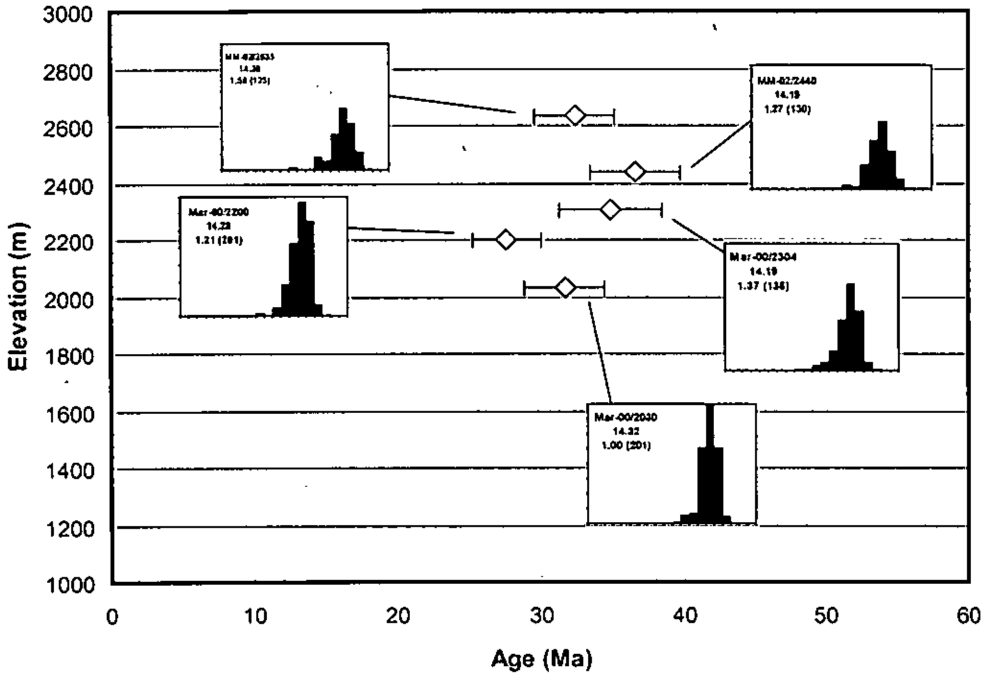

4.3b Maladeta AFT profile

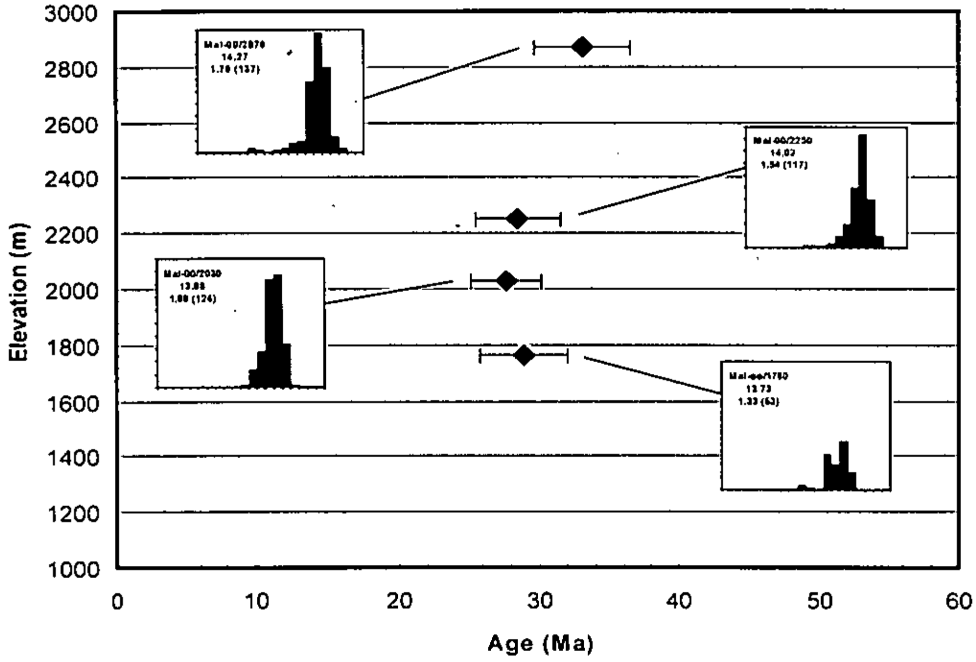

Figure 4.3 AFT and ZFT ages plotted against sampling elevation: (4.2a) Marimañi data; (4.2b) Maladeta data; (overleaf) (4.2c) Barruera data; (4.2d) Nogueres data; (4.2e) all apatite fission track data; (4.2f) all zircon fission track data. Histograms of track length information are inserted next to the appropriate data point. Each histogram lists the mean track length, the standard deviation of the mean track length, and the number of confined tracks measured to determine the mean track length.

Fig. 4.3
Fission track data

4.3c Barruera AFT profile

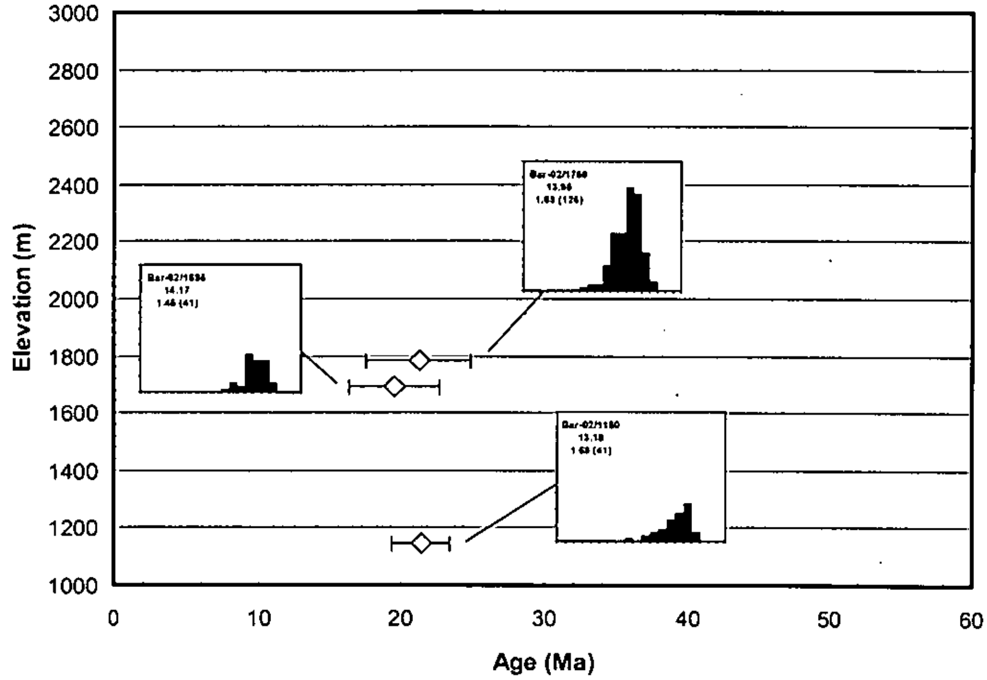

4.3d Nogueres AFT profile

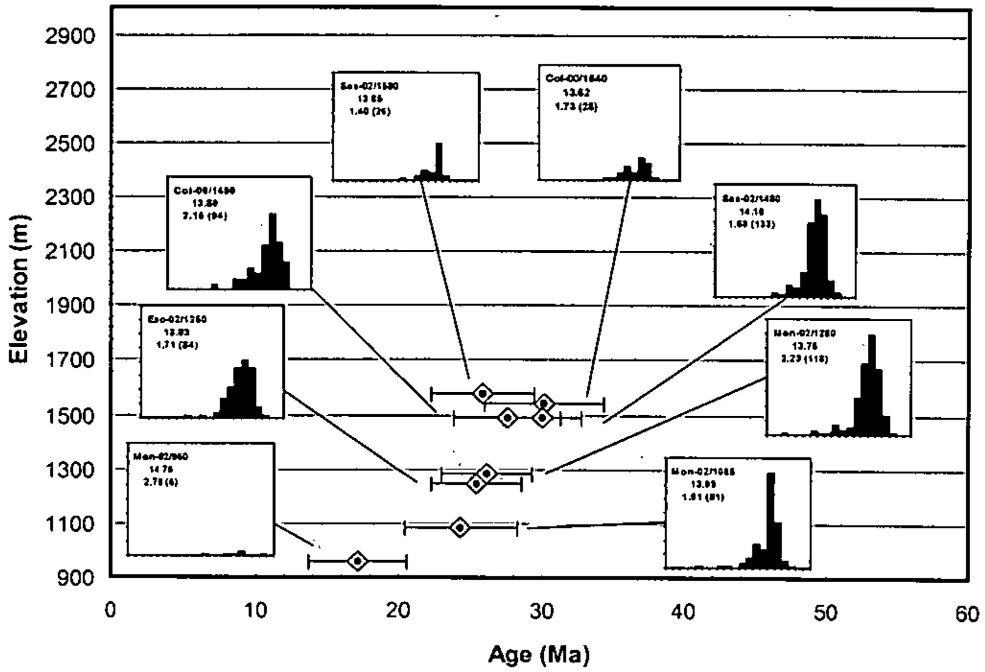

4.3e Compiled AFT profile

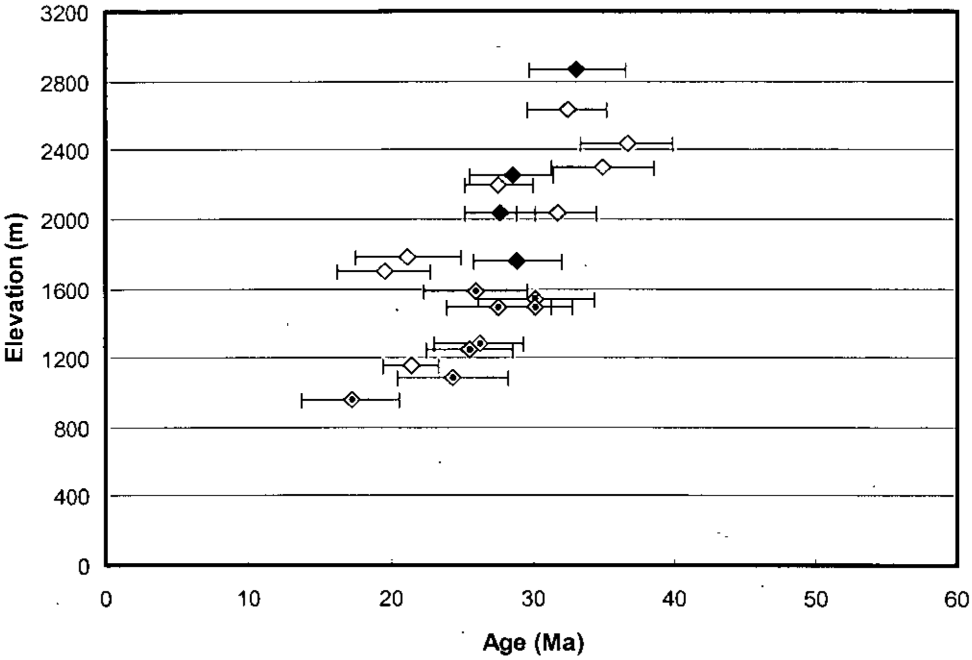

4.3f Zircon ZFT data

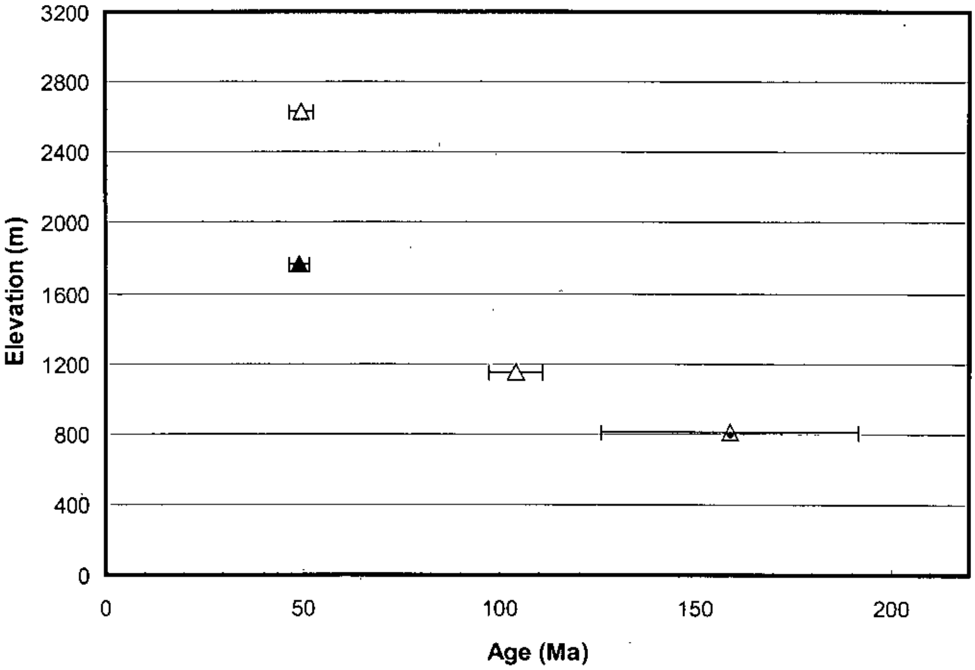

Fig. 4.3
Fission track data (continued)

Marimaña profile

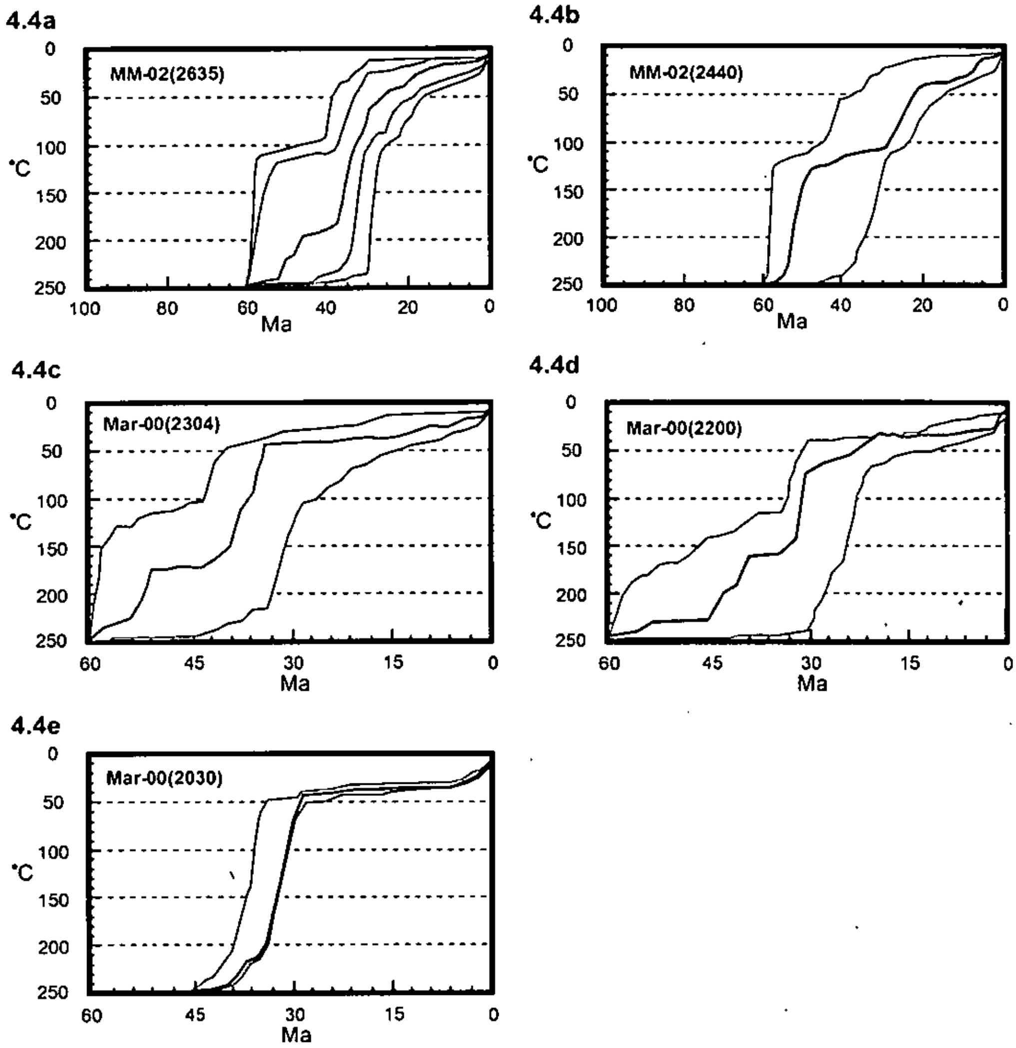

Maladeta profile

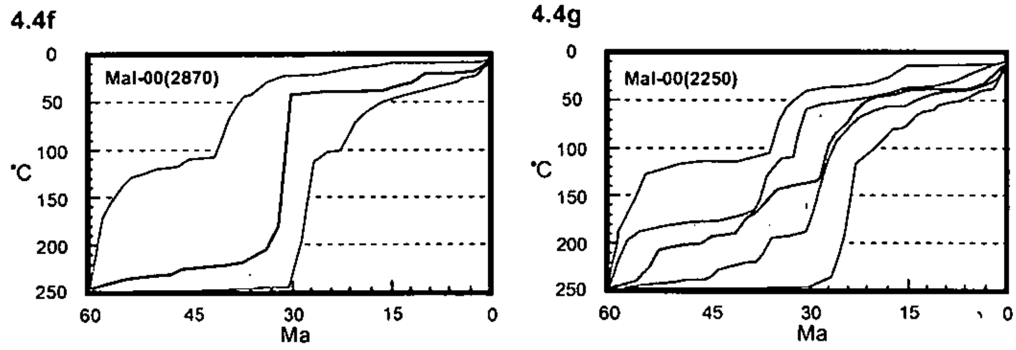

Figure 4.3 AFTSolve model outputs depicting time-temperature (t-T) envelopes defined by the t-T solutions generated from the AFT data. Dark grey envelopes in t-T space accommodate all the t-T solutions with a 'good' statistical fit with the measured data; light grey envelopes accommodate all the t-T solutions with an 'acceptable' statistical fit with the measured data. (4.4a-e) Marimaña model runs, (4.4f-i) Maladeta model runs, (overleaf) (4.4j-l) Barruera model runs, (4.4m-t) Nogueres model runs. Note, the horizontal scale (age) varies between model runs.

Fig. 4.4
AFTSolve thermal modelling

Maladeta profile (continued)

4.4h

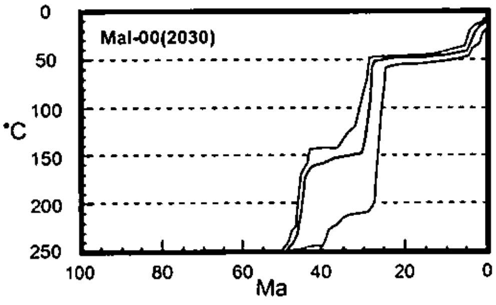

4.4i

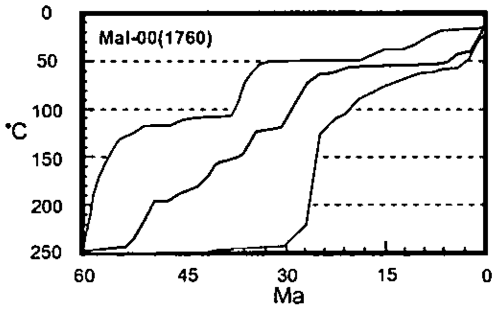

Barruera profile

4.4j

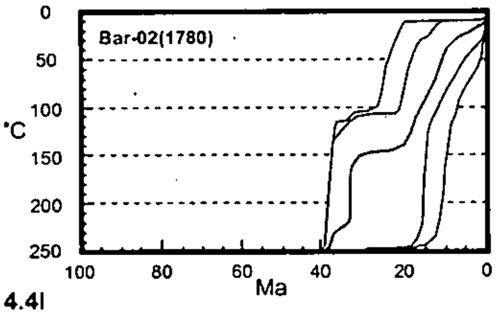

4.4k

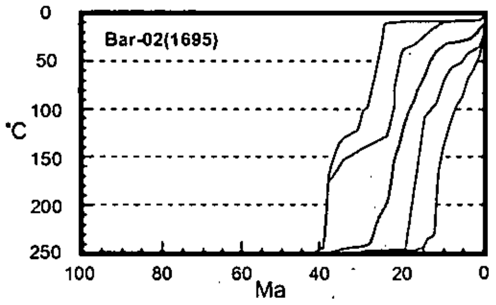

4.4l

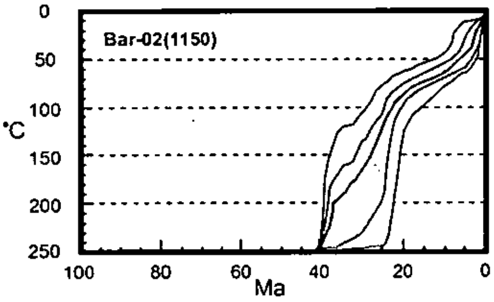

Nogueres profile

4.4m

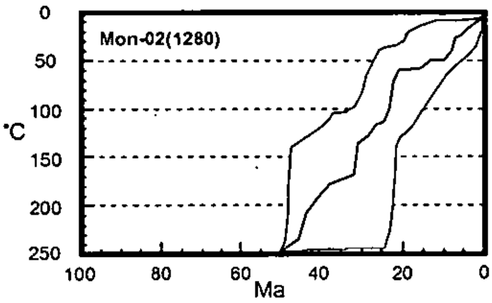

4.4n

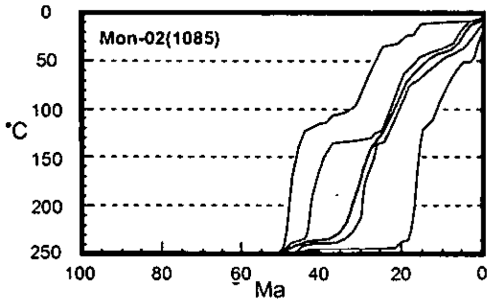

Fig. 4.4
AFTSolve thermal modelling (continued)

Nogueres profile (continued)

4.4o

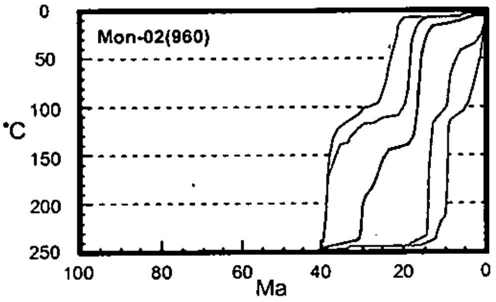

Nogueres single-elevation samples

4.4p

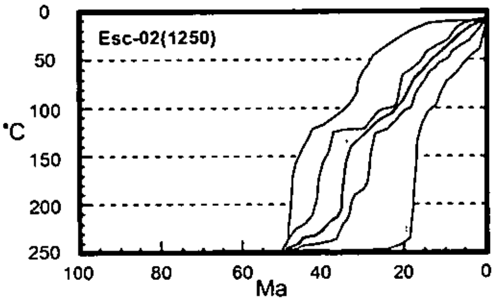

4.4q

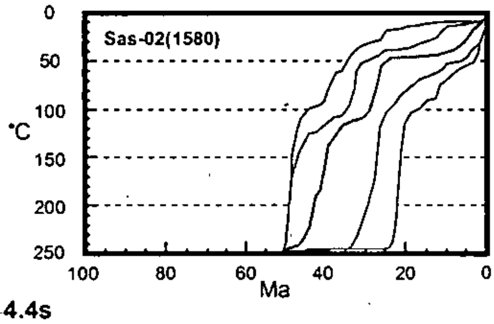

4.4r

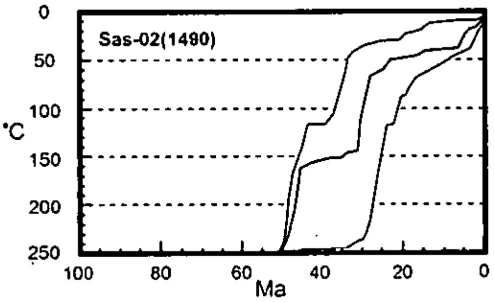

4.4s

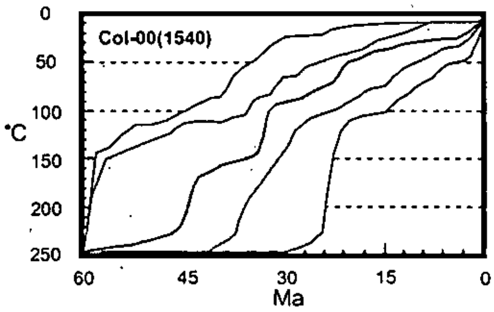

4.4t

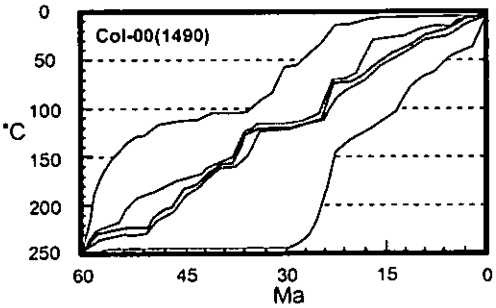

Fig. 4.4

AFTSolve thermal modelling (continued)

Sample	Grains	Av. Dia (μm)	4He (cc)	^{238}U (ng)	^{232}Th (ng)	Uncorrected AHe age (Ma)	Ft correction (Farley, 2002) (%)	Corrected AHe Age (Ma)	Uncertainty (± Ma)
Marimañi									
MM-02/2635:1	8	80	2.47E-09	0.761	1.031	20.8	0.64	32.4	1.9
MM-02/2635:2	9	73	1.70E-09	0.526	0.512	21.6	0.64	33.7	2.0
MM-02/2635:4	7	75	1.27E-09	0.399	0.374	21.4	0.65	32.8	2.0
MM-02/2440:1	7	80	1.67E-09	0.468	0.402	24.5	0.66	37.4	2.2
MM-02/2440:2	6	72	1.20E-09	0.408	0.395	19.8	0.63	31.5	1.9
MM-02/2440:3	7	72	1.70E-09	0.254	0.256	45.0	0.61	[73.8]	
Mar-00/2304:1	7	94	1.47E-09	0.612	0.381	17.2	0.70	24.4	1.5
Mar-00/2200:1	5	118	3.08E-09	0.967	0.530	23.2	0.79	29.2	1.8
Mar-00/2200:2	5	90	9.07E-10	0.391	0.261	16.4	0.71	23.2	1.4
Mar-00/2030:1	7	90	2.00E-09	0.771	0.873	16.8	0.71	23.5	1.4
Mar-00/2030:2	7	105	1.63E-09	0.612	0.529	18.2	0.73	24.9	1.5
Mar-00/2030:3	7	103	1.55E-09	0.576	0.538	18.1	0.72	25.2	1.5
Maladeta									
Mal-00/2870:1	6	92	1.40E-09	0.578	0.723	15.2	0.70	21.7	1.3
Mal-00/2870:2	8	70	1.10E-09	0.551	0.719	12.6	0.64	19.7	1.2
Mal-00/2870:4	5	117	4.70E-09	0.859	1.032	34.9	0.77	[45.4]	
Mal-00/2870:5	4	96	1.84E-09	0.404	0.496	29.0	0.72	[40.3]	
Mal-00/2870:6	5	58	9.58E-09	0.256	0.280	192.0	0.80	[240]	
Mal-00/2870:7	6	60	3.73E-09	0.313	0.434	12.5	0.55	22.7	1.4
Mal-00/2765-1	6	91	9.76E-10	0.318	0.423	19.0	0.73	26.1	1.6
Mal-00/2765-2	7	59	4.75E-10	0.347	0.466	9.0	0.55	16.3	1.0

Table 4.2

Apatite (U-Th)/He data

Sample	Grains	Av. Dia (μm)	4He (cc)	^{238}U (ng)	^{232}Th (ng)	Uncorrected AHe age (Ma)	Ft correction (Farley, 2002) (%)	Corrected AHe Age (Ma)	Uncertainty (± Ma)
(continued)									
Mal-00/2650:1	9	64	8.01E-10	0.147	0.553	23.7	0.62	[38.5]	
Mal-00/2650:2	10	72	1.45E-09	0.358	0.731	22.4	0.65	[34.7]	
Mal-00/2650:3	9	90	1.54E-09	0.605	0.946	15.3	0.70	21.8	1.3
Mal-00/2650:4	11	75	1.24E-09	0.557	0.613	14.6	0.63	23.3	1.4
Mal-00/2650:5	12	74	1.99E-09	0.843	1.032	15.1	0.64	23.5	1.4
Mal-00/2650:6	9	64	1.13E-09	0.984	0.724	7.2	0.61	11.8	0.7
Mal-00/2440:1	11	79	2.53E-09	0.902	1.155	17.7	0.67	26.4	1.6
Mal-00/2440:2	8	93	2.81E-09	0.559	0.473	34.4	0.71	[48.2]	
Mal-00/2440: 5	9	60	9.23E-10	0.353	0.446	17.0	0.57	29.9	1.8
Mal-00/2440: 6	8	62	6.12E-10	0.320	0.415	12.5	0.60	20.7	1.2
Mal-00/2360-1	5	83	7.26E-10	0.341	0.419	14.0	0.72	19.5	1.2
Mal-00/2360-2	6	58	9.70E-10	0.349	0.439	18.0	0.54	[33.1]	
Mal-00/2250:1	6	107	1.89E-09	1.053	1.285	11.4	0.76	15.0	0.9
Mal-00/2250:2	8	90	2.27E-09	1.131	1.331	12.8	0.71	18.1	1.1
Mal-00/2250:3	8	97	2.03E-09	1.592	1.176	8.3	0.72	11.6	0.7
Mal-00/2030:1	13	81	1.85E-09	2.452	1.584	5.3	0.68	7.8	0.5
Mal-00/2030:2	13	64	1.15E-09	1.041	1.097	6.5	0.60	10.9	0.7
Mal-00/1920:1	18	60	1.27E-09	1.239	1.082	6.9	0.58	12.0	0.7
Mal-00/1920:2	7	114	2.09E-09	1.989	1.504	6.9	0.76	9.1	0.5
Mal-00/1760:1b	8	103	9.74E-10	0.527	1.124	9.2	0.74	12.5	0.8
Mal-00/1760:1a	8	99	1.24E-09	0.950	0.909	8.1	0.74	10.9	0.7
Mal-00/1760:2b	7	116	1.90E-09	0.147	1.410	8.1	0.78	10.4	0.6

Table 4.2 (continued)

Table 4.2 (continued)

Sample	Grains	Av. Dia (µm)	4He (cc)	^{238}U (ng)	^{232}Th (ng)	Uncorrected AHe age (Ma)	Ft correction (Farley, 2002) (%)	Corrected AHe Age (Ma)	Uncertainty (± Ma)
(continued)									
Barruera									
Bar-02/1695:2	10	69	2.68E-10	0.137	0.672	7.4	0.63	11.8	0.7
Bar-02/1695:3	13	54	2.05E-10	0.108	0.506	7.4	0.55	13.5	0.8
Bar-02/1150:1	10	68	3.26E-10	0.242	0.220	9.3	0.62	14.9	0.9
Bar-02/1150:2	10	59	2.13E-10	0.311	0.225	4.9	0.64	7.6	0.5

4.5a **Marimaña AHe profile**

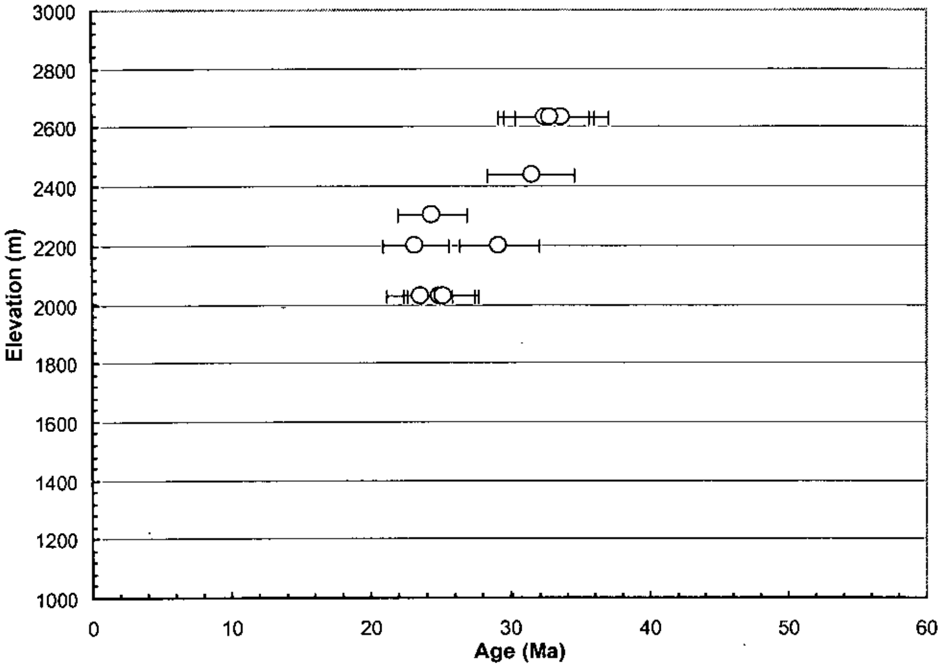

4.5b **Maladeta AHe profile**

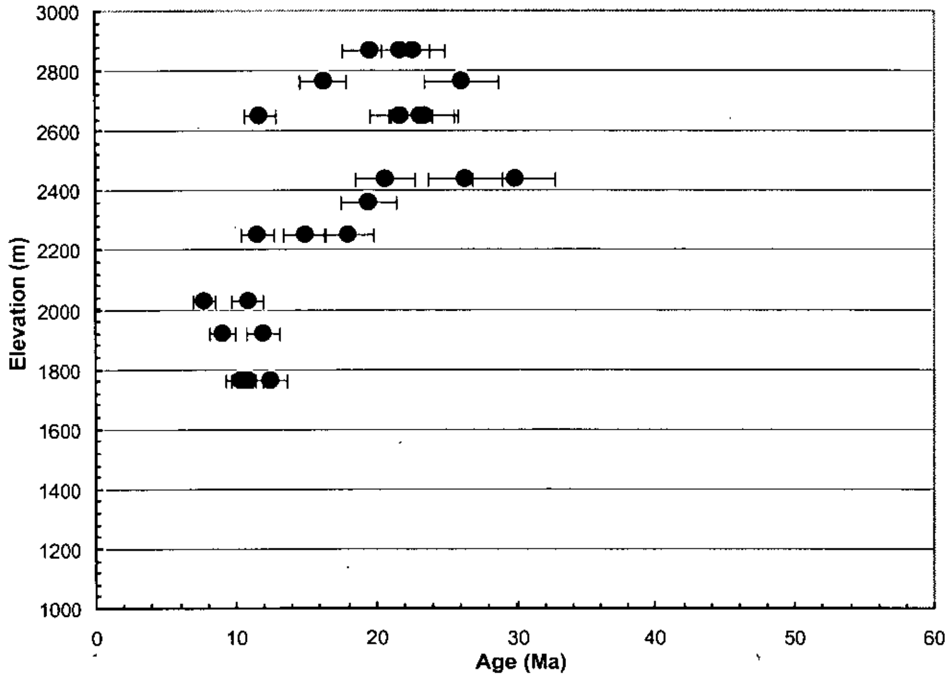

Figure 4.5 AHe ages plotted against sampling elevation: (4.5a) Marimaña data; (4.5b) Maladeta data; (overleaf) (4.5c) Barruera data. Analytical uncertainty of individual age determinations is ~6%. Replicates yielding ages in excess of the AFT or ZFT age omitted.

4.5c Barruera AHe profile

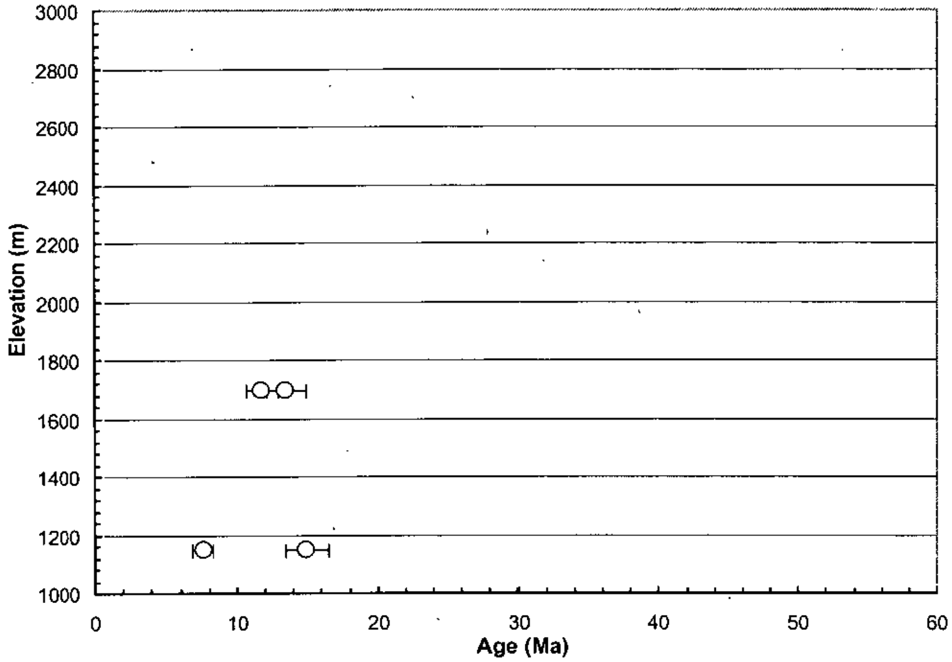

4.5d Composite AHe profiles

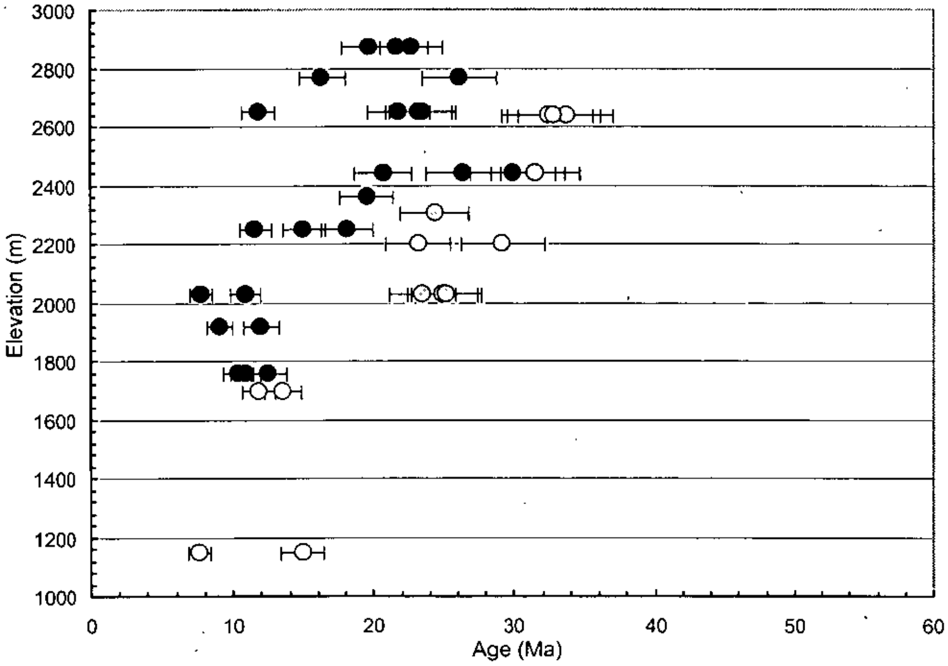

Fig. 4.5

AHe data (continued)

Marimañi profile

4.6a

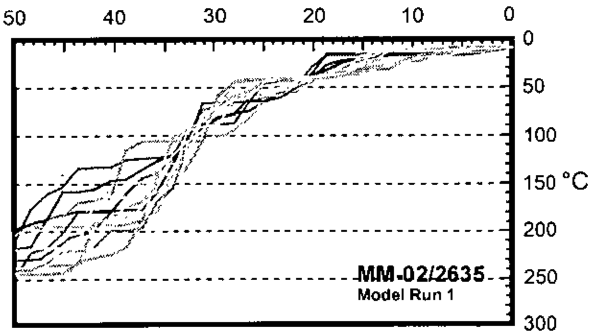

Runs: 20,000/Data: 0.5/Size: 70 um
t-T: 0 Ma (10°C), 50 Ma (200-250°C)
Modelled He age min/max: 20.9/23.5 Ma

4.6b

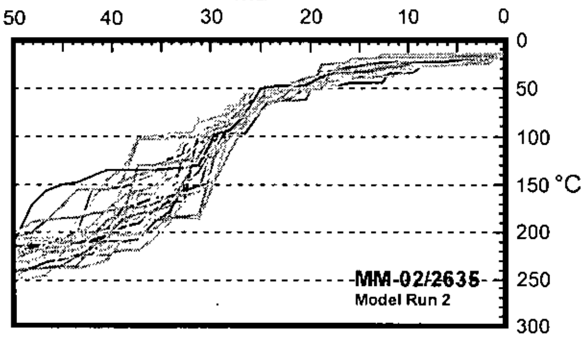

Runs: 20,000/Data: 0.05/Size: 70 um
t-T: 0 Ma (10°C), 50 Ma (200-250°C)
Modelled He age min/max: 18.7/23.7 Ma

4.6c

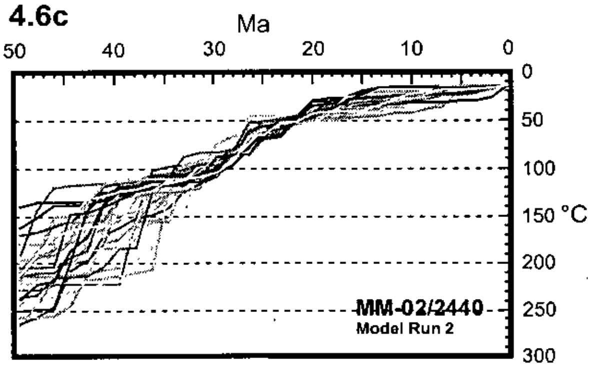

Runs: 50,000/Data. 0.05/Size: 70um
t-T: 0 Ma (10°C), 50 Ma (200-275°C)
Modelled He age min/max: 19.2-21.6 Ma

4.6d

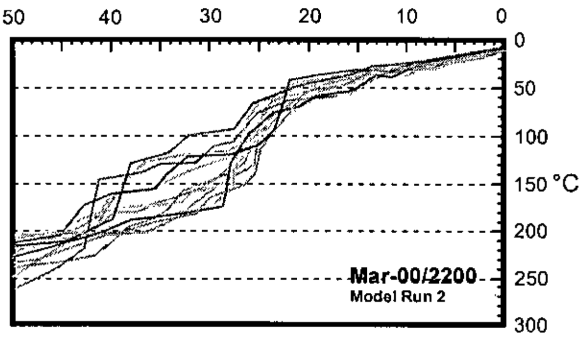

Runs: 50,000/Data: 0.01/Size 95um
t-T: 0 Ma (10°C), 50 Ma (200-275°C)
Modelled He age min/max: 18.4-20.9 Ma

4.6e

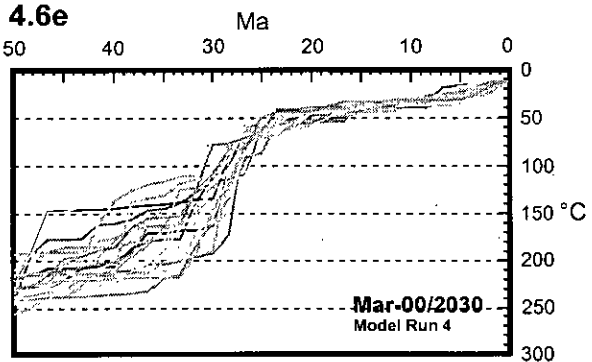

Runs. 250,000/Data· 0.05/Size 95um
t-T: 0 Ma (10°C), 50 Ma (200-275°C)
Modelled He age min/max: 17.5-20.2 Ma

Figure 4.6 Time-temperature solutions generated by DeComp/AFTSolve thermal modelling. Input values and parameters listed below each model run- 'Runs': amount of random t-T searches performed in AFTSolve; 'Data': standard of statistical precision delineated in AFTSolve; 'Size': model crystal size useed to generate AHe age (μm); 't-T':time-temperature constraints imposed on the model runs; 'He age min/max': range of model AHe ages generated for the given t-T paths. (4.6a-e) Marimañi model runs; (4.6i-f); (4.6j-k) Barruera model runs.

Maladeta profile

4.6f

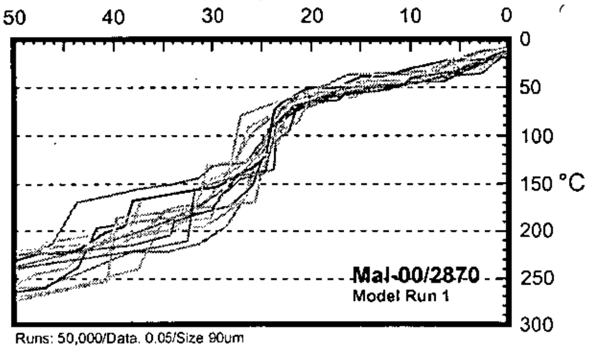

Runs: 50,000/Data. 0.05/Size 90um
t-T 0 Ma (10°C), 50 Ma (175-275°C)
Modelled He age min/max: 14.9-17.9 Ma

4.6g

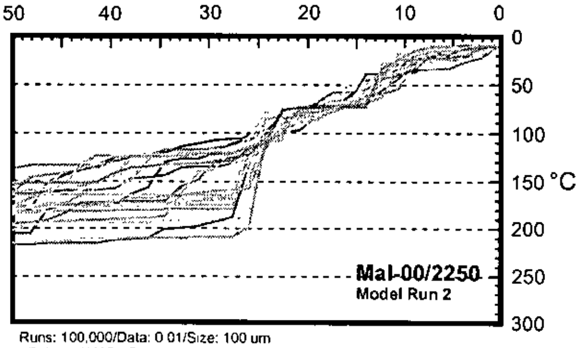

Runs: 100,000/Data: 0.01/Size: 100 um
t-T: 0 Ma (10°C), 50 Ma (175-225°C)
Modelled He age min/max: 12.8-14.6 Ma

Maladeta profile (continued)

4.6h

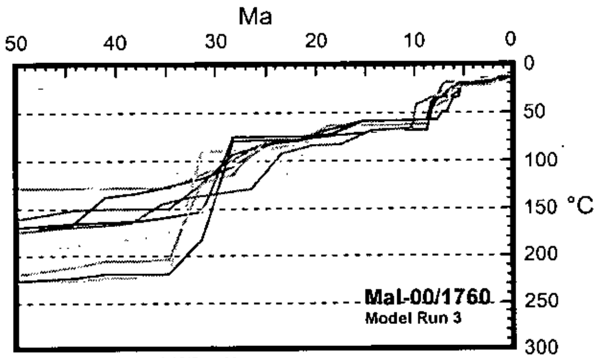

Runs: 250,000/Data: 0.05/Size 90um
t-T: 0 Ma (10°C), 8 Ma (30-120°C), 50 Ma (200-275°C)
Modelled He age min/max: 11.4-14.1 Ma

4.6i

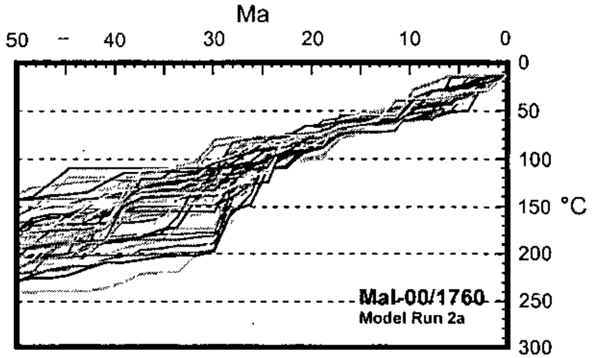

Runs: 50,000/Data: 0.05/Size: 90um
t-T: 0 Ma (10°C), 60 Ma (200-250°C)
Modelled He age min/max: 14.9-16.8 Ma

Barruera profile

4.6j

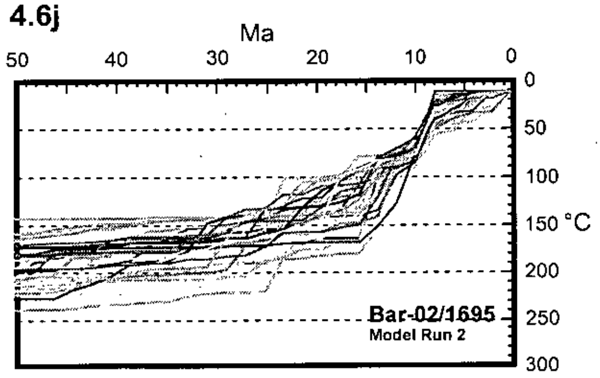

Runs: 50,000/Data: 0.05/Size: 65um
t-T: 0 Ma (10°C), 60 Ma (120-250°C)
Modelled He age min/max: 4.7-8.7 Ma

4.6k

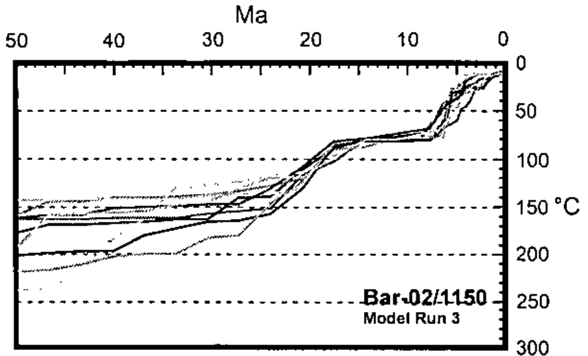

Runs: 100,000/Data: 0.05/Size: 60 um
t-T: 0 Ma (10°C), 60 Ma (150-250°C)
Modelled He age min/max: 5.4-6.4

Fig. 4.6

DeComp-AFTSolve integrated thermal modelling (continued)

4.7a

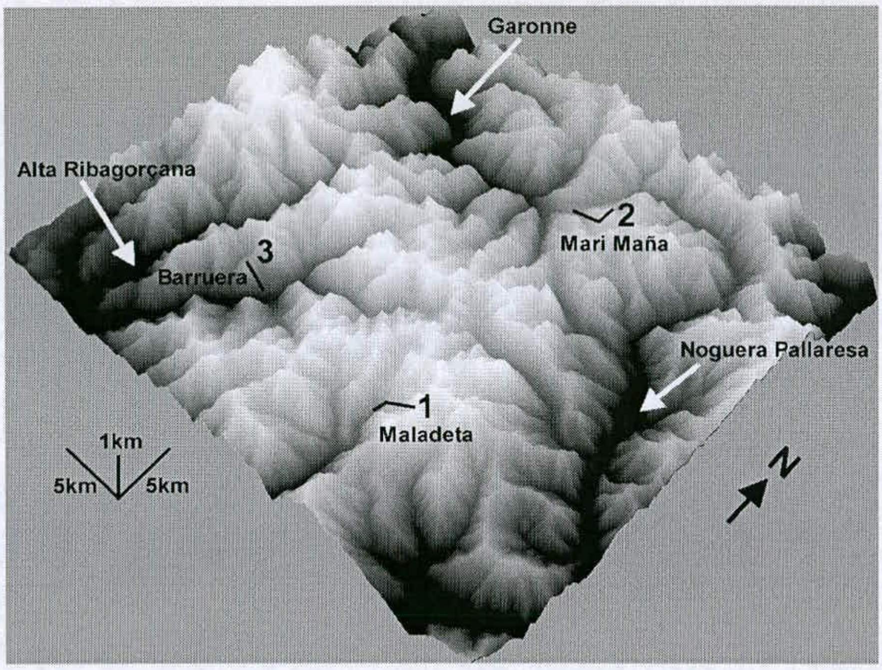

4.7b

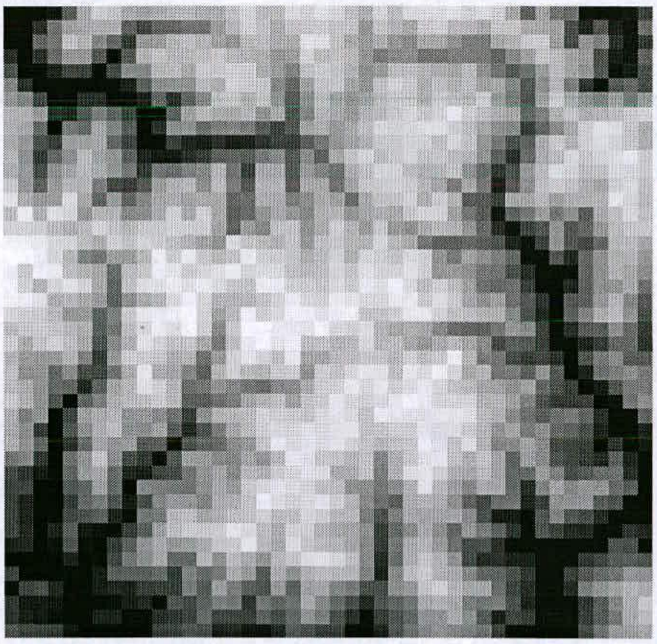

Figure 4.7 (Fig. 4.7a) A vertically-exaggerated (see scale) 44 km^2 tile of ~90m SRTM (Shuttle Radar Topography Mission) data (U.S.G.S., 2004), incorporating the three sampling localities (Marimaña, Maladeta and Barruera). Major valleys surrounding the sampling sites are also located (Noguera Pallaresa, Garonne, Alta Ribagorcana). This topography was downsampled to a grid of 1km^2 nodes (Fig. 4.7b) and used as the end-point of topographic evolution for all model runs. At the termination of all model runs (0 Ma) the time-temperature (t-T) history for each node containing a sampling site was forward-modelled in both AFTSolve (Ketcham et al., 2000) and DeComp (Dunai et al., 2003) to generate model fission track and AHe ages for a variety of topographic and exhumational scenarios.

Run Number	45-36 Myr KmMyr^{-1}	36-30 Myr KmMyr^{-1}	30-12 Myr KmMyr^{-1}	12-8 Myr KmMyr^{-1}	8-0 Myr KmMyr^{-1}	Topography[¥]	Total V since 30 Ma Km
1	0	0.5000	0.0000	0.2750	0.0625	Constant	1.60
2	0	0.5000	0.0530	0.0530	0.0530	Constant	1.60
3	0	0.5000	0.0000	0.2750	0.0625	Increasing	1.60
4	0	0.5000	0.0530	0.0530	0.0530	Increasing	1.60
5	0	0.5000	0.0000	0.2750	0.0625	Decreasing	1.60
6	0	0.5000	0.0530	0.0530	0.0530	Decreasing	1.60
7	0	0.5000	0.0000	0.2750	0.0625	Constant	1.60
8	0	0.5000	0.0530	0.0530	0.0530	Constant	1.60
9	0	0.5000	0.0000	0.1875	0.0625	Constant	1.25
10	0	0.5000	0.0416	0.0416	0.0416	Constant	1.25

Table 4.3

Exhumational velocities used in modelling

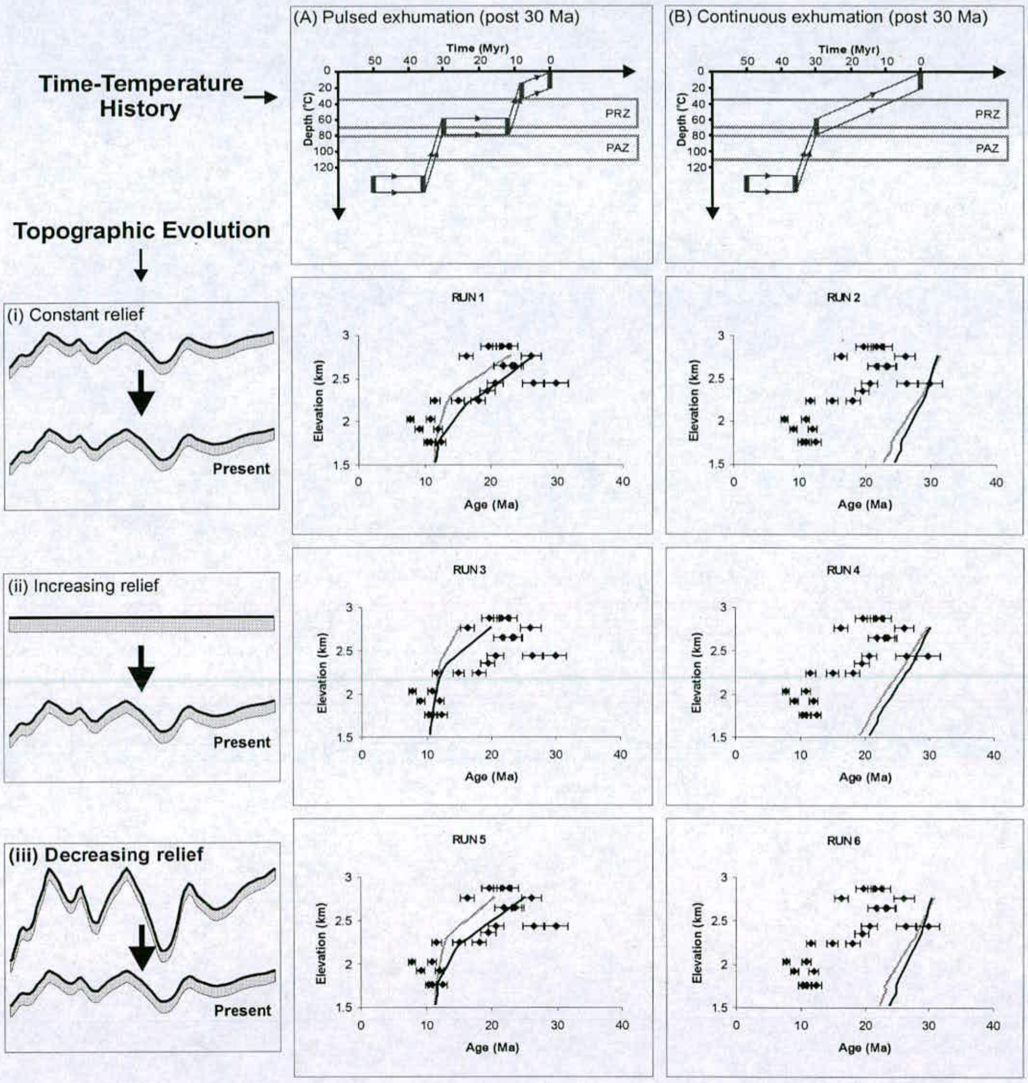

Figure 4.8 (a) Model AHe age profiles for different apatite dimensions (66μm (light grey line) and 133μm (black line)) generated from the *t*-T histories from the topographic nodes at the Maladeta profile. Measured AHe ages from the Maladeta site also plotted (black diamonds). Model runs 1, 3 and 5 have a 'pulsed' exhumational history (post 30 Ma) and three different topographic evolutions imposed (constant, increasing and decreasing, respectively). Model runs 2, 4 and 6 have a 'continuous exhumational history (post 30 Ma) and the same topographic evolutions imposed.

Fig. 4.8a

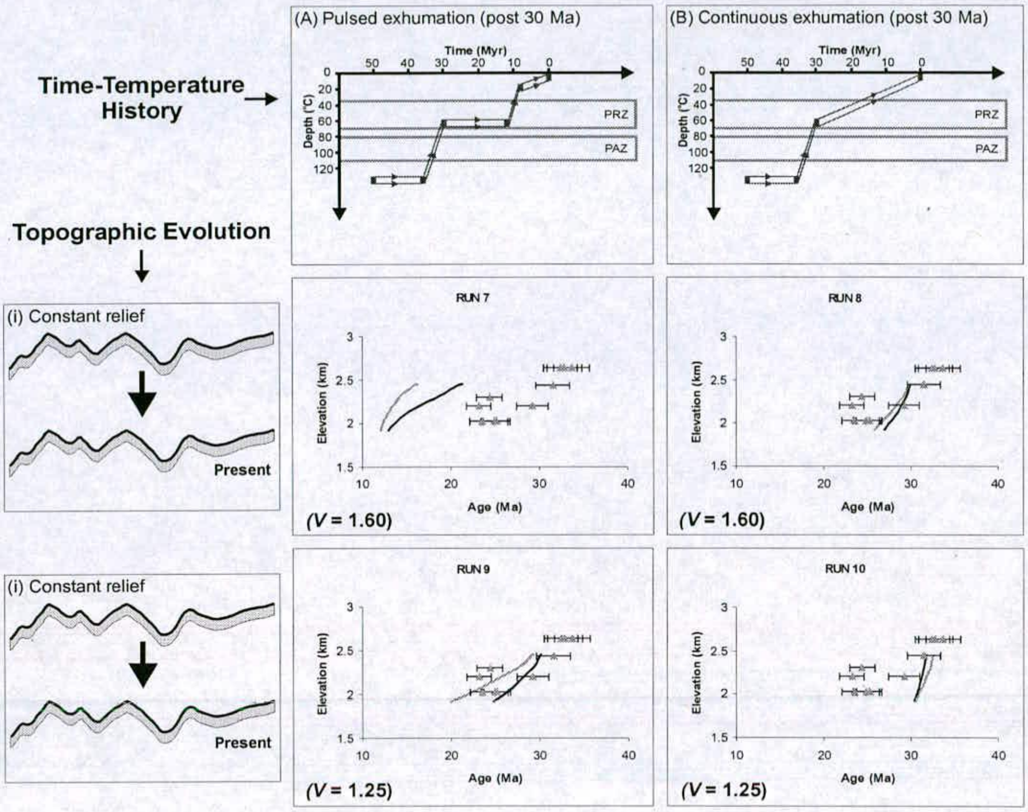

Figure 4.8 (b) Model AHe age profiles for different apatite dimensions (66μm (light grey line) and 133μm (black line)) generated from the *t*-T histories from the topographic nodes at the Marimaña profile. Measured AHe ages from the Marimaña site also plotted (grey triangles). Model runs 7 and 9 have a 'pulsed' exhumational history (post 30 Ma) but at different vertical velocities (0.275 and 0.1875 kmMyr^{-1}, respectively) and with a constant topographic relief. Model runs 8 and 10 have a 'continuous' exhumational history (post 30 Ma) but at different vertical velocities (0.0530 and 0.0416 kmMyr^{-1}, respectively) and with constant topographic relief. *V* = Total exhumation since 30 Ma. Variability in *V* is dictated by the position of the profile in the PRZ at 30 Ma; model runs with relatively high values of *V* were positioned at the base of the PRZ at 30 Ma, and model runs with lower values of *V* were positioned within the PRZ at 30 Ma.

Fig. 4.8b

Chapter 5

Geological field data

Objectives: The primary objective of this chapter is to present geological field data and brief interpretative summaries of a number of field areas in the southern and central Pyrenees. This information is used to constrain the tectonic evolution of the regions from which the thermochronological data are derived.

Chapter 5 – Geological field data

Strong spatial and temporal variability in erosional denudation occurred within the south-central Pyrenees over a ~50 Myr period. The thermochronological data described in Chapter 4 afford us a good documentation of this history, but offer few insights into the mechanisms that may have controlled it. Instead, this information may be recorded within the geological record preserved in the bedrock of the sampling areas, or within the sedimentary basins into which the eroded material was transported.

It is the objectives of this chapter to collate and assess both new and previously published geological data from five specific geographical regions of the south central Pyrenees (**Fig. 5.1 & 5.2**). The field areas represent different tectono-stratigraphic domains and are discussed in this chapter from north to south: (5.1) The North Maladeta Zone (areas a-d, Fig. 5.1), located within the central Axial Zone, comprises the upper reaches of the Garonne and Noguera Pallaresa valleys and the Bossost region; (5.2) The South Maladeta Zone (areas e-f, Fig. 5.1), located in the south central Axial Zone, comprises the Noguera Ribagorçana and eastern Baliera valleys, surrounding the villages of Estet and Aneto; (5.3) The Nogueres Zone (areas g-k, Fig. 5.1), located in a WNW-ESE trending linear strip south of the central Axial Zone, extends from the Escané area in the Noguera Ribagorçana to the village of Ancs in the Noguera Pallaresa; (5.4) The Morreres Zone (areas l-o, Fig. 5.1), located in the area surrounding the Morreres Backthrust, extends from the Massif de Sis to the region of La Pobla de Segur; (5.5) The Ebro Basin and Offshore Zone, located to the S of the Pyrenean chain and to the SE of the modern-day Catalonian and Valèncian coastline, respectively, includes the Ebro Delta area and València Trough.

Fieldwork was completed over two four-month intervals during the summer of 2001 and 2002. The areas selected for field study within the central Pyrenees were chosen as they represent major tectonic boundaries between the thermochronological sampling sites. This strategy was undertaken as much of the fieldwork was completed prior to the compilation of the thermochronological dataset. The focus of the fieldwork was on structures and sediments that were demonstrably of Alpine age, and which overprinted, deformed or truncated earlier structures. The older, pre-Alpine structures are briefly outlined for each area to provide a geological context for the new data.

5.1 The North Maladeta Zone – Geological review

The focus of the field research in the North Maladeta Zone was in area 'a' (Fig. 5.1) of the Port de la Bonaigua region. The primary objective of fieldwork in this area was to characterise the Alpine-age structures between the Marimaña and Maladeta thermochronological sampling sites. It is an area of relatively subdued relief between the high topography of the granodioritic batholiths, to the north and south, respectively. The stratigraphy comprises Cambrian- to Ordovician-age blue-black slates and phyllites, interbedded with coarse, oligomict conglomerates and coarsely crystalline white marbles of the Ransol Formation (Fig. 2.5: Regional geology map) (Zandvliet, 1960; Zwart, 1965). In the northwest of the area, Devonian-age limestones, and locally marbles, of the upper Seo Formation overlie Cambro-Ordovician sediments (Hartevelt, 1971). All the lithologies in this part of the Axial Zone have undergone low-grade regional metamorphism to lower greenschist facies during the Hercynian orogeny (Zwart, 1979).

At least two major periods of Hercynian-age folding have been documented in the region. These are demonstrably pre-Alpine in age as they are truncated at the contact with the Late Hercynian-age Marimaña and Maladeta Massifs and over-printed by the surrounding thermal metamorphic aureoles (Hartevelt, 1970; Zwart, 1979). The earliest phase of folding (F0, after Boschma, 1963; Hartevelt, 1970) is characterised by minor, N-S oriented, gentle to open folds (Hartevelt, 1970). The later main phase of deformation (F1, after Kleinsmiede, 1960) is characterised by E-W and WSW-ENE oriented, upright, moderately-inclined, tight to isoclinal folds of up to 0.5 km amplitude, with smaller, similarly-aligned parasitic folding of the order of cm's to m's (Kleinsmiede, 1960; Zwart, 1986; Losantos et al., 1986). Associated with these structures is a well developed, vertical to sub-vertical, axial planar and slaty cleavage in the pelitic, psammitic and calcareous lithologies (Zwart, 1979, Zwart, 1986). Low-angle, pre-Late Hercynian thrust surfaces that locally juxtapose Devonian and Cambro-Ordovician sediments are also folded by this main phase of deformation (Losantos et al., 1986). Locally developed crenulation cleavages, minor NE-SW folding and small-scale interference structures are linked with subsequent periods of lesser deformation (Zwart, 1963).

The Marimaña and Maladeta batholiths are intrusive, magmatic bodies that display no evidence of internal tectonic fabrics or preferred orientation. They are of typical granodioritic composition and have been interpreted as having been derived directly from melting of Cambro-Ordovician sediments similar to the surrounding country rock (Mey, 1968; Zwart, 1979). A well-defined thermal aureole of hornfels and spotted slates surrounds the igneous bodies within the Cambro-Ordovician units.

Large, WNW-ESE oriented, vertical to sub-vertical faults crosscut the Port de la Bonaigua region of area 'a'. These structures have previously been considered as an eastward continuation of the Gavarnie thrust zone (Muñoz et al., 1986). Outside the mapping area, there is evidence on linked structures of mylonitic ductile deformation through sinistal, strike-slip motion during Permian to Upper Cretaceous times (Soula et al., 1986). ^{40}Ar-^{39}Ar ages and fluid flow dating (Rb-Sr and U-Pb) indicate reactivation of these linked faults during Alpine-age deformation (~50 Ma) (McCaig and Miller, 1986; Wayne and McCaig, 1998).

5.1.1 North Maladeta Zone - Geological field data

Field data from the North Maladeta Zone is presented on a geological map and summary cross-section (**Fig. 5.3 & 5.4**) and in a series of field photographs and sketches (**Fig. 5.5 & 5.6**). Stratigraphical divisions and boundaries in the Palaeozoic sediments were confirmed from previous studies (Zandvliet, 1960; Losantos et al., 1986).

Large, WNW-ESE oriented, sub-vertical to steeply northward dipping, planar faults locally form tectonic boundaries between the granitoid massifs and the intervening metasediments (Fig. 5.5a & 5.5b). The thermal aureole at the igneous contacts and earlier thrusts and folds are truncated by these structures.

Within the Palaeozoic lithologies of the central area, the pervasive slaty cleavage is predominantly vertical to subvertical with an E-W to ESE-WNW strike (Fig. 5.4b). At the tectonic boundary with the granitoid massif the cleavages are disrupted by brittle dislocations (see below) but generally depict moderate to steep dips toward the S to SSW (Fig. 5.4b).

South-vergent, occasionally disharmonic, <0.5 m amplitude, tight to close folds and parasitic structures are well-developed in Cambro-Ordovician interbedded sands and marls in the area immediately south of the tectonic contact with the Marimaña Massif (Fig. 5.5c & 5.5d). Axial planar orientations persistently show a moderate (40-60°) southerly dip, with a gentle to moderately inclined fold axial plunge toward the W to WNW (Fig. 5.4b). Occasional symmetric folds of similar magnitude are also observed immediately north of the Maladeta tectonic contact. With increased distance from the Marimaña contact the folding decreases rapidly and is absent from the central region. The structures are not over-printed by subsequent fold generations but are occasionally cross-cut by brittle dislocations (see below).

Discontinuous shear fractures are common within the Palaeozoic metasediments in areas close to the tectonic contacts (less than ~250 m) with the granitoid massifs (Fig. 5.6a & 5.6b). They are characterised by distinct, well-defined bands of brittle shear, generally displaying a moderate to steep dip (~45-70°) toward the NNE or, less commonly, a shallow dip (~5-10°) toward the SSW (Fig. 5.4b). Each band has a surrounding zone of intensely fractured and finely brecciated rocks of variable thickness (8-100 mm) that is often preferentially weathered from the surrounding country rock. With increased proximity to the major tectonic contacts the shear structures increase in abundance. Small areas are often crosscut by numerous parallel, and occasionally, bifurcating, shear surfaces that bound chaotically disrupted wall rock. Individual shear fractures often truncate or deform the steeply dipping fabric and post-Hercynian small-scale fold structures. Kinematic analyses of the deformed fabrics are invariably consistent with south-directed displacement on the north dipping structures and north-directed displacement on the south dipping structures (Fig. 5.4b). Absolute displacement along the surfaces is generally difficult to constrain owing to the lack of clearly defined offset marker horizons. Occasional outcrops of shear fractures off-setting calcite-filled veins, however, suggest displacement along the smaller structures may be as little as 2 m.

Large-scale fault surfaces were only observed at a specific locality at the tectonic contact between the Marimaña Massif and the Palaeozoic meta-sediments (Fig. 5.6e). This may represent the actual bounding fault or a smaller offshoot of the main structure within the granodiorite. The fault surface is planar and oriented at a steep angle (72°) toward NNE. Slickenfiber lineations on the surface plunge toward NE. The direction of downstepping of stepped lineation surfaces is consistent with relative up-throw of the northern wall of the structure.

Field areas 'b', 'c' and 'd' (Fig. 5.1), located to the W, N and NW of field area 'a', respectively, were also briefly reconnaissance-mapped to determine the regional variability of structural features surrounding similarly-oriented large-scale faults. At all the localities similar fault kinematics to those in the Marimaña/Maladeta region were observed; ductile to brittle shear structures, including rotated and tailed porphyroblasts, C-S fabrics, pressure shadows, and discontinuous brittle shear fractures, were consistent with relative up-throw of the northern blocks.

5.1.2 North Maladeta Zone – Discussion

The structural framework of the North Maladeta Zone is dominated by the steeply northward dipping, planar faults that bound the Maladeta and Marimaña massifs. The abrupt truncation of the metamorphic thermal aureole surrounding the massifs is clear evidence that the structures post-date the Late Hercynian granodiorite emplacement age. Stepped and grooved fault surfaces indicate the structures represent reverse faults or over-steepened, south-vergent thrust faults. Smaller scale structures and fabrics, which deform or truncate the palaeozoic metasediments, increase in abundance and magnitude with increased proximity toward the faults, and all lithological boundaries terminate against them. Hence, it is probable that the structures represent the latest phase of major tectonic deformation within the area.

Localised deformation around the fault zones is restricted to the intervening Palaeozoic lithlogies and is absent from the granitoid rocks. The systematic orientation of the well-developed cleavage and the youngest minor fold structures (Fig. 5.4b), combined with their localised distribution adjacent to the major fault surfaces, may indicate they developed within the local shear zones during periods of south-directed thrusting.

The brittle shear fractures that cross-cut the folded meta-sediments, thus representing the youngest phase of deformation, are also restricted to the local shear zones surrounding the south-vergent tectonic contacts and are systematically oriented with the direction of shear orthogonal to the strike of the major structures (Fig. 5.4b). The majority of the shear fractures are parallel-aligned and are oriented at moderate angles toward the north, or at acute angles to the main line of faulting. This orientation combined with their synthetic kinematics is consistent with their development as secondary shear fractures to the main faults or Riedel (R_1) shears, within the fault zone (Fig. 5.4a) (Reidel, 1929; Cloos, 1955; Wilcox et al., 1973; Ramsay and Huber, 1987; Price and Cosgrove, 1991). The opposing shear fractures, which are less common, form a conjugate set at high angles to the main line of faulting and display antithetic displacement. These structures are consistent with their development as additional minor faults, or conjugate Riedel (R_2) shears within the fault zone (Fig. 5.4a) (Reidel, 1929; Cloos, 1955; Wilcox et al., 1973; Ramsay and Huber, 1987; Price and Cosgrove, 1991).

The shear structures are characterised by discrete planar displacement surfaces, local brecciation and the generation of fault gouge, and do not have an associated pervasive fabric or display evidence of associated ductile deformation. Hence, they are consistent with development under a strictly brittle deformational regime (Price, 1966; Ramsay and Graham, 1970; Twiss and Moore, 1992; McClay, 1997). Previous rheological studies indicate brittle deformation occurs in 'typical' continental crust, of dominantly granitic composition, at depths of less than ~10 km of the earth's surface (Byerlee, 1967; Rutter, 1974; Byerlee, 1978;

Knipe, 1989). The actual depths at which deformation occurred in this instance cannot be resolved as the regime of temperature, confining pressure and fluid pressure is unknown and the rate at which strain was imposed cannot be constrained. However, it is sufficient to recognise that the Palaeozoic shales, phyllites and marbles in which the shear fractures are found are likely to have a comparatively low mechanical strength and, hence, would deform in a brittle manner to only relatively shallow depths in the Brittle Zone (Byerlee, 1967; Davis and Reynolds, 1996). The complete lack of shear structures within the adjacent, and more mechanically competent, granitoid massifs is perhaps testament to relatively shallow level deformation.

It can be summarised, therefore, that the post-Hercynian structures in the North Maladeta Zone are consistent with south-directed shear and thrust displacement along the faults that bound the Marimaña and Maladeta massifs. Furthermore, the structures surrounding the faults indicate the rocks that are exposed at the present-day surface were undergoing active, south-vergent fault displacement within a brittle deformational regime in the shallow crustal realm (<10 km) (see Chapter 6 for further discussion).

5.2 The South Maladeta Zone – Geological review

The focus of the field research in the South Maladeta Zone was in areas 'e' and 'f' (Fig. 5.1) near the villages of Estet and Aneto. The primary objectives of field work in these adjacent areas was to characterise the Alpine-age structures south of the Maladeta thermochronlogical sampling area along major tectonic contacts.

Previous interpretations of the stratigraphy of the South Maladeta Zone have subdivided the pre-Hercynian strata, which was regionally metamorphosed to lower greenschist facies during the Hercynian orogeny, from the post-Hercynian cover rocks (Mey, 1968; Boersma, 1973). The pre-Hercynian strata range in age from Cambrian to Lower Carboniferous. Cambro-Ordovician rocks consist of monotonous, non-fossiliferous alternations of slates, phyllites, and thin quartzite bands, which pass upwards into Silurian-age friable, graptoliferous, black, carbonaceous shales, slates, and locally limestones (Mey, 1968). Devonian-age deposits are characterised by mainly shales and slates, which locally pass into coarser clastic lithologies, followed by a regional transition into dolomites, red, nodular limestones, slates and calc-shists (Mey, 1968; Boersma, 1973). These units are conformably overlain by a Pre-Hercynian Carboniferous sequence of radiolarian-bearing pelites and calcareous sandstones (Mey, 1968). Fine-grained, quartz-dolerite and aplite dykes of Upper Carboniferous age have intruded into the surrounding country rock and may be related to the emplacement of the Maladeta batholith to the north (Mey, 1968; Zwart, 1979). The majority of post-Hercynian age rocks of the south Maladeta Zone, however, are of Triassic age (Fig. 2.6: Stratigraphic column, Mey, 1968; Zwart, 1979). The Lower Triassic terrestrial sediments of the Bunter Formation (Mey et al., 1968) overlie a regional angular unconformity and comprise a greyish-red sequence of conglomerates, coarse-grained quartzose sandstones, and micaceous silt- and mudstones (Mey, 1968; Mey et al., 1968). These are overlain by limestones, dolomites and marl-gypsum sequences of the Pont de Suert Formation (Mey et al., 1968). This unit is generally represented by a chaotic mélange of limestone and dolomite slabs within a heavily deformed and incoherent gypsum matrix.

Pre-Hercynian lithologies in the area immediately to the south of the Maladeta batholith (area e, Fig. 5.1) (Sierra Negra Unit: Mey et al., 1968; Mey, 1968) are characterised by broadly E-W oriented, isoclinal folding with a well-developed axial planar slaty cleavage. Fabrics dip steeply (65-80°) to the north near the southern boundary of the granodioritic intrusion and decrease to moderate dips (40-55°) toward the south (Boschma, 1963; Mey, 1968). Local development of secondary fabrics, often as crenulation cleavages, is found within the central area (Mey, 1968). To the south (area f, Fig. 5.1) (Baliera and Ribagorçana Units: Mey, 1968), large, overturned, concentric folds are oblique to the regional E-W cleavage orientation, and represent an earlier phase of deformation. All episodes of folding and cleavage development in the pre-Hercynian lithologies are demonstrably Hercynian in age as they are truncated at the contact with the Late Hercynian-age Maladeta granodiorite and are overprinted by the associated contact thermal aureole (Mey, 1968).

The northern area (area e, Fig. 5.1) is crosscut by the large-scale, northward-dipping and southward-vergent Senet Thrust, which can be traced along strike to both the east and west for up to ~40 km (Mey, 1968; Zwart, 1979). The presence of Mesozoic rocks in the fault zone confirm the Alpine age of this structure (Zwart, 1979). Analysis of palaeomagnetic pole rotations with the igneous lithologies of the northern fault block indicate the Senet Thrust is likely to have had an initial orientation that was similar to its present steeply-north dipping attitude (70-85°) (McClelland and McCaig, 1989). The southern area (area f, Fig. 5.1) is crosscut by more gently northward-dipping structures (e.g. Estét Thrust, Bono Thrust; Mey, 1968) that, owing to the presence of deformed Triassic rocks, are also demonstrably Alpine in age (Mey, 1967). Palaeomagnetic studies suggest these structures have been over-steepened during a period of local doming after fault displacement (McClelland and McCaig, 1989).

5.2.1 The South Maladeta Zone: Area 'e' – Geological Field Data

Data from field area 'e', within the South Maladeta Zone, are presented on a geological map and cross-section (**Fig. 5.7a & 5.8a**) and in a series of field sketches and photographs (**Fig. 5.9 & 5.10**). Stratigraphical divisions and structures of Hercynian age were confirmed from previous studies of the Palaeozoic rocks (Boschma, 1963; Mey, 1967; Mey, 1968; Mey et al., 1968; McClelland and McCaig, 1989).

The Senet Fault is clearly discernable over km-scale outcrop and dips moderately steeply (45-60°) toward the N to NNW (Fig. 5.9a). The fault surface represents a planar, tectonic contact between black, carbonaceous shales and a heavily deformed marl-dolomite-gypsum succession.

Within the hanging-wall of the Senet Fault, the Palaeozoic lithlogies have a pervasive slaty cleavage that displays a moderate dip (37 to 60°) toward the N to NNW. In areas immediately adjacent to the tectonic contact (<~30 m) the cleavage is locally deformed by small-scale (2-10 cm amplitude) parallel folds and kink bands with moderately northward dipping axial surfaces. Spotted slates of the Hercynian basement, presumably derived from local heating during emplacement of the Maladeta granodiorite (Mey, 1967), display a systematic N-S stretching elongation of the contact metamorphic minerals (Fig. 5.10d), which have subsequently been weathered out.

The fault zone is characterised by incohesive, heavily foliated and brecciated, shales and muds with ubiquitous iron staining (Fig. 5.9c). The pervasive slatey cleavage is locally truncated by continuous brittle shear fractures oriented at gentle angles (15-35°) toward the north. Coherent blocks bound by shear fractures retain the rotated pervasive fabric of the Hercynian basement. The blocks are occasionally stacked in small-scale south-vergent thrust duplexes between parallel floor and roof thrusts (Fig. 5.9c). All the large-scale shear fractures are oriented sub-parallel to parallel to the main fault.

The mechanically incompetent marls and gypsums of the upper Triassic units located within the footwall of the fault, display non-concentric, disharmonious and ptygmatic folds and are highly variable over short distances (Fig. 5.9e).

Composite planar fabrics and foliations are pervasive within the more competent lithologies of the footwall immediately below the fault and are often deformed by low angle shear bands. The shear surfaces are aligned sub-parallel to the main fault zone and the intervening foliation is deformed into sigmoidal geometries at high angles to the shear surfaces (Fig. 5.10a). With increased distance from the main fault contact the spacing between the shear surfaces becomes progressively larger and less distinct. South-directed brittle shear fractures with a gentle northward dip (15-30°) disrupt and truncate the earlier foliation (Fig. 5.9f). These are characterised by finely brecciated fracture surfaces that preferentially weather from the surrounding bedrock.

5.2.2 The South Maladeta Zone: Area 'e' – Discussion

The large-scale, northward dipping Senet Thrust dominates the structural framework of field area 'e' of the South Maladeta Zone. The data collected in this study are consistent with previous interpretations of south-directed fault motion and the emplacement of older Hercynian basement over younger, unmetamorphosed cover rocks. The systematic orientation and kinematics of structures surrounding the Senet Thrust, such as shear foliations, fold structures and brittle shear fractures (Fig. 5.9f), are consistent with their development within a shear stress regime generated during active, south-vergent fault displacement (Fig. 5.8a). The brittle shear structures, representing the most recent period of compressive deformation, likely formed as minor Reidel shears (R1) or secondary shears to the main fault zone (Reidel, 1929; Cloos, 1955; Wilcox et al., 1973; Ramsay and Huber, 1987; Price and Cosgrove, 1991).

The localised deformation associated with thrust movement at the Senet fault can be broadly divided into two distinct categories. The first group is characterised by the development of penetrative foliations, distributed shear bands, and localised C-S-type fabrics surrounding the main thrust contact. These pervasive fabrics are likely to represent a semi-ductile to brittle-ductile response to distributed strain during thrust displacement (Simpson and Schmid, 1983; Hanmer and Passchier, 1991). The second group of structures, occurring within similar lithlogies, systematically overprint the first group and are characterised by discrete displacement surfaces along brittle shear fractures and the generation of brecciated surfaces and fault gouge. The nature of these structures is consistent with their development under a purely brittle deformational regime (Price, 1966; Ramsay and Graham, 1970; Hanmer and Passchier, 1991; McClay, 1997). As both groups of structures are oriented appropriately and are kinematically consistent with south-directed thrusting, it suggests the Senet Thrust was likely to have been active at a variety of crustal depths. However, the nature of the most recent structures indicates active fault displacement was maintained within the uppermost levels of the crust (<10 km) within a brittle deformational regime (Byerlee, 1967; Rutter, 1974; Byerlee, 1978; Knipe, 1989) (see Chapter 6 for further discussion).

5.2.3 The South Maladeta Zone: Area 'f' – Geological Field Data

Data from field area 'f', within the South Maladeta Zone, are presented on a geological map and cross-section (**Fig. 5.7b & 5.8b/c**) and in a series of field sketches and photographs (**Fig. 5.11 & 5.12**). The fault trace of the Estet Thrust runs in an approximately E-W orientation through the field area. It represents a planar structure with a N to NNE oriented, gentle to moderately inclined (25-40°) dip (Fig. 5.11a). The structure is the tectonic contact between intensely folded limestones, to the north, from gently folded psammitic and pelitic red-beds that unconformably overlie heavily deformed limestones and shales to the south. Well-defined mineral slickenside and groove lineations on small parallel faults within the Estet hangingwall yield plunge orientations of gentle to moderate dip (~30-40°) toward the N (Fig. 5.11c). Stepped mineral structures on large-scale fractures surfaces are consistent with upthrow of the northern block. A poorly defined cleavage within the older rocks dips moderately steeply (~40-70°) toward the N to NW (Fig. 5.12c).

The psammitic and pelitic red beds are deformed into a gently westward plunging, synform-antiform, open fold structure with a moderately inclined, northward dipping axial surface (Fig. 5.8b/c & 5.12c). Sedimentary way-up structures, including cross-stratification and erosive basal contacts, indicate the units have not been overturned and depict a syncline-anticline relationship (Fig. 5.11d).

A coarse but pervasive, fracture cleavage is ubiquitous throughout the red bed succession. Within the south dipping limbs of the anticline and syncline it forms a high angle with the bedding surfaces (Fig. 5.12a & 5.12b). The cleavage displays a moderate to steep dip (~40-65°) toward the NNW to NW (Fig. 5.12c).

5.2.4 The South Maladeta Zone: Area 'f' – Discussion

Data collected from field area 'f' are consistent with earlier interpretations of the Estet Fault as a south-directed thrust which caused the juxtaposition of Hercynian lithologies over unmetamorphosed Triassic redbeds. The deformation within the well-exposed younger units may have developed during overthrusting of the more northerly Hercynian basement, thus generating a local footwall syncline.

The formation of the coarse fracture cleavage within the red bed succession has previously been associated with the reactivation of the north-dipping basement cleavage below the unconformable contact (Mey, 1967; Zwart, 1979). However, data from this study depict a systematic discrepancy between the orientation of the basement cleavage and the overlying fracture cleavage (Fig. 5.12c). Instead, it is possible the fracture cleavage developed as an axial planar fabric as the footwall syncline was progressively tightened during southward thrusting on the Estet Thrust. The systematic orientation of the cleavage, with respect to the macro-scale fold structure is consistent with this interpretation (Fig. 5.12c). A more thorough investigation of the regional cleavage orientations of the region, of both basement and cover rock, would enable this interpretation to be better constrained.

In general, thrust-associated deformation within area 'f' is characterised by large scale folding and probably the development of a pervasive fracture cleavage within the cover rock succession. These structures and fabrics are likely to represent a semi-ductile to brittle-ductile response to distributed strain during active thrust displacement. There is no evidence of later overprinting by brittle structures to suggest the fault may have been active within the exclusively brittle regime of the shallow crustal realm (see Chapter 6 for further discussion).

5.3 The Nogueres Zone – Geological review

The focus of the field research in the Nogueres Zone was in five along-strike field areas (areas g-k: Fig. 5.1). The primary objective of field work in this area was to constrain the timing of deformation in the region of the Nogueres thermochronological sampling sites.

The term 'Nogueres Zone' was coined by Dalloni (1913) to refer to the narrow, WNW-ESE oriented stretch between the central Axial Zone and the south-dipping Jurassic and Cretaceous strata of the southern fold and thrust belt (Fig. 2.7: Cross-section). The stratigraphy of the region ranges from Devonian metasediments to Oligo-Miocene alluvial conglomerates, but is dominated by terrestrial deposits of Carboniferous to Triassic age (Mey et al., 1968; Nagtegaal, 1969).

The metamorphosed Devonian strata are of the same facies as in the South Maladeta Zone and their character is outlined in Section 5.2. The overlying unmetamorphosed cover rock succession are summarised in the stratigraphic logs of Mey (1968) and Zwart (1979) (Fig. 2.6). The basal units overlie an angular unconformity and are comprised of coarse, breccio-conglomerates and local coal stringers of the Upper Carboniferous Aguiró Formation (Mey et al., 1968; Nagtegaal, 1969). These pass upwards into a thick sequence of volcaniclastics, alluvial sandstones, siltstones, mudstones, and coals of the Erill-Castell and Malpas Formations, deposited in E-W oriented, fault-controlled, Stephanian-age basins (Zandvliet, 1960; Mey et al., 1968; Nagtegaal, 1969; Besley and Collinson, 1991; Soriano et al., 1996). The overlying Permian sediments of the Peranera Formation comprise monotonous, grey-red alternations of calcareous mud-, silt-, and sandstones, tuffs, breccia beds and nodular limestones (Zandvliet, 1960; Mey et al., 1968; Nagtegaal, 1969). These are overlain by a sharp, angular unconformity upon which quartz-rich successions of the Triassic age, Bunter Formation and gypsum-rich sediments of the Pont de Suert Formation are present, as described in Section 5.2. A conformable contact with marly limestones and dolomites marks the transition into the overlying Jurassic Bonansa Formation (Mey et al., 1968; Nagtegaal, 1969; Zwart, 1979). The youngest sediments in the region are Oligo-Miocene age, coarse, alluvial conglomerates of the Collegats and Sis Formations (Mey et al., 1968; Zwart, 1979; Vincent, 1993; Puigdefàbregas et al., 1993; Beamud et al., 2003). These sediments are deposited on an angular unconformity and progressively onlap northwards across the Nogueres Zone and into the Axial Zone (section 5.4).

The region is characterised by N-S structural repetition of the Devonian to Triassic succession. Large, cohesive blocks, up to km's scale, display normal and overturned strata and locally variable cleavage development (Seguret, 1964; Seguret, 1972; Choukroune and Seguret, 1973). The structural evolution and origin of these blocks has been disputed by a number of workers who have argued for both autochthonous and allochthonous origins (e.g., Dalloni, 1913; Jacob et al., 1926; Seguret, 1964; Mey, 1968; Seguret, 1972; Choukroune and Seguret, 1973; Zwart, 1979, Puigdefàbregas et al., 1989). Drill data from the region indicates the allochthonous models are likely to be the most accurate representation of the Nogueres Zone's structural history (Zwart, 1979; Bates, 1989). These models suggest the tectonic blocks, each consisting of a Hercynian basement core with Carboniferous to Triassic cover rocks, represent the southward plunging noses ('têtes plongeantes': Seguret, 1964) of synformal anticlines thrust from the Axial Zone region (Seguret, 1964; Seguret, 1972; Choukroune and Seguret, 1973; Soriano et al., 1996). The specific root zone of the blocks is difficult to constrain because the connecting thrust sheets have not been preserved. A number of Alpine age structures, both to the north and south of the Maladeta Massif, have been proposed as the possible structural roots, based upon stratigraphic similarities of the spatially variable Palaeozoic and Mesozoic succession (Zwart, 1979; Muñoz, 1986). This indicates that Nogueres Zone blocks may have been transported tens of kilometres from the north, prior to emplacement in their current position on the southern flank of the mountain belt. Below, and to the south of the Nogueres Zone, seismic imaging suggests the thrust faults branch into a sub-horizontal floor thrust, or decollement surface, that underlies the southern fold and thrust belt (Fig. 2.7: Cross-section) (Muñoz et al., 1986; Puigdefàbregas et al., 1992; Muñoz, 1992).

The timing of thrust block emplacement is constrained through palaeomagnetic remanence studies of basement thrust sheet rotations (Bates, 1989), and through magnetostratigraphic age dating of the unconformably overlying conglomerates of the La Pobla de Segur Formation (Rosell and Riba, 1966; Mey et al., 1968; Mellere et al., 1992; Beamud et al., 2003; Beamud pers comm.). These methods indicate tectonic emplacement of the Nogueres blocks occurred prior to ~38 Ma, or during upper Eocene times.

A number of steep, E-W oriented, planar faults have been identified within the northern Nogueres Zone that are not associated with the emplacement of south-directed thrust nappes (Mey, 1968). These have previously been attributed to either north-directed thrusting in autochthonous models (Mey, 1968), or to development during stacking of underlying Nogueres Zone thrust sheets (Soriano et al., 1996).

5.3.1 The Nogueres Zone – Geological Field Data

The field data from a number of N-S transects through the central Nogueres Zone (areas 'g' to 'k', Fig. 5.1) are presented in series of geological maps and cross-sections (**Fig. 5.13 to 5.18**) and in a collection of field phtotographs and sketches (**Fig. 5.19 to 5.26**). Each transect represents a traverse from the metamorphosed and heavily deformed basement (Hercynian age), on the southern border of the Axial Zone, to largely undeformed conglomerates (Oligo-Miocene) onlapping to the south. Bedrock exposure is good along N-S topographic ridges within the Carboniferous to Lower Triassic succession, but limited within lithologies younger than the Bunter Formation. As the sections are very similar in their structural and stratigraphic characteristics, they are discussed together to avoid repetition and are only individually referred to for specific examples.

The Hercynian basement, at the northern extreme of the sections comprises metamorphosed limestones with well-developed slaty and secondary cleavages, oriented at moderate to steep angles (~40-70°) toward the ~SW and ~NE, respectively. The secondary cleavage (S_2) is widely spaced (~10-50 cm) and is often manifested as kink bands within the primary foliation (Fig. 5.19a-c). To the south, the unmetamorphosed cover rocks unconformably overlie the basement and display a general southward younging direction. A pervasive, coarse fracture cleavage is often locally developed in the northern regions within the Carboniferous to Lower Triassic units. This foliation is most pronounced within the northern exposures of the cover rocks, though rarely within those directly overlying the Hercynian basement. The cleavage generally displays a moderate to steep, N to NE oriented attitude (Fig. 5.19d).

In all but the Vilaller section, the overlying conformable sequence to the south is disrupted by planar, southward oriented, steeply dipping (70-85°) fault surfaces (Fig. 5.20). Offset on these structures causes the stratigraphic repetition of readily recognizable facies, such as the Erill Castell volcanics, and of specific marker horizons, such as the Permo-Triassic angular unconformity (Fig. 5.21a). Exposure of the major fault surfaces is rare, but their trace is easily discernible by the stratigraphic discontinuities. Slickenslide and slickenfiber lineations along minor fault surfaces surrounding the main fault zones display moderate to steep plunges toward the S to SW (Fig. 5.21c). The orientation of these structures and the displacement measured between the marker horizons indicates dip-slip, reverse fault motion of up to ~200 m on individual faults. These structures form an along-strike fault zone that stretches tens of kilometres in a WNW-ESE orientation.

Within the coherent fault-bound blocks in the northern area, bedding has a similar attitude to the conformable sequence that directly overlies the basement and is laterally persistent along strike, up to hundreds of metres, in an E-W orientation. In general, deformation within the fault blocks is restricted to occasional meso-scale, chevron folds (1-3 m amplitude) within the Permian units (Fig. 5.21b). These display moderate to steep inclination of the axial surfaces toward the N to NNE and horizontal to subhorizontal fold axes (Fig. 5.26c). Deformation that affects the entire cover rock succession within the northern fault blocks is only observed within the Sas section (Fig. 5.15 & 5.18c). In this area the cover rocks have been deformed into a large, upright, open syncline adjacent to a steeply, south dipping fault. Minor, planar faults (~5-10 m displacement) are also observed in all the sections with variable orientations and down-throw directions.

With progressive younging toward the south, the Triassic age gypsum, marl and dolomite sequences outcrop toward the top of the cover rock succession. Stratification within these poorly exposed units has not been preserved and is instead represented by a chaotic melange of dolomitic slabs displaying no obvious preferred orientation. Lenses (~5-10 m) of the older Bunter Formation are also occasionally incorporated in the mélange, for example in the Coll d'Olli section (Fig. 5.16 & 5.18b) and display an E-W alignment and are heavily sheared and tectonised.

Synchronous with the appearance of the gypsum-marl lithologies is a marked shift in the structural character of all the sections compared to that observed in the northern areas. Repetition of the basement and lower cover succession occurs, though the attitude and orientation of bedding is highly variable, but predominantly at moderate to steep, northerly dips. Clear way-up structures are common, including tabular and trough cross-stratification, loadcasts, graded beds, scour structures, and desiccation cracks (Fig. 5.22a-5.22c). These indicate that conformable sequences of metamorphic basement and cover rocks have been overturned and rotated by more than 90°. Within both the Coll d' Olli and Sas sections, there is evidence of only one overturned block (Fig. 5.23). In the Ancs and Vilaller sections, numerous overturned blocks are evident, bound by heavily sheared, but poorly exposed tectonic surfaces.

The stratigraphy of the rotated blocks is characterised by metamorphosed limestones with strong slaty and secondary cleavages, comparable to the Devonian of the Axial Zone to the north. The cover rocks generally comprise a Carboniferous to Permian succession of highly variable thickness, with an extensive overlying sequence of Triassic red beds. Clear stratigraphic discrepancies between the overturned blocks and the immediately underlying succession to the north are evident. A good example of this can be found within the Coll d' Olli section (Fig. 5.16 & 5.18b), whereby the thick Carboniferous and Permian succession mapped to the north is absent within the overturned block, which is located less than 1000 m to the south. Likewise in the Sas section (Fig. 5.15 & 5.18c), the thick sequence of cover rocks between the basement and Bunter Formation are much reduced in the adjacent rotated block. In the Vilaller section (Fig. 5.13 & 5.18e), the overturned blocks display thick Carboniferous and Permian sequences, but these are not found in the gently deformed units to the north.

In general, the rotated blocks display very limited pervasive deformation. Exceptions to this general rule occur within the Vilaller section (Fig. 5.13 & 5.18e), whereby ~E-W oriented, mesoscale folding (~100 m amplitude) is evident within the overturned Triassic succession, and within the Ancs section (Fig. 5.17 & 5.18a), whereby an overturned, moderately southward dipping, syncline is mapped within a rotated block. Cleavage development occurs only very locally and is invariably a parting foliation sub-parallel to bedding, such as within the overturned Triassic of the Coll d' Olli section.

At the southern end of the Nogueres Zone, conglomerates and sandstones onlap onto a high-relief, angular unconformity above the overturned blocks. At the well-exposed onlap surface of the Coll d' Olli section (Fig. 5.16 & 5.18b) the basal units display a moderately steep dip (up to ~50°) toward the S to SE. The immediately overlying succession depicts progressively shallower dips toward the south, with the uppermost units oriented at shallow angles of <15° (Fig. 5.24). Lower in the conglomerate succession, adjacent to the villages of Perbes and Sarroca de Bellera (located in Fig. 5.27) (east and southeast of the base of the Coll d' Olli map area, respectively), the sediments are deformed by south-vergent thrusts oriented at gentle angles (10-20°) toward the N to NNE. Mesozoic carbonates overthrust the basal conglomerates and form local footwall synclines of <10 m amplitude, and associated axial planar fracture cleavages, within the deformed sediments (Fig. 5.25a & 5.25e). The displacement and lateral extent of these structures is difficult to ascertain owing to poor exposure of the onlap surface. Toward the southern end of the Senterada Basin, laterally-extensive brittle shear zones deform the basal conglomerates and cause brittle fracture and displacement (>10 m) of large, coherent boulder-grade clasts (Fig. 5.25c & 5.25d). The structures are oriented at gentle angles toward the N to NNE and display southward-vergent thrust displacement.

5.3.2 The Nogueres Zone – Discussion

The occurrence of isolated, overturned blocks of Hercynian basement and cover rocks bound by southward dipping faults classically characterises the structural nature of the Nogueres Zone. The structural geometries and stratigraphic variations observed in this study are consistent with previous interpretations from along-strike, with the blocks regarded as noses and flanks of south-directed thrust nappes transported from a source region within the central Axial Zone (e.g. Seguret, 1964; Choukroune and Seguret, 1973). As noted in Section 5.3, the timing of nappe emplacement is likely to have occurred prior to Upper Eocene times (>38 Ma). Since this time, the originally low-angle thrust structures that connected the source region to the overturned blocks have been exhumed and eroded from above the Axial Zone, and rotated and steepened toward the south in the exposed Nogueres Zone. As also previously noted, immediately to the south of the Nogueres Zone the structures branch into a sub-horizontal floor thrust that underlies the southern fold and thrust belt (Muñoz et al., 1986; Puigdefábregas et al., 1992; Muñoz, 1992).

The remaining parts of the mapped areas are characterised by relatively modest amounts of deformation; the Axial Zone basement unconformity and the overlying succession have been tilted steeply toward the south, the cover rocks have been offset in the north by north-directed, reverse faults or steep backthrusts, and, less commonly, in the south by gently dipping, south-directed thrusts. Both sets of structures display relatively limited dip-slip displacement of tens to hundreds of metres. The better-exposed north-directed set is laterally extensive over tens of kilometres. Previous interpretations of the structures have assumed they developed synchronously with the larger, nappe-bounding thrusts (e.g. Mey, 1968). However, it is difficult to envisage a single stress regime that might generate both sets of structures simultaneously. The undisturbed form of the north-directed structures and the intervening blocks suggest they probably postdate the emplacement of the large, overturned units immediately to the south and that they formed in-situ. Likewise, the south-directed structures deform the conglomerates that onlap onto the overturned Nogueres blocks. Hence, the development of both sets of minor thrusts must be associated with Nogueres Zone deformation that occurred after nappe emplacement, or after ~38 Ma.

A possible interpretation of the structures is that they formed in response to the development of compressive stresses on the internal arc, or the concave regions, of a regional WNW-ESE oriented synform that formed after the emplacement of the Nogueres nappes. The geometry of the synformal structure can be envisaged by considering the post-emplacement (<38 Ma) deformation of the nappe-bounding south-directed thrusts; to the north the structures have been uplifted and eroded above the present topography of the Axial Zone, in the Nogueres Zone the structures have been rotated to have a steep southward dipping attitude, and to the south the structures are sub-horizontal and branch into the floor thrust of the southern fold and thrust belt. Therefore, since emplacement of the Nogueres nappes at, or before, 38 Ma, the Nogueres Zone has acted as a linear flexure separating the northern limb, which was steepened toward the south, from the southern limb that was retained at sub-horizontal angles. This linear compressive stress regime, localised across the Nogueres Zone, could have promoted the development of 'fold-accommodation' faults or 'out-of-syncline' thrusts within the flexured unit (Stearns, 1964; Philip and Meghraoui, 1983; Burbank and Anderson, 2001; Mitra, 2002). These would be generated in two distinct sets oriented at steep angles toward the south, with north-directed thrust motion, and at gentle angles toward the north, with south-directed thrust motion (Stearns, 1964; Price, 1966; Price and Cosgrove, 1991), both of which are observed within the Nogueres Zone (Fig. 5.26a & 5.26b). With subsequent compressive deformation, or tightening of the synform, the thrusts in the flexure zone would have continued to passively rotate (Price and Cosgrove, 1991). Displacement of only tens to hundreds of metres on the observed structures, despite their extensive lateral persistence of many kilometres, is consistent with this mode of formation.

The development of the northward-dipping coarse fracture cleavage within the cover rocks of the Nogueres Zone has previously been attributed to the Alpine reactivation of upward shear movements along the youngest (S_2) Hercynian basement cleavage (Mey, 1967; Mey, 1968). However, it is difficult to reconcile the widely-spaced secondary foliation observed in the basement (Fig. 5.19a-5.19c) with the well-developed fracture cleavage of the cover rocks, particularly as they are often separated by thick sequences of non-cleaved mudstones and tuffs. A systematic discrepancy between the two sets of cleavages is also apparent, with the basement S_2 cleavage oriented at lower angles (Fig. 5.19d). A possible alternative is to suggest the north-dipping fabric developed as an axial planar cleavage within the flexure zone during tightening of the regional synform. This is consistent with the orientation of the cleavage bisecting the angle between the two sets of out-of-syncline thrusts (Fig. 5.26c). The development of mesoscale folds, with northward-oriented axial surfaces, within the flexure zone may also be linked to the development of the regional syncline as axial parasitic folds (Fig. 5.26c). However, as their occurrence is restricted to only the pre-Triassic cover rocks, the timing of their development is poorly constrained.

As noted previously, the formation and tightening of the regional synform, and the development of the associated thrust structures, must have occurred after emplacement of the Nogueres nappes (>38 Ma). The timing of this is further constrained by the depositional age of the deformed Senterada conglomerates, which range from ~33 to 21 Ma (Beamud et al., 2003; Beamud pers comm.; section 5.4.2). This indicates that the north-dipping, south-vergent thrusts were active during or after Oligocene and Lower Miocene times. The conglomerate units at the southern end of the Coll d'Olli section, which represent the uppermost fill of the Senterada Basin, have an estimated depositional age of ~21 Ma (Beamud et al., 2003; Beamud pers comm.; section 5.4.2). The succession in this region depicts evidence of southward rotation of the depositional surface during active sediment aggradation, or at least prior to deposition of the immediately overlying units. This synsedimentary deformation is consistent with the southward rotation of the Nogueres structures, or tightening of the regional synform, during Lower Miocene times (see Chapter 6 for further discussion).

5.4 The Morreres Zone – Geological review

The focus of the field research in the Morreres Zone was in area '1' (Fig. 5.1) in the vicinity of La Pobla de Segur. The primary objective of the field work in this region was to characterise the approximate timing and scale of deformation along the Morreres Backthrust, which represents the tectonic boundary between the inner orogen and the southern fold and thrust belt (Muñoz, 1992; Puigdefàbregas et al., 1989). The structure is aligned WNW-ESE with a steep dip toward the SSW. The fault trace outcrops for up to 80 km within the Noguera Pallaresa and Noguera Ribagorçana regions.

Within the south central Pyrenees, the structure juxtaposes the Lower Cretaceous succession against Triassic basaltic rocks, marls and gypsums of the Nogueres Zone to the north (Fig. 2.9) (Puigdefàbregas et al., 1989). Previously developed fold structures within the

Mesozoic stratigraphy are truncated, resulting in a subtractive contact and the omission of the entire Jurassic succession (Puigdefàbregas et al., 1989). Despite this stratigraphical cut out, the structure is regarded as a passive roof backthrust (Banks and Warburton, 1986) directed toward the north (Muñoz, 1992), rather than a fault with normal-sense displacement. Its' development is linked to the progressive deformation of the Bóixals thrust sheet in front of and over the Nogueres unit. The mechanically competent carbonates of the Jurassic and Cretaceous succession are regarded to have passively overthrust the underlying wedge of gypsums and marls during steepening of the structure, associated with the stacking of basement thrust sheets below the Nogueres Zone (Muñoz, 1992; Puigdefàbregas et al., 1989).

The fault trace is characterised by extreme topographic relief that correlates with the outcrop of the deformed Cretaceous succession of the hangingwall. Within the central region, the fault trace topography is onlapped by the La Pobla de Segur Conglomerate sequence (Rosell and Riba, 1966), also known as the Collegats Formation (Mey et al., 1968). In the western region it is onlapped by the conglomerates of the Sierra de Sis Formation (Vincent, 1993).

The Pobla de Segur conglomerates have a cumulative thickness of >3500 m and are preserved within plateau massifs between heavily incised canyons and gullies. The basin is regarded to represent an intramontane environment that was partitioned into two smaller sub-basins, either side of the relief of the Morreres backthrust (Mellere, 1992; Mellere, 1993). To the north of the structure, within the fault footwall lies the Senterada Basin. To the south, within the hangingwall, lies the Pobla de Segur basin (Mellere, 1992).

The conglomeratic sequence is regarded to represent an alluvial fan complex comprising more than 20 interfingering alluvial fan lobes that prograded into flood basin and shallow lacustrine environments (Mellere, 1993). Five main allogroups (Pessonada, Ermita, Pallaresa, Senterada and Antist) have been distinguished by Mellere (1993), based upon bounding unconformities, clast composition and palaeocurrent patterns. All five allogroups are represented within the Pobla de Segur basin, but only the two younger allogroups are found within the northern Senterada basin (Mellere, 1993). Magnetostratigraphic age dating of the sediments indicate the Pessonada to Pallaresa allogroups were deposited during Middle to Upper Eocene times (Ermita: 41.5-~40.5 Ma; Pallaresa: 40.5-33.5 Ma), and the Senterada and Antist allogroups were deposited during Lower Oligocene times (<33.5 Ma) (Beamud et al., 2003). The youngest sediments of the sequence, which have not been preserved, may have onlapped and backfilled across the entire Nogueres Zone and formed a high level aggradational alluvial plain extending into the central Axial Zone (Coney et al., 1996).

The Sierra de Sis conglomerates are located to the west of the Pobla de Segur Formation and are preserved within a single, linear massif oriented NNE-SSW (Vincent, 1993; Vincent, 2001). The sequence has a cumulative sedimentary thickness of >1400 m which overlies a regional angular unconformity (Puigdefàbregas et al., 1985; Vincent, 1993; Vincent, 2001). The geometry of the unconformable surface and the facies variations linked to a linear, NW-SE oriented axis, have been interpreted to indicate the Sierra de Sis represents a preserved intramontane palaeovalley and fluvial sediment transfer zone (Puigdefàbregas et al., 1985; Vincent, 1993; Vincent, 2001).

Four distinct stratigraphic formations have been discerned by Vincent (1993) (Cajigar, Cornudella, Sis, Collegats), based upon bounding disconformities and unconformities, palaeoflow and provenance data. Dating of the sediments has been constrained by biostratigraphic assemblages, magnetostratigraphic analysis and detrital fission track studies (Vincent, 1993; Bentham and Burbank, 1996; Fitzgerald et al., 2000). These indicate the Cajigar and Cornudella Formations were deposited during pre-Bartonian Middle Eocene times and the overlying Sis formation during Upper Eocene times (Bentham and Burbank, 1996; Fitzgerald et al., 2000). The Collegats formation, at the top of the succession, has been correlated with the Senterada and Antist Allogroups of the Pobla de Segur Conglomerates, and is regarded to be early Oligocene in age (Beamud et al., 2003).

5.4.1 The Morreres Zone – Geological Field Data

Field data from the Morreres Zone are presented on a geological map and cross-sections of the Pobla de Segur region (**Fig. 5.27 & 5.28**) and in a series of field photographs and sketches (**Fig. 5.29 to 5.32**). The focus of investigation was placed upon the Morreres Backthrust (hereafter referred to as the MBT) and the relationship with the sediments of the Pobla de Segur Formation that drape the structure. These are preserved to the north and south of the MBT, within the Senterada and Pobla Basins, respectively. The stratigraphical classification of the sediments into distinct allogroups used by Mellere (1993) is adhered to in this study. The four allogoups that are preserved within the field area are the Ermita, Pallaresa, Senterada and Antist. The Pallaresa and Senterada groups are further subdivided into subgroups (Montsor 1-3 and Senterada 1-3, respectively), following the classification of Mellere (1993).

The Morreres tectonic contact between the Pobla and Senterada basins is characterised by a steeply southward oriented, planar fault zone separating heavily-sheared limestones and breccias in the hangingwall from chaotic assemblages of basaltic rocks and marls in the footwall. Kinematic analysis of the ductile and brittle shear fabrics within the Morreres Backthrust fault zone indicate thay are compatible with relative upthrow of the southern block, or north-directed thrusting and, thus, consistent with previous interpretations (e.g. Puigdefàbregas et al., 1989).

The sediments of the Pobla Basin, which overlie the deformed hangingwall of the backthrust, display a regional, gentle (~5-20°) dip toward the NNE to NE (Fig. 5.29a). The onlap surface between the hangingwall and the overlying conglomerates is well preserved (Fig. 5.29b & 5.29c). Deformation within the sediments is characterised by interformational tilting and by long wavelength folding (Fig. 5.28a-5.28d): The Ermita allogroup, the stratigraphically lowest of the succession, and the overlying Montsor 1 subgroup (Pallaresa Allogroup) are gently tilted toward the NNE to NE and display no other localised deformation. The Montsor 2 subgroup displays a regionally similar dip at the base but is truncated by an intraformational unconformity. The Subgroup is hence further subdivided into the Montsor 2a group, below the unconformity, and the Montsor 2b group, above the unconformity. The erosional surface displays a dip toward the NNE to NE at a slightly higher angle than the underlying unit. Consequently, the Montsor 2a subgroup is progressively incised toward the north and culminates with a featheredge pinch out at the onlap surface (Fig. 5.28a/b & 5.30). Inter- and Intra-formational unconformities within the overlying units also result in subtle stratigraphic thinning toward the north. The Montsor 2b subgroup is deformed at the onlap surface into a local syncline with the northern limb oriented at a gentle to moderate angles toward the SSE to SE. The overlying Montsor 3 unit and Senterada and Antist allogroups also display a similar dip within their southern limb, but show progressive decline of deformation within the northern limb.

The sedimentary infill of the Senterada Basin, which overlies the footwall to the MBT, onlaps onto overturned blocks of Hercynian basement and Triassic cover rocks of the Nogueres Zone. Owing to the low weathering resistance of the Triassic marl-gypsum sequence, the onlap surface is rarely exposed. The two main allogroups represented within the basin (Senterada and Antist) are significantly thicker than observed within the Pobla Basin succession. The basal units display a marked contrast in facies from that of the overlying stratigraphy and have been tentatively linked to the uppermost sediments of the Pallaresa allogroup by Mellere (1992). The lowermost units are characterised by thick beds (2-3 m) of clast-supported, cobble- to boulder-grade, well-sorted conglomerates, which are massively dominated by extremely well rounded granitic and Hercynian basement clasts of 20-80 cm (b-axis) dimension (Fig. 5.31a & 5.31d). These pass abruptly into more typical

Senterada allogroup facies comprising interbedded sequences of cross-bedded sands, silts and well-sorted, cross-bedded and imbricated pebble grade conglomerates, the provenance of which is massively dominated by 4-16 cm (b-axis) dimension Permian and Triassic red bed clasts (Fig. 5.31a & 5.31b).

Deformation within the Senterada Basin is characterised by a gentle regional tilting of the northern side of the basin toward the SSW to SW. In the southern flank of the basin, which borders the Morreres fault zone, the basal units of the Senterada allogroup are deformed into an open, gently westward plunging syncline. Exposure of these units is limited and so it is difficult to determine if the deformed strata are bound by intraformational unconformities, as observed within the Pobla Basin. Where exposed, the onlap surface of the Senterada sediments is occasionally deformed by south-directed thrust surfaces, south-directed brittle shear fractures and syn-sedimentary rotation of the most northerly units. These structures are discussed in Section 5.3.1.

5.4.2 The Morreres Zone – Discussion

Kinematic analyses of shear structures within the MBT fault zone are consistent with previous interpretations from along-strike of north-directed thrusting. The history of kinematics and displacement along the structure can be further understood by considering the internal organisation and spatial distribution of the onlapping Pobla de Segur Formation.

The major units of the conglomeratic succession are often bound by sharp erosive surfaces oriented at shallow angles to the underlying succession, causing systematic truncation of progressively older and older strata. The occurrence of these inter- and intra-formational unconformities, or growth strata, is the result of the rotation of the depositional surface during active alluvial aggradation (Holl and Anastasio, 1993; Hardy and Poblet, 1993; Suppe et al., 1992). As approximately constant sedimentation rates (~0.1-0.2 kmMyr^{-1}) were maintained throughout the depositional history of the basin (Beamud et al., 2003), the growth stratal geometries and onlap-offlap relationships are a singular function of the localised uplift and rotation of the underlying substratum (Holl and Anastasio, 1993; Hardy and Poblet, 1993; Shaw and Suppe, 1994; Butler and Lickorish, 1997). This was likely to have been directly controlled by displacement along the MBT, upon which the Pobla and Senerada basins lie on the hangingwall and footwall, respectively. By attaching a sedimentological and chronological framework (Mellere, 1993; Beamud et al, 2003) to the succession, direct links between the stratal architecture and the local tectonic shortening history can be made (Fig. 5.32).

Prior to the onset of deposition of the Ermita allogroup during uppermost Middle Eocene times (~42 Ma: Beamud et al., 2003) significant shortening along the Morreres Backthust must have occurred. This is clearly evidenced by the considerable topographic relief upon which the conglomerates are deposited (Fig. 5.29a to 5.29c); the basal sediments onlap the Cretaceous substratum at ~500 m in the modern valley floors and the succession continues to 1500 m at the ridge crests. Therefore, before ~42 Ma, vertical topographic relief of more than 1000 m, as least as abrupt as found in the modern setting, had been generated along the hangingwall of the MBT.

During Middle to Upper Eocene times (~42 to 35 Ma) the Ermita allogroup and the Montsor 1 and 2a subgroups (Pallaresa allogroup) were deposited within the Pobla Basin (Mellere, 1993; Beamud et al., 2003; Beamud pers comm.). The parallel alignment and conformable nature of the surfaces bounding the Ermita and Montsor 1 units is consistent with their deposition on a stable, non-rotating substratum (Fig. 5.32a). The Montsor 2a unit, however, is vertically bound by a progressive unconformity that culminates in a featheredge pinch-out at the northern onlap surface. The progressive nature of this bounding surface is consistent with a northerly decrease in aggradation due to localised surface uplift and southward rotation of the regional depositional surface (Riba, 1976; Holl and Anastasio, 1993). This is likely to be associated with the rotation of the MBT hangingwall during tectonic shortening synchronous with deposition of the Montsor 2a unit (Fig. 5.32b). The absolute amount of tectonic shortening required to generate the differential uplift, thus causing the omission of ~120 m of the Montsor 2a stratigraphy in the north of the basin, cannot be accurately resolved as the subsurface geometry of the MBT is unconstrained (Holl and Anastasio, 1993; Hardy and Poblet, 1994). In the northern Pobla Basin area, the MBT surface trace is inferred from the outcrop of hangingwall lithologies and from the regional topographic form, and depicts a moderately steep dip of ~60° toward the south. If it is inferred that this ramp geometry is maintained below the surface, and that the ramp is of a similar size to that of the rotational wavelength documented in the Montsor 2a unit, approximately 70 m of horizontal tectonic shortening is sufficient to generate the local hangingwall uplift along the MBT. This period of shortening must have occurred prior to the deposition of the overlying Montsor 2b unit (~35 Ma).

During upper Eocene times (~35 to 33 Ma) the remaining subgroups of the Pallaresa allogroup (Montsor 2b and 3) were deposited within the Pobla Basin (Fig. 5.32c) (Mellere, 1993; Beamud et al., 2003; Beamud pers comm.). In the central and southern regions the units display an uninterrupted layer-cake stratigraphy. In the northern regions of the basin, both units are locally bound by intra- and inter-formational progressive unconformities, suggesting substratum rotation was again synchronous with continued sedimentation. Stratigraphic thinning of the units, associated with locally decreased aggradation, is very minor (cf. subgroup Montsor 2a), resulting in the reduction of the succession by <60 metres, and is restricted to the region of the northern onlap surface. The wavelength of this rotation is notably smaller than that documented in the Montsor 2a unit and, by inference, associated with a different control on the hangingwall uplift. This localised deformation may be linked to limited activity on smaller structures that splay from the MBT at shallower detachment levels. As noted previously, the lack of constraint on the subsurface fault geometries precludes a definitive analysis of the tectonic activity required to generate the localised rock uplift documented in the Pallaresa units. However, if it is assumed the dip of the minor structures are similar to that of the MBT, then an estimated ~35 m of horizontal shortening is sufficient to generate the required local rock uplift. In the western regions of the Pobla Basin, the Montsor 2b and 3 units also display significant southward tilting of the strata at the onlap surface, though notably without the formation of stratigraphic thinning or unconformities. This localised deformation must have occurred after deposition and likely indicates the lateral variability of the minor MBT-related structures that deform the blanketing conglomerates.

The sediments of the Senterada and Antist allogroups were deposited during post-Eocene times within both the upper Pobla Basin and in the Senterada Basin to the north (Mellere, 1993; Beamud et al., 2003). The omission of the Upper Senterada 1, and Senterada 2 and 3 subgroups from the Pobla Basin (Mellere, 1993) indicates sediment bypassing of the southern area must have occurred over extensive temporal intervals. This may be associated with the development of local relief in the area of the MBT, which caused deflection to the east or west at the southern end of the Senterada Basin. Chronographic constraints are only available for the lowermost units of the Senterada allogroup and indicate a Lower Oligocene depositional age (Beamud et al., 2003). If it is assumed that sediment aggradation was maintained at similar rates to the underlying allogroups, then to generate the maximum preserved thickness of the Senterada and Antist units would have required continued sedimentation until at least ~21 Ma. On the northern onlap region of the Pobla Basin, progressive intra- and inter-formational unconformities bound the Senterada allogroup. Stratigraphic reduction is similar to that observed in the underlying Pallaresa subgroups and is likely to be associated with small amounts of syn-depositional displacement along the minor MBT-related structures during Lower Oligocene times (Fig. 5.32d). Growth strata within the Senterada Basin are more difficult to identify owing to the relatively poor exposure. They may be inferred, however, by the progressive steepening of intra-formational surfaces within the Senterada 1 subgroup in the region of the southern onlap surface. Post-depositional tilting may have subsequently further steepened them toward the north. The orientation of the depositional surfaces and the inferred progressive unconformities are consistent with localised uplift and northward rotation of the structural footwall during displacement along the MBT, or related structures, during Lower Oligocene times. Time-equivalent Senterada 1 units from the onlap surfaces either side of the MBT show a marked asymmetry in their degree of rotation, with those in the Senterada Basin oriented at significantly steeper angles. This may suggest the southern flank of the Senterada Basin underwent more extensive deformation than the northern flank of the Pobla Basin during, or after, deposition of the Senterada 1 subgroup. This local variability in deformation may have been caused by different mechanical responses to MBT displacement in the footwall and hangingwall, which comprise gypsum-marl sequences and a competent limestone sequence, respectively. Alternatively, the additional deformation in the southern Senterada Basin may be linked to smaller blind thrust splays from the MBT that locally deformed the onlapping sediments. The central and northern regions of the Senterada Basin are characterised by a gentle southerly dip that is locally increased at the northern onlap surface of the youngest sediments (Fig. 5.32e). Intra-formational unconformities within this region are difficult to identify, but the undeformed nature of the immediately overlying units indicate deformation was syn-depositional. This localised tilting suggests southward rotation of the substratum occurred (section 5.3.2) and is unlikely to be linked to displacement along the MBT. As noted previously, these sediments are estimated to have a Middle Miocene depositional age (~21 Ma).

The entire Ermita to Antist allogroup succession within the Pobla Basin has been tilted gently toward the north (Fig. 5.32f). As north rotational growth strata are not observed within any of the sedimentary units, it must be assumed that tilting occurred at some point after deposition of the Antist allogroup. Analyses of the kinematic shear data within the MBT fault zone indicate it is unlikely that the structure was reactivated with normal fault displacement and hence accommodated regional northward tilting. Instead, tilting may have occurred in response to more regional scale sub-surface deformation (Muñoz, pers comm.).

In summary, clear insights into the structural evolution of the Morreres Zone can be achieved through careful consideration of the deformed Pobla de Segur conglomerates that blanket the region. A detailed reconstruction of the tectonic history of the area is achievable through high-resolution mapping of the Mesozoic basement and integration with sub-surface data and tight chronographic constraints, though this is beyond the scope of this study. Instead, broad constraints on the approximate values of overall horizontal tectonic shortening are estimated throughout the depositional history of the conglomerates during Upper Eocene to Lower Miocene times. From this, the following history can me summarised; The MBT had achieved the vast majority of its overall tectonic activity prior to deposition of the Ermita allogroup at ~42 Ma. This period of considerable fault displacement and intense deformation resulted in the generation of at least 1 km of local topographic relief and represented the main period of horizontal shortening. After a prolonged period of tectonic stability, the structure was reactivated causing the rotation of the Monstor 2a unit in Upper Eocene times. After ~35 Ma tectonic activity along the MBT continued, but deformation was localised in the northern region and probably associated with minor linked structures at shallower structural levels. During the depositional history of the Pobla de Segur sediments, horizontal shortening of the order of <200 metres was sufficient to generate the deformation preserved in the overlying sediments. The deposition of the Antist allogroup likely marks the onset of the post-tectonic period of the MBT. Deformation at the north of the Senterada Basin likely occurred during, or after, middle Miocene times (~21 Ma) and acted to rotate the onlapping sediments toward the south (see Chapter 6 for further discussion).

5.5 The Ebro Basin and Offshore Zone – Geological review

The focus of this section is to review the published data on the sedimentological record of the Ebro Foreland Basin, located to the south of the Pyrenean chain, and the offshore region, including the Valencia Trough. The primary objective of this is to provide additional constraints on the Pyrenean erosion history by assessing the detrital flux from the evolving orogen.

The Ebro foreland Basin, to the south of the mountain belt, formed by flexural subsidence in response to crustal loading primarily associated with the growth of the Pyrenees, but also due to the development of the Catalan Coastal Range and Iberian Range, to the southeast and southwest, respectively (Riba et al., 1983; Zoetemeijer et al., 1990; Puigdefabregas et al., 1992). The early stratigraphic history of the basin was dominated by the accumulation of deep-water turbidites during late Cretaceous times followed by a Palaeocene transition into continental alluvial and fluvial red beds in the north, with deep-water carbonates toward the west (Puigdefábregas et al., 1992). During late Eocene times the western seaward connection of the basin was closed through Pyrenean and Iberian Range tectonism (Riba et al., 1983). This marked the onset of a period of endorheic (internal) drainage for all fluvial catchments draining into the basin from the adjacent Pyrenean, Iberian and Catalan Coastal Range topographic barriers. During this time deltaic, fluvial and alluvial sediments progressively infilled the basin and onlapped across the topographic relief of the south Pyrenean fold and thrust belt and across the southern flank of the Pyrenees (Coney et al., 1996). Evidence for this period of regional sediment blanketing has been documented at a number of localities surrounding the Ebro region: The preserved high-elevation palaeovalleys of the Sierra de Sis and Sierra de Gurp (section 5.4), demonstrate that during Upper Eocene and Oligocene times the sediment dispersal systems that transported clastic detritus from the eroding mountain belt were progressively choked and back-filled (Vincent, 2001); Over 20 km to the south, on the high relief topographic ridge of the Montsec Range, karst caverns at ~1500 m elevation contain conglomerate cobbles of Axial Zone provenance (Carreras, 1965, 1967); In the northern Catalan Coastal Ranges, Late Oligocene age conglomerates unconformably overlie Hercynian basement (Anadón et al., 1989a); Within the southern Catalan Coastal Ranges, conglomerates are found capping pre-Tertiary cover rocks of high topographic relief, kilometres behind the orogenic thrust front (Colombo, 1980; Columbo and Vergés, 1992; Muñoz et al., 1997); In the south-eastern Iberian Range, the thin-skinned, frontal thrusts are buried and back filled by Oligocene age conglomerates (González et al., 1997; Muñoz et al., 1997); Within the central Ebro Basin, at least 3 km of Upper Eocene to Lower Miocene alluvial-fluvial channel and floodplain sandstones, shales and playa-lake deposits are preserved, which are the distal equivalents to the conglomeratic deposits mapped at the peripheral margins of the basin (Riba et al., 1983; Nichols, 1987).

Sedimentation in the central Ebro Basin continued up to at least ~14 Ma, as documented by the presence of magnetostratigraphically-dated lacustrine and alluvial sediments in the geographic centre of the basin (Pérez-Rivarés et al., 2002). Present-day exposures of these sediments are preserved undeformed on isolated hilltops, at up to ~800 m elevation, and are bound by steep valleys and canyons that have been deeply incised by the fluvial systems of the Ebro river and its tributaries.

The offshore Tertiary sedimentary record within the Gulf of València Basin (**Fig. 5.33**) can be subdivided into the Palaeogene 'Red Complex' and a Neogene sequence of marine facies (Martínez del Olmo, 1996). The 'Red Complex' comprises lacustrine and fluvial parasequences and continental molasse that formed from exposed and eroding basement fault block highs during compressional phases of the Catalan Coastal Range (Martínez del Olmo, 1996). The unit is capped by an erosional unconformity, upon which the marine Neogene facies is deposited. The Lower and Middle Miocene age (pre-Serravillian) deposits (Alcanar Group) are restricted to structurally-defined depocentres within Mesozoic half-graben (Ziegler, 1988; Martínez del Olmo, 1996) and are dominated by limestone and marl sequences and locally derived breccio-conglomerates (Anadón et al., 1989b; Roca and Desegaulx, 1992; Meléndez-Hevia and Alvarez de Buergo, 1996). In contrast, the Middle and Upper Miocene age (Serravallian and Tortonian) deposits (Castellón Group) are characterised by thick units of terrigenous sediments deposited in basinward (southeast) prograding clastic sequences (Johns et al., 1989; Roca and Desegaulx, 1992; Martínez del Olmo, 1996; Meléndez-Hevia and Alvarez de Buergo, 1996; Roca, 2001; Evans and Archie, 2002). Major intra-mid Miocene downlap surfaces within the succession (Ziegler, 1988; Johns et al., 1989) record the dramatic influx of large volumes of siliciclastic detritus that cover and homogenise the pre-existing Neogene basin topography (Anadón et al., 1989b; Roca and Desegaulx, 1992). Sedimentation rates increased progressively through the Serravallian and Tortonian until the onset of the Messinian Salinity Crisis (Dañobeitia et al., 1990), whereupon the unit is capped within the margins of the València Trough by an erosional unconformity and the deposition of evaporitic sequences in the deeper sections of the basin (Mulder, 1973; Roca and Desegaulx, 1992).

5.5.1 The Ebro Basin and Offshore Zone - Discussion

The timing and mechanism by which the Ebro Basin was reopened to a seaward connection, hence, redirecting the internally-drained fluvial systems to a new basin outlet, are poorly constrained. Upon reconnection, through whatever mechanism, the regional fluvial base level must have undergone a considerable drop in elevation and thus promoted the incision and seaward transport of the continental sediments infilling the Ebro Basin. A minimum value for this fall in base level is approximately 800 m, given by the vertical difference between the youngest preserved lacustrine deposits in the basin and the Mediterranean sea level.

A number of workers have linked basin opening to sediment overfilling and eventual lake capture, or piracy, by streams that drained into the Mediterranean Sea during Miocene times (Riba et al., 1983; Serrat, 1992). It is also postulated that the combination of Miocene rifting offshore of the Catalan Coastal Range and the drop in sea level associated with the Messinian Salinity Crisis at 5.97 Ma (Krijsman et al., 1999) may have triggered the drainage capture event (Dañobeitia et al., 1990; Coney et al., 1996). However, the role of the Messinian in initiating or contributing to basin capture is contentious. Recent studies of the geomorphic maturity of the Ebro drainage network, in comparison to the propagation of regressive fluvial incision in similar geological settings, has been used to suggest the area is unlikely to have been reconnected to the Mediterranean until significantly later than the Messinian event (Loget et al., 2004). Conversely, the presence of large-scale siliciclastic progradations into the Valencia Trough and increases in Ebro continental margin sedimentation rates from as early as the Middle Miocene (section 5.5) have been interpreted to support a Pre-Messinian age of basin capture (Evans and Archie, 2002). This notion is supported by 3D numerical simulations of the region which suggest the Messinian event was too short a duration for the base-level pulse to impose a first order impact on the timing of Ebro Basin opening (Garcia-Castellanos et al., 2003). These model predictions require a drainage opening between 13 and 8.5 Ma to enable the sedimentary infill of the Ebro Basin to be reworked by fluvial systems (Garcia-Castellanos et al., 2003) (see Chapter 6 for further discussion).

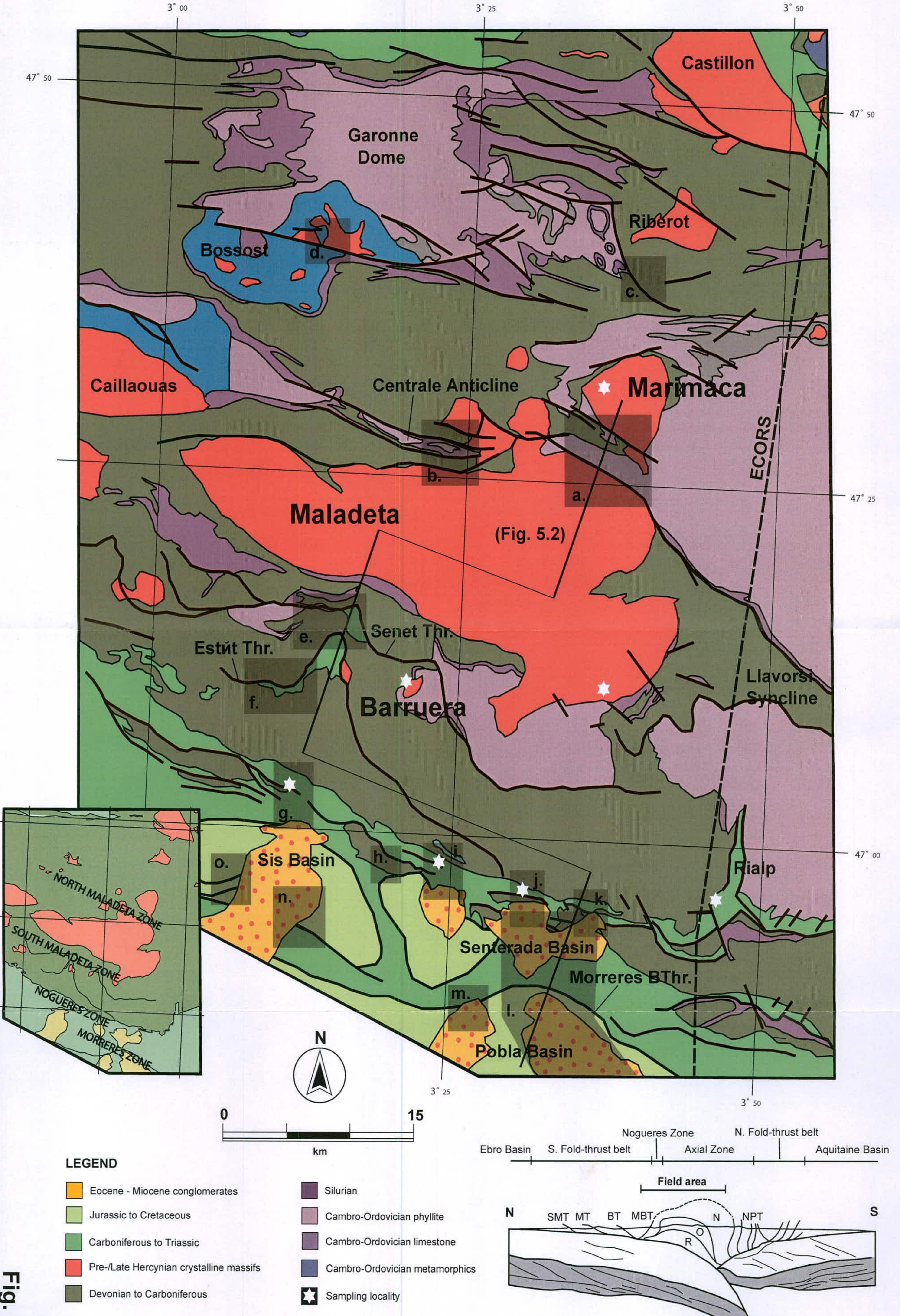

Fig. 5.1
Geological map/Location map of the south central Pyrenees

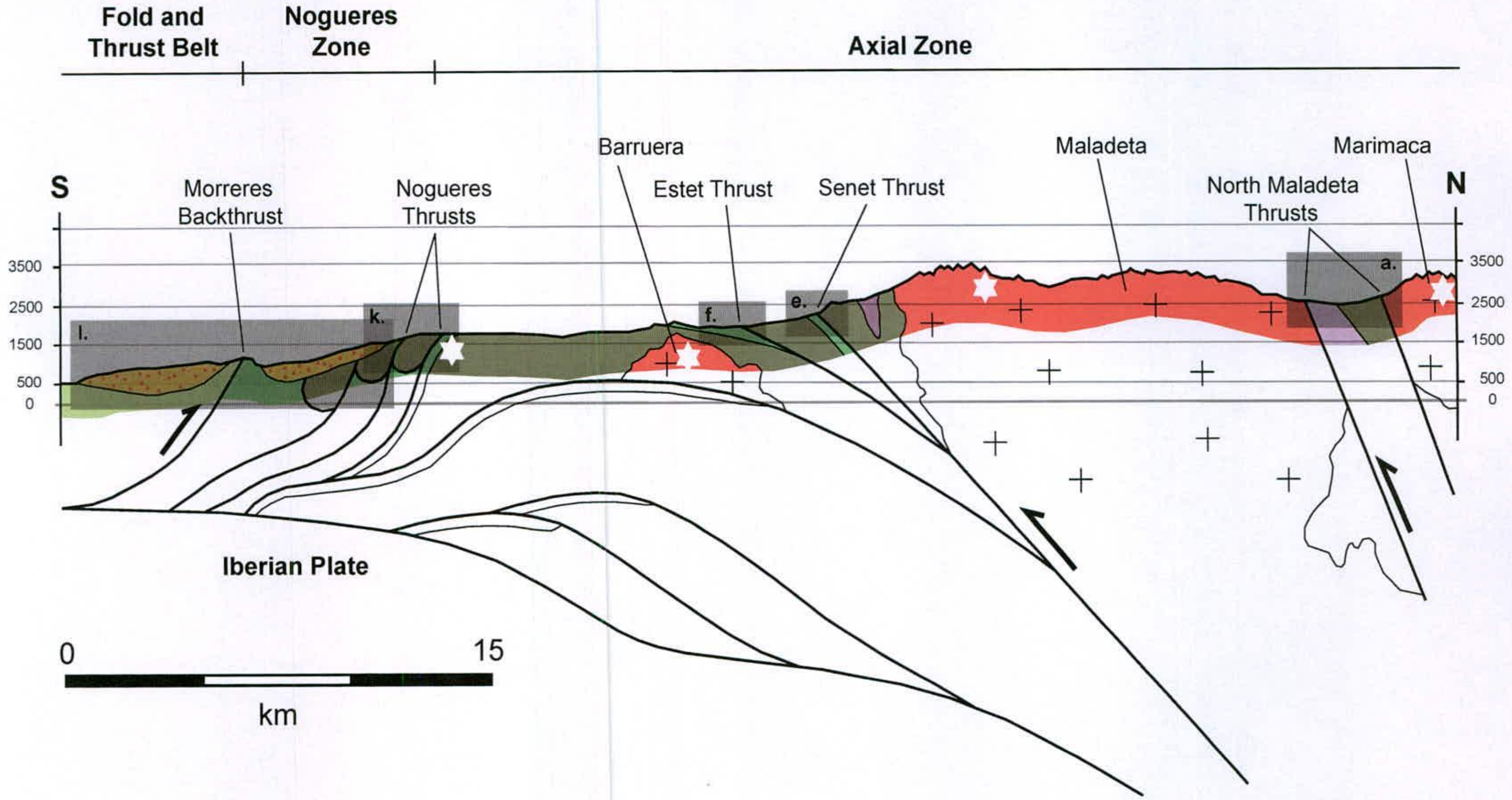

Figure 5.2 Geological cross-section of the south central Pyrenees (line of three compiled sections located in Fig. 5.1). Surface geology is constrained through field studies, presented in sections 5.1 to 5.4, and subsurface structural geometries collated from previous studies, though based upon the interpreted seismic section of the ECORS profile (Choukroune et al., 1989; Mucoz et al., 1992; Puigdefabregas et al., 1992). Specific field study areas located by shaded boxes, field areas denoted 'a-o' discussed and referred to in subsequent sections. Thermochronological sampling sites located by white star.

Fig. 5.2

Geological cross-section of the south central Pyrenees

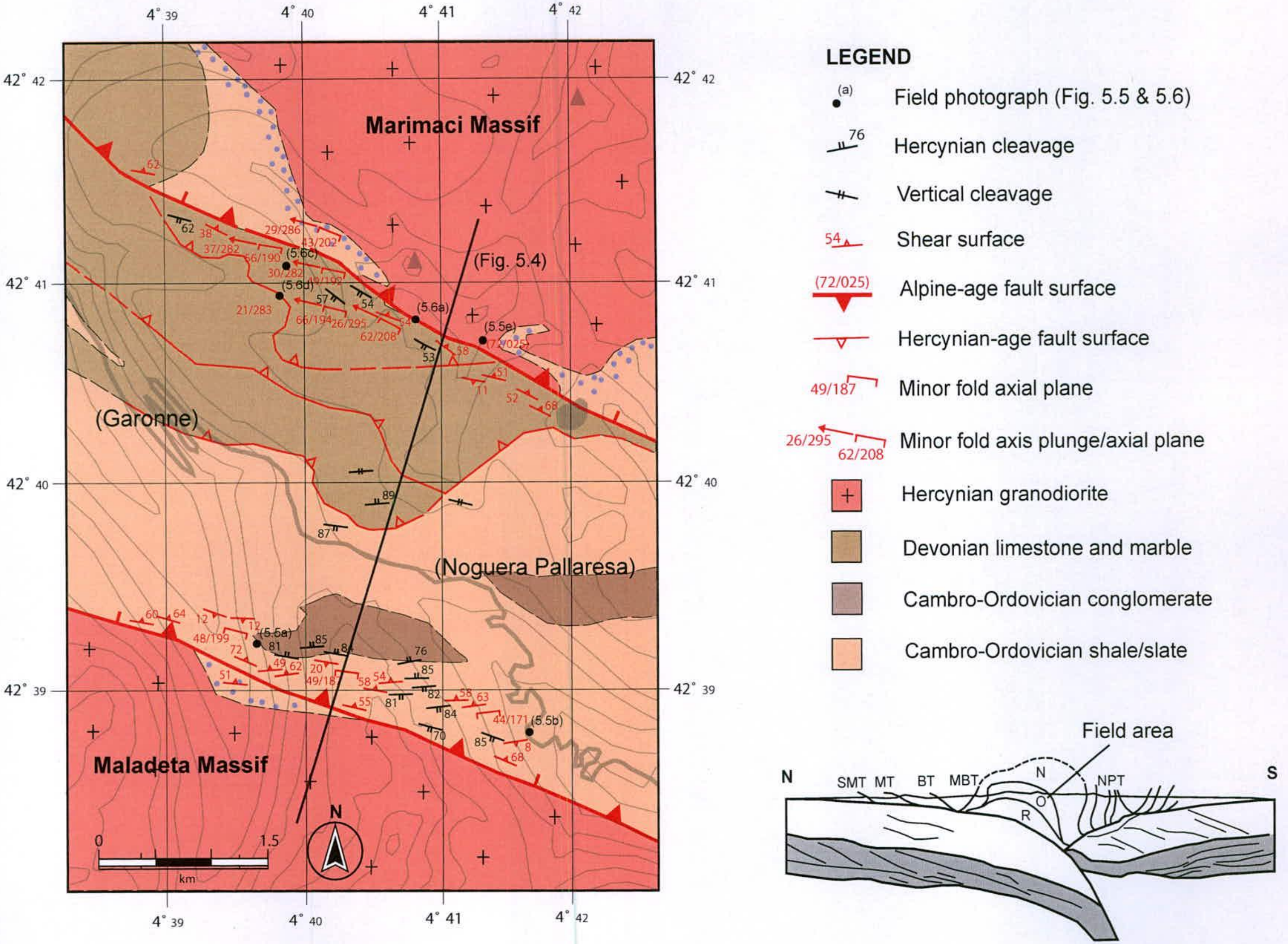

Fig. 5.3

Geological map of the North Maladeta Zone (area a)

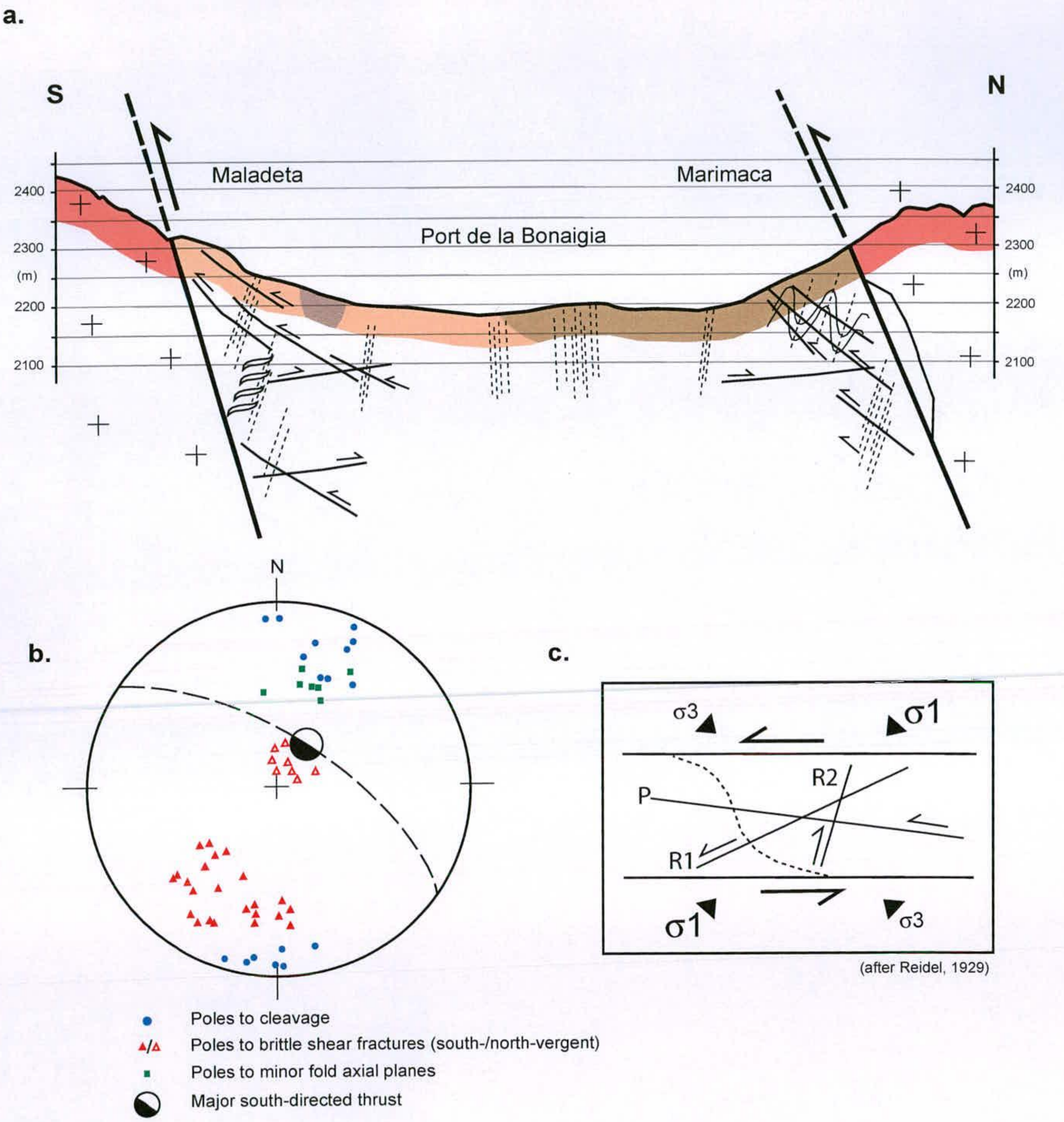

(after Reidel, 1929)

Figure 5.4 (a) Summary schematic cross-section of the North Maladeta Zone (approximate line of section located in Fig. 5.3). The large-scale, massif-bounding faults and the orientation of the structural features from the latest period of deformation are shown. (b) Stereoplot depicting poles to cleavage, poles to brittle shear fractures, and poles to minor fold axial planes with respect to the major, south-vergent thrust surfaces. (c) Summary diagram depicting the orientation of secondary shear features (Reidel shears) within and around a large scale shear zone; R1=Reidel 1 shears, R2=Reidel 2 shears (antithetic), P=P shears, dotted line=shear zone foliation.

Fig. 5.4

Summary cross-section of the North Maladeta Zone

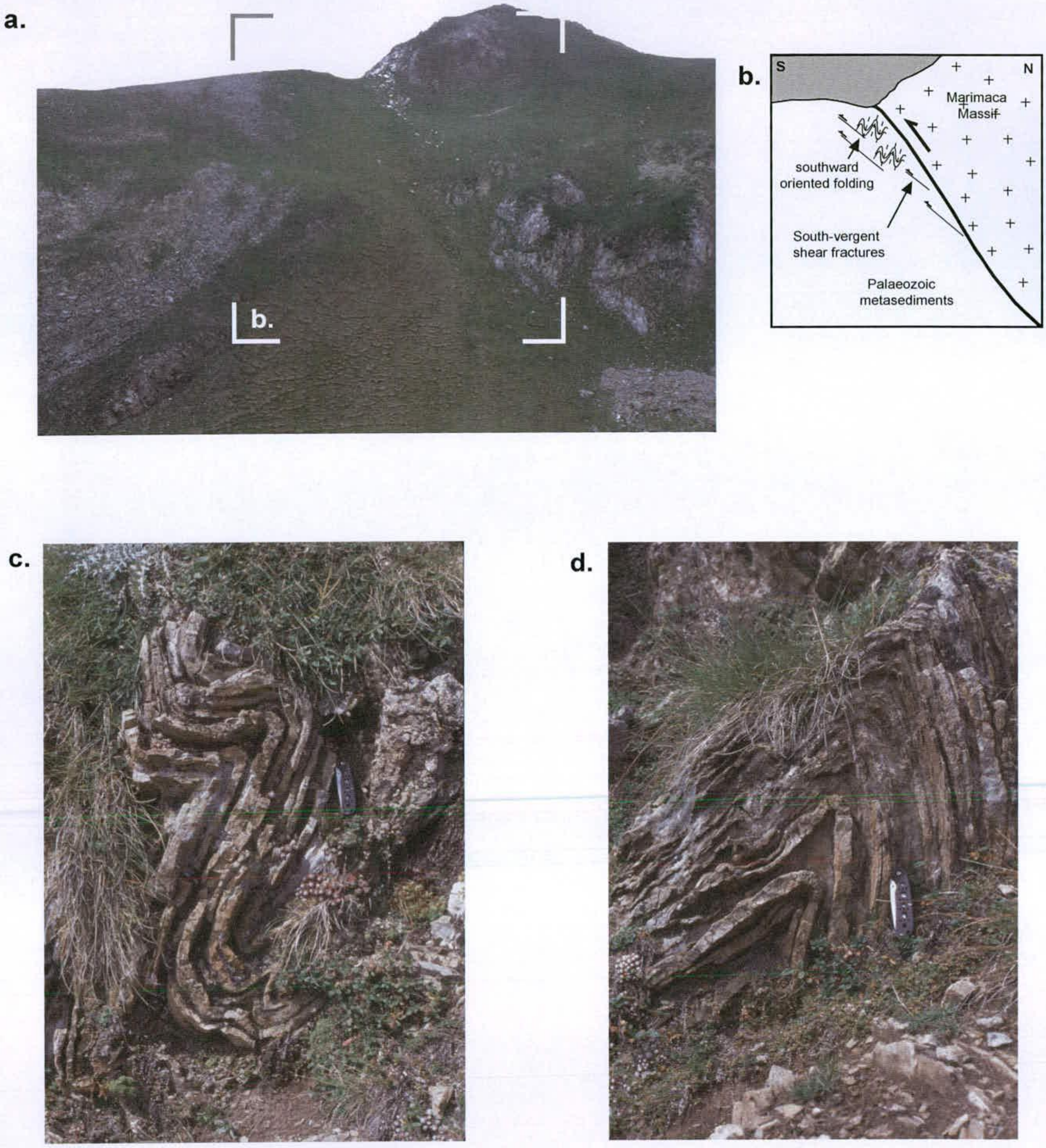

Figure 5.5 Field photographs of the geological features of the North Maladeta Zone (photographs located in Fig. 5.3). (a) View facing northwest toward the overthrust tectonic contact at the south of the Marimaca Massif (see sketch (b) for interpreted view) (field of view approximately 300 m left to right). (c & d) South-dipping axial surfaces in south-vergent folds within the palaeozoic metasediments immediately south of the Maladeta Massif (penknife for scale).

Fig. 5.5

Geological features of the North Maladeta Zone (area a)

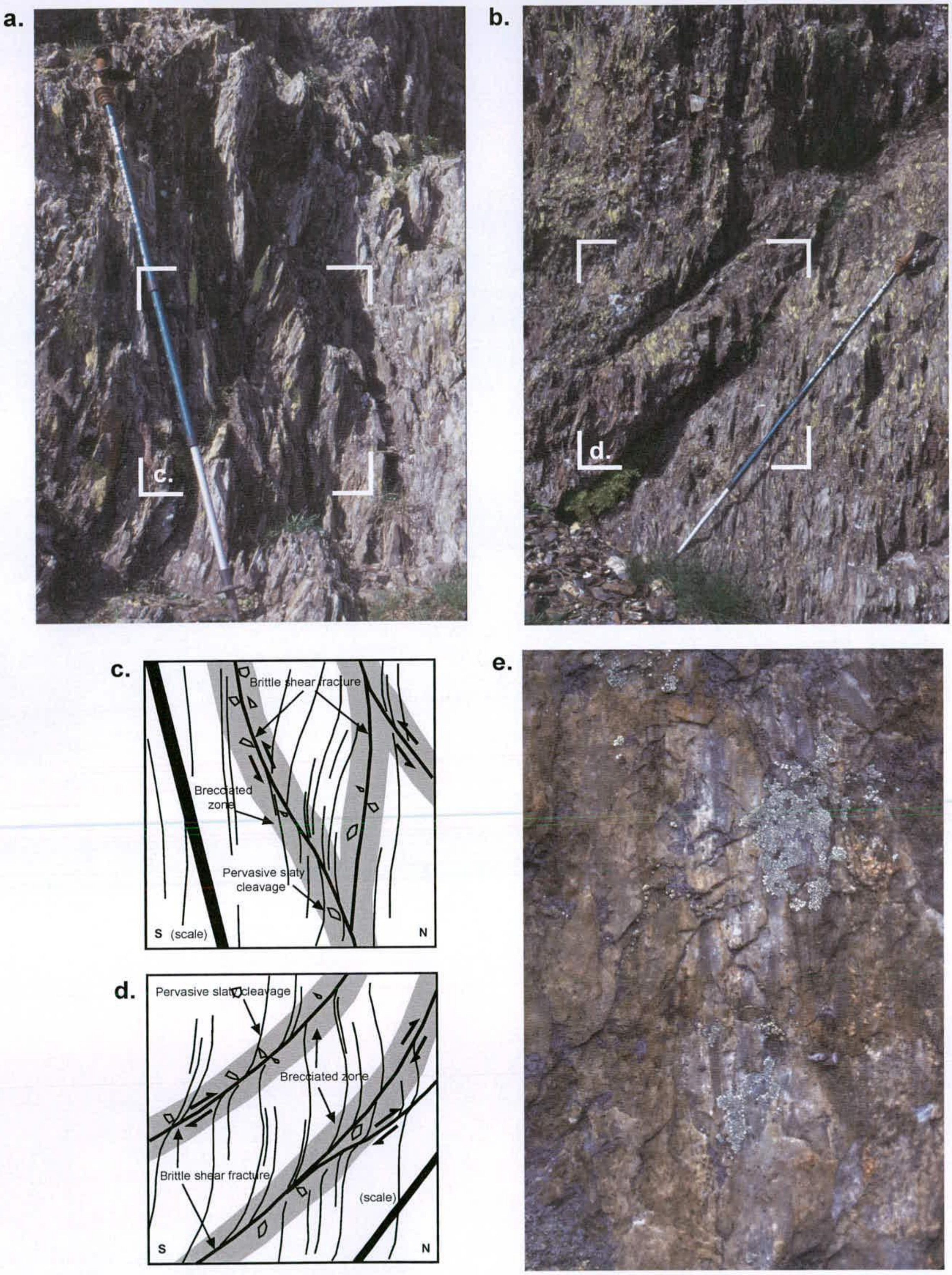

Figure 5.6 Field photographs of the geological features of the North Maladeta Zone (photographs located in Fig. 5.3). (a) South-vergent brittle shear fracture dipping steeply to the north offsets the pervasive regional cleavage and causes fine brecciation along the shear surface (see sketch (c) for detail). (b) North-vergent brittle shear fracture dipping gently to the south, with associated deformation as above (see sketch (d) for detail). (e) Stepped and grooved surface of sub-vertical fault plane immediately adjacent to the major fault bounding the Marimaca Massif, indicating northern block upthrow (field of view approximately 60 cm left to right).

Fig. 5.6

Geological features of the North Maladeta Zone (area a)

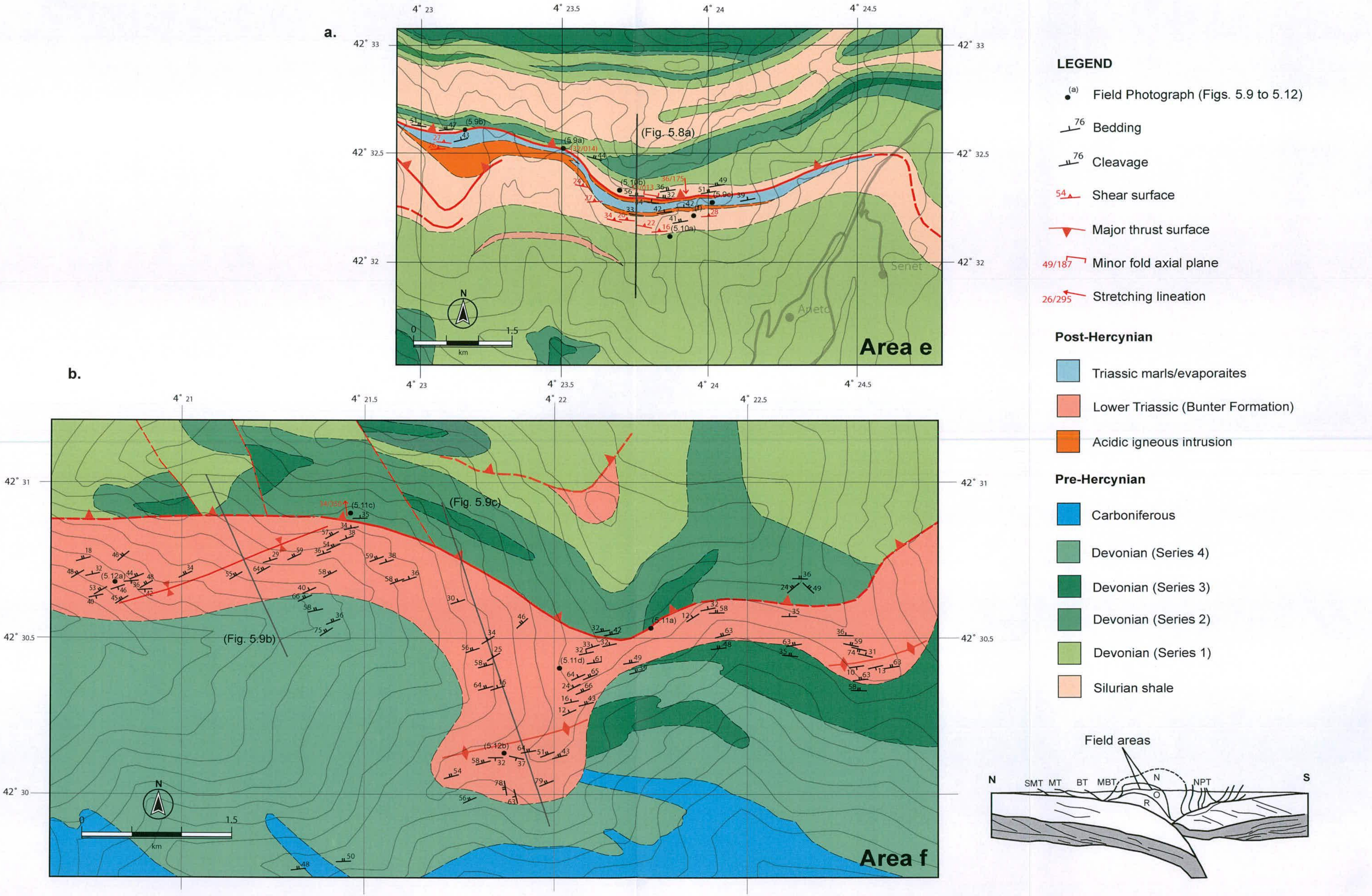

Fig. 5.7

Geological maps of the South Central Zone (areas e & f)

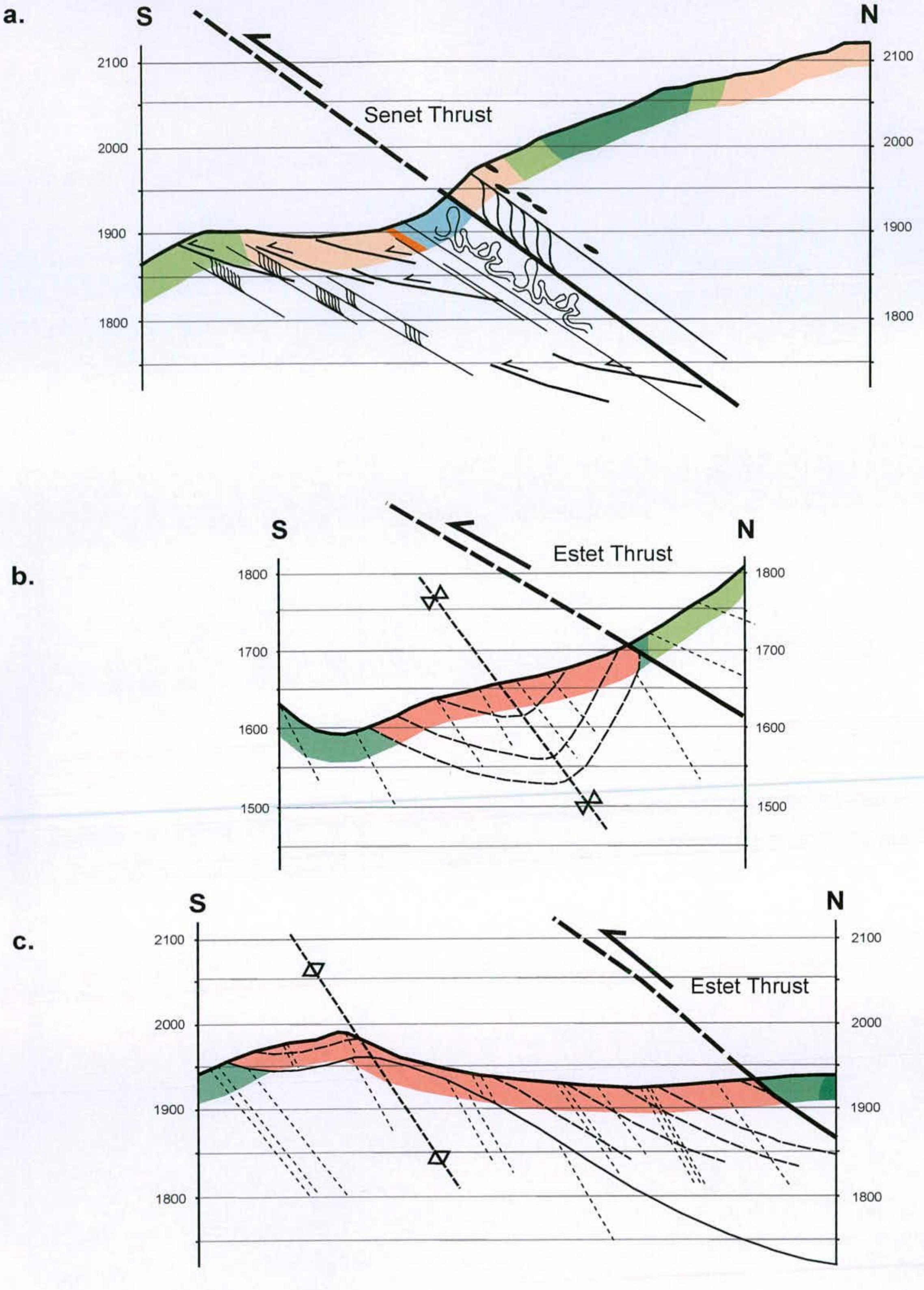

Figure 5.8 (a) Summary cross-section of the South Maladeta Zone (area e) (line of section located on Fig, 5.7a). The orientation of the major deformation structures around the Senet Thrust are schematically represented. (b & c) Cross-sections of the South Maladeta Zone (area f) (line of section located on Fig. 5.7b).

Fig. 5.8

Summary cross-section of the South Maladeta Zone (areas e & f)

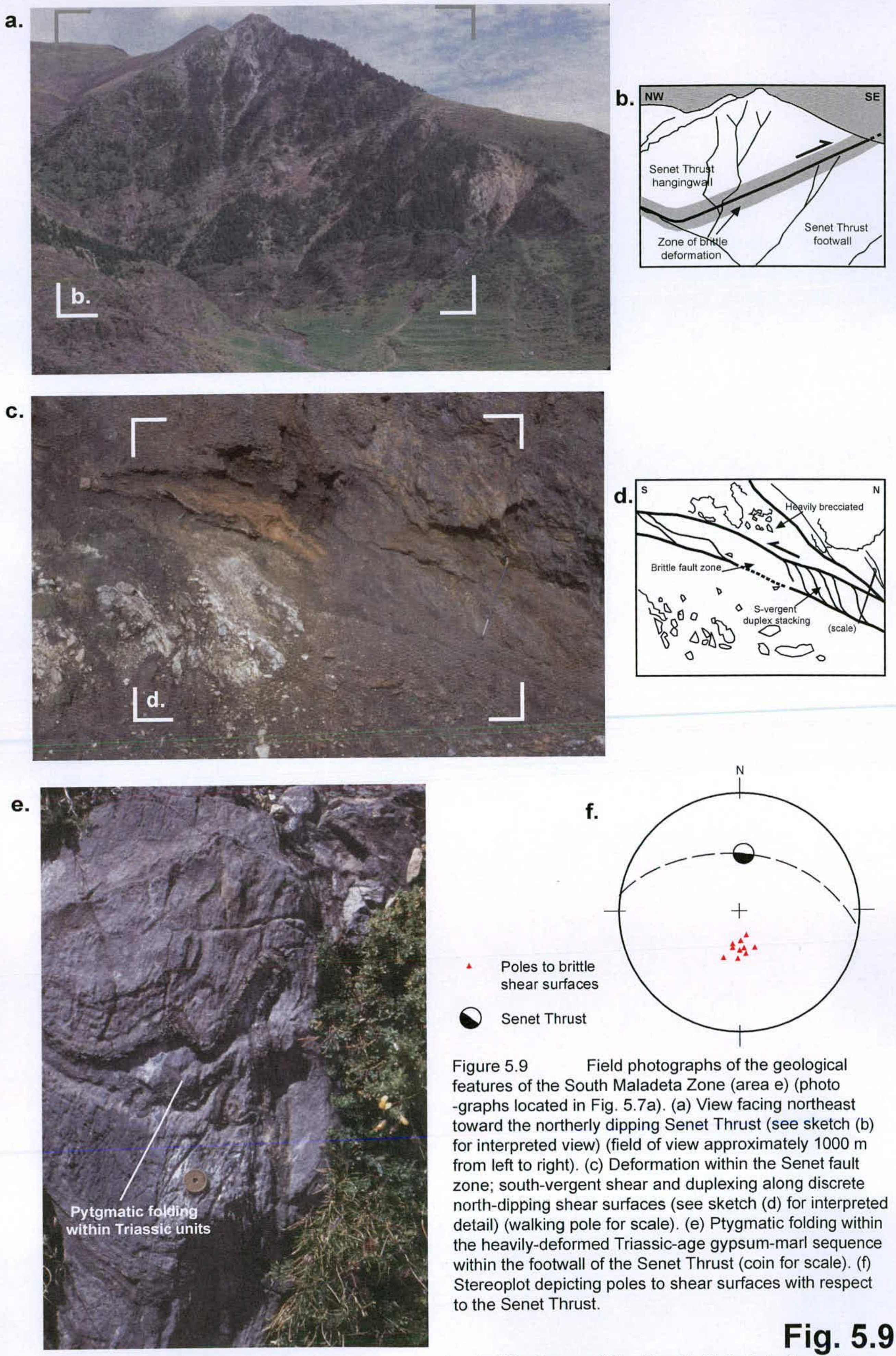

Figure 5.9 Field photographs of the geological features of the South Maladeta Zone (area e) (photographs located in Fig. 5.7a). (a) View facing northeast toward the northerly dipping Senet Thrust (see sketch (b) for interpreted view) (field of view approximately 1000 m from left to right). (c) Deformation within the Senet fault zone; south-vergent shear and duplexing along discrete north-dipping shear surfaces (see sketch (d) for interpreted detail) (walking pole for scale). (e) Ptygmatic folding within the heavily-deformed Triassic-age gypsum-marl sequence within the footwall of the Senet Thrust (coin for scale). (f) Stereoplot depicting poles to shear surfaces with respect to the Senet Thrust.

Fig. 5.9

Geological features of the South Maladeta Zone (area e)

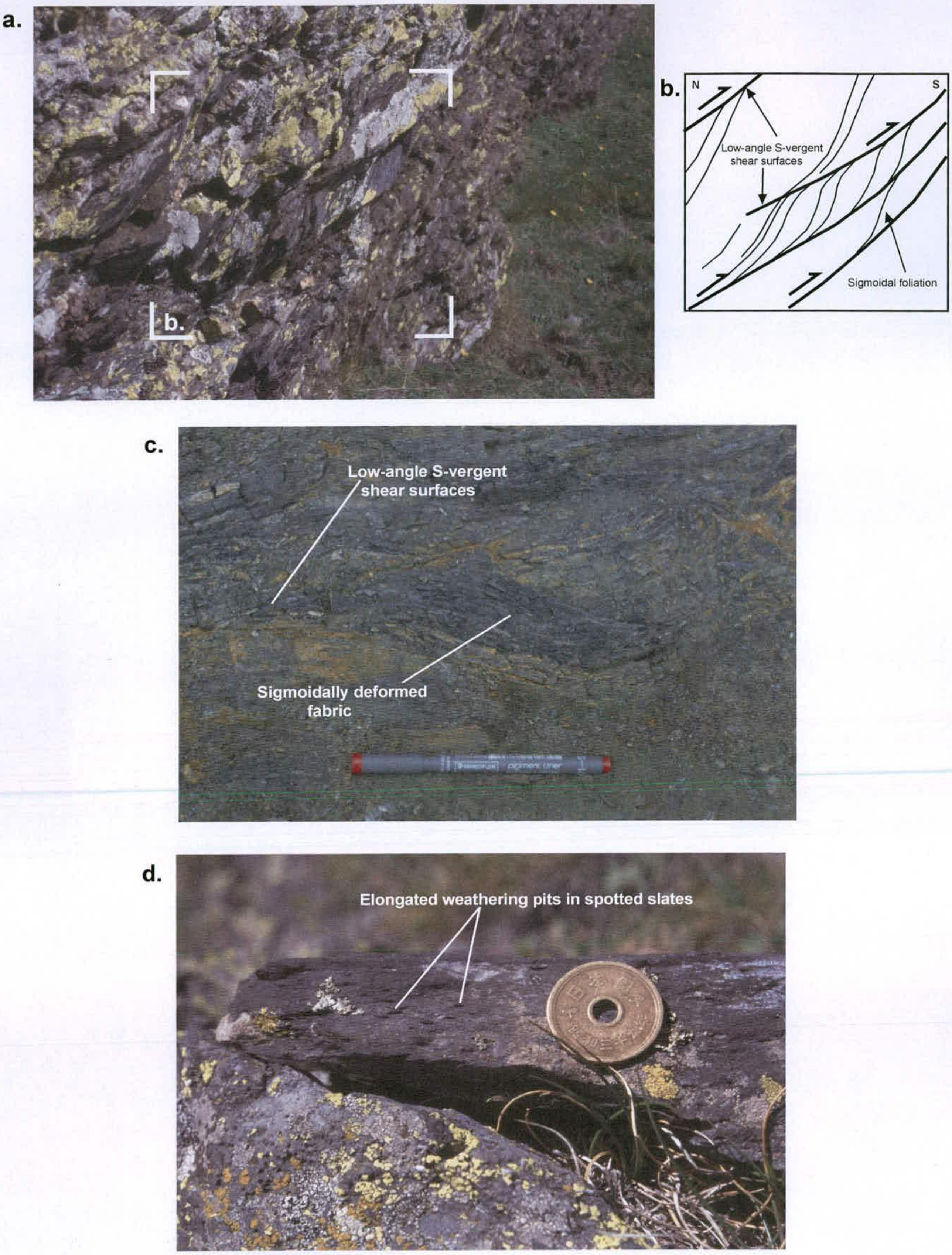

Figure 5.10 Field photographs of the South Maladeta Zone (photographs located within Fig. 5.7a). (a) Brittle-ductile deformation of the regional pervasive fabric into sigmoidal (C-S-type) morphologies by south-vergent, low-angle shear surfaces (see sketch (b) for detail) (field of view approximately 1 m left to right). (c) As above (pen for scale). (d) North-south elongation of metamorphic minerals close to Senet fault zone, which have been subsequently weathered out (coin for scale).

Fig. 5.10

Geological features of the South Maladeta Zone (area e)

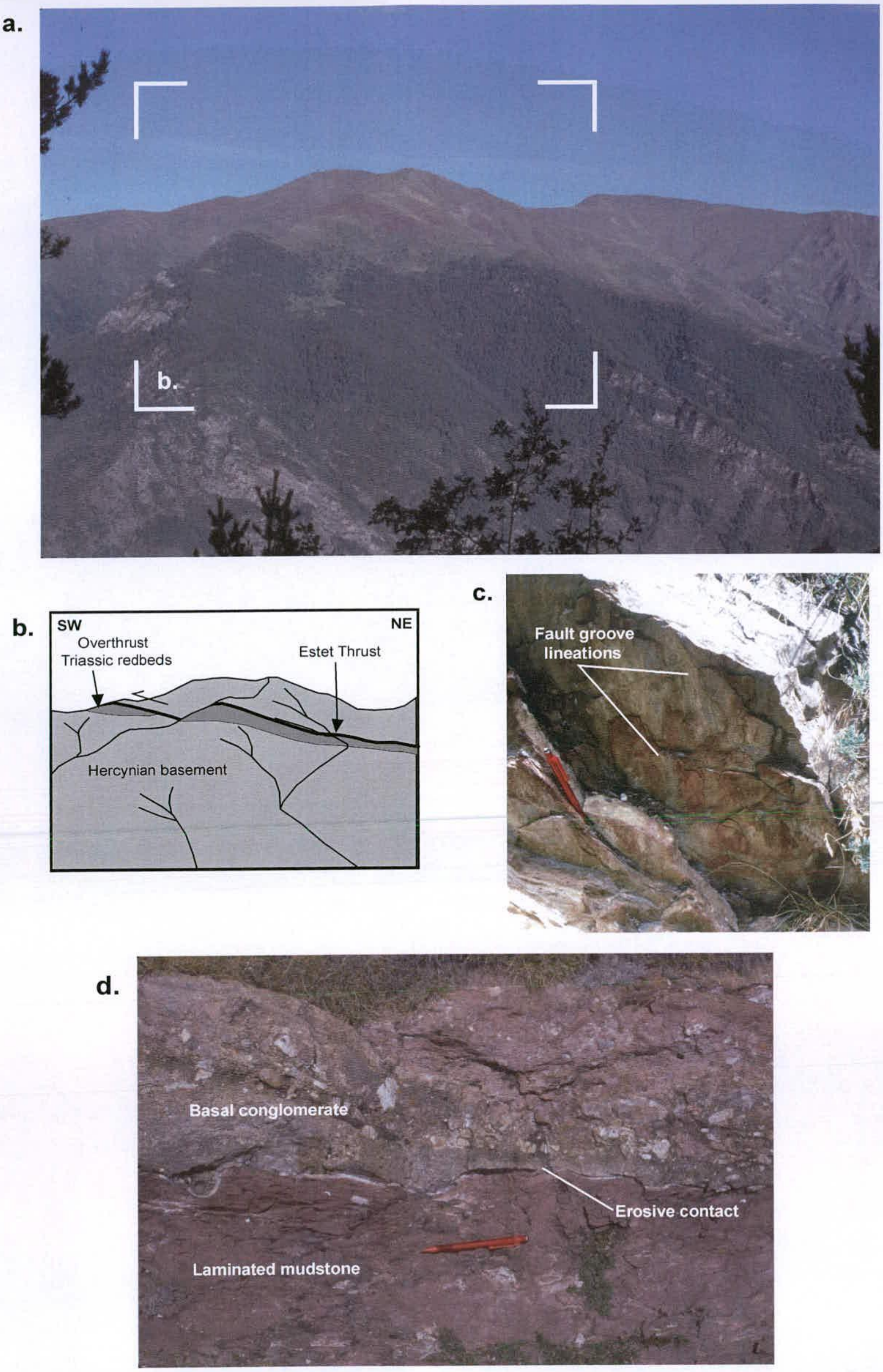

Figure 5.11 Geological features of the South Maladeta Zone (area f) (photographs located in Fig. 5.7b). (a) View facing north-west toward the north-dipping Estet Thrust, with the overthrust Triassic redbeds clearly visible (see sketch (b) for detail) (field of view approximately 4 to 5 km along the horizon). (c) Fault groove lineations along minor fault surface in the Estet fault zone (pen for scale). (d) Erosive contact depicting the northward younging direction of the footwall cover rocks (pen for scale).

Fig. 5.11

Geological features of the South Maladeta Zone (area f)

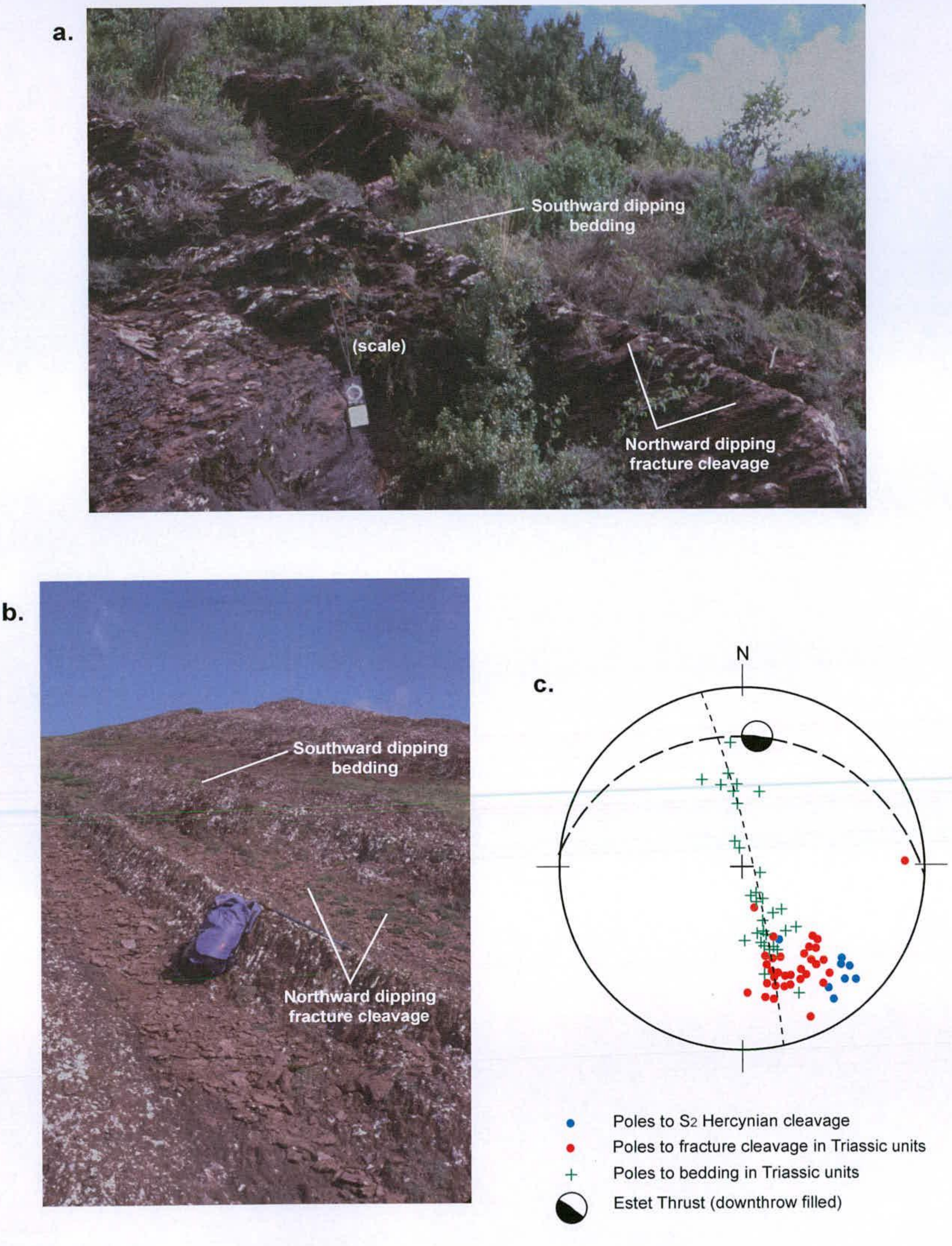

Figure 5.12 Field photographs of the geological features of the South Maladeta Zone (area f) (photographs located in Fig. 5.7b). (a) The well-developed, north-dipping fracture cleavage intersecting at a high angle with the south-dipping bedding on the northern limb of the syncline (clinometer for scale). (b) The same cleavage-bedding relationship observed on the southern limb of the anticline (bag for scale). (c) Stereoplot depicting the poles to the fracture cleavage in the Triassic units, poles to the S2 cleavage in the basement, and poles to the Triassic bedding (dotted line depicts pole-to-bedding girdle, dashed line depicts approximate orientation of Estet Thrust).

Fig. 5.12

Geological features of the South Maladeta Zone (area f)

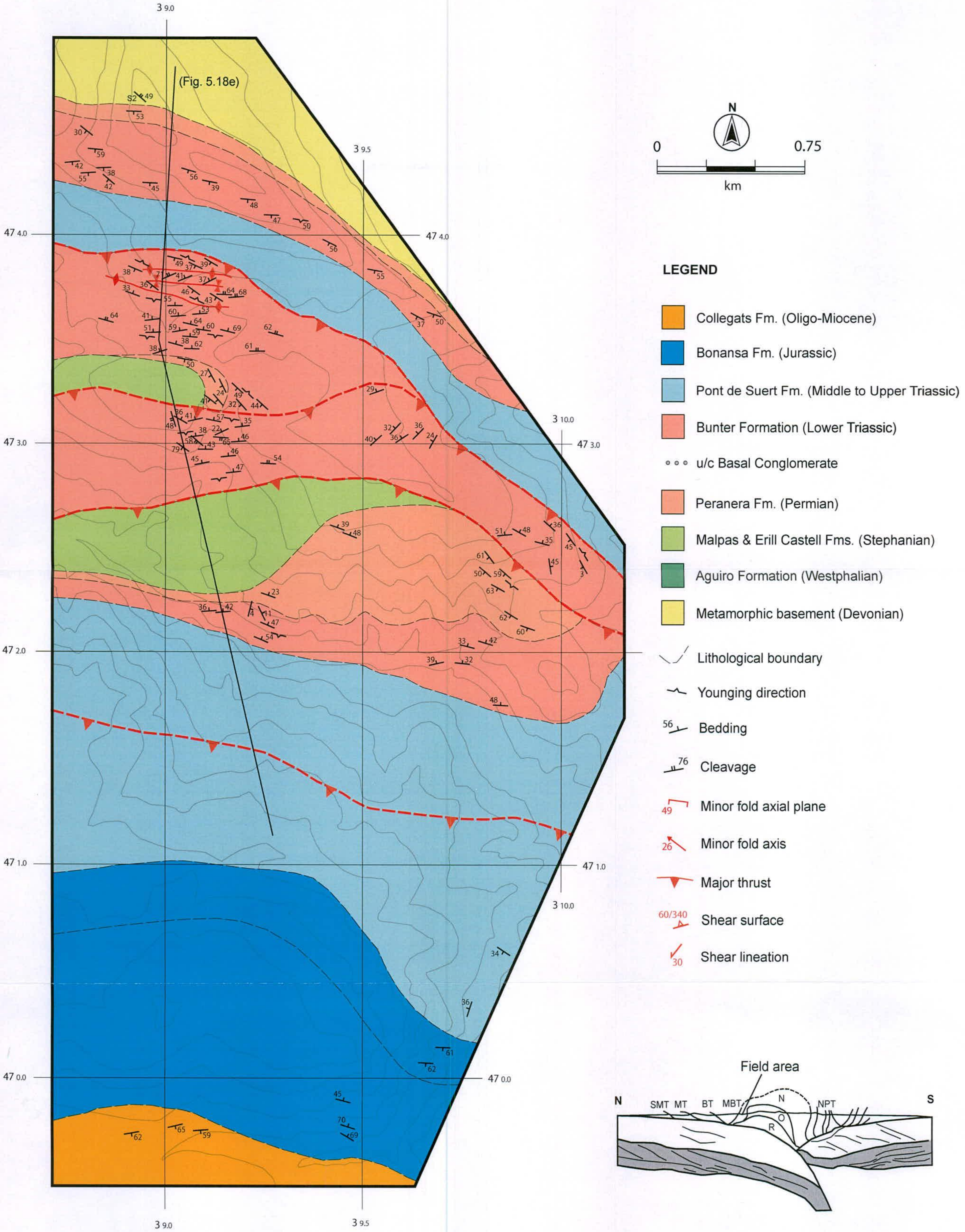

Fig. 5.13
Geological map of the Nogueres Zone (area g)

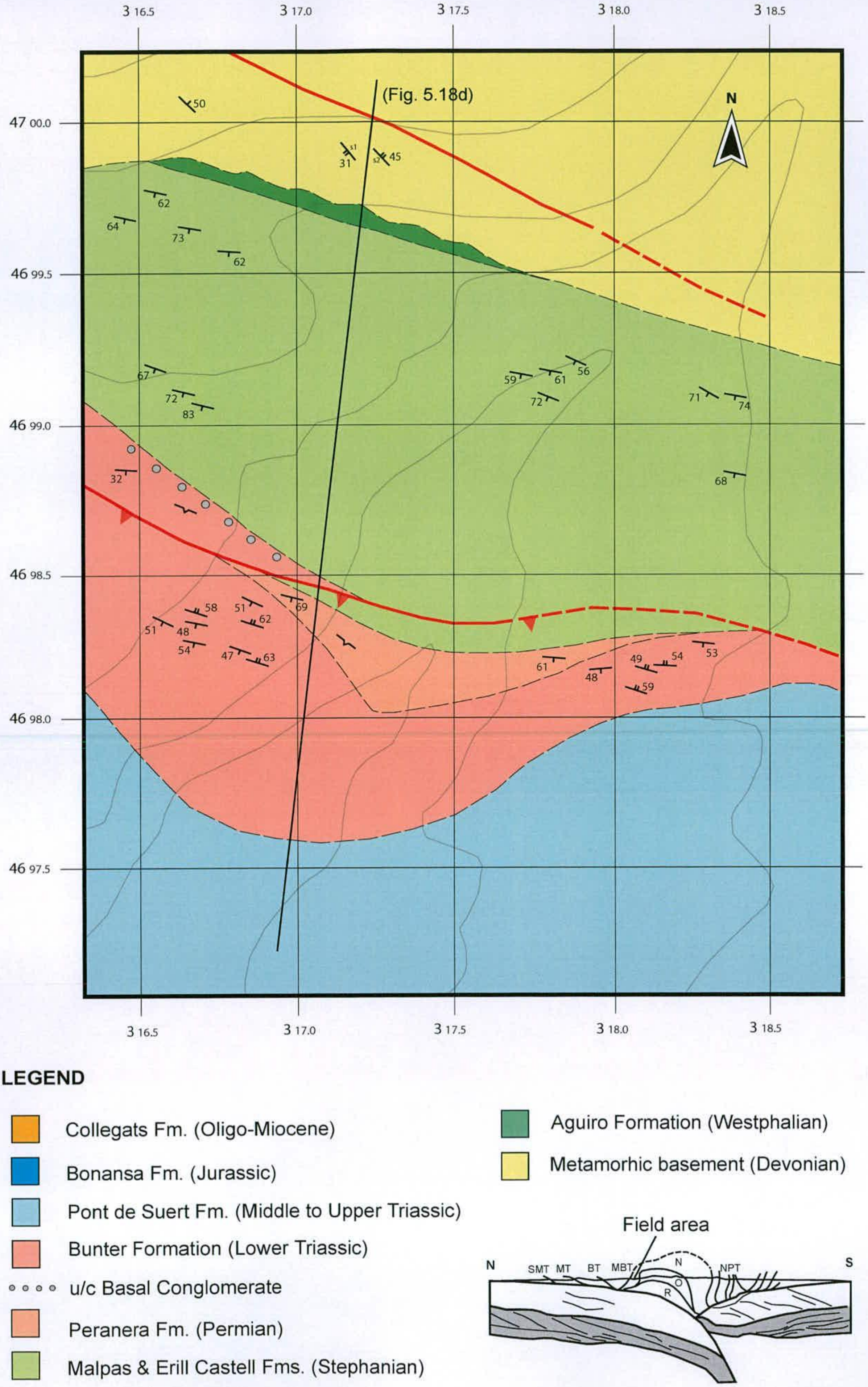

Fig. 5.14

Geological map of the Nogueres Zone (area h)

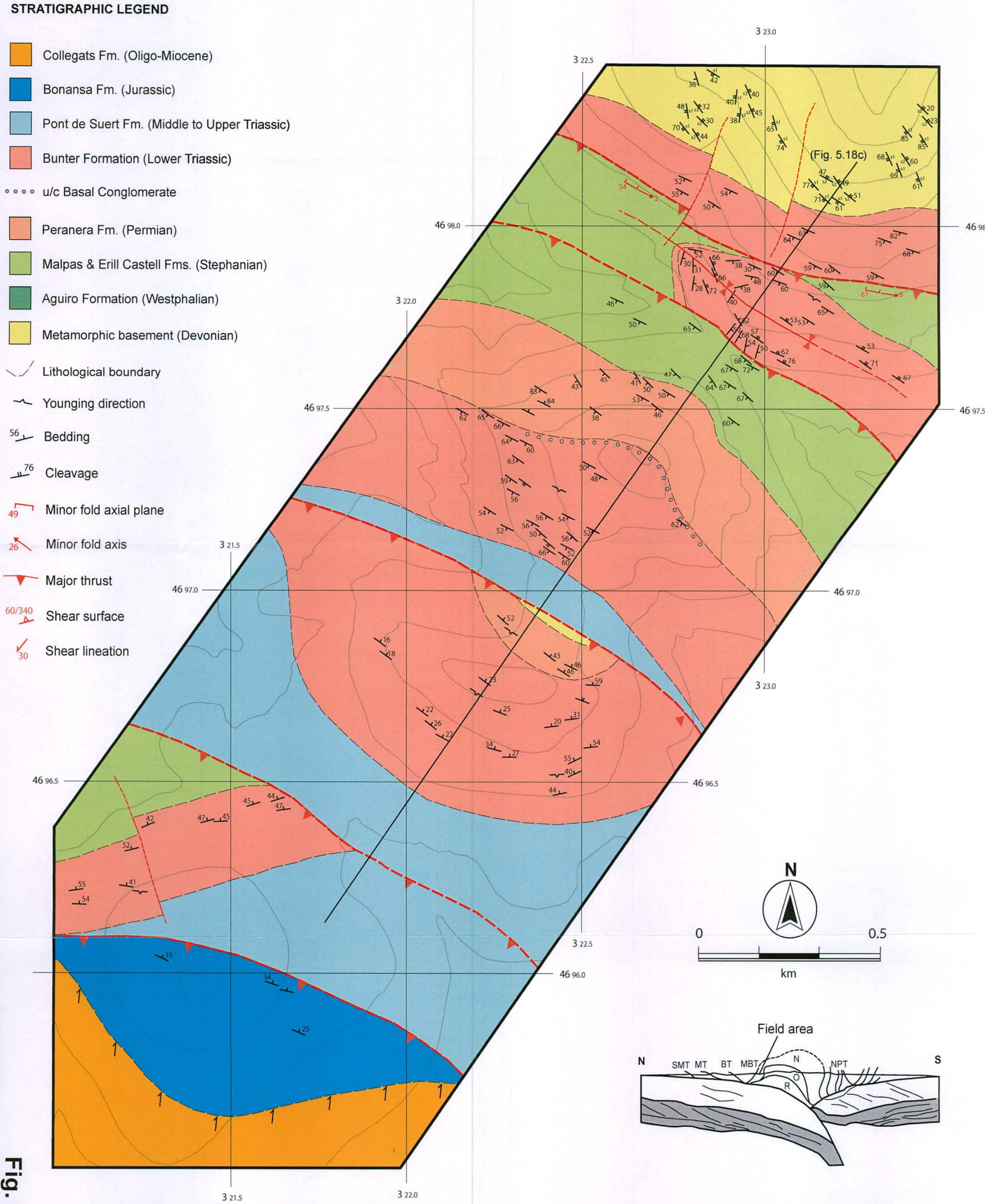

Fig. 5.15
Geological map of the Nogueres Zone (area g)

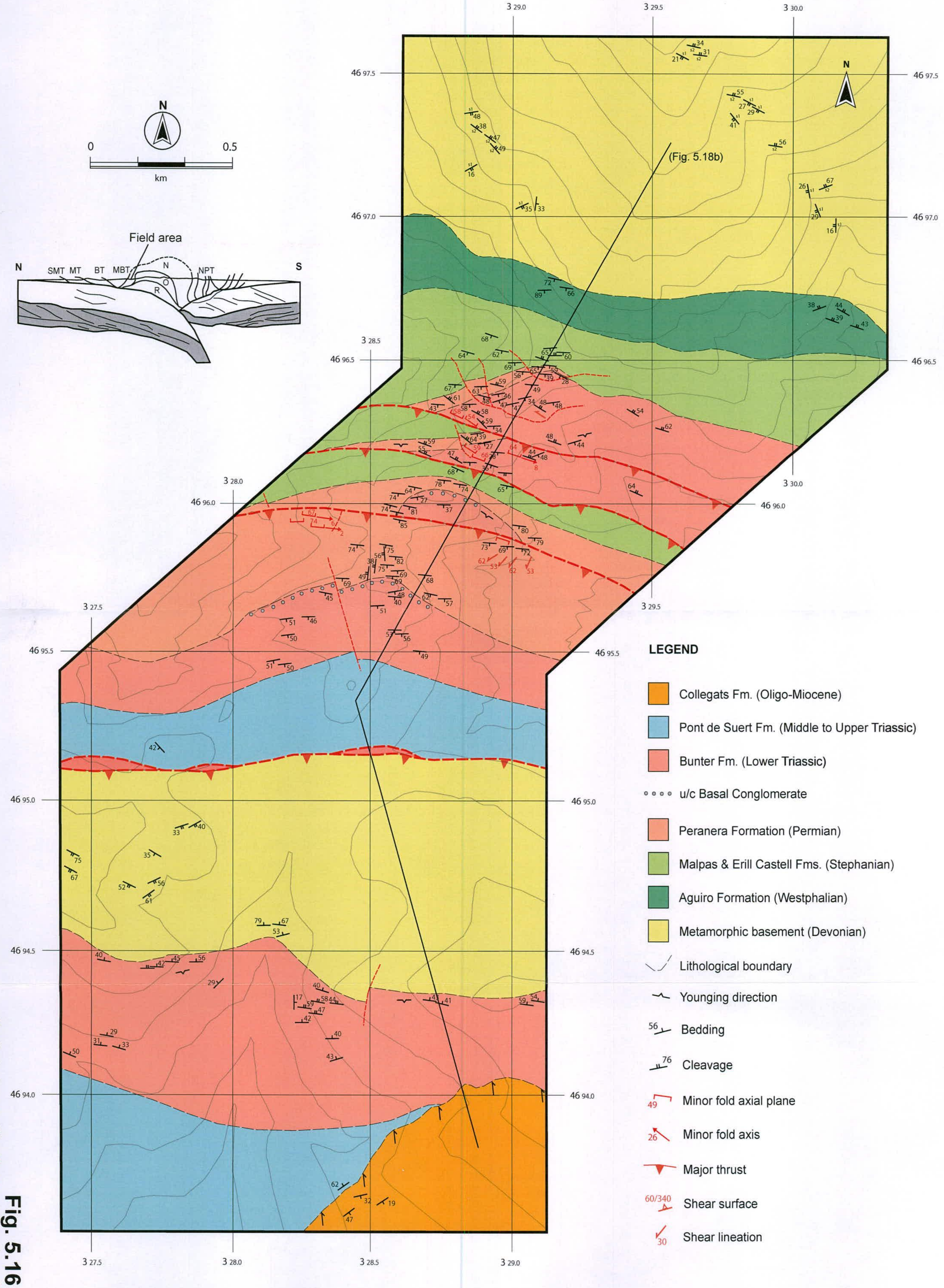

Fig. 5.16
Geological map of the Nogueres Zone (area j)

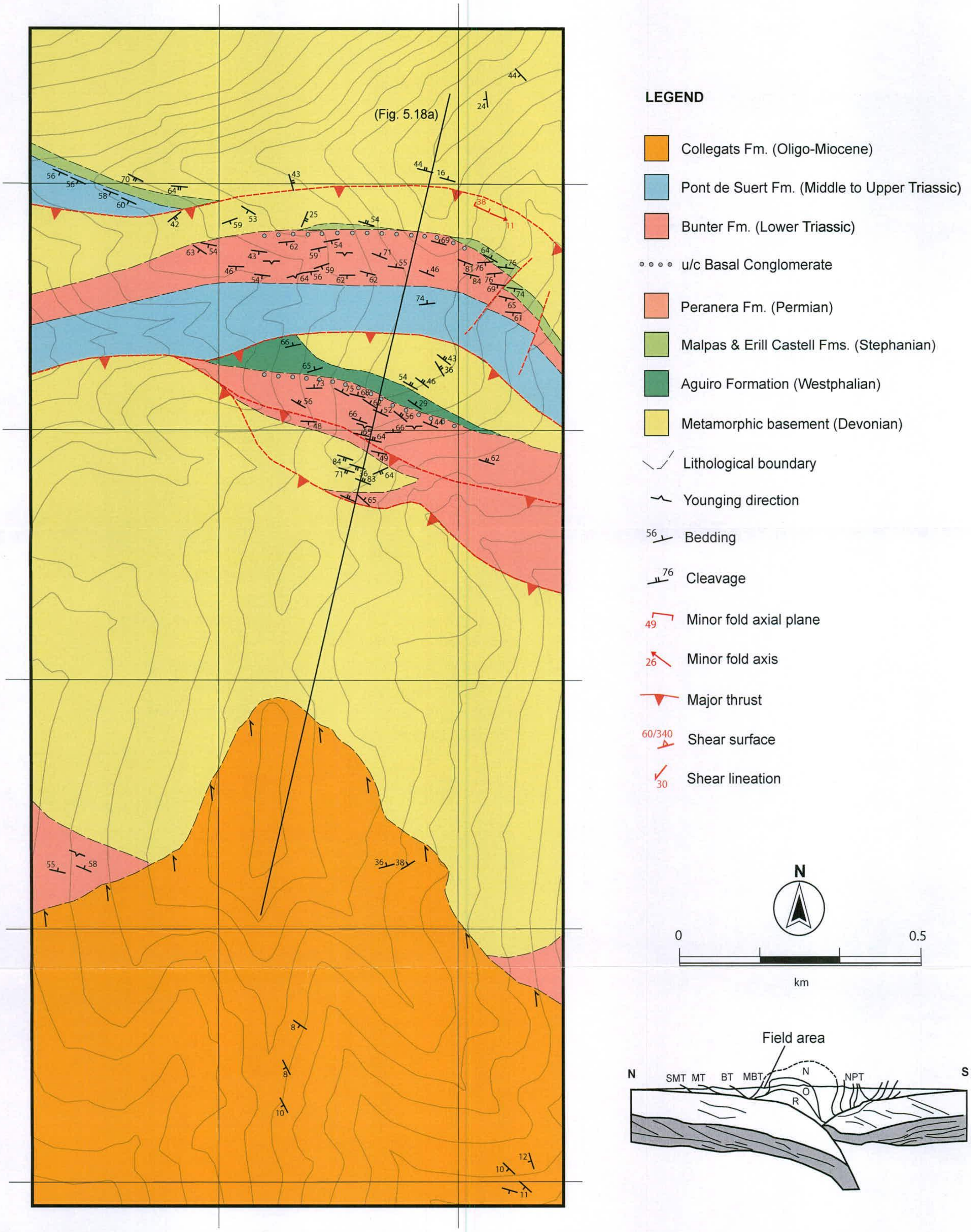

Fig. 5.17
Geological map of the Nogueres Zone (area k)

a. Ancs (area k)

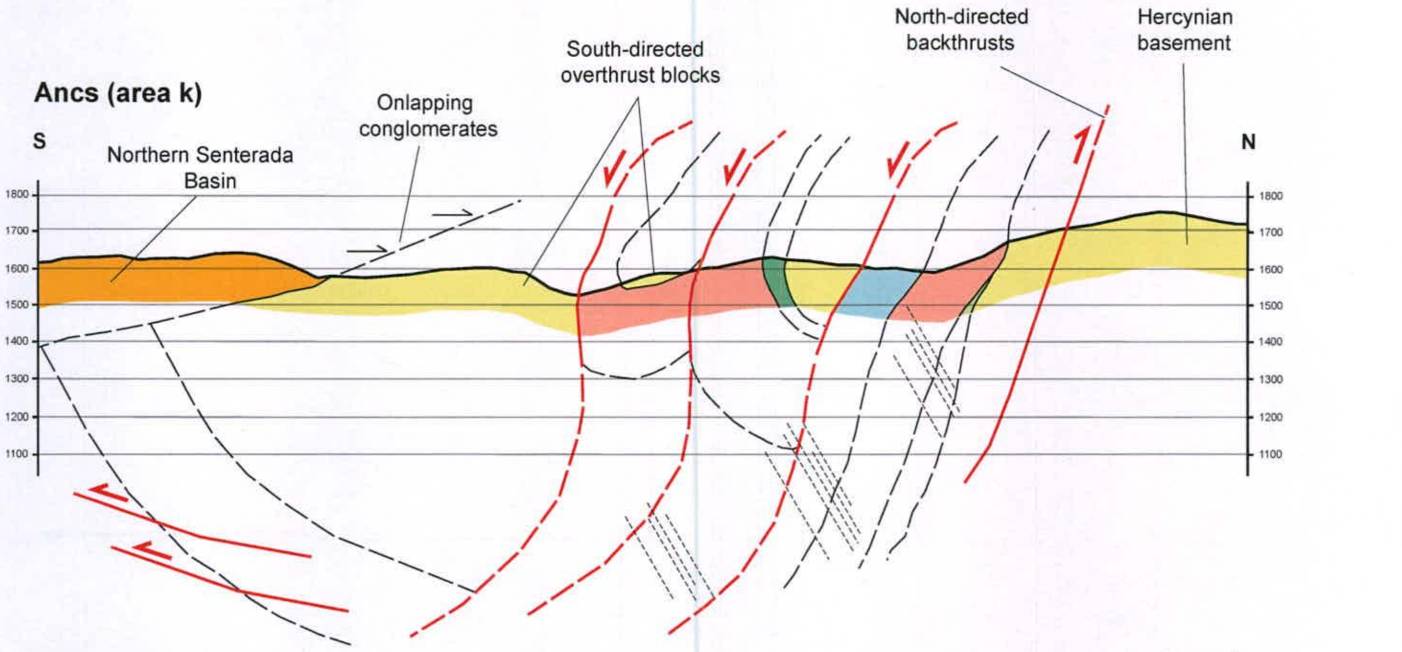

b. Coll d' Olli (area j)

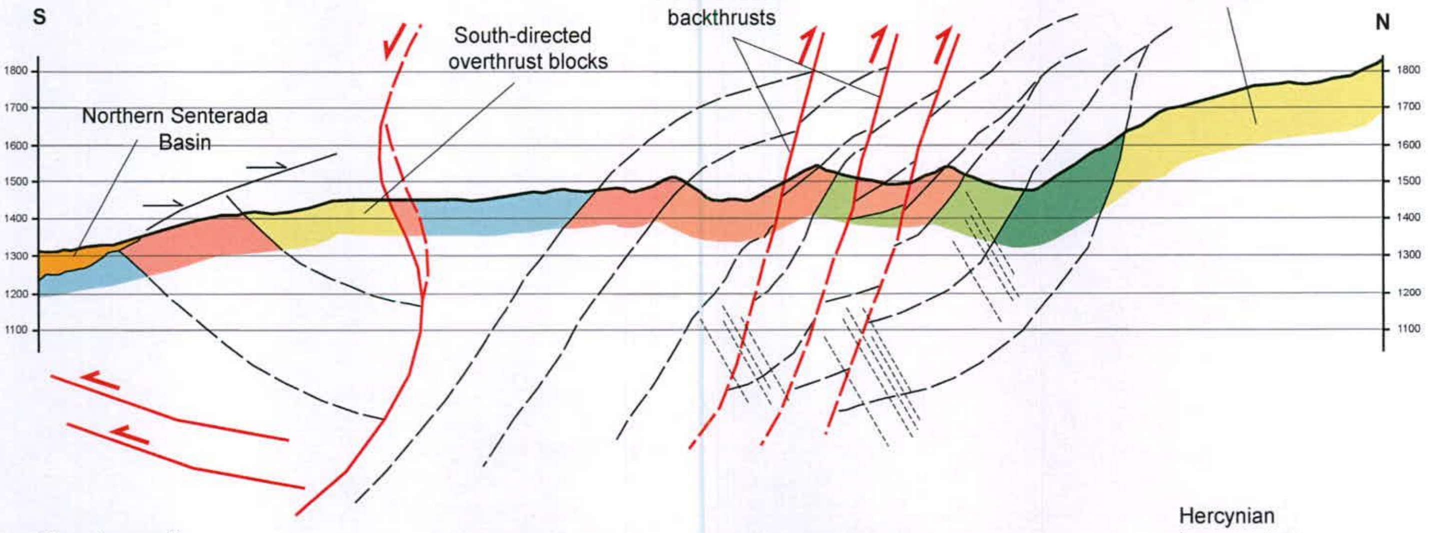

c. Sas (area i)

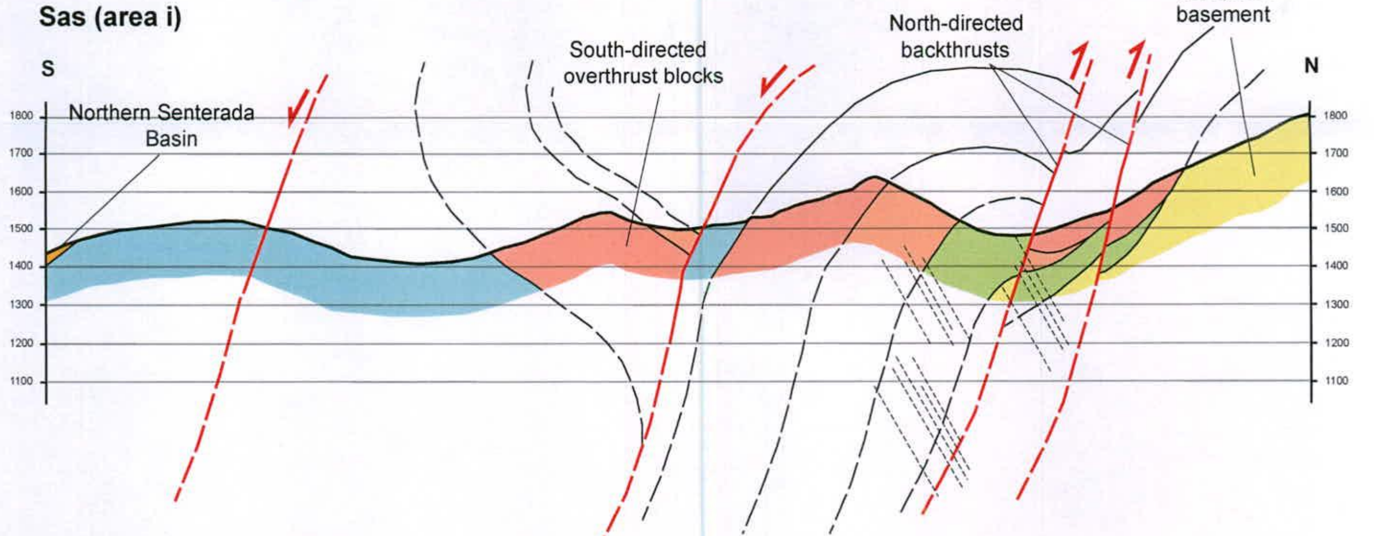

d. Erill (area h)

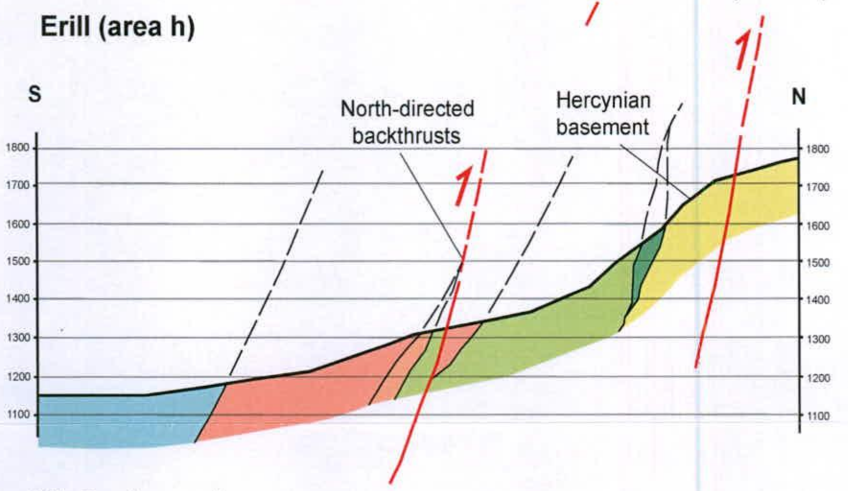

Figure 5.18 Geological sections from the five field areas of the Nogueres Zone (lines of section located on respective geological maps in Fig. 5.13 to 5.17) (Horizontal and vertical scales approximately equal). The stratigraphic legends are the same as used in the respective maps.

e. Vilaller (area g)

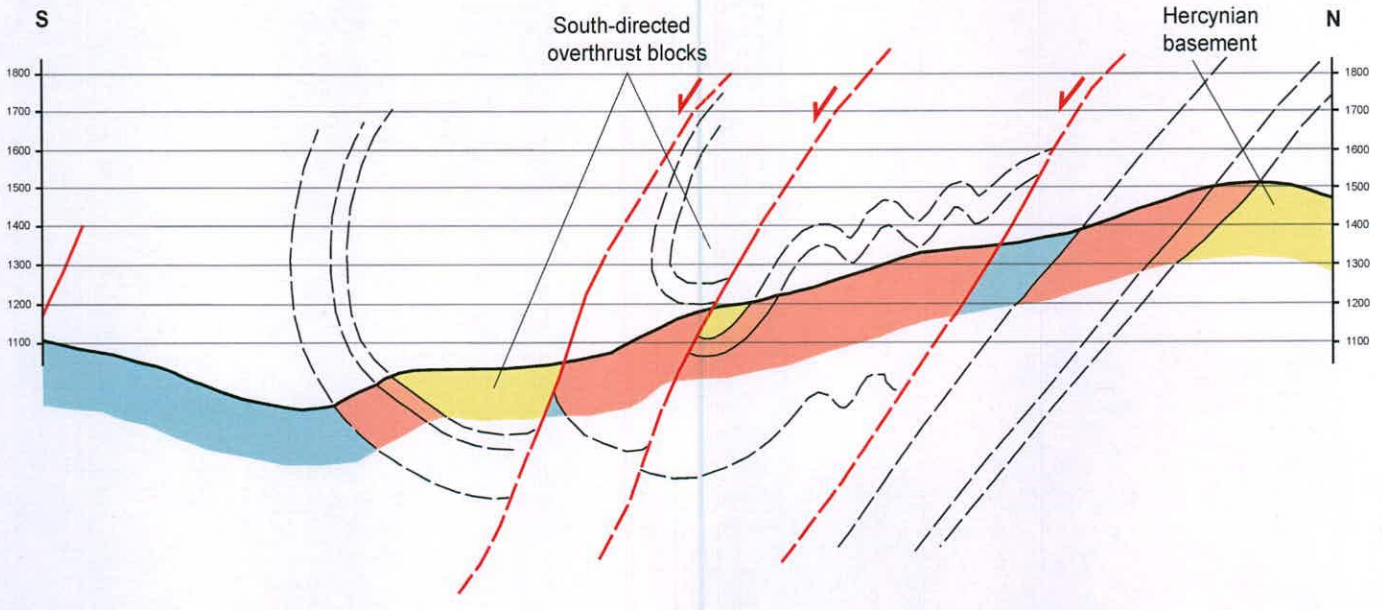

Fig. 5.18

Cross-sections from the Nogueres Zone (areas g-k)

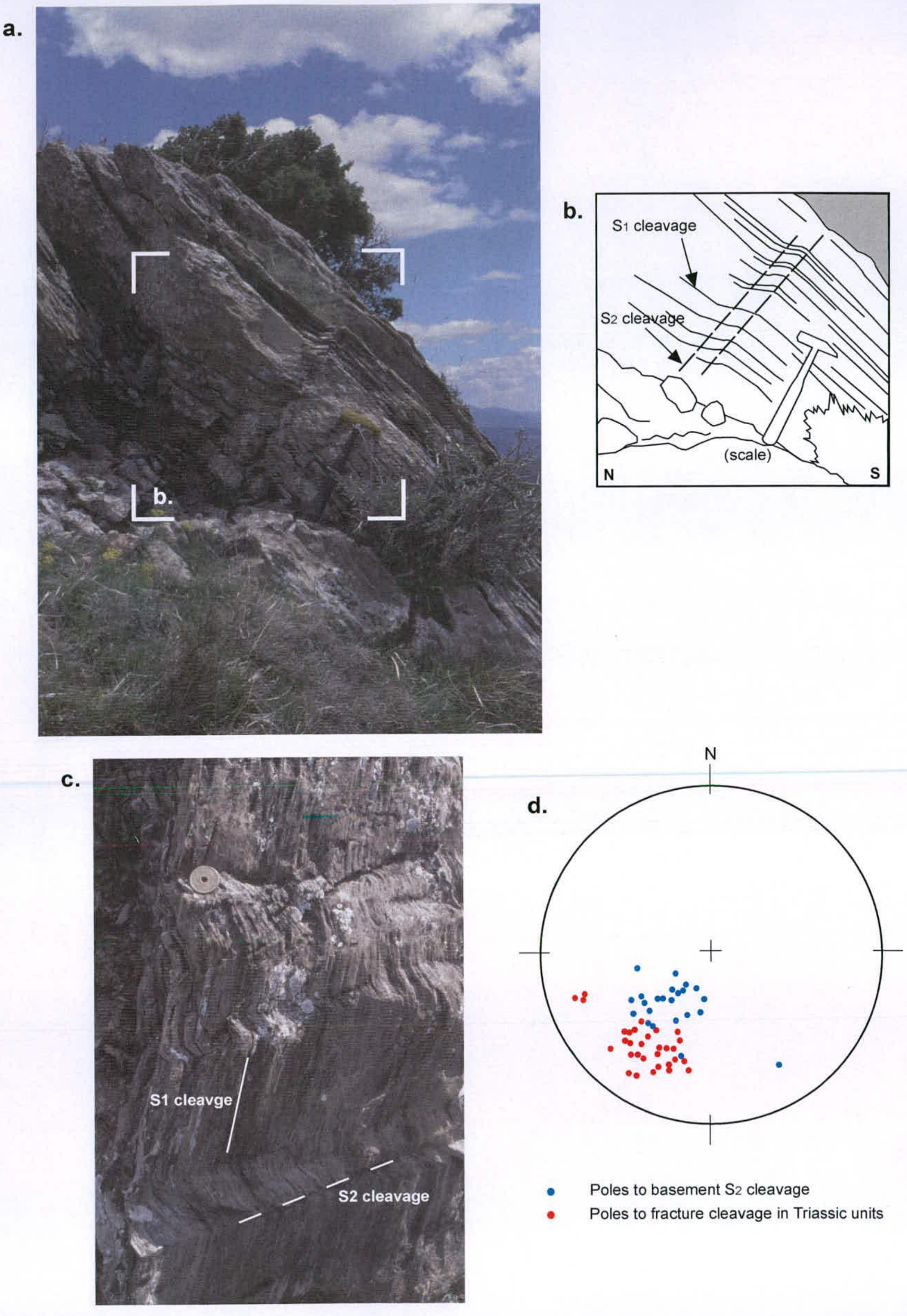

Figure 5.19 Field photographs of the basement lithologies in the Nogueres Zone. (a) The approximately orthogonal interception of the south-dipping S_1 and north-dipping S_2 clevage of the basement lithologies (see sketch (b) for detail) (hammer for scale). (c) Local variability in S_1 and S_2 orientations (cf. Photograph (a)) (coin for scale, north to left of image). (d) Stereoplot of the poles to S2 basement cleavage and the poles to fracture cleavage within the Triassic redbeds of the Sas and Coll d' Olli regions.

Fig. 5.19

Geological features of the Nogueres Zone (areas g-k)

Fig. 5.20
Geological features of the Nogueres Zone (areas g-k)

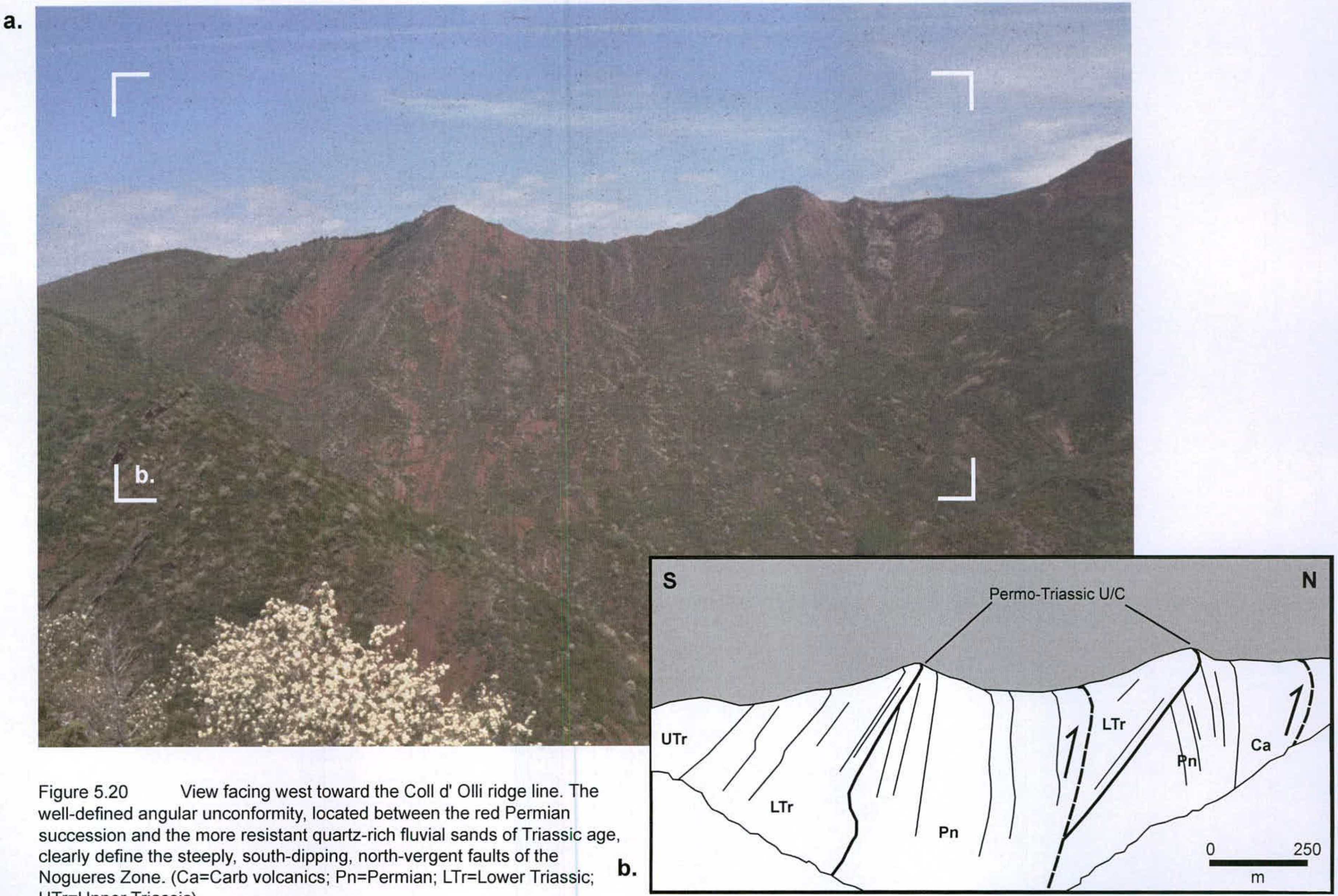

Figure 5.20 View facing west toward the Coll d' Olli ridge line. The well-defined angular unconformity, located between the red Permian succession and the more resistant quartz-rich fluvial sands of Triassic age, clearly define the steeply, south-dipping, north-vergent faults of the Nogueres Zone. (Ca=Carb volcanics; Pn=Permian; LTr=Lower Triassic; UTr=Upper Triassic)

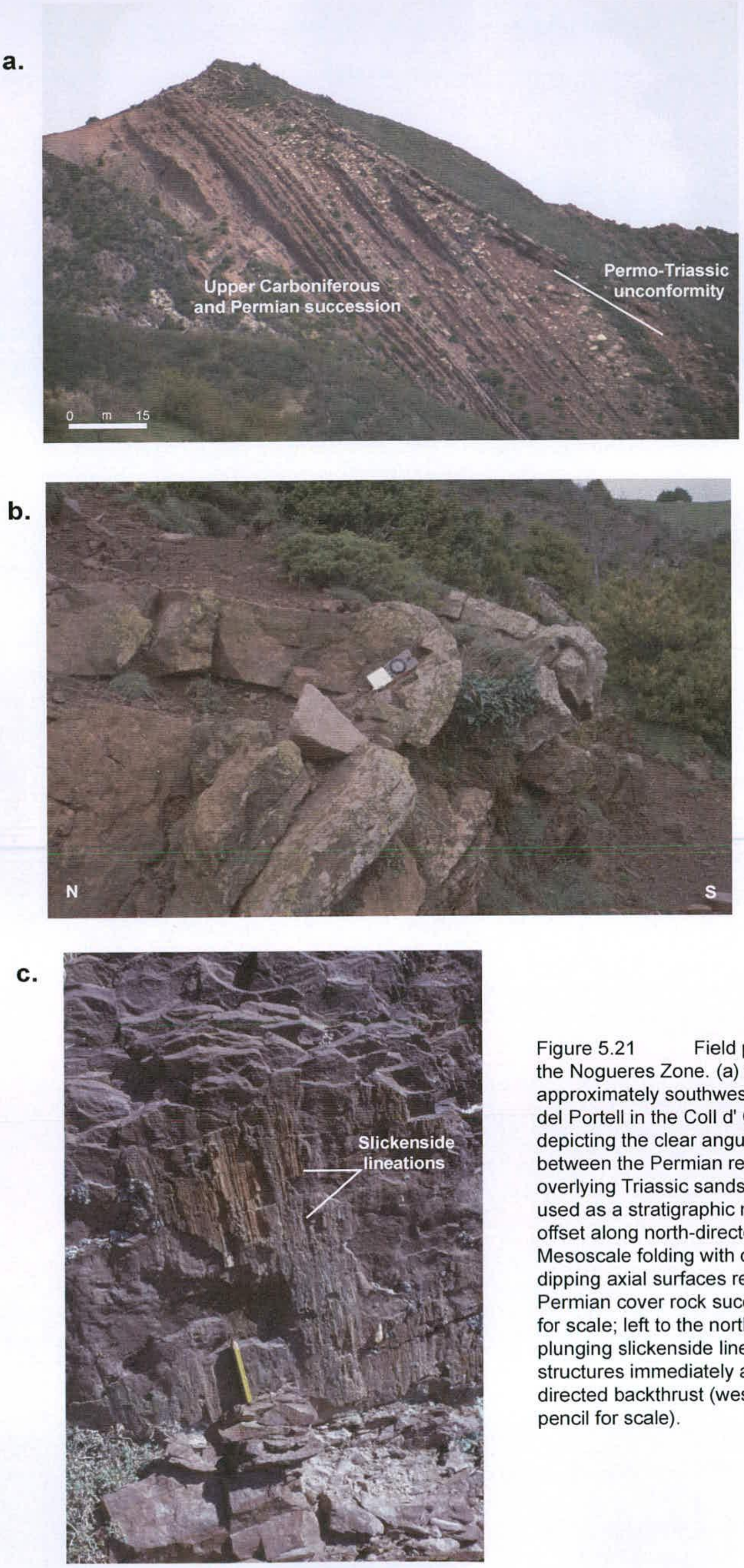

Figure 5.21 Field photographs of the Nogueres Zone. (a) View facing approximately southwest toward Tossal del Portell in the Coll d' Olli section depicting the clear angular unconformity between the Permian red muds and the overlying Triassic sands. This horizon was used as a stratigraphic marker to determine offset along north-directed backthrusts. (b) Mesoscale folding with consistent north-dipping axial surfaces restricted to the Permian cover rock succession (clinometer for scale; left to the north of image). (c) Steeply-plunging slickenside lineations on minor fault structures immediately adjacent to a north-directed backthrust (west to left of image; pencil for scale).

Fig. 5.21

Geological features of the Nogueres Zone (areas g-k)

a.

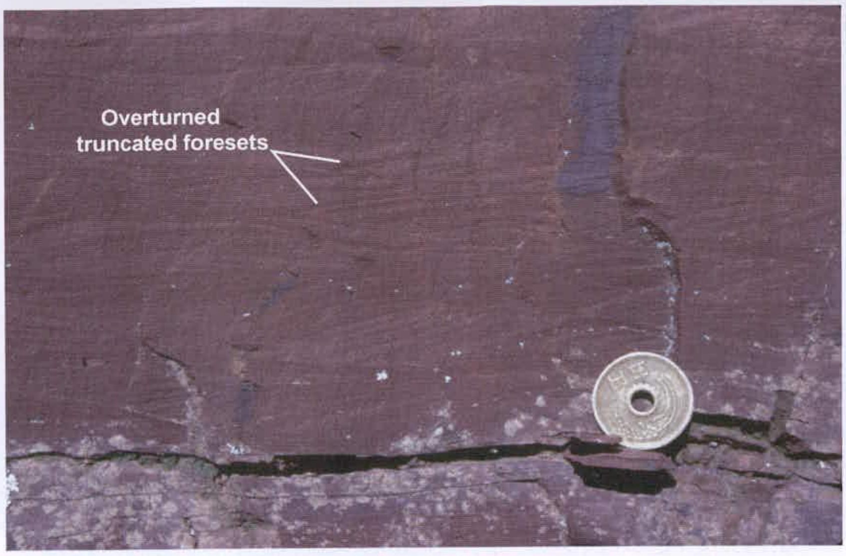

b.

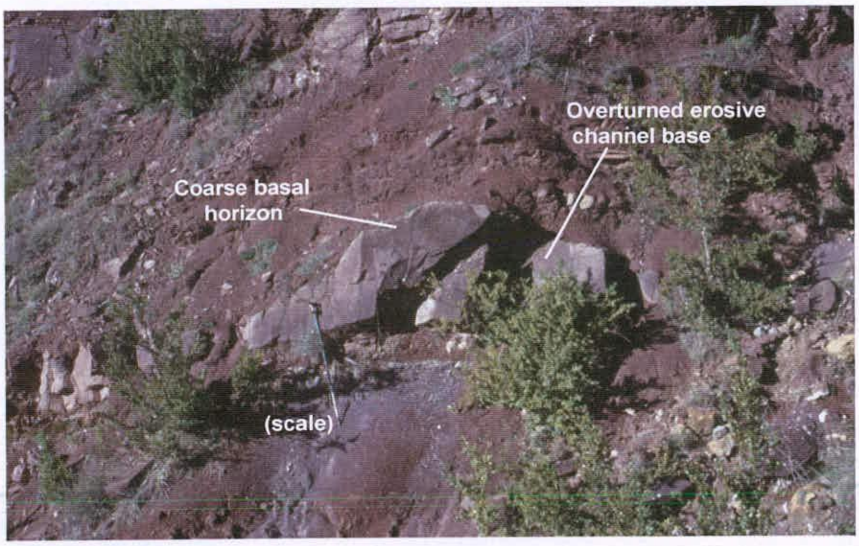

c.

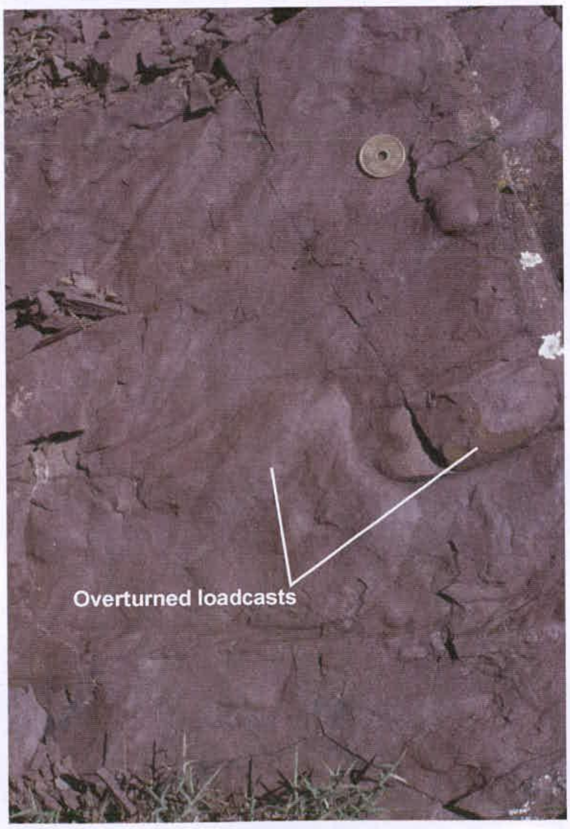

Figure 5.22 Field photographs of stratigraphic way-up structures within the Nogueres Zone, usd to determine the presence of overturned blocks in the hangingwalls of south-dipping thrusts. (a) Overturned trough cross-bedded fine sands in the Triassic Bunter Fm. (coin for scale). (b) Overturned coarse, sand-filled channel within red mud succession (walking pole for scale). (c) Over-turned loadcasts, and occasional directional markings in Triassic Bunter Fm. (coin for scale).

Fig. 5.22

Geological features of the Nogueres Zone (areas g-k)

Fig. 5.23

Geological features of the Nogueres Zone (areas g-k)

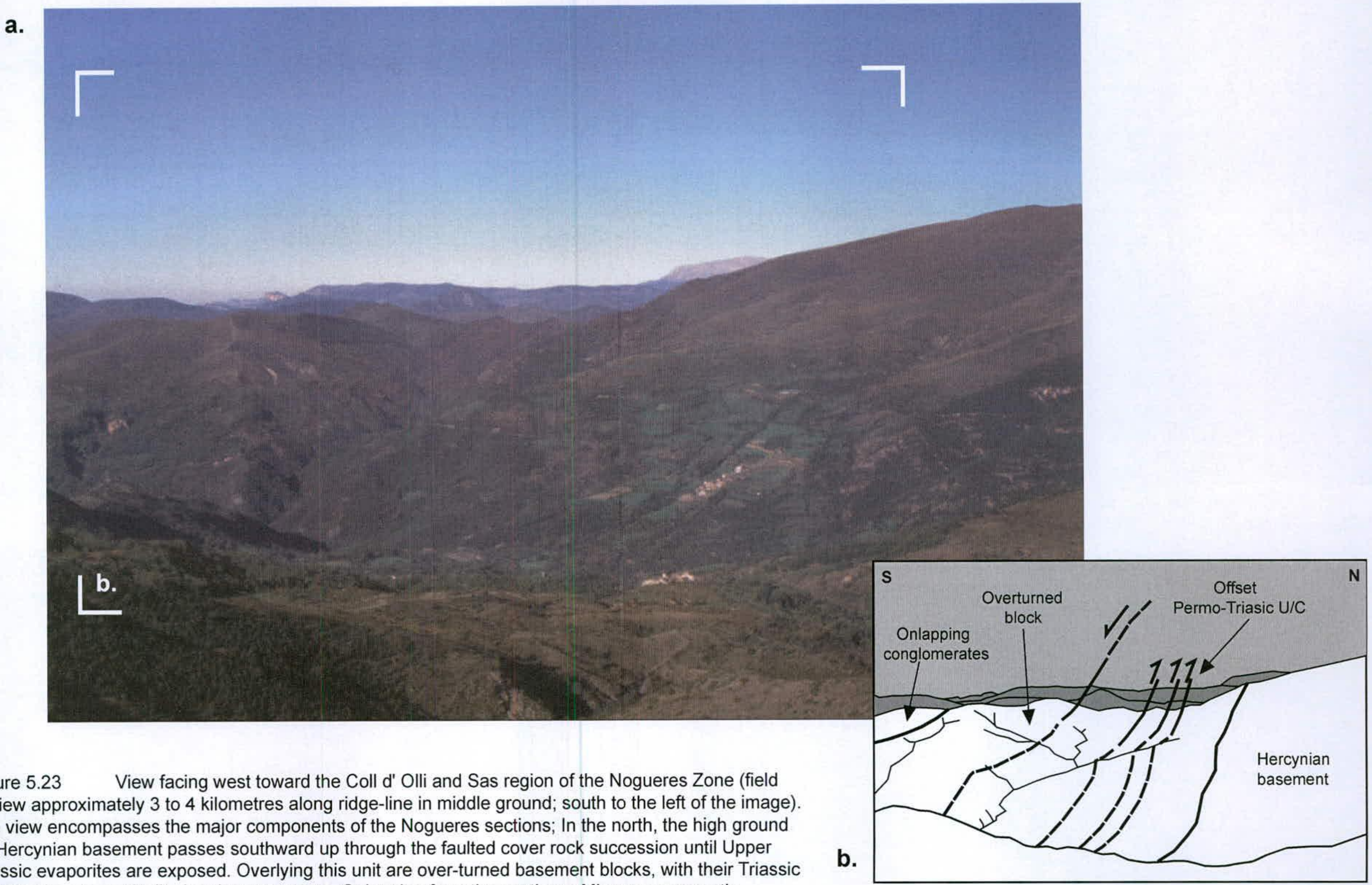

Figure 5.23 View facing west toward the Coll d' Olli and Sas region of the Nogueres Zone (field of view approximately 3 to 4 kilometres along ridge-line in middle ground; south to the left of the image). The view encompasses the major components of the Nogueres sections; In the north, the high ground of Hercynian basement passes southward up through the faulted cover rock succession until Upper Triassic evaporites are exposed. Overlying this unit are over-turned basement blocks, with their Triassic cover rocks, on south-dipping thrust contacts. Onlapping from the south are Miocene age gently deformed and south-rotated conglomerates of the northern Senterada Basin. (see sketch (b) for detail)

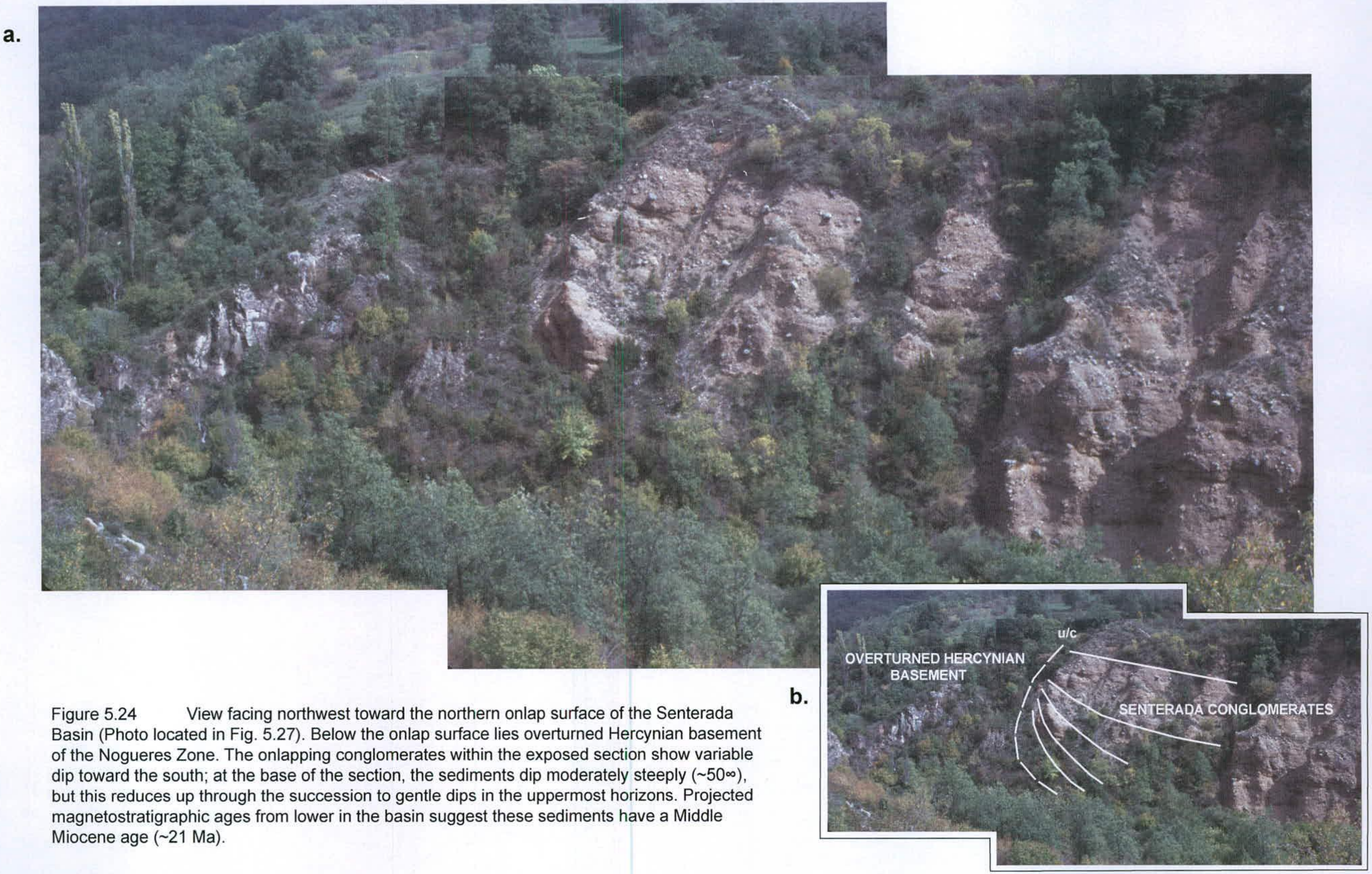

Figure 5.24 View facing northwest toward the northern onlap surface of the Senterada Basin (Photo located in Fig. 5.27). Below the onlap surface lies overturned Hercynian basement of the Nogueres Zone. The onlapping conglomerates within the exposed section show variable dip toward the south; at the base of the section, the sediments dip moderately steeply (~50∞), but this reduces up through the succession to gentle dips in the uppermost horizons. Projected magnetostratigraphic ages from lower in the basin suggest these sediments have a Middle Miocene age (~21 Ma).

Fig. 5.24

a.

b.

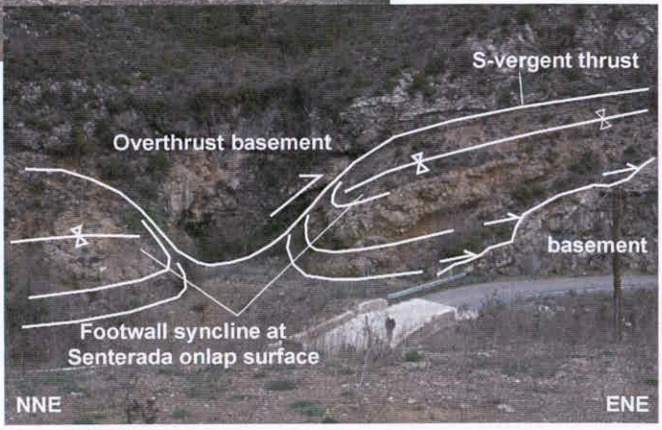

Figure 5.25 (a) Deformation at the base of the Senterada Basin by gently dipping, south-vergent thrusts; Mesozoic basement limestone has overthrust the onlapping Miocene sediments causing the formation of a local footwall syncline (see sketch (b) for detail and interpretation) (person on road for scale) (photo located in Fig. 5.27). (c & d) Gently-dipping, south-vergent thrusts cause brittle deformation of the 'granite-rich' conglomerates in the southern Senterada Basin (penknife and coin for scale).

c. d.

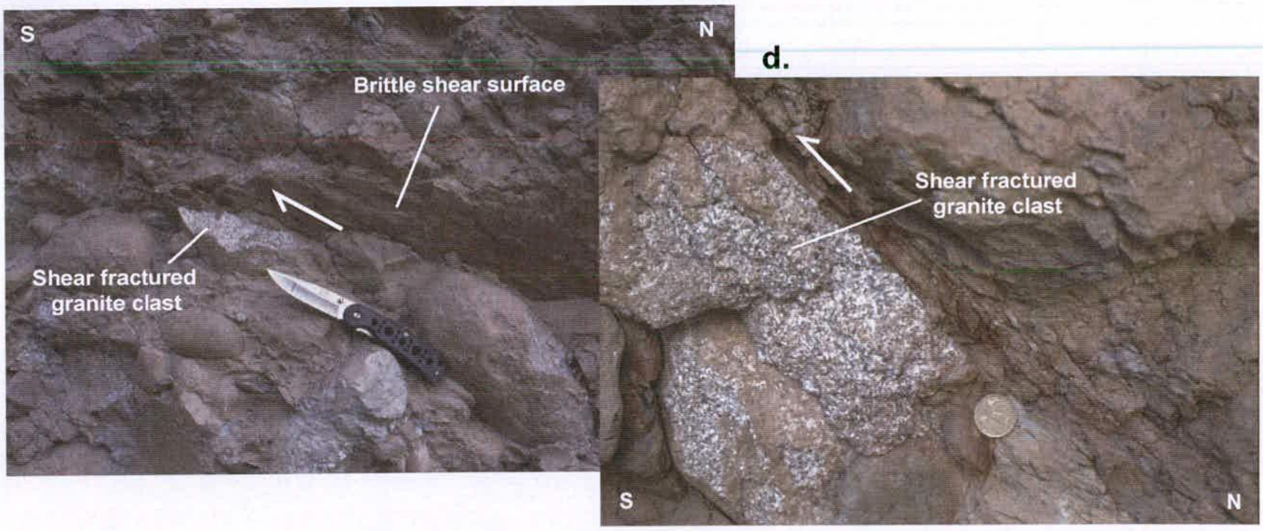

e.

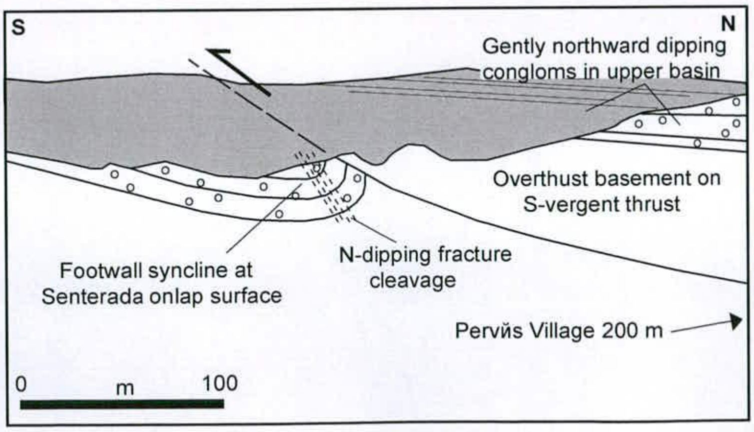

Figure 5.25 (e) Schematic cross section of the conglomerate onlap surface near the village of Perves, between the Sas and Coll d' Olli sections. Hercynian basement has overthrust the onlapping conglomerates causing the formation of a local footwall syncline and associated axial planar fracture cleavage. The overlying conglomerates to the north are undeformed and display a gentle southerly dip.

Fig. 5.25

Geological features of the Nogueres Zone (areas g-k)

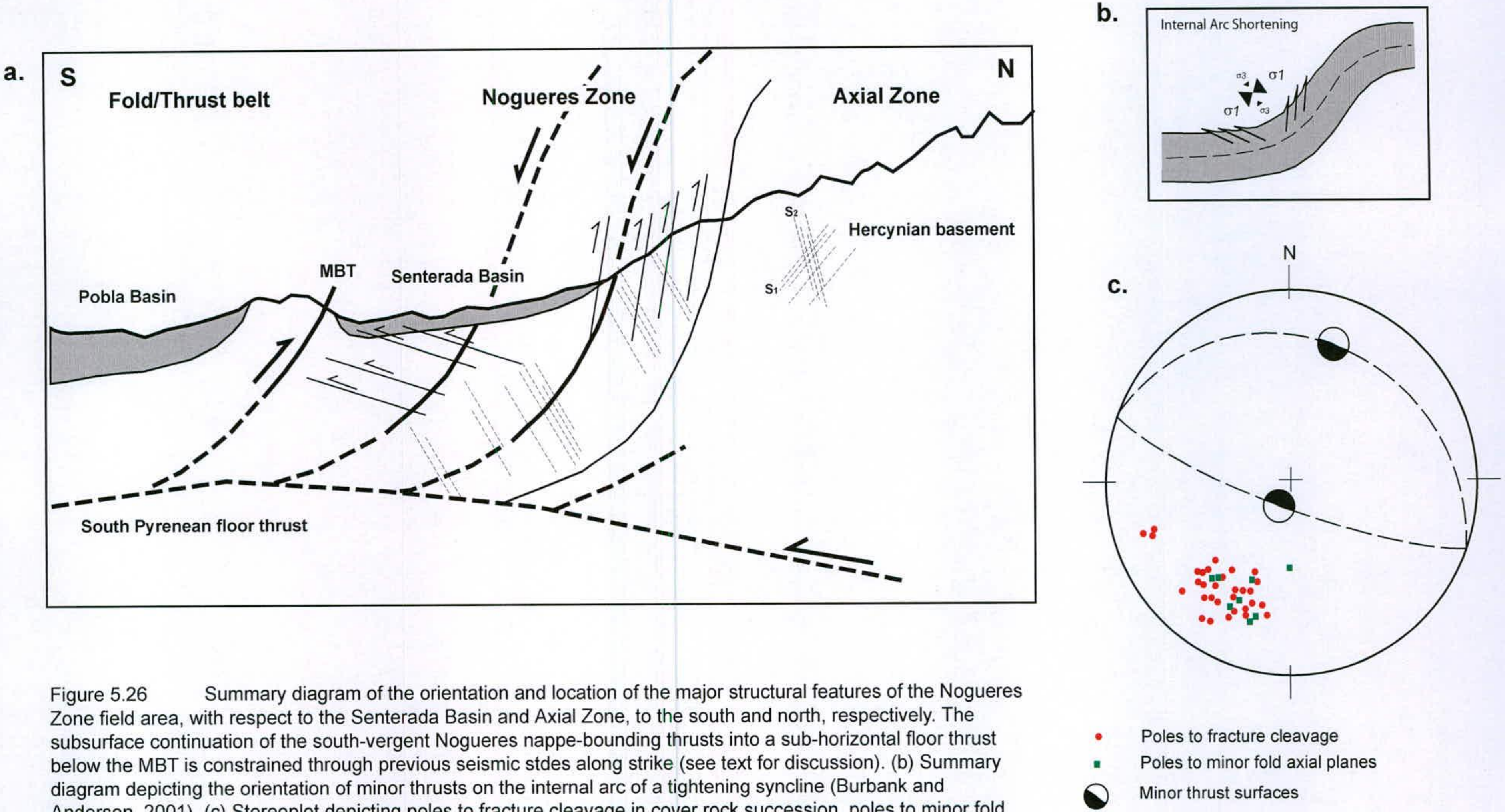

Figure 5.26 Summary diagram of the orientation and location of the major structural features of the Nogueres Zone field area, with respect to the Senterada Basin and Axial Zone, to the south and north, respectively. The subsurface continuation of the south-vergent Nogueres nappe-bounding thrusts into a sub-horizontal floor thrust below the MBT is constrained through previous seismic stdes along strike (see text for discussion). (b) Summary diagram depicting the orientation of minor thrusts on the internal arc of a tightening syncline (Burbank and Anderson, 2001). (c) Stereoplot depicting poles to fracture cleavage in cover rock succession, poles to minor fold axial surfaces in cover rock succession, with respect to the approximate orientations of the north-dipping and south-dipping thrust surfaces.

Fig. 5.26

Summary of the geological features of the Nogueres Zone

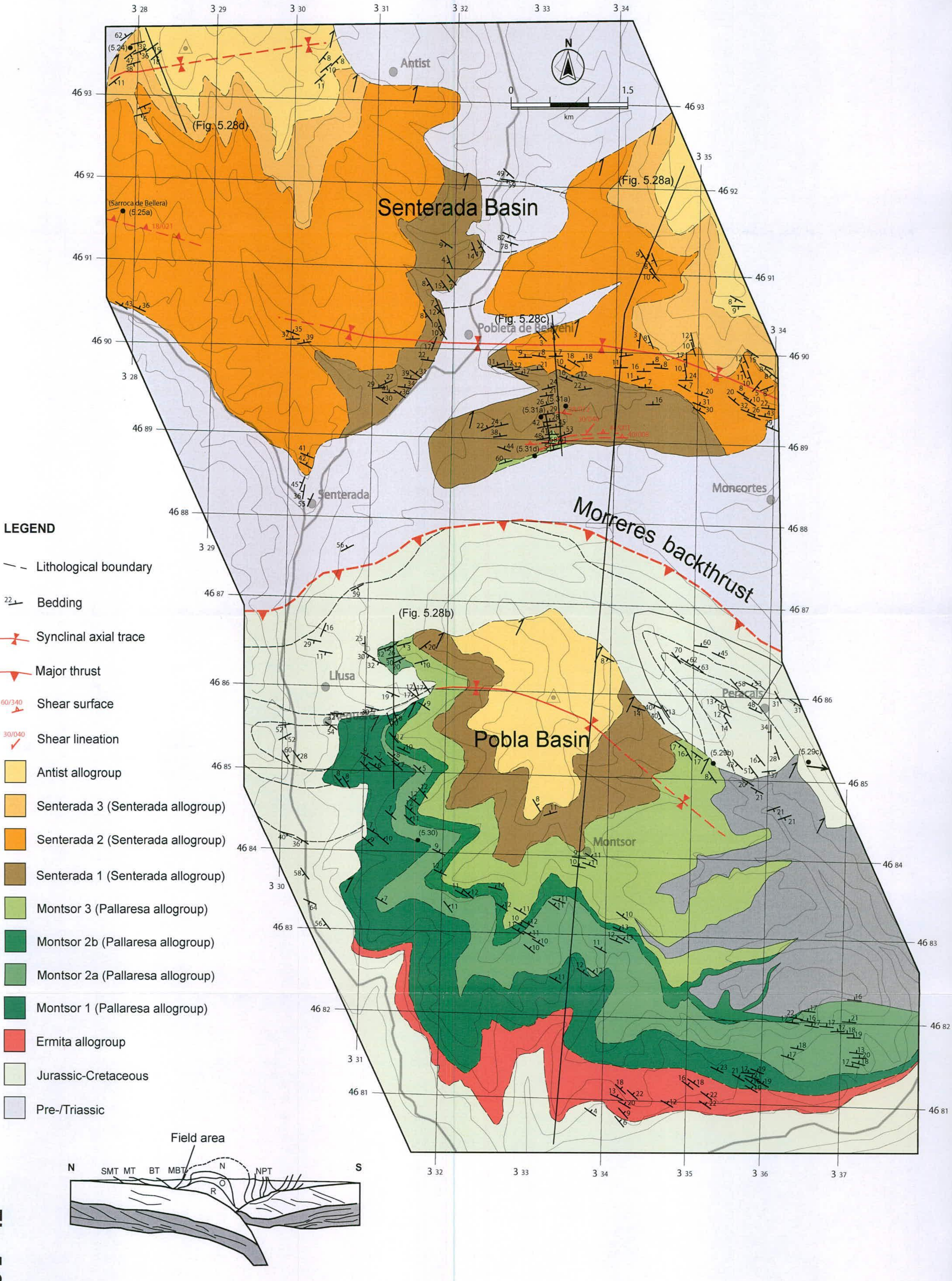

Fig. 5.27 Geological map of the Morreres Zone (area I)

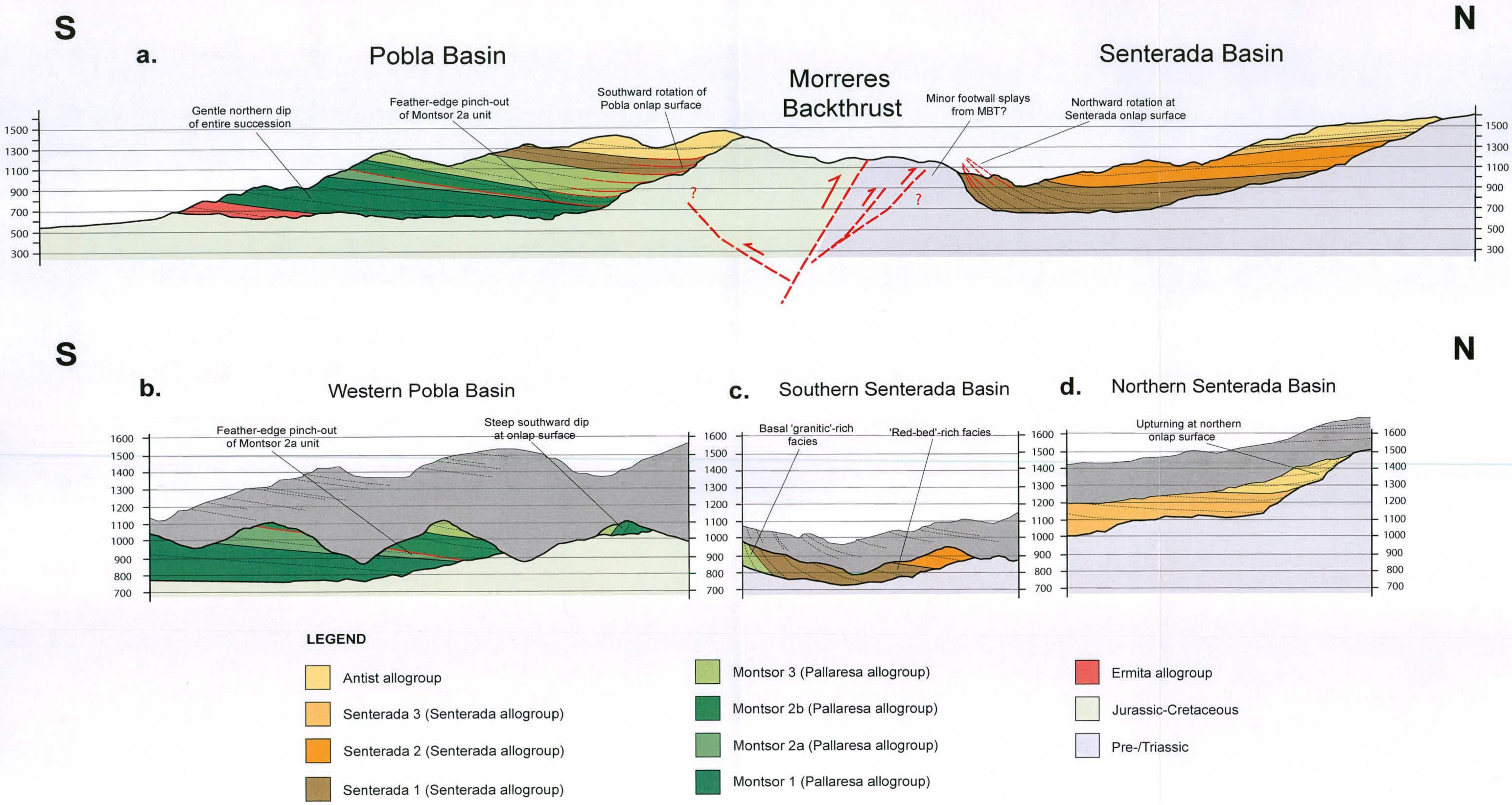

Figure 5.28 Geological cross-sections of the Morreres Zone. (a) N-S cross-section through the Pobla Basin (south), Morreres Backthust region, and Senterada Basin (north). (b) N-S cross-section through the western Pobla Basin depicting the feather-edge pinch-out of the Montsor 2a unit and local deformation at the onlap surface. (c) N-S section through the Southern Senterada Basin depicting the north-rotated basal strata and the contact between 'granite-rich' facies and the overlying 'red-bed-rich' facies. (d) N-S section through the Northern Senterada Basin depicting the upturning of the northern onlap surface.

Fig. 5.28
Cross sections of the Morreres Zone

a.

b.

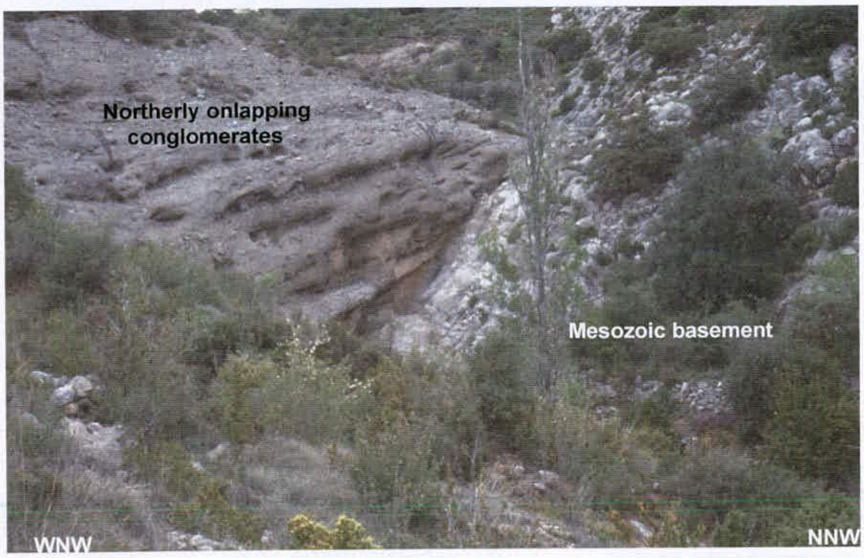

c.

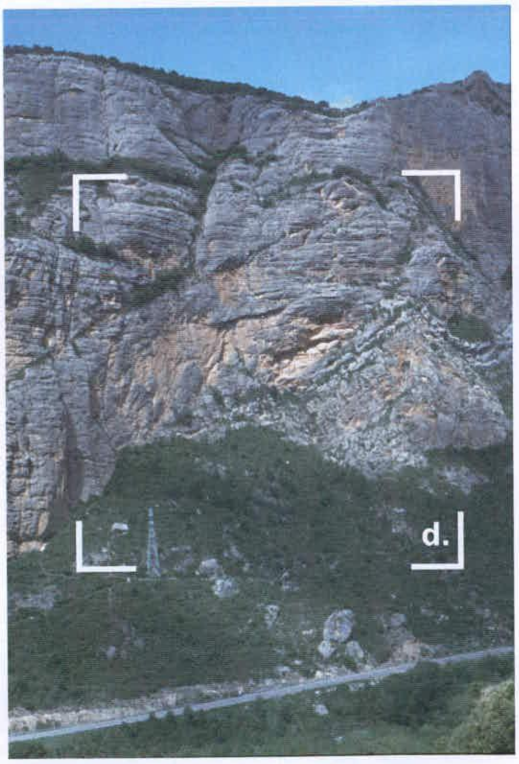

d.

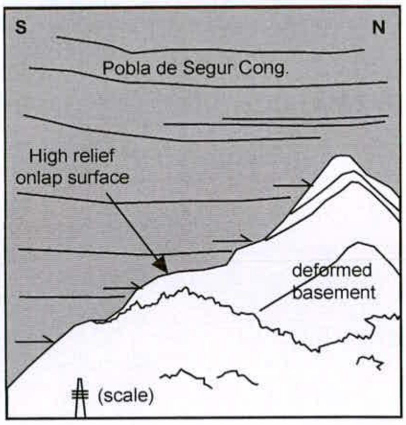

Figure 5.29 (a) View facing north depicting the subhorizontal sediments of the Pobla Basin onlapping onto the high relief of the MBT (craggy grey ridge line in middle ground) and northwards toward the Axial Zone (snow-capped peaks). (b) Onlap of the Pobla sediments onto the Mesozoic limestone basement (Field of view c. 40 m left to right) (Photo located in Fig. 5.27). (c & d) View facing northwest across the Collegats Canyon depicting MBT-related deformation, and subsequent erosion, prior to the deposition of the Sediments of the Pobla Basin (pylon for scale).

Fig. 5.29

Geological features of the Morreres Zone (area I)

a.

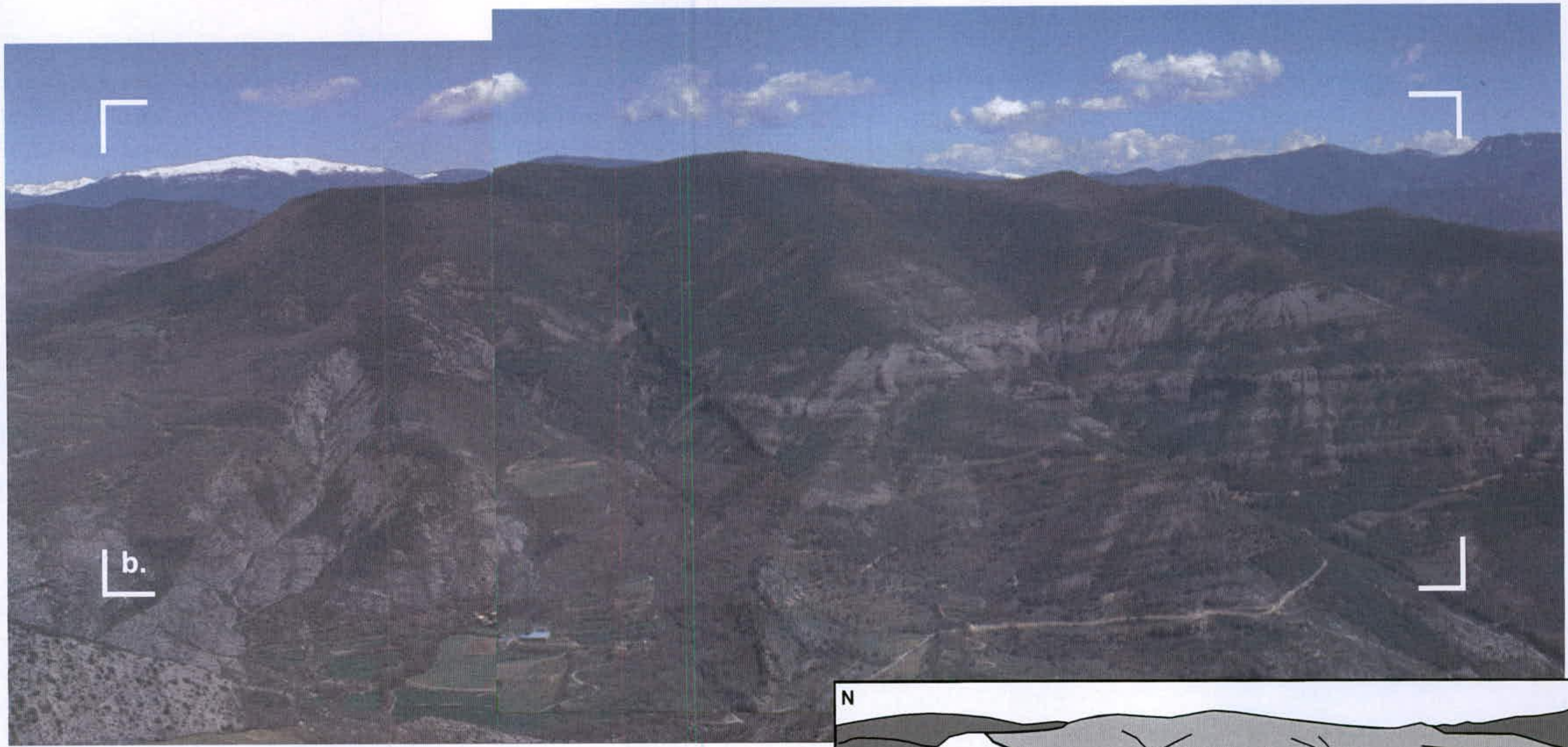

b.

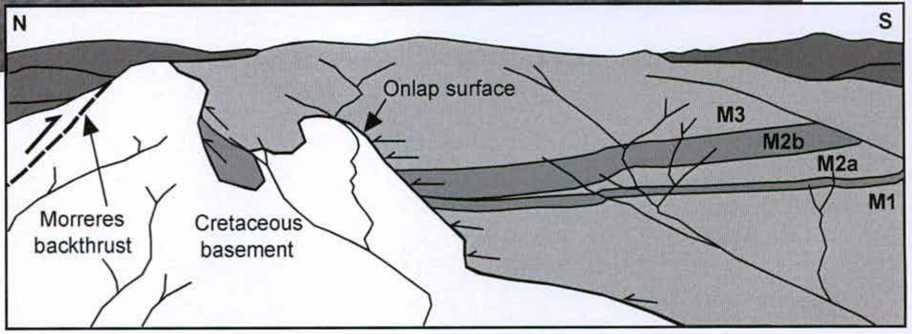

Figure 5.30 View facing west toward the eastern Pobla Basin in the vicinity of the Morreres Backthrust. The northward feather-edge pinch-out of the M2a unit is discernable between the well-exposed units above and below (M2b and M1, respectively) (see sketch (b) for detail and interpretation). The localised deformation at the northern onlap surface, causing the southward rotation of the M2b and M3 units, can also be clearly observed. (Field of view approximately 2 km left to right; farm buildings in foreground for scale). (Photograph located in Fig. 5.27)

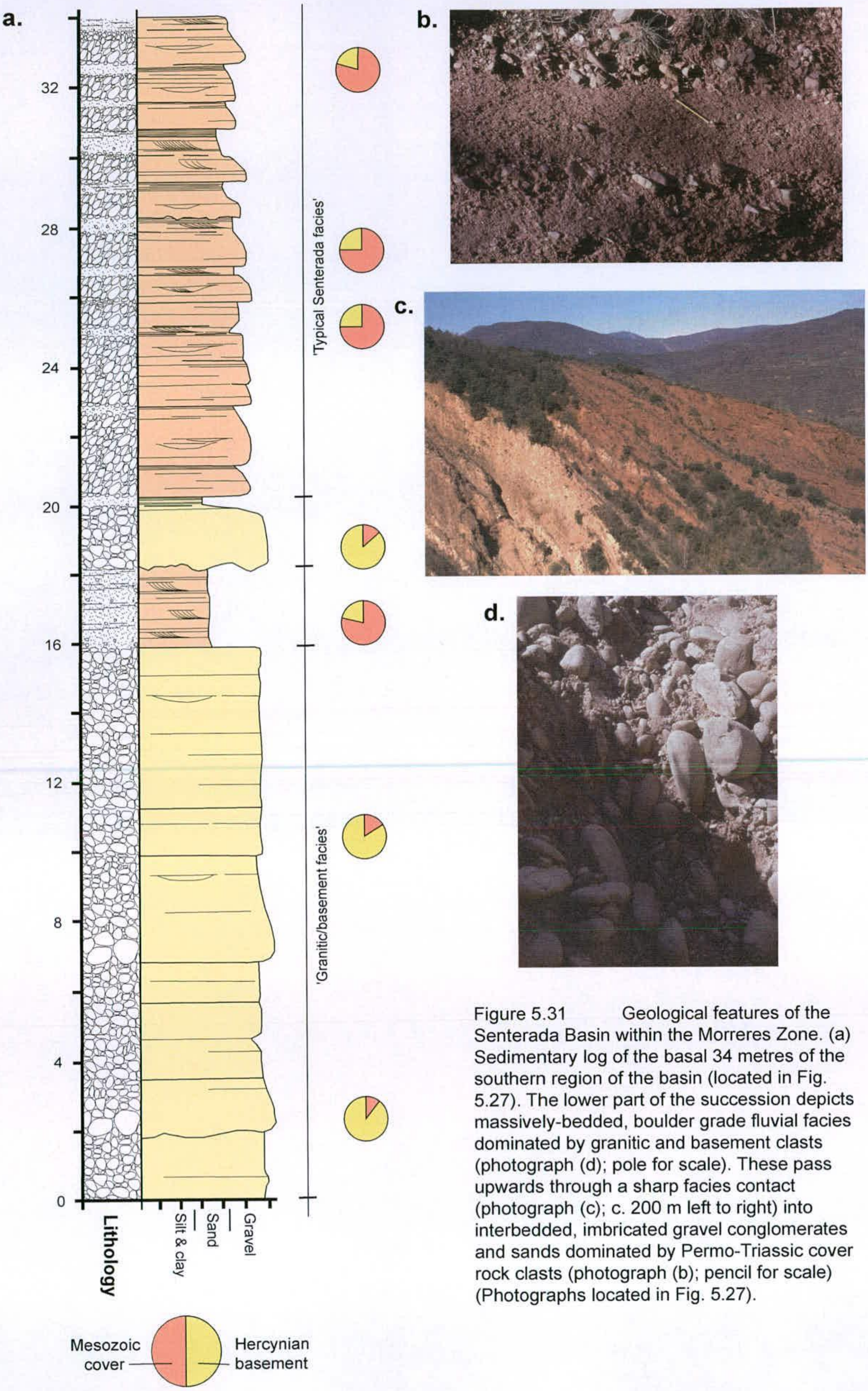

Figure 5.31 Geological features of the Senterada Basin within the Morreres Zone. (a) Sedimentary log of the basal 34 metres of the southern region of the basin (located in Fig. 5.27). The lower part of the succession depicts massively-bedded, boulder grade fluvial facies dominated by granitic and basement clasts (photograph (d); pole for scale). These pass upwards through a sharp facies contact (photograph (c); c. 200 m left to right) into interbedded, imbricated gravel conglomerates and sands dominated by Permo-Triassic cover rock clasts (photograph (b); pencil for scale) (Photographs located in Fig. 5.27).

Fig. 5.31

Geological features of the Morreres Zone (area I)

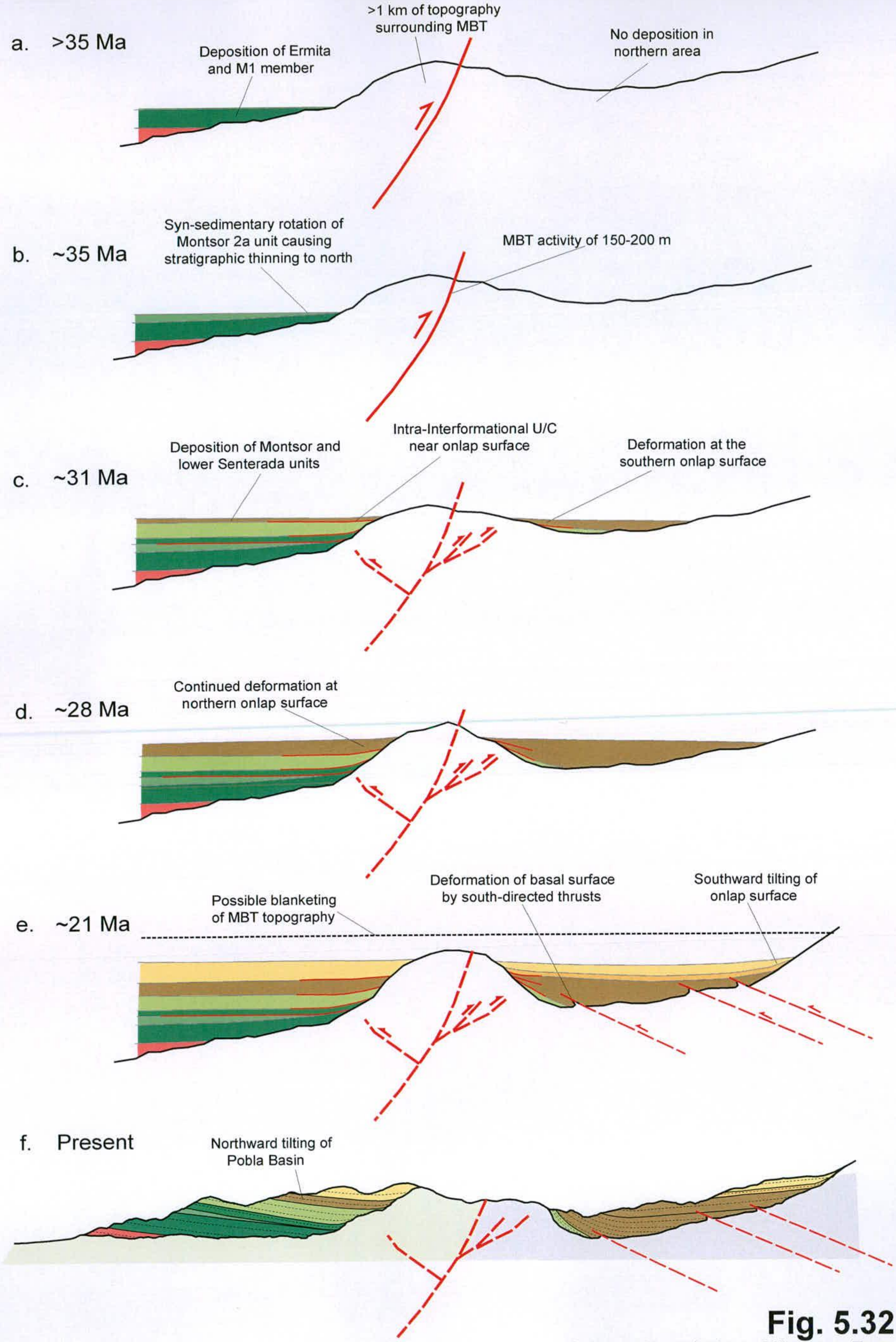

Fig. 5.32
Schematic evolution of Morreres Zone

Fig. 5.33

The offshore Tertiary sediment record in the Valencia Trough

(Ziegler et al., 1988)

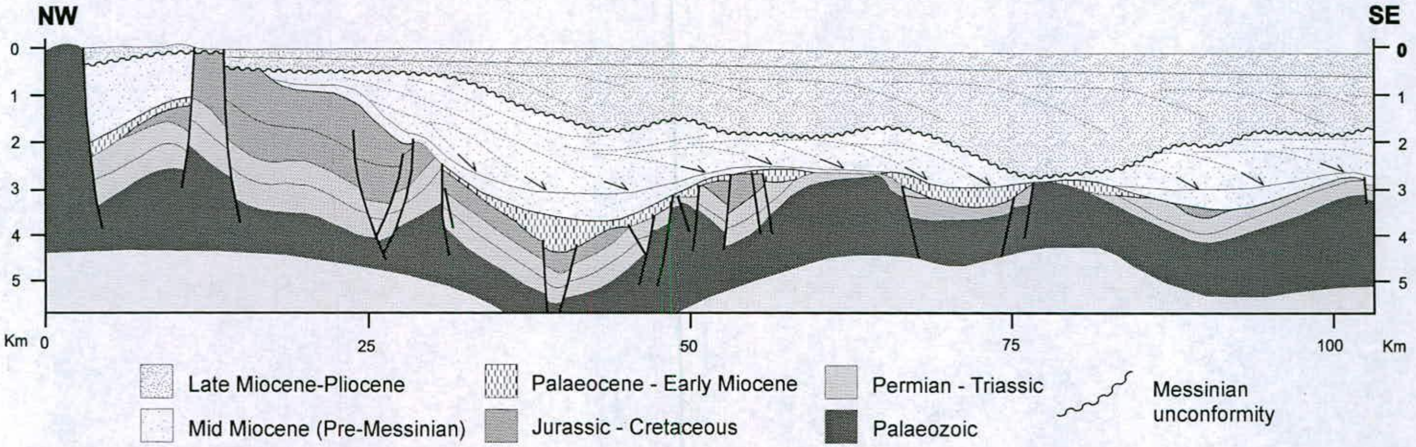

Figure 5.33 (Adapted from Ziegler, 1988) Interpreted seismic section along an approximarely NE-SW transect of the Valencia Trough, depicting the mid-Miocene age (Serravallian to Tortonian) siliciclastic Castellón Group prograding across a regional downlap surface. The overlying high-relief unconformity, associated with lowered base-levels during the Messinian Salinity Crisis, is overlain by thick Pliocene-age sediments.

Chapter 6

Synthesis: Mechanisms of localising erosional denudation

Objectives: The principal objective of this chapter is to synthesise the thermochronological data with the geological field data. This information is then used to constrain the mechanisms through which the distribution of erosional denudation was spatially and temporally controlled and to discuss the implications for existing models of Pyrenean development.

Chapter 6 – The Localisation of erosional denudation

The role of erosional denudation is widely recognised as the principal mechanism through which the interiors of compressional orogens are exhumed to the surface (Ring et al., 1999; Schlunegger and Willett, 1999; Willett, 1999; Beaumont et al., 2001). The spatial and temporal distribution of erosion within mountain belts is influenced by a host of factors that can be considered to be either internal or external to the orogenic system.

The primary internal forcing has long been regarded to be tectonically-driven rock uplift, whereby bedrock is forced upwards, relative to the geoid, by compressive tectonics, thus generating excess topographic relief which is modified or destroyed by erosion (e.g. Burbank and Beck, 1991; Kamp et al., 1992; Tippett and Kamp, 1993; Carrapa et al., 2003; Burbank et al., 2003; Wobus et al., 2003). The distribution of erosion in this case is consequently a function of the rock uplift patterns, as defined by the underlying structural framework. Further local variability in erosional denudation may be temporarily generated by a non-homogenous response to rock uplift, often associated with lithological contrasts and varied relief and slope thresholds (DeCelles and Mitra, 1995; Pazzaglia and Brandon, 1996; Summerfield and Brown, 1998).

External forcings that have previously been regarded to impose control on the distribution of denudation include climatic shifts, precipitation asymmetries, regional fluvial adjustments and base-level changes (e.g. Pazzaglia and Brandon, 1996; Harrison et al., 1998; Zhang et al., 2001; Reiners et al., 2003; Foeken et al., 2003; Cederbom et al., 2004). The association of these parameters to regional patterns of erosion is linked to the erosive capacity of rivers which can be approximated by a stream power function, whereby either increased discharge, through increased precipitation, or steeper channel slopes cause higher erosion rates (Howard, 1994).

In recent years both internal and external forcings have been considered to be mutually interactive within orogenic systems, whereby tectonic deformation, surface uplift, and erosion comprise a system which responds through positive feedback mechanisms of increased erosion through the orographic enhancement of precipitation (e.g. Koons, 1989; Willett, 1999). Numerical models that couple erosional processes with lithospheric deformation via gravitational feedbacks have indicated that denudation focused in this manner may exert first order control on orogen-scale tectonics (Willett, 1999; Beaumont et al., 2001).

The primary objective of this chapter is to develop an understanding of the specific mechanisms that controlled the spatial and temporal localisation of erosional denudation during the growth and decay of the Pyrenean orogen. This is achieved by synthesising the interpreted exhumation histories from Chapter 4 with the geological field data from Chapter 5. This also enables us to consider how published models of Pyrenean tectonic evolution might be revised to accommodate the new data.

6.1 Localised erosion in pre-Late Oligocene times

The thermochronological data, presented in Chapter 4, indicate that the large majority of the total Pyrenean exhumation, and hence the major period of orogenic growth of the mountain belt, occurred prior to Upper Oligocene times (~28 Ma). A major discontinuity in the exhumational record that may have lasted for up to 20 Myr is identified between the northern and southern regions. The maximum depths of exhumation occur in the region of the Marimaña and Maladeta Massifs where Pyrenean ZFT ages are found indicating erosional unroofing during Early Eocene times. This culminated with a period of extremely rapid exhumation through AFT annealing temperatures during Early Oligocene times. The area immediately to the south, including the Barruera Massif, maintained a pre-Pyrenean ZFT age and a post-Oligocene AFT age, indicating significantly less exhumation. The Nogueres Zone, located on the southern flank of the orogen, appears to have continued to cool progressively during this interval.

These data are difficult to reconcile with published models of Pyrenean evolution (e.g. Fig. 2.16). The distribution of exhumation has previously been regarded to be a function of accelerated erosional denudation promoted by large-wavelength, tectonically-forced rock uplift during internal thickening at mid-crustal levels and the development of the Axial Zone antiformal stack (Fitzgerald et al., 1999; Beaumont et al., 2000). Exhumation is proposed to have been a regional response across the south central Pyrenees but at a maximum at the locus of the structural culmination of the antiformal stack, directly along strike from the Barruera region (Fig. 2.16). Instead of this regional response centred in the Barruera region, the data from this study document abrupt and long-lived spatial discontinuities in exhumation focused on the Marimaña and Maladeta regions in the north. This distribution calls for a mechanism which enabled exhumation, and by inference erosional denudation, to be discretely partitioned in the northern area whilst allowing the southern flank to exhume more slowly.

It is difficult to envisage how this could be achieved by large-scale external forcings, such as climatic variations, base-level shifts or fluvial reorganisations. Likewise, as we have no knowledge of the nature of the lithologies at the surface at this time, we cannot assume the variations in rates of erosional denudation were due to lithological or erodibility contrasts, particularly as regions which appear to have undergone preferential exhumation are those predominantly comprised of more durable and weathering-resistant lithlogies. A plausible alternative is to suggest the local variability in erosional denudation in these areas was spatially partitioned by a tectonic forcing. Previous studies from other compressional orogenic systems have shown that abrupt discontinuities in thermochronological data can be generated by localised increases in rates of erosional denudation through structurally-controlled, accelerated rock uplift (e.g. Kamp et al., 1992; Wobus et al., 2003). Mechanically active and emergent large-scale displacement faults, such as the Insubric Line of the Swiss Alps or the Alpine Fault of the New Zealand Alps, have been interpreted to have preferentially uplifted and exhumed in excess of ten kilometres of hanging-wall rock, with respect to their adjacent foot-walls (Kamp et al., 1992; Tippett and Kamp, 1993; Seward and Manktelow, 1994).

The geological field data (section 5.1.1) indicates the Marimaña and Maladeta regions are structurally separated into two distinct tectonic blocks by steeply northward dipping faults of Alpine age. The structures are aligned broadly parallel with the orogenic strike and are laterally persistent for tens of kilometres. Secondary shear structures, developed around the faults, indicate active south-vergent, reverse fault motion within a shallow crustal stress regime. The orientation and kinematics of the structures are consistent with the relative upward displacement of the Marimaña region with respect to the Maladeta region. The Maladeta Massif is bounded to the south by the northward dipping Senet Thrust (section 5.2.2). The Alpine age and southward vergence of the structure is evidenced by the overthrust post-Hercynian strata in its footwall. The fault is laterally persistent along orogenic strike for up to 40 km and displays secondary shear structures associated with active displacement, most recently, within the shallow crustal realm. The orientation of the thrust surface and the surrounding secondary shear structures are consistent with the relative upward displacement of the Maladeta Massif with respect to the Barruera Massif, which lies in the structural footwall of the fault.

Previous orogenic models have assumed that all major basement thrusts within the Axial Zone were non-emergent and active only at low angles within the lowermost upper crust and have since been subsequently deformed and exhumed (Fig. 2.16) (Puigdefàbregas et al., 1989; Muñoz, 1992). The field data here indicates large-scale thrust structures were likely to have been active within a brittle regime in the shallow crustal realm. The thermal field in this section of the crust contains the relevant closure isotherms of the thermochronometers used in this study. Therefore, if the structures were emergent during active, south-vergent fault displacement, the preserved exhumation gradients may be directly physically related to differential tectonically-forced rock uplift (**Fig. 6.1a-b & 6.2a**). With increased rates of rock uplift in the structural hangingwalls would be an associated increase in the rate at which the erosional processes denuded the surface and, thus, exhumed the rock column through the relevant closure isotherms. Sustained rock uplift over millions of years could promote the required amount of cooling to cause closure within more than one thermochronometric system. It is plausible, therefore, that the thrusts to the north and south of the Maladeta Massif represent the locus of the exhumational discontinuities documented by the thermochronological data. If this is the case, the region to the north of the Senet Thrust, including the Marimaña and Maladeta massifs, would have undergone accelerated erosional denudation during active thrusting, with respect to the southern region. Likewise, the Marimaña region could have experienced enhanced erosional denudation during active thrusting, with respect to the more southerly Maladeta Massif. This distribution of focused exhumation is consistent with the thermochronological data.

The steeply-dipping structures could have developed as breach thrusts and truncated older and structurally higher thrusts in the antiformal stack (Fig. 6.1b). This interpretation is consistent with previous studies of palaeomagnetic pole rotations south of the Maladeta Massif, which indicate that the Senet Thrust, at least, was initiated at a steep, northward dipping orientation and post-dates the development of the other rotated and domed basement thrusts (McClelland and McCaig, 1989). The south-vergent Estet Thrust (section 5.2.3), which contains the Barruera Massif within the hanging-wall, is likely to be one of the older, deformed structures that was not emergent. The lack of constraint on the timing of thrust activity precludes a definitive linkage between the documented cooling histories and structurally controlled differential rock uplift. However, the concurrence between the thermal history data and the surrounding structural framework provide compelling evidence to suggest the two are inextricably associated (see section 6.4.2 for further discussion).

It is necessary to consider what are the possible implications for tectonic models of Pyrenean growth and how they can be revised to accommodate the new data. Published models have previously regarded Alpine-age thrusts in the Axial Zone to have been non-emergent and to be directly linked to the cover thrusts below the southern fold and thrust belt. Hence, all displacement along them was assumed to have been transferred directly to the cover thrust system (Muñoz, 1992; Puigdefàbregas et al, 1989; Puigdefàbregas et al., 1992). The data from this study instead suggest the development of emergent, out-of-sequence thrusting accommodated the upward flux of large volumes of basement rock within the central Axial Zone during the main period of orogenic growth. This implicitly suggests a significant proportion of tectonic shortening was not transmitted to the southern fold and thrust belt. Instead, it was partitioned within the inner regions of the mountain belt and compensated for by the removal of mass out of the system through processes of surface erosion. This is consistent with the synsedimentary growth strata from the Morreres Zone (section 5.4.1), which depicts tectonic shortening along the Morreres Backthrust to be of the order of only a few hundred metres from Middle Eocene to Late Oligocene times, despite the structure representing the major tectonic contact between the fold and thrust belt and the inner orogen. This documented shortening is likely to be due to passive backthrusting as regional exhumation continued within the entire southern Pyrenees. As suggested in previous models, this background exhumation is likely to have been driven by ongoing internal deformation beneath the antiformal stack duplex and is probably documented by the steady and protracted exhumation history depicted in the Nogueres Zone AFT profile.

It is also interesting to consider the potential physiographic implications of Axial Zone out-of-sequence thrusting in pre-Late Oligocene times. If rock uplift along the structures was maintained at higher rates than that which erosional processes denuded the surface, a net increase in local elevation would have been generated. This would have manifested itself as a linear physiographic discontinuity of increased relief at the locus of the thrust hanging-walls. This development of a high relief region within the central Axial Zone, comprising granite-rich basement lithologies, is compatible with documented expansions of the fluvial systems that drained into the southern foreland and with a huge increase in granitic clastic detritus at this time (Mellere, 1993; Vincent, 2001).

6.2 Localised erosion in Late Oligocene-Middle Miocene

The thermochronological data indicate a significant reduction in regional exhumation after ~28 Ma. AHe age profiles from the Marimaña and Maladeta regions suggest Late Oligocene to Middle Miocene times were characterised by a period of prolonged thermal and tectonic stability. Likewise, data from the Nogueres region indicate exhumation was likely to be continuous but slow and protracted during this interval. In contrast, data from the Barruera profile indicate the region exhumed rapidly through AFT annealing temperatures during Early Miocene times (20±2 Ma).

Again, it is difficult to reconcile the thermochronological data with published models of Pyrenean development (e.g. Fig. 2.16). Exhumational processes in the central Pyrenees have previously been regarded to have declined to negligible values by Late Oligocene and Early Miocene times, following a regional cessation in tectonics and exhumation (Fig. 2.19) (Fitzgerald et al., 1999). Data from this study indicate exhumation was maintained or rejuvenated in the Barruera region for an additional period of up to ~6 Myr. Importantly, these ages concur with previous sea-floor spreading data which indicate convergence between the Iberian and Eurasian plate was maintained until at least 23 Ma (Srivistava et al., 1990; Roest and Srivistava, 1991). As the 20±2 Ma signal does not appear to be recorded within the two northerly profiles or in the Nogueres profile to the south, it suggests the latest stages of orogenic exhumation may have been largely restricted to the intervening central area. Bearing this in mind, it is difficult to envisage how large-scale external forcings, such as climatic shifts or fluvial reorganisations, could have promoted processes of erosional denudation within such a small spatial domain. Instead, a mechanism is required by which exhumation could be localised in the central Barruera region.

The geological field data indicates that, unlike the Marimaña and Maladeta regions, the Barruera Massif is not bound by steeply dipping thrust surfaces that could have acted to preferentially uplift it. The Estet thrust to the south (section 5.2.4) dips at a relatively shallow angle and shows no evidence of activity within the brittle crustal realm. Previous palaeomagnetic studies indicate the structure was likely to have been initiated at a low angle and has since been deformed by localised doming with a N-S wavelength of approximately ~10 km (McClelland and McCaig, 1989). This doming has previously been regarded to have developed due to deformation on structurally lower thrust sheets during the formation of the Axial Zone antiformal stack (McClelland and McCaig, 1989). Field data from the Nogueres Zone and Senterada Basin (section 5.3.2 and 5.4.2) depict the deformation of Late Oligocene and Early Miocene age sediments by sets of small out-of-syncline thrusts, which are interpreted to have developed during the steepening of the Nogueres region and tightening of a regional synform. Syn-sedimentary deformation at the northern onlap surface of the Senterada Basin is consistent with the southward rotation of the Nogueres Zone during Early Miocene times.

If internal deformation below the Antiformal stack was maintained or rejuvenated until Early Miocene times, the Barruera region, which is located near the culmination of the antiform, could have undergone localised doming and rock uplift after the regions to the north and south had entered a period of relative thermal and tectonic stability (**Fig. 6.1c-d & 6.2b**). Rock uplift associated with doming would have promoted additional exhumation in the core region, centred around the Barruera Massif, and could have caused the cooling of the Barruera profile through the AFT closure isotherms. This would be consistent with the Barruera thermochronological data which depict a rapid transition through the thermal profile at this time. Areas located toward the periphery of the dome, such as the Nogueres Zone or Maladeta region, would have been rotated away from the locus of deformation, though would have undergone relatively little additional rock uplift. This is consistent with the thermochronological data and with the well-constrained timing of rotation and deformation of the Nogueres Zone and onlapping sediments of the Senterada Basin. (see section 6.4.3 for further discussion).

Sedimentological data from the basal units of the Senterada Basin depict two very distinct facies bound by a sharp conformable surface of Late Oligocene to Early Miocene age (section 5.4.1 & Fig. 5.31). The lowermost units are characterised by thick beds of clast-supported, cobble- to boulder-grade, well-sorted conglomerates which are massively dominated by extremely well-rounded granitic and Hercynian basement clasts. These pass abruptly into facies more typical of the upper basin-fill comprising interbedded sequences of cross-bedded sands, silts and well-sorted, cross-bedded pebble grade conglomerates, the provenance of which is massively dominated by Permian and Triassic cover rock clasts. This significant and rapid transition in the sedimentological character of the basin-fill may represent the transition from the early stages of growth of the mountain belt, which was accommodated by emergent out-of-sequence thrusts that exhumed granite-rich basement in the orogenic interior, to the later stages, which was accommodated by doming of granite-poor basement thrust sheets in more proximal regions. This would imply a major reorganisation of catchment headwaters and physiographic boundaries at this time.

It is also of importance to note that the exhumational event documented at 20±2 Ma in the Barruera region is the latest recorded orogenic deformation in the Pyrenees, post-dating deformation at the southern frontal thrust by up to 6 Myr (Meigs, 1997). Previous workers have postulated that the thick sediment draping of the southern fold and thrust belt, associated with the closure and infilling of the Ebro Basin, may have been important in lowering surface taper of the entire Pyrenean thrust wedge and, hence, modifying its growth (Coney et al., 1996; Sinclair et al., submitted). Analogue models have demonstrated that by decreasing thrust wedge surface taper angles, by for example sediment drapes, internal thickening at the rear of the orogenic wedge is encouraged and accretion and deformation at the front of the wedge discouraged (Storti and McClay, 1995). This is consistent with the shift of wedge deformation to the orogenic interior during Oligocene and Lower Miocene times as the synorogenic conglomerates, such as those preserved in the Senterada and Poble Basins, onlapped into the mountain belt.

6.3 Localised erosion in post-Middle Miocene times

AHe data and thermal modelling from the Maladeta and Barruera regions are consistent with an abrupt rejuvenation of accelerated exhumation at 10±2 Ma. The data from the Marimaña profile is ambiguous, though PeCube modelling suggests either the region did not undergo rejuvenated exhumation at 10±2 Ma, or did so but at significantly slower rates that in the Maladeta region. The regional patterns of exhumation are seemingly in conflict with empirical and theoretical models of the decay of post-tectonic, high-relief topography, which indicate that erosion occurs over protracted time periods at steady, slow rates which exponentially decline as topographic relief is progressively reduced (Pinet and Souriau, 1988; Pazzaglia and Brandon, 1996; Baldwin et al., 2003; Carrapa et al., 2003).

As noted in the previous section, plate convergence between Iberia and Eurasia, the driving force behind growth of the Pyrenean orogen, had ceased more than ten million years previously, during lowermost Miocene times. It is difficult, therefore, to attribute the rejuvenation of exhumation to tectonically-forced erosional denudation. Instead, an external forcing on the system must be considered.

Previous workers have documented dramatic increases in sediment accumulation rates and grain sizes, associated with enhanced rates of erosional denudation, from a number of tectonically-inactive mountain systems (Zhang et al., 2001). These have been linked to globally synchronous climatic instabilities, as documented in oxygen and carbon isotopes from Cenozoic deep-sea cores (Zhang et al., 2001). This is perhaps of particular importance for European mountain belts as palaeoceanographic records indicate that the reorganisation of ocean circulation systems likely enhanced atmospheric moisture content within the northern hemisphere (Haug and Tiedemann, 1998; Driscoll and Haug, 1998) and, by inference, the erosive capacity of surface processes (Cederbom et al., 2004). However, these climatic aberrations were restricted to Pliocene times (Zhang et al., 2001) and, thus, significantly post-date the documented 10±2 Ma event.

Similarly, the lowering of the Mediterranean Sea during the Messinian salinity crisis generated an increase in erosion rates in regions located within the drainage catchments of the basin (e.g. Foeken et al., 2003). This period of regional base-level fall has also been linked to capture of the closed Ebro Basin and with predicted increases in erosional denudation within the Pyrenees (Coney et al., 1996; Fitzgerald et al., 1999). The Messinian event, however, commenced at 5.97 Ma (Krijgsman et al., 1999) and thus cannot have influenced the increase in erosional denudation documented by the AHe data.

Instead, it is possible that the opening of the Ebro drainage system occurred during Middle to Late Miocene times (Serravallian to Tortonian) and caused a dramatic drop in fluvial base-levels that resulted in rejuvenated exhumation of the previously blanketed southern margin of the Pyrenees (**Fig. 6.2c**). Piracy of the palaeo-lake during this period would promote a rapid and irreversible reorganisation of regional drainage systems within the Ebro Basin and it's fluvial catchments (Garcia-Castellanos et al., 2003). The significant elevation difference between the Middle Miocene age lacustrine succession preserved on isolated hilltops within the modern basin (Pérez-Rivarés, 2002) and the Mediterranean Sea would represent a large and abrupt base-level drop of at least 800 m. The clastic infill of the basin would likely dictate that fluvial incision within the Ebro channel network, generated by the significantly lowered base-level, would follow transport-limited behaviour (Snow & Slingerland, 1987; Willgoose et al., 1991; Tucker & Whipple, 2002) and would rapidly propagate into the catchment hinterlands on the southern flank of the Pyrenees. Low-temperature thermochronometers within the mountain belt would thus record the thermal response to the abrupt acceleration of erosion processes and the subsequent thermal relaxation in the upper crust after the event. AHe ages from the Maladeta and Barruera profile suggest this denudation-induced thermal aberration was recorded in the central Pyrenees at 10±2 Ma. Drainage systems outside of the Ebro catchment, or north of the Pyrenean drainage divide, would be unaffected by this event. This is consistent with an apparent asymmetric distribution of exhumation focused upon the southern flank of the range, with less total exhumation recorded within the Marimañi profile.

The amount of exhumation at ~10 Ma required to cool the lower section of the Maladeta profile, which accounts for approximately 300 vertical metres of the rock column, through partial retention temperatures can be calculated for a given set of thermal parameters; for a geothermal gradient of ~30 to 35°Ckm^{-1} and a PRZ temperature range of ~40 to 80°C (Ehlers and Farley, 2003), between 1440 and 1630 m of exhumation must have occurred at this time. The vertical difference in elevation between the highest preserved Miocene sedimentary fill of the Ebro Basin and the modern sea level of the Mediterranean is approximately 1650 m in the central Nogueres Zone, south of the town of Geri de la Sal. If it is assumed this represents the maximum elevation of Ebro basin infill, and that it projected southwards to the Iberian Range and Catalan Coastal Range, which are of similar modern elevations, then fluvial incision and downcutting during the middle Miocene to near sea-level elevations (~100 m in the channel base of the central Ebro Basin) could have generated localised exhumation of up to ~1500 m. This scenario would suggest that the Miocene-age lacustrine deposits (~14 Ma: Peres-Rivarez et al., 2002) preserved on isolated hilltops in the central Ebro Basin do not represent the uppermost middle Miocene-age basin fill. With the removal of rock/sediment mass from the Ebro Basin would be an associated flexural isostatic rebound that would cause localised rock uplift, with respect to the geoid, and generate an additional increase in the rates of local exhumation. However, the absolute value of isostatic flexural rebound, and the implicit additional exhumation, cannot be reliably constrained with the available data.

A significant time-lag is assumed between capture of the basin drainage, the culmination of maximum fluvial incision efficiency, and the propagation of regressive erosion up the fluvial network to the orogen (Kooi & Beaumont, 1996; Garcia-Castellanos et al., 2003). As this lag is unconstrained, the timing of the basin opening can only be bracketed between the age of the youngest lacustrine sediments in the Ebro Basin (~14 Ma; Pérez-Rivarés, 2002) and the age of accelerated exhumation within the mountain belt (10±2 Ma), or during Serravallian to Tortonian times. This is compatible with both geodynamical numerical simulations of Ebro drainage evolution that predict basin capture between 13 and 8.5 Ma (Garcia-Castellanos et al., 2003), and with a number of independent observations on the offshore sediment record in the Ebro Delta and València Trough (Fig. 5.1.1) (e.g. Johns et al., 1989; Bartrina et al., 1992). This is the region in which the modern fluvial system flows through the Catalan Coastal Range, and where, by inference, the topographic barrier enclosing the isolated Ebro Basin was initially breached to the Mediterranean Sea (Coney et al., 1996).

6.4 Discussion

Inherent in achieving scientifically rigorous conclusions is the necessity to consider potential ambiguities, weaknesses or limitations in the presented models and to consider how future work might better constrain these issues. Within the three mechanisms interpreted to have influenced the localisation of erosional denudation, described above, there are a number of contentious points which warrant acknowledgement and, in the future, additional constraint.

6.4.1 Exhumation

The fundamental assumptions applied to derive information on exhumation from the thermochronological data, as outlined in Chapter 3, enabled a range of exhumation values and rates to be estimated according to a variety of reasonable input parameters. This approach was adopted as there were no independent constraints for parameters such as the palaeo-geothermal gradient, palaeo-topographic relief and orogen-scale macro-geomorphic form. A direct consequence of this approach, however, was that the minimum and maximum estimates of exhumation for specific intervals were relatively large. This did not preclude regional interpretations of the overall exhumation history but made quantitative comparisons and estimates of limited use. An integrated sensitivity study, assessing the interaction between variables such as the thermal regime, cooling rate, closure temperature and changing topography, would have provided additional insights into absolute closure depths at specific temporal intervals and enabled the range of exhumation values to be more tightly constrained for a given set of parameters. To some extent, this was achieved for the latest part of the exhumational history using PeCube, and the assumptions used were largely validated, though a more advanced study would be highly beneficial. Likewise, a sensitivity study that assessed the impact of an evolving, non-steady state, macro-geomorphic form on the thermal regime, and derived thermochronometric ages, would also enable the critical assessment of some of the assumptions outlined in Chapter 3.

Implicit in the procedure for calculating exhumation from a given closure depth to the surface is that the rock particles were transported along vertical kinematic geometries, and that erosion occurred perpendicular to that path. However, as inferred in the pre-Upper Oligocene interval (Model a: Fig. 6.2a), rock uplift was likely to have been controlled by breach thrusts that dipped at between 50 and 70° within the central Axial Zone. The implications of oblique rock trajectories for estimating exhumation values is of most importance for low-angle structures and becomes decreasingly significant at angles higher than ~20° (Morris et al., 1998; Batt et al., 2001). As the structures that are inferred to have controlled rock uplift trajectories during the pre-Upper Oligocene interval had a steeply-dipping attitude (~60°) similar to the present-day orientation (McClelland and McCaig, 1989), the non-vertical trajectories are unlikely to have greatly influenced the overall amount of exhumation. Nevertheless, the application of thermotectonic modelling (e.g. Ehlers et al., 2003; Ehlers and Farley, 2003), combining both the structural framework and the thermochronological data, would provide quantitative estimates of these effects. This would also provide an opportunity to estimate the magnitude of the thermal perturbation, caused by sustained differential uplift along discrete crustal dislocation surfaces, and to assess the potential impact on thermochronological samples transiting that thermal regime (Ehlers et al., 2003).

6.4.2 Thermochronological data

The suite of thermochronological data presented in this study comprehensively documents the exhumation history of a number of time intervals during the orogenic and post-orogenic periods. However, there are three specific stages of the exhumational record which, owing to the lack of thermochronological constraint, prohibit unambiguous interpretation or merit further thermochronological analyses.

Firstly, the early stages of the documented record, during Early to Middle Eocene times, are constrained only by single-elevation ZFT ages. These provide a minimum age for the onset of exhumation in the sampling regions and enable regional comparisons between areas with Pyrenean and pre-Pyrenean ages. However, it does not provide information on the manner in which exhumation was taking place at that time or, for the samples with pre-Pyrenean ages, at what part of the thermal regime above the ZFT closure temperature they resided. These issues generate a degree of uncertainty in interpreting the early histories and in deriving well-constrained exhumational differentials between adjacent sites from this early period. Additional ZFT analysis of samples from the remaining vertical profiles, perhaps combined with the application of an additional thermochronometer with an intermediate temperature sensitivity (e.g. zircon (U-Th)/He: T_c = ~170-190°C, Reiners et al., 2004), would provide considerably more constraint on the exhumational record at that time. Of particular benefit of applying these additional analyses would be to document the exhumational history of the Barruera region prior to Early Miocene times. This early history is poorly constrained by the current data, other than being bracketed between the AFT and ZFT partial annealing zones. If it could be demonstrated that the ~30 Ma exhumation event, as documented in the Marimaña/Maladeta regions, had little impact in the Barruera region, then the 'Breach Thrust Model' (Fig. 6.2a) would be well supported. If, on the other hand, the exhumation event was of a similar magnitude in the Barruera region, the spatial differential during Early Oligocene times would have been considerably less.

Exhumation at ~20 Ma in the interior of the mountain belt is only documented within the Barruera profile. The relatively short vertical span of this profile renders it difficult to accurately quantify the characteristics and magnitude of this event. By providing additional AFT ages from higher and lower elevations in the vicinity, the amount of exhumation during this interval could be better constrained. This is of particular importance because the interpreted model involving the late-stage development of the antiformal stack (Model b: 6.2b) assumes exhumation was of a relatively small vertical magnitude, as a large exhumational event is more likely to have been documented within the surrounding Maladeta and Nogueres profiles ie. On the limbs of a large wavelength antiformal stack.

The reactivation of exhumation processes within the post-orogenic period is reasonably well constrained by the thermochronological data. Despite the poor reproducibility of a number of samples in the Maladeta profile, the timing of the event at 10 Ma is also well constrained and consistent with the thermochronological modelling. The interpretation of rejuvenated south-draining fluvial networks influencing the exhumation patterns (Model c: 6.2c), however, is based upon an inferred physical relationship between orogenic exhumation and synchronous geological events in the distal regions of the foreland. This inference is based upon the interaction between a number of fundamental physical processes and has been to some extent corroborated in numerical simulations of the Ebro system (Garcia-Castellanos et al., 2003). Nevertheless, through the application of additional (U-Th)/He analsyses, the physical linkage could be further confirmed or negated. This could be achieved by testing the implicit predictions of the proposed model, whereby all upper, mountainous source regions of the Ebro river (e.g. southern flank of the Pyrenees, northeastern flank of the Iberian Range, northwestern flank of the Catalan Coastal Range) should record an acceleration of exhumation at approximately 10 Ma. Documentation of this event in these areas would provide considerable constraint and support for the proposed model.

6.4.3 Field data

The field data presented in this study enables the thermochronological ages to be interpreted within a rigid structural framework and, hence, to generate coherent models of the exhumational histories. However, a number of the interpretations from field localities would greatly benefit from additional data in order to minimise ambiguity or uncertainty.

In the northern areas, the presence of brittle shear structures, oriented at angles consistent with their development as secondary structures to adjacent major thrusts, is used to infer active thrust activity within the uppermost crustal realm and through low-temperature thermochronological closure isotherms. Timing of thrust activity, and the thermo-barometric regime in which it occurred, could be more tightly constrained by isotopic analysis (e.g. Rb-Sr or ^{40}Ar-^{39}Ar) of altered wall rocks, shear zone accessory minerals, or associated vein systems around the thrust surfaces (McCaig And Miller, 1986; Wayne and McCaig, 1998). Additional confirmation of active displacement within the brittle zone could also be provided by analysis of microstructural deformation fabrics within oriented samples in the thrust zone region (McCaig and Miller, 1986; Hanmer and Passchier, 1991).

The timing of deformation associated with the ~20 Ma exhumation event is constrained by the southward rotation and overthrusting of magnetostratigraphically-dated Miocene-age sediments. Owing to the poor preservation of the sediments of this age, however, it is difficult to quantify the magnitude and regional impact of deformation at this time. The south-vergent thrusts are interpreted to have formed during the steepening of the Nogueres Zone region and cause the deformation of the Senterada Basin onlap surface. This inferred relationship would be better understood by mapping of such structures over the entire Nogueres region, enabling a more critical assessment of their role in Nogueres deformation at ~20 Ma.

The link between orogenic exhumation and Ebro Basin opening at approximately 10 Ma is provided by data documenting the substantial flux of sediment into the offshore Valencia Trough at this time. The orientation of progradational advance suggest the flux was sourced from a region in the central Catalan Coastal Ranges. As noted previously, the large sediment volume is unlikely to be derived from a spatially-limited fluvial system draining only the basinward flank of the Catalan Coastal Range (Archie and Evans, 2002), and instead is likely to represent a breach in the topographic barrier of the Ebro Basin and the seaward transport of the infilling sediments. The provision of accurate provenance data on the Middle Miocene offshore sediments would allow this inference to be properly addressed.

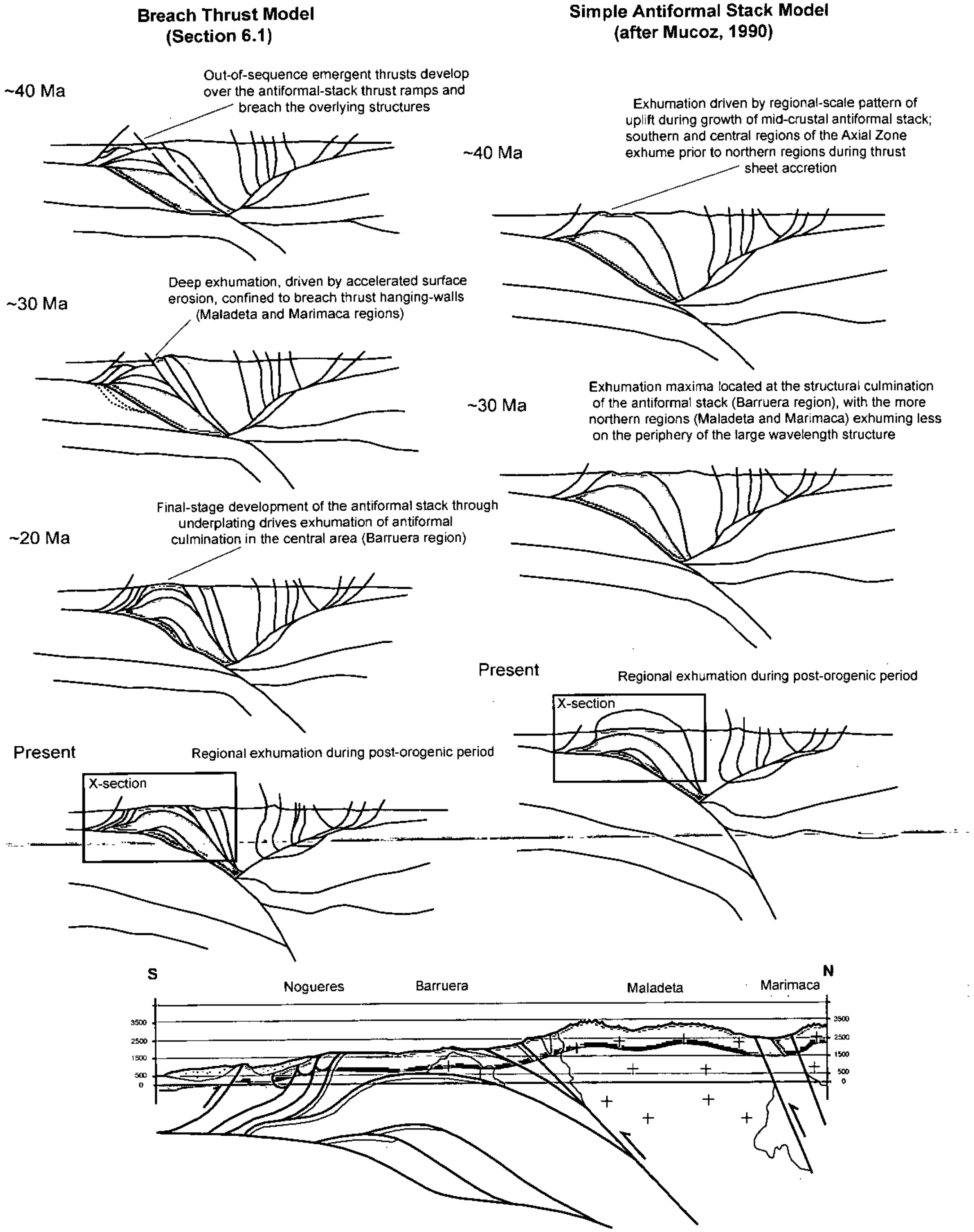

Breach Thrust Model (Section 6.1)

~40 Ma: Out-of-sequence emergent thrusts develop over the antiformal-stack thrust ramps and breach the overlying structures

~30 Ma: Deep exhumation, driven by accelerated surface erosion, confined to breach thrust hanging-walls (Maladeta and Marimaca regions)

~20 Ma: Final-stage development of the antiformal stack through underplating drives exhumation of antiformal culmination in the central area (Barruera region)

Present: Regional exhumation during post-orogenic period

Simple Antiformal Stack Model (after Mucoz, 1990)

~40 Ma: Exhumation driven by regional-scale pattern of uplift during growth of mid-crustal antiformal stack; southern and central regions of the Axial Zone exhume prior to northern regions during thrust sheet accretion

~30 Ma: Exhumation maxima located at the structural culmination of the antiformal stack (Barruera region), with the more northern regions (Maladeta and Marimaca) exhuming less on the periphery of the large wavelength structure

Present: Regional exhumation during post-orogenic period

Figure 6.1 A comparison of two models of tectonic evolution of the central Pyrenees; (i) The breach thrust model, as described in Chapter 6, suggests exhumation of the Maladeta and Marimaca regions during Oligocene times was principally accommodated by large out-of-sequence thrusting in the orogenic interior. By early Miocene times exhumation was driven by tectonic accretion or underplating during the final development of the Axial Zone antiformal stack. This proposed tectonic evolution is compatible with the deep exhumation of the Maladeta and Marimaca regions through ZFT/AFT Tc prior to ~30 Ma whilst the structural culmination of the antiformal stack (Barruera region) was retained at intermediate temperatures until ~20 Ma. Similar tectonic scenarios of internal emergent thrusting from thrust ramps in large-scale antiformal stacks have also been proposed in the Himalayan (Wobus et al., 2003) and Sevier orogens (DeCelles and Mitra, 1995). (ii) Antiformal stack model (Mucoz, 1990).

Fig. 6.1

Model of tectonic evolution of the central Pyrenees

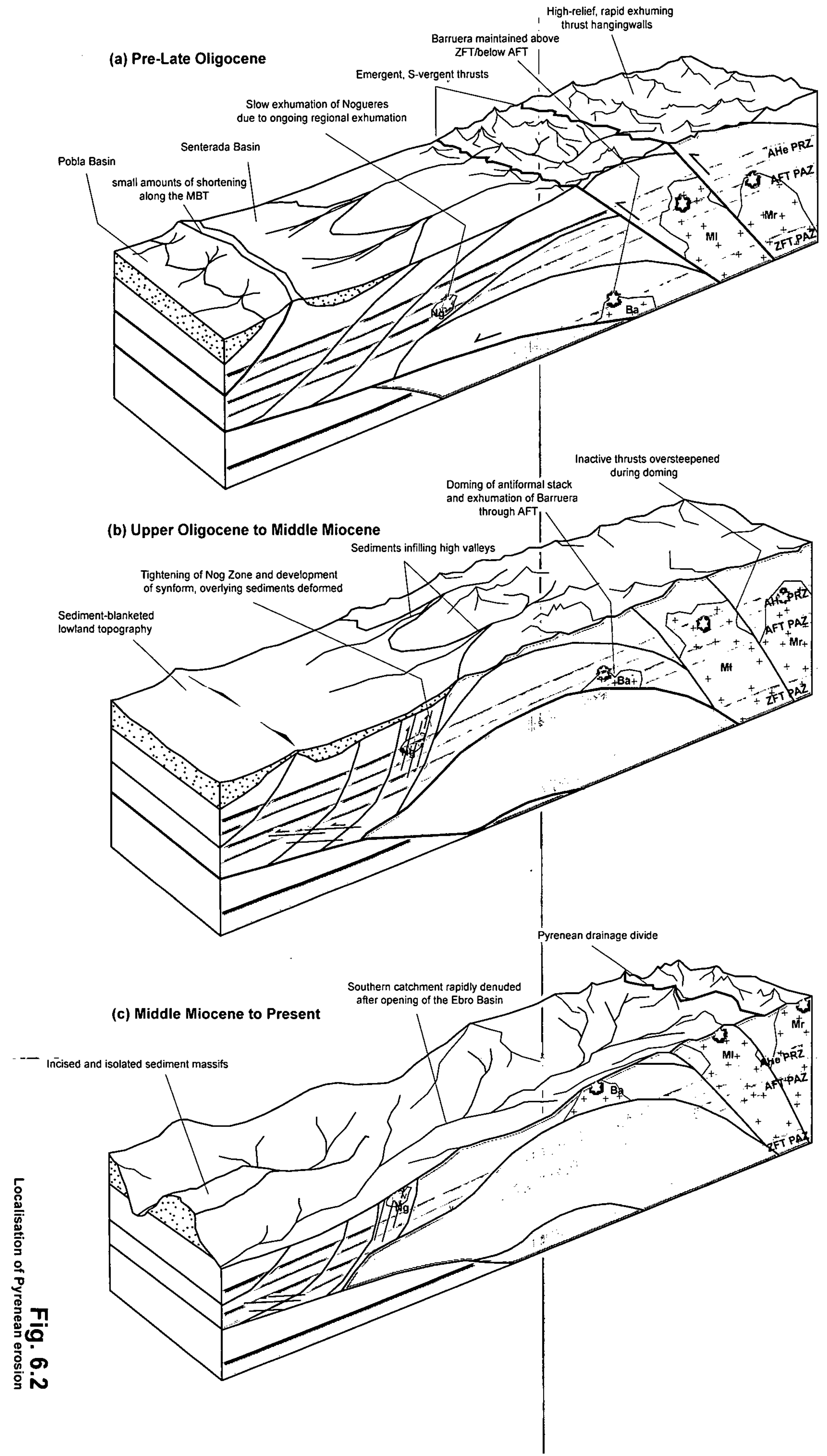

Figure 6.2 Summary diagram of the tectonic and topographic evolution of the central Pyrenees during and after Alpine orogenesis. (a) Prior to Late Oligocene times, exhumation was principally accommodated by large-scale out-of-sequence thrusts that were emergent to the surface. These enabled the Maladeta and Marimaca regions to exhume from below the ZFT PAZ to above the AFT PAZ at this time. More regional exhumation was also maintained across the southern mountain belt, progressively unroofing the Barruera and Nogueres regions, though from significantly shallower depths than in the north. This period of time likely corresponded to the generation of high topographic relief at the locus of the thrust hangingwalls and the delivery of large volumes of basement-derived clastic detritus toward the southern foreland. (b) During Upper Oligocene and Lower Miocene times, exhumation was principally driven by tectonic accretion of small thrust sheets below the Axial Zone antiformal stack causing uplift and exhumation in the central region. This likely caused the southward rotation and gentle deformation of the peripheral regions, such as the Nogueres Zone, at ~20 Ma. This period of time likely corresponded to a southward shift in the hinterlands of the southward-draining catchments and caused a change in the provenance of the southward flux of sedimentary detritus. (c) After Middle Miocene times the primary driving force of orogenic growth, the convergence of the Iberian and Eurasian plates, had ceased and the 'post-orogenic' period had commenced. Exhumation during this interval was controlled by externally-forced mechanisms. At 10 Ma the previously internally-drained Ebro Basin was opened to the Mediterranean and caused a regional drop in the base level of southward-draining fluvial systems. Erosion processes abruptly accelerated and caused the rapid exhumation of the southern flank of the range. Exhumation of the northern flank would have remained unaffected by this event, though the increase in relief in the south would promote the northward migration of the drainage divide. Exhumation since this time is likely to have been slow and continuous, though may have been temporarily accelerated by events such as the Messinian Salinity Crisis (~6 Ma) or by subsequent climatic instabilities that caused an increase in precipitation or glacial erosion.

Chapter 7

Summary and Conclusions

Objectives: The objectives of this chapter are to summarise the mechanisms through which the spatial and temporal distribution of erosional denudation was controlled during and after Pyrenean orogenesis, to consider the wider implications of this work, and to outline the main conclusions from this study.

Chapter 7 – Summary and Conclusions

7.1 Summary

In this thesis, the orogenic evolution and exhumational record of the Pyrenees has been investigated. The primary objectives of the study were (i) to document the magnitude and spatial distribution of Pyrenean exhumation gradients, as defined by variable erosional denudation, during active orogenesis and during the post-orogenic period, (ii) to investigate the mechanisms that may have controlled or influenced the spatial localisation of erosional denudation, (iii) to consider the implications for the tectonic evolution of the orogen. To this aim, a multidisciplinary approach was adopted.

In Chapters 1 and 2, an outline of this thesis and an introduction to the geological setting of the central Pyrenees is presented. Published geodynamical models of orogenic evolution are discussed along with thermochronological data that has been used to constrain them. In Chapter 3, the basic principles of (U-Th)/He and fission track thermochronology are summarised and the underlying assumptions used in applying the techniques are outlined. The specific methodology and assumptions used in this study are also described in detail.

In Chapter 4, the long-term cooling histories of four specific regions within the south central Pyrenees are presented, as documented by apatite (U/Th)/He, apatite fission track and zircon fission track thermochronology. The derived thermal histories were modelled, using AFTSolve and DeComp, and the topographic and thermal system synthetically reproduced using PeCube. In Chapter 5, new geological field data was collated with published material on the major tectonic contacts between the four main sampling regions and from the offshore sedimentary record in the Valencia Trough.

In Chapter 6, the thermochronological data was synthesised with the geological field data and used to develop viable models of the different mechanisms that controlled the distribution of erosional denudation within the Pyrenees. The compiled data indicate three discrete mechanisms through which this was achieved during the evolution of the orogen:

(i) The main phase of orogenic growth and exhumation was focused in the northern central Axial Zone, as documented in the Marimaña and Maladeta profiles, and culminated with a period of rapid unroofing during Early Oligocene times. During this interval the central and southern flank of the Axial Zone, recorded by the Nogueres and Barruera data, cooled slowly and progressively, with significantly less overall exhumation over the same time period. The geological data are consistent with the development or reactivation of steeply-dipping breach thrusts that partitioned the Marimaña and Maladeta regions from the central and southern area. Shear structures surrounding the thrusts indicate active fault displacement was occurring within a brittle regime in the shallow crustal realm. The thermal field in this section of the crust contains the relevant closure isotherms of the thermochronometers used in this study. The preserved exhumation gradient, therefore, may be attributed to tectonically-forced rock uplift along the hangingwalls of emergent thrusts on the northern flank of the Axial Zone antiformal stack. This may have resulted in a large amount of tectonic shortening not being transmitted to the southern fold and thrust belt but, instead, partitioned within the inner regions of the orogen. This is consistent with growth strata along the Morreres Backthrust, which depict very little tectonic shortening during the main period of orogenic growth of the mountain belt.

(ii) During Early Miocene times, focused exhumation in the central Axial zone, as documented in the Barruera region, was maintained or rejuvenated until at least 20±2 Ma, though this is not recorded in the surrounding regions. These ages concur with previous sea-floor spreading data which indicate convergence between the Iberian and Eurasian plate was maintained until Lower Miocene times (Srivistava et al., 1990; Roest and Srivistava, 1991). The 20±2 Ma signal is interpreted to be a response to tectonically-forced rock uplift during localised doming of the Barruera region, likely associated with the final stages of thrust sheet accretion below the Axial Zone antiformal stack. The geometry of the antiformal stack in the modern setting has been imaged along the ECORS profile. The geological field data are consistent with deformation of the Nogueres Zone at this time, causing the southward rotation and steepening of Nogueres Zone structures and gentle deformation of the onlapping sediments.

(iii) During Late Miocene times, after the cessation of plate convergence, rapid exhumation was abruptly rejuvenated in the Maladeta and Barruera regions. The data from the Marimaña profile is ambiguous, though modelling indicates exhumation since Middle Miocene times has been comparatively less in the northern area. Geological data from the Ebro Basin indicate a period of endorheic (internal) drainage occurred until ~14 Ma. At this time the base-level of the southern region was at least 800 m higher than the present level of the Mediterranean Sea. Interpreted seismic sections and drill data from the offshore sedimentary record in the Valencia Trough are consistent with a large influx of siliciclastic detritus from the Ebro Basin during Middle and Late Miocene times (Serravallian and Tortonian times). The 10±2 Ma signal is thus interpreted to mark the onset of a period of rapid denudation of the Miocene land surface caused by the abrupt fall in regional baselevel after the opening of the Ebro Basin to the Mediterranean Sea.

7.2 Wider context for orogenic studies

Previous models that interpreted exhumation during active Pyrenean orogenesis to be solely controlled through distributed, large-wavelength rock uplift, associated with mid-crustal internal thickening, are difficult to reconcile with the work presented in this thesis (Muñoz, 1992; Fitzgerald et al., 1999; Beaumont et al., 2000). Instead it is likely that the distribution of exhumation was largely governed by the spatial and temporal localisation of erosional denudation within discrete domains by a number of specific mechanical controls. The data presented here represent a significant step forward in understanding the evolution of the central Pyrenean orogen. It considerably embellishes existing thermochronological datasets that have been used to constrain the mechanical development of the orogenic interior. It is important to recognise, however, that in addition to contributing to our understanding of the central Pyrenean system, this study also has wider applications to more generic studies investigating orogenic growth and decay.

Numerical studies which model the interaction of the processes of erosion, sedimentation and accretionary growth, and their control on the gross geomorphic natural tendencies of comressional regimes, produce provocative but largely speculative predictions of orogenic evolution (e.g. Beaumont et al., 1999; Willet, 1999; Beaumont et al., 2000; Batt et al., 2001; Willet and Brandon, 2002; Naylor et al., in press). Continuum models are often used to make quantitative predictions of cooling paths, and hence thermochronometric age distributions, across orogens (Batt et al., 2001) and these are applied to assess the cumulative flux balance during mountain belt development (Batt et al., 2001; Willet and Brandon, 2002). However, owing to the scale at which the systems are modelled and the inherent need to reduce the natural complexity, the predictions are extreme simplifications of the natural systems.

By constraining the specific mechanisms through which mass flux is controlled at the regional scale, enables the gaps to be bridged between geological reconstructions and orogen-scale conceptual model predictions. By understanding, for example, the spatial and temporal evolution of exhumation associated with out-of-sequence thrusting during Lower Oligocene times within the Pyrenean orogenic interior, empirical constraints are placed upon the mechanical behaviour and flux partitioning in the evolving orogenic thrust wedge. These are the physical processes and specific mechanisms which cannot yet be addressed by the relatively coarse resolution of numerically-modelled systems, though they are the mechanisms through which the predicted cumulative flux paths are physically accommodated in natural orogenic systems such as the Pyrenees.

The lower temperature thermochronological data presented in this thesis has similarly provided a significant contribution to our understanding of the Pyrenees, though during the post-orogenic period. Empirical and theoretical models of post-orogenic decay of high-relief topography indicate exhumation is expected to occur over protracted periods at slow rates and exponentially decline as topography becomes increasingly subdued (Pinet and Souriau, 1988; Pazzaglia and Brandon, 1996; Baldwin et al., 2003; Reiners et al., 2003). The data from this study, however, indicate this predicted pattern was not followed in the Pyrenees and, instead, exhumation was abruptly rejuvenated and spatially partitioned by a specific, externally-forced mechansism at ~10 Ma.

Compilation of the post-orogenic exhumation histories with other geological data from the region provides clear insights into the landscape and drainage evolution of the Ebro system after the decline of major tectonics. Of additional significance, however, is the applicability of this work for providing empirical constraints on numerical model simulations of the Ebro fluvial network (e.g. Garcia-Castellanos et al., 2003; Loget et al., 2004). Through continued investigation, through both data collection and numerical model reconstructions of specific regions such as the Ebro, more generic issues such as the sensitivity and interplay between base-level variations, fluvial erosion and landscape evolution may be better assessed (e.g. Tucker and Whipple, 2002; Baldwin et al., 2003).

7.3 Conclusions

1. The application of three thermochronometric systems (apatite (U-Th)/He, apatite fission track and zircon fission track), comprising a range of temperature sensitivities, and vertical-profile sampling strategies, was used to characterise the spatial and temporal distribution of exhumation gradients within the central Pyrenees. Results indicate the history of erosional denudation during and after orogenesis is considerably more complex than previous models envisaged and is

governed by a number of discrete physical mechanisms. During active orogenesis, exhumation was controlled by the strongly spatially variable distribution of tectonically-forced rock uplift and the associated control on erosional denudation. During the post-orogenic period, spatial variability in exhumation was maintained, but was governed through the interaction with surface processes and a rejuvenated fluvial network on the southern flank;

2. Compilation of ZFT and AFT vertical profile data indicate that the locus of maximum exhumation within the central Pyrenees is located to the north of the culmination of the antiformal stack and comprises the Marimaña and Maladeta regions. Total exhumation in these areas is between approximately six to ten kilometres since Lower Eocene times. The central and southern regions of the Axial Zone have been retained above ZFT annealing temperatures throughout orogenesis, and hence have undergone significantly less exhumation;

3. Exhumation in the northern region culminated with a period of extremely rapid unroofing during Lower Oligocene times. This event is not recorded within the central and southern regions. This exhumation gradient is attributable to localised, tectonically-forced rock uplift of the structural hangingwalls of emergent south-vergent breach thrusts. Documentation of the northern contact between the orogenic interior and the southern fold and thrust belt, along the Morreres Backthrust, indicates large-scale tectonic shortening during this interval was principally accommodated within the orogenic interior and not transmitted toward the frontal regions of the orogenic wedge;

4. Vertical profile AFT data indicate exhumation was rejuvenated in the central Barruera region during Lower Miocene times. This event is not recorded in the thermochronological data from the areas to the north or south. This exhumation gradient is attributable to localised, tectonically-forced rock uplift at the crest of the Axial Zone antiformal stack and likely represents the final stage of active orogenic growth. Deformation and southward rotation in the Nogueres Zone to the south is consistent with Axial Zone doming at this time. The accommodation of late-stage deformation and internal thickening in the orogenic interior during Oligocene and

Lower Miocene times may be linked to the decrease in surface taper angle of the orogenic wedge due to sediment blanketing of the southern fold and thrust belt;

5. AHe age-elevation profiles and thermal modelling from samples in the Maladeta region record a period of accelerated exhumation after the cessation of major tectonics at 10±2 Ma. Thermal modelling of AHe ages from the Marimaña region, located immediately north of the main drainage divide, indicate lower rates of exhumation during the same interval. The 10±2 Ma event is linked to the opening of the internally-drained Ebro Basin to the Mediterranean Sea, by fluvial breaching of the intervening topographic barrier during Middle to Upper Miocene times. This abrupt fall in regional base-level and reorganisation of fluvial systems promoted accelerated rates of fluvial incision and erosional denudation within the basin and southern flank of the orogenic hinterland. Offshore sediment records, depicting the synchronous influx of large siliciclastic prograding wedges into the Adjacent Valencia Trough, support this model.

References

References

Albarede, F. and Michard-Vitrac, A., 1978, Age and significance of North Pyrenean metamorphism: Earth and Planetary Science Letters, v. 40, p. 327-332

Anadón, P., Julià, R., Roca, E. and Rosell, L., 1989a, Lacustrine oil-shale basins in Tertiary grabens from NE Spain (western European rift system): Palaeogeography, Palaeoclimatology, Palaeoecology, v. 70, p. 728

Anadón, P., Caberera, LL., Roca, E. and Rodríguez-Perea, A., 1989b, Sedimentary evolution in the València Trough: Terra Abstracts, v. 1, p. 46-47

Avouac, J. P. and Burov, E. B., 1996, Erosion as a driving mechanism of intracontinental mountain growth: Journal of Geophysical Research, v. 101, no. B8, p. 17747-17769

Baldwin, J. A., Whipple, K. X. and Tucker, G. E., 2003, Implications of the shear stress river incision model for the time-scale of post-orogenic decay of topography, Journal of Geophysical Research, v. 108, Bs, 2158

Balestrieri, M.L., Bernet, M., Brandon, M.T., Picotti, V., Reiners, P. and Zattin, M., 2003, Pliocene and Pleistocene exhumation and uplift of two key areas of the Northern Apennines: Quaternary International, v. 101-102, p. 67-73

Banks, C. J. and Warburton, J., 1986, 'Passive-roof' duplex geometry in the frontal structures of the Kirthar and Sulaiman mountain belts, Pakistan: Journal of Structural Geology, v. 8, p. 229-237

Barbarand, J., Carter, A., Wood, I.G. and Hurford, A.J., 2003, Compositional and structural control of apatite fission-track annealing: Chemical Geology, v. 198, p. 107-137

Barbarand, J., Hurford, T. and Carter, A., 2003, Variation in apatite fission-track length measurement: implications for thermal history modelling: Chemical Geology, v. 198, p. 77-106

Bates, M. P., 1989, Palaeomagnetic evidence for rotations and deformation in the Nogueres Zone, Central Southern Pyrenees, Spain: Journal of the Geological Society, London, v. 146, p. 459-476

Batt, G. E. and Braun, J., 1997, On the thermo-mechanical evolution of compressional orogens: Geophys. J. Int, v. 128, p. 364-382

Batt, G.E., Kohn, B.P., Braun, J., McDougall, I., and Ireland, T.R., 1999, New Insight into the dynamic development of the Southern Alps, New Zealand, from detailed thermochronological investigation of the Mataketake Range pegmatites, *in* Ring, U., Brandon, M.T., Lister, G.S., and Willett, S.D., Eds., Exhumation processes; normal faulting, ductile flow and erosion: Geological Society of London Special Publications, v. 154., p. 261-282

Batt, G. E. and Brandon, M. T., 2002, Lateral thinking: 2-D interpretation of thermochronology in convergent orogenic settings: Tectonophysics, v. 349, p. 185-201

Beamud, E., Garcés, M., Cabrera, L., Muñoz, J. A. and Almar, Y., 2003, A new middle to late Eocene continental chronostratigraphy from NE Spain: Earth and Planetary Science Letters, v. 216, p. 501-514

Beaumont, C., Fullsack, P. and Hamilton, J., 1991, Erosional control of active compressional orogens: *In*, Thrust Tectonics (Ed. by McClay, K.), Chapman and Hall, London, p. 1-18

Beaumont, C., Kooi, H. and Willet, S., 1999, Coupled tectonic-surface process models with applications to rifted margins and collisional orogens: In, Summerfield, M. A. (Ed.), Geomorphology and Global Tectonics, Wiley, New York, p. 29-55

Beaumont, C., Muñoz, J. A., Hamilton, J. and Fullsack, P., 2000, Factors controlling the Alpine evolution of the central Pyrenees inferred from a comparison of observations and geodynamical models: Journal of Geophysical Research, v. 105, no. B4, p. 8121-8145

Beaumont, C., Jamieson, R. A., Nguyen, M. H. and Lee, B., 2001, Himalayan tectonics explained by extrusion of a low-viscosity crustal channel coupled to focused surface denudation: Nature, v. 414, p. 738-742

Bentham, P. and Burbank, D. W., 1996, Chronology of Eocene foreland basin evolution along the western oblique margin of the south-central Pyrenees: *In*, Tertiary basins of Spain: The stratigraphic record of crustal kinematics (Eds P. F. Friend and C. J. Dario), Cambridge University Press, p. 144-152

Bernet, M., Brandon, M., Garver, J., Reiners, P. and Fitzgerald, P. G., 2002, Determining the zircon fission-track closure temperature: Contributions to tectonics and fission track dating in the Pacific northwest, Abstract Volume, Session No. 9, Geological Society of America Meeting Cordielerra Section), May 13-15

Besley, B. M. and Collinson, J. D., 1991, Volcanic and tectonic controls of lacustrine and alluvial sedimentation in the Stephanian coal-bearing sequence of the Malpás-Sort Basin, Catalonian Pyrenees: Sedimentology, v. 38, p. 3-26

Boschma, D., 1963, Successive Hercynian structures in some areas of the Central Pyrenees: Leidse Geologische Mededelingen, v. 28, p. 103-176

Boersma, K., Th., 1973, Devonian and Carboniferous conodont biostratigraphy, Central Spanish Pyrenees: Leidse Geologische Mededelingen, v. 49, p. 303-377

Boillot, G. and Capdevila, R., 1977, The Pyrenees, subduction and collision?: Earth and Planetary Science Letters, v. 35, p. 251-260

Boillet, G., 1984, Some remarks on the continental margins in the Aquitaine and French Pyrenees, Geological Magazine, v. 121, no. 5, p. 407-412

Bombolakis, E. G., 1994, Applicability of critical-wedge theories to foreland belts: Geology, v. 22, p. 535-538

Bond, R. M. G. and McClay, K. R., 1995, Inversion of a lower Cretaceous extensional basin, south central Pyrenees, Spain, *in* Buchanan, J. G. and Buchanan, P. G. (eds), 1995, Basin Inversion: Geological Society Special Publication, no. 88, p. 415-431

Brandon, M., Roden-Tice, M.K. and Garver, J.I., 1998, Late Cenozoic exhumation of the Cascadia accretionary wedge in the Olympic mountains, NW Washington State: Geological Society of America Bulletin, v. 110, p. 985-1009

Braun, J., 2002, Quantifying the effect of recent relief changes on age-elevation relationships: Earth and Planetary Science Letters, v. 200, p. 331-343

Brown, R.W. and Summerfield, M.A., 1997, Some uncertainties in the derivation of rates of denudation from thermochronologic data: Earth Surface Processes and Landforms, v. 22, p. 239-248

Brown, R.W., Summerfield, M.A. and Gleadow, A.J.W., 1994, Apatite fission track analysis: Its potential for the estimation of denudation rates and implications for models of long-term landscape development, *in* Kirkby, M.J. (Ed), 1994, Process models and theoretical geomorphology: John Wiley and Sons Ltd

Burbank, D. W. and Beck, R. A., 1991, Rapid, long-term rates of denudation: Geology, v. 19, p. 1169-1172

Burbank, D. W., Vergés, J., Muñoz, J. A. and Bentham, P., 1992, Coeval hindward- and forward-imbricating thrusting in the south-central Pyrenees, Spain: Timing and rates of shortening and deposition: Geological Society of America Bulletin, v. 104, p. 3-17

Burbank, D. W. and Pinter, N., 1999, Landscape evolution: the interactions of tectonics and surface processes: Basin Research, v. 11, p. 1-6

Burbank, D. W. and Anderson, R. S., 2001, Tectonic Geomorphology: Blackwell Science, Oxford

Burbank, D. W., Blythe, A. E., Putkonen, J., Pratt-Sitaula, B., Gabet, E., Oskin, M., Barros, A. and Ojha, T. P., 2003, Decoupling of erosion and precipitation in the Himalayas: Nature, v. 426, p. 652-655

Butler, R. W. H. and Lickorish, W. H., 1997, Using high-resolution stratigraphy to date fold and thrust activity: examples from the Neogene of south-central Sicily: Journal of the Geological Society, London, v. 154, p. 633-643

Byerlee, J. D., 1967, Frictional characteristics of granite under high confining pressure: Journal of Geophysical Research, v. 72, p. 3639-3648

Byerlee, J. D., 1978, Friction of rocks: Pure and Applied Geophysics, v. 116, p. 615-626

Carlson, W.D., Donelick, R.A. and Ketcham, R., 1999, Variability of apatite fission track annealing kinetics I: Experimental results: American Mineralogist, v. 84, p. 1213-1223

Carez, L., 1903-1909, La Geologie des Pyrenees Francaise: 6 vols. Paris: Imprimerie nationale

Carrapa, B., Wiljbrans, J. and Bertotti, G., 2003, Episodic exhumation in the Western Alps: Geology, v. 31, p. 601-604

Carreras, 1963, 1965

Casas, A., Kearey, P., Rivero, L. and Adam, C. R., 1997, Gravity anomaly map of the Pyrenean region and a comparison of the deep geological structure of the western and eastern Pyrenees, Earth and Planetary Science Letters, v. 150, p. 65-78

Cavet, P., 1957, Le Paleozoique de la zone axiale des Pyrenees orientales francaises entre le Roussillon et l'Andorre: Bulletine Serv. Carte Geologique, v. 55/254, p. 303-518

Cederbom, C. E., Sinclair, H. D., Sclunegger, F. and Rahn, M. K., 2004, climate-induced rebound and exhumation of the European Alps: Geology, v. 32, p. 709-712

Chery, J., Vilotte, J. P. and Daigniéres, M., 1991, Thermomechanical evolution of a thinned continental lithosphere under compression: Implications for the Pyrenees: Journal of Geophysical Research, v. 96, no. B3, p. 4385-4412

Choukroune, P. and Seguret, M., 1973, Tectonics of the Pyrenees: Role of compression and Gravity: In, Gravity and Tectonics, Interscience, Wiley and sons, New York, p. 141-156

Choukroune, P., 1976, Structure et evolution tectonique de la zone nord-pyreneenne (analise de la deformation dans une portion de chaine a schistosite subverticale): Memoires de la Societe Geologique de France, v. 127, p. 116

Choukroune, P. and ECORS Team, 1989, The ECORS Pyrenean deep seismic profile reflection data and the overall structure of an orogenic belt: Tectonics, v. 8, p. 23-39

Cloos, E., 1955, Experimental analysis of fracture patterns: Geological Society of America Bulletin, v. 66, p. 241-256

Colombo, F., 1980, Estratigrafia y sedimentologia del Terciario inferior continental de los Catalánides: PhD Thesis, University of Barcelona

Colombo, F. and Vergés, J., 1992, Geometría del margen S.E. de la Cuenca del Ebro: discordancias progresivas en el Grupo Scala Dei. Serra de La Llena (Tarragona): Acta Geológica Hispánica, v. 27, p. 33-53

Coney, P. J., Muñoz, J. A., McClay, K. R. and Evenchick, C. A., 1996, Syntectonic burial and post-tectonic exhumation of the southern Pyrenees foreland fold-thrust belt: Journal of the Geological Society, London, v. 153, p. 9-16

Curnelle, R., 1989, Magmatisme et volcanisma post-Hercyniens des Pyrenees et de l'Aquitaine: Bulletin of the Centre for Research of Exploration – Production, Elf-Aquitaine, v. 13, p. 101-103

Dahlen, F. A., 1984, Noncohesive critical coulomb wedges: An exact solution: Journal of Geophysical Research, v. 89, p. 10125-101333

Daigniéres, M., Gallart, J., Banda, E. and Hirn, A., 1982, Implication of the seismic structure for the orogenic evolution of the Pyrenean range: Earth and Planetary Science Letters, v. 57, p. 88-100

Dalloni, M., 1913, Stratigraphie et tectonique de la region des Nogueres (Pyrénées Centrales): Bulletin Sociéte Geologique France, v. 4/13, p. 243-263

Dalloni, M., 1930, Etude geologique des Pyrenees Catalanes: Universite de l'Aix Marseille faculte des Sciences annales, v. 26, p. 373

Dañobeitia, J. J., Belén, A. and Maldonado, A., 1990, Geological framework of the Ebro continental margin and surrounding areas: Marine Geology, v. 95, p. 265-287

Davis, D., Suppe, J. and Dahlen, F. A., 1983, Mechanics of fold-and-thrust belts and accretionary wedges: Journal of Geophysical Research, v. 88, p. 1153-1172

DeCelles, P. G. and Mitra, G., 1995, History of the Sevier orogenic wedge in terms of critical taper models, northeast Utah and southwest Wyoming: Geological Society of America Bulletin, v. 107, p. 454-462

Dempster, T. J., Jolivet, M., Tubrett, M. N. and Braithwaite, C. J. R., 2003, Magmatic zoning in apatite: a monitor of porosity and permeability change in granites: Contributions to Mineralogy and Petrology, v. 145, p. 568-577

De Sitter, L. U. and Zwart, H. J., 1962, Geological map of the Palaeozoic of the central Pyrenees, Sheets 1 and 2: Leidse Geologique Mededlingen, v. 27, p. 190-236

Deramond. J., Souquet, P., Fondecave-Wallez, M. J. and Specht, M., 1993, Relationships between thrust tectonics and sequence stratigraphy surfaces in foredeeps: model and examples from the Pyrenees (Cretaceous-Eocene, France, Spain), *In*, Williams, G. D. and Dobb, A., 1993, Tectonics and seismic sequence stratigraphy: Geological Society Special Publication, no. 71, p. 193-219

Desegaulx, P., Roure, F. and Villein, A., 1990, Structural evolution of the Pyrenees: tectonic inheritance and flexural behavior in the continental crust: Tectonophysics, v. 182; p. 211-225

Dinares, J., McClelland, E. and Santanach, P., 1992, Contrasting rotations within thrust sheets and kinematics of thrust tectonics as derived from palaeomagnetic data: an example from the Southern Pyrenees: *in* McClay, K. (ed), 1992, Thrust Tectonics: Chapman and Hall, London, p. 265-275

Donelick, R.A., Ketcham, R.A. and Carlson, W.D., 1999, Variability of apatite fission track annealing kinetics II: Crystallographic orientation effects: American Mineralogist, v. 84, p. 1224-1234

Dunai, T.J., Bikker, A. and Meesters, A.G.C.A., 2003, DeComp: A user-friendly forward modelling program for (U-Th)/He low-temperature geochronology: Geophysical Research Abstracts, v. 5, 14076

Ehlers, T.A. and Farley, K.A., 2003, Apatite (U-Th)/He thermochronometry: methods and applications to problems in tectonic and surface processes: Earth and Planetary Science Letters, v. 206, p. 1-14

Ehlers, T.A., Willet, S.D., Armstrong, P.A. and Chapman, D.S., 2003, Exhumation of the Central Wasatch Mountains, Utah: 2. Thermokinetic model of exhumation, erosion, and thermochronometer interpretation: Journal of Geophysical Research, v. 108, n. B3, p. 12-1 to 12-18

Ellis, M. A., Densmore, A. L. and Anderson, R. S., 1999, Development of mountainous topography in the Basin and Ranges, USA: Basin Research, v. 11, p. 21-41

Evans, G. and Archie, A., 2002, The flux of siliciclastic sediment from the Iberian Peninsular, with particular reference to the Ebro: *In*, Sediment flux to basins: Causes, controls and consequences (Ed. by S. J. Jones and L. E. Frostick), Geological Society, London, Special Publications, v. 191, p. 199-208

Farley, K., Wolf, R. and Silver, L., 1996, The effects of long alpha-stopping distances on (U-Th)/He ages: Geochimica et Cosmochimica Acta, v. 60, p. 4223-4229

Farley, K.A., 2000, Helium diffusion from apatite:general behavior as illustrated by Durango fluorapatite: Journal of Geophysical Research, v. 105, p. 2903-2914

Farley, K.A., 2002, (U-Th)/He dating: Techniques, calibrations, and applications, *in* Porcelli, P.D., Ballentine, C.J. and Wieler, R, (Eds.), 2002, Noble Gas Geochemistry: Reviews in Mineralogy and Geochemistry, v. 47, p. 819-843

Fechtig, H. and Kalbitzer, S., 1966, The diffusion of argon in potassium bearing solids, in Schaeffer, O.A. and Zahringer, J. (Eds.), 1966, Potassium-Argon dating: Heidelberg, Springer, p. 68-106

Fischer, M. W., 1984, Thrust tectonics in the North Pyrenees: Journal of Structural Geology, v. 6, no. 6, p. 721-726

Fitzgerald, P.G. and Gleadow, A.J.W., 1990, New approaches in fission track geochronology as a tectonic tool: examples from the Transantarctic Mountains: Nuclear Tracks, v. 17, p. 351-357

Fitzgerald, P.G., Sorkhabi, R.B., Redfield, T.F. and Stump, E., 1995, Uplift and denudation of the central Alaska Range: A case study in the use of apatite fission track thermochronology to determine absolute uplift parameters: Journal of Geophysical Research, v. 100, no. B10, p. 20175-20191

Fitzgerald, P. G., Muñoz, J. A., Coney, P. J. and Baldwin, S. L., 1999, Asymmetric exhumation across the Pyrenean orogen: implications for the tectonic evolution of a collisional orogen: Earth and Planetary Science Letters, v. 173, p. 157-170

Fleischer, R.L., Price, P.B. and Walker, R.M., 1975, Nuclear Tracks in Solids: Berkeley, University of California Press, p. 605

Foeken, J.P.T., Dunai, T.J., Bertotti, G. and Andriessen, P.A.M., 2003, Late Miocene to present exhumation in the Ligurian Alps (southwest Alps) with evidence for accelerated denudation during the Messinian salinity crisis: Geology, v. 31, no. 9, p. 797-800

Fontbote, J. M., Muñoz, J. A. and Santanach, P., 1986, On the consistency of proposed models for the Pyrenees with the structure of the eastern parts of the belt: Tectonophysics, v. 129, p. 291-301

Gallagher, K., 1995, Evolving temperature histories from apatite fission-track data: Earth and Planetary Science Letters, v. 136, p. 421-435

Gallagher, K., Brown, R. and Johnson, C., 1998, Fission track analysis and its application to geological problems: Annual Reviews in Earth and Planetary Science, v. 26, p. 519-572

Gallagher, K., 2000, The long and short of fission track annealing – From laboratory to geological timescales: 9th International Conference on Fission Track Dating and Thermochronology, Geological Society of Australia, Abstracts Number 58, p. 107-108

Garcia-Castellanos, D., Verges, J., Gaspar-Escribano, J. and Cloetingh, S., 2003, Interplay between tectonics, climate, and fluvial transport during the Cenozoic evolution of the Ebro Basin (NE Iberia): Journal of Geophysical Research, v. 108, p. 1-18

Garwin, L. J., 1985, Fission track dating and tectonics in the eastern Pyrenees: Unpublished PhD thesis, Cambridge University, Cambridge, England

Geotrack International Pty Ltd., 2004, THR™, AFTA®, ZFTA, (U-Th)/He, Basin Modelling: http://www.geotrack.com.au/

Gleadow, A.J.W. and Duddy, I.R., 1981, A natural long-term annealing experiment for apatite: Nuclear Tracks, v. 5, p. 169-174

Gleadow, A.J.W., Duddy, I.R., Green, P.F. and Lovering, J.F., 1986, Confined fission track lengths in apatite: A diagnostic tool for thermal history analysis: Contributions to mineralogy and Petrology, v. 94, p. 405-415

Gleadow, A.J.W. and Brown, R.W., 2000, Fission track thermochronology and the long-term denudational response to tectonics, *in* Summerfield, M.A., 2000, Geomorphology and Global Tectonics: John Wiley and Sons.

Goldberg, J. M., Maluski, H. and Leyreloup, A. F., 1986, Petrological and age relationship between emplacement of magmatic breccia, alkaline magmatism, and static metamorphism in the North Pyrenean Zone: Tectonophysics, v. 129, p. 275-290

González, A., Arenas, C. and Pardo, G., 1997, Discussion on syntectonic burial and post-tectonic exhumation of the southern Pyrenees foreland fold-thrust belt: Journal of the Geological Society, London, v. 154, p. 361-365

Green, P.F., Duddy, I.R., Gleadow, A.J.W., Tingate, P.R. and Laslett, G.M., 1986, Thermal annealing of fission tracks in apatite, 1. A qualitative description: Chemical Geology, v. 59, p. 237-253

Green, P.F., 1995, On Track article: v. 5, no. 2, p. 8-10, November issue

Guimera, J. 1984, Palaeogene evolution of deformation in the north-eastern Iberian Peninsular: Geol. Mag., v. 121, p. 413-420

Hanmer, S. and Passchier, C., 1991, Shear-sense indicators: A review: Geological Survey of Canada Paper 90-17, Energy, Mines and Resources Canada

Hardy, S. and Poblet, J., 1994, Geometric and numerical model of progressive limb rotation in detachment folds: Geology, v. 22, p. 371-374

Harrison, T. M., Yin, A. and Ryerson, F. J., 1998, Orographic eveolution of the Himalaya and Tibetan Plateau, *in* Crowley, T. J. and Burke, K. C. (eds), 1998, Tectonic boundary conditions for climate reconstructions: Oxford Monographs on Geology and Geophysics 39, Oxford University Press, New York, p. 39-72

Hartevelt, J. J. A., 1970, Geology of the Upper Segre and Valira valleys, Central Pyrenees, Andorra/Spain: Leidse Geologische Mededelingen, v. 45, p. 167-236

Hartevelt, J. J. A., 1971, Stratigraphic position of the limestones and conglomerates around the Marimaña granodiorite, Central Pyrenees: Geologische en Mijnbouw, v. 50, p. 691-697

Holl, J. E. and Anastasio, D. J., 1993, Palaeomagnetically derived folding rates, southern Pyrenees, Spain: Geology, v. 21, p. 271-274

House, M.A., Wernicke, B.P., Farley, K.A. and Dumitru, T.A., 1997, Cenozoic thermal evolution of the central Sierra Nevada, California, from (U-Th)/He thermochronometry: Earth and Planetary Science Letters, v. 151, p. 167-179

House, M.A., Farley, K.A. and Kohn, B., 1999, An empirical test of helium diffusion in apatite: borehole data from the Otway basin, Australia: Earth and Planetary Science Letters, v. 170, p. 463-474

House., M. A., Farley, K. and Stockli, D., 2000, Heliun chronometry of apatite and titanite using Nd-YAG laser heating: Earth and Planetary Science Letters, v. 183, p. 365-368

House, M.A., Kohn, B.P., Farley, K.A. and Raza, A., 2002, Evaluating thermal models for the Otway Basin, southeastern Australia, using (U-Th)/He and fission-track data from borehole apatites: Tectonophysics, v. 349, p. 277-295

Jager, E. and Zwart, H. J., 1968, Rb-Sr age determinations of some gneisses and granites of the Aston-Hospitalet Massif (Pyrenees): Geol. Mijnbouw, v. 47, p. 348-357

Johns, D. R., Hrber, M. A. and Schwander, M. M., 1989, Depositional sequences in the Catellón area, offshore northeast Spain: In, Atlas of seismic stratigraphy (Ed. by A. W. Bally), American Association of Petroleum Geology, Studies in Geology, v. 27, p. 181-184

Johnson, C., 1997, Resolving denudational histories in orogenic belts with apatite fission track thermochronology and structural data: an example from southern Spain: Geology, v. 25, p. 623-626

Kamp, P. J. J., Green, P. F. and Tippett, J. M., 1992, Tectonic architecture of the mountain front-foreland basin transition, South Island, New Zealand, assessed by fission track analysis: Tectonics, v. 11, No. 1, p. 98-113

Ketcham, R.A., Donelick, R.A. and Carlson, W.D., 1999, Variability of apatite fission track annealing kinetics III: Extrapolation to geological timescales: American Mineralogist, v. 84, p. 1235-1255

Ketcham ,R.A. and Donelick, R.A., 2000, AFTSolve Users Manual Version 1.1.3

Ketcham, R.A., Donelick, R.A. and Donelick, M.B., 2000, AFTSolve: A program for multi-kinetic modeling of apatite fission-track data: Geological Materials Research, v. 2, no. 1

Kleinsmiede, W. F. J., 1960, Geology of the Valle d'Aran (Central Pyrenees): Leidse Geologische Mededelingen, v. 24, p. 129-245

Knipe, R. J., 1989, Deformation mechanisms; recognition from natural tectonites: Journal of Structural Geology, v. 11, p. 127-146

Kohn, B.P. and Green, P.F., 2002, Low temperature thermochronology: From tectonics to landscape evolution: Tectonophysics, v. 349, p. 1-4

Koons, P. O., 1989, The topographic evolution of collisional mountain belts: A numerical look at the Southern Alps, New Zealand: American Journal of Science, v. 289, p. 1041-1069

Krifgsman, W., Higen, F. J., Raffi, I., Sierro, F. J. and Wilson, D. S., 1999, Chronology, causes and progression of the Messinian salinity crisis: Nature, v. 400, p. 652-655

Laslett, G.M., Kendall, W.S., Gleadow, A.J.W. and Duddy, I.R., 1982, Bias in measurement of fission track length distributions: Nuclear Tracks, v. 6, p. 79-85

Laslett, G.M., Gleadow, A.J.W. and Duddy, I.R., 1984, The relationship between fission track length and track density in apatite: Nuclear Tracks, v. 9, p. 29-38

Laslett, G.M., Green, P.F., Duddy, I.R. and Gleadow, A.J.W., 1987, Thermal annealing of fission tracks in apatite, 2. A quantitative analysis: Chemical Geology, v. 65, p. 1-13

Lawton, T. F., Boyer, S. E. and Schmitt, J. G., 1994, Influence of inherited taper on structural variability and conglomerate distribution, Cordilleran fold and thrust belt, western United States: Geology, v. 22, p. 339-342

Lippolt, H.J., Leitz, M., Wernicke, R.S. and Hagedorn, B., 1994, (U+Th)/He dating of apatite experience with samples from different geochemical environments: Chemical Geology, v. 112, p. 179-191

Lock, J. and Furlong, K., 2003, Geomorphic and thermal steady state regimes: reality or wishful thinking?: Geophysical Research Abstracts, Vol. 5, 07518, European Geophysical Society 2003

Loget, N., Babault, J., Castelltort, S., Van den Driessche, J., Bonnet, S. and Davy, P., 2004, When does the Ebro River connect to the Mediterranean?: Geophysical Research Abstracts, v. 6, 07710, EGU 2004

Losantos, M., Palau, J. and Sanz, J., 1986, Considerations about Hercynian thrusting in the Marimaya Massif (Central Pyrenees): Tectonophysics, v. 129, p. 71-79

Mancktelow, N.S. and Grasemann, B., 1997, Time-dependent effects of heat advection and topography on cooling histories during erosion: Tectonophysics, v. 270, p. 167-195

Martínez del Olmo, W., 1996, Depostional sequences in the Gulf of Valencia Tertiary Basin: *In*, Tertiary basins of Spain: The stratigraphic record of crustal kinematics: World and regional geology (Eds. Friend, P. F. and Dabrio, C. J.), Cambridge University Press, New York, p. 55-67

Mattauer, M. and Henry, J., 1974, Pyrenees, *in* Spencer, A. M. ed., Mesozoic-Cenozoic orogenic belts: Data for orogenic studies: Geological Society of London Special Publication 4, p. 3-22

Masson, D. G. and Miles, P. R., 1984, Mesozoic seafloor spreading between Iberia, Europe and North America: Marine Geology, v. 56, p. 279-287

McCaig, A., 1986, Thick- and thin-skinned tectonics in the Pyrenees: Tectonophysics, v. 129, p. 319-342

McCaig, A. M. and Miller, J. A., 1986, 40Ar-39Ar age of mylonites along the Merens fault, Central Pyrenees: Tectonophysics, v. 129, p. 149-172

McClelland, E. A. and McCaig, A. M., 1989, Palaeomagnetic estimates of total rotation in basement thrust sheets, Axial Zone, Southern Pyrenees: Cuadernos de Geologia Iberica, v. 12, p. 181-193

Meesters, A.G.C.A. and Dunai, T.J. 2002, Solving the production-diffusion equation for finite diffusion domains of various shapes, Part II. Application to cases with α-ejection and nonhomogenous distribution of the source: Chemical Geology, v. 186, p. 347-363

Meigs, A. J., Vergés, J. and Burbank, D. W., 1996, Ten-million-year history of a thrust sheet: Geological Society of America Bulletin, v. 12, p. 1608-1625

Meigs, A. J., 1997, Sequential development of selected Pyrenean thrust faults, Journal of Structural Geology, v. 19, no. 3-4, p. 481-502

Meigs, A. J. and Burbank, D. W., 1997, Growth of the South Pyrenean orogenic wedge: Tectonics, v. 16, no. 2, p. 239-258

Meléndez-Hevia, F. and Alvarez de Buergo, E., 1996, Oil and gas resources of the Tertiary Basins of Spain:

In, Tertiary basins of Spain: The stratigraphic record of crustal kinematics: World and regional geology (Eds. Friend, P. F. and Dabrio, C. J.), Cambridge University Press, New York, p. 26-43

Mellere, D., 1992, I conglomerati di Pola de Segur: Stratigrafia fisica e relazioni tettonica-sedimentazione, Tesi di Dottorato in Scienzi della Terra: Universita degli Studi di Padova, Padua, 1992

Mellere, D., 1993, Thrust-generated, back-fill stacking of alluvial fan sequences, south-central Pyrenees, Spain (La Pobla de Segur Conglomerates: Special Publications of the International Association of Sedimentologists, v. 20, p. 259-276

Mey, P. H. W., 1967, The geology of the upper Ribagorçana and Baliera valleys, Central Pyrenees, Spain: Leidse Geologische Mededelingen, v. 41, p. 153-220

Mey, P. H. W., Nagtegaal, P. J. C., Roberti, K. J. and Hartevelt, J. J. A., 1968, Lithstratigraphic subdivisions of Post-Hercynian deposits in the south-central Pyrenees, Spain: Leidse Geologische Mededelingen, v. 41, p. 221-228

Mey, P. H. W., 1968, The geology of the upper Ribagorçana and Tor valleys, Central Pyrenees, Spain: Leidse Geologische Mededelingen, v. 41, p. 229-292

Mitra, S., 2002, Fold-accomodation faults: American Association of Petroleum Geologists, v. 86, No. 4, p. 671-693

Montigny, R., Azambre, B., Rossy, M. and Thuizat, R., 1986, K-Ar study of Cretaceous magmatism and metamorphism in the Pyrenees: Age and length of rotation of the Iberian Peninsular: Tectonophysics, v. 129, p. 257-273

Moore, M.A. and England, P.C., 2001, On the inference of denudation rates from cooling ages of minerals: Earth and Planetary Science Letters, v. 185, p. 265-284

Moreau, G. M., Berthou, J. Y. and Malod, J. A., 1997, New paleomagnetic Mesozoic data from the Algarve (Portugal): fast rotation of Iberia between the Hauterivian and the Aptian: Earth and Planetary Science Letters, v. 146, p. 689-701

Morris, R. G., 1998, Implications of surface processes on mountain belt development; a Pyrenees case study: Unpublished PhD Thesis, University of Birmingham, Birmingham

Morris, R. G., Sinclair, H. D. and Yelland, A. J., 1998, Exhumation of the Pyrenean orogen: implications for sediment discharge: Basin Research, v. 10, p. 69-85

Muñoz, J. A., Martínez, A. and Vergés, J., 1986, Thrust sequences in the eastern Spanish Pyrenees: Journal of Structural Geology, v. 8, p. 399-405

Muñoz, J. A., 1992. Evolution of a continental collision belt: ECORS-Pyrenees crustal balanced cross-section, *in* McClay, K. (ed), 1992, Thrust Tectonics: Chapman and Hall, London, p. 235-246

Muñoz, J. A., Coney, P. J., McClay, K. R. and Evenchick, C. A., 1997, Discussion on syntectonic burial and post-tectonic exhumation of the southern Pyrenees foreland fold-thrust belt: Journal of the Geological Society, London, v. 154, p. 361-365

Mulder, C. J., 1973, Tectonic framework and distribution of Miocene evaporites in the Mediterranean: *In*, Messinian events in the Mediterranean (Ed. by C. W. Drooger), Netherlands, Amsterdam, 44-59

Nagtegaal, P. J. C., 1969, Sedimentology, palaeoclimatology and diagenesis of post-Hercynian continental deposits in the south-central Pyrenees, Spain: Leidse Geologische Mededelingen, v. 42, p. 143-238

Naylor, M., Sinclair, H. D., Willet, S. and Cowie, P., in press, A discrete element model for orogenesis and accretionary growth: Journal of Geophysical Research

Nicols, G. J., 1987, Structural controls on fluvial distributary systems: The Luna system, northern Spain: *In*, Ethrighe, F. G., Flores R. M. and Harvey, M. D., (eds) Recent developments in Fluvial Sedimentology: Society of economic palaeontologists and mineralogists Special Publications, v. 39, p. 269-277

Paul, T. and Fitzgerald, P.F., 1992, Transmission electron microscope investigation of fission tracks in apatite: American Mineralogist, v. 77, p. 336344

Pazzaglia, F. J. and Brandon, M. T., 1996, Macrogeomorphic evolution of the post-Triassic Appalachian mountains determined by deconvolution of the offshore basin sedimentary record: Basin Research, v. 8, p. 255-278

Pérez-Rivarés, F. J., Garcz0233s, M., Arenas, C. and Pardo, G., 2002, Magnetochronología de la sucesión Miocena de la Sierra de Alcubierre (sector central de la cuenca del Ebro): Rev. Soc. Geol. Esp., v. 15, p. 211-225

Peybernes, B. and Souquet, P., 1984, basement blocks and tectono-sedimentary evolution in the Pyrenees during Mesozoic times: Geological Magazine, v. 121, no. 4, p. 397-405

Pocovi, J., 1978, Estudio geologico de las Sierras Marginales Ctalanas: unpublished PhD Thesis, Universitat de Barcelona, Barcelona

Philips and Meghraoui, 1983 (see Burbank and Anderson, 2002?)

Pinet, B., Montadert, L., Curnelle, R., Cazes, M., Marillier, F., Rolet, J., Tomassino, A., Galdeano, A., Patriat, Ph., Brunet, M. F., Olivet, J. L., Schaming, M., Lefort, J. P., Arrieta, A. and Riaza, C., 1987, Crustal thinning on the Aquitaine shelf, Bay of Biscay, from deep seismic data: Nature, v. 325, p. 513-516

Pinet, P. and Souriau, M., 1988, Continental erosion and large-scale relief, Tectonics, v. 7, p. 563-582

Platt, J. P., 1986, Dynamics of orogenic wedges and the uplift of high pressure metamorphic rocks: Geological Society of America Bulletin, v. 97, p. 1037-1054

Price, N. J., 1966, Fault and joint development in brittle and semi-brittle rocks: Pergammon Press, Oxford

Price, N. J. and Cosgrove, J. W., 1991, Analysis of geological structures: Cambridge University Press, Cambridge, p. 144-157

Puigdefàbregas, C., Samso, J. M., Serra-Kiel, J. and Tosquella, J., 1985, Facies analysis and faunal assemblages of the Roda Sandstone Formation, Eocene of the Southern Pyrenees: In, VI Regional European Meeting, Lerida, Spain. IAS abstracts, p. 639-642

Puigdefàbregas, C. and Souquet, P., 1986, Tecto-sedimentary cycles and depositional sequences of the Mesozoic and Tertiary from the Pyrenees: Tectonophysics, vol. 129, p. 173-203

Puigdefàbregas, C., Nijman, W. and Muñoz, J. A., 1989, Alluvial deposits of the successive foreland basin stages and their relation to the Pyrenean thrust sequences: 4th International Conference on Fluvial Sedimentology, Sitges, Spain, Excursion guidebook, 10

Puigdefàbregas, C., Muñoz, J. A. and Vergés, J., 1992, Thrusting and foreland basin evolution in the southern Pyrenees: In, Thrust Tectonics (Ed. By K. McClay), Chapman and Hall, London, p. 247-254

Rahl, M. K., Brandon, M. T., Batt, G. E. & Garver, J. I., 2004, A zero-damage model for fission track annealing in zircon: American Mineralogist, April issue expected (in print)

Ramsay, J. G. and Graham, R. H., 1970, Strain variation in shear belts: Canadian Journal of Earth Sciences, v. 7, p. 786-813

Ramsay, J. G. and Huber, M. I., 1987, The techniques of modern structural geology, Volume 2: Folds and fractures: Academic Press, London, p. 529-530

Reidel, W., 1929, Zur mechanik geologischer Brucherscheinungen. Ein Beitrag zun problem der 'Fiederspalten': Centralblatt für Mineralogie, Geologie, und Paleontologie, Part B, p. 354-368

Reiners, P. W. and Farley, K. A., 2001, Influence of crystal size on apatite (U-Th)/He thermochronology: An example from the Bighorn Mountains, Wyoming: Earth and Planetary Science Letters, v. 188, p. 413-420

Reiners, P. W., Zhou, Z., Ehlers, T. A., Xu, C., Brandon, M. T., Donelick, R. A. and Nicolescu, S., 2003, Post-orogenic evolution of the Dabie Shan, Eastern China, from (U-Th)/He and fission track thermochronology, American Journal of Science, v. 303, p. 489-518

Reiners, P. W., Ehlers, T. A., Mitchell, S. G., Montgomery, D. R., 2003, Coupled spatial variations in precipitation and long-term erosion rates across the Washington Cascades: Nature, v. 426, p. 645-647

Reiners, P. W., Spell, T. L., Nicolescu, S. and Zanetti, K. A., 2004, Zircon (U-Th)/He thermochronometry: He diffusion and comparisons with ^{40}Ar/^{39}Ar dating: Geochimica et Cosmochimica Acta, v. 68, p. 1857-1887

Reynolds, A. D., 1987, Tectonically controlled fluvial sedimentation in the South Pyrenean foreland basin: unpublished PhD Thesis, University of Liverpool, Liverpool, p. 309

Riba, O., 1976, Tectogenése et sedimentation: Deax modéeles de discordances syntectoniques pyrénéennes: [France] Bureau de Recherches Géologiques et Miniéres, Bulletin, v. 1, p. 383-401

Riba, O., Reguant, S. and Villena, 1983, Ensayo de síntesis estratigráfica y evolutiva de la cuenca terciaria del Ebro: In, Libro Jubliar (Ed. By J. M. Rios), Geologique España, 2, 131-159

Ring, U., Brandon, M.T., Willett, S.D. and Lister, G.S., 1999, Exhumation processes, *in* Ring, U., Brandon, M.T., Lister, G.S. and Willett, S.D. (eds) Exhumation processes: Normal Faulting, Ductile Flow and Erosion: Geological Society, London, Special Publication 154, p. 1-27

Roca, E. and Desegaulx, P., 1992, Analysis of the geological evolution and vertical movements in the València Trough area, Western Mediterranean: Marine and Petroleum Geology, v. 9, p. 167-185

Roca, E., 2001, The northwest Mediterranean Basin (Valencia Trough, Gulf of Lions and Liguro-Provençal basins): structure and dynamic evolution: in, Peri-Tethyan Rift/Wrench Basins and Passive Margins (Ed. by P. A. Ziegler, W. Cavazza, A. H. F. Robertso and S. Crasquin-Soleau), Peri-Tethys Memoir 6, Mém. Mus. Natn. Hist. Nat., v. 186, p. 671-706

Roest, W. R. and Srivastava, S. P., 1991, Kinematics of the plate boundaries between Eurasia, Iberia and Africa in the North Atlantic from the Late Cretaceous to the present, Geology, v. 19, p. 613-616

Rosell, J. and Riba, O., 1966, Nota sobre la disposicion sedimentaria de los Conglomerados de Pobla de Segur: Instituto Estudios Pirenaicos, Zaragoza, p. 1-16

Roure, F., Choukroune, P., Berastegui, X., Muñoz, J. A., Villien, A., Matheron, P., Bareyt, M., Séguret, M., Camara, P. and Deramond, J., 1989, ECORS deep seismic data and balanced cross sections: geometric constraints on the evolution of the Pyrenees: Tectonics, v. 8, no. 1, p. 41-50

Rutter, E., 1974, The influence of temperature, strain rate and interstital water in the experimental deformation of calcite rocks: Tectonophysics, v. 22, p. 311-330

Sans, M., Muñoz, J. A. and Vergés, J., 1996, Triangle zone and thrust wedge geometries related to evaporitic horizons (southern Pyrenees): Bulletin of Canadian Petroleum Geology, v. 44, no. 2, p. 375-384

Sanz de Galdeano, C. M., 1996, Tertiary tectonic framework of the Iberian Peninsula: Friend, P. (ed), 1996, Tertiary basins of Spain; a stratigraphic record of crustal kinematics: Cambridge University Press, Cambridge, p. 9-14

Schlunegger, F. and Willett, S., 1999, Spatial and temporal variations in exhumation of the central Swiss Alps and implications for exhumation mechanisms, *in* Ring, U., Brandon, M.T., Lister, G.S. and Willett, S.D. (eds) Exhumation processes: Normal Faulting, Ductile Flow and Erosion: Geological Society, London, Special Publication 154 , p.157-179

Schmidt, K. M. and Montgomery, D. R., 1995, Limits to relief: Science, v. 270 (5236), p. 617-620

Scott, R.J., Foster, D.A., and Lister, G.S., 1998, Tectonic implications of rapid cooling of lower plate rocks from the Buckskin-Rawhide metamorphic core complex, west central Arizona: Geological Society of America Bulletin, v. 110, p. 588-614.

Seguret, M., 1964, Sur le style en têtes plongeantes des structures pyrénéennes de la zone des Nogueres (versant Sud des Pyrénées centrals: Comptes Rendus Hebdomadaires des Seances de l' Acadamie des Sciences, v. 259, p. 2895-2898

Séguret, M., 1970, Etude tectonique des nappes et serie decollees de la partie centrale du versant sud des Pyrenees: Publications de l'Universite de Sciences et Techniques de Languedoc, serie Geologie Structurale, n. 2, Montpellier

Seguret, M., 1972, Etude tectonique des nappes et series décollées de la partie centrale du versant sud des Pyrénées; caractére synsédimentaire, role de la compression et de la gravité: Thése Fac. Sci., Montpellier, Publ. U.S.T.E.L.A., Série Geol. Struct., v. 2

Séguret, M. and Daigniéres, M., 1985, Coupes balancees d'echelle crustale des Pyrenees: C. R. Academie Sciences Paris, Ser. II, v. 301, p. 341-346

Séguret, M. and Daigniéres, M., 1986, Crustal scale balanced cross-sections of the Pyrenees; discussion: Tectonophysics, v. 129, p. 303-318

Seward, D. and Mancktelow, N. S., 1994, Neogene kinematics of the central and western Alps: Evidence from fission track dating: Geology, v. 22, p. 803-806

Serrat, D., 1992, La xarxa fluvial dels Països Catalans: In, Historia Natural dels Països Catalanas, Geologia II, Enciclopedia Catalana, Barcelona, Spain, 375-389

Shaw, J. H. and Suppe, J., 1994, Active faulting and growth folding in the eastern Santa Barbera Channel, California: Geological Society of America Bulletin, v. 106, p. 607-626

Simpson, C. and Schmid, S. M., 1983, An evaluation of criteria to deduce the sense of movement in sheared rocks: Geological Society of America Bulletin, v. 94, p. 1281-1288

Smith, A. G., 1996, Cenozoic latitudes, positions and topography of the Iberian Peninsula: Friend, P. (ed), 1996, Tertiary basins of Spain; a stratigraphic record of crustal kinematics: Cambridge University Press, Cambridge, p. 6-8

Soom, M. and Hurford, A.J., 1990., Fission track dating of apatites and zircons along the western profile of Swiss National Research Project PNR20 (External massifs and Penninic nappes, Swiss Alps): Nuclear Tracks, v. 17, 428

Soriano, C., Martí, J. and Casas, J., 1996, Palinspastic reconstruction of Permo-Carboniferous basins involved in Alpine deformation: The Erill Castell-Estac basin, Southern Pyrenees, Spain: Geologie en Mijnbouw, v. 75, p. 43-55

Soula, J. C., Lambouroux, C., Viallard, P., Bessiére, G., Debat, P. and Ferret, B., 1986, The mylonite zones in the Pyrenees and their place in the Alpine tectonic evolution: Tectonophysics, v. 129, p. 115-147

Spotila, J. A., Bank, G. C., Reiners, P. W., Naeser, C. W., Naeser, N. D. and Henika, B. S., 2004, Origin of the Blue Ridge escarpment along the passive margin of Eastern North America: Basin Research, v. 16, no. 1, p. 41-64

Srivastava, S. P., Schouten, H., Roest, W. R., Klitgord, K. D., Kovacs, L. C., Verhoe, J. and Macnab, R., 1990, Iberian plate kinematics: a jumping plate boundary between Eurasia and Africa: Nature, v. 344, p. 756-759

Stearns, D. W., 1964, Macrofracture patterns on Teton Anticline N. W. Montana (Eos): Transcripts of the American Geophysical Union, v. 45, p. 107

Stockli, D.F., Farley, K.A. and Dumitru, T.A., 2000, Calibration of the apatite (U-Th)/He thermochronometer on an exhumed fault block, White Mountains, California: Geology, v. 28, no. 11, p. 983-986

Stüwe, K., White, L. and Brown, R., 1994, The influence of eroding topography on steady-state isotherms. Application to fission-track analysis: Earth and Planetary Science Letters, v. 124, p. 63-74

Stüwe, K. and Hintermüller, M., 2000, Topography and isotherms revisited: the influence of laterally migrating drainage divides: Earth and Planetary Science Letters, v. 184, p. 287-303

Summerfield. M. A. and Brown, R. W., 1998, Geomorphic factors in the interpretation of thermochronologic data, *in*, Van Den Haute, P. and De Corte, F. (eds), 1998, Advances in fission track geochronology: Kluwer, Dordrecht, p. 269-284

Suppe, J., Chou, G. T. and Hook, S. C., 1992, Rates of folding and faulting determined from growth strata: *In*, Thrust Tectonics (Ed. By K. McClay), Chapman and Hall, London, p. 105-121

Tagami, T., Ito, H., and Nishimura, S., 1990, Thermal annealing characteristics of spontaneous fission tracks in zircon: Chemical Geology, v. 80, p. 159-169

Tagami, T., Hurford, A.J., and Carter, A., 1995, Natural long-term annealing of the zircon fission-track system in Vienna Basin deep borehole samples; constraints upon the partial annealing zone and closure temperature: Chemical Geology, v. 130, p.147-157.

Tippet, J. M. and Kamp, P. J. J., 1993, Fission Track Analysis of the late Cenozoic Vertical Kinematics of Continental Pacific Crust, South Island, New Zealand: Journal of Geophysical

Tucker, G. E. and Whipple, K. X., 2002, Topographic outcomes predicted by stream erosion models: Sensitivity analysis and intermodel comparison: Journal of Geophysical Research, v. 107, no. B9, 2179

Twiss, R. J. and Moores, E. M., 1992, Structural Geology: Freeman & Company, USA

Van der Beek, P., Braun, J., Bernet, M. and Labrin, E., 2004, Using thermochronology to track recent relief development in the French western Alps: EGU Nice abstract, 2004

Vergés, J., 1993, Estudi tectonic del vessant sud del Pirineu oriental I central: Evolucio cinematica en 3D: PhD Thesis, Universitat de Barcelona, Barcelona

Vergés, J., Millan, H., Roca, E., Muñoz, J. A., Marzo, M., Cires, J., Den Bezemer, T., Zoetemeijer, R. and Cloetingh, S., 1995, Eastern Pyrenees and related foreland basins: pre-, syn- and post-collisional crustal-scale cross-sections: Marine and Petroleum geology, v. 12, no. 8, p. 893-915

Vergés, J. and Muñoz, J. A., 1990, Thrust sequences in the southern central Pyrenees: Bulletin Societe Geologique France, v. 2, p. 265-271

Vergés, J., Muñoz, J. A. and Martines, A., 1992, South Pyrenean fold and thrust belt: The role of foreland evaporitic levels in thrust geometry: *in* McClay, K. (ed), 1992, Thrust Tectonics: Chapman and Hall, London, p. 255-264

Vielzeuf, D. and Kornprobst, J., 1984, Crustal splitting and the emplacement Pyrenean lherzolites and granulites: Earth and Planetary Science Letters, v. 67, p. 383-386

Vincent, S. J., 1993, Fluvial palaeovalleys in mountain belts: An example from the South Central Pyrenees: Unpublished PhD thesis, University of Liverpool, Liverpool, 1993

Vincent, S. J., 2001, The Sis palaeovalley: a record of proximal fluvial sedimentation and drainage basin development in response to Pyrenean mountain building: Sedimentology, v. 48, p. 1235-1276

Wagner, G. A. and Van Den Haute, P., 1992, Fission Track Dating: Dortrect, Netherlands, Kluwer Academic Publishers, p. 285

Warnock, A.C., Zeitler, P.K., Wolf, R.A. and Bergman, S.C., 1997, An evaluation of low-temperature apatite U-Th/He thermochronometry: Geochimica et Cosmochimica Acta, v. 61, p. 5371-5377

Wayne, D. M. and McCaig, A. M., 1998, Dating fluid flow in shear zones: Rb-Sr and U-Pb studies of syntectonic veins in the Néouvielle Massif, Pyrenees, *In* Parnell, J., 1998, Dating and duration of fluid flow and fluid-rock interaction: Geological Society, London, Special Publication, v. 144, p. 129-125

Wilcox, R. E., Harding, T. P. and Seely, D. R., 1973, Basic wrench tectonics: American Association of Petroleum Geologists Bulletin, v. 57, p. 74-96

Willet, S. D., Beaumont, C. and Fullsack, P., 1993, Mechanical model for the tectonics of doubly vergent compressional orogens: Geology, v. 21, p. 371-374

Willet, S. D., 1999, Orogeny and orography: The effects of erosion on the structure of mountain belts: Journal of Geophysical Research, v. 104, no. B12, p. 28957-28981

Willet, S. D., Slingerland, R. and Hovius, N., 2001, Uplift, shortening, and steady-state topography in active mountain belts: American Journal of Science, v. 301, p. 455-485

Williams, G. D., 1985, Thrust tectonics in the south central Pyrenees: Journal of Structural Geology, v. 7, no. 1, p. 11-17

Williams, G. D. and Fischer, M. W., 1984, A balanced section across the Pyrenean orogenic belt: Tectonics, v. 3 (7), p. 773-780

Wobus, C. W., Hodges, K. V. and Whipple, K. X., 2003, Has focused denudation sustained active thrusting at the Himalayan topographic front?: Geology, v. 31, p. 861-864

Wolf, R.A., Farley, K.A. and Silver, L.T., 1996, Helium diffusion and low-temperature thermochronometry of apatite: Geochimica et Cosmochimica Acta, v. 60, p. 4231-4240

Wolf, R.A., Farley, K.A. and Kass, D.M., 1998, Modeling of the temperature sensitivity of the apatite (U-Th)/He thermochronometer: Chemical Geology, v. 148, p. 105-114

Yamada, R., Tagami, T., Nishimura, S., and Ito, H., 1995, Annealing kinetics of fission tracks in zircon: an experimental study: Chemical Geology, v. 122, p. 249-258.

Yelland, A. J., 1990, Fission track thermotectonics in the Pyrenean orogen: Nuclear Tracks and Radiation Measurements, v. 17, p. 293-299 Zwart, H. J., 1979, The geology of the central Pyrenees: Leidse Geologique Mededlingen, v. 50, p. 1-74

Young, E., Myers, A., Munsen, E. and Conklin, N., 1969, Mineralogy and geochemistry of fluorapatite from Cerro de Mercado, Durango, Mexico: United States Geological Survey, Professional Paper, v. 650-D, p. D84-D93

Zandvliet, J., 1960, The geology of the Upper Salat and Pallaresa valleys, Central Pyrenees, France/Spain: Leidse Geologische Mededelingen, v. 25, p. 1-127

Zaun, P.E. and Wagner, G.A., 1985, Fission track stability in zircons under geological Conditions: Nuclear Tracks and Radiation Measurements, v. 10, p. 303-307.

Ziegler, P. A., 1988, Evolution of the Arctic-North Atlantic and the Western Tethys: American Association of Petroleum Geologists Memoirs, v. 43, p. 198

Zeitler, P.K., Herczig, A.L., McDougall, I. And Honda, M., 1987, U-Th-He dating of apatite: a potential thermochronometer: Geochimica et Cosmochimica Acta, v. 51, p. 2865-2868

Zeyen, H. and Fernández, M., 1994, Integrated lithospheric modelling combining thermal, gravity, and local isostasy analysis: application to the NE Spanish Geotransect: Journal of Geophysical Research, v. 99, p. 18089-18102

Zhang, P., Molnar, P. and Downs, W. R., 2001, Increased sedimentation rates and grain sizes 2-4 Myr ago due to the influence of climate change on erosion rates: Nature, v. 410, p. 891-897

Ziegler, J.F., 1977, Helium: Stopping powers and ranges in all elemental matter: New York, Pergamon, p.367

Zoetemeijer, R., Deselgaulx, P., Cloetingh, S., Roure, F. and Moretti, I., 1990, Lithspheric dynamics and tectono-stratigraphic evolution of the Ebro Basin: Journal of Geophysical Research, v. 95, p. 2701-2711

Zwart, H. J., 1963, The structural evolution of the Palaeozoic of the Pyrenees: Geologische Rundschau, v. 53, p. 170-205

Zwart, H. J., 1965, Geological map of the Palaeozoic of the Central Pyrenees, sheet 6, Aston, France, Andorra, Spain, 1:50,000: Leidse Geologische Mededelingen, v. 33, p. 191-254

Zwart, H. J., 1979, The geology of the central Pyrenees: Leidse Geologische Mededelingen, v. 50, p. 1-78

Zwart, H. J., 1986, The Variscan geology of the Pyrenees, Tectonophysics, v. 129, p. 9-27

Appendices

Appendix I	Mineral separation procedures
	(U-Th)/He analysis procedures
	AFT analysis procedures
Appendix II	Apatite geochemical spectra analyses
	AHe analysis data
	Errata: Table 4.2 (Revised)
Appendix III	Gibson et al. (submitted to Basin Research)

Appendix I

Mineral Separation Procedures

All mineral separation was performed at the Grant Institute (University of Edinburgh), the Gregory Building (University of Glasgow) and at the Scottish Universities Environmental Research Centre (SUERC), East Kilbride. The techniques used to extract heavy mineral separates (including apatite and zircon) from rock samples is outlined below;

- Rock samples weighed, measured and the outer-surface removed, where weathered;
- Individual blocks disaggregated using sledge hammer, hydraulic rock splitter, and jaw crusher (med and max aperture). All equipment was cleaned with pressured air, water and acetone in between samples;
- Coarse fraction (300 μm aperture sieve) separated through dry sieving and reduced in size (to <300 μm) using Rock Roller Mill;
- Sediment dry sieved into four grain-size fractions (<70 μm, 70-250 μm, 250-350 μm, >350 μm) using electronic sieve agitator. Sieves washed in warm water in Ultra-Sonic bath for ~20 mins and wire-brushed when dry to clean in between samples;
- Size fractions of <350 mm washed in cold tap water and dried at room temperature in open-top trays for up to 2 weeks;
- Dry samples entered into Frantz Isodynamic separator twice (1.0 Amp, 7/20 followed by 1.5 Amp, 7/20) and the magnetic separate removed and stored;
- 0.25 kg of Non-magnetic separates placed into 0.5 litres of Lithium Polytungstate (LST: density 2.82 gmL^{-1}, viscosity 10cP) diluted with 40 ml of de-ionised MilliQ water in glass density separating funnel, stirred, and allowed to settle for 30 mins. Dense fraction at the base of the funnel tapped off into Whatman wet-strengthened filter papers (113/11.0 cm) within ceramic Buchaner funnel attached to air-sealed concial flask and motorised vacuum pump. All glassware and apparatus cleaned under high power water jet and immersed in hot water in Ultra Sonic bath for 30 mins in between samples;
- Heavy fraction, when dried, inspected under binocular microscope to confirm apatite/zircon crystals. Unpure seperates re-entered into pure LST solution following the procedure described above;
- Individual apatite crystals, when chosen from the resultant apatite yield, were screened under plane and cross-polarised light at x218 magnification for mineral contaminents, structural defects, appropriate morphology and size. The physical dimensions of between 5 and 15 inclusion-free crystals per sample were measured, using a calibrated graticule within the microscope lens, and packed into stainless steel capsules and wrapped in degassed Cu foil.

(U-Th)/He analysis produres

All (U-Th)/He analyses were performed at SUERC by M. Gibson following the procedure outlined below;

- Capsules were loaded into the Monax glass 'Christmas tree' above a double-walled resistively heated vacuum furnace. After pumping and furnace outgassing, a hot blank was performed until an acceptable blank was obtained;
- Subsequently each capsule was dropped into the furnace and heated at 950°C for 35 minutes to completely outgas inclusion free apatites. The gases obtained were then spiked with a known amount of ^{3}He and purified using liquid nitrogen-cooled charcoal traps and TiZr getters. The gases were then admitted into the Hiden HAL3F quadrupole mass spectrometer and the ^{4}He abundance was measured relative to a 99.9% pure ^{3}He spike;
- After analysis the entire system was pumped out for 10 mins using Turbo/Ion pumps. The samples were then reheated to check for quantitative degassing. The reheat step ensured ^{4}He levels indistinguishable from the initial blank;
- After He analysis, the capsules were retrieved from the furnace, opened and placed in Teflon beakers, they were then inspected to ensure all grains were still present. Apatites were spiked with 3 ng ^{230}Th and ^{235}U and dissolved in 5% HNO_3. The ^{230}Th/^{232}Th and ^{238}U/^{235}U ratios are measured directly on these solutions by VG PlasmaQuad 2 ICP-MS;
- Based on reproducibility of pure standard gases and aqueous standard solutions, the overall analytical precision of He ages determined by this procedure was ~2%.

Fission track analysis procedures

All fission track analysis was performed at Apatite to Zircon Inc., Idaho, USA. By Ray Donelick. M. Gibson spent 3 months working alongside Ray Donelick at the laboratories in Idaho in the summer of 2003. Fission track slides were prepared following the procedures outlined below;

- Coarse apatite fractions were mounted in epoxide resin and cured for 1 hour at 90°C. Internal crystal surfaces were exposed using 0.3 μm Al_2O_3 slurries on a polishing wheel. Spontaneous fission tracks intersecting the surface were then etched in 5.5N HNO_3 for 20 seconds (±0.5) at 21°C and densities counted using both reflected and unpolarised transmitted light at 1562.5x magnification;
- For apatite length analysis the grain mounts were irradiated with ^{252}Cf-derived fission fragments in a nominal vacuum chamber to maximise track-length distribution measurements following the procedure of Donelick and Miller (1991). After etching, as outlined above, the length and crystallographic orientation, with respect to the c-axis, of natural, horizontal confined track lengths was determined under 1562.5x magnification with attached projection tube and digitising tablet;
- Fission track ages were determined by placing low-Uranium muscovite sheets against the polished and etched grain mounts prior to irradiation at the Washington State University nuclear reactor (45 minutes at thermal neutron fluence of 10^{16} neutron/cm^2 at 1 MW power level). Similar mica sheets were placed next to 235-doped CN-1 glass for standardisation purposes. The mica sheets were immersed in 48% HF at 20°C (±1°C) for 15 minutes (±15 seconds) in order to reveal fission tracks induced through irradiation;
- Fission track ages were calculated using the radioactive decay equation with an analyst zeta calibration factor of 113.8±2.9. Annealing kinetics were inferred using the arithmetic mean of 1-4 measured Dpar values (μm units) per grain.

Appendix II

Apatite geochemical spectra analyses

Geochemical spectra of the background crystal composition of apatites from 14 samples (in order from top left to bottom right, (MM-02/2635, Mar-00/2304, Mar-00/2030, Mal-00/2870, Mal-002650, Mal-00/2360, Mal-00/2140, Mal-00/1920, Mal-00/1760, Bar-02/1695, Mon-02/1280, Esc-02/1250, Sas-02/1490, Col-00/1540). Major elemental peaks (plus Cl) noted in each spectra.

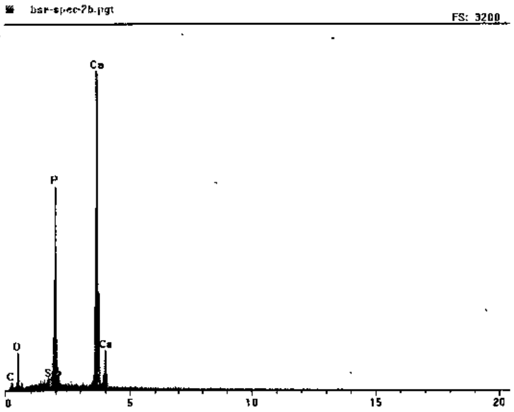

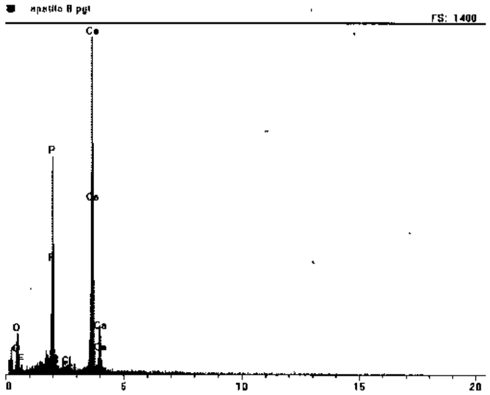

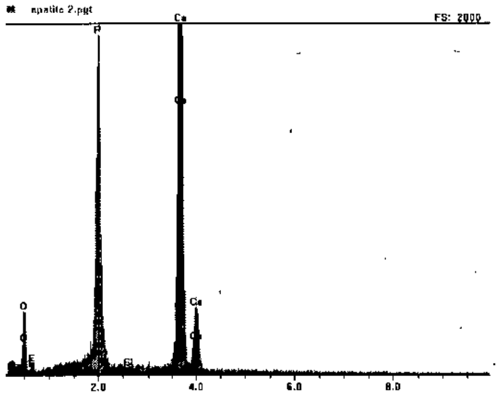

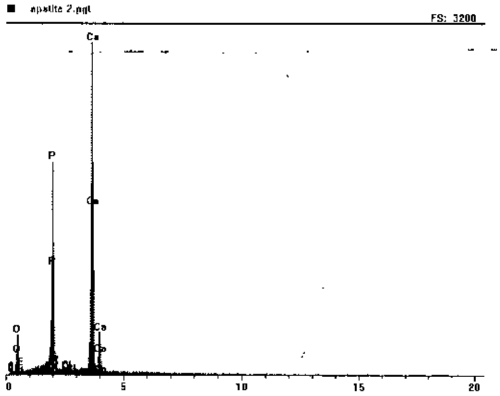

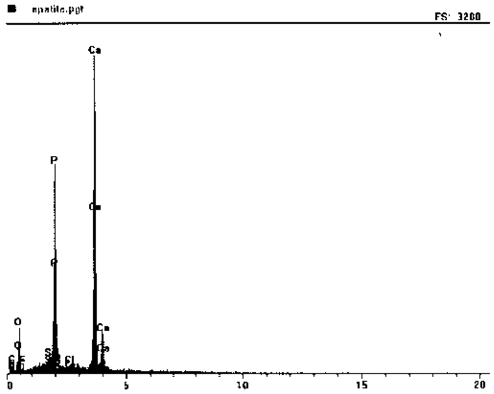

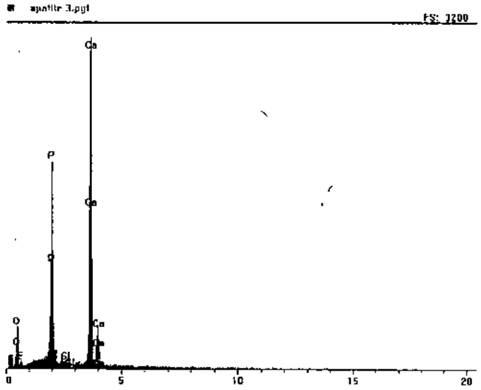

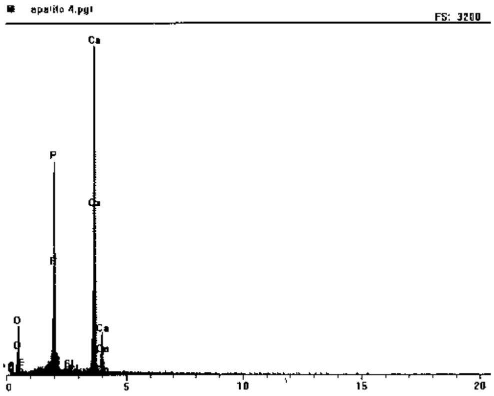
apatite 4.pgt
FS: 3200
Ca
P
Ca
P
O
O
Ca
Ca
F
Cl
0
5
10
15
20

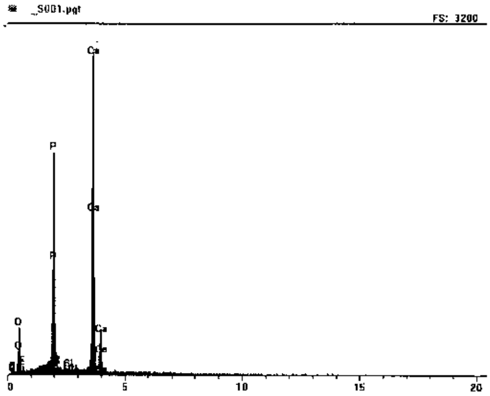
_S001.pgt
FS: 3200
Ca
P
Ca
P
O
O
Ca
Ca
F
Cl
0
5
10
15
20

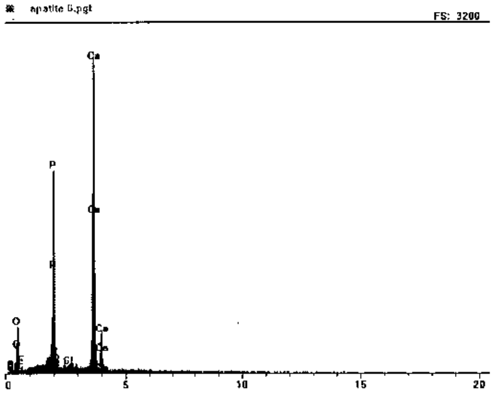
apatite 6.pgt
FS: 3200
Ca
P
Ca
P
O
O
Ca
Ca
F
Cl
0
5
10
15
20

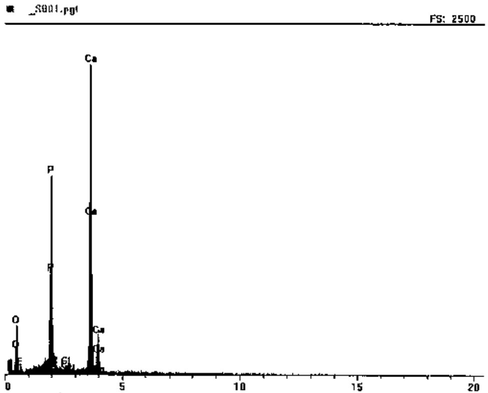
_S001.pgt
FS: 2500
Ca
P
Ca
P
O
O
Ca
Ca
F
Cl
0
5
10
15
20

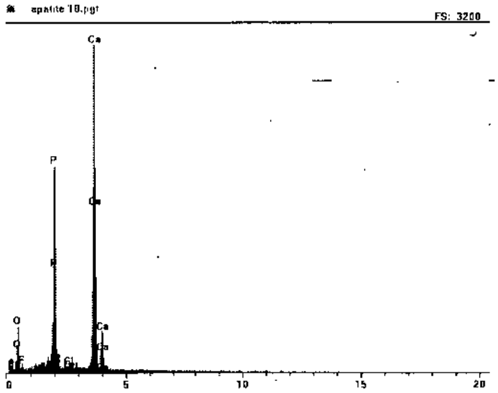
apatite 10.pgt
FS: 3200
Ca
P
Ca
P
O
O
Ca
Ca
F
Cl
0
5
10
15
20

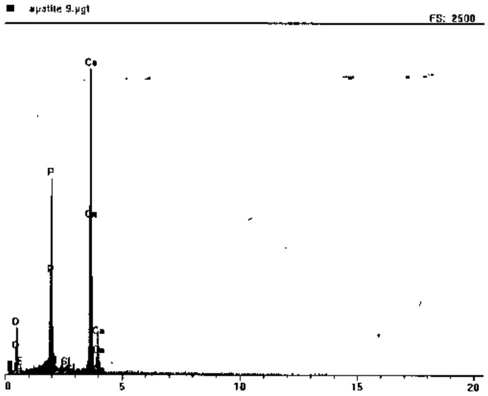
apatite 9.pgt
FS: 2500
Ca
P
Ca
P
O
O
Ca
Ca
F
Cl
0
5
10
15
20

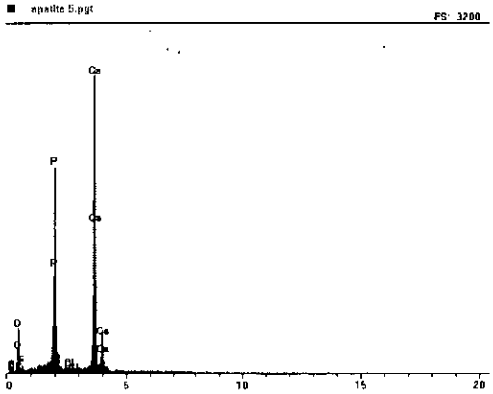
apatite 5.pgt
FS: 3200
Ca
P
Ca
P
O
O
Ca
Ca
F
Cl
0
5
10
15
20

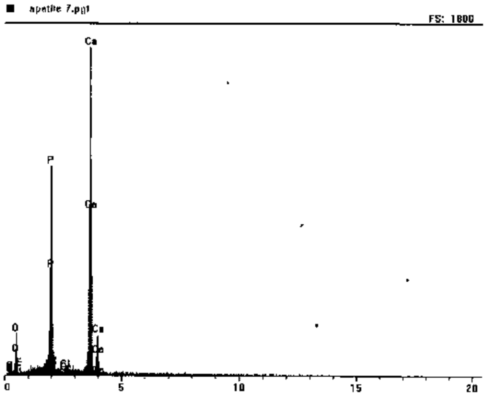
apatite 7.pgt
FS: 1800
Ca
P
Ca
P
O
O
Ca
Ca
F
Cl
0
5
10
15
20

Appendix II

AHe analysis data (1 of 9)

Sample Name	MAR 00/2030:2	MAL 00/2440:1	MAL 02/2440:2	mal00/2140:2	mar00/2200:1
U-TH DATA					
230/232 sample.natural	0.000001385	0.000001385	0.000001385	0.000001385	0.000001385
235/238 sample.natural	0.00725268	0.00725268	0.00725268	0.00725268	0.00725268
230Th/232Th spike	10000	10000	10000	10000	10000
1 sigma error	10	10	10	10	10
235U/238U spike	10000	10000	10000	10000	10000
1 sigma error	10	10	10	10	10
conc 230Th spike (ng/g)	15	15	15	15	15
1 sigma error	0.02	0.02	0.02	0.02	0.02
conc 235U spike (ng/g)	8.8	8.8	8.8	8.8	8.8
1 sigma error	0.01	0.01	0.01	0.01	0.01
mass of 230Th spike added (g)	0.03111	0.02864	0.03112	0.03088	0.02196
1 sigma error	0.0003111	0.0002864	0.0003112	0.00021	0.00021
mass of 235U spike added (g)	0.03031	0.03086	0.03036	0.03076	0.02932
1 sigma error	0.0003031	0.0003086	0.0003036	0.00021	0.00021
mass of 230Th spike added (ng)	0.46665	0.4296	0.4668	0.4632	0.3294
1 sigma error	0.004707797	0.004334018	0.004709311	0.003209973	0.003180471
mass of 235U spike added (ng)	0.266728	0.271568	0.267168	0.270688	0.258016
1 sigma error	0.002684446	0.002733158	0.002688875	0.001873425	0.001871115
Measured ratios					
230Th/232Th sample	0.843265306	0.364295322	0.960371158	0.49680136	0.596633693
1 sigma error	0.117247249	0.043468072	0.105584671	0.185587698	0.091613014
235U/238U sample	0.417377504	0.300805108	0.469069767	0.307986554	0.2594404
1 sigma error	0.055795383	0.037867149	0.056826712	0.121895391	0.041969553
235U/238U standard (interpol.)	0.9356	0.9688	0.9594	0.9398	0.9398
1 sigma error	0.0011	0.0015	0.0021	0.0014	0.0014
235/238 standard (true)	0.9997	0.9997	0.9997	0.9997	0.9997
1 sigma error	0.0009997	0.0009997	0.0009997	0.0009997	0.0009997
MASS BIAS	1.068512185	1.031895128	1.04200542	1.063736965	1.063736965
1 sigma error	0.00164922	0.001901952	0.002507565	0.001908554	0.001908554
MASS BIAS per amu (f)	0.022837395	0.010631709	0.014001807	0.021245655	0.021245655
1 sigma error	3.52489E-05	1.9596E-05	3.36951E-05	3.81189E-05	3.81189E-05
230/232 sample.lincorr	0.881781272	0.372041486	0.987265021	0.517911101	0.62198544
err f*meas	0.002677787	0.000462195	0.00147873	0.003942978	0.001946511
1 sigma error	0.196637709	0.168755405	0.15549942	0.528304013	0.217159692
235/238 sample.lincorr	0.445972949	0.310399326	0.48877324	0.327616682	0.275976344
err f*meas	0.001274306	0.000402636	0.000795834	0.002589774	0.000891725
1 sigma error	0.189059582	0.178039214	0.171345585	0.559722488	0.228783706
232/230 sample.lincorr	1.134068087	2.687872287	1.012899251	1.930833299	1.607754677
1 sigma error	0.150792909	0.314041932	0.108326166	0.691892693	0.236808199
238/235 sample.lincorr	2.242288466	3.221656483	2.045938521	3.05234762	3.623498974
1 sigma error	0.280531236	0.393025804	0.237868912	1.135678143	0.551049519
HELIUM DATA					
4He in pipette cc	6.2631E-09	6.2631E-09	6.2631E-09	6.26279E-09	6.26279E-09
1 sigma	6.2631E-11	6.2631E-11	6.2631E-11	6.26279E-11	6.26279E-11
% error	1	1	1	1	1
Comment	35 min @ 16%	35 min @ 16%	35 min @ 16%	35 min @ 16%	35 min @ 16%
Measured 4He (std-spike) torr	3.71E-09	3.71E-09	3.998E-09	3.292E-09	3.292E-09
4He cc/torr factor =	1.68816677	1.68816677	1.566557958	1.902425912	1.902425912
1st 3He/4He (std-spike)=	1.142	1.142	1.133	1.151	1.151
1 sigma error					
2nd 3He/4He (std-spike)=	1.137	1.137	1.14	1.146	1.146
1 sigma error					
Average 3He/4He (std-spike) =	1.1395	1.1395	1.1365	1.1485	1.1485
1 sigma error	0	0	0	0	0
3He (spike) cc =	7.1368E-09	7.1368E-09	7.11801E-09	7.19281E-09	7.19281E-09
1 sigma error	7.1368E-11	7.1368E-11	7.11801E-11	7.19281E-11	7.19281E-11
3He/4He (sample)	4.334	2.804	2.522	2.929	2.326
1 sigma error					
3He/4He (re-extract 1)	514.9	465.11	420.273	493.246	547.042
1 sigma error					
3He/4He (re-extract 2)	1E+20	1E+20	1E+20	1E+20	1E+20
1 sigma error	1E+20	1E+20	1E+20	1E+20	1E+20
Measured 4He (sample) cc =	1.6467E-09	2.54522E-09	2.82237E-09	2.45572E-09	3.09235E-09
Measured 4He (re-extract1) cc =	1.38606E-11	1.53443E-11	1.69366E-11	1.45826E-11	1.31486E-11
Measured 4He (re-extract2) cc =	7.1368E-29	7.1368E-29	7.11801E-29	7.19281E-29	7.19281E-29
Blank 4He (sample) torr	9.434E-12	1.005E-11	8.706E-12	6.771E-12	7.88E-12
Blank 4He (re-extract1) torr	7.475E-12	9.311E-12	1.046E-11	7.879E-12	7.1E-12
Blank 4He (re-extract2) torr			8.801E-12		
Blank 4He (sample) cc =	1.59262E-11	1.69661E-11	1.36385E-11	1.28813E-11	1.49911E-11
Blank 4He(re-extract1) cc =	1.2619E-11	1.57185E-11	1.63862E-11	1.49892E-11	1.35072E-11
Blank 4He(re-extract2) cc =	0	0	1.37873E-11	0	0
Corrected 4He(sample) cc =	1.63077E-09	2.52826E-09	2.80873E-09	2.44284E-09	3.07736E-09
Corrected 4He(re-extract1) cc =	1.24151E-12	-3.74192E-13	5.50442E-13	-4.06612E-13	-3.58673E-13
Th (ng)	0.529212986	1.15471036	0.472821466	0.894362246	0.529594529
1 sigma error	0.070569776	0.135414471	0.050791151	0.320544715	0.078172061
U (ng)	0.612251355	0.902139754	0.558751394	0.85089003	0.966915153
1 sigma error	0.076845811	0.110430373	0.065205592	0.316642958	0.147212292
4He sample (cc)	1.63202E-09	2.52788E-09	2.80928E-09	2.44243E-09	3.077E-09
1 sigma error	#REF!	#REF!	#REF!	#REF!	#REF!
Th/U	0.864372093	1.279968382	0.846210803	1.051090287	0.547715616
Copy to iterative calc. 238U	0.612251355	0.902139754	0.558751394	0.85089003	0.966915153
Copy to iterative calc. 235U	0.004440465	0.006542934	0.004052447	0.006171236	0.00701273
Copy to iterative calc. 232Th	0.529212986	1.15471036	0.472821466	0.894362246	0.529594529
Copy to iterative calc. 4He	1.63202E-09	2.52788E-09	2.80928E-09	2.44243E-09	3.077E-09
Uncorrected age (Ma, iterative)	18.2	17.7	34.4	ERROR	23.2

Appendix II

AHe analysis data (2 of 9)

Sample Name	mar00/2200:2	Mal-00/2765-2	bar02/1695:1	bar02/1695:2	mal00/2870:4
U-TH DATA					
230/232 sample.natural	0.000001385	0.000001385	0.000001385	0.000001385	0.000001385
235/238 sample.natural	0.00725268	0.00725268	0.00725268	0.00725268	0.00725268
230Th/232Th spike	10000	10000	10000	10000	10000
1 sigma error	10	10	10	10	10
235U/238U spike	10000	10000	10000	10000	10000
1 sigma error	10	10	10	10	10
conc 230Th spike (ng/g)	15	15	15	15	15
1 sigma error	0.02	0.02	0.02	0.02	0.02
conc 235U spike (ng/g)	8.8	8.8	8.8	8.8	8.8
1 sigma error	0.01	0.01	0.01	0.01	0.01
mass of 230Th spike added (g)	0.02856	0.0305	0.03098	0.02958	0.03071
1 sigma error	0.00021	0.000305	0.00021	0.00021	0.00021
mass of 235U spike added (g)	0.02931	0.0312	0.0301	0.03089	0.03093
1 sigma error	0.00021	0.000312	0.00021	0.00021	0.00021
mass of 230Th spike added (ng)	0.4284	0.4575	0.4647	0.4437	0.46065
1 sigma error	0.00320137	0.004615488	0.003210359	0.003205073	0.003209321
mass of 235U spike added (ng)	0.257928	0.27456	0.26488	0.271832	0.272184
1 sigma error	0.001871099	0.00276327	0.001872353	0.001873639	0.001873705
Measured ratios					
230Th/232Th sample	1.57171601	0.9322	0.927796879	0.633375351	0.428113457
1 sigma error	0.191291131	0.0075	0.129541494	0.060920076	0.062907556
235U/238U sample	0.630545846	0.7438	2.437394247	1.889473684	0.306691236
1 sigma error	0.106690544		0.34052708	0.215230793	0.037755879
235U/238U standard (interpol.)	0.9398	0.925	0.9398	0.9398	0.9398
1 sigma error	0.0014	0.0016	0.0014	0.0014	0.0014
235/238 standard (true)	0.9997	0.9997	0.9997	0.9997	0.9997
1 sigma error	0.0009997	0.0009997	0.0009997	0.0009997	0.0009997
MASS BIAS	1.063736965	1.080756757	1.063736965	1.063736965	1.063736965
1 sigma error	0.001908554	0.002159341	0.001908554	0.001908554	0.001908554
MASS BIAS per amu (f)	0.021245655	0.026918919	0.021245655	0.021245655	0.021245655
1 sigma error	3.81189E-05	5.37837E-05	3.81189E-05	3.81189E-05	3.81189E-05
230/232 sample.lincorr	1.638500283	0.982387632	0.967220184	0.6602883	0.446304559
err f*meas	0.004064547	0.000208024	0.002752421	0.001294512	0.001336612
1 sigma error	0.172131102	0.011552125	0.197464451	0.136035435	0.207814152
235/238 sample.lincorr	0.670734924	0.803866876	2.59274636	2.009903003	0.326238804
err f*meas	0.002266838	4.00043E-05	0.007235317	0.004573286	0.000802234
1 sigma error	0.239296566	0.00199799	0.197587186	0.161103691	0.174109022
232/230 sample.lincorr	0.610314206	1.017928124	1.033890748	1.514489958	2.240622417
1 sigma error	0.071252777	0.007771332	0.1384708	0.139731149	0.315820391
238/235 sample.lincorr	1.49090194	1.243987071	0.38569141	0.497536448	3.065239286
1 sigma error	0.237150525	0	0.050656081	0.053278772	0.354742603
HELIUM DATA					
4He in pipette cc	6.26279E-09	6.26275E-09	6.26279E-09	6.26279E-09	6.26279E-09
1 sigma	6.26279E-11	6.26275E-11	6.26279E-11	6.26279E-11	6.26279E-11
% error	1	1	1	1	1
Comment	35 min @ 16%	35 min @16%	35 min @ 16%	35 min @ 16%	35 min @ 16%
Measured 4He (std-spike) torr	3.38E-09	9.699E-09	3.359E-09	3.317E-09	3.279E-09
4He cc/torr factor =	1.852895297	0.645711397	1.86447934	1.888087459	1.909968314
1st 3He/4He (std-spike)=	1.143	1.137	1.151	1.143	1.145
1 sigma error					
2nd 3He/4He (std-spike)=	1.14	1.133	1.146	1.14	1.145
1 sigma error					
Average 3He/4He (std-spike) =	1.1415	1.135	1.1485	1.1415	1.145
1 sigma error	0	0	0	0	0
3He (spike) cc =	7.14897E-09	7.10823E-09	7.19281E-09	7.14897E-09	7.17089E-09
1 sigma error	7.14897E-11	7.10823E-11	7.19281E-11	7.14897E-11	7.17089E-11
3He/4He (sample)	7.767	14.442	19.184	25.384	1.521
1 sigma error					
3He/4He (re-extract 1)	408.298	348.512	533.75	547	561.9
1 sigma error					
3He/4He (re-extract 2)	1E+20	421.342	1E+20	1E+20	1E+20
1 sigma error	1E+20	1E+20	1E+20	1E+20	1E+20
Measured 4He (sample) cc =	9.20429E-10	4.92191E-10	3.74938E-10	2.81633E-10	4.71459E-09
Measured 4He (re-extract1) cc =	1.75092E-11	2.03959E-11	1.3476E-11	1.30694E-11	1.27619E-11
Measured 4He (re-extract2) cc =	7.14897E-29	1.68704E-11	7.19281E-29	7.14897E-29	7.17089E-29
Blank 4He (sample) torr	7.2E-12	2.527E-11	7.4E-12	7.4E-12	8.26E-12
Blank 4He (re-extract1) torr	9.4E-12	3.294E-11	7.2E-12	7E-12	7.082E-12
Blank 4He (re-extract2) torr		2.727E-11			
Blank 4He (sample) cc =	1.33408E-11	1.63171E-11	1.37971E-11	1.39718E-11	1.57763E-11
Blank 4He(re-extract1) cc =	1.74172E-11	2.12697E-11	1.34243E-11	1.32166E-11	1.35264E-11
Blank 4He(re-extract2) cc =	0	1.76085E-11	0	0	0
Corrected 4He(sample) cc =	9.07088E-10	4.75874E-10	3.61141E-10	2.67661E-10	4.69881E-09
Corrected 4He(re-extract1) cc =	9.19817E-14	-8.73802E-13	5.17391E-14	-1.47197E-13	-7.64534E-13
Th (ng)	0.261458648	0.465702211	0.480449128	0.671979363	1.032143051
1 sigma error	0.030587162	0.005891874	0.064432941	0.062188455	0.145660316
U (ng)	0.391488201	0.347087463	0.103170638	0.136692847	0.859288365
1 sigma error	0.062336852	0.003493213	0.013569874	0.014668067	0.099621906
4He sample (cc)	9.0718E-10	4.75E-10	3.61193E-10	2.67514E-10	4.69805E-09
1 sigma error	#REF!	#REF!	#REF!	#REF!	#REF!
Th/U	0.66785831	1.341743106	4.656839761	4.915980443	1.201160278
Copy to iterative calc. 238U	0.391488201	0.347087463	0.103170638	0.136692847	0.859288365
Copy to iterative calc. 235U	0.00283934	0.002517316	0.000748264	0.00099139	0.006232147
Copy to iterative calc. 232Th	0.261458648	0.465702211	0.480449128	0.671979363	1.032143051
Copy to iterative calc. 4He	9.0718E-10	4.75E-10	3.61193E-10	2.67514E-10	4.69805E-09
Uncorrected age (Ma, iterative)	16.4	9	ERROR	7.4	34.9

Appendix II

AHe analysis data (3 of 9)

Sample Name	mal00/2870:5	Mal-00/2870-6	Mal-00/2870:7	Mal-00/2360:2	Mal-00/2765-1
U-TH DATA					
230/232 sample.natural	0.000001385	0.000001385	0.000001385	0.000001385	0.000001385
235/238 sample.natural	0.00725268	0.00725268	0.00725268	0.00725268	0.00725268
230Th/232Th spike	10000	10000	10000	10000	10000
1 sigma error	10	10	10	10	10
235U/238U spike	10000	10000	10000	10000	10000
1 sigma error	10	10	10	10	10
conc 230Th spike (ng/g)	15	15	15	15	15
1 sigma error	0.02	0.02	0.02	0.02	0.02
conc 235U spike (ng/g)	8.8	8.8	8.8	8.8	8.8
1 sigma error	0.01	0.01	0.01	0.01	0.01
mass of 230Th spike added (g)	0.02652	0.029	0.0316	0.0301	0.0313
1 sigma error	0.00021	0.00029	0.000316	0.000301	0.000313
mass of 235U spike added (g)	0.02665	0.0315	0.0317	0.0311	0.0311
1 sigma error	0.00021	0.000315	0.000317	0.000311	0.000311
mass of 230Th spike added (ng)	0.3978	0.435	0.474	0.4515	0.4695
1 sigma error	0.003194343	0.004388496	0.004781948	0.004554957	0.004736549
mass of 235U spike added (ng)	0.23452	0.2772	0.27896	0.27368	0.27368
1 sigma error	0.001867117	0.00278984	0.002807554	0.002754414	0.002754414
Measured ratios					
230Th/232Th sample	0.769470405	1.469	1.034	0.979	1.055
1 sigma error	0.098381015	0.0086	0.0044	0.0084	0.0055
235U/238U sample	0.556750823	1.013	0.8326	0.7404	0.8108
1 sigma error	0.074497488				
235U/238U standard (interpol.)	0.9398	0.922	0.9204	0.9278	0.9264
1 sigma error	0.0014	0.0022	0.0022	0.0016	0.0016
235/238 standard (true)	0.9997	0.9997	0.9997	0.9997	0.9997
1 sigma error	0.0009997	0.0009997	0.0009997	0.0009997	0.0009997
MASS BIAS	1.063736965	1.084273319	1.086158192	1.07749515	1.079123489
1 sigma error	0.001908554	0.002805222	0.002814254	0.002147957	0.002153637
MASS BIAS per amu (f)	0.021245655	0.028091106	0.028719397	0.025831717	0.026374496
1 sigma error	3.81189E-05	7.2677E-05	7.44124E-05	5.14948E-05	5.26363E-05
230/232 sample.lincorr	0.802166211	1.55153167	1.093391714	1.029578501	1.110650187
err f*meas	0.002090375	0.000264123	0.000147947	0.000222766	0.000155326
1 sigma error	0.180823869	0.008674085	0.006552011	0.012296871	0.007638017
235/238 sample.lincorr	0.592236431	1.098368872	0.904335311	0.797777409	0.874953325
err f*meas	0.00158289	7.36218E-05	6.19558E-05	3.81268E-05	4.26775E-05
1 sigma error	0.189241019	0.002587191	0.002591017	0.001993473	0.001995728
232/230 sample.lincorr	1.246624436	0.644524388	0.91458531	0.971271252	0.900373503
1 sigma error	0.152891229	0.003572541	0.003680452	0.00792429	0.004458698
238/235 sample.lincorr	1.688514835	0.910440951	1.105784534	1.253482474	1.14291811
1 sigma error	0.212398472	0	0	0	0
HELIUM DATA					
4He in pipette cc	6.26279E-09	6.26275E-09	6.26275E-09	6.26275E-09	6.26275E-09
1 sigma	6.26279E-11	6.26275E-11	6.26275E-11	6.26275E-11	6.26275E-11
% error	1	1	1	1	1
Comment	35 min @ 16%	35 min @ 16%	35 min @ 16%	35 min %16%	35min @16%
Measured 4He (std-spike) torr	3.385E-09	9.845E-09	9.845E-09	1.106E-08	9.845E-09
4He cc/torr factor =	1.850158376	0.636135585	0.636135585	0.566252698	0.636135585
1st 3He/4He (std-spike)=	1.145	1.139	1.139	1.137	1.139
1 sigma error					
2nd 3He/4He (std-spike)=	1.145	1.14	1.14	1.139	1.14
1 sigma error					
Average 3He/4He (std-spike) =	1.145	1.1395	1.1395	1.138	1.1395
1 sigma error	0	0	0	0	0
3He (spike) cc =	7.17089E-09	7.13641E-09	7.13641E-09	7.12702E-09	7.13641E-09
1 sigma error	7.17089E-11	7.13641E-11	7.13641E-11	7.12702E-11	7.13641E-11
3He/4He (sample)	3.875	0.743	18.17	7.252	7.169
1 sigma error					
3He/4He (re-extract 1)	555.568	326.45	391.3	419.064	449.149
1 sigma error					
3He/4He (re-extract 2)	1E+20	411.8	388.1	586.32	586.32
1 sigma error	1E+20	1E+20	1E+20	1E+20	1E+20
Measured 4He (sample) cc =	1.85055E-09	9.60486E-09	3.92758E-10	9.82765E-10	9.95454E-10
Measured 4He (re-extract1) cc =	1.29073E-11	2.18606E-11	1.82377E-11	1.7007E-11	1.58887E-11
Measured 4He (re-extract2) cc =	7.17089E-29	1.73298E-11	1.83881E-11	1.21555E-11	1.21715E-11
Blank 4He (sample) torr	7.082E-12	3.203E-11	2.739E-11	2.418E-11	2.977E-11
Blank 4He (re-extract1) torr	7.106E-12	3.78E-11	3.233E-11	2.885E-11	2.527E-11
Blank 4He (re-extract2) torr		2.977E-11	3.203E-11		
Blank 4He (sample) cc =	1.31028E-11	2.03754E-11	1.74238E-11	1.3692E-11	1.89378E-11
Blank 4He(re-extract1) cc =	1.31472E-11	2.40459E-11	2.05663E-11	1.63364E-11	1.60751E-11
Blank 4He(re-extract2) cc =	0	1.89378E-11	2.03754E-11	0	0
Corrected 4He(sample) cc =	1.83745E-09	9.58448E-09	3.75334E-10	9.69073E-10	9.76516E-10
Corrected 4He(re-extract1) cc =	-2.39912E-13	-2.18528E-12	-2.32857E-12	6.70594E-13	-1.86412E-13
Th (ng)	0.495907312	0.280368155	0.43351352	0.438529057	0.42272544
1 sigma error	0.060950369	0.0032273	0.004708599	0.005689766	0.004750738
U (ng)	0.403724779	0.255842218	0.313154968	0.348640066	0.317631035
1 sigma error	0.050886201	0.002574888	0.003151704	0.003508839	0.003196753
4He sample (cc)	1.83721E-09	9.5823E-09	3.73005E-10	9.69744E-10	9.7633E-10
1 sigma error	#REF!	#REF!	#REF!	#REF!	#REF!
Th/U	1.228330136	1.095863527	1.384341825	1.257827483	1.33086945
Copy to iterative calc. 238U	0.403724779	0.255842218	0.313154968	0.348640066	0.317631035
Copy to iterative calc. 235U	0.002928088	0.001855543	0.002271214	0.002528576	0.002303677
Copy to iterative calc. 232Th	0.495907312	0.280368155	0.43351352	0.438529057	0.42272544
Copy to iterative calc. 4He	1.83721E-09	9.5823E-09	3.73005E-10	9.69744E-10	9.7633E-10
Uncorrected age (Ma, iterative)	29	192	12.5	18	19

Appendix II

AHe analysis data (4 of 9)

Sample Name	Mal-00/2360-1	mar00/2030:3	mm02/2635:4	bar02/1695:3	mar00/2304:1
U-TH DATA					
230/232 sample.natural	0.000001385	0.000001385	0.000001385	0.000001385	0.000001385
235/238 sample.natural	0.00725268	0.00725268	0.00725268	0.00725268	0.00725268
230Th/232Th spike	10000	10000	10000	10000	10000
1 sigma error	10	10	10	10	10
235U/238U spike	10000	10000	10000	10000	10000
1 sigma error	10	10	10	10	10
conc 230Th spike (ng/g)	15	15	15	15	15
1 sigma error	0.02	0.02	0.02	0.02	0.02
conc 235U spike (ng/g)	8.8	8.8	8.8	8.8	8.8
1 sigma error	0.01	0.01	0.01	0.01	0.01
mass of 230Th spike added (g)	0.0313	0.02677	0.02707	0.02782	0.02419
1 sigma error	0.000313	0.00021	0.00021	0.00021	0.00021
mass of 235U spike added (g)	0.0312	0.03015	0.0305	0.02918	0.02784
1 sigma error	0.000312	0.00021	0.00021	0.00021	0.00021
mass of 230Th spike added (ng)	0.4695	0.40155	0.40605	0.4173	0.36285
1 sigma error	0.004736549	0.003195177	0.003196187	0.003198762	0.003186936
mass of 235U spike added (ng)	0.27456	0.26532	0.2684	0.256784	0.244992
1 sigma error	0.00276327	0.001872433	0.001873	0.001870896	0.001868853
Measured ratios					
230Th/232Th sample	1.068	0.715881054	1.041437932	0.790815608	0.913076342
1 sigma error	0.0094	0.107777931	0.15058331	0.108398258	0.089567316
235U/238U sample	0.7621	0.443219773	0.643707094	2.257826888	0.386066523
1 sigma error		0.048574644	0.103771501	0.462466561	0.046210121
235U/238U standard (interpol.)	0.930375	0.9398	0.9398	0.9398	0.9398
1 sigma error	0.0012	0.0014	0.0014	0.0014	0.0014
235/238 standard (true)	0.9997	0.9997	0.9997	0.9997	0.9997
1 sigma error	0.0009997	0.0009997	0.0009997	0.0009997	0.0009997
MASS BIAS	1.074512965	1.063736965	1.063736965	1.063736965	1.063736965
1 sigma error	0.00175366	0.001908554	0.001908554	0.001908554	0.001908554
MASS BIAS per amu (f)	0.024837655	0.021245655	0.021245655	0.021245655	0.021245655
1 sigma error	4.05363E-05	3.81189E-05	3.81189E-05	3.81189E-05	3.81189E-05
230/232 sample.lincorr	1.121053231	0.746299778	1.085689994	0.824418399	0.951874152
err f*meas	0.000237454	0.002289975	0.003199487	0.002303189	0.001903235
1 sigma error	0.012553738	0.212921437	0.204491453	0.193856635	0.138737475
235/238 sample.lincorr	0.818886331	0.471469256	0.684735031	2.401733922	0.410673232
err f*meas	3.08927E-05	0.001032138	0.00220483	0.009825782	0.000981875
1 sigma error	0.001632051	0.155001033	0.227991287	0.28967634	0.169283391
232/230 sample.lincorr	0.892018302	1.33994412	0.92107324	1.212976325	1.050559045
1 sigma error	0.007479549	0.193509912	0.127751253	0.15948761	0.098853145
238/235 sample.lincorr	1.221170708	2.121029074	1.460418929	0.416365856	2.435026007
1 sigma error	0	0.218525874	0.22132629	0.080173446	0.273996055
HELIUM DATA					
4He in pipette cc	6.26275E-09	6.26279E-09	6.26279E-09	6.26279E-09	6.26279E-09
1 sigma	6.26275E-11	6.26279E-11	6.26279E-11	6.26279E-11	6.26279E-11
% error	1	1	1	1	1
Comment	35 min @ 16%	35 min @ 16%	35 min @ 16%	35 min @ 16%	35 min @ 16%
Measured 4He (std-spike) torr	9.699E-09	3.553E-09	3.553E-09	3.553E-09	3.394E-09
4He cc/torr factor =	0.645711397	1.762675514	1.762675514	1.762675514	1.84525224
1st 3He/4He (std-spike)=	1.137	1.157	1.157	1.157	1.156
1 sigma error					
2nd 3He/4He (std-spike)=	1.133	1.155	1.156	1.156	1.156
1 sigma error					
Average 3He/4He (std-spike) =	1.135	1.156	1.1565	1.1565	1.156
1 sigma error	0	0	0	0	0
3He (spike) cc =	7.10823E-09	7.23978E-09	7.24291E-09	7.24291E-09	7.23978E-09
1 sigma error	7.10823E-11	7.23978E-11	7.24291E-11	7.24291E-11	7.23978E-11
3He/4He (sample)	9.545	4.632	5.642	33.03	4.873
1 sigma error					
3He/4He (re-extract 1)	507.858	580.833	527.5	573.611	535.135
1 sigma error					
3He/4He (re-extract 2)	586.32	1E+20	1E+20	1E+20	1E+20
1 sigma error	1E+20	1E+20	1E+20	1E+20	1E+20
Measured 4He (sample) cc =	7.44707E-10	1.56299E-09	1.28375E-09	2.19283E-10	1.48569E-09
Measured 4He (re-extract1) cc =	1.39965E-11	1.24645E-11	1.37306E-11	1.26269E-11	1.35289E-11
Measured 4He (re-extract2) cc =	1.21235E-11	7.23978E-29	7.24291E-29	7.24291E-29	7.23978E-29
Blank 4He (sample) torr	2.687E-11	7.106E-12	7.2E-12	8E-12	7.4E-12
Blank 4He (re-extract1) torr	2.418E-11	7.2E-12	8E-12	7.2E-12	7.4E-12
Blank 4He (re-extract2) torr					
Blank 4He (sample) cc =	1.73503E-11	1.25256E-11	1.26913E-11	1.41014E-11	1.36549E-11
Blank 4He(re-extract1) cc =	1.56133E-11	1.26913E-11	1.41014E-11	1.26913E-11	1.36549E-11
Blank 4He(re-extract2) cc =	0	0	0	0	0
Corrected 4He(sample) cc =	7.27357E-10	1.55047E-09	1.27106E-09	2.05181E-10	1.47204E-09
Corrected 4He(re-extract1) cc =	-1.61682E-12	-2.26785E-13	-3.70765E-13	-6.43927E-14	-1.2598E-13
Th (ng)	0.418802672	0.538054687	0.374001861	0.506175132	0.381195428
1 sigma error	0.005493911	0.077821782	0.051956876	0.066667199	0.03602479
U (ng)	0.34066455	0.575570193	0.398964307	0.107995814	0.611564917
1 sigma error	0.00342857	0.059438935	0.060527053	0.020810046	0.068972975
4He sample (cc)	7.2574E-10	1.55024E-09	1.27069E-09	2.05117E-10	1.47191E-09
1 sigma error	#REF!	#REF!	#REF!	#REF!	#REF!
Th/U	1.229369689	0.934820277	0.937431881	4.686988438	0.623311471
Copy to iterative calc. 238U	0.34066455	0.575570193	0.398964307	0.107995814	0.611564917
Copy to iterative calc. 235U	0.002470732	0.004174428	0.002893562	0.000783259	0.004435487
Copy to iterative calc. 232Th	0.418802672	0.538054687	0.374001861	0.506175132	0.381195428
Copy to iterative calc. 4He	7.2574E-10	1.55024E-09	1.27069E-09	2.05117E-10	1.47191E-09
Uncorrected age (Ma, iterative)	14	18.1	21.4	7.4	17.2

Appendix II

AHe analysis data (5 of 9)

Sample Name	Mal-00/2440: 5	MAL-00/2650:4	MAL-00/2650:5	MM-02/2440:1	MM-02/2440:2
U-TH DATA					
230/232 sample.natural	0.000001385	0.000001385	0.000001385	0.000001385	0.000001385
235/238 sample.natural	0.00725268	0.00725268	0.00725268	0.00725268	0.00725268
230Th/232Th spike	10000	10000	10000	10000	10000
1 sigma error	10	10	10	10	10
235U/238U spike	10000	10000	10000	10000	10000
1 sigma error	10	10	10	10	10
conc 230Th spike (ng/g)	15	15	15	15	15
1 sigma error	0.02	0.02	0.02	0.02	0.02
conc 235U spike (ng/g)	8.8	8.8	8.8	8.8	8.8
1 sigma error	0.01	0.01	0.01	0.01	0.01
mass of 230Th spike added (g)	0.0311	0.03116	0.03016	0.0308	0.03111
1 sigma error	0.000311	0.0003116	0.0003016	0.000308	0.0003111
mass of 235U spike added (g)	0.0309	0.03121	0.03099	0.03101	0.031
1 sigma error	0.000309	0.0003121	0.0003099	0.0003101	0.00031
mass of 230Th spike added (ng)	0.4665	0.4674	0.4524	0.462	0.46665
1 sigma error	0.004706284	0.004715364	0.004564036	0.004660886	0.004707797
mass of 235U spike added (ng)	0.27192	0.274648	0.272712	0.272888	0.2728
1 sigma error	0.002736701	0.002764156	0.002744671	0.002746443	0.002745557
Measured ratios					
230Th/232Th sample	0.9972	0.734845668	0.421467556	1.10145224	1.131718717
1 sigma error	0.0042	0.0807253	0.044945878	0.192107994	0.128066956
235U/238U sample	0.7304	0.476757587	0.314184768	0.558993711	0.637676972
1 sigma error		0.072632088	0.043390198	0.092693778	0.092999371
235U/238U standard (interpol.)	0.93155	0.94662331	0.943230445	0.939837579	0.936355691
1 sigma error	0.0012	0.0019	0.002	0.0021	0.002275
235/238 standard (true)	0.9997	0.9997	0.9997	0.9997	0.9997
1 sigma error	0.0009997	0.0009997	0.0009997	0.0009997	0.0009997
MASS BIAS	1.07315764	1.056069493	1.059868249	1.063694432	1.067649836
1 sigma error	0.001750069	0.002368184	0.002484703	0.002603917	0.002805119
MASS BIAS per amu (f)	0.02438588	0.018689831	0.019956083	0.021231477	0.022549945
1 sigma error	3.97677E-05	4.1911E-05	4.67841E-05	5.19745E-05	5.92472E-05
230/232 sample.lincorr	1.045835199	0.76231395	0.438289239	1.148223156	1.182759107
err f*meas	0.00010983	0.001509057	0.00089716	0.004079138	0.002888681
1 sigma error	0.006175581	0.155372361	0.150831892	0.246669897	0.160056055
235/238 sample.lincorr	0.783834341	0.503489144	0.33299446	0.594598497	0.680815714
err f*meas	2.90463E-05	0.001357629	0.000866023	0.00196824	0.002097471
1 sigma error	0.001630766	0.215461381	0.19532273	0.234521314	0.206266885
232/230 sample.lincorr	0.956173593	1.311795487	2.281598339	0.870910846	0.845480702
1 sigma error	0.003839925	0.138912694	0.233974349	0.145711167	0.091547078
238/235 sample.lincorr	1.275779777	1.986140143	3.003052961	1.681807143	1.468826261
1 sigma error	0	0.286515624	0.391306997	0.262182057	0.200641548
HELIUM DATA					
4He in pipette cc	6.26275E-09	6.2628E-09	6.2628E-09	6.2628E-09	6.2628E-09
1 sigma	6.26275E-11	6.2628E-11	6.2628E-11	6.2628E-11	6.2628E-11
% error	1	1	1	1	1
Comment	35 min @ 16%	35 min @ 16%	35 min @ 16%	35 min @ 16%	35 min @ 16%
Measured 4He (std-spike) torr	1.106E-08	3.24E-09	3.24E-09	3.038E-09	3.292E-09
4He cc/torr factor =	0.566252698	1.93296189	1.93296189	2.061486677	1.902429078
1st 3He/4He (std-spike)=	1.137	1.157	1.157	1.152	1.152
1 sigma error					
2nd 3He/4He (std-spike)=	1.139	1.159	1.159	1.147	1.147
1 sigma error					
Average 3He/4He (std-spike) =	1.138	1.158	1.158	1.1495	1.1495
1 sigma error	0	0	0	0	0
3He (spike) cc =	7.12702E-09	7.25232E-09	7.25232E-09	7.19908E-09	7.19908E-09
1 sigma error	7.12702E-11	7.25232E-11	7.25232E-11	7.19908E-11	7.19908E-11
3He/4He (sample)	7.574	5.765	3.6238	4.287	5.936
1 sigma error					
3He/4He (re-extract 1)	529.494	381.69	359.46	560	568.9
1 sigma error					
3He/4He (re-extract 2)	586.32	559.23	568.72	1E+20	1E+20
1 sigma error	1E+20	1E+20	1E+20	1E+20	1E+20
Measured 4He (sample) cc =	9.40984E-10	1.25799E-09	2.0013E-09	1.67928E-09	1.21278E-09
Measured 4He (re-extract1) cc =	1.346E-11	1.90005E-11	2.01756E-11	1.28555E-11	1.26544E-11
Measured 4He (re-extract2) cc =	1.21555E-11	1.29684E-11	1.2752E-11	7.19908E-29	7.19908E-29
Blank 4He (sample) torr	2.885E-11	1.055E-11	1.001E-11	6.356E-12	6.49E-12
Blank 4He (re-extract1) torr	2.136E-11	9.843E-12	5.47E-12	3.673E-12	6.356E-12
Blank 4He (re-extract2) torr					
Blank 4He (sample) cc =	1.63364E-11	2.03927E-11	1.93489E-11	1.31028E-11	1.23468E-11
Blank 4He(re-extract1) cc =	1.20952E-11	1.90261E-11	1.05733E-11	7.57184E-12	1.20918E-11
Blank 4He(re-extract2) cc =	0	0	0	0	0
Corrected 4He(sample) cc =	9.24648E-10	1.2376E-09	1.98195E-09	1.66618E-09	1.20044E-09
Corrected 4He(re-extract1) cc =	1.36489E-12	-2.5598E-14	9.60229E-12	5.28367E-12	5.62555E-13
Th (ng)	0.446055068	0.613133352	1.032195427	0.402360886	0.394543642
1 sigma error	0.004843457	0.06522179	0.106361016	0.067440843	0.04290548
U (ng)	0.352617366	0.557361331	0.843099765	0.467885823	0.407864242
1 sigma error	0.003548868	0.080598996	0.110185687	0.073091998	0.055865237
4He sample (cc)	9.26013E-10	1.23757E-09	1.99156E-09	1.67146E-09	1.201E-09
1 sigma error	#REF!	#REF!	#REF!	#REF!	#REF!
Th/U	1.26498327	1.10006439	1.224286224	0.859955284	0.967340605
Copy to iterative calc. 238U	0.352617366	0.557361331	0.843099765	0.467885823	0.407864242
Copy to iterative calc. 235U	0.002557422	0.004042365	0.006114736	0.003393428	0.00295811
Copy to iterative calc. 232Th	0.446055068	0.613133352	1.032195427	0.402360886	0.394543642
Copy to iterative calc. 4He	9.26013E-10	1.23757E-09	1.99156E-09	1.67146E-09	1.201E-09
Uncorrected age (Ma, iterative)	17	14.6	15.1	24.5	19.8

Appendix II
AHe analysis data (6 of 9)

Sample Name	MM-02/2440:3	BAR-02/1150:1	BAR-02/1150:2	Mal-00/2440-6
U-TH DATA				
230/232 sample.natural	0.000001385	0.000001385	0.000001385	0.000001385
235/238 sample.natural	0.00725268	0.00725268	0.00725268	0.00725268
230Th/232Th spike	10000	10000	10000	10000
1 sigma error	10	10	10	10
235U/238U spike	10000	10000	10000	10000
1 sigma error	10	10	10	10
conc 230Th spike (ng/g)	15	15	15	15
1 sigma error	0.02	0.02	0.02	0.02
conc 235U spike (ng/g)	8.8	8.8	8.8	8.8
1 sigma error	0.01	0.01	0.01	0.01
mass of 230Th spike added (g)	0.03114	0.0313	0.03104	0.0309
1 sigma error	0.0003114	0.000313	0.0003104	0.000309
mass of 235U spike added (g)	0.03099	0.0313	0.03108	0.0316
1 sigma error	0.0003099	0.000313	0.0003108	0.000316
mass of 230Th spike added (ng)	0.4671	0.4695	0.4656	0.4635
1 sigma error	0.004712337	0.004736549	0.004697204	0.004676018
mass of 235U spike added (ng)	0.272712	0.27544	0.273504	0.27808
1 sigma error	0.002744671	0.002772127	0.002752642	0.002798697
Measured ratios				
230Th/232Th sample	1.743113176	2.042186354	1.976432197	1.055
1 sigma error	0.241396431	0.200447191	0.227980976	0.0055
235U/238U sample	1.019925857	1.078776645	0.835889571	0.8108
1 sigma error	0.131231485	0.099457705	0.1119347	0.0083
235U/238U standard (interpol.)	0.936266669	0.936177646	0.934822392	0.9188
1 sigma error	0.00235	0.002425	0.00215	0.0022
235/238 standard (true)	0.9997	0.9997	0.9997	0.9997
1 sigma error	0.0009997	0.0009997	0.0009997	0.0009997
MASS BIAS	1.06775135	1.067852885	1.069400999	1.08804963
1 sigma error	0.002884894	0.002965049	0.002681948	0.002823333
MASS BIAS per amu (f)	0.022583783	0.022617628	0.023133666	0.029349877
1 sigma error	6.10178E-05	6.28011E-05	5.80169E-05	7.61587E-05
230/232 sample.lincorr	1.821845357	2.134565177	2.067876444	1.11692824
err f*meas	0.005452682	0.004535454	0.005275282	0.000180315
1 sigma error	0.195867139	0.1388374	0.163148469	0.007815987
235/238 sample.lincorr	1.089027211	1.151974752	0.893901142	0.88219064
err f*meas	0.002964357	0.002250517	0.002589914	0.000251308
1 sigma error	0.181983624	0.130412841	0.189395175	0.014707738
232/230 sample.lincorr	0.548894008	0.468479487	0.483587887	0.895312666
1 sigma error	0.072729035	0.043992752	0.053315003	0.004408716
238/235 sample.lincorr	0.918250701	0.868074581	1.118691937	1.133541839
1 sigma error	0.110652335	0.0749467	0.140083104	0.010664812
HELIUM DATA				
4He in pipette cc	6.2628E-09	6.2627E-09	6.2628E-09	6.26275E-09
1 sigma	6.2628E-11	6.2627E-11	6.2628E-11	6.26275E-11
% error	1	1	1	1
Comment	35 min @ 16%	35 min @ 16%	35 min @ 16%	35 min @16%
Measured 4He (std-spike) torr	3.071E-09	3.292E-09	3.292E-09	9.699E-09
4He cc/torr factor =	2.03933459	1.902400585	1.902429078	0.645711397
1st 3He/4He (std-spike)=	1.156	1.156	1.156	1.137
1 sigma error				
2nd 3He/4He (std-spike)=	1.148	1.148	1.148	1.133
1 sigma error				
Average 3He/4He (std-spike) =	1.152	1.152	1.152	1.135
1 sigma error	0	0	0	0
3He (spike) cc =	7.21474E-09	7.21463E-09	7.21474E-09	7.10823E-09
1 sigma error	7.21474E-11	7.21463E-11	7.21474E-11	7.10823E-11
3He/4He (sample)	4.212	21.34	32.189	11.27
1 sigma error				
3He/4He (re-extract 1)	576.73	612	622.39	428.359
1 sigma error				
3He/4He (re-extract 2)	1E+20	1E+20	1E+20	586.32
1 sigma error	1E+20	1E+20	1E+20	1E+20
Measured 4He (sample) cc =	1.7129E-09	3.3808E-10	2.24137E-10	6.30721E-10
Measured 4He (re-extract1) cc =	1.25097E-11	1.17886E-11	1.1592E-11	1.65941E-11
Measured 4He (re-extract2) cc =	7.21474E-29	7.21463E-29	7.21474E-29	1.21235E-11
Blank 4He (sample) torr	6.327E-12	6.327E-12	5.96E-12	2.727E-11
Blank 4He (re-extract1) torr	6.327E-12	5.964E-12	5.84E-12	2.687E-11
Blank 4He (re-extract2) torr				
Blank 4He (sample) cc =	1.29029E-11	1.20365E-11	1.13385E-11	1.76085E-11
Blank 4He(re-extract1) cc =	1.29029E-11	1.13459E-11	1.11102E-11	1.73503E-11
Blank 4He(re-extract2) cc =	0	0	0	0
Corrected 4He(sample) cc =	1.7E-09	3.26044E-10	2.12798E-10	6.13113E-10
Corrected 4He(re-extract1) cc =	-3.93131E-13	4.427E-13	4.81809E-13	-7.56178E-13
Th (ng)	0.256388431	0.219951152	0.225158554	0.414977499
1 sigma error	0.034070065	0.020773454	0.024927181	0.004658586
U (ng)	0.253873561	0.242313145	0.310643325	0.320068026
1 sigma error	0.030699142	0.021062182	0.039024334	0.004409618
4He sample (cc)	1.69961E-09	3.26487E-10	2.1328E-10	6.12356E-10
1 sigma error	#REF!	#REF!	#REF!	#REF!
Th/U	1.009905994	0.907714486	0.724813751	1.296529067
Copy to iterative calc. 238U	0.253873561	0.242313145	0.310643325	0.320068026
Copy to iterative calc. 235U	0.001841265	0.001757421	0.002252998	0.002321352
Copy to iterative calc. 232Th	0.256388431	0.219951152	0.225158554	0.414977499
Copy to iterative calc. 4He	1.69961E-09	3.26487E-10	2.1328E-10	6.12356E-10
Uncorrected age (Ma, iterative)	45	9.3	4.9	12.5

Appendix II

AHe analysis data (7 of 9)

	MAL 2650-1	MAL 2650-2	MAL 2650-3	MAL 2250-1	MAL 2250-2	MAL 1760: 1b
Sample Name --->	3	11	2	4	5	8
230/232 sample.natural	1.38504E-06	1.38504E-06	1.38504E-06	1.38504E-06	1.38504E-06	1.38504E-06
235/238 sample.natural	0.007252683	0.007252683	0.007252683	0.007252683	0.007252683	0.007252683
230Th/232Th spike	10000	10000	10000	10000	10000	10000
1 sigma error	10	10	10	10	10	10
235U/238U spike	10000	10000	10000	10000	10000	10000
1 sigma error	10	10	10	10	10	10
conc 230Th spike (ng/g)	15	15	15	15	15	15
1 sigma error	0.015	0.015	0.015	0.015	0.015	0.015
conc 235U spike (ng/g)	8.8	9.8	10.8	11.8	12.8	14.8
1 sigma error	0.0088	0.0098	0.0108	0.0118	0.0128	0.0148
mass of 230Th spike added (g)	0.21	0.21	0.21	0.21	0.21	0.20922
1 sigma error	0.00021	0.00021	0.00021	0.00021	0.00021	0.00020922
mass of 235U spike added (g)	0.21	0.21	0.21	0.21	0.21	0.20655
1 sigma error	0.00021	0.00021	0.00021	0.00021	0.00021	0.00020655
mass of 230Th spike added (ng)	3.15	3.15	3.15	3.15	3.15	3.1383
1 sigma error	0.004454773	0.004454773	0.004454773	0.004454773	0.004454773	0.004438226
mass of 235U spike added (ng)	1.848	2.058	2.268	2.478	2.688	3.05694
1 sigma error	0.002613467	0.002910452	0.003207436	0.003504421	0.003801406	0.004323166
MEASURED RATIOS						
230Th/232Th sample	4.864	4.059	2.917	2.326	2.239	3.251
1 sigma error	0.0848	0.0226	0.0124	0.0181	0.005	0.0108
235U/238U sample	10.1	5.3	3.12	2.198	2.21	2.97
1 sigma error	0.0994	0.0099	0.0277	0.024	0.014	0.0057
235U/238U standard (interpol.)	0.7951	0.9147	0.8248	0.9247	0.9207	0.914
1 sigma error	0.004	0.0014	0.006	0.006	0.004	0.0014
235/238 standard (true)	0.9997	0.9997	0.9997	0.9997	0.9997	0.9997
1 sigma error	0.0009997	0.0009997	0.0009997	0.0009997	0.0009997	0.0009997
MASS BIAS	1.257326123	1.092926643	1.212051406	1.081107386	1.085804279	1.093763676
1 sigma error	0.006449125	0.001998175	0.008899975	0.007097683	0.004840649	0.002000778
MASS BIAS per amu (f)	0.085775374	0.030975548	0.070683802	0.027035795	0.028601426	0.031254559
1 sigma error	0.000439962	5.66319E-05	0.000519024	0.000177495	0.000127509	5.71727E-05
230/232 sample.lincorr	5.69842284	4.310459495	3.329369302	2.45177052	2.367077188	3.454217141
err f*meas	0.007582016	0.000736822	0.001749398	0.000640242	0.000319307	0.00038534
1 sigma error	0.025183576	0.008083628	0.009489955	0.012814382	0.005463395	0.005041655
235/238 sample.lincorr	12.69899384	5.792511206	3.781600388	2.376274035	2.399627457	3.248478118
err f*meas	0.009614555	0.000429102	0.002540836	0.000757115	0.000489637	0.000246111
1 sigma error	0.01483316	0.003212614	0.014545215	0.016779502	0.010006762	0.00327304
232/230 sample.lincorr	0.175487153	0.231993828	0.300357188	0.407868515	0.422461931	0.289501198
1 sigma error	0.002611479	0.001216358	0.001118659	0.003011057	0.00089237	0.000905158
238/235 sample.lincorr	0.078746396	0.172636697	0.264438306	0.420826885	0.416731354	0.307836459
1 sigma error	0.000616379	0.000295054	0.001936995	0.004250286	0.00243131	0.000540151
4He measured V	0.003252	0.005883	0.006273	0.007672	0.009203	0.005032
Error	0.000041	0.000044	0.000046	0.000048	0.00002	0.000024
4He MAP3 conversion factor	0.00406162	0.00406162	0.00406162	0.00406162	0.00406162	0.00406162
Th (ng)	0.552784597	0.730780649	0.946125264	1.284786002	1.330755273	0.908541726
1 sigma error	0.008263222	0.003968461	0.003769258	0.009657295	0.003382803	0.003117729
U (ng)	0.146632908	0.358239282	0.605134166	1.053374317	1.1314893	0.949791262
1 sigma error	0.001166336	0.000794697	0.004514429	0.010742707	0.00679255	0.00214048
4He sample (cc)	8.00666E-10	1.44844E-09	1.54446E-09	1.8889E-09	2.26584E-09	1.23891E-09
1 sigma error	1.00945E-11	1.08331E-11	1.13255E-11	1.18179E-11	4.92414E-12	5.90897E-12
Th/U	3.769853614	2.039923272	1.563496689	1.21968609	1.176109462	0.956569894
Copy to iterative calc. 238U	0.146632908	0.358239282	0.605134166	1.053374317	1.1314893	0.949791262
Copy to iterative calc. 235U	0.001063482	0.002598196	0.004388847	0.007639791	0.008206334	0.006888535
Copy to iterative calc. 232Th	0.552784597	0.730780649	0.946125264	1.284786002	1.330755273	0.908541726
Copy to iterative calc. 4He	8.00666E-10	1.44844E-09	1.54446E-09	1.8889E-09	2.26584E-09	1.23891E-09
Age (Ma, iterative)	23.7	22.4	15.3	11.4	12.8	8.1

Appendix II

AHe analysis data (8 of 9)

	MAL 1760: 2b	MAL 1920: 1	MAL 1920:2	MAL 2030: 2	MAL 2030: 1	MAL 2650-6
Sample Name --->	15	12	13	14	6	16
230/232 sample.natural	1.38504E-06	1.38504E-06	1.38504E-06	1.38504E-06	1.38504E-06	1.38504E-06
235/238 sample.natural	0.007252683	0.007252683	0.007252683	0.007252683	0.007252683	0.007252683
230Th/232Th spike	10000	10000	10000	10000	10000	10000
1 sigma error	10	10	10	10	10	10
235U/238U spike	10000	10000	10000	10000	10000	10000
1 sigma error	10	10	10	10	10	10
conc 230Th spike (ng/g)	15	15	15	15	15	15
1 sigma error	0.015	0.015	0.015	0.015	0.015	0.015
conc 235U spike (ng/g)	16.8	17.8	18.8	19.8	20.8	22.8
1 sigma error	0.0168	0.0178	0.0188	0.0198	0.0208	0.0228
mass of 230Th spike added (g)	0.20699	0.20883	0.20942	0.20922	0.20994	0.21
1 sigma error	0.00020699	0.00020883	0.00020942	0.00020922	0.00020922	0.00021
mass of 235U spike added (g)	0.20955	0.20974	0.19817	0.20978	0.2102	0.21
1 sigma error	0.00020955	0.00020974	0.00019817	0.00020978	0.00020978	0.00021
mass of 230Th spike added (ng)	3.10485	3.13245	3.1413	3.1383	3.1383	3.1491
1 sigma error	0.004390921	0.004429953	0.004442469	0.004438226	0.004438226	0.004454136
mass of 235U spike added (ng)	3.52044	3.733372	3.725596	4.153644	4.363424	4.79256
1 sigma error	0.004978654	0.005279785	0.005268788	0.00587414	0.006170813	0.00677448
MEASURED RATIOS						
230Th/232Th sample	2.02	2.725	1.957	2.653	1.869	4.221
1 sigma error	0.0062	0.0088	0.007	0.0074	0.01	0.0267
235U/238U sample	2.21	2.78	1.72	3.6	1.65	4.7
1 sigma error	0.0155	0.0067	0.0031	0.008	0.0072	0.0258
235U/238U standard (interpol.)	0.8804	0.9136	0.908	0.8942	0.9168	0.9562
1 sigma error	0.0024	0.0014	0.002	0.0022	0.0025	0.0026
235/238 standard (true)	0.9997	0.9997	0.9997	0.9997	0.9997	0.9997
1 sigma error	0.0009997	0.0009997	0.0009997	0.0009997	0.0009997	0.0009997
MASS BIAS	1.135506588	1.094242557	1.100991189	1.117982554	1.090423211	1.045492575
1 sigma error	0.003297129	0.002002269	0.002663315	0.002969096	0.003167084	0.00302895
MASS BIAS per amu (f)	0.045168863	0.031414186	0.03366373	0.039327518	0.03014107	0.015164192
1 sigma error	0.000131155	5.74824E-05	8.14331E-05	0.000104445	8.75434E-05	4.3933E-05
230/232 sample.lincorr	2.202482205	2.896207312	2.088759838	2.861671811	1.981667321	4.349016105
err f*meas	0.000385507	0.000317738	0.000284475	0.000401839	0.000342957	0.000445331
1 sigma error	0.005222313	0.004919934	0.005607148	0.004755356	0.008104973	0.009403073
235/238 sample.lincorr	2.509469559	3.041994308	1.893704846	4.024737195	1.799198298	4.913815101
err f*meas	0.000757746	0.000264265	0.000174667	0.000490267	0.000260693	0.000442382
1 sigma error	0.010334975	0.00386848	0.003514028	0.004114562	0.006820447	0.008286113
232/230 sample.lincorr	0.45403318	0.34527915	0.478752981	0.349446081	0.504625569	0.229937065
1 sigma error	0.001278106	0.001049116	0.001604431	0.000903633	0.00254647	0.001411657
238/235 sample.lincorr	0.398490588	0.328731713	0.528065396	0.248463428	0.555803105	0.203507861
1 sigma error	0.002461319	0.000724032	0.000864444	0.000493873	0.002224203	0.001068519
4He measured V	0.007705	0.00514	0.008499	0.004673	0.007503	0.004595
Error	0.000023	0.000022	0.00003	0.000023	0.000026	0.000024
4He MAP3 conversion factor	0.00406162	0.00406162	0.00406162	0.00406162	0.00406162	0.00406162
Th (ng)	1.409705125	1.08156982	1.503906963	1.096666785	1.583666662	0.724094901
1 sigma error	0.004440964	0.003624827	0.005470381	0.003232263	0.008299486	0.004561902
U (ng)	1.416845238	1.23888222	1.98884194	1.041179487	2.452182989	0.983650487
1 sigma error	0.008977751	0.003242706	0.004302421	0.002539919	0.010407852	0.005348552
4He sample (cc)	1.89703E-09	1.2655E-09	2.09251E-09	1.15053E-09	1.84729E-09	1.13132E-09
1 sigma error	5.66277E-12	5.41656E-12	7.38622E-12	5.66277E-12	6.40139E-12	5.90897E-12
Th/U	0.994960555	0.873020698	0.756172189	1.05329273	0.645819121	0.736130272
Copy to iterative calc. 238U	1.416845238	1.23888222	1.98884194	1.041179487	2.452182989	0.983650487
Copy to iterative calc. 235U	0.01027593	0.008985221	0.014424441	0.007551345	0.017784907	0.007134106
Copy to iterative calc. 232Th	1.409705125	1.08156982	1.503906963	1.096666785	1.583666662	0.724094901
Copy to iterative calc. 4He	1.89703E-09	1.2655E-09	2.09251E-09	1.15053E-09	1.84729E-09	1.13132E-09
Age (Ma, iterative)	8.1	6.9	6.9	6.5	5.3	7.2

Appendix II

AHe analysis data (9 of 9)

	MAL 1760: 1a	MAL2250-3
Sample Name --->	10	17
230/232 sample.natural	1.38504E-06	1.38504E-06
235/238 sample.natural	0.007252683	0.007252683
230Th/232Th spike	10000	10000
1 sigma error	10	10
235U/238U spike	10000	10000
1 sigma error	10	10
conc 230Th spike (ng/g)	15	15
1 sigma error	0.015	0.015
conc 235U spike (ng/g)	15.8	23.8
1 sigma error	0.0158	0.0238
mass of 230Th spike added (g)	0.21	0.21
1 sigma error	0.00021	0.00021
mass of 235U spike added (g)	0.21	0.21
1 sigma error	0.00021	0.00021
mass of 230Th spike added (ng)	3.15	3.15
1 sigma error	0.004454773	0.004454773
mass of 235U spike added (ng)	3.318	4.998
1 sigma error	0.004692361	0.007068239
MEASURED RATIOS		
230Th/232Th sample	2.6383	2.593
1 sigma error	0.0084	0.0054
235U/238U sample	5.8	3.02
1 sigma error	0.0138	0.0289
235U/238U standard (interpol.)	0.9141	0.953
1 sigma error	0.0014	0.0026
235/238 standard (true)	0.9997	0.9997
1 sigma error	0.0009997	0.0009997
MASS BIAS	1.093644021	1.049003148
1 sigma error	0.002000406	0.003048112
MASS BIAS per amu (f)	0.031214674	0.016334383
1 sigma error	5.70954E-05	4.74632E-05
230/232 sample.lincorr	2.803007348	2.677710108
err f*meas	0.000302393	0.000151417
1 sigma error	0.004860012	0.00413728
235/238 sample.lincorr	6.343135324	3.167989507
err f*meas	0.00054334	0.000493346
1 sigma error	0.003829871	0.013841795
232/230 sample.lincorr	0.356759678	0.373453421
1 sigma error	0.001069131	0.000753124
238/235 sample.lincorr	0.157650743	0.315657611
1 sigma error	0.000342982	0.002879588
4He measured V	0.003958	0.0082625
Error	0.000022	0.000031
4He MAP3 conversion factor	0.00406162	0.00406162
Th (ng)	1.123793139	1.176378437
1 sigma error	0.003723929	0.00289754
U (ng)	0.527375411	1.592422856
1 sigma error	0.00136845	0.014700409
4He sample (cc)	9.74488E-10	2.03429E-09
1 sigma error	5.41656E-12	7.63242E-12
Th/U	2.130916831	0.738734962
Copy to iterative calc. 238U	0.527375411	1.592422856
Copy to iterative calc. 235U	0.003824887	0.011549339
Copy to iterative calc. 232Th	1.123793139	1.176378437
Copy to iterative calc. 4He	9.74488E-10	2.03429E-09
Age (Ma, iterative)	9.2	8.3

Sample	Elevation (m)	Grains	Av. Dia (μm)	^{4}He (cc)	^{238}U (ng)	^{232}Th (ng)	Raw age (Ma)	Ft correction (%)	Corrected age (Ma)	Uncertainty (± Ma)
Marimaña										
MM-02/2635:1	2635	8	80	2.47E-09	0.510	1.031	27.0	0.68	39.9	4.0
MM-02/2635:2	2635	9	73	1.70E-09	0.353	0.512	29.5	0.64	46.0	4.6
MM-02/2635:4	2635	7	75	1.27E-09	0.267	0.374	29.4	0.66	44.3	4.4
MM-02/2440:1	2440	7	80	1.67E-09	0.605	0.402	23.7	0.67	35.2	3.5
MM-02/2440:2	2440	6	72	1.20E-09	0.273	0.395	27.0	0.72	37.7	3.8
Mar-00/2304:1	2304	7	94	1.47E-09	0.410	0.381	24.2	0.71	34.2	3.4
Mar-00/2200:1	2200	5	118	3.08E-09	0.648	0.530	32.7	0.76	[43.0]	-
Mar-00/2200:2	2200	5	90	9.07E-09	0.262	0.261	23.0	0.71	32.3	3.2
Mar-00/2030:1	2030	7	90	2.00E-09	0.517	0.873	22.8	0.72	31.8	3.2
Mar-00/2030:2	2030	7	105	1.63E-09	0.410	0.529	25.1	0.73	34.3	3.4
Mar-00/2030:3	2030	7	103	1.55E-09	0.386	0.538	24.9	0.72	34.5	3.5
Maladeta										
Mal-00/2870:1	2870	6	92	1.40E-09	0.388	0.723	20.6	0.71	29.2	2.9
Mal-00/2870:2	2870	8	70	1.10E-09	0.369	0.719	16.9	0.64	26.4	2.6
Mal-00/2870:4	2870	5	117	4.70E-09	0.576	1.032	47.0	0.77	[61.0]	-
Mal-00/2870:5	2870	4	96	1.84E-09	0.271	0.496	38.9	0.72	[53.7]	-
Mal-00/2870:6	2870	5	58	9.58E-09	0.172	0.280	323.7	0.76	[582.2]	-
Mal-00/2870:7	2870	6	60	3.73E-09	0.210	0.434	9.9	0.57	17.3	1.7
Mal-00/2765:1	2765	6	91	9.76E-09	0.213	0.423	25.7	0.74	34.9	3.5
Mal-00/2765:2	2765	7	59	4.75E-09	0.233	0.466	11.4	0.56	20.4	2.0

Table 4.2 [Revised]

Apatite (U-Th)/He data

Sample	Elevation (m)	Grains	Av. Dia (μm)	^{4}He (cc)	^{238}U (ng)	^{232}Th (ng)	Raw age (Ma)	Ft correction (%)	Corrected age (Ma)	Uncertainty (± Ma)
(continued)										
Mal-00/2650:1	2650	9	64	8.01E-10	0.098	0.553	28.7	0.62	[46.8]	-
Mal-00/2650:2	2650	10	72	1.45E-09	0.216	0.731	30.6	0.65	[47.7]	-
Mal-00/2650:3	2650	9	90	1.54E-09	0.331	0.946	22.9	0.71	32.6	3.3
Mal-00/2650:4	2650	11	75	1.24E-09	0.374	0.613	19.7	0.64	30.8	3.1
Mal-00/2650:5	2650	12	74	1.99E-09	0.565	1.032	20.3	0.65	31.4	3.1
Mal-00/2650:6	2650	9	64	1.13E-09	0.255	0.724	21.8	0.62	[35.4]	-
Mal-00/2440:1	2440	11	79	2.53E-09	0.605	1.155	23.7	0.67	[35.2]	-
Mal-00/2440:2	2440	8	93	2.81E-09	0.375	0.473	47.4	0.72	[66.3]	-
Mal-00/2440:5	2440	9	60	9.23E-09	0.236	0.446	22.3	0.58	[38.6]	-
Mal-00/2440:6	2440	8	62	6.12E-09	0.215	0.415	16.2	0.62	26.1	2.6
Mal-00/2360:1	2360	5	83	7.26E-10	0.228	0.419	17.3	0.72	24.0	2.4
Mal-00/2360:2	2360	6	58	9.70E-10	0.233	0.439	23.7	0.55	[42.8]	-
Mal-00/2250:1	2250	6	107	1.89E-09	0.527	1.285	18.7	0.77	24.5	2.5
Mal-00/2250:2	2250	8	90	2.27E-09	0.521	1.331	22.2	0.71	31.3	3.1
Mal-00/2250:3	2250	8	97	2.03E-09	0.395	1.176	24.8	0.73	[34.3]	-
Mal-00/2140:2	2140	10	80	2.44E-09	0.570	0.894	25.7	0.68	[37.9]	-
Mal-00/2140:3	2140	9	68	1.25E-09	0.382	0.682	18.9	0.63	30.2	3.0
Mal-00/2030:1	2030	13	81	1.85E-09	0.696	1.584	14.2	0.69	20.8	2.1
Mal-00/2030:2	2030	13	64	1.15E-09	0.31	1.097	16.3	0.61	26.8	2.7
Mal-00/1920:1	1920	18	60	1.27E-09	0.411	1.082	15.6	0.57	27.9	2.8
Mal-00/1920:2	1920	7	114	2.09E-09	0.624	1.504	17.5	0.77	22.8	2.3
Mal-00/1760:1a	1760	8	99	9.74E-10	0.197	1.124	17.3	0.74	23.4	2.3
Mal-00/1760:1b	1760	8	103	1.24E-09	0.379	0.909	17.1	0.75	22.9	2.3
Mal-00/1760:2b	1760	7	116	1.90E-09	0.498	1.410	18.9	0.79	23.9	2.4

Table 4.2 [Revised] (continued)

Sample	Elevation (m)	Grains	Av. Dia (μm)	^{4}He (cc)	^{238}U (ng)	^{232}Th (ng)	Raw age (Ma)	Ft correction (%)	Corrected age (Ma)	Uncertainty (± Ma)
Barruera										
Bar-02/1695:1	1695	8	74	3.61E-10	0.069	0.480	16.3	0.67	[24.3]	-
Bar-02/1695:2	1695	10	69	2.68E-10	0.092	0.672	8.8	0.64	13.8	1.4
Bar-02/1695:3	1695	13	54	2.05E-10	0.072	0.506	8.8	0.56	15.9	1.6
Bar-02/1150:1	1150	10	68	3.26E-10	0.162	0.220	12.6	0.63	[20.1]	-
Bar-02/1150:2	1150	10	59	2.13E-10	0.208	0.225	6.8	0.65	10.5	1.1

Table 4.2 [Revised](continued)

Appendix III

Gibson et al. (submitted to Basin Research)

POST-OROGENIC EXHUMATION OF THE PYRENEES LINKED TO REJUVENATION OF THE EBRO BASIN: INSIGHTS FROM (U-TH)/HE THERMOCHRONOMETRY

M. Gibson, * H. D. Sinclair, * G. J. Lynn,.*, & F. M. Stuart†

*School of GeoSciences, The University of Edinburgh, Grant Institute, Kings Buildings, West Mains Road, Edinburgh, EH9 3JW, UK
†Scottish Universities Environmental Research Centre, Scottish Enterprise Technology Park, Rankine Avenue, East Kilbride, Glasgow, G75 OQF, UK

Correspondence: Matthew Gibson, School of GeoSciences, The University of Edinburgh, Grant Institute, Kings Buildings, West Mains Road, Edinburgh, EH9 3JW, UK. Email: matthew.gibson@glg.ed.ac.uk

ABSTRACT

Apatite (U-Th)/He thermochronometry and 3D thermal modelling are applied to constrain the post-orogenic exhumation history of the central Pyrenees, Spain. Cooling ages from south of the drainage divide range from 7.8 to 29.9 Ma. The age-elevation relationships and forward modelling of simulated time-temperature (*t*-T) histories are consistent with an abrupt rejuvenation of exhumation during upper Miocene times (10±2 Ma). In contrast, the cooling ages from similar elevation samples from immediately north of the drainage divide range from 23.2 to 33.7 Ma; *t*-T modelling indicates these ages are consistent with either very slow and continuous exhumation, or with an exhumational pulse at 10±2 Ma that was significantly smaller than documented on the southern flank of the range. This acceleration of exhumation is up to 20 Myr after the documented cessation of major tectonics within the central Pyrenees. Consequently, it is proposed that the exhumation event was initiated and driven by an external forcing which acted to locally increase rates of erosional denudation. This is attributed to an abrupt lowering of regional base-levels in south-draining catchments, associated with the opening of the internally-drained Ebro Basin to the Mediterranean Sea. This timing of events is closely compatible with large siliciclastic progradations and increases in sedimentation rates within the offshore Valencia Trough.

INTRODUCTION

Understanding the factors that govern the decay of high-relief topography within post-orogenic environments, and the associated late-stage exhumation history of orogens, remains at the forefront of deciphering long-term landscape evolution (e.g. Pazzaglia & Brandon, 1996; Baldwin et al., 2003; Reiners et al., 2003). Rock cooling histories obtained through the application of isotopic thermochronometers can be used as a proxy for exhumation and provide quantitative constraints on the temporal and spatial variability of erosional denudation (e.g. Reiners et al., 2003; Foeken et al., 2003; Spotila et al., 2004a). In tectonically-inactive mountain systems this enables the geomorphic response to changing environmental parameters, or particular geological events, to be accurately assessed without the ambiguity of a combined tectonically-driven forcing (e.g. Cederbom et al., in press).

Empirical and theoretical models of the decay of high-relief topography indicate that post-orogenic erosion occurs over protracted time periods at steady, slow rates and may exponentially decline through time as topographic relief is progressively reduced (Pinet & Souriau, 1988; Pazzaglia & Brandon, 1996; Baldwin et al., 2003; Reiners et al., 2003; Carrapa et al., 2003). However, recent studies indicate that external forces acting on tectonically-inactive mountainous topography, such as climatic changes, palaeoceanographic aberrations or fluvial reorganisations, may exert sufficient influence on the rates of erosional denudation to induce non-monotonic patterns of exhumationally-driven cooling (Zhang et al., 2001; Baldwin et al., 2003; Reiners et al., 2003; Foeken et al., 2003; Cederbom et al., in press). At present the extent to which such external forces individually contribute to the acceleration of exhumation, and the time-scales on which they influence the system, remain poorly constrained.

The Pyrenees of western Europe (Fig. 1) represent an Alpine-age collisional mountain belt that has experienced more than 20 Myr of post-orogenic decay (Fitzgerald et al., 1999). Apatite fission track studies in the central Pyrenees have been interpreted to record rapid Axial Zone exhumation during late Eocene to early Oligocene times, followed by abrupt deceleration and cessation of exhumation processes at ~30-32 Ma (Fitzgerald et al., 1999). Localised exhumation has also been identified on a smaller scale in the western central Pyrenees up to ~20 Ma (Sinclair et al., submitted). The decline of erosional denudation is regarded to coincide with the termination of major compressional tectonics and with a rise in fluvial base-levels and reduction of local relief (Fitzgerald et al., 1999). This is associated with the closure and infilling of the Ebro foreland basin and the onlap of alluvial sediments onto the southern flank of the range (Coney et al., 1996; Fitzgerald et al., 1999). Forward modelling of the fission track length distributions has predicted that a 'post-orogenic' rejuvenation of rapid exhumation rates may have occurred after a period of thermal quiescence of more than 20 Myr (Fitzgerald et al., 1999). Importantly, as there is no structural or metamorphic evidence to suggest the central Pyrenees has experienced any significant tectonic denudation during its Neogene evolution, a rejuvenation of exhumation requires accelerated rates of erosional denudation. It has been postulated that such a sudden rejuvenation of exhumation may be linked to the re-excavation of the Ebro foreland Basin on the southern flank of the Pyrenees, possibly during the Messinian salinity crisis at 5.97 Ma (Coney et al., 1996; Krijgsman et al., 1999; Fitzgerald et al., 1999). As the proposed post-orogenic rejuvenation of exhumation in the Pyrenees has not been documented, and as the timing and duration of the Ebro Basin capture and re-excavation is still poorly constrained, our understanding of the late-stage exhumation history of the mountain belt and it's postulated linkage to Ebro drainage evolution is purely speculative.

Here, we test for the presence of accelerated post-orogenic exhumation in the central Pyrenees using apatite (U-Th)/He (hereafter referred to as AHe) thermochronology. This radiometric system can be used to constrain the timing of rock cooling in the upper crust, with a temperature sensitivity over the 40-80°C range and with a closure temperature of ~70°C (for 10°C Myr^{-1} cooling rate; 80μm effective radius) (Zeitler et al., 1987; Wolf et al., 1996; Farley, 2000). AHe ages and modelled thermal histories are used to consider if the Pyrenees has undergone an exhumational history which is characterised by slow and steadily-declining erosion, as predicted for areas of progressively reducing high relief (e.g. Pinet & Souriau, 1988; Baldwin et al., 2003) or by a more punctuated history as predicted by previous thermochronometer studies (Fitzgerald et al., 1999). Integration of the derived exhumation histories with existing geological data is used to critically assess and discriminate between a number of possible mechanisms which could have influenced exhumation after the cessation of major tectonics. In particular, the postulated dynamic linkage between fluvial reorganisation, associated with the opening of the internally-drained Ebro Basin to a seaward connection, and rates of erosional denudation in the orogenic hinterland are considered.

GEOLOGIC AND GEOMORPHIC SETTING

The Pyrenean orogen extends over 1500 km from the Mediterranean Sea in south-west France to the Cantabrian platform in northern Spain, and separates the Iberian peninsula from the rest of the European continent. The range forms a ~150 km-wide west-northwest to east-southeast trending linear zone of high topography and relief with the main drainage divide running down the axis of the orogen (Fig. 2). Elevation and local relief is intimately linked to lithostratigraphic variation, with highest mean and peak elevations associated with metamorphic basement lithologies of the Axial Zone and a number of crystalline massifs distributed across the central orogen.

The mountain belt formed by Afro-Iberian and European plate convergence, initiated during late Cretaceous times determined by the opening of the Central Atlantic and the rotation of Iberia to open the Bay of Biscay (Roest and Srivastava, 1991). The ECORS deep seismic profile (Choukroune et al., 1989) and seismic tomography data (Souriau & Granet, 1995) indicate the Iberian plate was partially subducted below the European plate during active convergence.

The orogen comprises an Axial Zone, of dominantly Palaeozoic meta-sediments and Hercynian-age crystalline massifs, flanked to the north and south by folded and thrusted Mesozoic and Cenozoic sedimentary cover rocks (Fig. 1) (Zwart, 1979; Muñoz, 1992). The central Axial zone is characterised by a complex antiformal duplex structure of stacked thrust nappes which accommodated a significant component of the estimated 165 km of overall tectonic shortening (Muñoz, 1992; Beaumont et al., 2000). Rapid rates of exhumation during upper Eocene and Lower Oligocene times, on the southern flank of the range, have been linked to temporally-variable, tectonically-driven rock uplift, associated with internal deformation in the upper crust below the basement antiformal stack (Muñoz, 1992; Fitzgerald et al., 1999).

To the north and south of the respective deformation fronts are the Aquitaine and the Ebro foreland basins. Analysis of Iberian plate kinematics indicate convergence had ceased by early Miocene times as Iberia had begun to move as part of the Eurasian plate, with its southern boundary along the Azores-Gibraltar Fracture Zone (Srivistava et al., 1990; Roest and Srivistava, 1991). This is consistent with the youngest age-constrained compressive deformation in the South Pyrenean fold and thrust belt (Meigs et al., 1996; Meigs, 1997) and in the Iberian and Catalan Coastal Range (Guimera, 1984).

The Ebro foreland basin, to the south of the mountain belt, formed by flexural subsidence in response to crustal loading primarily associated with the growth of the Pyrenees, but also due to the development of the Catalan Coastal Range and Iberian Range, to the southeast and southwest, respectively (Fig. 1 and 2) (Riba et al., 1983; Zoetemeijer et al., 1990; Puigdefàbregas et al., 1992). The early stratigraphic history of the basin was dominated by the accumulation of deep-water turbidites during late Cretaceous times followed by a Palaeocene transition into continental alluvial and fluvial red beds in the north, with deep-water carbonates toward the west (Puigdefàbregas et al., 1992). During late Eocene times the western seaward connection of the basin was closed through Pyrenean and Iberian Range tectonism (Riba et al., 1983). This marked the onset of a period of endorheic (internal) drainage for all fluvial catchments draining into the basin from the adjacent Pyrenean, Iberian and Catalan Coastal Range topographic barriers. During this time deltaic, fluvial and alluvial sediments progressively infilled the basin and onlapped across the low relief topography of the south Pyrenean fold and thrust belt and across the southern flank of the Pyrenees (Coney et al., 1996). Sedimentation in the Ebro Basin continued up to at least ~14 Ma, as documented by the presence of magneto-stratigraphically-dated lacustrine and alluvial sediments in the geographic centre of the basin (Pérez-Rivarés et al., 2002). Present-day exposures of these sediments are preserved, undeformed, at up to ~800m elevation; these have been deeply incised by fluvial systems down-cutting since basin capture. It is interpreted this incision has been caused by the considerable fall in base-level upon reconnection of the Ebro Basin to the Mediterranean Sea (Riba et al., 1983; Coney et al., 1996).

The timing of reopening and excavation of the Ebro Basin has not been established but has been tentatively linked to sediment overfilling and eventual capture, or piracy, by streams that drained into the Mediterranean Sea during Miocene times (Riba et al., 1983; Serrat, 1992). It has been postulated that the combination of Miocene rifting offshore of the Catalan Coastal Ranges and the drop in sea level associated with the Messinian salinity crisis at 5.97 Ma (Krijgsman et al., 1999) may have triggered the capture of the Ebro drainage (Dañobeita et al., 1990; Coney et al., 1996). However, the role of the Messinian event in initiating or contributing to basin capture remains poorly constrained. Recent studies of the geomorphic maturity of the Ebro drainage network, in comparison to the propagation of regressive fluvial incision in similar geological settings, has been used to suggest the area is unlikely to have been reconnected to the Mediterranean until significantly later than the Messinian event (Loget et al., 2004). Conversely, the presence of large-scale siliciclastic progradations into the Valencia Trough from the Ebro Delta (Ziegler et al., 1988; Johns et al., 1989; Roca and Desegaulx, 1992; Bartrina et al., 1992; Roca, 2001) from as early as the middle Miocene (middle Serravallian; Martínez del Olmo, 1996), and pre-Messinian increases in Ebro continental margin sedimentation rates (Dañobeitia et al., 1990; Martínez del Olmo, 1996) have been interpreted to support a Pre-Messinian age of basin capture (e.g. Evans & Archie, 2002). This notion is supported by 3D numerical simulations of the region which suggest the Messinian event was too short a duration for the base-level pulse to impose a first order impact on the timing of Ebro basin opening (Garcia-Castellanos et al., 2003). These model predictions require a drainage opening between 13 and 8.5 Ma to enable the sedimentary infill of the Ebro basin to be reworked by fluvial systems (Garcia-Castellanos et al., 2003). Low temperature thermochronology is used here to distinguish between these alternative scenarios by documenting the late-stage erosion history of the southern Pyrenees.

THERMOCHRONOMETRY

Methodology

Three vertical profiles were sampled from high-relief Hercynian-age granodioritic massifs (Barruera, Maladeta and Marimaña) from coherent structural blocks within the central Axial Zone (Fig. 1 and 2). All samples were fresh, unweathered bedrock located at least 100 m from hydrothermal vein systems or from evidence of small-scale fault or shear structures. The two southern profiles (Barruera and Maladeta) are located south of the modern Pyrenean watershed within the hinterlands of catchments entering the southern Ebro modern drainage system. The northern profile (Marimaña) is located immediately north of the main Pyrenean watershed within a catchment draining into the northern Aquitaine drainage system. Profile localities were chosen to sample the maximum local vertical topographic relief with minimal horizontal separation between samples.

Apatite crystals were separated from the host rock for analysis using standard magnetic and gravimetric differentiation techniques after disaggregation and sieving. Individual crystals were screened under polarised light at 218X magnification for mineral inclusions, structural defects, appropriate morphology and size. The physical dimensions of between 5-15 inclusion-free crystals per sample were measured and packed into stainless steel capsules and wrapped in degassed Cu foil. Variation of grain diameter was minimised within individual aliquots to reduce the standard deviation of the recoil correction within each population to ±0.5% (Farley et al., 1996). Where enough inclusion-free apatite was recovered individual sample analyses were reproduced in duplicate or triplicate (Ehlers and Farley, 2002). Samples were heated in a double-walled resistance furnace at 950°C for 35-minute intervals. Liberated gas was purified on hot and cold TiZr getters and liquid nitrogen-cooled charcoal trap for 10 minutes after heating. ^{4}He abundance was measured relative to a 99.9% pure ^{3}He spike in a Hiden HAL3F mass spectrometer. Samples were checked for quantitative degassing of He by a subsequent reheating for 35-minutes. Capsules were extracted from the furnace and the samples dissolved in 5% nitric acid and spiked with 3 ng ^{230}Th and 1.3 ng ^{235}U, and U and Th concentrations measured by VG PlasmaQuad 2 ICP-MS. All laboratory He ages are corrected for the effects of α-ejection following the methods of Farley (2002). The analytical uncertainty on age determinations is ≤6%. Typically, multiple aliquots of the same sample yield a reproducibility of ±8-10% (Persano et al., 2002).

Fission track analysis was also undertaken on a number of apatite crystals extracted from the same samples and profiles. Methodology, data and interpretations of these analyses are presented by Sinclair et al. (submitted), though the fission track ages are also considered in this study to help constrain the derived thermal histories from the AHe data (House et al., 1997). In addition, a number of fission track slides were also used to characterise the relative distribution of U (and by inference Th) in a large selection of apatite crystals from the samples used for AHe analysis. This was undertaken as a number of previous workers have demonstrated the potentially significant impact a non-homogenous distribution of parent elements may have on measured AHe ages if undetected and unaccounted for (Farley et al., 1996; Meesters and Dunai, 2002).

Results

U, Th and He concentration measurements are summarised (Table 1) and He ages, after α-ejection correction (Farley, 2002), are plotted against elevation for each of the sampling profiles (Fig. 3). The distribution of U and Th are homogenous for the representative samples. Thus it is assumed that all apatite crystals used for AHe analysis possessed a similar U and Th distribution and no additional corrections were applied. As the isotherms for which AHe dating is sensitive are higher in the thermal structure of the crust than for apatite fission track dating, it logically follows that fission track ages must be older than, or effectively equal to, those for the AHe system. Three AHe ages which were older than the apatite fission track ages from the corresponding samples were regarded to be erroneously high, and are omitted from thermal modelling calculations.

AHe ages from the Marimañi profile are early Oligocene, or younger, and range from 23.2±2.3 Ma (Mar-00/2200:2) to 33.7±3.4 Ma (MM-02/2635:2) (Fig. 3a). AHe ages from the Maladeta profile are late

Oligocene, or younger, and range from 7.8±0.8 Ma (Mal-00/2030:1) to 29.9±3.0 Ma (Mal-00/2440:5) (Fig. 3b). AHe ages from the Barruera profile are of middle Miocene age, or younger, and range from 7.6±0.8 Ma (Bar-02/1150:2) to 14.9±1.5 Ma (Bar-02/1150:1) (Fig. 3c).

AHe data reproducibility

AHe age reproducibility is variable. A number of samples reproduce in duplicate or triplicate well within the prescribed analytical uncertainty. This reproducibility is an indispensable demonstration of the quality of specific AHe ages (e.g. Bar-02/1695, Mal-00/1760, Mal-00/2650, Mal-00/2870, Mar-00/2030, MM-02/2635) (Ehlers & Farley, 2003). However, the standard of precision for a number of the remaining samples is significantly lower (e.g. Mal-00/2250 and Mar-00/2200). As noted by a number of previous workers (e.g. House et al., 1997; Mesters and Dunai, 2002; Farley, 2002; Ehlers and Farley, 2003; Foeken et al., 2003; Spotila et al., 2004) there are several factors which may commonly and adversely affect the reproducibility of an AHe age. Variation in He loss, such as grain size variations, undetected parent element zonation, variability in kinetic parameters, or the presence of sub-microscopic U or Th-rich mineral or fluid inclusions all may affect AHe ages in replicates from the same sample (Ehlers & Farley, 2003). In this study, grain size variability can be effectively discounted as grain size variation between aliquots was not large enough to induce age differences larger than the analytical uncertainty. Likewise, parent element zonation is unlikely to have played a significant role. The most likely factor which affected the reproducibility within certain samples was the inclusion of sub-microscopic U and Th-rich mineral inclusions within the apatite crystals (House et al., 1997; Foeken et al., 2003; Spotila et al., 2004). Owing to the destructive nature of AHe analysis, it cannot be unequivocally determined which factors influenced the AHe age of the crystals used. Bearing this in mind, it is inappropriate to be selective and to discriminate between any of the AHe ages which are younger than their respective fission track age. Consequently, the only circumspect approach to deal with the data is to consider the span of measured ages for each sample, plus their individual uncertainty bounds. Following this inclusive and non-interpretative treatment of the data, the profiles still delineate clear age-elevation trends and hold important implications for the patterns of exhumation.

Interpretation

Fission track ages of ~28 to 36 Ma (Fig. 3e) and high mean track lengths (~14 μm) for all samples from the Marimañi and Maladeta profiles (Fig. 3e and Appendix: Table 3) were interpreted by Sinclair et al. (submitted) to document rapid cooling of both profiles to crustal depths above the fission track Partial Annealing Zone (PAZ) (Naeser, 1979; Gleadow & Fitzgerald, 1987) during lower Oligocene times. This was also consistent with a previous interpretation of fission track data from similar elevations along orogenic strike in the Maladeta Massif by Fitzgerald et al. (1999), which linked rapid cooling and exhumation in the southern Pyrenees during this period to accelerated tectonic rock uplift. Fission track data from the Barruera profile suggest limited exhumation may have occurred up to ~20 Ma. However, as this signal is not documented in any of the surrounding sampling localities it is assumed this was a localised effect which did not significantly influence regional patterns of exhumation.

In contrast to the fission track data, the AHe ages from this study show a marked asymmetry between the Marimaña and Maladeta sampling areas (Fig. 3a, b). AHe ages from the Marimañi profile depict a positive, linear age-elevation relationship which is tightly constrained within the uncertainty bounds by the high quality ages from the uppermost and lowermost samples. The uppermost AHe age is indistinguishable, within error from the corresponding fission track age. This probably reflects the rapid cooling of the sample through both the fission track and AHe closure isotherms during rapid exhumation associated with accelerated erosional denudation during Pyrenean mountain-building (Fitzgerald et al., 1999; Sinclair et al., submitted). The remaining AHe ages from the profile decrease consistently with decreasing elevation. This age-elevation relationship may document the progressive cooling of the samples at a given vertical velocity during upper Oligocene and early Miocene times, or may simply represent static residence in the AHe Partial Rention Zone (PRZ) (e.g. Wolf et al., 1996; Wolf et al., 1998; Warnock et al., 1997; House et al., 1999).

AHe ages from the Maladeta profile, however, yield markedly younger ages (~10 Myr younger) for similar elevations to those in the Marimañi. A positive linear age-elevation gradient is clearly discernible in the upper section of the profile (above ~2100m) which steepens to a vertical relationship in the lower section of the profile below ~2100m. The reproducibility of the AHe ages improves in the lower elevation samples. The age-elevation relationship depicted by the data is consistent with the progressive cooling of the upper elevation samples, or their protracted stasis in a PRZ, followed abruptly by a period of rapid cooling of the lower elevation samples (below ~2100m) through the AHe closure isotherm at ~10±2 Ma. The discernible improvement of reproducibility in the lower elevation ages is also consistent with their rapid transition through temperatures at which the AHe system is sensitive (Ehlers and Farley, 2003). However, it is important to recognise that owing to the spread of measured ages, particularly in the upper samples, this interpretation of the data is non-unique and a number of alternative scenarios could also be equally plausible. The most simplistic scenario, or null hypothesis, is to interpret the AHe age-elevation profile as simply depicting a linear age-elevation relationship, thereby suggesting exhumation rates had been largely slow and broadly continuous in the post-tectonic era, and did not accelerate at ~10±2 Ma. This is perhaps the predicted exhumational history for a tectonically inactive region with decreasing relief (e.g. Pinet & Souriau, 1988; Reiners et al., 2003; Baldwin et al., 2003) and will be considered further in the 3D thermal modelling of the data.

The limited number of data from the Barruera profile, and the poor reproducibility from the lowermost sample, render it difficult to interpret the AHe ages confidently. However, a primary observation to make is that the AHe age ranges, as defined by the uncertainty of each analysis, are consistent with the lower samples of the Maladeta profile.

In summary, despite sharing very similar fission track age profiles and interpreted exhumation histories during the upper Eocene-lower Oligocene (Fitzgerald et al., 1999; Sinclair et al., submitted), AHe data from the Marimañi and Maladeta profiles indicate the two areas may have undergone markedly contrasting histories of exhumation in the post-tectonic period. The Marimañi profile suggests progressive exhumation during the upper Oligocene and lower Miocene. The Maladeta profile, which includes the same sampling elevations, suggests progressive exhumation during the lower and middle Miocene followed by an abrupt acceleration of exhumation rates at ~10±2 Ma. AHe age data from the lower Barruera profile are also broadly consistent with a similar period of rapid exhumation at ~10+2 Ma.

Despite these well-defined differences in the age-elevation relationships, a number of important uncertainties regarding the interpretation of the data still persist and cannot be reliably discounted without synthetic analysis of the age-elevation relationships. The most important of these is to assess whether the age-elevation relationships, and the interpretations therein, are simply an artefact of deformation of the subsurface thermal regime at the time of mineral closure. This may be associated with effects such as thermal advection during rapid rock uplift (Mancktelow and Grasemann, 1997; Brown and Summerfield, 1997), thermal relaxation after rapid exhumation (Brown and Summerfield, 1997; Moore and England, 2001), or the subsurface perturbation of relevant isotherms by long wavelength topography or rapidly changing relief (Mancktelow and Grasemann, 1997; Braun, 2002). Secondly, it is vital to assess if the interpreted thermal histories can be reliably discriminated from alternative scenarios. Primarily, it must be resolved whether the uncertainty of the data permit the simplest interpretation, or null hypothesis, of a linear age-elevation relationship suggesting steady slow exhumation after ~30 Ma.

In order to critically assess these issues it is necessary to couple the AHe data with 3-dimensional topographic and thermal modelling . This enables model AHe ages to be generated for a number of topographic and thermal end-member scenarios, and the compatibility between the derived age-elevation predictions with the actual AHe data to be considered.

THERMAL MODELLING

Methodology

To simulate different thermal and topographic evolutions in the Marimaña and Maladeta sampling areas we apply the finite-element code 'Pecube' (Braun, 2003). The code was developed to solve the three-dimensional heat transport equation in uplifting and eroding lithospheric blocks which have an evolving, finite-amplitude surface topography (Braun, 2003). Time-temperature (*t*-T) histories of specific rock particles, defined by delineating specific nodes on the imposed topographic surface, can be generated for a given history of exhumation.

These *t*-T paths can then be input into thermochronometer-specific software, such as AFTSolve (Ketcham et al., 2000) or DeComp (Dunai et al., 2003) in order to forward-model cooling ages (Braun, 2002; Braun, 2003).

The boundary conditions used to simulate the upper crustal thermal structure are defined by the following parameters which were assumed to be spatially uniform and non-variant with time: heat diffusivity (25 km^2Myr^{-1}), heat production (23.44 $°CMyr^{-1}$), crustal thickness (20 km), and crustal basal temperature (500°C). Each model run was initiated at 45 Ma and terminated at present-day (0 Ma). At the start of each experiment (45 Ma), isotherms are distributed uniformly with depth, giving a geothermal gradient of $25°Ckm^{-1}$. However, during periods of exhumation, the isotherms are advected towards the cooling surface (Brown and Summerfield, 1997), thus temporarily increasing the geothermal gradient during model runs up to values of $\sim 40°Ckm^{-1}$.

A 44 km^2 sample of ~90m SRTM (Shuttle Radar Topography Mission) data (U.S.G.S., 2004) topography from the central Pyrenees (Fig. 4), incorporating the sampling localities, was downgraded in resolution to a grid of $1km^2$ nodes using ArcInfo software (ESRI, 2000). For each experiment, this grid was delineated as the end-point topographic configuration reached by the model before present-day (0 Ma). The model AHe ages generated between 45 and 0 Ma were thus a function of the only two variables imposed on each experiment, namely a temporally-variant exhumation history and a specific topographic evolution. Individual AHe ages were calculated for a range of apatite crystal sizes (66 to 130μm diameter) at the geographical location and elevation of the samples in the Marimaña and Maladeta profiles. A period of rapid exhumation, with a vertical velocity of 0.5 $kmMyr^{-1}$, was imposed on all runs from 36 to 30 Ma to simulate the late Eocene to early Oligocene tectonically-driven exhumation documented by previous apatite fission track studies (Fitzgerald et al., 1999; Sinclair et al., submitted). This rate represents a minimum value based on previous estimates (Fitzgerald et al., 1999) and may be significantly increased with little effect on the derived model ages. Importantly, it generates model fission track ages of ~30 Ma with high track lengths (~14μm) for the samples from both profiles. This is consistent with previously published data (Fig. 3e) (Sinclair et al., submitted) and provides a good thermal constraint for the subsequent *t*-T history in each model run.

Two exhumation histories were tested by the model. The first scenario assumes that after the decline of tectonism at ~30 Ma the exhumation velocities have been slow and continuous (0.053 $kmMyr^{-1}$) to present-day (0 Ma). This rate represents the minimum value required to exhume the samples from above the fission track closure depth to the modern surface over a 30 Myr interval. This protracted history of continuous exhumation is intended to represent a simplified modelling analogy for that predicted for post-orogenic settings (Pinet & Souriau, 1988; Pazzaglia & Brandon, 1996; Baldwin et al., 2003; Reiners et al., 2003). However, as model predictions would suggest the rates should decrease exponentially through time (e.g. Pinet & Souriau, 1988), the generated model ages can be regarded as minimum values which would increase in age if an exponential decay was also applied. The second scenario assumes that exhumation is negligible immediately after the decline of tectonism at ~30 Ma, but resumes at accelerated rates (0.275 $kmMyr^{-1}$) for a 4 Myr period between 12 to 8 Ma, and then significantly declines (0.0625 $kmMyr^{-1}$) from 8 Ma to present. The vertical velocities are the minimum values required to exhume samples through the AHe PRZ during the 12 to 8 Ma interval, and subsequently to their present elevations during the 8 to 0 Ma interval. Alternative values are also used in the Marimaña model profile in order to assess the impact of varying exhumation rates (Table 2). For simplicity it is assumed rates were continuous during the designated intervals, however, it is the total amount of exhumation during the given time-period that is of primary importance and not the maintenance of a singular vertical velocity. This scenario of pulsed exhumation is intended to represent the history interpreted directly from the Maladeta AHe ages and age-elevation profile, namely an abrupt rejuvenation of exhumation at 10±2 Ma after a prolonged period of thermal quiescence.

In order to test the relative impact of different topographic evolutions on model AHe ages, three end-member topographic scenarios were tested against both exhumational histories. As there are no independent constraints on the topographic development in the area, it is necessary to assess for the impact of decreasing, increasing and unchanging relief, with respect to the modern topography. For the pulsed exhumational history it was assumed that the abrupt changes in vertical velocity coincided with the changes in relief, and for the continuous exhumational history it was assumed the relief changes occurred progressively through time. For the first topographic scenario we assume a topography identical to that in the modern system was created by 30 Ma and has been retained to present-day (0 Ma). For the second scenario we assume a very low amplitude (essentially flat) topography was sustained until at least 30 Ma. The modern topography was then carved from this progressively from 30 Ma (continuous exhumation) or carved quickly between 12 to 8 Ma (pulsed exhumation). For the third scenario we assume a high amplitude topography (50% larger than the modern system) was present until 30 Ma. This amplitude was then reduced to the modern topography progressively from 30 Ma (continous exhumation) or reduced relatively rapidly between 12 to 8 Ma (pulsed exhumation).

Model age-elevation profiles were generated for each combination of tectonic and exhumational scenario at the appropriate nodes for both the Marimañi and Maladeta profiles. Modelling of the *t*-T histories and AHe ages at the nodes relevant to the Barruera profile was omitted due to the lack of reproducible AHe data with which to compare the model results.

Model results and discussion

Model ages are presented as two linear age-elevation profiles, corresponding to the ages predicted for crystals of 66 and 130 μm apatite crystal diameter, and are plotted with the measured AHe data to allow direct comparison (Fig. 5 & 6). The corresponding *t*-T profile and topographic scenario is located above and to the side, respectively, of the age-elevation plots for each model run.

Model ages for the Maladeta profile (Fig. 5) display a very small degree of variability as a function of the changing topographic scenario. In contrast, the two exhumational scenarios yield markedly different results; age-elevation profiles generated from the pulsed exhumational history show a good fit to the measured AHe ages (Runs 1, 3 and 5), whereas profiles generated from the continuous exhumational history depict a linear trend significantly outside the uncertainty bounds of the AHe data (≤15 Myr) (Runs 2, 4 and 6). Owing to the negligible impact of topographic variation, only the constant relief scenario is presented for the Marimaña profile (Fig. 6). Instead, the two exhumational scenarios are run with varying vertical velocities (Table 2). For the scenario of pulsed exhumation, the model ages are consistent with the measured data when rates are significantly reduced (Run 9) and show a large discrepancy when the same values are imposed as those used for the Maladeta profile (Run 7). For the continuous exhumation scenario, however, the model ages fit with the measured data by applying the same rates as used in the Maladeta profile (Run 8), but show much reduced compatibility when the rates are lowered (Run 10).

The modelling results clearly demonstrate the very limited influence of topographically-induced isothermal perturbation and thermal advection imposed on the AHe ages and derived *t*-T histories. A bigger impact would have been documented if the profiles had a significantly larger horizontal spatial component, thereby sampling the larger wavelength of the orogen. However, in this case, no additional corrections are necessary and it can be assumed that the interpreted age-elevation relationships from the Marimañi and Maladeta profiles are likely to be a singular function of the exhumation history. Furthermore, as the evolution of topography in the area is unlikely to have undergone such an extreme history as depicted in the end-member scenarios, the true extent of thermal perturbation caused by this effect is likely to be considerably less than that depicted in the models.

Results from the continuous exhumation model demonstrate that the appropriate fission track and AHe ages for samples from the Maladeta profile cannot be resolved by a *t*-T history characterised by slow and protracted, or exponentially declining, exhumation. Conversely, the age elevation relationship can be accurately reproduced by a model that imposes a period of protracted thermal stability after the 36-30 Ma event followed by an abrupt rejuvenation of exhumation at approximately 10 Ma. During the initial period of modelled exhumation (36-30 Ma), the simulated 1100m of rock column is exhumed rapidly through the apatite fission track PAZ. This is consistent with the generation of a vertical age-elevation profile of lower Oligocene apatite fission track ages combined with high mean track lengths in the Maladeta profile (Fitzgerald et al., 1999; Sinclair et al., submitted). Exhumation subsequently declines and the profile languishes at constant or negligibly decreasing depths, with the upper elevation samples being held within the AHe partial retention zone, and the lower samples below it, for at least 18 Myr. Exhumation processes are abruptly rejuvenated at 12 Ma and the lower samples rapidly transit temperatures at which the AHe system is sensitive. This is compatible with the upper samples from the profile (>2100m) depicting a palaeo-PRZ and the lower samples, yielding elevation-invariant ages, recording rapid exhumation at 8-12 Ma.

Simulations of the Marimaña profile, in contrast, indicate a markedly different *t*-T history is required in order to generate model ages which are compatibile with the data. The two scenarios, which cannot be discriminated from each other, suggest the Marimaña either progressively exhumed at slow rates from 30 to 0 Ma, or underwent a history of pulsed exhumation between 12 to 8 Ma but at rates significantly less than at the Maladeta.

In summary, the modelling results from the Maladeta profile are consistent with the age-elevation interpretation which indicates an abrupt rejuvenation of exhumation occurred at 8-12 Ma, during the post-orogenic period. The similarity of the Barruera AHe ages suggest this event affected the region encompassing both sites located south of the main Pyrenean drainage divide. Modelling results from the Marimaña profile, located to the north of the drainage divide, indicate this event either was not recorded or had a significantly reduced impact.

MECHANISMS FOR POST-TECTONIC ACCELERATED EXHUMATION

A mechanism is required to explain the proposed increases in erosional denudation at 10±2 Ma. As noted previously, there is no evidence to suggest that either tectonic denudation or localised tectonically-driven rock uplift played a significant role in the central Pyrenees during this period. Consequently, we must consider alternative controls on erosional denudation at this time and, in addition, why their effects were focused to the south of the main Pyrenean drainage divide

Previous workers have documented dramatic increases in sediment accumulation rates and grain sizes, associated with enhanced rates of erosional denudation, from a number of tectonically-inactive mountain systems (Zhang et al.; 2001). This has been linked to globally synchronous climatic instabilities, as documented in oxygen and carbon isotopes from Cenozoic deep-sea cores (Zhang et al., 2001). This is perhaps of particular importance for European mountain belts as palaeoceanographic records indicate that the reorganisation of ocean circulation systems likely enhanced atmospheric moisture content within the northern hemisphere (Haug and Tiedemann, 1998; Driscoll and Haug, 1998) and, by inference, the erosive capacity of surface processes (Cederbom et al., in press). However, these climatic aberrations were restricted to Pliocene times (Zhang et al., 2001) and, thus, significantly post-date the 10±2 Ma event.

Similarly, the lowering of the Mediterranean Sea during the Messinian salinity crisis generated an increase in erosion rates in regions located within the drainage catchments of the basin (e.g. Foeken et al., 2003). This period of regional base-level fall has also been linked to capture of the closed Ebro Basin and with predicted increases in erosional denudation within the Pyrenees (Coney et al., 1996; Fitzgerald et al., 1999). The Messinian event, however, commenced at 5.97 Ma (Krijgsman et al., 1999) and thus cannot have influenced the increase in erosional denudation documented by the AHe data.

Instead, it is proposed the opening of the Ebro drainage system occurred during middle to upper Miocene times (Serravallian to Tortonian) and caused a dramatic drop in fluvial base-levels that resulted in rejuvenated exhumation of the previously blanketed southern margin of the Pyrenees. Piracy of the palaeo-lake during this period would promote a rapid and irreversible reorganisation of regional drainage systems within the Ebro Basin and it's fluvial catchments (Garcia-Castellanos et al., 2003). The significant elevation difference between the lacustrine succession preserved on isolated hilltops within the modern basin (Pérez-Rivarés, 2002) and the Mediterranean Sea would represent a large and abrupt base-level drop of at least 800m. The clastic infill of the basin would likely dictate that fluvial incision within the Ebro channel network, generated by the significantly lowered base-level, would follow transport-limited behaviour (Snow & Slingerland, 1987; Willgoose et al., 1991; Tucker & Whipple, 2002) and would rapidly propagate into the catchment hinterlands on the southern flank of the Pyrenees. Low-temperature thermochronometers within the mountain belt would thus record the thermal response to the abrupt acceleration of erosion processes and the subsequent thermal relaxation in the upper crust after the event. AHe ages from the Maladeta and Barruera profile suggest this denudation-induced thermal aberration was recorded in the central Pyrenees at 10±2 Ma. Drainage systems outside of the Ebro catchment, or north of the Pyrenean drainage divide, would be unaffected by this event. This is consistent with an apparent asymmetric distribution of exhumation focused upon the southern flank of the range, with less total exhumation recorded within the Marimañi profile.

Implicit in this mechanism is an isostatic response to the removal of mass from the Pyrenees, both during and after the onset of accelerated exhumation. This would provide additional rock uplift over the region and, thus, continue to promote increased rates of erosional denudation beyond that predicted for ancient and tectonically-inactive topography. This component is an inherent requirement of the proposed model, as a base-level fall of at least 800m, as defined by the vertical distance between the preserved lacustrine deposits and the Mediterranean Sea, is likely to be exceeded by the vertical distance required to rapidly exhume the lower 300m of the Maladeta profile through PRZ temperatures. For a geothermal gradient of ~30 to 35°Ckm^{-1} and a PRZ temperature range of ~40 to 80°C, a conservative estimate of this value is between ~1440 to 1630 m, suggesting that ~640 to 830m more exhumation is required, which is interpreted as the isostatic component. Simple Airy isostasy would predict ~670m of rock uplift in response to 800m of erosional denudation (Molnar and England, 1990). This suggests, that the actual base-level fall may have been greater than 800m and that the lacustrine sediments preserved in isolated hilltops of the Ebro Basin do not represent the uppermost basin fill during Middle Miocene times.

A significant time-lag is assumed between capture of the basin drainage, the culmination of maximum fluvial incision efficiency, and the propagation of regressive erosion up the fluvial network to the orogen (Kooi & Beaumont, 1996; Garcia-Castellanos et al., 2003). As this lag is unconstrained, the timing of the basin opening can only be bracketed between the age of the youngest lacustrine sediments in the Ebro Basin (~14 Ma; Pérez-Rivarés, 2002) and the age of accelerated exhumation within the mountain belt (10±2 Ma), or during Serravallian to Tortonian times. This is compatible with both geodynamical numerical simulations of Ebro drainage evolution that predict basin capture between 13 and 8.5 Ma (Garcia-Castellanos et al., 2003), and with a number of independent observations on the offshore sediment record in the Ebro Delta and València Trough (e.g. Johns et al., 1989; Bartrina et al., 1992). This is the region in which the modern fluvial system flows through the Catalan Coastal Range, and where, by inference, the topographic barrier enclosing the isolated Ebro Basin was initially breached to the Mediterranean Sea (Coney et al., 1996).

Within the offshore València Trough, the pre-Serravillian Miocene deposits (Aquitanian to Langhian) of the Alcanar Group are restricted to structurally-defined depocentres within Mesozoic half-graben (Ziegler, 1988; Martínez del Olmo, 1996) and are dominated by limestone and marl sequences and locally-derived breccio-conglomerates (Anadón et al., 1989; Roca and Desegaulx, 1992; Meléndez-Hevia & Alvarez de Buergo, 1996). In contrast, the Middle and Upper Miocene Castellón Group, of Tortonian and Serravillian age (Roca and Desegaulx, 1992; Martínes del Olmo, 1996), are characterised by thick units of terrigenous sediments deposited in basinward (southeast) prograding clastic sequences (Johns et al., 1989; Marínez del Olmo, 1996; Roca & Desegaulx, 1992; Meléndez-Hevia & Alvarez de Buergo, 1996; Roca, 2001; Evans & Archie, 2002). Major intra-mid Miocene downlap surfaces within the succession (Ziegler, 1988; Johns et al., 1989) record the dramatic influx of large volumes of siliciclastic detritus that cover and homogenise the pre-existing Neogene basin topography (Fig. 7; Ziegler, 1988; Anadón, et al., 1989; Roca & Desegaulx, 1992). Sedimentation rates increase progressively through the Serravallian and Tortonian until the onset of the Messinian Salinity Crisis (Dañobeitia et al., 1990), whereupon the unit is capped within the margins of the València Trough by an erosional unconformity and the deposition of evaporitic sequences in the deeper sections of the basin (Mulder, 1973; Roca & Desegaulx, 1992).

The substantial sediment volume within the Castellón Group (Martínez del Olmo, 1996) is unlikely to be derived from a spatially-limited fluvial system draining only the basinward flank of the Catalan Coastal Range (Evans & Archie, 2002). Instead, it may account for the large discrepancy previously observed (Garcia-Castellanos et al., 2003) between the calculated volume of detritic material eroded from the Ebro Basin since capture and the estimated volume of post-Messinan sediment within the Ebro Delta (Nelson, 1990). The lack of accurate provenance data precludes a definitive linkage between the substantial clastic influx and the opening of the Ebro Basin through the Catalan Coastal Range. However, the close compatibility between the onset of rejuvenated Pyrenean exhumation, the age of the youngest Ebro Basin lacustrine sediments, and the large pre-Messinian sedimentary influx of clastic detritus into the Valencia trough provide compelling evidence to suggest the events are inextricably associated.

An implication of the proposed model is that all the upper, mountainous source regions of the Ebro River should record an acceleration of erosional denudation at 10±2 Ma. Hence, the model predicts the event should also be recorded within both the Iberian Range and Catalan Coastal Ranges, and is thus testable through the application of additional AHe thermochronometry in these regions.

CONCLUSIONS

Age-elevation relationships of apatite (U-Th)/He data from sub-vertical profiles sampled in the central Pyrenees record a period of accelerated exhumation after the cessation of major tectonics. Thermal modelling of a number of pre-defined scenarios confirms the negligible impact on the thermal structure of the upper crust of an evolving topography on the AHe data, owing to the small wavelength of local relief in the sampling areas. However, varied exhumational histories are demonstrated to have a strong influence on model ages and the most compatible time-temperature history requires an acceleration of exhumation during middle to late Miocene times (10±2 Ma). Thermal modelling of AHe ages from the Marimaña profile, located immediately north of the main drainage divide, indicate lower rates of exhumation during the post-orogenic period.

As tectonic activity is considered negligible within the central Pyrenees during this period, a mechanism to promote rates of erosional denudation is required to explain the 10±2 Ma event. Models involving accelerated denudation associated with climatic instabilities and with the Messinian Salinity Crisis are disregarded as they significantly post-date the period of rapid exhumation. Instead, post-orogenic rejuvenated exhumation is linked to the opening of the internally-drained Ebro basin to the Mediterranean Sea, by fluvial breaching of the intervening topographic barrier (Catalan Coastal Ranges) during Serravallian to Tortonian times (Fig. 8). This abrupt fall in regional base-level and reorganisation of fluvial systems promoted accelerated rates of fluvial incision and erosional denudation within the basin and on the southern flank of the orogenic hinterland. Offshore sediment records, depicting the influx of large siliciclastic prograding wedges into the adjacent Valencia Trough during Tortonian and Serravallian times, support this model.

ACKNOWLEDGEMENTS

We thank C. Persano and S. Diskin for assistance in the He laboratory. We also acknowledge constructive and helpful advice from Peter Reiners and an anonymous reviewer on an earlier version of this manuscript. This work was supported by the Scottish Universities, NERC (GR3 R9840, NER/S/A/2000/03351 (MG) and NER/S/A/2001/06170 (GJL)) and a SHEFC RDG grant (CRUST).

REFERENCES

ANADÓN, P., CABERERA, LL., ROCA, E. & RODRÍGUEZ-PEREA, A. (1989) Sedimentary evolution in the València Trough. *Terra Abstracts*, **1**, 46-47

BALDWIN, J.A., WHIPPLE, K.X. & TUCKER, G.E. (2003) Implications of the shear stress river incision model for the timescale of postorogenic decay of topography. *Journal of Geophysical Research*, **108**, Bs, 2158

BARTRINA, M.T., CABRERA, L., JURADO, M.J., GUIMERA, J. & ROCA, E. (1992) Evolution of the central Catalan margin of the Valencia Trough (Western Mediterranean). *Tectonophysics*, **203**, 219-247

BEAUMONT, C., MUÑOZ, J.A., HAMILTON, J. & FULLSACK, P. (2000) Factors controlling the Alpine evolution of the central Pyrenees inferred from a comparison of observations and geodynamical models. *Journal of Geophysical Research*, **105**, B4, 8121-8145

BRAUN, J. (2002) Quantifying the effect of recent relief changes on age-elevation relationships. *Earth and Planetary Science Letters*, **200**, 331-343

BRAUN, J. (2003) Pecube: a new finite-element code to solve the 3D heat transport equation including the effects of a time-varying, finite amplitude surface topography. *Computers and Geosciences*, **29**, 787-794

BROWN, R.W. & SUMMERFIELD, M.A. (1997) Some uncertainties in the derivation of rates of denudation from thermochronologic data. *Earth Surface Processes and Landforms*, **22**, 239-248

BREWER, I.D., BURBANK, D.W. & HODGES, K.V. (2003) Modelling detrital cooling-age populations: insights from two Himalayan catachments. *Basin Research*, **15**, 305-320

CARRAPA, B., WIJBRANS, J. & BERTOTTI, G. (2003) Episodic exhumation in the Western Alps. *Geology*, **31**, 601-604

CEDERBOM, C., SINCLAIR, H.D., SCHLUNNEGGER, F. & RAHN, M. (in press) Climate-induced rebound and exhumation of the European Alps. *Geology*

CHOUKROUNE, P. and ECORS Team (1989) The ECORS Pyrenean deep seismic profile reflection data and the overall structure of an orogenic belt. *Tectonics*, **8**, 23-39

CONEY, P.J., MUÑOZ, J.A., McCLAY, K.R. & EVENCHICK, C.A. (1996) Syntectonic burial and post-tectonic exhumation of the southern Pyrenees foreland fold-thrust belt. *Journal of the Geological Society London*, **153**, 9-16

DAÑOBEITIA, J.J., BELÉN, A. & MALDONADO, A. (1990) Geological framework of the Ebro continental margin and surrounding areas. *Marine Geology*, **95**, 265-287

DRISCOLL, N.W. & HAUG, G.H. (1998) A short circuit in thermohaline circulation: A cause for northern hemisphere glaciation? *Science*, **282**, 436-438

DUNAI, T.J., BIKKER, A. & MEESTERS, A.G.C.A. (2003) Decomp: A user-friendly forward modelling program for (U-Th)/He low-temperature geochronology. *Geophysical Research Abstracts*, **5**, 14076

EHLERS, T.A. & FARLEY, K.A. (2002) Apatite (U-Th)/He thermochronometry: methods and applications to problems in tectonic and surface processes. *Earth and Planetary Science Letters*, **206**, 1-14

EHLERS, T.A., WILLET, S.D., ARMSTRONG, P.A. & CHAPMAN, D.S. (2003) Exhumation of the central Wasatch Mountains, Utah: Thermockinematic model of exhumation, erosion, and thermochronometer interpretation. *Journal of Geophysical Research*, **108**, B3, 2173

ESRI (2000) ArcInfo. Environmental Systems Reseach Institute, Redlands, Ca.

EVANS, G. & ARCHIE, A. (2002) The flux of siliciclastic sediment from the Iberian Peninsula, with particular reference to the Ebro. In: *Sediment flux to basins: Causes, Controls and Consequences* (Ed. by S.J. Jones & L.E. Frostick), Geological Society, London, Special Publications, **191**, 199-208

FARLEY, K.A. (2000) Helium diffusion from apatite: general behavior as illustrated by Durango fluorapatite. *Journal of Geophysical Research*, **105**, 2903-2914

FARLEY, K.A. (2002) (U-Th)/He dating: Techniques, calibrations, and applications. In *Noble Gas Geochemistry: Reviews in Mineralogy and Geochemistry* (Ed. by P.D. Porcelli, C.J. Ballentine & R. Wieler), **47**, 819-843

FITZGERALD, P.G., SORKHABI, R.B., REDFIELD, T.F. & STUMP, E. (1995) Uplift and denudation of the Central Alaska Range: A case study in the use of apatite fission track thermochronology to determine absolute uplift parameters. *Journal of Geophysical Research*, **100**, B10, 20175-20191

FITZGERALD, P.G., MUÑOZ, J.A., CONEY, P.J. & BALDWIN, S.L. (1999) Asymmetric exhumation across the Pyrenean orogen: Implications for the tectonic evolution of a collisional orogen. *Earth and Planetary Science Letters*, **173**, 157-170

FOEKEN, J.P.T., DUNAI, T.J., BERTOTTI, G. & ANDRIESSEN, P.A.M. (2003) Late Miocene to present exhumation in the Ligurian Alps (southwest Alps) with evidence for accelerated denudation during the Messinian salinity crisis. *Geology*, **31**, 9, 797-800

GARCIA-CASTELLANOS, D., VERGÉS, J., GASPAR-ESCRIBANO, J. & CLOETINGH, S. (2003) Interplay between tectonics, climate, and fluvial transport during the Cenozoic evolution of the Ebro Basin (NE Iberia). *Journal of Geophysical Research*, **108**, 1-18

GLEADOW, A.J.W. & FITZGERALD, P.G. (1987) Uplift history and structure of the Transantarctic Mountains: New evidence from fission track dating of basement apatites in the Dry Valleys area, Southern Victoria Land. *Earth and Planetary Science Letters*, **82**, 1-14

GUIMERA, J. (1984) Palaeogene evolution of deformation in the north-eastern Iberian Peninsula. *Geology Magazine*, **121**, 413-420

HAUG, G.H. & TIEDEMANN, R. (1998) Effect of the formation of the Isthmus of Panama Atlantic Ocean thermohaline circulation. *Nature*, **393**, 673-676

HOUSE, M.A., WERNICKE, B.P., FARLEY, K.A. & DUMITRU, T.A. (1997) Cenozoic thermal evolution of the central Sierra Nevada, California, from (U-Th)/He thermochronometry. *Earth and Planetary Science Letters*, **151**, 167-179

HOUSE, M.A., FARLEY, K.A. & KOHN, B. (1999) An empirical test of helium diffusion in apatite: borehole data from the Otway basin, Australia. *Earth and Planetary Science Letters*, **170**, 463-474

JOHNS, D.R., HERBER, M.A. & SCHWANDER, M.M. (1989) Depositional sequences in the Castellón area, offshore northeast Spain. In Atlas of Seismic Stratigraphy (Ed. by A.W. Bally), *American Association of Petroleum Geology*, Studies in Geology, **27**, 181-184

KETCHAM, R.A., DONELICK, R.A. & DONELICK, M.B. (2000) AFTSolve: A program for multi-kinetic modeling of apatite fission-track data. *Geological Materials Research*, **2**, 1

KOHN, B.P. & GREEN, P.F. (2002) Low temperature thermochronology: From tectonics to landscape evolution. *Tectonophysics*, **349**, 1-4

KRIJGSMAN, W., HIGEN, F.J., RAFFI, I., SIERRO, F.J. & WILSON, D.S. (1999) Chronology, causes and progression of the Messinian salinity crisis. *Nature*, **400**, 652-655

LOGET, N., BABAULT, J., CASTELLTORT, S., VAN DEN DRIESSCHE, J., BONNET, S. & DAVY, P. (2004) When does the Ebro River connect to the Mediterranean? *Geophysical Research Abstracts*, **6**, 07710, EGU 2004

MANCKTELOW, N.S. & GRASEMANN, B. (1997) Time-dependent effects of heat advection and topography on cooling histories during erosion. *Tectonophysics*, **270**, 167-195

MARTÍNEZ DEL OLMO, W. (1996) Depositional sequences in the Gulf of València Tertiary Basin. In *Tertiary Basins of Spain: the stratigraphic record of crustal kinematics: World and Regional Geology* (Ed. by P.F. Friend & C.J. Dabrio), Cambridge University Press, New York, 55-67

MEESTERS, A.G.C.A. & DUNAI, T.J. (2002) Solving the production-diffusion equation for finite diffusion domains of various shapes Part I. Implications for low-temperature (U-Th)/He thermochronology. *Chemical Geology*, **186**, 333-344

MEIGS, A.J., VERGES, J. & BURBANK, D.W. (1996) Ten-million year history of a thrust sheet. *Geological Society of America Bulletin*, **12**, 1608-1625

MEIGS, A.J. (1997) Sequential development of selected Pyrenean thrust faults. *Journal of Structural Geology*, **19**, 481-502

MELÉNDEZ-HEVIA, f. & ALVAREZ DE BUERGO, E. (1996) Oil and Gas resources of the Tertiary Basins of Spain. In *Tertiary Basins of Spain: the stratigraphic record of crustal kinematics: World and Regional Geology* (Ed. by P.F. Friend & C.J. Dabrio), Cambridge University Press, New York, 26-43

MOORE, M.A. & ENGLAND, P.C. (2001) On the inference of denudation rates from cooling ages of minerals. *Earth and Planetary Science Letters*, **185**, 265-284

MORRIS, R.G., SINCLAIR, H.D. & YELLAND, A.J. (1998) Exhumation of the Pyrenean orogen: implications for sediment discharge. *Basin Research*, **10**, 69-85

MULDER, C.J. (1973) Tectonic framework and distribution of Miocene evaporites in the Mediterranean. In *Messinian Events in the Mediterranean* (Ed. by C.W. DROOGER), Netherlands, Amsterdam, 44-59

MUÑOZ, J.A. (1992) Evolution of a continental collision belt: ECORS-Pyrenees crustal balanced cross-section. In: *Thrust Tectonics* (Ed. by K. McClay), Chapman and Hall, London, 235-246

NAESER, C.W. (1979) Thermal history of sedimentary basins: Fission track dating of subsurface rocks. In *Aspects of Diagenesis* (Ed. by P.A. Scholle & P.R. Schluger), Special Publication, Society of Economic Palaeontologists and Mineralogists, 26, 109-112

NELSON, C.H. (1990) Estimated post-Messinian sediment supply and sedimentation rates on the Ebro continental margin, Spain. *Marine Geology*, **95**, 395-418

NIEMANN, J.D., GASPARINI, N.M., TUCKER, G.E. & BRAS, R.L. (2001) A quantitative evaluation of Playfair's Law and its use in testing long-term stream erosion models. *Earth Surface Processes and Landforms*, **26**, 1317-1332

PAZZAGLIA, F.J. & BRANDON, M.T. (1996) Macromorphic evolution of the post-Triassic Appalachian mountains determined by deconvolution of the offshore basin sedimentary record. *Basin Research*, **8**, 255-278

PÉREZ-RIVARÉS, F.J., GARCÉS, M., ARENAS, C. & PARDO, G. (2002) Magnetocronología de la sucesión Miocena de la Sierra de Alcubierre (sector central de la cuenca del Ebro). *Rev. Soc. Geol. Esp*, **15** (3-4), 211-225

PERSANO, C., STUART, F.M., BISHOP, P. & BARFOD, D.N. (2002) Apatite (U-Th)/He age constraints on the development of the Great Escarpment on the southeastern Australian passive margin. *Earth and Planetary Science Letters*, **200**, 79-90

PINET, P. & SOURIAU, M. (1988) Continental erosion and large-scale relief. *Tectonics*, **7**, 563-582

PUIGDEFÀBREGAS, C., MUÑOZ, J.A. & VERGÉS, J. (1992) Thrusting and foreland basin evolution in the southern Pyrenees. In *Thrust Tectonics* (Ed. by K. McClay), Chapman and Hall, London, 247-254

REINERS, P.W., ZHOU, Z., EHLERS, T.A., XU, C., BRANDON, M.T., DONELICK, R.A. & NICOLESCU, S. (2003) Post-orogenic evolution of the Dabie Shan, Eastern China, from (U-Th)/He and fission track thermochronology. *American Journal of Science*, **303**, 489-518

RIBA, O., REGUANT, S. & VILLENA, J. (1983) Ensayo de síntesis estratigráfica y evolutiva de la cuenca terciaria del Ebro. In: *Libro Jubilar* (Ed. by J. M. Rios), Geologique España, **2**, 131-159

ROEST, W.R. & SRIVASTAVA, S.P. (1991) Kinematics of the plate boundaries between Eurasia, Iberia and Africa in the north Atlantic from the Late Cretaceous to the present. *Geology*, **19**, 613-616

ROCA, E. & DESEGAULX, P. (1992) Analysis of the geological evolution and vertical movements in the València Trough area, Western Mediterranean. *Marine and Petroleum Geology*, **9**, 167-185

ROCA, E. (2001) The Northwest Mediterranean Basin (Valencia Trough, Gulf of Lions and Liguro-Provençal basins): structure and geodynamic evolution. In *Peri-Tethyan Rift/Wrench Basins and Passive Margins* (Ed. by P.A. Ziegler, W. Cavazza, A.H.F. Robertson & S. Crasquin-Soleau), Peri-Tethys Memoir 6, Mém. Mus. Natn. Hist. Nat., **186**, 671-706

SERRAT, D. (1992) La xarxa fluvial dels Països Catalans. In: *Historia Natural dels Països Catalanas, Geologia II*, Enciclopedia Catalana, Barcelona, Spain, 375-389

SINCLAIR, H.D., GIBSON, M., NAYLOR, M. & MORRIS, R.G. Asymmetric growth of the Pyrenees revealed through measurement and modelling of orogenic fluxes (submitted to American Journal of Science)

SNOW, R.S. & SLINGERLAND, R.L. (1987) Mathmatical modelling of graded river profiles. *Journal of Geology*, **95**, 15-33

SOURIAU, A., & GRANET, M.A. (1995) A tomographic study of the lithosphere beneath the Pyrenees from local and teleseismic data. *Journal of Geophysical Research*, **100**, B9, 18117-18134

SPOTILA, J.A., BANK, G.C., REINERS, P.W., NAESER, C.W., NAESER, N.D. & HENIKA, B.S. (2004a) Origin of the Blue Ridge escarpment along the passive margin of Eastern North America. *Basin Research*, **16**, 41-63

SPOTILA, J.A., BUSCHER, J.T., MEIGS, A.J. & REINERS, P.W. (2004b) Long-term glacial erosion of active mountain belts: Example of the Chugach-St. Elias Range, Alaska. *Geology*, **32**, 6, 501-504

SRIVASTAVA, S.P., SCHOUTEN, H., ROEST, W.R., KLITGORD, K.D., KOVACS, L.C., VERHOE, J. & MACNAB, R. (1990) Iberian plate kinematics: a jumping plate boundary between Eurasia and Africa. *Nature*, **344**, 756-759

TUCKER, G.E. & WHIPPLE, K.X. (2002) Topographic outcomes predicted by stream erosion models: Sensitivity analysis and intermodel comparison. *Journal of Geophysical Research*, **107**, B9, 2179

U.S.G.S. (United States Geological Survey) (2004) ftp://edcftp.cr.usgs.gov/pub/data/srtm/

WARNOCK, A.C., ZEITLER, P.K., WOLF, R.A. & BERGMAN, S.C. (1997) An evaluation of low-temperature apatite (U-Th)/He thermochronometry. *Geochemica et Cosmochimica Acta*, **61**, 5371-5377

WILLGOOSE, G., BRAS, R.L. & RODRIGUE-ITURBE, I. (1991) A coupled channel network growth and hillslope evolution model. *Water Resources Res.*, **27(7)**, 1671-1684

WOBUS, C.W., HODGES, K.V. & WHIPPLE, K.X. (2003) Has focused denudation sustained active thrusting at the Himalayan topographic front? *Geology*, **31**, 10, 861-864

WOLF, R.A., FARLEY, K.A. & SILVER, L.T. (1996) Helium diffusion and low-temperature apatite U-Th/He thermochronometry of apatite. *Geochimica et Cosmochimica Acta*, **60**, 4231-4240

WOLF, R.A., FARLEY, K.A. & KASS, D.M. (1998) Modelling of the temperature sensitivity of the apatite (U-Th)/He thermochronometer. *Chemical Geology*, **148**, 105-114

ZHANG, P., MOLNAR, P. & DOWNS, W.R. (2001) Increased sedimentation rates and grain sizes 2-4 Myr ago due to the influence of climate change on erosion rates. *Nature*, **410**, 891-897

ZEITLER, P.K., HERCZIG, A.L., McDOUGALL, I. & HONDA, M. (1987) U-Th-He dating of apatite: a potential thermochronomter. *Geochimica et Cosmochimica Acta*, **51**, 2865-2868

ZIEGLER, P.A. (1988) Evolution of the Arctic-North Atlantic and the Western Tethys. *American Association of Petroleum Geologists Memoirs*, **43**, 198

ZOETEMEIJER, R., DESELGAULX, P., CLOETINGH, S., ROURE, F. & MORETTI, I. (1990) Lithosperic dynamics and tectono-stratigraphic evolution of the Ebro Basin. *Journal of Geophysical Research*, **95**, 2701-2711

ZWART, H.J. (1979) The geology of the central Pyrenees. *Leidse Geologique Mededlingen*, **50**, 1-74

FIGURE & TABLE CAPTIONS

Fig. 1. (a) Location map and simplified geological map of the Pyrenees, Catalan Coastal Range, Iberian Range, Ebro Basin and Aquitaine Basin. Inset depicts the outline of the Iberian peninsular, south-west France and north Africa. The major thrust fronts are delineated and the various lithostratigraphic divisions of the area noted in the legend below. (b) Detailed geological map delineating the main lithostratigraphic divisions and structural contacts (bold lines) within the area of the Axial Zone sampled for AHe thermochronology. The Marimañi, Maladeta and Barruera sampling localities are also located (black stars).

Fig. 2. (a) Shaded relief elevation map of north-east Iberian peninsular, including Pyrenees, and adjacent foreland basins, Catalan Coastal Range and the Iberian Range (locations depicted in Fig. 1). Elevation scale depicted in legend at bottom right. The map was generated from ~90m SRTM data (Shuttle Radar Topography Mission) (U.S.G.S., 2004) using ArcInfo and ArcView software (ESRI, 2000). (b) Shaded relief elevation map of 44 km^2 grid within the Axial Zone of the central Pyrenees. AHe sampling localities are highlighted (1- Maladeta Massif, 2- Marimañi Massif, 3- Barruera Massif). Main Pyrenean drainage divide (dotted line) extracted using ArcInfo software (ESRI, 2000). (c) Topographic section (A-A'; Fig2a) extracted using ArcInfo software (ESRI, 2000) depicts the low topographic relief of the Ebro Basin bound by the high relief terrains of the Pyrenees and the Catalan Coastal Ranges.

Fig. 3. (a-c) AHe ages plotted against sampling elevation for the Marimaña, Maladeta and Barruera sampling localities, respectively (Table 1). (d) Composite plot depicting all the AHe ages from this study plotted against sampling elevation. (e) Fission track ages (Table 3) from the samples from the Marimaña (open triangles) and Maladeta (open diamonds) profiles presented in Sinclair et al., (submitted) and used as a thermal modelling constraint in this study.

Fig. 4. A vertically-exaggerated (see scale) 44 km^2 tile of ~90m SRTM (Shuttle Radar Topography Mission) data (U.S.G.S., 2004), incorporating the three sampling localities (Marimaña, Maladeta and Barruera). Major valleys surrounding the sampling sites are also located (Noguera Pallaresa, Garonne, Alta Ribagorcana). This topography was downsampled to a grid of 1km^2 nodes and used as the end-point of topographic evolution for all model runs. At the termination of all model runs (0 Ma) the time-temperature (t-T) history for each node containing a sampling site was forward-modelled in both AFTSolve (Ketcham et al., 2000) and DeComp (Dunai et al., 2003) to generate model fission track and AHe ages for a variety of topographic and exhumational scenarios.

Fig. 5. Model AHe age profiles for different apatite dimensions (66µm (light grey line) and 133µm (black line)) generated from the t-T histories from the topographic nodes at the Maladeta profile. Measured AHe ages from the Maladeta site also plotted (black diamonds). Model runs 1, 3 and 5 have a 'pulsed' exhumational history (post 30 Ma) and three different topographic evolutions imposed (constant, increasing and decreasing, respectively). Model runs 2, 4 and 6 have a 'continuous exhumational history (post 30 Ma) and the same topographic evolutions imposed.

Fig. 6. Model AHe age profiles for different apatite dimensions (66µm (light grey line) and 133µm (black line)) generated from the t-T histories from the topographic nodes at the Marimaña profile. Measured AHe ages from the Marimaña site also plotted (grey triangles). Model runs 7 and 9 have a 'pulsed' exhumational history (post 30 Ma) but at different vertical velocities (0.275 and 0.1875 kmMyr^{-1}, respectively) and with a constant topographic relief. Model runs 8 and 10 have a 'continuous' exhumational history (post 30 Ma) but at different vertical velocities (0.0530 and 0.0416 kmMyr^{-1}, respectively) and with constant topographic relief. V = Total exhumation since 30 Ma. Variability in V is dictated by the position of the profile in the PRZ at 30 Ma; model runs with relatively high values of V were positioned at the base of the PRZ at 30 Ma, and model runs with lower values of V were positioned within the PRZ at 30 Ma.

Fig. 7. (Adapted from Ziegler, 1988) Interpreted seismic section B-B' (located in Fig. 2) along an approximately northeast-southwest transect of the Valencia Trough, depicting the mid-Miocene age (Serravallian to Tortonian) siliciclastic Castellón Group prograding across a regional downlap surface. The overlying high-relief unconformity, associated with lowered base-levels during the Messinian Salinity Crisis, is overlain by thick Pliocene-age sediments.

Fig. 8. Sequential reconstruction of the post-orogenic erosional history of the southern Pyrenees and Ebro Basin. (a) At approximately 20 Ma the Ebro Basin was fully ponded, with alluvial fans accumulating in the peripheral regions (speckled fill), and lacustrine sediments in the core of the basin (lined fill). The height of the upper Ebro basin sediments is defined here by the height of the Catalan Coastal Ranges which acted as the barrier to the Mediterranean. The upper elevation of basin-fill at this time likely exceeded the elevation of middle Miocene-age lacustrine sediments (800m) preserved in the modern setting. Carbonate mudstones of the Alcanar Group accumulated in the Valencia Trough during this period. (b) Sometime after 14 Ma, base-level in the Ebro Basin started to fall as the barrier of the Catalan Coastal Ranges was breached. At this time, siliciclastic sedimentation was initiated in the region of the present-day Ebro Delta with accumulation of the Castellón Group. (c) At 10±2 Ma, the fluvial base-level fall in the Ebro Basin resulted in accelerated erosion in the upper reaches of the catchments, in the vicinity of the Maladeta and Barruera Massifs, but not at the Marimaña Massif. The elevation difference between the youngest, preserved Ebro Basin sediments and sea level, indicates at least 800 metres of denudation can be accounted for by base-level fall. In reality, it is likely the sedimentary fill of the Ebro Basin was higher than that preserved today, and so the relative base-level fall, and associated denudation, may have been much more significant. Additional denudation will have also occurred due to increased rates of isostatically-driven rock uplift associated with the rapid removal of mass from the region. (d) Present-day topography of the Pyrenees, Ebro Basin and Catalan Coastal Range. Within the Valencia Trough, down-lapping foresets of the Castellón Group are now truncated by a Messinian-age erosional unconformity and post-Messinian sediments.

Table 1. (U-Th)/He analysis data for samples from the Marimaña, Maladeta and Barruera profiles. All samples measured at Scottish Universities Research & Reactor Centre. ‡ Analytical uncertainty (≤10%) calculated following the procedures of Persano et al. (2002). † Mass Weighted Average Radius (MWAR). § α-ejection correction (F_T) following the procedures of Farley (2002). Quantitative analysis of the elemental composition of representative crystals from the same samples used for fission track analysis were determined to be Fluorapatites. This was achieved using the Backscatter Electron Detector method (20keV and 10mm working distance) and Energy Dispersive Spectrometry (EDS) and a PGT Spirit X-Ray analysis system at the University of Edinburgh.

Table 2. Exhumational velocities and the time intervals in which they were imposed on model runs (1-10). All rates given in KmMyr^{-1}. ¥ The topographic scenario (see text for discussion) imposed upon the various exhumation histories.

Table 3. (Appendix; supplied as is unpublished) (Taken from Sinclair et al., submitted) All fission track data was prepared and analysed at Apatite to Zircon, Inc., Apatite crystals were separated from the host rock using standard magnetic and gravimetric differentiation techniques and then mounted in epoxide resin and cured for 1 hour ar 90°C. Internal crystal surfaces were exposed using 0.3mm Al_2O_3 slurries on a polishing wheel. Spontaneous fission tracks intersecting the polished surface were then etched in 5.5N HNO_3 for 20 seconds (±0.5) at 21°C and densities counted using both reflected and unpolarized transmitted light at 1562.5x magnification. For apatite track length analysis the grain mounts were irradiated with ^{252}Cf-derived fission fragments in a nominal vacuum chamber to maximise track length distribution measurements following the procedures of Donelick & Miller (1991). After re-etching, as outlined above, the length and crystallographic orientation, with respect to the c-axis, of natural, horizontal confined track lengths was determined under 1562.5x magnification with attached projection tube and digitising tablet. Fission track ages were determined by placing low-uranium muscovite sheets against the polished and etched grain mounts prior to irradiation at the Washington State University nuclear reactor (45 minutes at thermal neutron fluence of 10^{16} neutrons/cm^2 at 1MW power level; position D9). Similar mica sheets were placed next to ^{235}U-doped CN-1 glass for standardisation purposes. The mica sheets were immersed in 48% HF at 20°C (±1°C) for 15 minutes (±15 seconds) in order t reveal fission tracks induced through irradiation. Fission track ages were calculated using the radioactive decay equation with an analyst zeta calibration factor of 113.8±2.9. Annealing kinetics were inferred using the arithmetic mean of 1-4 measured Dpar values (mm units) per grain. Quantitative analysis of the elemental composition of representative crystals from the same samples used for fission track analysis were determined to be Fluorapatites. This was achieved using the Backscatter Electron Detector method (20keV and 10mm working distance) and Energy Dispersive Spectrometry (EDS) and a PGT Spirit X-Ray analysis system. Rho-S and Rho-I are the spontaneous and induced track densities measured (tracks cm^{-2}). The bracketed numbers are the numbers of spontaneous and induced tracks counted. Rho-D is the induced track density in the external detector adjacent to the CN-1 glass. Bracketed is the number of tracks counted in determining Rho-D.

Figure 1

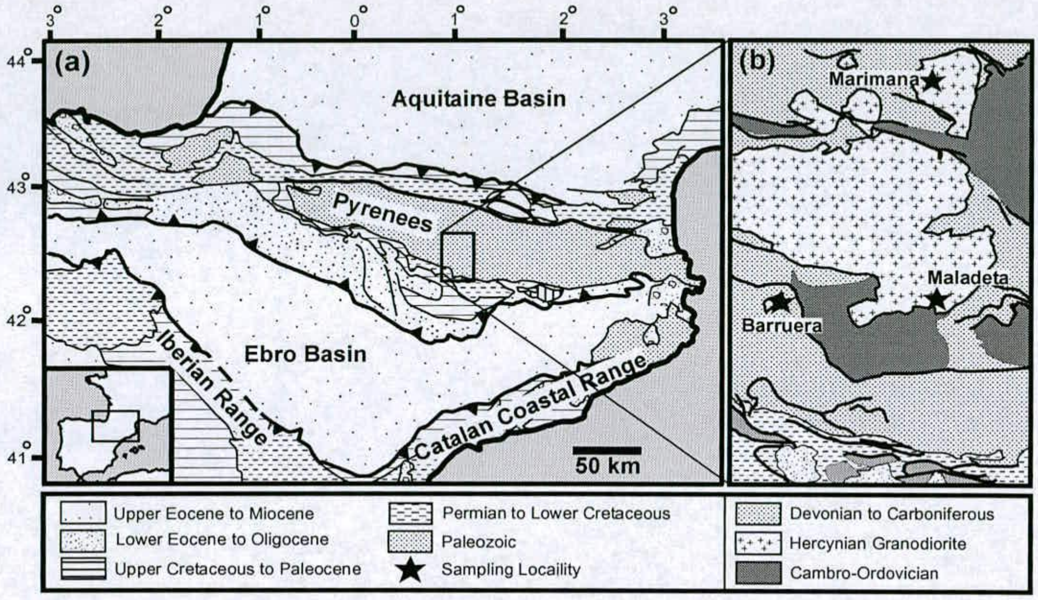

Figure 2

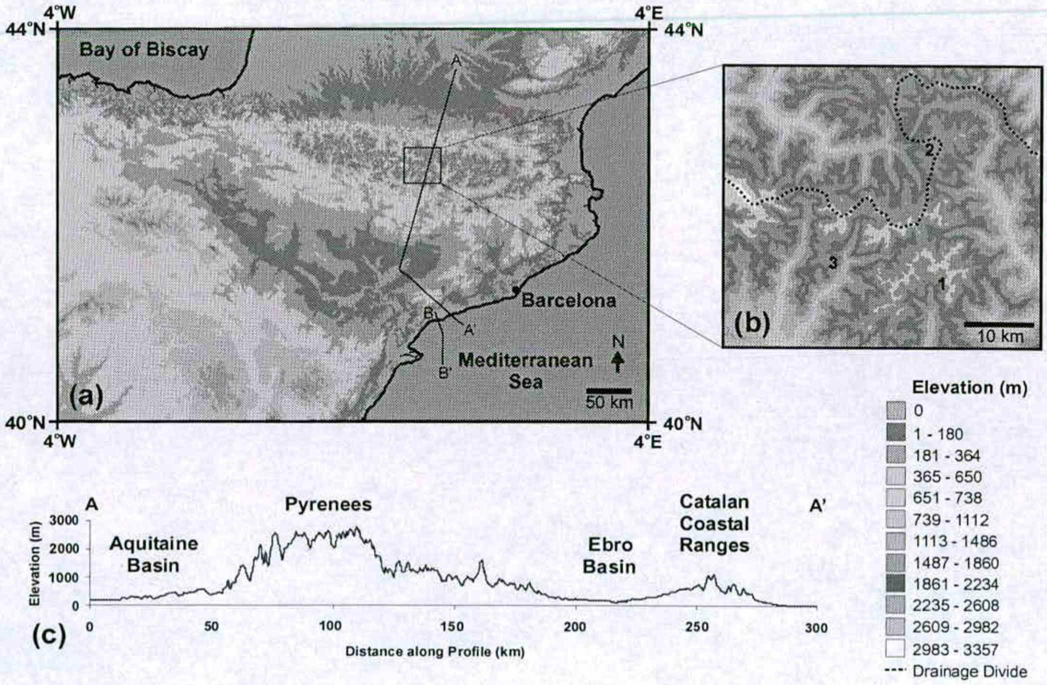

Figure 3

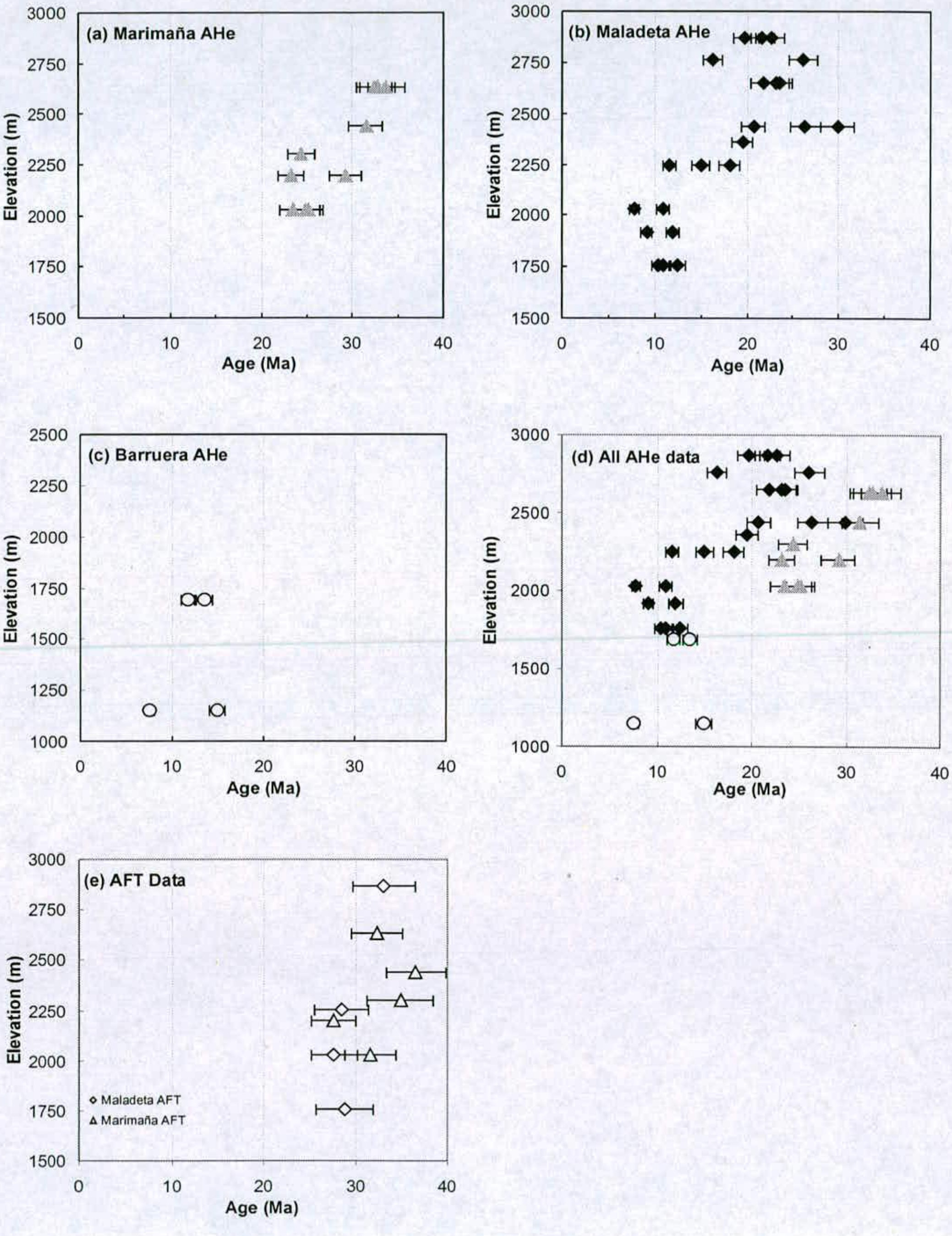
(a) Marimaña AHe
(b) Maladeta AHe
(c) Barruera AHe
(d) All AHe data
(e) AFT Data
Elevation (m)
Age (Ma)
3000
2750
2500
2250
2000
1750
1500
1250
1000
0
10
20
30
40
◇ Maladeta AFT
△ Marimaña AFT

Figure 4

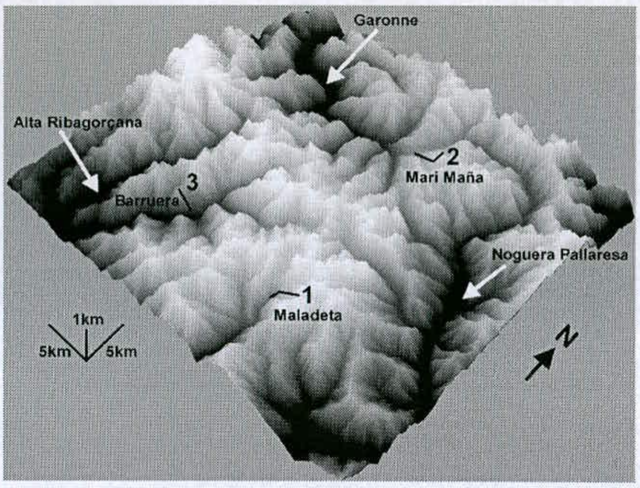

Figure 5

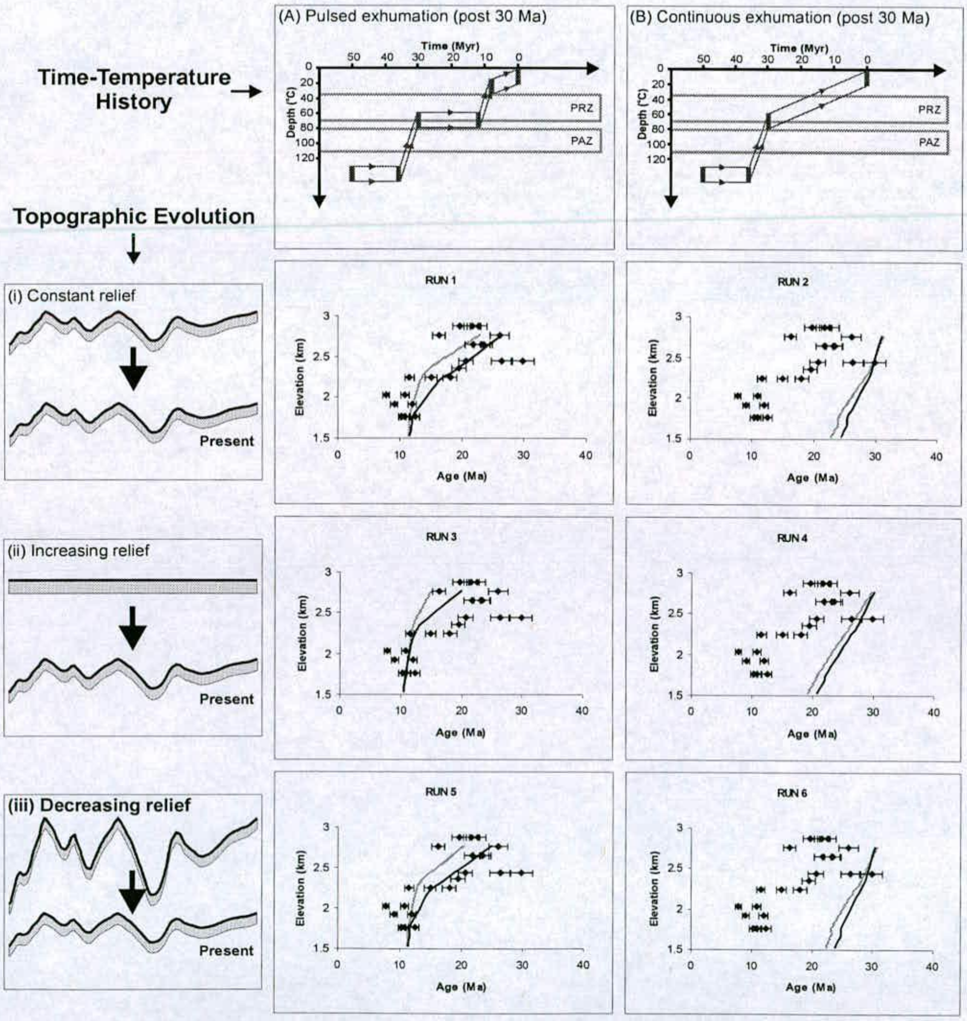

Figure 6

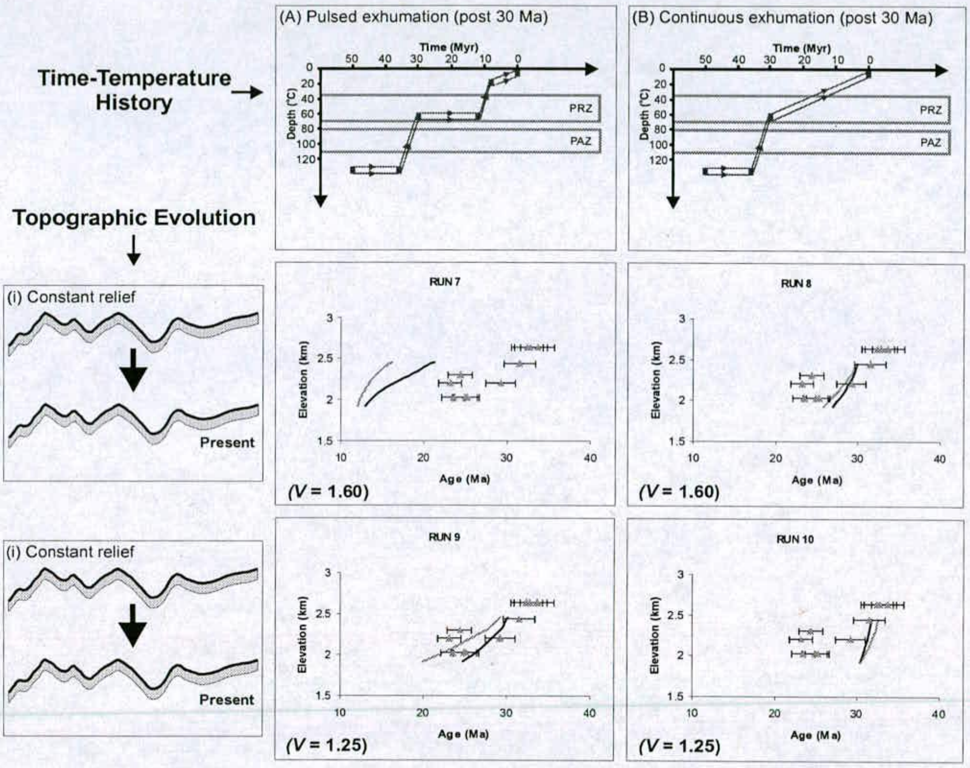

Figure 7

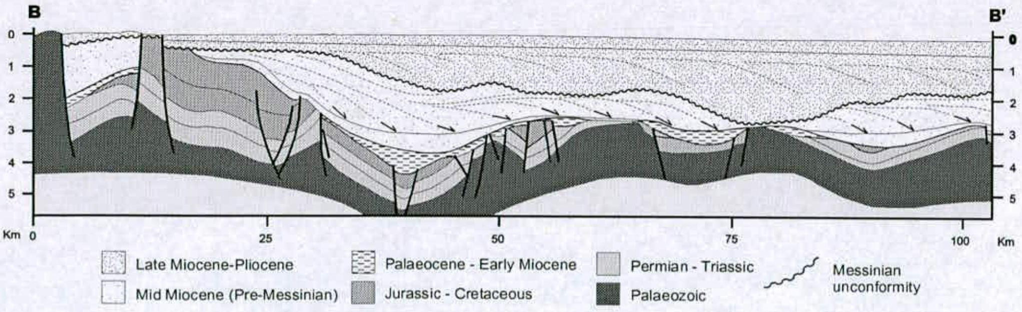

Figure 8

(a) ~20 Ma

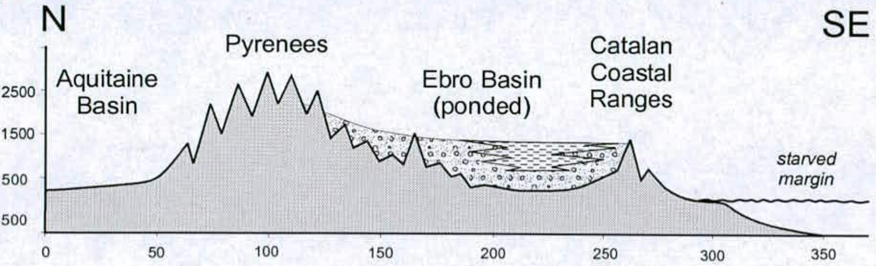

(b) post 14 Ma

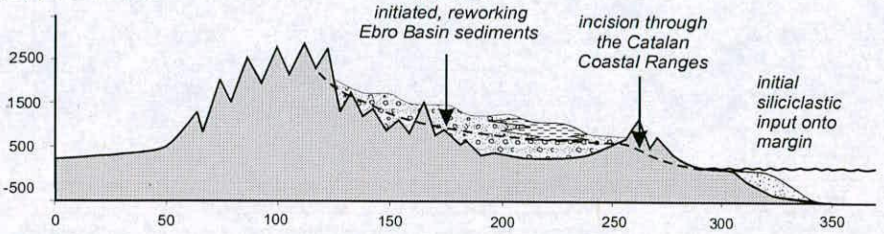

(c) ~10 Ma

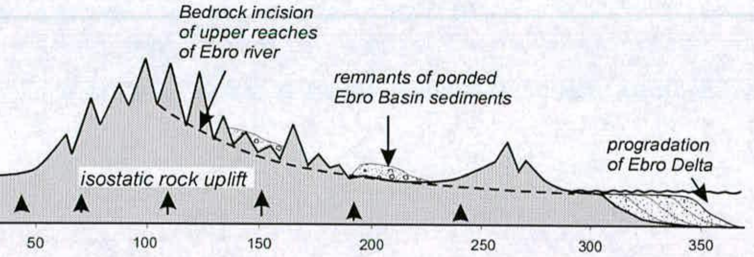

(d) Present-day